In-situ analysis of the influence of gases and ions on biological interfaces

Dissertation
for obtaining the academic degree
Doctor rerum naturalium
(Dr. rer. nat.)
from the TU Dortmund University

submitted to the Faculty of Physics by

Susanne Dogan
from Menden

Dortmund 2020

1. Supervisor and Referee: Prof. Dr. Metin Tolan

2. Referee: Prof. Dr. Matthias Schneider

Contents

Chapter 1

Introduction

Biological membranes, which consist of a lipid bilayer, form the boundary of a cell. These barriers regulate the transfer of molecules and ions between the intra- and extracellular region. While small non-polar molecules are able to penetrate lipid membranes, other substances require transport systems to pass them. In addition to the external separation by the plasma membrane, eukaryotic cells are segmented by intracellular membranes into individual organelles, such as mitochondria, chloroplasts and lysosomes. Biological membranes have functions that are essential for life. These include signal acquisition, recognition, further processing and transmission, as well as energy storage, conversion and biosynthesis. Charge and concentration gradients across the membrane drive numerous biochemical processes. These complex functions rely on an efficient and specific composition of a variety of lipids and proteins and a high mobility of these components. Ion transport or catalysis of reactions are performed by membrane proteins, whilst lipids establish the environment for the binding of substrates, reactions and diffusion of proteins and their products.

The natural environment of biomembranes is an electrolyte solution and the interaction between ions and lipids influences the properties of membranes. The polar headgroups of the lipids can directly interact with the ions in solution, which in turn can affect the electrostatic membrane potential and lipid phase transitions and modify the dynamics and fusion affinity of the membrane.

Besides the lipid bilayers that organise the cellular environment, there are also films of lipids and proteins at the alveolar epithelium which allow animal breathing. The respiratory pulmonary gas exchange takes place across a complex physical barrier. The so-called lung surfactant facilitates the gas exchange and is essential for the alveolar stability. Nowadays, the human lung is exposed to various potentially harmful molecules, such as solvents and volatile substances used in paints, varnishes, plasticisers, detergents and anaesthetic agents. On the other hand, substances such as perfluorocarbons (PFCs) have promising properties that might support injured lung surfactants. Perfluorocarbons are compounds that contain only carbon and fluorine.

In this work the structural response of biomembranes interacting with gases or vaporised compounds and ions was studied. The investigations aim on a deeper under-

standing of supporting and destructive effects of gaseous substances of different shapes and sizes on the lung surfactant with a particular focus on PFCs and of the role of ions in membrane processes.

Well-defined models of complex natural membranes are a powerful tool for the investigation of membrane-associated interfacial phenomena. In this work, lipid monolayers were applied to mimic the liquid/gas-interface of the alveoli. Solid-supported membranes produced by spin-coating were used in gaseous and aqueous environment as a model system for the lung surfactant or cellular membranes. Surface-sensitive x-ray scattering techniques, such as x-ray reflectivity (XRR) and grazing-incidence x-ray diffraction (GIXD) are well-suited techniques for the investigation of membrane-associated processes and enable to detect changes of the interfacial structure *in-situ* with subangstrom resolution. By combining the two techniques, insights into the lateral and vertical structure of lipid systems can be derived and a more comprehensive knowledge of the interfacial structure can be obtained.

The lung surfactant facilitates the expansion of the alveoli during inhalation and prevents the collapse of the alveoli during exhalation by reduction of the surface tension. Any impairment or the absence of the lung surfactant can lead to severe respiratory dysfunction with fatal consequences. There are numerous respiratory diseases in which the lung surfactant is either absent or inactivated. An unusually high surface tension of the alveolar lining fluid is related with serious and potentially lethal conditions, such as acute respiratory distress syndrome (ARDS). In the course of ARDS, protein-rich oedema fluid leaks into the alveolar air space as a consequence of the increasing permeability of the alveolar-capillary barrier and surface-active serum proteins hinder the adsorption of lung surfactant at the alveolar lining fluid interface. The neonatal respiratory distress syndrome (NRDS) is caused by the lack of surfactant of immature lungs of preterm birth babies. Both respiratory diseases, ARDS and NRDS, share similar symptoms with different underlying pathophysiological origins. A variety of lung surfactant substitutes consisting of purified and enriched lung extracts from porcine or bovine tissue have proven to be highly beneficial in the treatment of NRDS. For the clinical condition of ARDS the treatment is more difficult. The efficacy of surfactant substitutes has shown limited improvement in human clinical trials and the mortality remains high. It was recognised that the inactivation of surfactant is an essential mechanism in ARDS and that the ineffectiveness of exogenous surfactant preparations is a consequence of this inactivation. Besides the treatment via mechanical ventilation, the medical therapy options are limited. However, the oxygenation of patients leads to a series of pathophysiological mechanisms and causes ventilator-induced injuries. Different and novel approaches are thus necessary to induce the reversion of lung surfactant inactivation and to design more efficient substitute preparations that are not affected by inactivation in ARDS. A promising approach is the ventilation with aerolised and vaporised perfluorocarbons. Sustainable improvement of gas exchange and lung compliance has already been shown in ARDS animal models. Perfluorocarbons are being studied for a wide range of biomedical diagnosis and therapy applications because of their unique biophysical properties, such as low water solubility, biological and chemical inertness, high gas-dissolving capacity and low surface tensions. In addition, new alternative syn-

thetic surfactant replacement compositions are needed to minimise the risks associated with mixtures of animal origin. These have the inherent disadvantage of contamination, pathogen transmission and immunological reactions, high costs of preparation and purification as well as quality variation from batch-to-batch. It has already been shown, that perfluorocarbons have an effect on the phase behaviour of the primarily component of the lung surfactant 1,2-dipalmitoyl-*sn*-glycero-3-phosphocholine (DPPC) and lung surfactant substitutes [1–4]. An incooperation into DPPC monolayers and an inhibition of the formation of a liquid condensed phase was observed. Nevertheless, studies that investigate the structural response of monolayers to their interaction with perfluorocarbons are rare. The studied perfluorocarbons are shown in the figure 1.1. The perfluoroalkylated substances (PFAS), here perfluorooctyl bromide (F-octyl bromide), have to be distinguished from the substance class of perfluorocarbons. For simplicity it is classified here as perfluorocarbon. In this thesis, gaseous perfluorocarbons are denoted as gFCs (C_3F_8, C_4F_{10}) and the vaporised compounds as vFCs (F-decalin and F-octyl bromide).

The examination of the interaction of PFCs with phospholipids may also have implication for further biomedical applications, including those based on the injection of PFC-containing phospholipid-based microbubble agents and emulsions. These involve microbubbles for contrast-enhanced ultrasound and emulsions for intravascular oxygen delivery (artificial blood substitutes), (targeted) drug and gene delivery, use in ophthalmology, organ cell preservations, cell aggregation control, molecular imaging and diagnostics. The majority of commercially available soft-shelled microbubbles are composed of a fluorine gas core, mostly C_3F_8 and C_4F_{10}. F-octyl bromide is dispersed in water with a suitable emulsifier used for fluorine-19 magnetic resonance imaging (^{19}F-MRI). In these systems, phospholipids (DMPC and DPPC) form the shells of the bubbles and droplet walls. The effect of (gaseous) perfluorocarbons on phospholipid-based interfaces is relevant for the development of stable microbubbles and the design of perfluorocarbon-phospholipid emulsions. Studies aiming a better understanding of the interactions of non-polar, non-amphiphilic perfluorocarbons with phospholipid monolayers are very scarce and the interaction of the interfacial film composed of DPPC or other phospholipids with the gas compounds were not considered so far. The implications of the fluidising properties of PFCs on phospholipid monolayers have also been poorly considered in the context of medical microbubbles or emulsions.

The second field of research examined in this thesis is the interaction of mono- and divalent cations with zwitterionic and anionic membrane systems. Metal ions are ubiquitous entities in cell biology. Since present theories cannot explain the large number of effects involving ions, they are often referred as “ion-specific”. The Hofmeister or ion-specific effects in biological and biochemical systems are known since Hofmeister (1888) published a series of salts according to their ability to precipitate proteins from whole egg white solutions. The ions that occur most frequently in biologically relevant electrolytes are Na^+, Ca^{2+}, Mg^{2+} and Cl^-. Sodium in the form of the Na^+ cation is the most important extracellular electrolyte in terms of quantity. Among the various ions found in the cell, calcium is especially important. Calcium is necessary for a proper cell function, since it acts as a second messenger and its binding to mem-

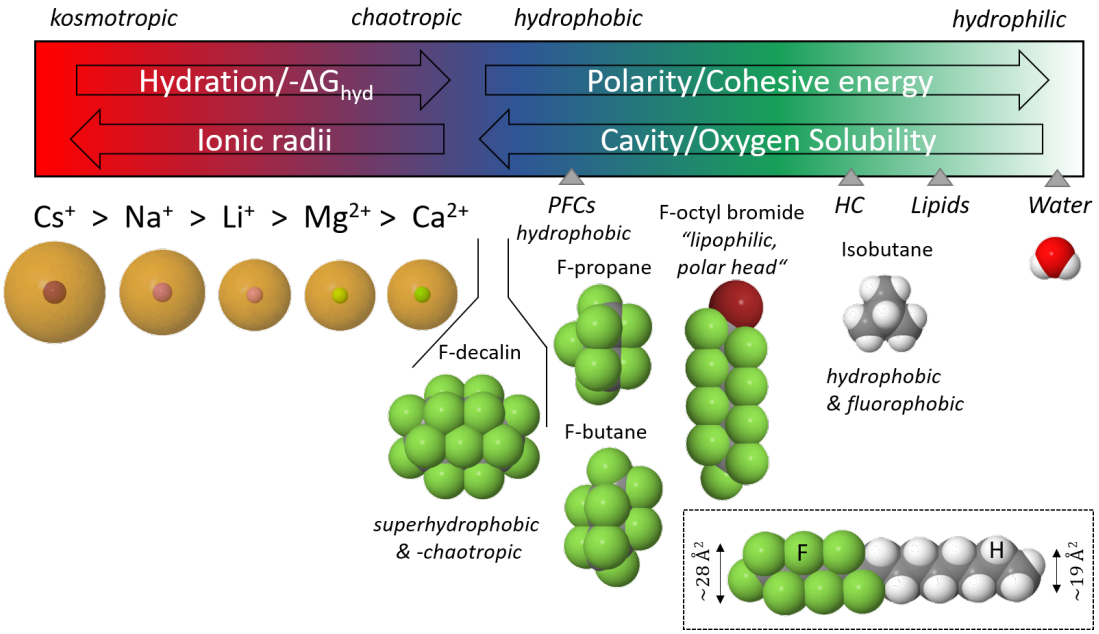

Figure 1.1: Illustration of the substances studied in interaction with lipid systems. Left: Presentation of the cations used in this thesis within the Hofmeister scale. The direction of the arrow indicates an increase. The van der Waals radii of the cations are shown. Right: Polarity scale with the relative positions of water, hydrocarbon (HC) and perfluorocarbons (PFCs). Cavity building due to less cohesive energy and resulting high oxygen solubility of PFC. Water, a high cohesive material due to the hydrogen bonds, is a poor oxygen solvent. F-octyl bromide and F-decalin are reversed on the oxygen solubility scale. The molecules are represented in the space-filling model. Inset, bottom right: Semifluorinated alkane molecule $C_6F_{13}C_8H_{17}$ to emphasise the differences between fluorocarbon and hydrocarbon chains with different cross-sectional areas. The cations and molecules were visualised using Jmol [5, 6] and ChemDraw (Chem3D).

branes regulates membrane fusion events, endozytosis and protein signalling. There is convincing evidence, that ions interact in a very specific way with membrane lipids. However, the molecular details of the binding, the adsorption sites and binding affinities, especially of sodium cations to zwitterionic phospholipid bilayer membranes, are highly under debate. Currently, there is also a lack of consistency in the literature regarding the binding stoichiometry (Ca^{2+}:lipid) and adsorption sites of the calcium binding to membranes. Despite the multitude of experimental and theoretical studies on the interaction of biological important cations with phospholipid bilayers, there is no consensus in the scientific literature. In order to shed more light on the structural influence of the binding of biological important cations to membranes, XRR measurements were conducted. Besides the physiologically important cations, lithium and caesium were studied at solid-supported DMPC bilayers. Lithium and caesium have pharmacological potential and medical significance. Lithium is strongly hydrated and exhibits a high affinity to zwitterionic membranes. It acts like a polyvalent ion. In contrast, caesium

is weakly hydrated and is known to behave as a hydrophobic ion in contact with membranes. The binding patterns of the cations are not entirely known. The physical origin for diverse effects of ions on lipid bilayers is not well understood.

This thesis is organised in the following way. The first part (**chapters 2-4**) of this work describes the biological and scientific background, the theoretical basics of the applied surface-sensitive x-ray scattering and diffraction techniques and the experimental procedures, while the second part of this thesis (**chapters 5-7**) is focused on the results and interpretation of the different studies performed in this work.

Chapter 2 provides a description of the biological background. Section 2.1 deals with the lipid classes and phase behaviour of biological and biomimetic membranes as well as the specification of the used model membrane systems, Langmuir films and solid-supported bilayers. The section 2.2 explains the lung surfactant complex and the diseases associated with its absence and inactivation. The unique properties of perfluorocarbons are also explained in this section. The chapter also contains information on the Hofmeister series and the cellular cationic environment as well as the current state of research on the cation/membrane-interaction. Finally, the chapter is closed by the brief description of protein chemistry in section 2.4, where the basics of protein structure, folding and adsorption are presented.

The description of the theoretical background of the utilised x-ray scattering methods is summarised in **chapter 3**. The experimental procedures used in this work are given in **chapter 4**. A brief explanation of the beamline end-stations as well as data treatment is given.

Chapter 5 presents the results of the surface/gas-interaction studies. The first section 5.1 discusses the liquid/gas-interfaces. Subsection 5.1.2 deals with the response of Langmuir films to elevated gas pressures and vaporised F-octyl bromide and F-decalin at varying lipid surface coverage. The influence of fluorine gas molecules and vaporised perfluorocarbons on the lateral structure of DPPA Langmuir films were examined by means of GIXD to obtain additional information on the adsorption sites and influence on the crystalline lipid film phases. The results are presented in subsection 5.1.3. Gas pressure-dependent measurements of the surface tension with different initial surface pressures of the DPPC- and DPPA-films provide further evidence of the co-surfactant ability and insertion of molecules from the gas phase into the Langmuir films. The chapter carries on with the studies of the influence of gas molecules on solid-supported lipid mono- and multilayers. The subsequent and last section 5.3 of the chapter deals with protein-containing systems at liquid/gas-interfaces. Two well-known model proteins, lysozyme and bovine serum albumin (BSA) were selected for adsorption studies. The influence of gaseous and vaporised perfluorocarbons on the protein adsorption behaviour was investigated at a DPPA-film and at the water/gas-interface.

The study of the interaction of cations within the Hofmeister series and model membranes is summarised in **chapter 6**. The first section presents the results of the influence of mono- and divalent cations, namely sodium and calcium cations, on DPPC and DPPA Langmuir films. The section is closed by the study of the BSA adsorption in dependence of the pH-value and magnesium chloride addition at DPPA-films. The electrostatic interaction strength between the surface and proteins can be enhanced or

suppressed by variation of the pH-value and the ionic strength of the solution. The results concerning the interaction between mono- and divalent cations and solid-supported DMPC bilayers are afterwards presented in section 6.2.

Chapter 7 summarises the results obtained in this thesis and gives an outlook for future studies in the considered research fields, cation/membrane-interactions and the influence of perfluorocarbon compounds on biological lipid systems.

Chapter 2

Biological and scientific background

This chapter summarises biological and scientific background information. The chapter is subdivided into four sections. At first, section 2.1 introduces biological membranes and model membranes with regard to lipid classes and the phase behaviour of lipid bilayers. A particular focus lies on Langmuir films and solid-supported bilayers. Section 2.2 provides information on the lung surfactant, perfluorocarbons and gas adsorption at interfaces. On this bases, the current state of research concerning the potential of perfluorocarbons for the treatment of lung diseases is discussed. In section 2.3 the Hofmeister series, the role of ions in the cellular environment and specific effects of cations on membranes are addressed. The last section 2.4 briefly summarises basics about design and structure of proteins. Subsequently, thermodynamic and kinetic aspects of proteins adsorption at interfaces are described. Finally, the relevance of model proteins in research is outlined and the model proteins which were applied in the framework of this thesis are introduced.

2.1 Biological and biomimetic model membranes

Lipids are the structure-making building blocks of membranes in living organisms. Lipid research has become an increasingly important field, due to the diverse biological roles that lipids play in cell biology, physiology and pathophysiology. Lipid biology, in the context of genomics and proteomics, the *lipodomics* a branch of metabolomics, deals with the comprehensive analysis of lipid molecules for the understanding of cell biology and pathology [7, 8]. Lipids exhibit a remarkable structural diversity driven by a number of different molecular transformations, such as variable chain length, different headgroups and connections between head- and tailgroups, as well as a variety of oxidative, reductive, substitutive and ring-forming biochemical transitions or modification with sugar residues [9]. The intrinsic physical phase behaviour of lipids and their interactions with membrane proteins are created through their unique composition. A higher eukaryotic cell allows the existence of more than 1000 different lipid species [10–12].

The membranes of Gram-positive and Gram-negative bacteria differ in composition and significantly in the structure from mammalian cell membranes [13, 14]. For information on Gram-positive, Gram-negative bacterial membranes and archaea membrane lipids please refer to the literature [14–19]. Further information and differences in membrane structure between animal, bacteria and yeast cells as well as lipid diversity and functions can be found in Dowhan et al. [20, 21]. This paragraph focuses on eukaryotic animal cell membranes[1].

Lipids fulfil three general functions: First, they are used as efficient energy storage and source (lipid droplets) [25] and for the membrane biogenesis. Second, they act as first and second messenger in signal transduction and signal acquisition, further processing and signal transmission [12, 26, 27]. Recent studies show a regulatory function of lipids due to their ability to modulate proteins by specific lipid/protein-interactions or via membrane-mediated interactions [28–30]. Third, the matrix of cellular membranes is formed by lipids, which consists of a hydrophilic and hydrophobic region. The tendency of hydrophobic moieties to aggregate and self-associate in an aqueous environment due to the hydrophobic effect and the tendency of hydrophilic moieties to interact with water and each other is the physical basis for spontaneous membrane formation. The amphiphathy of lipids enabled the first cells to segregate their internal constituents from the external environment. The same principle allows the cell to produce discrete organelles, such as mitochondria and nucleus (double bilayer), endoplasmic reticulum, golgi apparatus and lysosomes [12]. This compartmentalisation provides biochemical efficiency and limited dissemination of reaction products within the cell.

Typically, biological membranes are organised as bilayers that consist of two opposite leaflets of lipids orienting their hydrophobic moieties towards each other [31]. The first protein containing "semi-permeable" membrane was introduced by Danielli and Davson with data from 1935 as the *sandwich model* [32]. The bilayer structure was soon verified by electron microscopic images. The two dark lines that enclosed a cell and also cell compartments in these images led Robertson in 1958 to formulate the *unit membrane model* [33]. The famous asymmetric model of the organisation of a biological membrane was developed in 1972 by Singer and Nicholson and is called the *fluid mosaic model* [34]. The model was refined in terms of molecular composition and structural organisation [35–37]. An important step towards an improved understanding of biological membranes was the discovery of tightly packed aggregates, so-called *lipid rafts* [38–41].

These about 50 - 70 nm large microdomains exhibit an increased concentration of sphingolipids and cholesterol and are characterised by high rigidity and order [12, 44–47]. The function and exact physiological relevance of *lipid rafts* is controversially discussed in literature. It is assumed that they play a decisive role, especially in protein induced signal transduction processes, membrane transport and protein sorting [48–52]. A schematic illustration of a biomembrane, more precisely a plasma membrane, is shown in figure 2.1.

[1] One should keep in mind that due to the endosymbiotic theory [22–24], the lipids produced in mitochondia have "bacterial origin": some glycerophospholipids (PS, PE, PG) and CL. The organelle also harbours the bacterial enzyme PS-decarboxylase (half of the cellular PE is synthesised here).

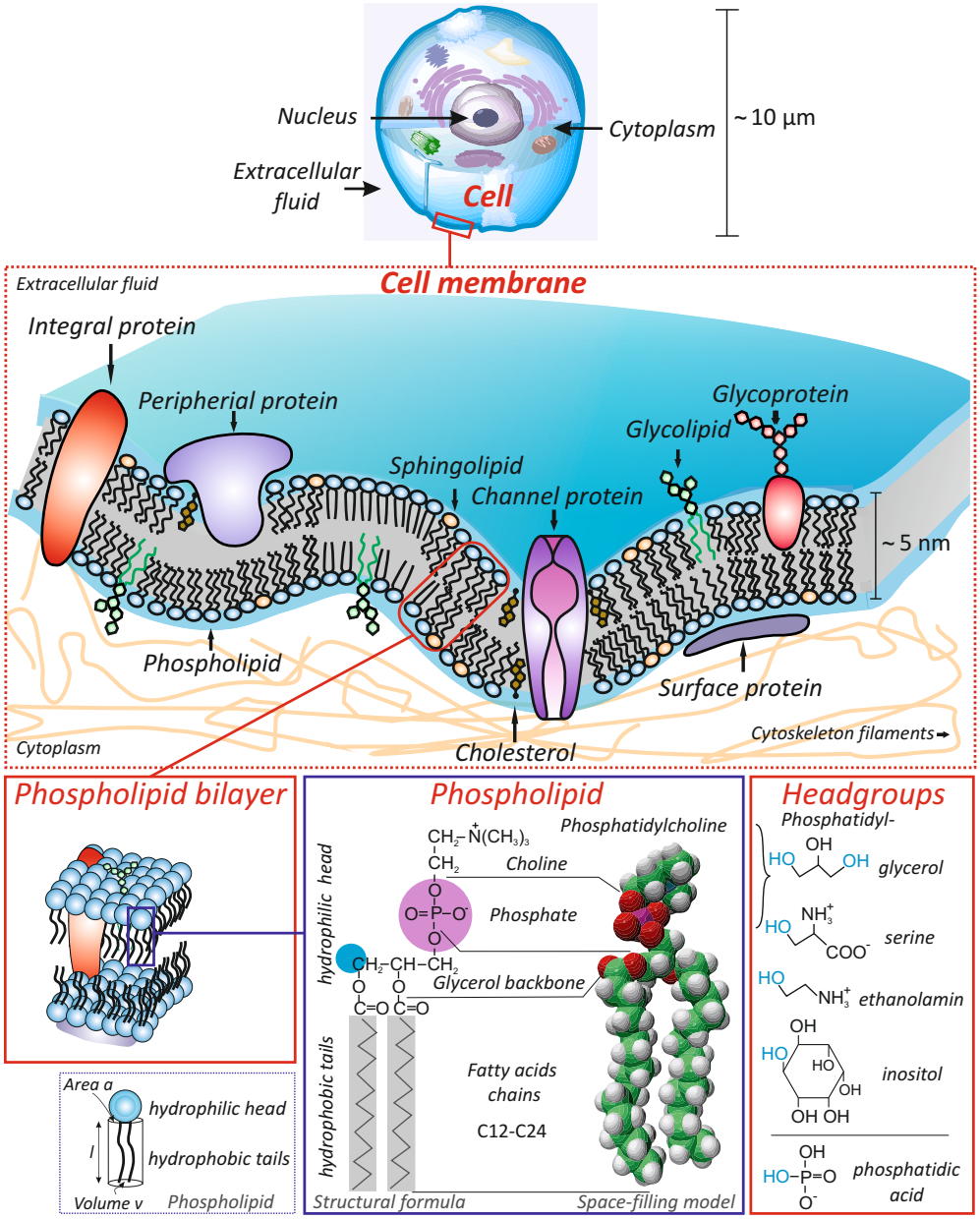

Figure 2.1: Schematic representation of a cell (top) and a cell membrane (center) illustrating the lipid asymmetry as well as microdomains. The membrane components are very dynamically and heterogeneously organised in the membrane plane. More or less ordered, sub-micrometer lipid/protein hot-spots (*lipid rafts*) coexist with fluid regions. Molecular structure and space-filling model with polar head- and hydrophobic tailgroup of the phosphatidylcholine DPPC (bottom center) with different polar headgroup alcohols (bottom right). The blue highlighted OH groups are able to bind to the phosphate moiety. The phosphoric acid binds to the *sn*-3 position of the glycerol backbone yielding a phosphatidic acid. Furthermore, the alkyl chains can vary in length, saturation and branching. Membrane lipids exhibit a cylindrical shape (bottom left) [12, 42, 43].

The plasma membrane contains transport systems to control the uptake and release of specific molecules by the cell. The transport systems are the basis of the selective permeability of the plasma membrane which is their key feature. Smaller non-polar molecules can penetrate the membrane without any further transport system. Apart from the barrier and separation function, membranes have additional biological roles that are essential for the function of a cell, e.g., signalling, transport function (budding, tubulation, fission and fusion) and biosynthesis. These properties are essential for cell division, biological reproduction and intracellular membrane trafficking. Proteins are responsible for most biological processes that takes place at or in the near of membranes and can be regulated via lipid interactions.

The membrane is an asymmetric multicomponent structure and is build up of a number of different amphiphilic molecules, proteins and carbohydrates [53]. The weight ratio of proteins and lipids varies depending on the function of the membrane and is between 1:4 and 4:1 [54, 55]. For example, in the nervous system the myelin sheath which is a multilayered membrane structure that covers axons and is necessary for optimal saltatory signal conductivity [56–58], contains 79 % lipids and 18 % proteins. The ratio can also vary within a membrane, e.g., the inner mitochondrial membrane exhibits a protein/lipid ration of 32, whereas the outer membrane of mitochondria only displays a ration of 1.1 [53, 59]. Many integral membrane proteins span the entire lipid bilayer, some are only partially inserted into the membrane via e.g. lipid anchors [60, 61]. Integral membrane proteins are involved in numerous biological processes from signalling to transport [62–65]. Peripheral membrane proteins are bound to the membrane by electrostatic interactions and hydrogen bonds, also to be seen in the schematic representation in figure 2.1.

The three main groups of lipids found in mammalian membranes are glycerophospholipids (65 mol%), shingolipids (phospho- and glycosphingolipids, ~ 10 mol%) and sterols[2] (~ 25 mol%) [34, 41, 68, 69]. Glycerophospholipids, abbreviated as phospholipids, consist of a semi-polar glycerol unit. These are esterified at the *sn*-1 and *sn*-2 position at two hydroxyl groups with fatty acid chains, resulting in a diacylglycerol. The fatty acid chains can be saturated or *cis*-unsaturated hydrocarbons of different lengths. The third carbon atom (*sn*-3) connects the polar phospholipid headgroup, which is composed of the phosphate group and an alcohol residue (see also figure 2.1). With the different headgroups, the phospholipids found in eukaryotic cells and their membranes can be divided into phosphatidylcholine (PC), phosphatidylethanolamine (PE), phosphatidylserine (PS), phosphatidylinositol (PI) and phosphatidic acid (PA) [12, 70]. Phosphatidylglycerol (PG) is highly abundant in the monolayer structure of the lung surfactant at the alveolus/air-interface [71] and in the inner leaflet of mitochondria [72]. The (semi-) hydrophobic region of the lipid molecules is the diacylglycerol. The polar headgroups can be zwitterionic or negatively charged. The phospholipids PG, PS, PI, and PA represent negatively charged lipids. PC and PE have a neutral net charge due to their zwitterionic nature. The proportion and distribution of charged lipids in both leaflets

[2]Cholesterol, the main sterol in mammalian cells, is often equimolar with phospholipids in many membranes,e.g. in erythrocytes [66, 67]. It does not form membranes by itself.

can induce a surface potential and can dramatically affect biological processes [73–77].

The cylindrical shaped phosphatidylcholines are the most abundant lipids in eukaryotic membranes with more than 50 mol% and spontanously self-organise as planar bilayers [12, 47, 68, 78]. Phosphatidyletholamines occur in concentration of 20 mol% in most membranes and is crucial for budding, fission and fusion as they induce curvature stress onto the bilayer [47, 79]. The curvature stress exerted by PEs and PAs can be modulated due to the interaction with divalent cations [12, 73].

In this thesis the prototypical PCs [12, 80] DPPC (di-palmitoyl PC, 1,2-dipalmitoyl-*sn*-glycero-3-phosphocholine) and DMPC (di-myristoyl PC, 1,2-dimyristoyl-*sn*-glycero-3-phosphocholine) are investigated.

The phospholipid DMPC is commonly used for monolayer studies, primarily because of its phase transition properties at physiologically relevant temperatures. It is further very well-suited for the use in lipid bilayer studies and preparations of stable solid-supported multilayer systems [81–84]. The di-palmitoyl phospholipid DPPC is the major lipid present in lung surfactant and is used to reconstruct the alveolus/air-interface. This is further discussed in section 2.2. Furthermore, the negatively charged lipid DPPA (1,2-dipalmitoyl-*sn*-glycero-3-phosphate) was chosen to mimic the anionic portion of the lung surfactant and study the interaction of salt solutions with anionic interfaces. Phosphatidic acid is the key intermediate in the biosynthesis of main membrane phospholipids and triglycerides [85] and occurs in eukaryotic cells in minor proportions (1 - 2 mol % [86]). However, it plays an important role in membrane dynamics, e.g. the fission and fusion [20, 87–90], and has an unique signalling function [91–93]. The signalling seems to be pH-value dependent [94, 95]. PA affects lipid-gated ion channels, for example the TREK-1 potassium channels through a putative site in the transmembrane domain [96, 97]. Furthermore, PA recruits cytosolic proteins to appropriate membranes [98]. PA can directly influence the activity of protein kinases. For example, the protein kinase C-ζ can only be activated in the absence of PA and protein kinase C-α can only be stimulated by PA in the presence of calcium [98, 99]. PA can be found in the outer leaflet of the human erythrocyte membrane [100]. Relatively new published reviews gives a comprehensive overview on the biochemical properties and functions of DPPA [20, 90, 101–107].

Since DPPA has unique biophysical properties resulting from its molecular shape and negative headgroup, it can exist in the non-bilayer and bilayer phase, depending on the microenvironment [20, 102] (pH-value and ionic strength) [89, 108]. Furthermore, by cations a phase separation [109, 110] and domain building [111–113] of DPPA/DPPC mixed and DPPA containing membranes can be induced.

In contrast to glycerophospholipids, sphingolipids constitute of a hydrophobic ceramide (Cer) backbone consisting of a sphingoid base which is linked to a fatty acid. In eukaryotes, the most frequently represented subcategory of this lipid class are sphingomyelins (SMs) and glycosphingolipids (GSLs). These contain mono-, di- or oligosaccharides as headgroup based on glucosylceramide (GlcCer) and sometimes galactosylceramide (GalCer) [12, 114]. Sphingolipids may also contain different saturated or unsaturated hydrocarbon chains [115]. The cholesterol (chol) content in cell membranes varies according to the membrane under consideration. In the plasma membrane it is

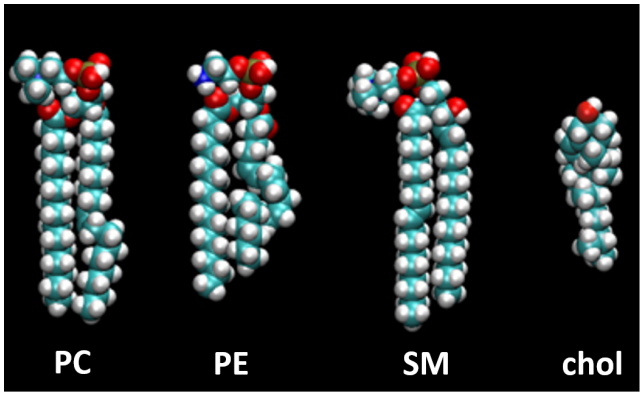

Figure 2.2: Calotte model representation of common membrane lipids of eukaryotic cells. Unsaturated phosphatidylcholine (PC) fluidises membranes, phosphatidylethanolamine (PE) creates stress in the bilayer and a negative curvature of the PE containing monolayer due to the small headgroup. Sphingomyelin (SM) leads to more ordered, rigid membrane systems, but is fluidised by cholesterol (chol), which has a high affinity for the fatty acid region of SM due to its flat structure. Modified from van Meer (2005) [47].

about 20 to 50 %, on the contrary, in the membranes of the organelles less than 10 %.

The major lipids in animal cells are shown in figure 2.2. In a review of van Meer et al. (2008) the lipid metabolism, composition and distribution of lipids in mammalian and yeast cells are given [12]. A lipid map of the mammalian cell can be found in van Meer and de Kroon (2011), describing the different lipid content of organelle membranes, lipid localisations and dynamics [68]. The lipid composition of membranes from diverse mammalian sources may vary, examples can be found in [30, 116–118]. The variation in lipid composition between different cells of one mammalian organism, as well as the organelles of the same cell, even the two leaflets of a bilayer may have a variable composition [12, 68]. This results in an asymmetrical distribution of the lipids in the membrane [119–121]. Mitochondria contain a high proportion of charged lipids, mainly cardiolipin, an organelle-specific lipid and very few sphingolipids [122], while plasma membranes are high in cholesterol and sphingolipids content. As example for the asymmetry of the leaflets, the outer leaflet (luminal side) of mammalian plasma membranes contains predominantly phosphatidylcholine and sphingomyelin as well as GSLs, whereas the aminophospholipids PS and PE are actively concentrated in the cytosolic leaflet [68, 123].

The properties of functional membranes, e.g. organisation and curvature are not encoded in the genome, they are direct consequences of the chemical structure and of the collective self-aggregation processes. Depending on their structure and microenvironment membrane lipids can arrange in various phases, such as lamellar phases, micellar aggregates and non-lamellar mesomorphic phases of different topology [124]. This is also known as *lyothrophic mesomorphism* or *lipid polymorphism* [42, 125–127]. This supramolecular phase organisation is driven by the shape of the lipids and external variables such as water content, temperature, pressure and aqueous phase compositions (pH, ionic strength). The structure is commonly predicted by the surfactant packing parameter[3] $p = v/la$ [128–131]. Here, v is the volume of a single lipid molecule, a is

[3]In model systems the parameter p works very reasonably, but should be applied with great care in

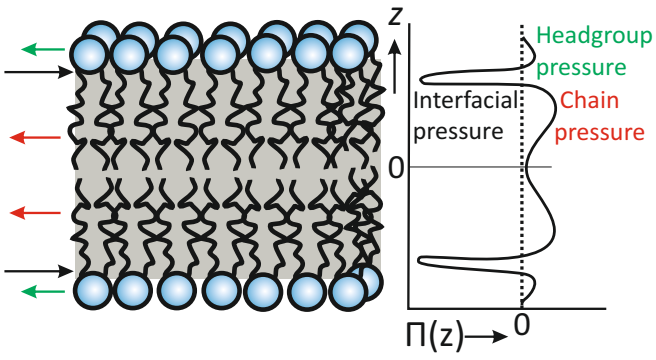

Figure 2.3: Transbilayer structure (left) and schematic illustration of the lateral pressure profile Π(z). The repulsive forces between the headgroups and between the fatty acid chains generate positive contributions to the pressure profile. These are compensated by the interfacial tension forces which act at the fluid hydrocarbon/water-interface due to the exposure of the lipid chains to water. The area below the lateral pressure profile curve becomes zero.

the cross-sectional area of the headgroup and l is the maximum (critical) length of the hydrocarbon chain, see also figure 2.1. It predicts in a simple manner the conditions for, e.g., micelles ($p \leqslant 1/3$) and planar bilayers ($p \approx 1$). A transition between the interrelated different types of aggregates and phases is possible and occurs via different types of phase transitions [132–134]. Non-bilayer lipid phases, like cubic or hexagonal phases may be related to transient biomembrane events (fussion, budding, fission) [12, 135, 136]. The forces for the self-assembly process and the organisation are weak. The organisation of the structures reflects the lipid packing at the lowest free energy needed to balance the repulsive headgroup interactions and the hydrophobic chain effects [137, 138]. The driving force is the exclusion of water molecules, the so-called "hydrophobic effect" [139–142].

Lipids with two chains and a cylindrical shape are likely to form bilayers, for example the phospholipids DPPC and DMPC. Figure 2.3 shows the transversal structure of a lipid bilayer with the so-called lateral pressure profile on the right. The shape of the lateral pressure profile is highly non-trivial. It is composed of a microscopic tension at the interface between the hydrophilic and hydrophobic region due to attractive hydrophobic forces, a positive chain pressure which arises from the entropic interchain repulsion of the fatty acid chains, and a weakly positive contribution from the hydrophilic headgroup region [79, 131, 134, 137, 142, 143]. The incorporation of proteins [79, 144] as well as their conformation [130, 143] and activity [145] can be influenced by the pressure profile, curvature and lipid composition. Furthermore, the linkage with the cytoskeleton plays an important role for the lateral pressure of biological membranes [146, 147]. As a domain-forming lipid, cholesterol also contributes significantly to membrane properties [146, 148, 149].

In its function as a separating layer between two media of different composition, especially concerning the ion concentrations, the natural membrane plays a decisive role for the electrostatic and electrodynamic processes in and around cells. In addition to mechanical properties such as lateral pressure, these functional membranes also have

in-vivo systems.

electrical properties that determine their function as a barrier between the internal and external medium. Due to the hydrophobic fatty acid region, the passage of hydrated ions requires considerable high energy. Therefore a membrane is a very good isolator and in the hydrophobic region the ion concentration is negligible [150, 151]. For smooth muscle cells, for example, Tomita (1966) determined membrane resistance densities of $10^9\,\Omega\,\mathrm{cm}^2$ [152], for model membranes, however, values up to maximal $10^4\,\Omega\,\mathrm{cm}^2$ were found [151]. As a charge-separating element especially the hydrophobic area has a capacity. Fettiplace et al. (1971) compare the specific capacity of cells with model membranes. They described values of around $1\,\mu\mathrm{F/cm}^2$ for cell membranes and only $0.5\,\mu\mathrm{F/cm}^2$ for the model membranes [153]. The inner membrane potential is explained in [154, 155]. Cevc (1999) summarised electrostatic models and the influence of the interfacial structure on the thermodynamics of charged membranes [156]. Furthermore, it provides information about ion binding effects on membranes. In section 2.3.3 the electrical double layer as atomistic model for the interaction of cations with lipid membranes will be explained in further detail.

The permeation of uncharged molecules and ions between intra- and extracellular region, which is necessary to maintain the vital cell functions, is controlled by the membrane. Even model membranes composed exclusively of lipids are permeable to a limited extent for molecules and even for ions and protons. This is called *simple diffusion*. It is attributed to transient defects that allow the molecules to enter the headgroup of lipids. From there they can diffuse through the hydrophobic region [157, 158]. Biological membranes allow different molecules to pass through by active and passive transport mechanisms facilitated by specific proteins. Passive transport mechanisms include highly specific transport mediated by carrier proteins and channel-mediated diffusion. If the transport is directed against a concentration gradient, energy in the form of adenosintriphosphat (ATP) is necessary (active transport).

Many physiological processes, such as transport and signal transduction at the membrane depend on its fluidity. The degree of fluidity of a membrane is a function of the lipid chain length and the ratio of saturation of the lipids and also the cholesterol content [55, 159]. Depending on their composition and the environmental conditions, such as temperature, pH-value, ionic strength and pressure, different lamellar phases can dominate in biomembranes. The fluid or liquid-crystalline phase has the highest lateral diffusion coefficient and associated mobility of the lipids. By increasing the concentration of *cis*-unsaturated alkyl chains or cholesterol, the biological membrane adapt to changing environmental conditions without losing its physiological functionality. The main transition temperature from the gel-to-fluid phase thus depends sensitively on the environment and the lipid composition. The most common lipid bilayer phases in the order of their occurrence upon increasing the temperature are the crystalline or subgel phase L_c, a gel phase with tilted chains $L_{\beta'}$, the ripple gel phase $P_{\beta'}$ and the liquid crystalline phase L_α, see also figure 2.4. This is the so-called *thermotrophic mesomorphism* (thermotrophic phase transitions) [160]. It should be noted that the nomenclature is not uniform in literature. Within this thesis, the nomenclature introduced by Luzzati is applied [125]. The phase transitions are first order phase transitions.

For the understanding of the interaction of different molecules with membranes on

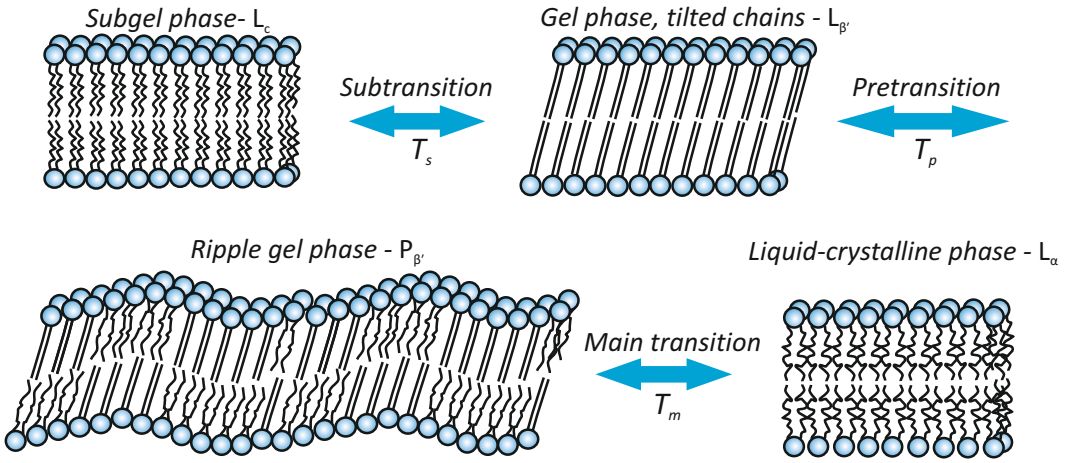

Figure 2.4: The thermotropic lamellar lipid membrane phases. Lamellar states in which the headgroups form parallel layers are indicated by L. An undulating super structure is marked with P. The phases are designated by the indices, where α describes the liquid-crystalline phase, β gel-like phases and c the solid-crystalline subgel phase. The main phase transition takes place at T_m. For some lipids there is a preliminary transition to the intermediate phase $P_{\beta'}$ at the pretransition temperature T_p. T_s is the subtransition temperature where the subgel phase transforms into gel phases.

the molecular level the state of the mimicked membrane is relevant. The crystalline L_c phase is characterised by a crystalline arrangement of the hydrocarbon chains, whereby the free rotation of the lipids is restricted. The molecules are highly ordered and tightly packed in a hexagonal lattice with a spacing of roughly 0.4 nm in all-*trans* configuration [161]. The lateral lipid diffusion is substantially reduced and the headgroups exhibit a low hydration level. Upon heating, the L_c phase transforms into a lamellar gel phase L_β or $L_{\beta'}$[4] at the subtransition temperature T_s. At high chemical heterogeneity of the fatty acid chains and low hydration, in the L_β phase the chains align perpendicular to the membrane surface without tilting [162]. The molecular area is increased but the lateral mobility of the lipids is still reduced. The hydrocarbon chains are rigid, extended, and in all-*trans* conformation and have some rotational freedom along their chain axis. The phase is organised on a two-dimensional triangular lattice. PE membranes have no chain tilt, whereas PCs exhibit tilt angles about 30° [133]. With further heating, the gel phase L_β undergoes a melting transition into the liquid-crytalline phase L_α at the main phase transition temperature. The gel to liquid-crystalline ($L_\beta \rightarrow L_\alpha$) phase transition is also referred to as (chain-)melting transition. This phase transition is the most important event in the lipid bilayers, which occurs with a large enthalpy change. It is associated with a rotameric disorder of hydrocarbon chains, increased headgroup hydration and increased intermolecular entropy [163]. The energy required to expand the hydrocarbon

[4]The nomenclature of the two forms is not uniform in the literature. The version without tilting is partly called L_β phase and the one with tilting is called $L_{\beta'}$ phase. However, it is common to subsume both under the generic term L_β, which is also done in this work.

chain region against attractive van der Waals interactions and to increase the bilayer area (increased hydrophobic exposure at the polar-apolar interface) contributes to the large transition enthalpy change [163, 164]. The rates and amplitudes of intra- and intermolecular motion are greatly increased, the phase is characterised by a high mobility of the hydrocarbon chains due to the formation of *gauche* isomers [165].

The chain melting process within a membrane is a cooperative process. The ripple gel phase $P_{\beta'}$ is a stable intermediate between the tilted gel phase $L_{\beta'}$ and the liquid-crystalline phase L_α. If this phase is omitted, the L_α phase is formed directly at T_m. The ripple phase is constituted by undulation of the $L_{\beta'}$ phase and is accompanied by a certain loss of liquid crystalline order [166]. The periodicity of the undulations is typically around 15 - 30 nm [133]. Because of the formation of rotational isomers and the resulting reduced chain length, the thickness of the lipid bilayer in the L_α phase is lower than in the gel phases and the occupied area increases [132, 167]. The bilayer thickness is a characteristic parameter which is directly accessible in x-ray reflectivity studies. The model membranes can be designed in such a way that a physiologically relevant state is represented in order to draw conclusions about possible *in-vivo* processes. The phases and phase transitions for lipid monolayers are described in the next subsection 2.1.1.

Through the development of surface-sensitive x-ray scattering techniques, such as x-ray reflectivity and grazing-incidence x-ray diffraction, studies at various (solid/liquid-, liquid/liquid- and liquid/gas-) interfaces are possible in order to investigate membranes in their fluid phase in or on the surface of liquid media. The phase diagram of several lipids have already been published [133, 168–173]. An extensive review of structural parameter data of fully hydrated bilayers is given by Nagle (2000, 2001) [167, 174] and Tristram Nagle (2004) [175]. Information covering all aspects of the physical properties of lipid bilayers can be found in Phospholipid bilayers by Cevc and Marsh (1987) [176] and in the CRC Handbook of Lipid Bilayers (Marsh, 1990) [177].

Diffusion coefficients are used to characterise the dynamics within a lipid layer. The lateral diffusion coefficient D_L of a lipid molecule can range from 10^{-7} to $10^{-8}\,\mathrm{cm^2\,s^{-1}}$ in a fluid membrane phase and from 10^{-8} to $10^{-9}\,\mathrm{cm^2\,s^{-1}}$ in more ordered membrane structures [178–181]. Concerning rotational movements, two forms are distinguished: axial rotation around tilted lipid axis and the fluctuating rotation perpendicular to the membrane axis (*wobble rotation*). Values of $10^7\,\mathrm{s^{-1}}$ for the axial rotation frequency of membrane lipids and $10^8\,\mathrm{s^{-1}}$ for the *wobble rotation* are assumed [182, 183]. The transversal diffusion, i.e. the spontaneous flipping of a lipid molecule from one side of the membrane to the other, the so-called *flip-flop* mechanism, is very slow with time constants of several minutes or even days ($10^{-15}\,\mathrm{s^{-1}}$) [142, 184–186]. Nevertheless, some membrane components, like ceramide, diacylglycerol and cholesterol can flip-flop very fast since their effective polar headgroup area is very small. For instance cholesterol is only limited by one hydroxyl group [187–191]. In addition to the spontaneous flip-flop process, there are translocation enzymes that can move phospholipids actively through the membrane and thus maintain the asymmetry of the membrane [184, 192–195].

Even if only the lipid species of the cell membrane and its organelles are considered, the diversity and heterogeneity is very high and it will not be possible or very compli-

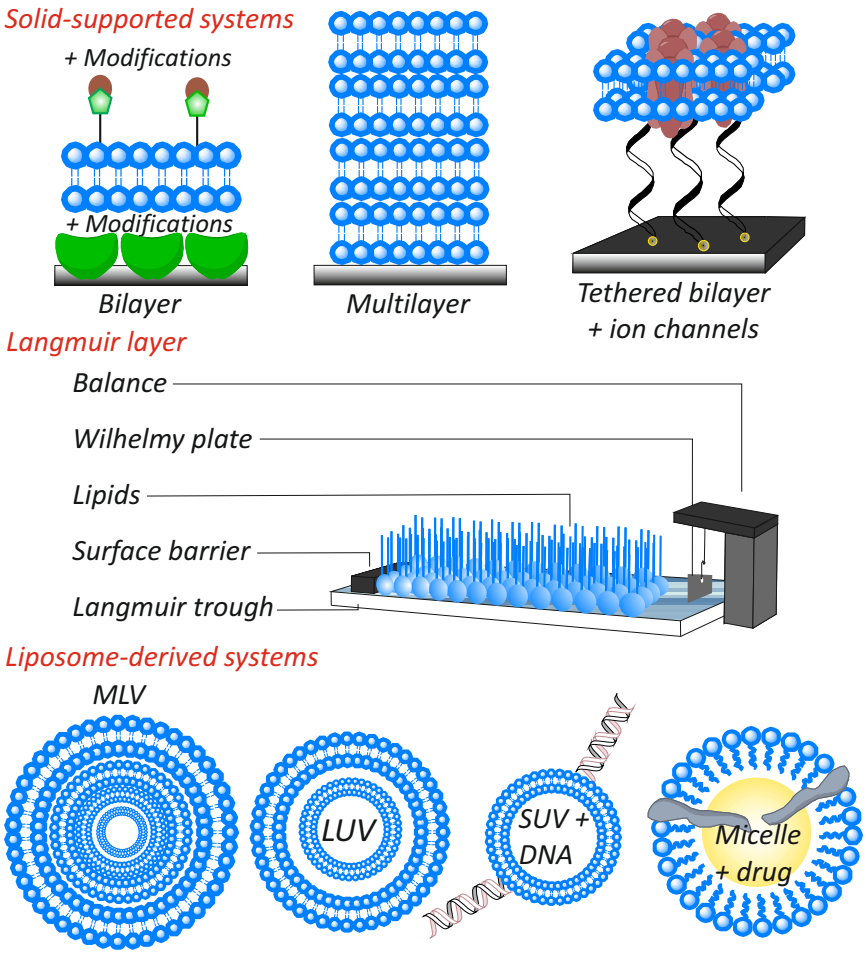

Figure 2.5: Schematic illustration of different model membranes. Top: Solid-supported lipid layer systems. Center: Langmuir trough with a Langmuir film, Wilhelmy balance and plate for measuring the surface pressure and surface barrier for compressing the lipid film. Bottom: Different liposome-derived systems, MLV: multilamellar, LUV: large unilamellar and SUV: small unilamellar vesicles and micelles can be filled or modified. These structures can be used for immobilization as well as for the investigation of surface recognition reactions and deposition on a substrate to create supported lipid layers or for the study in solution.

cated to generate meaningful results with experimental methods that can be interpreted. Even for single lipid model systems with a defined composition it can be difficult to understand the interaction of all factors leading to structural changes. Therefore, it is necessary to reduce and simplify the diversity of natural occurring biological systems to simple lipid model systems and extend the experiments in the further steps.

Figure 2.5 shows various schematic representations of the frequently used model systems. References [180, 196–201] review some commonly used systems. In this thesis substrate-bound lipid membranes on silicon substrates as well as the well-known Langmuir films were used as biomimicking model membranes for the investigation of

interactions with different cations and gases and in the interplay with proteins at the molecular level.

The coupling of lipid membranes to a surface offers a number of advantages. These include a high stability, the possibility to study membrane topology and also lateral properties when the mobility of individual lipids can be preserved [202] and the applicability of surface-sensitive techniques [196, 203]. In most cases the membrane is only accessible from one side and fluidity and phase behaviour are altered by interactions with the substrate compared to the natural situation [204–206]. Fluidity and phase behaviour are also significantly regulated by the coupling to the cytoskeleton, which none of these model systems can reproduce adequately [207]. However, the directly coupled or so-called integrated [199] solid-supported bilayer systems were chosen because they offer high mechanical stability and can be reliably reproduced with a sufficient homogeneous morphology.

2.1.1 Langmuir films

In order to investigate adsorption processes at membranes *in-vitro* with surface-sensitive methods, reproducible and representative membrane models should be applied. A technique more than 100 years old for the generation and analysis of molecular lipid monolayers is the use of Langmuir films [208–211]. This subsection first introduces the mechanisms that lead to the formation of Langmuir films. A brief explanation of the structural phase transitions with regard to the surface pressure-area isotherm of Langmuir films closes the subsection.

Liquid/gas-interfaces play an important role for the human organism, such as the alveolus/gas-interface, where the gas exchange takes place, or the tear film on the eye for maintaining a healthy ocular surface. To fulfil their function, these interfaces are covered with so-called "surfactant" (**surf**ace-**act**ive **a**ge**nt**). Langmuir films are particularly suitable for studying the processes at the alveolar tissue/- or eye fluid/air-interface because they perfectly simulate the structure and conditions of these systems.

By definition, a Langmuir film is a monomolecular layer of amphiphilic molecules which are oriented at a hydrophobic interface, e.g. the water/air-interface. Basic requirement is that the film-forming component is poorly soluble in the subphase. The hydrophobic effect essentially determines the formed structures of the amphiphilic molecules in bulk water. At sufficiently low concentrations of amphiphilic molecules, however, the formation of a monolayer is preferred at the water/air-interface. Especially phospholipids do not form micelles due to their two bulky fatty acid chains. The hydrophobicity and thus the chain length of the tailgroup plays a decisive role. Fatty acid chain lengths shorter than 12 carbon atoms are more likely to lead to the formation of spherical micelles. If the chains are too long, no monolayer can be formed because of the crystallisation of the lipids at the water surface. Geometric factors of the headgroups also influence the structure [212], these are not further discussed. If lipids are dissolved in non-polar volatile solvents such as isopropanol or chloroform and are brought to a water surface, the solvent evaporates and the amphiphilic molecules arrange on the surface as a monomolecular film. This process is called spreading. The

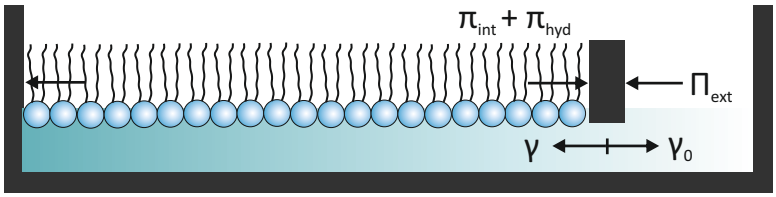

Figure 2.6: Langmuir trough with a compressed Langmuir film at a balance experiment. The surface pressure results from the difference between the surface tension of the pure water phase γ_0 and the surface tension γ with spread lipids. The external pressure Π_{ext} is generated by the barriers and is counteracted by an internal pressure composed of $\pi_{\text{hyd}} + \pi_{\text{int}}$. Redrawn from Marsh (1996) [215].

solvent acts as a spreading agent and should evaporate leaving no solvent residues that influence the final monolayer [213, 214].

Due to its high cohesive forces, water has a high surface tension γ_{water} of about $72\,\text{N}\,\text{m}^{-1}$. The surface tension can be understood as the energy required to increase the surface area and thus can be given in energy per unit area, $[\gamma] = 1\,\text{J}\,\text{m}^{-2} = 1\,\text{N}\,\text{m}^{-1}$. The interfacial tension can thus be reduced by surface-active molecules (surfactants) like phospholipids. At a water/air-interface, the hydrophilic headgroup remains in the water phase due to the strong interaction with the water molecules. The water molecules form an ordered hydrate structure around the polar headgroup and thus produce an energy gain. The energetically unfavourable contact between the hydrophobic region and the water is avoided by orienting the hydrophobic tailgroups into the less polar air phase. Thus, the formation of a monolayer results from the amphiphilic nature of these molecules.

Figure 2.6 schematically shows a Langmuir film at the water/air-interface. With one or two Teflon barriers the pressure Π_{ext} is generated by an externally applied force, which acts on the film. In this way, the area available to the monolayer can be reduced. This increases the surface density of the surfactant molecules and, therefore, the surface tension decreases depending on the intermolecular distances. An internal pressure created by the internal interaction between the lipids π_{int} and the hydration of the headgroups π_{hyd} counteracts the externally applied pressure. This internal counterpressure causes a reduction of the surface tension γ compared to the pure water surface γ_0 [176, 215]. The surface tension is then given as the difference between the surface tension of pure water γ_0 and the surface tension with lipid γ by

$$\Pi = \gamma_0 - \gamma. \tag{2.1}$$

The free energy, F_{m}, of a monolayer at the water/air-interface can be expressed in a form equivalent to that of a bilayer [215]

$$F_{\text{m}} = n_{\text{m}}\Phi_{\text{m}}(A_{\text{m}}) = n_{\text{m}}\left[\Phi_{\text{hyd}}(A_{\text{m}}) + \Phi_{\text{int}}(A_{\text{m}}) + \Phi_{\text{m-u}}(A_{\text{m}})\right]. \tag{2.2}$$

Here, A_{m} is the occupied area per lipid molecule and n_{m} is the number of lipid molecules in the monolayer. The contributions of hydration of the headgroups, the interaction

between the lipids, the degree of interaction between the fatty acid chains of the lipids and the upper phase are denoted by $\Phi_{\mathrm{hyd}}(A_{\mathrm{m}})$, $\Phi_{\mathrm{int}}(A_{\mathrm{m}})$ and $\Phi_{\mathrm{m\text{-}u}}(A_{\mathrm{m}})$. In contrast to a bilayer, the monolayer is only in equilibrium under the influence of an externally applied surface pressure Π_{ext}, otherwise it can expand indefinitely, see also figure 2.6. The surface pressure of a monolayer is given by the first derivative of the free energy F_{m} with respect to the molecular area A_{m} as

$$\begin{aligned}\Pi_{\mathrm{m}}(A_{\mathrm{m}}) = -\left(\frac{\partial F_{\mathrm{m}}(A_{\mathrm{m}})}{\partial A_{\mathrm{m}}}\right)_{n_{\mathrm{m}}} &= \pi_{\mathrm{int}}(A_{\mathrm{m}}) + \pi_{\mathrm{hyd}}(A_{\mathrm{m}}) - \phi'_{\mathrm{m\text{-}u}}(A_{\mathrm{m}}) \\ &\approx \pi_{\mathrm{int}}(A_{\mathrm{m}}) + \pi_{\mathrm{hyd}}(A_{\mathrm{m}}).\end{aligned} \tag{2.3}$$

The equation represents the equilibrium condition for the monolayer. Since the van der Waals interaction between the hydrophobic lipid tails and the air is very low, the term $\phi'_{\mathrm{m\text{-}u}}(A_{\mathrm{m}})$ can be neglected for the water/air-interface. A comparison of the derivation of free energy from lipid monolayers with lipid bilayers reveals the conditions that cause a monolayer to be in the same state as lipid bilayers. An analysis shows that corresponding states are archived when the surface pressure of the monolayer is numerically equal to the density of the hydrophobic free energy of a lipid bilayer [215]. In the range of 20 - 40 mN/m the properties of a condensed lipid monolayer are in equivalence to the lipid packing density of bilayers or cell membranes [79, 176, 215–218]. It should also be noted that monolayers often exhibit phase transformations similar to those observed in bulk systems [212, 215, 219, 220]. A film balance is typically used for the continuous measurement of the surface pressure Π of a Langmuir layer. As shown in figure 2.7 it consists of a microbalance as force sensor and a sample plate, the so-called Wilhelmy plate. The determination of the surface tension with the Wilhelmy plate method is based on the measurement of the force acting on a plate which is brought into contact with the surface of the liquid. This force is proportional to the surface tension. The plate can consist of a piece of filter paper and hangs freely movable at the end of the balance arm of the force sensor. The force F_{w} measured by the force sensor can be calculated as [221]

$$\begin{aligned}F_{\mathrm{w}} &= F_{\mathrm{g}} + F_{\mathrm{b}} + F_{\gamma} \\ &= g(\rho_{\mathrm{p}} l_{\mathrm{p}} W_{\mathrm{p}} t_{\mathrm{p}} - \rho_{\mathrm{s}} h_{\mathrm{p}} W_{\mathrm{p}} t_{\mathrm{p}}) + 2\gamma t_{\mathrm{p}} W_{\mathrm{p}} \cos(\theta_{\mathrm{B}}).\end{aligned} \tag{2.4}$$

The gravitational force F_{g} can be determined from the mass of the plate which is given as the product of its density ρ_{p} and its volume $W_{\mathrm{p}} \cdot l_{\mathrm{p}} \cdot t_{\mathrm{p}}$. F_{g} is counteracted by the buoyancy force F_{b} which depends on the mass of the displaced subphase which is obtained as product of the subphase density ρ_{s} and the displaced volume $W_{\mathrm{p}} \cdot t_{\mathrm{p}} \cdot h_{\mathrm{p}}$. The last is F_{γ}, which describes the force due to the interfacial tension and wetting of the plate. It is a function of the surface tension γ of the subphase and the contact angle $\cos(\theta_{\mathrm{B}})$. For Wilhelmy plates of platinum or iridium with high surface energies and paper plates that soak up the subphase one can assume a complete wetting which results in contact angles of $0°$ ($\cos(\theta = 0) = 1$) and the F_{γ} is a linear function of the surface tension [222]. The force difference between the force exerted by a subphase in absence and presence of a Langmuir film provides the surface pressure. After calibrating

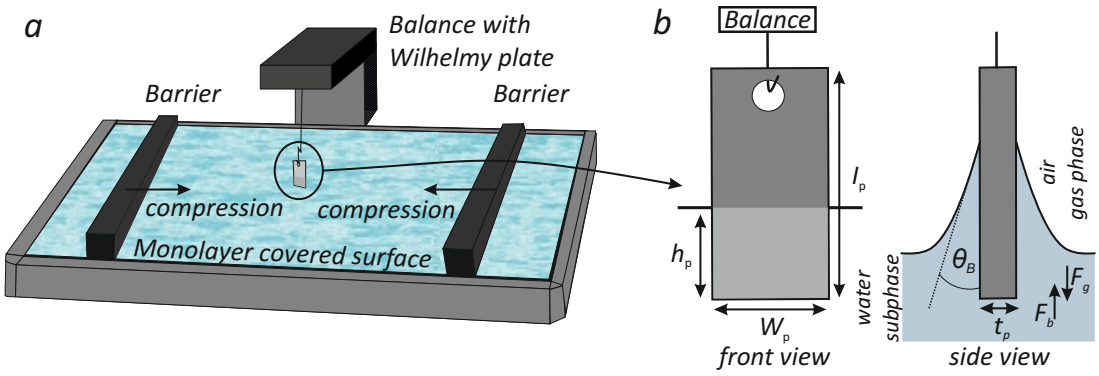

Figure 2.7: (a) Schematic representation of a Langmuir trough with two adjustable barriers for compression and a balance with a Wilhelmy plate for surface pressure measurements of the Langmuir layer. (b) Wilhelmy plate. The platelet dimensions are marked as t_p, W_p and l_p and reflect the thickness, width and length of the platelet. The rise height of the water lamella is designated as h_p. The contact or wetting angle is given by θ_B.

the film balance on the empty surface, the surface pressure of a Langmuir film can be measured. According to Gaines (1966) [223, 224] it is given as

$$\Pi = \gamma_0 - \gamma = \frac{\Delta F_\mathrm{w}}{2(t_\mathrm{p} + W_\mathrm{p})}, \tag{2.5}$$

where ΔF_w is the difference between the occurring surface forces with and without a Langmuir film on a water subphase.

With successive compression of a Langmuir layer the surface pressure increases. The compression behaviour of a Langmuir film at constant subphase temperature is described by the surface pressure-area (Π-A) isotherm, where A is the mean area per molecule. The Langmuir films exhibit different phases depending on the surface pressure, as shown schematically in figure 2.8. The shape of a Π-A isotherm is influenced by various parameters, such as the composition and physicochemical properties of the lipids and the temperature of the subphase. Before compression, a lipid molecule has an available area of several hundred square angstroms, in this so-called gaseous phase there are no interactions between the lipids. Thus, the law for ideal two-dimensional gases, from the Gibbs adsorption equation, can be assumed for ideal surface film systems and the surface pressure can be approximated by [213, 226]

$$\Pi A_\mathrm{m} = k_\mathrm{B} T. \tag{2.6}$$

With decreasing area per molecule, the monolayer changes to what is traditionally referred to as the liquid-expanded phase (LE) and can be described by the van der Waals equation for a non-ideal gas [215, 227]

$$\left(\Pi + \frac{a_\mathrm{int}}{A_\mathrm{m}^2}\right)(A_\mathrm{m} - A_\mathrm{e}) = \Pi_\mathrm{eff} A_\mathrm{eff} = k_\mathrm{B} T. \tag{2.7}$$

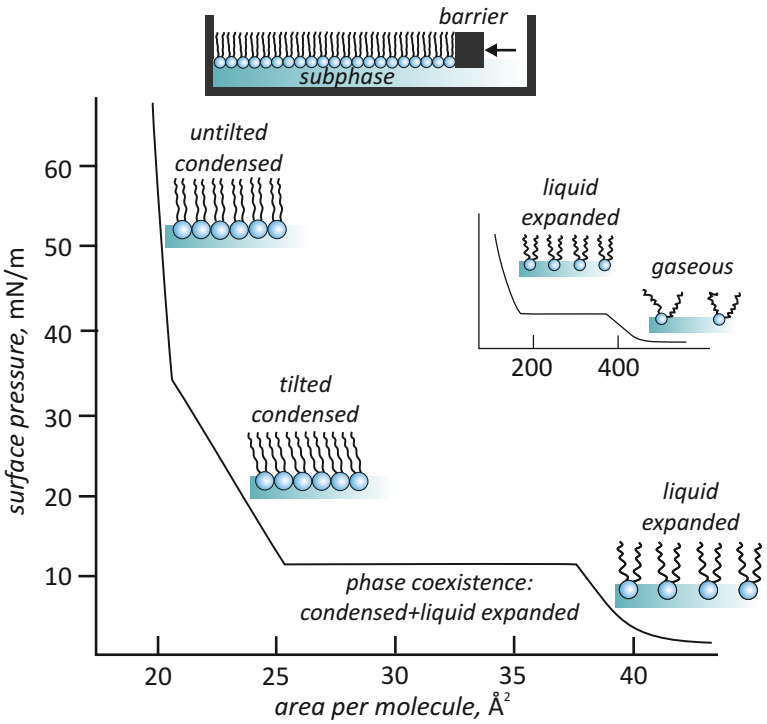

Figure 2.8: Top: Sketch of a Langmuir trough with a compressed Langmuir layer. Bottom: Schematic Π-A isotherm of a Langmuir film with schemes showing the structure of the corresponding phases. Adapted from Kaganer et al. (1999) [225].

By introducing an effective surface pressure Π_{eff} and en effective area per molecule A_{eff}, this expression is equivalent to equation (2.6). The correction term for the surface pressure increases upon compression with A_{m}^{-2} and is due to a weak repulsive interaction between the lipids. The parameter a_{int} describes the strength of the interaction. The area per molecule is reduced by the excluded area per lipid A_{e} [176, 215]. In this state no long range ordering occurs. The heads of the molecules are translatorically disordered and the chains are conformationally disordered [225]. A further compression leads to a coexistence phase of the liquid-condensed and liquid-expanded phase (LC+LE). In this regime, the isotherm is characterised by a first-order phase transition and has a horizontal course. According to the Gibb's phase rule, a coexistence of liquid-condensed and liquid-expanded phase over a wide range of the surface pressure is allowed and was experimentally confirmed [228, 229]. This course is not observed in reality, most systems show a minor positive slope, due to contamination or impurities and the formation of small micelles and aggregates on the surface [230, 231]. With further reduction of the film area, the coexistence phase is followed by a tilted condensed phase (TC), which has a compact arrangement of lipids. The hydrocarbon chains of the lipids exhibit a tilt angle with respect to the surface plane. The system reacts to the increasing repulsive intermolecular interactions by a reorientation of the hydrocarbon chains. Different conformations of the tailgroups can be observed. With further compression, the

hydrocarbon chains straighten up and the tilt angle reduces. A new phase transition into an untilted condensed phase (UC) occurs, where the molecules are densely packed and the surface pressure rises enormously at a low compressibility. This arrangement is the closest possible packing for aliphatic saturated hydrocarbons. X-ray diffraction experiments have shown that the tilted and untilted condensed phase can be treated as two-dimensional crystals [225]. A further surface reduction leads to film collapse.

2.1.2 Spin-coated lipid films on solid substrates

Solid-supported lipid bilayers are popular and commonly used model systems for cell membranes [206, 232]. A wide range of conceptually different solid-supported systems has been described and developed (see also figure 2.5) [199, 206, 233]. There is a multitude of experimental methods for the preparation of lipid layers on a solid substrate: vesicle fusion [232, 234–238], Langmuir-Blodgett [213, 239, 240], Langmuir-Schäffer [241], drop casting (solvent thinning) [242, 243] and spin-coating [82, 244–246].

For the preparation of bilayers the Langmuir-Schäffer technique or the vesicle spreading method are suitable, whereas for the preparation of multilayers spin-coating can be used. Monocrystalline silicon wafers are particularly suitable as spin-coating substrates for x-ray reflectivity studies. To produce a high quality membrane with high homogeneity and high lipid mobility, the substrates should be hydrophilic, smooth and clean.

Forces in a multilayer stack can be described at least with two different fundamental forces, according to the DLVO theory [247, 248]: attractive short-ranged van der Waals [249] and repulsive electrostatic double layer forces. Also short-ranged hydration forces [249, 250] as well as thermodynamic fluctuations (Helfrich undulation forces) [251–254] contribute to the interaction within the bilayers in a multilayer stack. The force contributions were experimentally confirmed in x-ray diffraction experiments with DPPC [250, 255] and force measurements [256] on PE and PC membranes. An adsorption of ions to a net neutrally charged membrane leads to an additional repulsive contribution between individual lipid membranes [250, 255].

The multilayer structure is highly stable at air. Solid-supported multilayer tend to detach upon hydration and heating [81, 257, 258]. However, the remaining bilayer in direct contact to the substrate is highly stable and provides a high homogeneity [82, 246, 257, 259]. Therefore, the spin-coating technique with low concentrations of the lipid solution follow by hydration and tempering of the sample is feasible for the production of a single bilayer attached to a solid substrate.

An important factor is the influence of the solid support on membrane properties [257, 260], such as the thermotropic phase behaviour [261, 262], the lateral lipid mobility, the structural coupling of the interleaflet interaction [263] and the lipid distribution [264]. So far not all aspects of this interaction are known and understood in detail since the parameter space of the involved forces is large and effects are difficult to separate [260, 265].

In this work fully-hydrated DMPC bilayers on silicon substrates were used. Therefore, a brief introduction to the bilayer/substrate-interaction potential is given. As it will be demonstrated later, the influence of the substrate could affect the specific ion

binding characteristics. In the simplified case, the interaction of DMPC and the chemically homogeneous substrate is non-specific. Similar to the forces within a multilayer stack, the van der Waals force, the electric double layer force and entropic forces act [249]. A further contribution is the solvation or hydration force that causes a repulsion between the lipids and substrate. It can be understood as the fore required to displace water molecules from the space between bilayer and substrate [256, 266, 267]. The Helfrich undulation force in comparison to the bilayer/bilayer-interaction potential is often neglected since solid supports usually suppress undulation fluctuations [268].

The interaction can be simplified to the DLVO theory, as it explains the interaction of two charged or uncharged surfaces in electrolyte solutions and gives a rough estimate. Permanent, instantaneous or induced dipoles can correlate and generate attractive forces between molecules. The attractive van der Waals potential for two planar surfaces is given as

$$w_{\mathrm{vdW}}(d) = -\frac{H_{\mathrm{eff}}}{12\pi d^2}, \tag{2.8}$$

with the spacing d and the system specific Hamaker constant H_{eff}, which has a value around $10^{-20}\,\mathrm{J}$ for hydrocarbon material in water [134, 257, 269]. The inner leaflet of the first lipid bilayer is directly attached to the substrate and acting van der Waals forces can be varied by using solids of different Hamaker constants [199]. As will be seen later, the van der Waals interaction can lead to a vertical asymmetry in the lipid density of the leaflets near the main phase transition temperature [268, 270].

The repulsive electric double layer potential is caused by the counterions and a diffuse layer outside the surface (double layer). When two similar charged surfaces approach each other, the ions outside the surfaces are confined to a shrinking space, thus reducing the entropy of the double layers at the overlap of the electrical double layer potentials. This yields in a repulsive force. The double layer repulsion for two charged planar surfaces is

$$w_{\mathrm{EDL}}(d) = \frac{z_{\mathrm{m}} z_{\mathrm{s}}}{\epsilon\epsilon_{\mathrm{o}}\kappa}\exp(-d\kappa), \tag{2.9}$$

with the charge per unit area of the membrane z_{m} and the surface z_{s} in $\mathrm{C/m^2}$. The surface charge density of a planar silica surface at a pH-value of 7 is around $-0.038\,\mathrm{C/m^2}$ [271, 272]. The surface charge of the membrane depends on it's composition and can be influenced by adsorption of salt ions from the surrounding solution. The Debye length $1/\varkappa$ is defined by the electrolyte concentration and the ion valency. For sodium chloride, it is given as $1/\varkappa = 0.304/\sqrt{\mathrm{c_{NaCl}}}\,\mathrm{nm}$, the concentration [c] is expressed in M [142].

The first atomistic simulation of a solid-supported bilayer studying the substrate (hydroxylated silicon)/bilayer-interaction revealed distances of around 3.5 nm and adhesion energies of $30\,\mathrm{mJ/m^2}$ [273–277]. Equilibrium distances of 0.5 - 2 nm were measured experimentally between membranes supported on colloidal glass beads and membranes on glass [278–280]. Membranes produced with the spin-coating process often exhibit no (detectable) water layer between the substrate and the bilayer in the hydrated state when tested by x-ray reflectivity experiments [81, 84, 246, 258, 259, 281, 282]. The adhesion energy for a DPPC-substrate system were reported to be $0.5\,\mathrm{mJ/m^2}$ [256].

2.2 Lung surfactant and diseases

The gas exchange in the lungs takes place as simple diffusion across the very thin alveolar-capillary membrane (blood-air barrier) according to Fick's law [283–285]. This barrier in humans ~ 0.6 - $2.2\,\mu$m thick [286, 287] and is folded into about 300 million alveoli in a pair of lungs generating a large surface of about 70 - 145 m^2 [287–289]. The alveoli are closely connected to the capillary system of the lung via a surrounding network (enveloping capillaries). Pulmonary alveoli are the smallest functional unit of the lower respiratory tract and located in the alveolar sac structures. They are connected to the air through the airways (by alveolar duct, they connect the respiratory bronchioles to the alveolar sacs). The diameter of the sac-like structure is between 200 and 500 µm (alveolus: 5 - 10 µm [290, 291]) [292, 293]. They expand and contract during the respiratory cycle. The inner surface of the alveoli are covered with the alveolar lining fluid. This is composed of a thin hypophase coated by a phospholipid-rich surfactant film, the lung surfactant [294–296].

The area between the outer surface of the lungs and the inner thoracic wall is the pleural space which is usually filled with pleural fluid. This forms a seal which holds the lungs against the thoracic wall by surface tension. When the thoracic cavity expands or reduces, the lungs act accordingly. Boyle's law defines that the gas volume is inversely proportional to pressure at a constant temperature. The inspiration process is initiated by the motion of the diaphragm and of the external intercostal muscles. The flattening of the diaphragm cause an extending of the superior/inferior dimensions of the thoracic cavity. The elevation of the ribs and sternum generate an extending of the anterior/posterior dimensions of the thoracic cavity. The increase of the volume of the thoracic cavity leads to an increase of the lung volume and according to Boyle's law to a decrease of the pressure in the lungs. The thoracic cavity which is normally at a slight negative gauge pressure becomes more negative, the lungs expand into the cavity, and induce a reduction of pressure on the outside of the alveoli (p_{out}) [297]. The resulting inflation of the alveoli generates a reduced pressure in the alveolar airspace (p_{alv}) in relation to the outside atmosphere, which leads to the inflow of air into the lung. In accordance with the Laplace equation, the pressure difference required to inflate an alveolus with radius R depends on the surface tension γ of the alveolar mucosa fluid $\Delta p = \mid p_{\text{out}} - p_{\text{alv}} \mid = 2\gamma/R$. The surface tension of the alveolar lining fluid is regulated by a surfactant complex, called lung surfactant, allowing efficient respiratory cycles [298, 299]. With the reduction of the surface tension of the alveolar lining fluid by the lung surfactant, it increases the compliance of the lungs and therefore decreases the work required for (re)inflating of the alveoli. Moreover, the lung surfactant prevents the collapse of the smaller alveoli by reducing the surface tension to near-zero values during expiration and very low lung volumes. In such a way that the retractile forces are similar within separate units as well as between respiratory units[5] [294, 305]. The

[5]The lung stability and the large alveolar surface for efficient gas exchange, even at low lung volumes, is maintained by this effect, and the alveolar interdependence [300–302]. The alveoli are inter-connected via the lung parenchyma (alveolar duct and embraced by peripheral and axial connective elastic fibers, that are connected to the pleura). Important points to consider regarding the application and restriction

surface tension is reduced by a factor of around 15, so that the pressure difference of only 1 mmHg is sufficient to inflate the alveoli [306, 307].

The lung surfactant (LS) is an unique and complex multicomponent system of lipids and proteins forming a monolayer at the liquid/air-interface of the alveolar compartment of the lungs [71, 295, 308, 309]. An alveoli with the alveolar lining fluid and the life cycle of lung surfactant is shown in figure 2.9. The lung surfactant is synthesised, secreted and recycled though endo- and exozytosis by the alveolar type II pneumocytes [307, 310]. The lung surfactant is composed of around 90 % lipids and 8 - 10 % proteins by mass. The phospholipid fraction of the mammalian lung surfactant include mainly zwitterionic phosphatidylcholine (70 - 80 % by mass) and phosphadidylethonenolamin (2 - 3 %), anionic species, such as phosphatidylglycerol (7 - 18 %) and phosphatidylinositol (2 - 4 %) and neutral lipids, mostly cholesterol (3 - 8 % by mass) [311, 312]. The most abundant and major compartment PC in the phospholipid LS-fraction is DPPC with about 40 - 70 % [313, 314]. The composition differs depending on the detection method. The specific surfactant proteins (SP) can be divided into two families. SP-A and SP-D are hydrophilic surfactant glycoproteins that belong to the Ca^{2+}-dependent carbohydrate-binding collectin family [313–315]. Contrary to SP-A, SP-D is not associated with the the membrane. The proteins SP-B (saposin-like protein family) and SP-C are hydrophobic proteins that bind to negative charged phospholipids [316, 317]. The most abundant protein SP-A is involved with SP-D in the host defence system [318, 319]. In addition, it can accelerate the adsorption of surfactant lipids to the liquid/air-interface. SP-B and SP-C are crucial for lipid packaging, reorganisation and adsorption at the air-liquid interface during the respiration cycle [310, 320]. For further information, see [308, 318, 321, 322] and surfactant lipids [311, 323].

Depending on the phase behaviour of the pure component, single LS components can be characterised either as good stabilisers with low surface tension or as good fluidisers [334, 335]. However, these properties are mutually exclusive. Good stabilisers with low surface tension adsorb poorly from the solution and propagate slowly from a collapsed state, while good fluidisers cannot achieve low surface tensions [336]. These conflicting requirements are achieved by the above mentioned combination of special compounds that act synergistically to enhance adsorption and propagation during the dynamic compression-expansion cycle. Pure DPPC-films can reduce the surface tension of an water/air-interface to near-zero values by forming a semi-crystallised liquid-condensed phase upon compression (core body temperature $< T_m$ of DPPC), but cannot re-spread efficiently and fast enough during expansion due to the high cohesive lateral forces within the two-dimensional domains [285, 305, 337]. Therefore, the presence of unsaturated lipids and the amphiphilic proteins SP-B and SP-C is necessary to maintain the proper re-spreading of the monolayer at the interface and fluidise the film. In turn, to obtain a highly compressed DPPC-enriched monolayer at the interface, the minor components, pre-dominantly non-phosphatidylcholine compounds are squeezed out. The interplay between the individual components of this complex lipid-protein system ensures a rapid adsorption at the interface after secretion, a proper generation

of the law of Laplace in biological systems are presented in Prange's article from 2003 [303, 304].

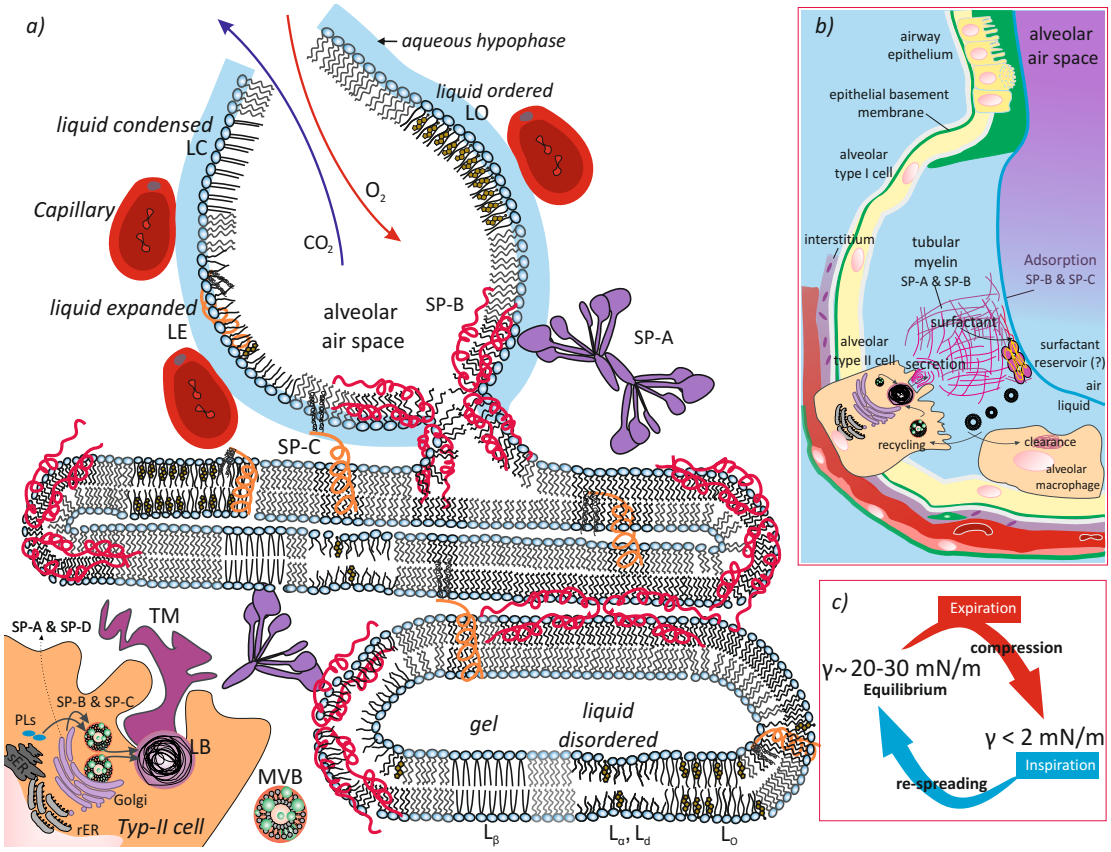

Figure 2.9: Sketch of the life cycle of lung surfactant (a and b) and location of the components within an alveolus. Part a) shows the structure of the lipid phases [295, 308] and membrane-associated proteins in the LS. The LO (in the monolayer structure) or L_o as well as L_d (in the bilayer structure) phases are additionally formed in the presence of cholesterol. The phospholipids were synthesised at the smooth endoplasmatic reticulum (sER), the exact transportation mechanism to the lamellar bodies are unknown. In comparison, the low-molecular weight hydrophobic proteins SP-B and SP-C undergo post-translational processing during trafficking rough ER (rER) to Golgi apparatus and from multivesicular bodies (MVB) to the final lamellar body (LB) [323–325]. SP-A and SP-D were significantly modified in the rER and Golgi apparatus and bypass the LB and are constitutively released (non-LB pathway) [324, 326–328]. The LB secretion occurs via exozytosis across the plasma membrane of the alveolar epithelial type II cell into the hypophase. After unravel and swelling of the LB, tubular myelin is formed consisting lipids and proteins (SP-A and SP-B). Large surface-active aggregates transfers the lipids to the air/liquid-interface (supported by SP-B and -C) as well as to the surfactant reservoir. Upon compression of the mixed monolayer, some lipids are squeezed out into the surface-associated phase (multilayer) and the film undergoes a molecular restructuring with the final capability to reduce the surface tension to near-zero values. By expansion (inspiration), the lipids re-enter the surface film. After inactivation, the lipids are finally recycled via endocytosis back into the type II cells or undergo the clearance pathway via alveolar macrophages. c) The equilibrium surface tension is around 20 - 30 mN/m [329–333].

of near-zero surface tensions during expiration and a good re-spreading ability of the surfactant to reduce the surface tension during inspiration [294, 305, 308, 310]. The concept of "surface-associated phases" or "surfactant reservoirs" was developed to consider the fast phospholipid uptake, that cannot be explained by *de-novo* adsorption alone [285, 313, 337]. The anionic phospholipids have a key role for the interaction with cationic hydrophobic surfactant proteins [295, 308, 336, 338, 339]. Further they are important for the fluidising due to regulation of the chain melting temperature of the monolayer [291]. The physiological calcium concentration in the aqueous hypophase is around 1.5 mM [340, 341] (in the extracellular space of alveoli around 0.2 - 0.5 mM [342]). The formation of tubular myelin and vesicle aggregation (also in cooperation with SP-A) and adsorption at the interface among other processes require calcium ions [291, 340, 342–346]. The concentration of calcium ions are furthermore 5-fold higher than in the surrounding alveolar environment [347]. There are some challenging general questions open. For example, the precise mechanism of the surface tension variation from breath-to-breath. The classical model of the squeeze-out theory [309, 333, 348], that leads to DPPC-rich LS-films is controversial and some recent studies disprove this model [291, 336].

Since the lung continuously undergoes compression-expansion cycles and the volume varies by 20 %, it is obvious that the viscoelastic properties of the pulmonary surfactant monolayer are a crucial determinant of lung functionality [305, 349]. The absence or impairment of pulmonary surfactant or a modification of the quantitative or qualitative composition leads to numerous serious diseases [297, 332]. For example, the deficiency of an effective surfactant due to the immaturity of the lungs in premature infants leads to neonatal (infant) respiratory distress syndrome (IRDS or NRDS) [350–352]. About 60 % to 80 % of premature infants ($<$ 28-th week of pregnancy) develop a respiratory distress syndrome [349, 353]. This is the most frequent cause of death in the neonatal period. The surfactant absence in NRDS leads to progressive lung failure and it manifests by alveolar collapse (atelectasis), decreased lung compliance, reduced functional residual capacity, systemic profound hypoxia (largely attributable to shunting of blood past unventilated lung units) and lung oedema [283, 349, 354, 355]. One therapeutic approach is the endotracheal or bronchoscopic application of animal or synthetic surfactant as LS replacement that significantly reduces mortality rates [285, 294, 305, 356–359]. Currently, the most effective LS substitution are from animal-derived sources, for example bovine-derived Survanta (Abbott Laboratories, North Chicago, IL, US) or porcine-extracted Curosurf (Chiesi Farmaceutici, Parma, Italy). The replacement surfactants usually contain high amounts of DPPC ($>$ 98 % by weight), fatty acids, phosphaditylglycerols and small fractions of specific surfactant proteins ($\leqslant$ 2 wt%) [309, 340, 360, 361]. As natural preparations, even when they are highly purified, they can be potentially virus contaminated and have inherent immunological risks that can cause undesirable immunological reactions. In addition, the purification process is very costly and batch-to-batch consistency cannot be guaranteed. Hence, there is a obvious need for alternative synthetic lung surfactant substitutes [287, 337, 349, 362, 363].

Surfactant inactivation in newborns may be caused by meconium inhalation immediately before or during the birth, such as in meconium aspiration syndrome [349,

364, 365]. The acute respiratory distress syndrome (ARDS) is also attributed to a LS inactivation and can affect children and adults of all ages. ARDS has a more complicated pathophysiology than NRDS [366–368]. There are direct lung injuries (pneumonia (bacterial and viral), aspiration, toxic inhalation, lung contusion, thorax trauma or near-drowning) and indirect lung injuries (sepsis, acute pancreatitis and shock, trauma and cardiopulmonary bypass (major surgery), transfusion-related acute lung injury, burns) that may cause ARDS [367, 369–379]. The inactivation of LS can be induced by blood proteins, like serum albumins which leak into the alveolar air space of the lungs due to injuries or diseases [380, 381]. The analysis of extracted bronchial fluid of ARDS patients report a up to 16-fold increase in serum albumin concentrations in the lining fluid compared to healthy lungs [382–385]. The surface-active serum albumins compete with the LS for the adsorption at the alveolar/air-interface [386–389]. Upon reaching the interface, albumin (or the other competitors) forms a steric and electrostatic barrier that kinetically inhibits the subphase adsorption of LS components and also hinders the LS re-spreading upon expansion during inspiration [285, 294, 381, 390]. Consequently, ARDS and NRDS share many symptoms [391]. Studies on the interfering and inhibiting effects of different blood plasma proteins like albumin [392–395], fibrinogen and also hemoglobin [287, 396, 397] on the surface tension of pulmonary surfactant or its components by competitive adsorption have been published. Unfortunately, in the case of ARDS the inactivation mechanism affects endo- and exogenous surfactants. the usual treatment with LS replacement only leads to a moderate and temporary improvement of lung function in ARDS patients with high concentrated LS replacement therapy [398–402]. The lethality of ARDS is around 62 % [391], it has a high mortality (≈ 50 % [403, 404]) for which no satisfactory treatment is available yet.

One potential approach for new lung surfactant replacement preparations for the treatment of NRDS and promising strategy for the therapy of ARDS/MAS is the ventilation of vaporised or gaseous perfluorocarbons (v- and gFCs), which has shown positive effects in animal models with significant and long-term improvement of gas exchange, lung compliance and alveolar recruitment (oleic acid injured ARDS sheep [362, 405–408], piglet models [406, 409–412] and rats [413]). This perfluorocarbon application is a less invasive mode and may open new strategies. The significantly lower amounts of liquid applied during evaporation compared to liquid ventilation (total and partial) represent a significant therapeutic advance [411, 414–416].

In 1966, Clark and Gollan demonstrated the possibility of total immersion of mice in perfluorocarbon solution equilibrated with oxygen at atmospheric pressure. In some cases for well over an hour, the mice survived this experiment without visible damage [417]. Based on the knowledge gained, further studies on liquid ventilation were carried out. Over the time, two different strategies were development. On the one hand, the total liquid ventilation in which the airways are completely filled with a perfluorocarbon solution [418–420]. This technique is not used in clinical routine due to the technically very complex requirements. On the other hand, the experience was used to develop partial liquid ventilation as respiratory support. Here, the lung is only partially filled with liquid perfluorocarbon up to a volume corresponding to the functional residual capacity. The partial liquid ventilation offers the advantage that it can be performed

with a conventional ventilator. Thus, it considerably reduces the amount of equipment required [421]. Experiments [422–424] and first clinical studies [425, 426] showed an improvement in oxygenation as well as an increase in lung compliance and surfactant function. The first study with infants were conducted in 1989 [427]. Further studies followed [428, 429], also in neonates [430], and adults [418, 426, 431]. With regard to the study endpoint criteria mortality and ventilator free days, partial liquid ventilation could not prevail in the treatment of ARDS [432–434]. There is no clear recommendation for partial liquid ventilation in the treatment of adults [435, 436]. Partial liquid ventilation is used in the USA for the treatment of NRDS (LiquiVent, Alliance Pharm. Corp., San Diego, USA, F-octyl bromide) [429]). However, some tasks, for example the monitoring, the regulation of the volume filling of the lungs and evaporation loss are not yet definitely solved for the partial liquid ventilation. Moreover, the weaning leads to a deterioration in gas exchange. The ventilation with vaporised or aerolised perfluorocarbons seems to be a good solution for these problems since it also reduces ventilation-associated lung failure. Bronchopulmonary dysplasia is a chronic lung disease that occurs primarily in prematurely born children of low birth weight who are artificially ventilated for long time periods due to oxygen injury [437], for example to treat NRDS [438, 439]. An association between reduced lysozyme activity and bronchopulmonary dysplasia in newborns is suspected.

So far, little is known about how v- and gFC influence the properties and structures of the lung surfactant. Therefore, DPPC- and DPPA-films and the response to different g- and vFCs were studied in this thesis. Studies on the structural change and behaviour under elevated gFC and vFC atmosphere of lipid layers in sub-angstrom resolution are rare. Previous studies reported an effect on the physical properties of a two-dimensional surfactant film at the liquid/air-interface when perfluorocarbons were present in the gas phase [1, 440, 441]. There are no reports on structural behaviour of the DPPC and DPPA monolayers upon elevated gas pressures and treatment with vaporised perfluorocarbons at constant area and the alteration of the surface tension.

Chapter 5 presents results of the adsorption behaviour of BSA at the water/air-interface and the interaction with an overlying vFC-(perfluorodecalin) atmosphere to test the inactivation ability of the perfluorocarbon on the surface-activity of BSA. Since interaction and displacement studies are available, a mechanism for a possible denaturation or alteration can be given [2, 442, 443]. To get further information about the interaction of perfluorocarbons with DPPA-films in association with lysozyme at the water/air-interface, this was also investigated. The concentration of the protein is elevated in the bronchoalveolar lavage in patients with chronic bronchitis [444]. Therefore, an understanding of the effect of gFCs on the adsorption behaviour of lysozyme would be helpful for the consideration of FCs as aerosol spray ingredient.

2.2.1 Physicochemical properties of perfluorocarbons

Perfluorocarbons (PFCs) or fluorocarbons (FCs) are hydrocarbon compounds in which all hydrogen atoms are substituted by fluorine atoms. The prefixal symbol “F-” conventionally stands for perfluoro- and is used through this thesis (IUPAC notation) [445–

447]. Perfluorocarbons have properties that significantly distinguish them from their alkylated analogues [448–452]. While low-molecular fluorocarbons (less than 5 carbon atoms) are gaseous at room temperature, high-molecular fluorocarbons (more than 5 carbon atoms) are colourless liquids [453, 454]. The physicochemical PFC properties are defined by their chain length, the carbon chain branching and the degree of fluorination and substitution [454–456]. Thus, two gaseous linear and small PFCs, C_3F_8 and C_4F_{10}, and two further compounds, the bicyclic F-decalin and the linear F-octyl bromide, that consists of a further halogen atom (bromide), were chosen for this study. These are the most frequently investigated PFCs for biomedical applications [445, 457]. F-octyl bromide is more precisely a perfluoroalkyl substance (PFAS).

The differences in comparison with hydrocarbons can be explained mainly by the properties of fluorine [458]. Fluorine is the element with the highest electronegativity and has very special properties. It has a high ionisation potential and a very low polarisability [459, 460]. Nevertheless, the relatively small fluorine atom is much larger than hydrogen (van der Waals radius of 1.47 Å vs. 1.20 Å) [461]. Perfluoroalkylated chains are more bulky than their hydrogenated counterparts (cross-sections: 30 $Å^2$ and 20 $Å^2$ [457, 460, 462, 463]) and the average volumes are estimated for CF_2 and CF_3 groups to be 38 $Å^3$ and 92 $Å^3$ respectively, compared to 27 $Å^3$ and 54 $Å^3$ for the CH_2 and CH_3 groups [140, 462]. Another consequence of the larger size of the fluorine atom is the higher rigidity of the perfluorinated chains [464, 465] which is related to the loss of *gauche-trans* freedom. The *gauche-trans* energy difference is approx. 2.0 kJ mol^{-1} and 4.6 kJ mol^{-1} for hydrocarbon and fluorocarbon chains, respectively [460, 466]. To minimise steric hindrance, perfluorinated chains adopt a helical conformation [446, 460].

Primarily due to the extremely strong covalent bonds between fluorine and carbon atoms ($\approx$ 485 kJ mol^{-1} compared to $\approx$ 425 kJ mol^{-1} for a C-H bonds), PFCs are highly thermally and chemically stable [416, 446, 448–450]. Furthermore, PFCs are weak hydrogen-bond acceptor [446, 452] and considerably more hydrophobic than the corresponding H-chains. This effect is due to the larger surface area of the fluorinated chains (the "hydrophobic" - sometimes refereed as "superhydrophobic" [445, 457] effect of the chain is approximately proportional to its contact area with water [468, 469]). They are also biologically inert and cannot be metabolised or undergo enzymatic changes [470]. Thus, the PFCs are not subject to any metabolism after application and are therefore extremely biocompatible. They are 99 % bronchially eliminated by exhalation [455, 471, 472]. The C-F bond is the most stable single bond found in the organic chemistry [445, 473]. Additionally, the dense electron cloud of fluorine atoms leads to a repulsive and sterically shell around the "skeletal" C-C bonds and protects it from the approach of reagents (shielding effect) [446, 457]. The intermolecular forces in PFCs are very weak, in comparison to their strong intramolecular bonds. The low polarisability of fluorine leads to low van der Waals interactions between fluorinated chains and low cohesive energy densities in liquid fluorocarbons. Hence, liquid PFCs act like almost ideal, gas-like fluids [457, 474, 475]. These low intermolecular forces are responsible for the valuable characteristic physicochemical properties of fluorinated compounds that are critical for liquid ventilation and other biomedical applications [457]. Due to the weak van der Waals forces, PFCs have high vapour pressures relative to their molecular weight, and

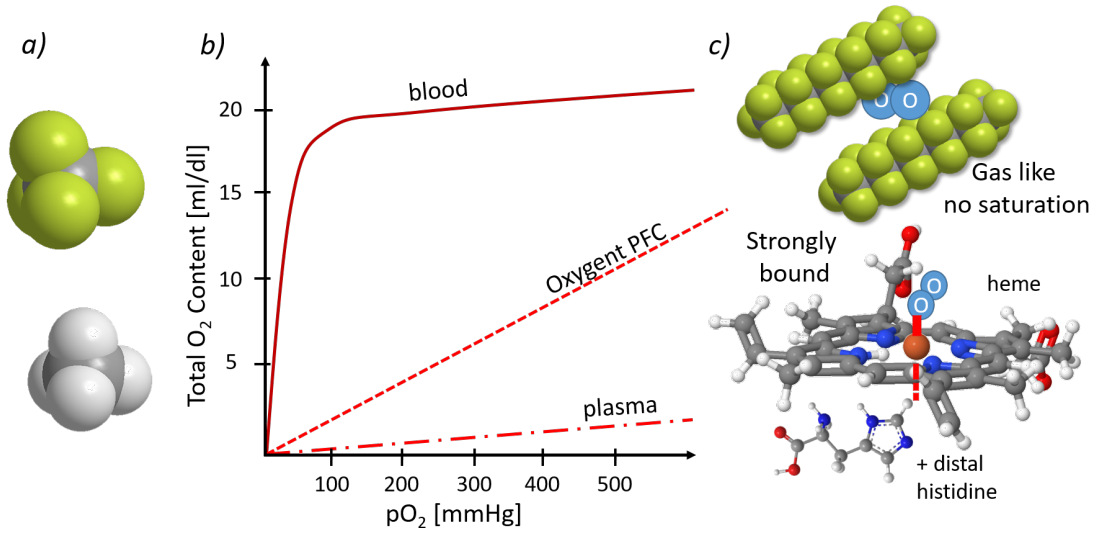

Figure 2.10: (a) Size difference of CF_4 and CH_4. (b) The sigmoidal binding curve of blood is shown as well as the direct linear relationship between the partial pressure of oxygen and the dissolved amount of di-oxygen in PFCs, here Oxygent. (c) Dissolution of oxygen via physically binding by PFCs and di-oxygen binding via the central iron atom in heme [445, 467].

are quite volatile, the typically used PFCs for liquid ventilation evaporates at or below physiological temperatures [445–447]. Moreover, PFCs have very low surface tensions ($< 20\,\mathrm{mN/m}$) and therefore an excellent spreadability for lowering the surface tension at the injured alveolar/air-interface [376, 431, 476]. Perfluorocarbons are about twice as dense as water and are not soluble in water or lipids. An effective penetration into the tiny spaces between the small airways and alveoli because of gravity and the denser nature, furthermore, archives the surfactant-like activities. These are not impaired by mediators in the alveolar edema fluid. A gently opening of collapsed or atelectatic regions is possible. Finally and most importantly, due to their low cohesive energy, PFCs are excellent solvents for gases (with similar low cohesivety: O_2, CO_2, N_2, NO). The gas is physically dissolved by insertion to an intermolecular site (non-directional van der Waals interactions) within the solvent (PFC) [445, 469, 477]. In addition to oxygen, it is also possible to dissolve other respiratory gases and thus ensure the removal of physiologically produced carbon dioxide (solubility of $\sim 50\,\mathrm{ml}$ O_2 and ~ 140 - $210\,\mathrm{ml}$ CO_2 per dl of PFC [478, 479]). The binding of O_2 to hemoglobin, which undergoes conformational changes during this process results in a sigmoidal oxyhemoglobin dissociation curve [480]. In contrast, O_2 solubility in PFCs is a linear function of the partial pressure of the gas [457, 481–483]. Figure 2.10 illustrates this relationship by showing the oxygen content as a function of the oxygen partial pressure in blood and a PFC solution (Oxygent). PFCs are immiscible with almost all physiological compounds (water or lipids) except gases [445, 479].

Due to the difference in cohesive energy densities between H- and F-chains, the mix-

ture of these compounds is highly non-ideal [446, 484–486]. Thus, phase separation and domain building can be observed in different mixed systems (e.g. solutions, membranes, colloids).

The relatively homogeneous and unique group of perfluorinated compounds are hence characterised by biological and chemical inertness (in the kinetic sense), stability (in the thermodynamic sense), intense hydrophobic and lipophobic effects, a low water solubility, low surface tension and high gas solubility. In addition to therapeutic applications, PFCs are also used in diagnostic applications (e.g. x-ray tomography, ultrasound imaging and magnetic resonance imaging [449, 487]).

2.2.2 Perfluorocarbon-based drugs

This subsection briefly presents biomedical application of PFCs beyond the treatment of lung diseases and the contact of PFCs with biological membranes *in-vivo*. Many of these applications are based on the injection of lipid-coated PFC droplet emulsions or microbubbles. Their further development can benefit from the structural insights into the lipid/PFC-interaction on a molecular level, which this thesis provides. Therefore, this subsection offers an overview of this medical field.

Perfluorocarbons are unique substances for the design of a wide range of stable colloidal systems. These colloidal systems consists of a dispersions of encapsuled droplets or bubbles with an internal fluorine core in a distinct external phase. The various biomedical uses of PFC-based colloids, such as targeted drug and gene delivery, molecular imaging and *in-vivo* oxygen delivery (artificial blood substitutes) have been reviewed in literature [458, 488–496].

Due to the low water solubility and the high volatility PFC gases are suitable for the design of injectable dispersions, that can served as *in-vivo* reflectors (micron-size microbubbles) in contrast-enhanced ultrasound imagining (CEUS) (figure 2.11a) or (submicron size) liquid PFC-based droplet emulsions for oxygen delivery and fluorine-19 magnetic resonance imaging (^{19}F-MRI) [499–502] (figure 2.11b). Gas-filled microbubbles, mostly C_3F_8 and C_4F_{10} (second and third generation agents) [500, 503–505], are highly echogenic, since the compressibility of the gases are multiple orders of magnitude higher than of biological tissue (different acoustic impedance) [498, 506]. Simple air bubbles dissolve fast within seconds as a result of the blood pressure and surface tension pressure [469]. The reduction of the partition coefficient prevents this fast dissolution of the bubbles and increases the lifetime. This can be realised by introducing a voltaire PFC. The water soluble gases (CO_2, N_2 and O_2) are in equilibrium with the gases within the plasma whilst the very poorly water-soluble PFCs remain in the bubbles and balance the blood pressure and Laplace pressure. PFCs are not generally suitable for intravenous application. Other parameters such as the possibility of forming emulsions and the organ retention time must also be taken into account [457, 507]. For this reason and because of the poor solubility of PFCs they must be processed, e.g., emulsified or encapsulated [508, 509]. The surface of commercially available microbubbles for CEUS or droplet emulsions for oxygen delivery and molecular imaging with MRI are mostly composed of denaturated serum albumins, polymers and phospholipid shells (e.g. Sonazoid,

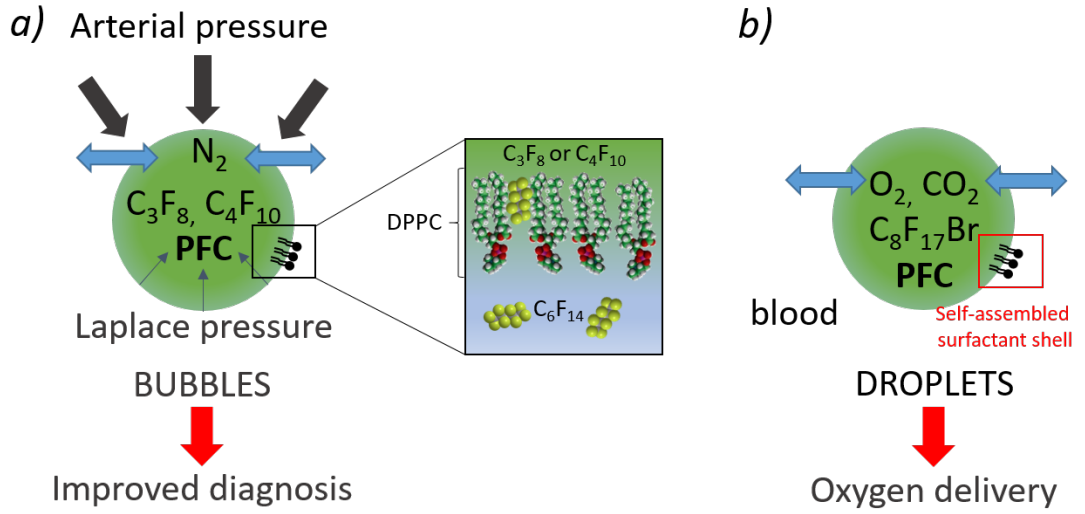

Figure 2.11: Injectable colloids with a PFC core and lipid shell. (a) Stabilised PFC microbubble for diagnostic ultrasound imaging, with DPPC shell and intercalated PFC molecules [497]. (b) PFC droplet emulsion for intravascular oxygen delivery to tissues [469]. Blue arrows indicate the gas exchange through the interface, the partial pressure inside the bubble is equal to the partial blood pressure. The PFC partial pressure is balanced as sum of Laplace pressure and blood pressure [498].

a contrast agent from GE Healthcare (Amersham, UK): C_4F_{10} and lipids), to produce biocompatible materials [505, 510, 511]. One interesting approach is the stabilisation of DPPC or DMPC shells with high molecular weight perfluorocarbons in the outer phase, see figure 2.11a [497, 510, 512]. Apart from this, the interaction between the fluorine gas phase and the interfacial phospholipid monolayer has not been considered so far [4]. Hence, it is crucial to understand the mechanism how the PFC molecules interact with the DPPC shell and how they affect structure and surface tension. In this work, the Langmuir monolayer technique which provides a controlled model membrane was applied in combination with x-ray scattering methods which enable to resolve structures with sub-angstrom resolution to address these questions.

The knowledge about the interaction of perfluorocarbons with the interfacial phospholipid droplet wall is also important for the design and control of other self-assembled colloidal systems like liquid PFC droplet emulsions for oxygen supply [4, 469, 497]. Especially F-decalin and F-octyl bromide, are excellent nominees for oxygen carrier solutions and artificial blood substitutes [469, 513]. An overview of approved other PFC-based emulsions for different applications can be found in [514].

The perfluorocarbons, especially the gases F-butane, F-propane and the liquid F-decalin are commonly used in the field of ophthalmology [453, 515–521].

2.2.3 Gas adsorption at interfaces

Many physical and chemical processes occur at interfaces. Adsorption appears in a wide range of natural physical, biological and chemical systems and is one of the main basic surface phenomena. In an adsorption process spontaneous accumulation of a gas takes place at the solid surface. In the framework of this thesis, the behaviour of different alkanes, especially perfluoroalkanes, at different lipid layer systems, monolayers on a buffer subphase or solid-supported lipid systems on silicon wafer is studied in order to examine their effects on the lung surfactant.

The adsorption process is generally classified either as physisorption or as chemisorption. The processes which are studied in the framework of this thesis can be categorised as physissorption since they are reversible, have a low enthalpy of adsorption and the intermolecular forces are weak (van der Waals forces, hydrogen bonding). They are also highly non-specific. Different types of adsorption occur depending on the interfacial tension between the substrate and the adsorbate: complete wetting, partial wetting and frustrated complete wetting, also known as pseudo-partial wetting [522–524]. Due to the adsorption the surface energy is reduced.

This subsection takes a brief look at the thermodynamics and basic theory of the adsorption of gas molecules on solid or liquid surfaces for systems where the adhesive interactions between the gas molecules and the liquid or solid surface is greater than the cohesive interactions between the adsorbed molecules. With this condition only the complete wetting, where a closed layer is formed in the equilibrium state, is considered. The amount of the adsorbed substance at equilibrium depends on the temperature, the pressure and the condensation pressure of the gas and the specific surface area of the interface. The chemical nature of the gas and solid plays also a significant role. The Keesom interaction, the Debye force and the London dispersion force contribute to the van der Waals force which is always present between atoms and molecules. The reason for the adsorption of a gas molecule on a solid or liquid surface is the van der Waals interaction between the substrate and gas molecule. The van der Waals interaction is caused by fluctuating dipoles. These can be permanent dipoles or induced dipoles. The potential energy of the inverse sixth-power attractive van der Waals interaction $w(r)_{\mathrm{vdW}}$ between two atoms or molecules can be described as a function of the distance r

$$w(r)_{\mathrm{vdW}} = -\frac{C}{r^6}. \tag{2.10}$$

Here C is a substance specific constant. The Lennard-Jones potential $w(r)_{\mathrm{LJ}}$ approximates the total intermolecular interaction potential between a pair of neutral particles by adding a Pauli repulsion to the attractive van der Waals contribution

$$w(r)_{\mathrm{LJ}} = 4\epsilon \left[\left(\frac{\psi}{r} \right)^{12} - \left(\frac{\psi}{r} \right)^{6} \right]. \tag{2.11}$$

Here, ψ is the finite distance at which the interaction potential is zero, r is the distance between the particles and ϵ the depth of the potential. In the following, the system which is illustrated in figure 2.12a is further considered. Upon increasing the gas pressure in

the container in figure 2.12a (dotted black arrows), the chemical potential of the gas μ_g increases approaching μ_0, and a fluid phase μ_f might be formed. As illustrated in figure 2.12c two different possibilities arise at $\mu_g = \mu_f = \mu_0$: first, a closed (macroscopically thick) layer is formed indicated by the curve CW (complete wetting), and reaches the adsorbed amount Γ, second, the adsorbed amount reaches a finite limited value (Γ_0) and partial wetting occurs. Therefore, a distinction is made between two phenomena in the adsorption of gases.

We now assume that the gas phase and the molecular thin film on the substrate are in a thermodynamically equilibrated state and a complete wetting occurs. The free energy or Gibbs energy G in its minimum describes a stable thin film on a substrate. The Gibbs energy includes the interaction energy between the adsorbate and substrate, and the free energy of the adsorbed film, which is a function of the gas pressure in the system. The pressure dependence of μ_g is given by $\mu = \mu_0 + RT\ln(p/p_0)$ with the gas constant $R = 8.31\,\mathrm{J/(K \cdot mol)}$, the gas pressure p and the condensation pressure p_0 which is set to the value at the given temperature T. Therefore, μ_0 is the chemical potential of the gas at condensation. Now, it is possible to calculate the Gibbs free energy with $G = n \cdot \mu$ with the amount n in mol. By the particle density difference of the gas phase and adsorbed liquid $\Delta\rho_l$ with a layer thickness l, it is possible to write the free energy per unit area as [142, 525]

$$\begin{aligned} G &= \left(\frac{\mu_0}{N_A} - \frac{\mu}{N_A}\right)\Delta\rho_l l \\ &= \left(\frac{\mu_0}{N_A} - \left(\frac{\mu_0}{N_A} - k_B T \ln\left(\frac{p}{p_0}\right)\right)\right)\rho_l l. \end{aligned} \tag{2.12}$$

If a adsorbed film is considered on the liquid substrate, with the assumption of van der Waals interactions, which can be simplified described by two parallel surfaces, see equation (2.8), the free energy per unit area can be calculated with [526, 527]

$$F = \gamma_s + \gamma_f - \frac{H_{eff}}{12\pi l^2} + l k_B T \Delta\rho_l \ln\left(\frac{p}{p_0}\right). \tag{2.13}$$

Here, γ_s and γ_f are the surface tension of the substrate and the film. H_{eff} is the effective Hamaker constant. It is assumed, that the interaction is non-retarded and additive between the two surfaces. It is typically in the order of 10^{-19} J for interactions of fluids or solids in vacuum. For most condensed phases it is in the range of $(0.4\text{-}4)\cdot 10^{-19}$ J. It is a key property for determining the wetting behaviour and can be calculated with regard to the dielectric properties of the three materials. It is a highly system specific value that depends on the properties of the interaction materials and on the geometry of the system [142, 528, 529].

The following expression for the Hamaker constant is valid for non-retarded van der

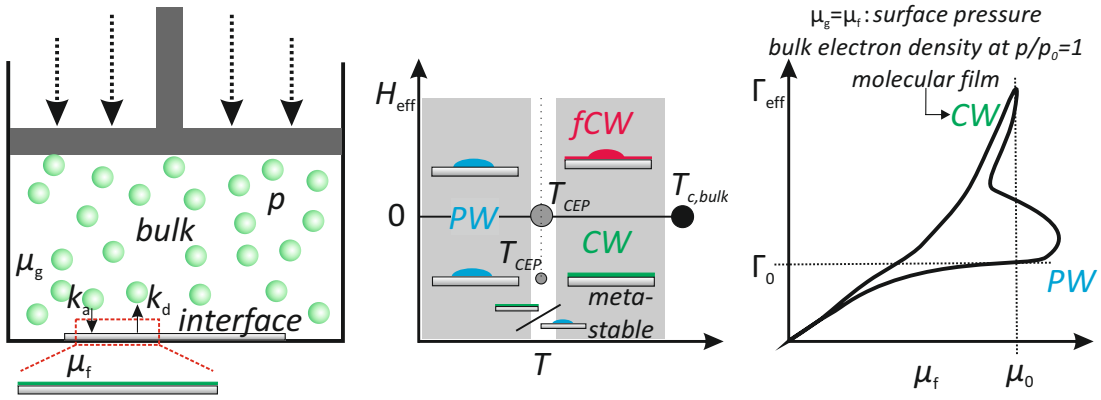

(a) Adsorption-induced wetting. **(b)** Schematic phase diagram. **(c)** Adsorption isotherm.

Figure 2.12: (a) Schematic sketch of adsorption-induced wetting, (b) wetting phase diagram ($T_{\mathrm{c,bulk}}$ is the bulk critical temperature) modified from [523] and (c) adsorption isotherm, redrawn from [530].

Waals forces, i.e. for short distances compared to a typical wavelength in the UV [142]

$$\begin{aligned} H_{\mathrm{eff}} =& A_{\nu=0} + A_{\nu>0} \approx \frac{3}{4} k_{\mathrm{B}} T \left(\frac{\epsilon_{\mathrm{s}} - \epsilon_{\mathrm{f}}}{\epsilon_{\mathrm{s}} + \epsilon_{\mathrm{f}}}\right)\left(\frac{\epsilon_{\mathrm{g}} - \epsilon_{\mathrm{f}}}{\epsilon_{\mathrm{g}} + \epsilon_{\mathrm{f}}}\right) \\ &+ \frac{3h\nu_e}{8\sqrt{2}} \frac{(n_{\mathrm{s}}^2 - n_{\mathrm{f}}^2)(n_{\mathrm{g}}^2 - n_{\mathrm{f}}^2)}{(n_{\mathrm{s}}^2 + n_{\mathrm{f}}^2)^{1/2}(n_{\mathrm{g}}^2 + n_{\mathrm{f}}^2)^{1/2}\left((n_{\mathrm{s}}^2 + n_{\mathrm{f}}^2)^{1/2} + (n_{\mathrm{g}}^2 + n_{\mathrm{f}}^2)^{1/2}\right)}. \end{aligned} \tag{2.14}$$

Here, the indices s (substrate) and g (gas) denote the material in the two halfspaces and f (film) is the intermediate film. Further, h is the Planck's constant and ν_e the main electronic absorption frequency in the ultraviolet regime (typically $\approx 3 \cdot 10^{15}\,\mathrm{s}^{-1}$). The refractive index n and the dielectric permittivity ϵ for the materials are given in the spectral range of visible light. The Hamaker constant can be approximated from the surface energy, which is the surface tension for liquids. A stable film is formed when the free energy of the system is minimal, i.e. by the first derivation of the free energy with $\partial F/\partial l \stackrel{!}{=} 0$. The layer thickness l_{stable} at the potential minimum can subsequently calculated with [526]

$$l_{\mathrm{stable}} = \left(\frac{H_{\mathrm{eff}}}{6\pi\Delta\rho_{\mathrm{l}} k_{\mathrm{B}} T \ln\left(\frac{p}{p_0}\right)}\right)^{\frac{1}{3}}. \tag{2.15}$$

At a given temperature in dependence of the condensation pressure the equation describes a Frenkel-Halsey-Hill isotherm [531–533]. The film thickness increases with increasing gas pressure and diverges as soon as the gas pressure reaches the condensation pressure, corresponding to macroscopic adsorption. Furthermore, it can be seen from equation (2.15) that the effective Hamaker constant has to be negative, otherwise no

stable film can be formed and, thus, no or only partial adsorption occurs. This can be also seen in figure 2.12b.

A different approach for the determination of the wetting type is given by Young's equation. Here, only the interfacial and surface tensions of the involved phases are taken as basis for the calculation of the wetting behaviour, without considering the Hamaker constant. Through the Young's equation, the relations between the equilibrium contact angle θ_{eq} of the drop and the surface as well as the three surface tensions or energies are given as [142]

$$\gamma_{\mathrm{s,g}} = \gamma_{\mathrm{s,f}} + \gamma_{\mathrm{f}} \cos(\theta_{\mathrm{eq}}). \tag{2.16}$$

When the three surface tensions are known, the state of wetting follows directly. Complete wetting or spreading occurs, when the contact angle θ_{eq} is zero, i.e. for the case that the inequation $\gamma_{\mathrm{s,g}} \geqslant \gamma_{\mathrm{s,f}} + \gamma_{\mathrm{f,g}}$ is valid. On the contrary, for contact angles $\theta_{\mathrm{eq}} > 0°$ islands are formed on the substrate, partial wetting results.

Besides the two states of complete and partial wetting, a third wetting state has been reported. The frustrated-complete wetting (fCW or pseudo-partial wetting) is characterised by a mesoscopic film of a drop with a finite contact angle, where the surface free energy is very close to that required for complete wetting [522, 523]. By changing thermodynamic variables, e.g. the temperature, the surface tensions or the chemical composition of the adsorbate or of the surface, the sign of the effective Hamaker constant can change and consequently also the contact angle and wetting transition can occur [522–524, 528]. Figure 2.12b illustrates a generic phase diagram for wetting transitions for systems where wetting below the critical bulk temperature occurs [523]. It is depicted here to illustrate temperature and effective Hamaker constant dependent wetting transitions. The configurations at the partial, complete and frustrated-complete wetting is also shown.

2.3 The Hofmeister series

Studies and theories dealing with the behaviour of macromolecules in electrolyte solutions date back to the nineteenth century. One of the most important observations in this respect was made by Hofmeister in 1888, who showed that different salts can dissolve or precipitate proteins [534, 535]. However, we now tend to discuss specific ion interactions rather than the influence of salts. It was initially assumed that ions influence the physical properties of macromolecules in aqueous solution by forming or breaking up the water bond structures [536, 537]. While so-called kosmotropes (e.g. small cations with high charge density and anions) were believed to strengthen the water-hydrogen bonding network, chaotropes (e.g. large cations and anions) have the opposite effect [538–540]. Indeed, previous studies have shown, that ions do not have significant effects on the structure of the water and the hydrogen bonding network and do not offer long-range structural perturbations effects [541–544]. Hence, the current hypothesis is that direct ion/macromolecule-interactions and also the interaction with water of the first hydration shell of the macromolecule, are largely responsible for most aspects of the phenomena associated with the Hofmeister series [541, 545–547]. Despite

the fact that Hofmeister effects are common to macromolecules in aqueous solution, the mechanisms by which ions interact with them at the molecular level are still in an early stage of elucidation [546–550]. The Hofmeister series is not yet fully understood. The essential effects are based on a very complex interaction between the ions, the solvent and the dissolved organic molecules [550].

There are many theoretical approaches to explain the Hofmeister series, for example classical theories as Debye-Hückel theory [551, 552] and the DLVO-theory [553–557], but also recently developed approaches, as the ion-pairing hypothesis or Collin's law of matching water affinities [549, 558–561] and extended Debye-Hückel theory [551, 562–564] for instance. Furthermore, work on the ion-specific parameters and hydration the Jones Dole viscosity B coefficient and Setchenow constant, shall be mentioned [558, 560, 565–570]. A recent concept is also the introduction of ionic dispersion and van der Waals forces acting on ions at the interface [571–573]. In extension to the law of matching water affinities, Kunz et al. proposed a Hofmeister-like ordering for the binding of ions to charged surfactant headgroups [574, 575]. The phosphatidic acid for example, is classified as a "hard" (chaotropic) headgroup that favourably interacts with also hard ions. As with all concepts, the simplifications should be considered with care. The choline and phosphate group of phosphatidylcholines can be regarded as chaotrope and kosmotrope group [574, 576].

A wide range of phenomena related to ions cannot be explained by current theories and are therefore often referred to as "ion-specific". However, the Hofmeister series is proposed for salts and not for specific ions [575]. These specific ion interactions can follow the Hofmeister series or not, and are not restricted to proteins or even biomolecules [577, 578]. Typically, the polar headgroups of lipid membranes are susceptible for perturbations, they can directly interact with the ions in solution [579, 580]. This in turn can influence the properties of the membrane, for example the lipid phase transitions [581] modify the membrane surface potential (e.g. nerve cell action potentials) [582, 583], the dipole potential [584], the structure and dynamics of the lipid molecules [585, 586] can change the hydration layer [587] or influence the intermembrane forces [588], and are essential and able to regulate the protein/membrane-interactions.

Numerous examples of specific ion effects are known and there is a vast majority of reviews concerning the Hofmeister or lyotrophic series [549, 562, 589–592]. Specific ion effects can be investigated with a wide number of experimental techniques and can be further subdivided and categorised in simple solutions, complex mixtures and well-defined surfaces, the two books of Ninham & Nostro and Kunz gives a further overview [575, 593]. Two further reviews of Cevc [156] and Eisenberg [583] documented the consensus until 1990 that multivalent cations interact very strongly with phospholipid bilayers, while the interaction with monovalent ions, except for lithium, is weak - the relative binding affinities generally followed the Hofmeister series. The consistency regarding the relative binding affinities is currently missing, this is further discussed in section 2.3.2.

The structural response, and also probably possible adsorption sites, of lipid systems upon salt addition can be studied with surface-sensitive x-ray scattering methods, like x-ray reflectivity. The structural reorganisation upon salt addition and ion binding does

not affect only one lipid molecule but often the entire membrane [156].

2.3.1 Cellular cation environment and specific ion effects

The intracellular region of the mammalian cell is a very crowded environment containing a variety of proteins, RNA (ribonucleic acid) and ions, beside many other solutes [594]. Ions and specific ion effects are ubiquitous in the biology. Metal cations, especially Ca^{2+}, Mg^{2+}, Na^{+} and K^{+} play a vital role in cell function and regulation [55, 595, 596]. They take part in a variety of chemical reactions within the cell.

Since the beginnings of molecular biology it is known, that living cells retain certain ions, such as potassium, and reject others, such as sodium. In fact, the intracellular concentration of potassium and sodium are 145 mM and 5 - 10 mM, respectively. In contrast, the extracellular concentration is higher for sodium with about 145 mM and the potassium concentration is around 5 mM. This yields an electrochemical gradient across the membrane which is called the resting potential. The electric potential of an excitable cell is of fundamental cell physiological importance for the excitation conduction of the nerves, the control of muscle contraction, as well as the electrophoretic material transport through the membrane [78, 597]. The concentrations of cations and their fluxes into and out of the cell are strictly regulated [595].

In contrast to monovalent cations, divalent cations are more scarce in the intracellular milieu [597]. Calcium is involved in many signal transduction pathways (cascades) and plays a crucial role in cell fusion and endocytosis. The reason why this ion is often used as an intracellular messenger is due to several properties. Firstly, local and temporary changes in calcium concentration are detected quickly and easily. Transport systems keep the cytosolic concentration at about 1 - 100 nM, several powers of ten below the extracellular concentration which is about 1 - 2 mM. Due to the low local concentrations slight changes can be detected quickly. Another reason why calcium is so well-suited as a messenger substance is that it is able to bind very tightly to proteins and can induce substantial restructuring. It can bind coordinatively to up to eight oxygen atoms [597, 598].

Up to now, we have seen some examples for specific ion effects, such as the calcium triggered fusion of lamellar bodies with the type II pneumocyte plasma membrane. This is promoted by extracellular calcium ions [599, 600]. Moreover, the structure of tubular myelin is maintained by calcium ions. Further, the surfactant protein A binds calcium-mediated to the phospholipid structures and is important for formation of tubular myelin [599–601]. The strictly controlled regulation of calcium signals is crucial for adequate cell function, as shown by the role in cell proliferation, gene transcription and cell death. Certain specific features of the calcium signalling are also altered in some cancers [602, 603]. Calcium is also an important cofactor in metallo enzymes, here the binding is highly specific in the active site of the protein. Further, as second messenger it is crucial for the propagation of neuronal signals. The membrane fusion of the neurotransmitter-rich vesicles and the neuron synapsis membrane is mediated trough calcium ions [604, 605]. Due to the modulation of the charge property of the lipids, calcium ions play an important role in the T-cell receptor activation (adaptive immune sys-

tem) [606]. Another "bridging" role of calcium ions is the protein/membrane-interaction of the C2 domains and annexins [607, 608]. Unspecific effects of metal ions can lead to complications, for example the mediation of the interaction of amyloidogenic peptides with membranes [609]. Since Ca^{2+} is an important signal molecule that causes many cellular reactions, it is possible that part of its effect is transmitted by changes in the physical properties of membranes. Indeed, during the phase transition charged lipid membranes emit interfacial bound ions. This enables the generation of ion pulses [156]. The local concentration of cations can be temporally enhanced due to transient signal responses to external stimuli, for example at the signal transmission in neurons ("synaptic plasticity") [610, 611].

Magnesium is the second most abundant ion in the interior of a cell and is an essential element for biological functions [612]. It occurs typically as Mg^{2+} ion. It is deeply involved in the cellular metabolism. In fact, Mg^{2+}-dependent enzymes occur in almost every metabolic pathway. Examples are DNA polymerase and hexokinase. Further, the main energy source of the cell, ATP, must bind to a magnesium ion to be active. It stabilise polyphosphate compounds in the cells, including those involved in the synthesis of DNA and RNA [613, 614]. The magnesium ion tends to sense in the other direction as calcium. For example, magnesium binds weakly to proteins and the cell can regulate the enzymatic activity through a local change of the magnesium concentration. Further, the two cations (magnesium and calcium) cannot be exchanged in biologically complex processes. For example, the sugar/lipid-interactions mediated by Ca^{2+} which regulates the presentation of sugars present in $PI(4,5)P_2$ lipid and finally modulates the phospholipase C delta 1 pleckstrin homology domain (PLC δ_1-PH) cannot performed by magnesium ions [615]. This is an example for the high selectivity of the present ions. The total concentration of magnesium ions in a mammalian cell is about 30 mM, the free cytoplasmatic Mg^{2+} concentration is in the range of 1.5 mM. The latter pool is stored in intracellular compartments or bound to chelators, e.g. ATP [613, 614, 616, 617].

Beside the effects of the global change of the ionic distributions trough cell homeostasis, stronger localised alterations of the cation distributions are important, e.g. in membrane fusion events and signal transmission. Furthermore, the selective accumulation of cations at the surface of a membrane can effectively modify its interaction with the environment and modulate its physical properties [618–620]. Indeed, magnesium and calcium ions can catalyse the membrane fusion (or endocytosis/exocytosis) and are able to bind to multi-anionic sites of the membrane and due to the cross-linking membrane stabilisation can be enhanced [577, 621, 622].

In the last few decades, considerable progress has been made in elucidating the role of ions in signal transmission [623, 624] and in cell membrane-related processes. Yet, there is strong evidence that ions interact in a very specific way with membranes [620, 625–627]. However, the experimental description of the direct and specific effects between ions and zwitterionic membranes is still lacking and the quantitative aspects as well as the underlying molecular details are still under debate [626, 628]. In order to obtain more information, in this work different ions were used to investigate the structural response upon membrane binding. Due to the selection of various ion sizes,

properties (e.g. polarisability), hydration states and concentrations different features can be screened.

2.3.2 Specific ion effects on membrane systems

This subsection briefly summarises previous studies and the current status of the research field of the interaction of ions or salt-induced effects on membranes, especially work conducted with solid-supported membranes. As already described, the environment of biological membranes is rich in ionic species, and the physicochemical mechanism for the multiple effects of ions that were observed at lipid bilayers is generally not well understood. The ionic distribution of the aqueous environment is particularly important, since it directly controls and regulates the properties of a lipid membrane. The lipid bilayer as biological interface is sensitive to the interference by ions which typically bind to the polar headgroup [579, 580, 588, 629]. The direct measurement of ion/membrane-interactions in the complex biological system is not possible or very difficult. Therefore, simplified lipid bilayers are often used as mimicry model system to shed light on the role of ions in complex biological systems [156, 630, 631].

The interest in understanding the effects of various ions on biological systems has led to intensive studies on the interactions between ions and phospholipid membranes. Salt effects has been widely studied in order to obtain more knowledge. A number of model systems were used: monolayers [632–635], bilayers [583, 588, 636], micelles and liposomes [637–640]. The book from Kunz [575] summarises specific ionic effects divided into different model systems. The reviews from Friedman (2018) [577] and Leontidid (2017) [591] give an overview of current experimental and computational methods that are used to investigate ion/membrane-interactions with corresponding results.

Since biological membranes constitute more than 50 % of zwitterionic lipid species, DPPC and DMPC were used to investigate effects upon salt addition. Any adsorption of cations onto a zwitterionic membrane leads to a positive net charge, this can be measured via zeta-potential measurements and the electrophoretic mobilities [637, 641, 642]. Further, to change the electrostatics of the system, DPPA, an anionic lipid with unique biophysical properties that is important in signalling and promotes curvature in bilayer membranes, was chosen.

As already mentioned, until 1990 the consensus was that multivalent cations (and lithium) interact strongly with zwitterionic phospholipid bilayers, whereas monovalent cations only display weak affinities. The relative binding affinities were generally in agreement with the Hofmeister series [156, 576, 579, 583, 643–647]. These findings have been confirmed and supported by further studies that show that bilayer properties are unaltered upon addition of sub-molar concentrations of monovalent ions like sodium chloride [644, 648, 649]. Since 2000, a different view has evolved indicating much stronger interactions between phospholipids and monovalent cations, especially a strong binding of sodium cations [54, 579, 580, 645–647, 650–654].

At sub-molar concentrations of NaCl in different experimental setups [54, 646, 647, 650–654] and molecular dynamics (MD) simulations [54, 580, 585, 655–659] indications were found, that a strong binding of sodium occurs at phospholipid bilayers. The

publication of Catte et al. clearly shows these discrepancies and attempts to solve the obvious inconsistencies [626]. It was concluded that the current MD simulations are not sufficient for the interpretation of cation/membrane-interactions [626, 628]. Currently, however, there is no consensus in the literature.

Indeed, non-invasive spectroscopic methods generally indicate that Na^+ ions have negligible binding to PC lipid bilayers. In comparison, Ca^{2+} is observed to bind specifically phosphate groups of a few PC molecules [644, 648, 649, 660–664]. A stronger membrane binding of cations is predicted by MD simulations with atomistic resolution [626, 628]. These simulations show varying Na^+ accumulation at the lipid interface [54]. For Ca^{2+} strong bonds with up to four PC lipids at once are reported [580], whereby these interactions are not only limited to the phosphate group [580, 620, 625]. So far, the significant binding of calcium cations to PC bilayer membranes at sub-molar concentrations is agreed in literature [156, 584, 643, 661]. The interpretation of NMR (nuclear magnetic resonance) spectroscopy and scattering experiments, on the contrary, reveal that one calcium cation interacts with two PC headgroups [661, 663–665]. However, the molecular details of the calcium/membrane-interactions are still under debate and despite the previous studies, an understanding on a molecular- or atomistic level is still lacking.

In order to shed more light on the binding of biological important cations, in particular sodium and calcium were investigated with XRR at fully hydrated DMPC bilayers. This study was conducted in cooperation with the University of Helsinki and the experimental results will be combined with state-of-the-art molecular dynamics (MD) simulations. The experimental findings and the development of force fields goes hand-in-hand [666] and further information can help to validate molecular dynamic simulations with improved parameters for the binding of cations. For recent reviews that compare experimental findings and bilayer simulations, see [667, 668] and current state-of-the-art biomembrane simulations and discussion of limitations, see [666, 669].

Calcium and magnesium cations were further shown to enhance the permeability and fusion of lipid membranes [576, 638, 639, 670–672]. Moreover, the main transition temperature increases in dependence of the ion type and concentration of the solution in lamellar model systems [627, 673] as well as in monolayer systems [674]. Frequently also domain formation, phase separation and transient poration of membrane systems upon alkaline and alkaline earth cation addition was reported [117, 674–678].

The binding of ions to lipid membranes seems to be entropy driven due to the expel of hydration shell water molecules of the ions and PC headgroups, since the process is endothermic [579]. Klasczyk et al. used zeta potential measurements and isothermal titration calorimetry (ITC) as well as differential scanning calorimetry (DSC) with PC vesicles and found that the molar enthalpies follow the Hofmeister series. The greatest gain in entropy was facilitated by the smallest ion under consideration. They explained the mechanism of cation/membrane-interaction as “binding-by-dehydration”. Furthermore, various studies have shown that metal cations can cause dehydration of the headgroup and increase the chain melting temperature through ion bridge formation [676, 679–681]. It was reported, that monovalent alkali cations inefficently adsorb at a zwitterionic membrane but adsorb more strongly when negatively charged lipids are

present [620, 636]. Calcium ions have also an affinity to interact with neutral lipids [625].

Le et al. (2019) [627] studied the distribution of Na^+, Ca^{2+}, Mg^{2+} ions in single DMPC model membranes on quartz chips using differential scanning calorimetry, quartz crystal microbalance and computer simulations. Beside the observation of the absence of water molecules in the hydrophobic core of the bilayer, they found an accumulation of ions in the headgroup region indicated by an increased phase transition temperature of the supported membrane. It is believed that this explains the effect of ions on the size of liposomes [576, 648, 682, 683]. An association with Cl^- was not found. The preferred binding sites of the ions regarding to their MD simulations are: Na^+ and Ca^{2+} both bind to the ester moiety, while Mg^{2+} (hydrated) bind to the phosphate. The results for NaCl, however, contradict the assumption of a negligible sodium binding affinity.

Metal ions can also affect the interlamellar water layer in bilayer stacks or multilamellar membranes. A swelling of the interlamellar water layer thickness was observed [588, 648, 684–687]. This effect is curvature independent [688]. Alsop et al. (2016) [689] investigated the effect of the ions of the Hofmeister series on solid-supported DMPC multilayer stacks with x-ray diffraction. They found a swelling of the bilayers that was differently pronounced following the sequence: Fe^{2+}>Mg^{2+}>Ca^{2+}>Zn^{2+}. In the used dehydrated gel phase the thermal fluctuations of the bilayer are suppressed, but sensitivity to subtle hydration events caused by ions is enhanced. However, an increase of the water layer thickness, i.e., an increase in the number of water molecules bound per lipid molecule is explained by the positioning and hydration strength of the present ion. The exact mechanism is not known and different possibilities are proposed by the group. The observation of the increased interlamellar water thicknesses in oriented bilayers and multilamellar vesicles by monovalent ions is explained by a shielding effect of the van der Waals attraction [588, 648, 687].

Garcia-Celma et al. (2007) [576] used for the measurements of currents and the estimation of ion binding a special solid-supported membrane - a hybrid bilayer, consisting of an alkanethiol bound to a gold electrode and a terminating lipid layer. Different lipids were examined. The results showed that cation binding to PC was related to its hydration-free energies (G_{hyd}). They found a reversed Hofmeister-like series [574, 575].

Solid-supported DMPC bilayers prepared via Langmuir-Blodgett were also used in FRAP analysis to reveal the effect and influence of NaCl ionic strength on substrate/bilayer-interactions [647]. However, these effects are highly under debate since an interaction of sodium with the fluorescent dye is suspected [626, 649]. Therefore, surface-sensitive tracer- and dye-free methods with sub-angstrom resolution such as XRR are highly suitable for the investigation of details without side-effects.

Beside Ca^{2+}, Mg^{2+} and Na^+ the monovalent cations Li^+ and Cs^+ were chosen in the framework of this thesis. Lithium, a less common ion, may have significant and important effects on membranes. It is biological very important [690–692]. Lithium has a pharmacological potential in the treatment of maniac-depression and bipolar illnesses [693, 694]. Roux and Bloom found in a deuterium NMR study with POPS and POPC membranes that lithium penetrates the membrane more deeply and changes the structure in a higher degree than sodium, but less pronounced than divalent cations [695].

In a microelectrophoresis study and studies based on zeta potential it was found that lithium has the highest affinity of alkali metals for mixed PC-PG membranes and the highest overall membrane affinity [696, 697]. More information on the interaction of lithium with membranes and the biological significance in several different contexts can be found in Jakobsson et al. [698].

Caesium cations which are weakly hydrated have medical significance. The chemical properties of potassium and caesium are very similar. Caesium ions are slightly hydrophobic compared to potassium ions. A biodistribution of Cs^+ can be observed in the regions of high potassium concentrations (e.g. muscle cells, interior of cells). Potassium channels can serve as entrance to cells, whereas it was also reported that caesium ions inhibit these channels. Therefore, the uptake in cells or even in living bodies has not been resolved and a permeability of Cs^+ across the membrane is assumed [699, 700].

Solid-supported membranes are a convenient model system for biological membranes and are proven in the study of the Hofmeister series. The research performed with solid-supported lipid membranes has given insights into the ion-specific effects and mechanism of the Hofmeister series and are increasingly used in biophysics to study specific ion effects. However, high precision measurements of the structure of bilayers interacting with ions, like it is provided by x-ray reflectivity, is still missing. Accurate and careful measurements between ions and lipid bilayers are also urgently needed for the development and validation of more accurate molecular dynamic simulation starting models. Since the binding mode for calcium ions depends on the concentration [625], different sub-molar and higher concentrations of the salt solutions were applied. In addition, the collected data could be helpful in evaluating the inconsistencies regarding sodium binding to zwitterionic phospholipid bilayers.

2.3.3 The electrical double layer

To understand the ion binding at membranes or surfaces in general, an atomistic picture of the underlying conditions should be considered since the distribution of ions near the solid/liquid-interface is different to that in the bulk phase. Sufficiently far away from the interface in the volume phase, the anions and cations of the electrolyte solution are more or less uniformly distributed. The ions are differently hydrated depending on their nature and charge density. The attractive and repulsive interaction forces of every single charged species are balanced, and the sum of the forces exerted on a particle across space is zero.

In the proximity of the solid/liquid-interface this equilibrium is disturbed in a sensitive manner since the properties of the charged surface are entirely distinct from the bulk. In 1853 Helmholtz developed the first simple model to describe the distribution of near-surface ions and proposed the term *electric double layer* [701]. He assumed that the surface charge is compensated by the redistribution of attracted near-surface counterions and that the interface therefore remains neutral. These counterions build a defined layer. The Helmholtz double layer consists of the aforementioned Helmholtz layer and the oppositely charged surface. It is assumed that the spatial proximity is limited to the ion radius and one single hydration shell. Gouy and Chapman stud-

ied the thermal motion of ions and they introduced the concept of a diffuse region determined by a Boltzmann distribution, the so-called *diffuse double layer* [702, 703]. They considered the ions to be point charges that could reach infinitely close to the substrate. Therefore, the Gouy-Chapman model predicts very high unrealistic surface concentrations. These two models were then further combined by Stern to explain the near-surface ion distribution in a two-layer model. The presented concept also takes the limitation of the Gouy-Chapman model into account by positioning the center of the first ion layer at an average distance from the solid surface [704]. The last compact layer is the Stern layer, which is adjacent to the surface and screens most of the surface charge. The Stern layer in the case of a mixture of ions is divided into the inner and the outer Helmholtz layer with specifically adsorbed ions (inner) and counterions to these inner layer. The potential within this layer is linearly reduced and drops from the Nernst potential Ψ_0 of the charged surface to the Stern potential Ψ_s. Beyond this, the ion distribution based on the Gouy-Chapman picture of the diffuse layer and is determined by the Poisson-Boltzmann equation. These two layers form the two main regions. Further, in an aqueous system water molecules adopt a preferred orientation at the Helmholtz plane, this results in a reduced dielectric permittivity [705].

In the diffuse layer region, the excess ion concentration decays exponentially and asymptotically approaching zero at infinite distance. To eliminate an infinite thickness, the thickness of the electric double layer is defined as the point at which the potential reaches 1/e. It can be calculated with the reciprocal Debye parameter $\varkappa$ of the electrolyte solution [142]

$$1/\kappa = \left[\frac{\epsilon RT}{F^2 \sum_i c_i z_i^2} \right]^{1/2} . \tag{2.17}$$

Here, ϵ is the dielectric constant of the solution, F the Faraday constant, c_i the concentration and z_i the valence of the ions. Figure 2.13 illustrates the electrical double layer with the used notations. In this case, a negatively charged surface and a NaCl solution was used as an example to represent the double layer structure. For the Debye length, see subsection 2.1.2. The adsorption and binding of ions at phospholipid membranes is mostly described by the Gouy-Chapman theory [591, 637, 697, 706]. As already mentioned, the electrochemical potential of the ions in the diffuse layer of the Gouy-Chapman model is described by the Poisson-Boltzmann equation. This mean-field theory operates well at low electrolyte concentrations, but fails above a certain value depending on the electrolyte ($\sim 100\,\mathrm{mM}$). The Poisson-Boltzmann theory has further limitations: finite sizes and discrete nature of the ions are neglected, the surface charge density is assumed to be homogeneous and flat on the molecular scale, to give some examples [142, 707].

The adsorption or binding process is highly complex. Beside the electrostatic forces for a sufficiently description additional repulsion forces due to steric hydration (of the membrane and ions), van der Waals forces and thermodynamic contributions should be considered. In addition, the phase of the membrane and ion key properties for example, should not be neglected. A further important issue is that this model does not consider

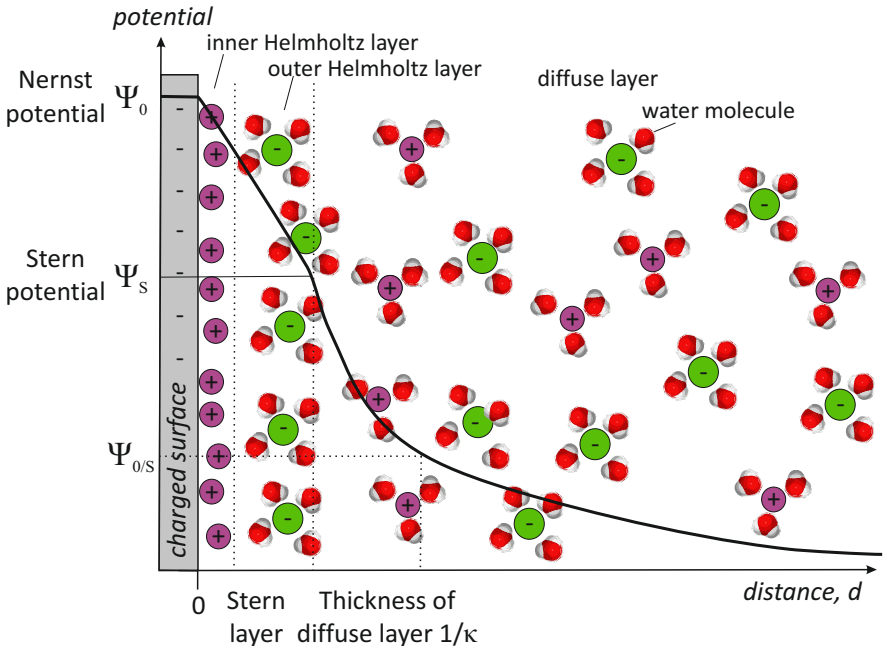

Figure 2.13: Sketch of an electric double layer of a negatively charged surface with adsorbed Na^+ and Cl^- ions with the potential course.

the penetration of ions.

2.4 Proteins

This section describes details of the protein structure and folding. Moreover, the adsorption of proteins at interfaces will be discussed and insights into the mechanistic descriptions will be given. The last part is dedicated to the model proteins applied in this work, lysozyme and bovine serum albumin.

Among the macromolecules of living systems proteins are the most versatile. They have a decisive function in almost all biological processes [708]. An understanding of protein chemistry is of fundamental importance for the entire biochemistry. The elucidation of the structure/function-relationship of proteins is the subject of current research. The primary sequence (amino acid sequence) is encoded as a sequence of the base pairs of DNA (deoxyribonucleic acid) in the genes. Many proteins are further modified co- or posttranslationally. This is the key mechanism to create and to increase the proteomic diversity. The precise amino acid sequence allows the protein to fold into a well-defined three-dimensional structure or conformation. This three-dimensional structure determines their function and specific activity [78, 708]. Proteins perform their functions mainly through protein/protein-interactions, which can also occur in the vicinity of membranes. Despite the variety of tasks, they consist of only 20 different building blocks, the proteinogenic amino acids, which are linked by peptide bonds. A

linear polypeptide chain consisting of less than 100 amino acids is called a polypeptide.

Some proteins primarily have the function of forming defined structures and give the cell form and shape. Further, proteins can be peripherally attached to or integrated in the different membranes of the cell [62, 63]. They form channels and ion pumps with which the flow of nutrients, information and the regulation of these in and out of the cell and the various organelles can be controlled. In addition, specialised proteins act as receptors, antibodies, toxins, hormones, growth factors, enzymes and control cell differentiation. Structural proteins are proteins that primarily serve as scaffolds in tissues or cells. Besides globular proteins and membrane proteins, they form a main class of proteins. These proteins often have no catalytic function, i.e. they do not act as enzymes, but are significantly involved in the formation of fibres, giving cells their shape and tissues their rigidity and elasticity. Enzymes perform almost all of the chemical reactions that occur in cells. They are also involved in translation and transcription processes (DNA/RNA processing). Peptide or protein hormones transmit signals to coordinate biological processes. They are very specific and act on their certain target organ via receptor mediated binding (in or outside the cell). Storage or ligand binding proteins carry atoms and small molecules through cells or the whole organism. Antibodies are large Y-shaped proteins used by the immune system to identify and neutralise pathogens (or antigens).

Before the explanation of the classical theory, the following passage first summarises the recently gained knowledge of protein structure and folding. Over the last two decades, progress in biochemistry, biophysical and molecular dynamic techniques has revealed a multitude of deviations from the "one sequence $\rightarrow$ one structure $\rightarrow$ one function" paradigm [709]. In terms of structure, there are indications of so-called metamorphic proteins. These are single amino acid sequences, which can occupy different folded conformations with similar Gibbs energies in the native environment and changes (rate of $\sim 1\,\mathrm{s}^{-1}$) reversibly between these structures [709–713]. The term was coined by Murzin in 2008 to describe this findings [714]. Furthermore, a structural plasticity of protein sequences could be shown in NMR-based and molecular modelling studies. Indeed, this intrinsic flexibility is necessary to accomplish the protein's function [715, 716]. The description of the native conformation, therefore, also contains the internal dynamics and a certain flexibility. So-called "intrinsically unstructured or disordered regions" in proteins or peptides are surprisingly common, especially in functional proteins [717–720]. These unordered structures gives the proteins the ability to interact with many different targets, and to adopt multiple conformations upon binding in dependence of the binding event [721, 722]. Furthermore, it becomes clear that so-called "molten globules", a term commonly used in the context of protein folding [723, 724], are important for some vital cell functions [725–727]. Hence it is not absolutely necessary for a protein to adopt an overall defined structure in order to perform its function(s) [721]. It can be stated, that these two basic principles, spontaneously folded domains and intrinsically disordered regions, represent the two functional building blocks [709, 720].

2.4.1 Protein structure and folding

As discussed above, a protein does not have a statically fixed form. It is conformationally flexible. A rigid form would impede different active states, the regulatory function and the substrate conversion. Protein structures can be regarded on four organisation levels and are divided into primary, secondary, tertiary and quaternary structures.

The primary structure is the amino acid sequence of a polypeptide chain. Usually there are 20 types of amino acid side chains in proteins, which differ in size, shape, ability to form hydrogen bridge bonds, hydrophobic character and chemical reactivity. They determine the physicochemical properties of the protein. The amino acids have a central carbon atom (α-carbon). The amine (-NH_2) and carboxyl (-COOH) functional groups accompanied by a side chain (-R) unique to each amino acid, are bound to the α-carbon. The carbon atom is thus chiral. A peptide bond, or amide bond, is formed by the reaction of the carboxyl group of one amino acid with the amino group of another, causing the release of water. Peptide bonds have a planar *trans*-configuration due to their double bond character, thus, the number of conformations is limited [598]. The N-C_α and C_α-C bonds can rotate, the resulting bond angles are called Φ and Ψ. The spatial arrangement of a protein or peptide is created by interactions between the individual atoms of the polypeptide scaffold and bonds between the amino acid side chains.

The secondary structure is the composition of the protein from particularly frequently occurring motives for the spatial arrangement of the amino acids, without considering the side groups. The structures are stabilised by hydrogen bonds. Since the secondary structures are local, different secondary structures can be present in the same protein molecule. A distinction is made between the following structure types: α-helix, β-sheet (parallel or anti-parallel) and turns. By turns and loops (ω-loops, hairpin-bend, multiple turns, linker) the secondary structure elements are connected and a direction change of the polypeptide chain can be induced.

In contrast to the α-helix structure the β-sheet structure is flat and the polypeptide chain is almost stretched. There are also mixed β-sheets with parallel and antiparallel sequences. Proteins that play a role in lipid metabolism are almost exclusively composed of this structural motif. The tertiary structure is the overall arrangement of a protein. The tertiary structure is stabilised by non-covalent interactions, mainly by the formation of a hydrophobic core. Disulfide bridges connect areas of the sequence covalently that are distant from each other and give the structure additional stability. In addition, hydrogen bonds, salt bridges, van der Waals and ionic interactions play an important role. The protein continues to fold through these bonds and interactions. The quaternary structure is constituted by several polypeptide chains or protein molecules, usually referred to in this context as subunits, which operate as a single protein complex [78, 598].

Despite their molecular diversity, all proteins have the same ability to quickly and spontaneously fold into a well-defined spatial structure that is crucial for their specific function. Protein folding is a highly cooperative process. Other temporary thermodynamically unstable transition states exist between the stable native state and the unfolded state. The determination and existence of the transitions as well as their in-

termediates with respect to the structure and the conditions under which they occur is an intensive research field. Protein folding is achieved by progressive stabilisation of the intermediate products. The basic principle is therefore a cumulative selection in which partially correctly folded intermediates are retained, and not a random testing (Levinthal's paradoxon) [728, 729]).

In-vitro studies showed that protein folding takes place within milliseconds [730]. The development of novel experimental techniques for measuring in the ms to ns range and with higher resolution enabled to obtain more detailed information about the various intermediates, their conformations and kinetics [731–736]. Furthermore, molecular dynamic simulations allowed better interpretation of the experimentally obtained data [737, 738]. With the obtained data, different mechanistic models for protein folding [739–741] and also mixed models [742–744] were postulated. The protein folding process can be illustrated using a funnel-shaped potential energy surface, a so-called folding funnel [729]. The driving force in this process is the decrease of free enthalpy. The height of the folding funnel reflects the energy of the folding protein, while the lateral expansion at this energy level indicates the entropy of the system [729, 745]. The unfolded states are characterised by a high degree of conformational entropy and a high free enthalpy. Pits at the edge of the folding funnel represent metastable intermediate products. On the way along the funnel the protein can adopt less and less alternative conformations and the entropy of the system reduces. The correct native structure is formed at the lowest point of the funnel. The native state of proteins can be determined well by high-resolution methods such as x-ray crystallography or NMR spectroscopy [746–749].

The metastable intermediate structures on the way to the correct native conformation can also initiate protein aggregation [729, 750, 751]. The folding intermediates expose hydrophobic regions. Through intermolecular interactions, which compete with intramolecular interactions, insoluble protein aggregates [729, 752, 753] are formed via different intermediate stages. Similar to the intramolecular folding, the aggregation pathway is driven by hydrophobic forces. Amyloid fibrils are the most thermodynamically stable form [729, 753]. *In-vivo*, these anomalies and the loss of the functional structure can cause protein misfolding diseases, so-called amyloidosis.

2.4.2 Protein adsorption at interfaces

Almost two decades ago, Nakanishi et al. has described the phenomena when a protein adsorbs to a solid interface as "[...] a common but very complicated phenomenon" [754]. Proteins and polypeptides are intrinsically surface-active and tend to adsorb and accumulate at interfaces. The understanding of protein/interface-interactions is fundamental for a broad spectrum of research areas, such as biology, biotechnology, pharmacology and medicine. The process of the protein adsorption has implications in diverse fields, for example in the design of biocomparable medical implants and surgical tools, tissue engineering, drug discovery and delivery, biofouling, biosensors, food industry and immunological assays [755, 756]. It also plays an important role in the economic field [757].

In-vivo, proteins interact with lipid membranes of different compartments, these

interactions are highly specific and relevant for the proper performance of biological processes. Complex interactions between proteins and membranes or protein/protein-interactions can take place at membranes. For example, blood coagulation or energy conversion as well as signal transmission events are membrane-associated processes. Another important aspect of protein adsorption is the aggregation of proteins. They can aggregate at the membrane and thus hinder signal transduction [758, 759] and other important cellular processes [760–762].

By diffusion, Brown molecular motion and far-reaching interaction forces the protein approaches the surface [763]. Adsorption of proteins results in a concentration gradient. According to Fick's first law, the particle current density J is proportional to the concentration gradient against the diffusion direction. The proportional constant is the diffusion coefficient D

$$J = -D\frac{\partial c}{\partial z}. \tag{2.18}$$

According to the Stokes-Einstein relation, D is proportional to the root mean square velocity μ of the particles, which depends on the temperature T, the viscosity of the fluid η and the size of the particles R_0

$$D = \frac{k_\mathrm{B}T}{6\pi\eta R_0}. \tag{2.19}$$

The diffusion coefficient for biological materials normally ranges from 10^{-11} to $10^{-10}\,\mathrm{m^2/s}$. For example, lysozyme and BSA have diffusion coefficients in water ($T = 298.15\,\mathrm{K}$) of about $1.28 \cdot 10^{-10}\,\mathrm{m^2/s}$ and $0.72 \cdot 10^{-10}\,\mathrm{m^2/s}$ [764].

Different types of interactions and factors can result in an attraction or repulsion of the protein from the surface. The interactions and driving forces that facilitate protein adsorption have been discussed by many authors [765–769].

Thermodynamic approach According to the current state of research, surface activity and, thus, protein adsorption results from a variety of direct and indirect causes and cannot be determined by a structural element of the protein. Independent of the mechanism and kinetics of the adsorption process, protein adsorption can only occur when the free Gibbs energy ΔG_ads of the system decreases, provided that temperature and pressure are constant [765]. This includes enthalpic (ΔH_ads) and entropic (ΔS_ads) contributions. The relationship is given by

$$\Delta G_\mathrm{ads} = \Delta H_\mathrm{ads} - T \cdot \Delta S_\mathrm{ads} < 0. \tag{2.20}$$

The lower the free Gibbs energy ΔG_ads is, the more stable is the system and the more likely a protein adsorbed at the interface. In addition, entropy ($\Delta S_\mathrm{ads} > 0$) can be increased or enthalpy ($\Delta H_\mathrm{ads} < 0$) reduced at constant pressure and temperature.

Protein adsorption relies on different intermolecular surface interaction forces acting between the surface and the proteins. In a simplified approach, the energetic contributions consist of enthalpic effects of protein/protein-interaction and protein/surface-interactions as well as the entropic contribution of adsorption with respect to the

(de)solvation entropy. For example, adsorption results in entropy loss due to loss of the translational and rotational degree of freedom of the protein; conformational entropy can also be considered here. The desolvation enthalpy of protein and surface as well as the corresponding entropies and the entropy contribution of the released water are also considered. During the adsorption process, the free Gibbs energy is composed of a multitude of interactions. Interactions that can lead to a reduction in enthalpy and, thus, to adsorption are the van der Waals interaction and the electrostatic interaction between the proteins and between the proteins and the surface [769]. The most important interaction forces are the hydrophobic interaction, electrostatic or Coloumb interactions and van der Waals interactions. The actual binding energies of the interactions mentioned above vary strongly.

Due to the amphoteric character of the proteins, the electrostatic interaction depends sensitively on the charge distribution of the protein surface, which in turn depends on the pH-value. Furthermore, there may be a shielding effect by counterions which causes a repulsion. In fact, an entropy gain from the detachment of adsorbed water molecules and ions from the surface, which is due to the hydrophobic effect and the conformational change during adsorption of the protein [769–771], is often described as the driving force of protein adsorption. The Gibbs fundamental equation considers the system in a state of equilibrium. By calculating the energy minimum of the free energy, equilibrium models of adsorption can be assumed taking into account conditions, such as pH-value, ionic strength, temperature, surface condition and protein structure. The result is the access to adsorption isotherms or other specific information [772, 773].

Kinetic approach Kinetic models consider the process of adsorption and desorption of a protein at an interface. It is assumed that a thermodynamic equilibrium between free and bound phase is established. The models are determined partly on the basis of physical considerations, but also empirically. The aim of the models is to find a relationship between the concentration of the respective component in the bulk and adsorbed phase. The simplest and yet most common model was designed by Langmuir in 1918 [774]. The Langmuir model is based on the basic assumption that equivalent and equidistant adsorption sites are present on the surface, that there is no interaction potential between the proteins and that the adsorbed proteins are laterally immobile but can desorb again. The change of the surface coverage Γ over time t depends on the kinetic rate constants of the adsorption k_{ad} and the desorption k_{de}, the concentration at the interface $\mathrm{c_g}$ and the maximum coverage Γ_{max}

$$\frac{\partial \Gamma}{\partial t} = k_{\mathrm{ad}} \cdot \mathrm{c_g} \left(1 - \frac{\Gamma}{\Gamma_{\mathrm{max}}}\right) - k_{\mathrm{de}} \cdot \Gamma. \tag{2.21}$$

The degree of coverage at $\Gamma = \Gamma_{\mathrm{max}} = 1$ reaches a saturation value corresponding to a completely filled monomolecular adsorption layer. For spherical objects in a hexagonal densest package, this value is about 91 % [763].

One of the major weaknesses of the Langmuir model was overcome with the development of the random sequential adsorption (RSA) model. In this model, the proteins can adsorb to any random site on the surface. The maximum possible coverage of the

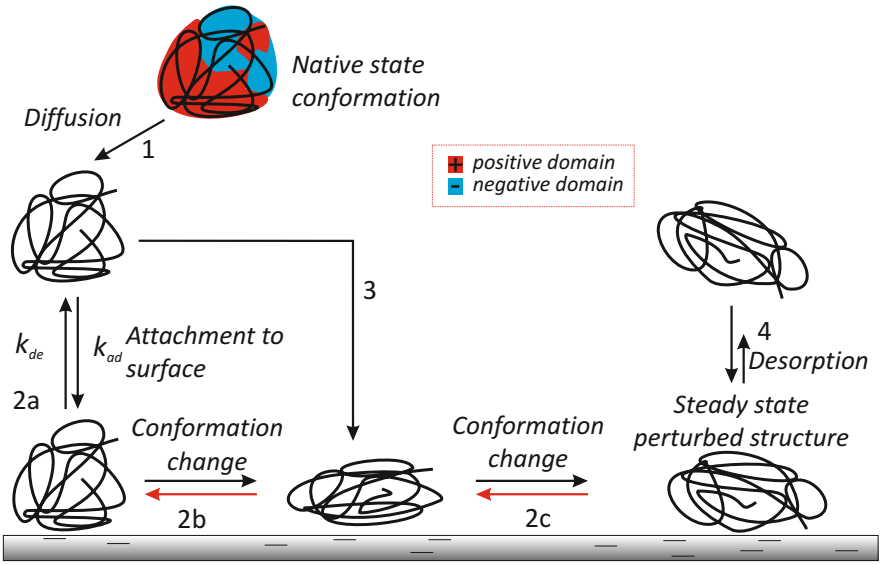

Figure 2.14: Schematic representation of protein adsorption. Shown is the Langmuir model (1, 2a), the two-state model (1, 2a, 3, excl. red arrow) and the multiple-state model (1, 2a, 2b, 2c, incl. red arrows). Structural arrangements through increased interaction points and alterations of protein's secondary and tertiary structure. This occurs frequently at hydrophobic interfaces. Adapted from Norde et al. [777].

RSA model is 55 % [775]. Further extensions of the model, considering different desorbtion events, diffusion and structural rearrangements can be found in Schaaf et al. [776]. Another model, the two-state model, takes into account the observation that proteins only desorb apparently from the surface after rinsing with protein-free buffer solution. The model is shown in figure 2.14. Since proteins are flexible macromolecules that can undergo conformational changes intrinsically or by influencing interaction potentials, the inclusion of different conformational states in an adsorption model is realistic. The model indicates two possible reaction pathways, whereby the protein can either adsorb in the native conformation (2a) and a conformational change follows (2b) or it carries out the structural transformation directly during adsorption (3) [777]. The ability of desorption is almost lost after structural transformation, since the protein can denature on the surface and is thus irreversibly bound. For unfolded proteins this is less probable than for native state conformations due to a high number of interaction sites with the surface and a higher binding stability after protein unfolding. An extension of this kinetic model is the multiple-state model, where several conformations are possible depending on the surface affinity. This is illustrated in the figure by the pathway (2c) [778].

A large number of models have been postulated for the adsorption kinetics of proteins. Different factors were taken into account and various assumptions were used,

e.g., overshoot phenomena, different conformational states that can be occupied during or before the adsorption process, the interaction of proteins with each other and the formation of clusters on the surface [779]. Each model describes with its characteristic adsorption curve the degree of coverage as a function of time, taking into account the adsorption and desorption rate. The review article by Rabe et al. provides an overview of the generally used models [763].

The adsorption kinetic is often measured by the amount of adsorbed protein per surface area Γ, as a measure for the strength of adsorption over the time t. Popular methods are SPR-(surface plasmon resonance) ([780]), CD-(circular dichroism) [781] and ATR-IR-(attenuated total reflection infrared) spectroscopy [782, 783], as these can be used label-free. As a surface-sensitive method, x-ray reflectivity provides insights to the adopted surface structure of the protein at the binding process and access to the mass density.

2.4.3 Model proteins

This paragraph gives a brief overview of the proteins, that served as model proteins in this thesis. Further details on the structural properties which are relevant for the data interpretation are summarised in chapter 4.1.

Lysozyme, muramidase Lysozyme, a well-known single-chain protein (129 aa) has emerged as a model for investigations on protein structure and function since its discovery by Fleming in 1922 [771, 784].

In mammals, the antimicrobial enzyme occurs in many secretions, such as tear fluid, saliva, respiratory secretions, blood serum, cerebrospinal fluid, amniotic fluid, cervical mucus, milk and in professional phagocytes, including macrophages, neutrophils and dendric cells. At mucosal surfaces it can reach concentrations of 1 mg/ml [786–788]. Lysozyme is also found in phagocyte-like cells in non-mammalian organisms indicating that lysozyme plays a conserved role in host defence throughout the animal kingdom [786, 788, 789]. All lysozymes have a similar overall structure (figure 2.15) and share the ability to hydrolyse the bacterial wall consisting of peptidoglycan. The tertiary structure, the protein folding and the function of hen egg-white lysozyme are nearly identical to those of human lysozyme [790]. Hen egg-white lysozyme can therefore serve as suitable model protein for the study of protein aggregation in the context of developing a deeper understanding of lysozyme amyloidosis. The adsorption of lysozyme onto liquid or solid interfaces and the formation into amyloid fibrils is in the focus of current research.

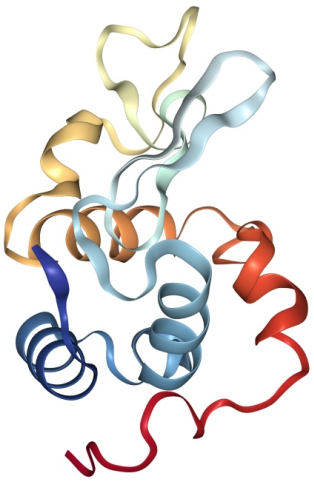

Figure 2.15: Hen egg-white lysozyme structure at ambient pressure. PDB entry 1GXV [785].

In-vitro, different conditions were studied which induce the fibrillation of hen egg-white lysozyme. Due to the abundant knowledge about lysozyme and its *in-vitro* aggregation behaviour it is an ideal model protein for the study of amyloidogenesis [790–792]. An aggregation of lysozyme at anionic and neutral phospholipid membranes was observed. *In-vitro* the protein clustering close to membranes can lead to (proto)fibrillar structures [793–795]. On the contrary, the function of lysozyme, including its antimicrobial, antitumor and immunemodulatory activities, has been suggested to be linked with its lipid binding properties [793, 796, 797]. Since lysozyme bears positive charges over a broad range of pH-values, it has an intrinsic affinity for anionic phospholipids [798, 799]. Further investigations of partially unfolded states and native conformations are also of interest, since protein-rich clusters may act as precursors of amyloid fibrils [800–802]. Apart of the aggregation of lysozyme in solution or at membranes, a mutation in the LYZ gene leads to a rare hereditary form of amyloidosis in humans [803, 804]. Human lysozyme has semi-disordered regions (residues 39-52 and 67-75) [805] which were also detected in a partially unfolded state via H/D exchange (residues 36-102) [806] and within the cross-β-sheet fibril core (residues 32-108) [807]. The adsorption behaviour in contact with perfluorocarbons under lipid monolayers or at the bare water interface was not investigated so far. It might be possible to influence the protein adsorption by perfluorocarbon treatment and prevent self-aggregation.

A low surface tension of the tear film of the eye is essential for its function. It consists of salts, lysozyme, mucins and other proteins [808]. At high surface tensions, the clinical condition called “dry eye” can occur [809]. The interaction and penetration behaviour of lysozyme and other proteins of the tear fluid, mucin and lactoferrin, at the meibomian phospholipid monolayer causes this condition which is not completely understood [810–814]. Other causes, in particular evaporation and dysfunction of the meibomian gland are intensively discussed [815]. In addition to the perfluorocarbons used in ophthalmology, there are freely available semifluorinated eye drops [816]. An entirely perfluorocarbon-based drug for the treatment of dry eye is currently in phase III clinical trials (May 2020) [817, 818].

Although lysozyme is one of the best studied proteins, its adsorption behaviour and the resulting structures at hydrophobic liquid/gas-interfaces is still controversial.

Serum albumins (BSA and HSA) Further, serum albumin protein of cows and humans were used as model proteins. Serum albumins are the most abundant blood proteins of mammals and were recognised as a major component already in 1839 [819]. In healthy humans, the protein contributes to approx. 50 % to the total plasma protein pool (0.6 mM or 5 g/ml [820, 821]). Serum albumins are large globular proteins with a high α-helical content. They are the smallest, water soluble monomeric blood proteins. They contribute to the colloid osmotic pressure (80 %), regulate the pH-value of the blood, and operate as plasma carrier for different substances by non-specific reversible binding. It has binding capacity for substances as water, Ca^{2+}, Na^{+}, K^{+}, and for less polar substances, such as fatty acids, several hydrophobic steroid hormones, bilirubin and various drugs. It plays an important role for the transport and deposition of endogenous and exogenous substances [820, 822–827]. Moreover, serum album catalyses

a variety of different reactions [828–831]. It is also able to bind free radicals via the free Cys-34 thiol group, this is characterised by a high antioxidant activity [832–834].

Another novel function is the chaperon-like activity (anti-aggregatory and anti-amyloid properties) of BSA at physiological levels and conditions and in the presence of divalent cations (Ca^{2+}, Cu^{2+}). It inhibits the aggregation and amyloid formation of wild-type and (mutation variant) of L55P transthyretin [835], but also the fibril formation and aggregation of amyloid-β by binding [836–838] and insulin [839]. Further, under non-physiological conditions BSA and HSA are able to form well-ordered β-sheet rich aggregate structures which do not correspond to the common cross-β structures. BSA still has a α-helical core and lack of cytotoxicity [840, 841]. The fibrillation of HSA was also observed [842]. The polymorphism and the universality of the fibrillation mechanism are also underlined by the mosaic structures of well-known aggregation-prone peptides [843–845].

Serum albumin is the most known multifunctional transport protein and performs multiple functional roles that seem otherwise unrelated. It is a so-called moonlighting protein [709, 846]. Therefore, it is difficult to categorise albumins. They seem to be proteins with "catalytic promiscuity" [847]. A large majority of the known binding sites of serum albumin are characterised by a "dual personality" with ordered and flexible/unordered residues. The intrinsic disordered regions are related to the functions of this important serum protein [848]. Further information of the gene locus, the expression rate, lifetime in the blood, related diseases, processing and degradation are found in references [821, 849, 850].

The serum albumin molecule is structured in three homologous domains I-III, see figure 2.16. Each domain consists of two subdomains (A and B). The domains are not topologically identical, but have very similar 3D structures. The disulfid bonds stabilise the domain structures. The secondary structure of HSA and BSA is mainly α-helical (67 %), where the remaining polypeptide chain occurs alternately and in extended or flexible regions between the subdomains. Thereby, β-sheets are not described. Furthermore, HSA and BSA are the only plasma proteins that are not glycosylated under physiological conditions, due to the absence of the tripeptide Asn-X-Ser/Thr (X: any amino acid except proline) which is necessary for recognition by an oligosaccharyltransferase, and it further does not carry any prosthetic groups.

The primary sequence of the serum albumins is well-known [851, 852]. Akdogan et al. quantitatively compare structural identities in the crystal state of BSA and HSA in their ligand-free form (PDB entry (BSA) 3V03 [851] and PDB entry (HSA) 1BM0 [853]) [854]. The structures were aligned with the MUSTANG algorithm. The results show a root mean square of 1.361 Å and a sequence identity of 75.52 % over 572 aligned residues (76 % for the whole primary sequence [820, 821]). There are two regions showing the significant differences between HSA and BSA both localised on the subdomain IB. BSA thus serves as good model for the human variant since it has similar biological functions and structure. Further, due to the lack of prosthetic groups or carbohydrates it is very stable and can be produced at low costs.

The ability of albumin to undergo major reversible conformational changes or isomerisation processes upon changing the microenvironment, for example the pH-value.

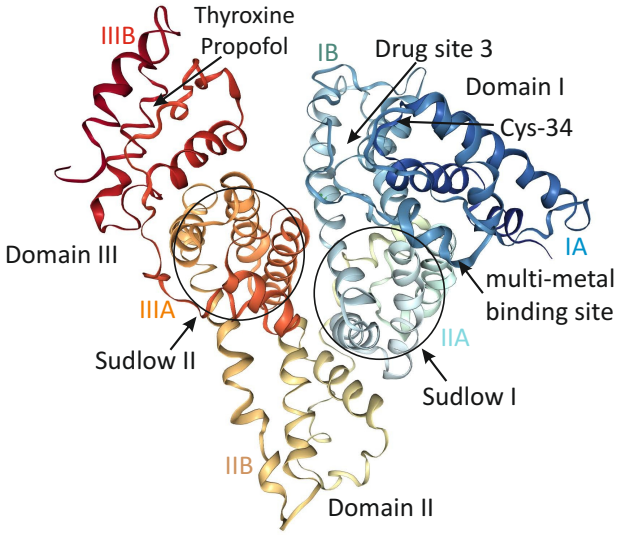

Figure 2.16: Crystal structure of ligand-free HSA, PDB entry 1UOR [855] with the representation of domains, subdomains and Sudlow's binding sites I and II. Albumin has two major binding sites (drug binding via Sudlow I and II [856–858]) and other sites like Cys-34 (free thiol) and metal ion binding sites [856, 859]. The binding sites for metal ions are isolated from the Sudlow sites [860, 861]; fatty acid binding sites may overlap with the Sudlow sites [862, 863]. Examples of the binding sites for endogenous and exogenous ligands for which crystal structures have been solved and predicted binding is summarised in [864] and [827].

This was first demonstrated by Luetscher in 1939 [865]. The transitions occur at pH 2.7, 4.3, 8 and 10. Early works describe the conformational structure of albumin in solutions with neutral pH based on a variety of experimental methods [866–873] as a prolate ellipsoid or partially expanded cigar-shaped structure (later referred to "F"-isoform). Foster characterised the different forms [874, 875]. With the designation "N" for a normal form, which is predominately at a neutral pH-value. Later, this conformation was also called the heart-shaped form. The dimensions are commonly approximated as 30 Å thick equilateral triangle with an edge length of 80 Å [855, 859, 876]. The cigar-shaped model is still commonly used and persisted as occupied form at neutral pH-values [877–879]. The majority of the contemporary evidence pointed to the heart-shaped structure and several research groups demonstrated that the spherical molecule has the dimensions of around 80 Å [880–883]. These observations could only be interpreted by the heart-shaped structure, which was determined from x-ray crystallographic data of HSA [820, 855]. In the meantime, x-ray structure data are also available for BSA and a heart-shaped structure has been demonstrated for example in PDB file 3V03 [851].

Two additional conformations can be observed with decreasing pH-value of the solution, the N-form at neutral pH is followed by the "F"-(fast migrating) form, this cigar-shaped structure ($140 \times 40 \times 35$ Å^3 [821, 866, 884]) is produced abruptly in aque-

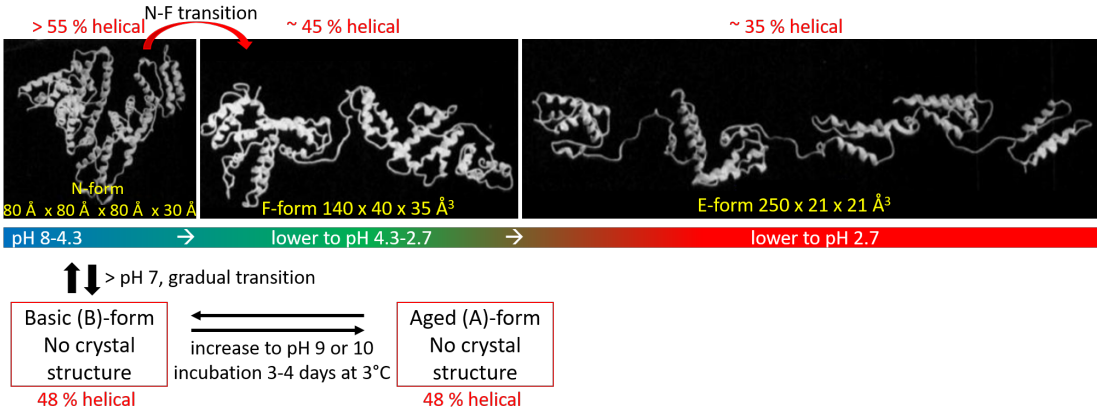

Figure 2.17: Diagram of the five conformational forms of the BSA molecule. The (confirmed) crystal structure of the N-conformer and the proposed configurations, as ribbon diagrams of the F- and E-forms, from [820, 882, 898, 899] are shown. The well-known structural transitions are reversible.

ous environment with pH-values below 4. The "E"-(expanded) form occurs at pH-values less than 2.7 with the dimensions 250 x 21 x 21 $Å^3$. The "B"-(basic) form occurs at pH-values above 8 and an "A"-(aged) form is present with time at pH-values higher than 8.0 [874]. The five forms adopt different content of α-helices, β-sheets and other structural motifs. The expanded form (35 % - 50 % α-helix content) of BSA corresponds to the fully extended dimensions of the protein allowed by the disulfid bonds [820, 885]. The multiple conformations of BSA are shown in figure 2.17. During the N→F-isoform transition BSA and HSA pass the isoelectric point. The net charge of BSA changes from -18 to +100 from pH-value of 7.4 to 3.5 [885–889]. The transition is associated with unfolding of domain III (C-terminus) with remaining intact domains I and II [876, 890–892]. This F-form is less compact, longer and coupled with a decrease in helical content [893, 894]. During the F→E transition all six subdomains separate from the compact structure and the protein denaturates and changes into the fully extended E-isoform. A high α-helical content could be still observed [892]. The described transformations also occur for HSA [885, 895, 896]. Moreover, conformational changes occur within the adsorption of BSA to surfaces. This can be explained by the low conformational stability [897].

As mentioned above, the folding of BSA and HSA is very sensitive to the microenvironment. Therefore, pH-value dependent experiments in the range of pH 3 - 9 of the adsorption behaviour to DPPA-films were conducted. Furthermore, the influence of the BSA ligand $MgCl_2$ was examined. Since DPPA's protonation state is sensitive to the pH-value, the change of the electrostatic properties of the monolayer has to be considered. Serum albumin is the major circulatory protein involved in the handling of Ca^{2+} and Mg^{2+} in mammals controlling the "biologically active" levels of these metals in the blood [821, 851, 885]. The interactions between metal complexes with serum albumin can result in disrupting the disulfide bonds which can lead to a partial loss of α-helix conformation with the subsequent unfolding of the protein [900–903].

The interaction of metal ions with serum albumins is of biomedical and physiological importance and have been intensely studied [861, 904–906]. They are still under debate. However, the study of the adsorption behaviour of BSA at different pH-values on DPPA-films with the influence of ions is still lacking.

Chapter 3

Basic principles of experimental methods: Surface-sensitive x-ray scattering

The aim of this thesis is to resolve molecular processes at interfaces, in particular, the interaction of thin lipid films with gases, ions and proteins. This is realised by the application of x-ray scattering techniques. Hard x-ray radiation has a wavelength of $\sim 1\,\text{Å}$, therefore it is suited to resolve objects at an atomic length scale. Due to its high transmission through, e.g., aqueous environments it is able to provide insight into the structure of buried interfaces. Moreover, the occurrence of external total reflection enables to achieve low penetration depth and, thus, high surface-sensitivity.

In the following chapter the theoretical background of the most common *in-situ* surface-sensitive x-ray scattering and diffraction techniques are presented. X-ray reflectivity (XRR) and grazing-incidence x-ray diffraction (GIXD) became essential characterisation working tools for determining structures, properties and processes at interfaces on the atomic length scale. GIXD provides information on the lateral organisation, including lattice constants, mean crystallite size, length of the lipid molecules, molecular tilt angles, and tilt directions. XRR yields a laterally averaged electron density profile along the surface normal. The electron density profile can subsequently be interpreted to acquire information about interfacial structure, including molecular arrangements and ionic distributions. By combining XRR and GIXD it is possible to obtain a complete molecular picture of the sample system *in-situ* under near physiological conditions.

First, in section 3.1 the scattering geometry for XRR and GIXD will be introduced. The basic principles of the methods are discussed in section 3.2 and 3.3. The theory of the x-ray reflectivity technique is based on the textbooks: *X-Ray Scattering from Soft-Matter Thin Films, Materials Science Basic Research* by Metin Tolan [907] and *Elements of modern X-ray physics* of J. Als-Nielsen and D. McMorrow [908]. For a detailed and complete description of the surface-sensitive x-ray scattering techniques, the reader is referred to the textbooks and literature [909–914].

3.1 Scattering geometry

The following section deals with the geometry of XRR and GIXD. A sketch of the scattering layout is shown in figure 3.1.

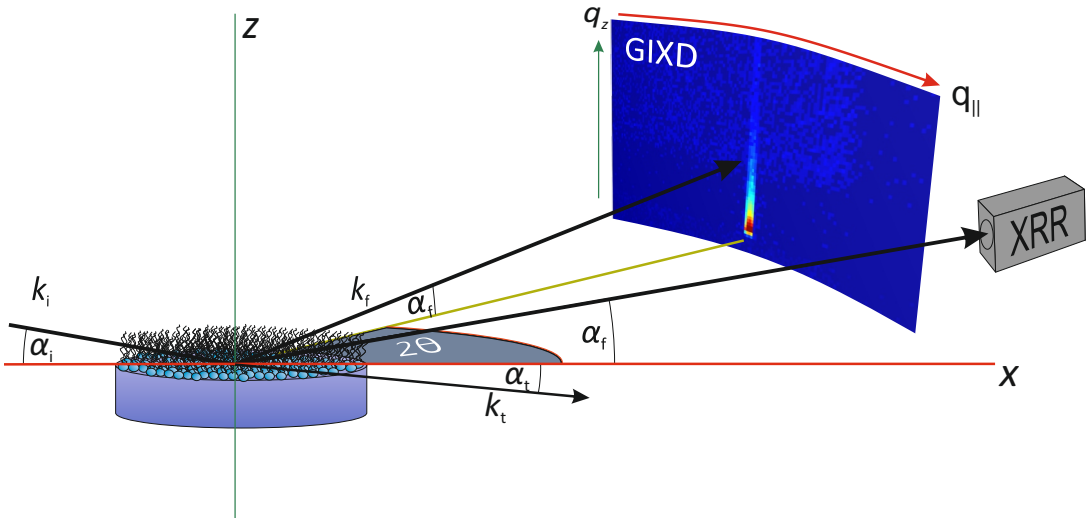

Figure 3.1: Geometry for XRR ($\alpha_i = \alpha_f$, $2\theta = 0$) and GIXD ($\alpha_i < \alpha_c$, $2\theta \neq 0$) experiments.

An incoming x-ray beam hits the sample surface under an angle α_i and is scattered under a vertical angle α_f and a horizontal angle 2θ into the volume above the surface. A part of the x-ray beam is refracted into the medium under an angle α_t. The incoming, scattered and transmitted components are described by plane waves $\vec{E}_i(\vec{k}_i)$, $\vec{E}_f(\vec{k}_f)$, $\vec{E}_t(\vec{k}_t)$ with the wave vectors $\vec{k}_i$, $\vec{k}_f$ and $\vec{k}_t$, respectively. In the following only the elastic scattering is considered, meaning that the wavelength λ is preserved. Therefore, the absolute value of the wave vectors $|\vec{k}_i| = |\vec{k}_f| = k = 2\pi/\lambda$ is constant, only the direction of the radiation changes. In x-ray scattering experiments the scattered intensity is detected as a function of the wave vector transfer $\vec{q} = \vec{k}_f - \vec{k}_i$.

From the scattering geometry sketched in figure 3.1, the wave vector transfer can be written as

$$\vec{q} = \frac{2\pi}{\lambda} \begin{pmatrix} \cos(\alpha_f)\ \cos(2\theta) - \cos(\alpha_i) \\ \sin(\alpha_f)\ \sin(2\theta) \\ \sin(\alpha_i) + \sin(\alpha_f) \end{pmatrix}. \tag{3.1}$$

In XRR experiments, the specular reflected intensity is detected. Therefore, the incident angle α_i, and the vertical exit angle α_f are equal while the horizontal angle of deflection 2θ is zero ($\alpha_i = \alpha_f$ and $2\theta = 0$). The expression 3.1 simplifies to

$$\vec{q}_{XRR} = \begin{pmatrix} q_x \\ q_y \\ q_z \end{pmatrix} = \frac{4\pi}{\lambda} \begin{pmatrix} 0 \\ 0 \\ \sin(\alpha_i) \end{pmatrix}. \tag{3.2}$$

Only the wave vector transfer perpendicular to the sample surface is not equal to zero

and consequently, XRR measurements only give information about the vertical electron density distribution.

In GIXD experiments, the x-ray beam hits the surface under grazing incidence with a shallow incidence angle α_i (see figure 3.1). The horizontal angle of deflection 2θ differs from zero. If for a first approximation $\alpha_\mathrm{i} = \alpha_\mathrm{f} \approx 0$ is assumed, the wave vector transfer has only lateral components

$$\vec{q}_\mathrm{GIXD} = \begin{pmatrix} q_x \\ q_y \\ 0 \end{pmatrix} \approx \frac{2\pi}{\lambda} \begin{pmatrix} \cos(2\theta) - 1 \\ \sin(2\theta) \\ 0 \end{pmatrix} \tag{3.3}$$

which can be summarised as

$$\begin{aligned} |\vec{q}_\parallel| = |\vec{q}_\mathrm{GIXD}| &= \sqrt{q_x^2 + q_y^2} \\ &= \frac{2\pi}{\lambda} \sqrt{(\cos(\alpha_\mathrm{f})\cos(2\theta) - \cos(\alpha_\mathrm{i}))^2 + (\cos(\alpha_\mathrm{i})\sin(2\theta))^2} \\ &\approx \frac{4\pi}{\lambda} \sin(\theta). \end{aligned} \tag{3.4}$$

Therefore, GIXD probes the lateral structure of the sample. The incident beam in GIXD experiments is kept below the critical angle for total reflection to enhance the sensitivity to surface scattering. In case of lipid samples, many crystallites with statistically distributed orientations contribute to the scattering pattern and can be considered as 2D powder samples.

Depending on the interest of information, the optimal scattering geometry must be selected. By combining the GIXD and XRR methods, the structure of Langmuir films can be precisely characterised[1].

3.2 X-ray reflectivity (XRR)

In the following, the theoretical basics of XRR are briefly explained. Starting from the Fresnel reflectivity of ideally smooth surfaces the reflectivity of multilayer systems will be discussed, the so-called "effective-density model". In an x-ray reflectivity measurement one significant parameter is the index of refraction n of the sample. The medium composed of N atoms per unit volume can be described as harmonic oscillators which are stimulated by an electromagnetic wave with the frequency ω and the respective resonance frequencies ω_j, the refractive index is then calculated by the Drude-Lorentz model as

$$n^2(\vec{r}) = 1 + N\frac{e^2}{\epsilon_0 m_e} \sum_{j=1}^{N} \frac{f_j}{\omega_j^2 - \omega^2 - 2\mathrm{i}\omega\eta_j}, \tag{3.5}$$

the factors f_i describe the forced oscillation strength of each single atom and η_j are damping factors. The elementary charge is denoted as e, the electron mass as m_e and

[1] Grazing incidence x-ray diffraction experiments have also been successfully performed at solid-supported lipid systems [915–918].

the electric field constant is ϵ_0. The oscillation strength f_j is essentially a complex expression

$$f_j = f_j^0 + f_j'(\omega) + \mathrm{i}f_j''(\omega). \tag{3.6}$$

The energy-dependent dispersion and absorption correction are taken into account by the $f_j'(\omega)$ and $f_j''(\omega)$. In the hard x-ray regime, the frequencies of the radiation are much larger than the resonance frequencies of the system ($\omega \gg \omega_j$). By taking the scattering geometry into account, i.e. shallow incidence angles, equation (3.6) simplifies to

$$n = 1 - \delta + \mathrm{i}\beta. \tag{3.7}$$

The real part describes the dispersion $\delta = \frac{\lambda^2}{2\pi} r_e \rho$, with the classical electron radius r_e and the electron density ρ, while the imaginary part represents the absorption $\beta = \frac{\lambda}{4\pi}\mu$ with the energy- and material-dependent linear absorption coefficient μ. The dispersion is in a range of 10^{-5} - 10^{-7} for the discussed systems. Since the real part of the refractive index $\Re(n)$ is smaller than one for x-rays, the refractive index n is smaller than the refractive index of vacuum, implying that x-rays undergo total external reflection. This is a peculiarity of x-rays, compared to visible light.

Total external reflection occurs below a critical angle ($\alpha_\mathrm{i} \leq \alpha_\mathrm{c}$). For the relationship between incident and transmitted beam the Snell's law of refraction applies. Since the absorption β is typically much smaller than δ ($\beta \ll \delta$), the critical angle can be approximated as

$$\alpha_\mathrm{c} \cong \sqrt{2\delta} = \lambda\sqrt{\frac{r_e\rho}{\lambda}}. \tag{3.8}$$

For $\alpha_\mathrm{i} < \alpha_\mathrm{c}$ the wave field penetrates only a few nm into the sample and an exponentially decaying wave, a so-called evanescent wave propagates parallel to the surface. With a penetration depth of

$$\Lambda = \frac{\lambda}{\sqrt{2\pi}}\left\{\sqrt{(\alpha_\mathrm{i}^2 - \alpha_\mathrm{c}^2)^2 + 4\beta^2} - (\alpha_\mathrm{i}^2 - \alpha_\mathrm{c}^2)\right\}^{-1/2} = \frac{1}{2k_\mathrm{i}\Im(\alpha_\mathrm{t})} \tag{3.9}$$

the wave field inflates into the medium. The penetration depth of x-rays with incident angles $\alpha_\mathrm{i} \to 0$ tends to $\Lambda_0 = \lambda/(2\pi\alpha_\mathrm{c}) = 1/\sqrt{4\pi r_e\rho}$ and gets independent of the wavelength. For the most materials Λ_0 is around 50 Å, the scattering derives with this very shallow angles from the near-surface area of the sample.

3.2.1 Smooth surfaces and multiple interfaces

The scattering at smooth surfaces can be described by the Fresnel formulas[2]

$$r = \frac{k_{\mathrm{i},z} - k_{\mathrm{t},z}}{k_{\mathrm{i},z} + k_{\mathrm{t},z}}, \quad t = \frac{2k_{\mathrm{i},z}}{k_{\mathrm{i},z} + k_{\mathrm{t},z}}, \tag{3.10}$$

with $k_{\mathrm{i},z} = k\sin(\alpha_\mathrm{i})$ and $k_{\mathrm{t},z} = kn\sin(\alpha_\mathrm{t})$.

[2]In the case of x-rays, p- and s- polarised waves differ only by the factor n^2 and are practically the same. Therefore, no distinction is made in this thesis.

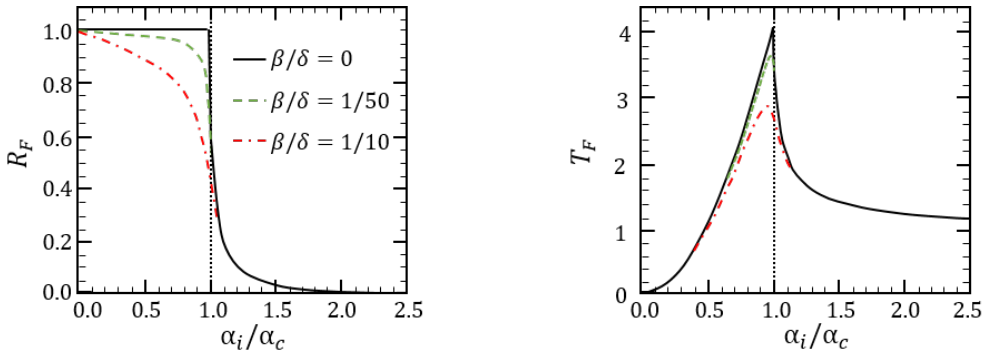

(a) Fresnel reflectivity R_F.

(b) Fresnel transmission T_F.

Figure 3.2: Fresnel reflectivity (a) and Fresnel transmission (b) of a silicon/vacuum-interface with different absorption/dispersion (β/δ) ratios with $\lambda = 1.54\,\text{Å}$.

Considering Snell's law $k_{\mathrm{t},z} = k\sqrt{n_2^2 - \cos^2(\alpha_\mathrm{i})}$ follows. The z component of the corresponding wave vector is described by the index z. The Fresnel reflectivity results from the square of the reflection coefficient as $R_\mathrm{F} = |r^2|$. Figure 3.2a and 3.2b shows the Fresnel reflectivity (R_F) and the square of the transmission function ($|t|^2$, Fresnel transmission T_F), respectively.

The incident angle α_i is normalised by the critical angle α_c. The Fresnel transmission function 3.2b shows a maximum at $\alpha_\mathrm{i} \approx \alpha_\mathrm{c}$ (depending on the absorption β), which can be explained by constructive interference of the reflected and transmitted waves increasing the amplitude by a factor of two. It approaches unity for higher angles. The figure 3.2a shows that the reflected intensity below the critical angle is equal to one (plateau of total external reflection). Above the critical angle the intensity decreases strongly (see also figure 3.4b). For $\alpha_\mathrm{i} > 3\alpha_\mathrm{c}$ the Fresnel reflectivity can be approximated by $R_\mathrm{F} \approx (q_{\mathrm{c},z}/2q_{\mathrm{i},z})^4$, or $R_\mathrm{F} \approx (\alpha_\mathrm{c}/2\alpha_\mathrm{i})^4$. X-ray reflectivity measurements therefore are generally shown on logarithmic scales. The recorded reflectivity data are often normalised to R_F in order to highlight even small changes (compare figure 3.4a and 3.4b).

So far, only the reflectivity of an single surface has been considered. However, sample systems usually consist of a substrate and one or more additional layers. In this case, multiple scattering of the electromagnetic wave at the different interfaces occurs. The components interfere and, thus, modulate the reflected signal. From the scattering of two interfaces in a distance d oscillations arise in the reflectivity curve, the so-called "Kiessig-Fringes" [919], also to be seen in figure 3.4a and 3.4b. The thickness d of the included layer can be calculated considering the oscillation period via

$$d = \frac{2\pi}{\Delta q_z} \approx \frac{\lambda}{2\Delta\alpha_\mathrm{i}}, \tag{3.11}$$

here Δq_z and $\Delta\alpha_\mathrm{i}$ are the distances of two subsequent minima.

Parratt published a method in 1954 which is commonly known as recursive Parratt's algorithm to describe the reflectivity of a system consisting of arbitrary number of layers

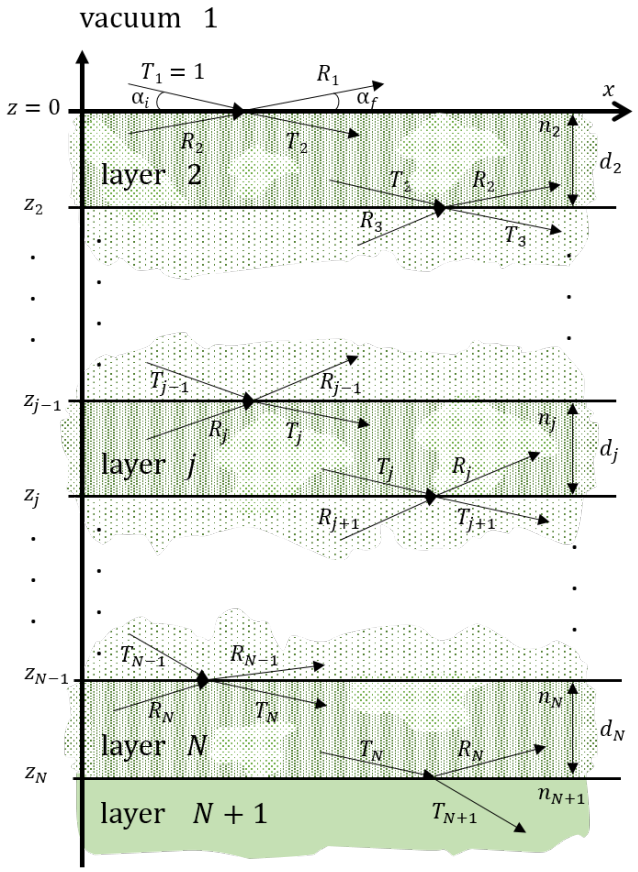

Figure 3.3: Sketch of a multilayer stack with $N+1$ layer and N interfaces. Each layer has a thickness of d_j and a refractive index of n_j. The incident radiation is reflected (R_1) and transmitted (T_1) at the first interface. This applies analogously to all other transmitted beams at the lower layers, except for T_{N+1}. Picture based on Tolan (1999) [907].

[920]. The basic situation is shown in figure 3.3.

The vacuum counts as "layer 1", the semi-infinite substrate counts as "layer $N+1$" with an overlying layer with the last interface at $z = z_N$. Every layer has a different refractive index n_j with the thickness d_j. The reflectivity of a multilayer system thus can be computed via

$$X_j = \frac{R_j}{T_j} = \exp(-2ik_{z,j}z_j)\frac{r_{j,j+1} + X_{j+1}\,\exp(2\mathrm{i}k_{z,j+1}z_j)}{1 + r_{j,j+1}X_{j+1}\,\exp(2\mathrm{i}k_{z,j+1}z_j)} \tag{3.12}$$

for the X_j-th layer, when X_{j+1} is known.
The Fresnel coefficient of layer j is given as (compare with equation (3.10))

$$r_{j,j+1} = \frac{k_{z,j} - k_{z,j+1}}{k_{z,j} + k_{z,j+1}}, \tag{3.13}$$

where $k_{z,j} = k(n_j^2 - \cos^2\alpha_\mathrm{i})^{1/2}$ is the z component in the layer j. The substrate is

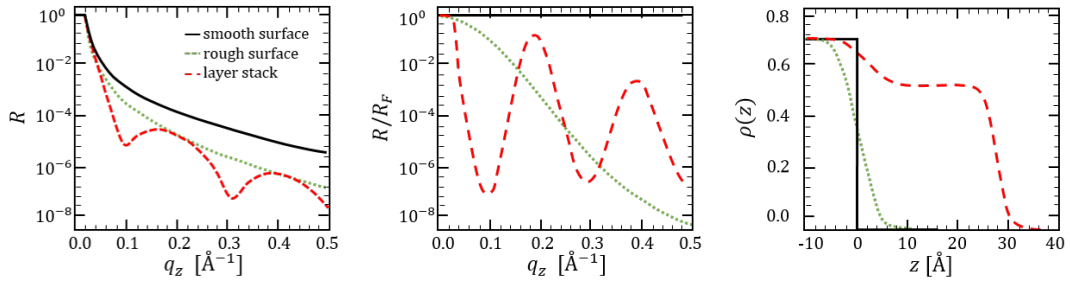

(a) Normalised R. **(b)** Fresnel normalised R. **(c)** Electron density profiles.

Figure 3.4: X-ray reflectivity curves (a) calculated from the corresponding electron density profiles (c) with the additional Fresnel normalised representation (b) for a better visualisation of small changes. The black curve represents the Fresnel reflectivity of a silicon/air-interface. The same interface with roughness (5 Å) is shown in green. An extra layer with a thickness of 30 Å is added on top and shown in red.

assumed to be much thicker than the penetration depth of x-rays (see equation (3.9)), consequently there is no reflected component in the substrate, i.e. it is possible to begin the recursion at the bottom with the starting conditions: $R_{N+1} = X_{N+1} = 0$.

3.2.2 Real interfaces and Effective-density model

Up to this point, the reflectivity of ideally sharp and smooth interfaces has been discussed. In reality, especially in biological systems, the assumption of ideally smooth boundaries is not appropriate. Instead, every interface has a finite roughness σ. Therefore, the specular reflected intensity is damped in comparison to the Fresnel reflectivity. The difference of the Fresnel reflectivity and the reflectivity of a rough interface can be seen in figure 3.4a.

Since, the wave vector transfer $\vec{q}$ has only a component in z direction, the refractive index of a rough surface is laterally averaged over (x, y) as $n_j(z) = \int\int n_j(x, y, z)\mathrm{d}y\ \mathrm{d}x$ yielding a continuous variation of the refractive index $n(z)$. To describe the refractive index transition of a rough layer at position z_j, the mean height function at the coordinates z_{j+z} is weighted with a probability density function $P_j(z)$. This results in a rms ("root-mean-square") roughness of the boundary of

$$\sigma_j^2 = \int (z - \mu_j)^2 P_j(z)\mathrm{d}z \tag{3.14}$$

with the mean value of the probability distribution $\mu_j = \int z\ P_j(z)\mathrm{d}z$.
Taking the roughness into account, a layer system can be described by using Parratt formalism under consideration of modified Fresnel coefficients

$$\tilde{r}_{j+1,j} = \frac{f_j(k_{z,j+1} + k_{z,j})}{f_j(k_{z,j+1} - k_{z,j})} r_{j+1,j} \tag{3.15}$$

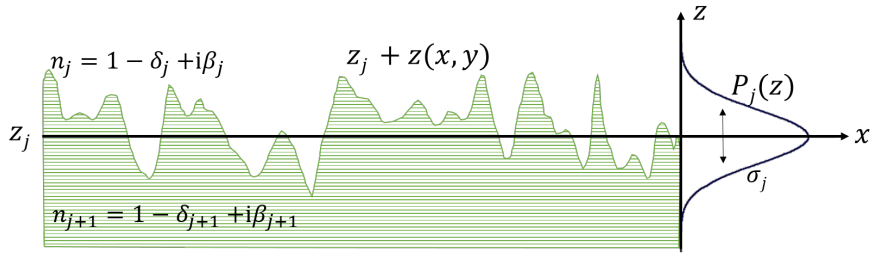

Figure 3.5: Sketch of a rough surface. The average height is z_j. The height function $z(x,y)$ describes the fluctuations around z_j. The interface is substituted by a set of smooth surfaces with the probability density function $P_j(z)$ at coordinates $z_j + z$. Picture is redrawn from Tolan (1999) [907].

$$\tilde{t}_{j+1,j} = \frac{1}{f_j(k_{z,j+1} - k_{z,j})} t_{j+1,j}, \tag{3.16}$$

with the expected value[3] $f_j(k)$ of the rms roughness regarding to $P_j(z)$

$$\begin{aligned} f_j(k) &= \Big\langle \exp\{-ik(z-\mu_j)\} \Big\rangle_{P_j(z)} \\ &= \exp(ik\mu_j) \int \exp(ikz)\ P_j(z) dz. \end{aligned} \tag{3.17}$$

The choice of the probability density $P_j(z)$ determines the course of the refractive index at an interface, for example between the layer j and $j+1$, a continuous refractive index $n_j(z)$

$$n_j(z) = \frac{n_j + n_{j+1}}{2} - \frac{n_j - n_{j+1}}{2} \mathrm{erf}\left(\frac{z - z_j}{\sqrt{2}\sigma_j}\right) \tag{3.18}$$

with the error-function $\mathrm{erf}(z) = \frac{2}{\sqrt{2\pi}\sigma_j} \int_0^z \exp(-t^2) dt$ corresponds to a Gaussian probability distribution, see also figure 3.5,

$$P_j(z) = \frac{1}{\sqrt{2\pi}\sigma_j} \exp\left(-\frac{z^2}{2\sigma_j^2}\right) \tag{3.19}$$

and finally resulting in the modified Fresnel coefficients

$$\tilde{r}_{j+1,j} = r_{j,j+1} \exp(-2\ k_{z,j} k_{z,j+1} \sigma_j^2), \tag{3.20}$$

$$\tilde{t}_{j+1,j} = t_{j,j+1} \exp\left\{(k_{z,j} - k_{z,j+1})^2 \sigma_j^2 / 2\right\}. \tag{3.21}$$

Since $|r|^2$ is the Fresnel reflectivity of a smooth surface, equation (3.20) describes the reflectivity of a rough surface with

$$R(q_z) = R_\mathrm{F}(q_z)\ \exp\{-q_z^2 \sigma^2\}. \tag{3.22}$$

[3]The function $f_j(k)$ for real k-values is the Fourier transform of $P_j(z)$.

Roughness thus causes an exponential decrease in reflectivity. The exponential decrease of the reflected intensity with $-q_z^2$ on a rough surface is the result of the special case of the erf function profile, as represented in equation (3.18). In many cases equation (3.18) can be successfully applied further to describe a refractive index transition at a rough interface.

There are functions beside the erf function described in the literature that work well with other systems. In the case of liquid/vapour-interfaces [921] and a component between two immiscible polymers [922, 923] the refractive index follows a hyperbolic tangent function. An improvement is to replace $\tanh(z)$ by $\sqrt{2}\tanh(z/2)/[3-\tanh^2(z/2)]^{1/2}$ [924]. Some soft-matter interfaces, especially vapour/liquid-interfaces, seem to be asymmetric and can be described with modified tanh profile [925, 926]. The refractive index profiles of the erf and tanh function and the respective probability densities are very similar and the differences are always being less than 5 %.

Using the Parratt algorithm with the modified Fresnel coefficients the dispersion profiles for multilayer systems with rough interfaces can be calculated for the measured reflectivity curve. However, it only applies for the conditions $\sigma_j \ll d_j$, i.e. otherwise the transitions regions of the refractive index at different heights overlap and the layers cannot be treated as independent. For systems with the conditions $\sigma_j \approx d_j$, for example oxide layers or complex biological systems such as peptide adsorbate at membranes, the Parratt algorithm leads to discontinuous dispersion profiles, also shown in figure 3.6a. Within the j-th layer, the assigned refractive index n_j is not reached, the density profile becomes discontinuous. The assumption of independent layers is invalid. Nevertheless, a simple parametrisation of the complete dispersion profile, which is still based on the layer structure, is possible through the introduction of the so-called "effective-density model". In the first step, an initial continuous density profile based on freely adjustable parameters, the thickness, the roughness and the dispersion, that have to be refined later is guessed. By an odd function $Y_j(z)$ which is ± 1 for $z \to \pm\infty$ a continuous transition between the layers is implemented. In this thesis $Y_j(z) = \mathrm{erf}\left(\frac{z}{\sqrt{2}\sigma_j}\right)$ is utilised. Using the connection points

$$\zeta_j = \frac{\sigma_j z_{j-1} + \sigma_{j-1} z_j}{\sigma_j + \sigma_{j-1}} \tag{3.23}$$

the fraction of material j at position z can be determined as

$$W_j(z) = \begin{cases} \frac{1}{2}\left(1 + Y_j(z - z_j)\right) & \text{for } z \le \zeta_j, \\ \frac{1}{2}\left(1 - Y_j(z - z_{j-1})\right) & \text{for } z > \zeta_j. \end{cases} \tag{3.24}$$

This produces the dispersion profile

$$\delta(z) = \left(\sum_{j=1}^{N+1} \delta_j W_j(z)\right) \Bigg/ \left(\sum_{j=1}^{N+1} W_j(z)\right). \tag{3.25}$$

In the following the "primary-profile" is subdivided into many very thin discrete layers with the thickness ε_j and the uniform density δ_j with sharp interfaces, as sketched in

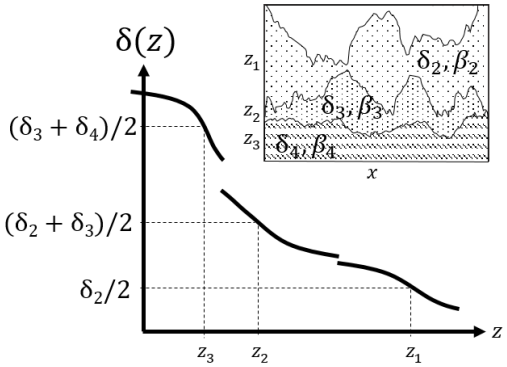

(a) Layer stack with large roughnesses, $d_j \approx \sigma_j$, and associated discontinuous dispersion profile. The layers were treated independently with approximation of tanh functions and individual rms roughnesses.

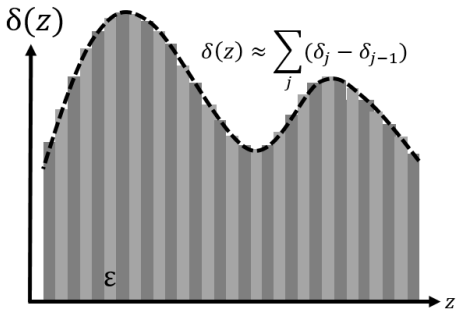

(b) Initial guessed continuous dispersion profile is (dashed line) sliced into thin layers ε with the thickness d, sharp interfaces and constant δ_j. The Parratt formalism is applicable with $\delta(z) \approx \sum_j (\delta_j - \delta_{j-1})$.

Figure 3.6: (a) Layer stack with large roughnesses $d_j \approx \sigma_j$ and associated dispersion profile. (b) The density profile in the effective-density model, which assures a continuous density profile, also with large interface roughnesses. Based on Tolan (1999) [907].

figure 3.6b. The Parratt algorithm can be applied to the resulting layer system. In the context of the effective-density model the density profile at a selected depth z is to be understood as the "effective density at depth z". More information and mathematical details can be found in [907]. The program LSFit [927] was utilised to evaluate the data in this thesis, it uses the recursive Parratt algorithm in association with the "effective-density model".

A more comprehensive approach for the calculation of reflectivities is offered by the kinematical or (first-order) Born approximation [907, 910]. The kinematic approximation is valid for the range where the scattering cross section for the scattered radiation is small. Here, only single scattering processes are considered and multiple scattering events can be neglected. Therefore, the approximation is not exact near the critical angle and is sufficiently well at angles $\alpha_\mathrm{i} > 3\alpha_\mathrm{c}$. Since the q_z range in an experiment is limited, the resulting electron density profile is not unambiguous. By using the kinematic approximation, the reflectivity can be expressed as the Fourier transformed of the change of the electron density profile with

$$R(q_z) = R_\mathrm{F}(q_z)\left|\frac{1}{\Delta\rho}\int \frac{\mathrm{d}\rho(z)}{\mathrm{d}z}\exp(\mathrm{i}q_z z)\mathrm{d}z\right|^2 . \tag{3.26}$$

Equation (3.26) contains the Fresnel reflectivity R_F for an ideally smooth substrate, the electron density contrast $\Delta\rho$ between the substrate and the surrounding medium, and the changes in electron density $\rho(z)$ perpendicular to the surface.

As seen in this section, laterally averaged electron density profiles, with roughnesses, thicknesses and electron density differences of samples, i.e. multilayer and buried in-

terfaces can be determined by means of XRR without any tracer or marker with sub-angstrom resolution. In order to obtain a comprehensive molecular picture of the samples, it is necessary to combine different techniques to gain detailed insights, e.g. into the lateral structure. One method to receive information about the sample's lateral structure is the GIXD technique, which is discussed in the next section.

3.3 Grazing-incidence x-ray diffraction (GIXD)

The following section briefly describes the grazing-incidence x-ray diffraction (GIXD) technique, used in this work as the second surface-sensitive x-ray scattering method for the investigation of the influence of gas molecules on the structural behaviour of *in-vitro* biomimetic membranes. The first GIXD measurements of compressed lipid monolayers at liquid/vapour-interfaces were carried out by two research groups in 1987 [928, 929]. It is a well-suited tool for the structural investigation of soft thin films on liquid subphases and solid surfaces.

Grazing-incidence x-ray diffraction relies on combining Bragg scattering with the surface-sensitivity of using very small incident angles in the region of the critical angle [930, 931]. The incident angle is adjusted in the range of 60 % - 80 % of the value of the critical angle. With equation (3.9), a typically penetration depth of about 50 Å results, which is close to the thickness of a lipid monolayer [907, 932].

Compressed lipid Langmuir films form two-dimensional crystals (see section 2.1.1). They are composed of randomly oriented crystallites, hence they can be treated as a "2D powder". This implies, that the Bragg condition is always fulfilled. Due to the lack of vertical containment Bragg reflections occur as Bragg rods. The scattering of a lipid film arranged as a 2D lattice, that is defined by $\vec{r}_G = m_1\vec{r}_1 + m_2\vec{r}_2$, with $m_{1,2} \in \mathbb{Z}$, is given by two key factors: the geometrical structure factor [172]

$$S_G(q_\parallel) = \sum_{\vec{r}_G} \exp(-\mathrm{i}\vec{q}\cdot\vec{r}_G) \tag{3.27}$$

which contains the information of the 2D lattice structure and the molecular form factor

$$f(q_\parallel, q_z) = \int_{Lipid} d^3r \rho_e(\vec{r}_G + \vec{r}) \exp(-\mathrm{i}\vec{q}\cdot\vec{r}) \tag{3.28}$$

which describes the scattering of a single lipid based on its electron density distribution.

The geometrical structure factor depends only on $q_\parallel$. This does not apply for the molecular form factor, as the alignment of the lipids modulates also the vertical scattering intensity.

In this thesis the response of DPPA-films to g- and vFCs was investigated with GIXD. Special attention was paid to the influence of the gas on the formation and destruction of the crystalline structures of the Langmuir film. Due to the small headgroups of this lipid, no tilting of the alkyl chains above surface pressures of 15 mN/m is observed [109, 933]. Moreover, the dense gas phase decreased the signal-to-noise ratio. Therefore, it was not possible to resolve the q_z dependence of the Bragg rods. Hence,

the further explanations focus on the determination of lattice parameters and not of the alignment of the lipid molecules in the unit cell. The extraction of the 2D unit cell parameter and the 2D crystallite size are considered separately in the following subsections. The observed intensity distributions are derived from the periodic formation of the tailgroups. Until now no diffraction pattern has been observed by the headgroup itself [928, 934]. For further descriptions, including detailed discussion of the influence of the molecular form factor, please refer to the following literature [229, 911, 913, 914, 935–943] and detailed reviews [944–947].

3.3.1 2D unit cell of a Langmuir film

Equation (3.27) shows, that the geometrical structure factor becomes maximal and reflexes in the scattering patterns appears if the argument of the exponential function corresponds to a multiple of 2π. This is the case for wave vector transfers that are integer linear combinations of vectors $\vec{g}_i$ that are defined by $\vec{r}_i \cdot \vec{g}_j = 2\pi\delta_{ij}$. This is equivalent to the Laue condition $\vec{q} = \vec{G}_{hk}$ [948] with the reciprocal lattice vector $\vec{G}_{hk} = h\vec{g}_1 + k\vec{g}_2$ (h, $k \in \mathbb{Z}$) and the Miller indices h and k. The geometric structure factor, equation (3.27), is then given by

$$S_{G_{hk}} = \sum_{m_1,m_2} \exp(-\mathrm{i}2\pi(hm_1 + km_2)). \tag{3.29}$$

A simple geometric approach which yields the same scattering angles for constructive interference as the Laue condition is provided by the Bragg condition $m\lambda = 2d\sin(\theta)$ with $m \in \mathbb{Z}$ [949]. The situation is illustrated in figure 3.7a.

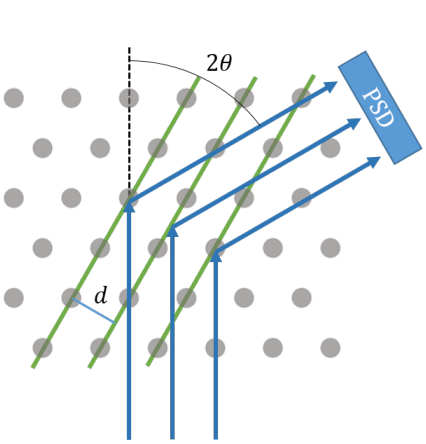

(a) Bragg reflection at a surface.

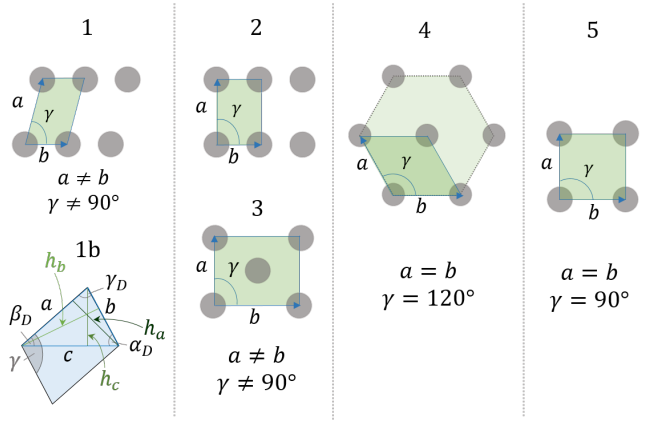

(b) Bravais lattices: oblique (1), unit cell (1b), rectangular (2), centered rectangular (3), hexagonal (4), square (5).

Figure 3.7: Scattering at a two-dimensional lattice under Bragg conditions with a position sensitive detector (PSD). Scheme of the five two-dimensional Bravais lattices and the primitive unit cell of an oblique lattice (1b).

Taking equation (3.4) into account, the wave vector transfer $q_\parallel$ can be directly linked to the spacings d of the lattice planes involved in the scattering process

$$d = \frac{m\lambda}{2\sin(\theta)} \approx \frac{2\pi}{q_\parallel}. \tag{3.30}$$

The lattices that fill a two-dimensional space with periodically recurring units without leaving gaps or overlaps are called Bravais lattices. There are five of them in two dimension, see also 3.7b. The square, rectangular, oblique and hexagonal lattice are primitive ones, the centered rectangular is the only not primitive.

The unit cell can be described geometrically by a parallelogram spanned by the lattice vectors $\vec{a}$ and $\vec{b}$. The sketch 3.7b shows the primitive unit cell of an oblique cell (blue) which has the lowest symmetry and is the most universal one, because it is defined by $a \neq b$ and $\gamma \neq 90°$ and is therefore not subject to any restriction of the grid vectors $\vec{a}$, $\vec{b}$ and the grid angle γ. As a consequence of the limited number of grid types, it is possible to calculate the parameters of the unit cell using only the lowest order Bragg peak positions. These corresponds to a spacing that is given by heights h_a, h_b and h_c (green) of the triangle spanned from sides a and b, with

$$h_i = \frac{2\pi}{q_{\parallel,i}}. \tag{3.31}$$

With the relationships between the edges and heights

$$\sin(\alpha_D) = \frac{h_c}{b} = \frac{h_b}{c} \tag{3.32}$$

$$\sin(\beta_D) = \frac{h_a}{c} = \frac{h_c}{a} \tag{3.33}$$

$$\sin(\gamma_D) = \frac{h_b}{a} = \frac{h_a}{b} \tag{3.34}$$

and the crystallographic conventions $q_{\parallel,a} \leqslant q_{\parallel,b} \leqslant q_{\parallel,c}$ it is possible to calculate the angle α_D

$$\begin{aligned} \alpha_D =& \arccos\left[\frac{h_c}{2h_b} + \frac{h_b}{2h_c} - \frac{h_b h_c}{2h_a^2}\right] \\ \Leftrightarrow \alpha_D =& \arccos\left[\frac{1}{q_{\parallel,b}}\left(\frac{q_{\parallel,b}^2}{2} + \frac{q_{\parallel,c}^2}{2} - \frac{q_{\parallel,a}^2}{2}\right)\right] \end{aligned} \tag{3.35}$$

as a function of the horizontal components of the wave vector transfers $\vec{q}$ of the Bragg reflexes in the scattering pattern. The angle between the vectors $\vec{a}$ and $\vec{b}$ are further connected by

$$\gamma = \alpha_D + \beta_D = 180 - \gamma_D. \tag{3.36}$$

Moreover, it is possible to calculate the area A of the two-dimensional unit cell via

$$A = ah_a = \frac{4\pi^2}{q_{\parallel,b} q_{\parallel,c} \sin(\alpha_D)}. \tag{3.37}$$

and thus determine the area per lipid molecule.

3.3.2 2D crystallite size of a Langmuir film

In the previous section it was shown that information about the shape of the unit cell can be obtained from the positions of the Bragg reflexes. The intensity distribution along $q_\parallel$, i.e. the shape of the Bragg reflexes will be investigated in more detail.

In the experiment, reflections with small wave vector transfers are investigated. The potentially observable reflexes are therefore the reflexes with large distances between the lattice planes with the Miller indices for the oblique lattice (the low order reflections are) (0,1), (0,$\bar{1}$) (first reflection), (1,0),($\bar{1}$,0) (second reflection) and (1,$\bar{1}$), ($\bar{1}$,1) (third reflection).

If one consider the geometrical structure factor, see equation (3.29), for the reflection at the net plane set ($\bar{1}$,0),

$$S_{G_{\bar{1},0}} = \sum_{m_1,m_2} \exp(-\mathrm{i}2\pi(-1m_1 + 0m_2)) = \sum_{m_1} \exp(\mathrm{i}2\pi m_1) \tag{3.38}$$

it depends only on the lattice vectors $\vec{r}_G = m_1\vec{r}_1$ in the direction of the primitive lattice vector $\vec{r}_1$. The intensity distribution of the ($\bar{1}$,0) reflection can be analysed in dependence of the parallel component of the wave vector transfer $q_\parallel$ using equation (3.27)

$$S_{G_{\bar{1},0}} = \sum_{r_G} \exp(-\mathrm{i}\vec{q}\cdot\vec{r}_G) = \sum_{m_1}^{M_1-1} \exp(-\mathrm{i}m_1 q_\parallel h_b) \tag{3.39}$$

with the lattice spacing h_b. Thus, the geometrical structure factor becomes dependent from the number of lattice planes which are involved in the scattering M_1. When scattered at M_1 lattice planes for small-size crystallites as they appear in polycrystalline Langmuir films the structure factor results in

$$S_{G_{\bar{1},0}} = \frac{1-\exp(-\mathrm{i}h_b M_1 q_\parallel)}{1-\exp(-\mathrm{i}h_b q_\parallel)} \tag{3.40}$$

and the scattered intensity using equation (3.4) yields in

$$\begin{aligned} I_{G_{\bar{1},0}}(\theta) \propto \left|S_{G_{\bar{1},0}}\right|^2 =& \frac{\sin^2\left(M_1\frac{h_b q_\parallel}{2}\right)}{\sin^2\left(\frac{h_b q_\parallel}{2}\right)} \\ =& \frac{\sin^2(M_1 h_b \frac{2\pi}{\lambda}\sin\theta)}{\sin^2(h_b\frac{2\pi}{\lambda}\sin\theta)}. \end{aligned} \tag{3.41}$$

This function becomes maximal for $h_b\frac{2\pi}{\lambda}\sin\theta_{\bar{1},0} = n\pi$ with $n\pi \in \mathbb{Z}$ with respect to the Bragg condition. By developing around the maximal value $\theta_{\bar{1},0}$ with $\sin(\theta_{\bar{1},0}+\vartheta) = \sin(\theta_{\bar{1},0} + \vartheta\cos(\theta_{\bar{1},0})$ the following intensity distribution around the maxima results

$$\begin{aligned} I(\theta_{\bar{1},0}+\vartheta) &\propto \frac{\sin^2[M_1 h_b\frac{2\pi}{\lambda}(\sin(\theta_{\bar{1},0}) + \vartheta\cos(\theta_{\bar{1},0}))]}{\sin^2[h_b\frac{2\pi}{\lambda}(\sin(\theta_{\bar{1},0}) + \cos(\theta_{\bar{1},0}))]} \\ &\propto \frac{\sin^2[M_1 h_b\frac{2\pi}{\lambda}\vartheta\cos(\theta_{\bar{1},0})]}{\sin^2[h_b\frac{2\pi}{\lambda}\vartheta\cos(\theta_{\bar{1},0})]} \end{aligned} \tag{3.42}$$

with the full width at half maximum (FWHM)

$$2\vartheta_{1/2} = \frac{0.444\lambda}{M_1 h_b \cos(\theta_{\bar{1},0})}. \tag{3.43}$$

At the experiment, the angle is defined with respect to the incident beam and not to the lattice plane. Therefore, the intensity maxima are found at $2\theta_{\bar{1},0}$ and the intensity fall by half at $2\vartheta_{1/2}$. For the measured half width of the ($\bar{1}$,0)-reflex in the experiment thus results in

$$\mathrm{FWHM}_{\bar{1},0} = 4\vartheta_{1/2} = \frac{0.888\lambda}{M_1 h_b \cos(\theta_{\bar{1},0})}. \tag{3.44}$$

Thus, the half width $\mathrm{FWHM}_{\bar{1},0}$ provides information about the size $L_{\bar{1},0}$ of the crystallites perpendicular to the ($\bar{1}$,0)-lattice planes

$$L_{\bar{1},0} = M_1 h_b = \frac{0.888\lambda}{\mathrm{FWHM}_{\bar{1},0} \cos(\theta_{\bar{1},0})}. \tag{3.45}$$

Similarly, the dimensions $L_{0,\bar{1}}$ of the crystallites vertical to the (0,$\bar{1}$)-lattice planes can be calculated with

$$L_{0,\bar{1}} = M_2 h_a = \frac{0.888\lambda}{\mathrm{FWHM}_{0,\bar{1}} \cos(\theta_{0,\bar{1}})}. \tag{3.46}$$

This is the Scherrer formula [950]. According to the Scherrer equation, the dimensionless shape factor K includes several contributions and can vary [951, 952]. The width of the Bragg reflexes provides details about the number of lattice planes which contribute to the scattering and thus the average size of the crystallites of the polycrystalline structure in a Langmuir layer.

Chapter 4

Experimental setup and data processing

The aim of this thesis is to explore interaction mechanisms of biological membranes with different molecules. As the thickness of the lipid membranes is typically a few nanometres, x-ray scattering techniques are ideally suited to study their structure. By preparing lipid layers at interfaces between two media with a proper electron density contrast, it is possible to resolve the structure of a single membrane in detail. The experiments were performed at various synchrotron radiation facilities and at the laboratory diffractometer D8. In the following, the applied samples (section 4.1) and sample cells (section 4.2) are described and the different experimental end-stations are introduced (section 4.3). Then, the preparation of the lipid surfaces is explained (section 4.4) and a general description of the data processing is given (section 4.5).

Figure 4.1 shows an outline of the different model systems used to mimic natural biomembranes (center), in order to obtain deeper insights into the interaction with different gases and vFCs (chapter 5) and with different physiological important ions (chapter 6).

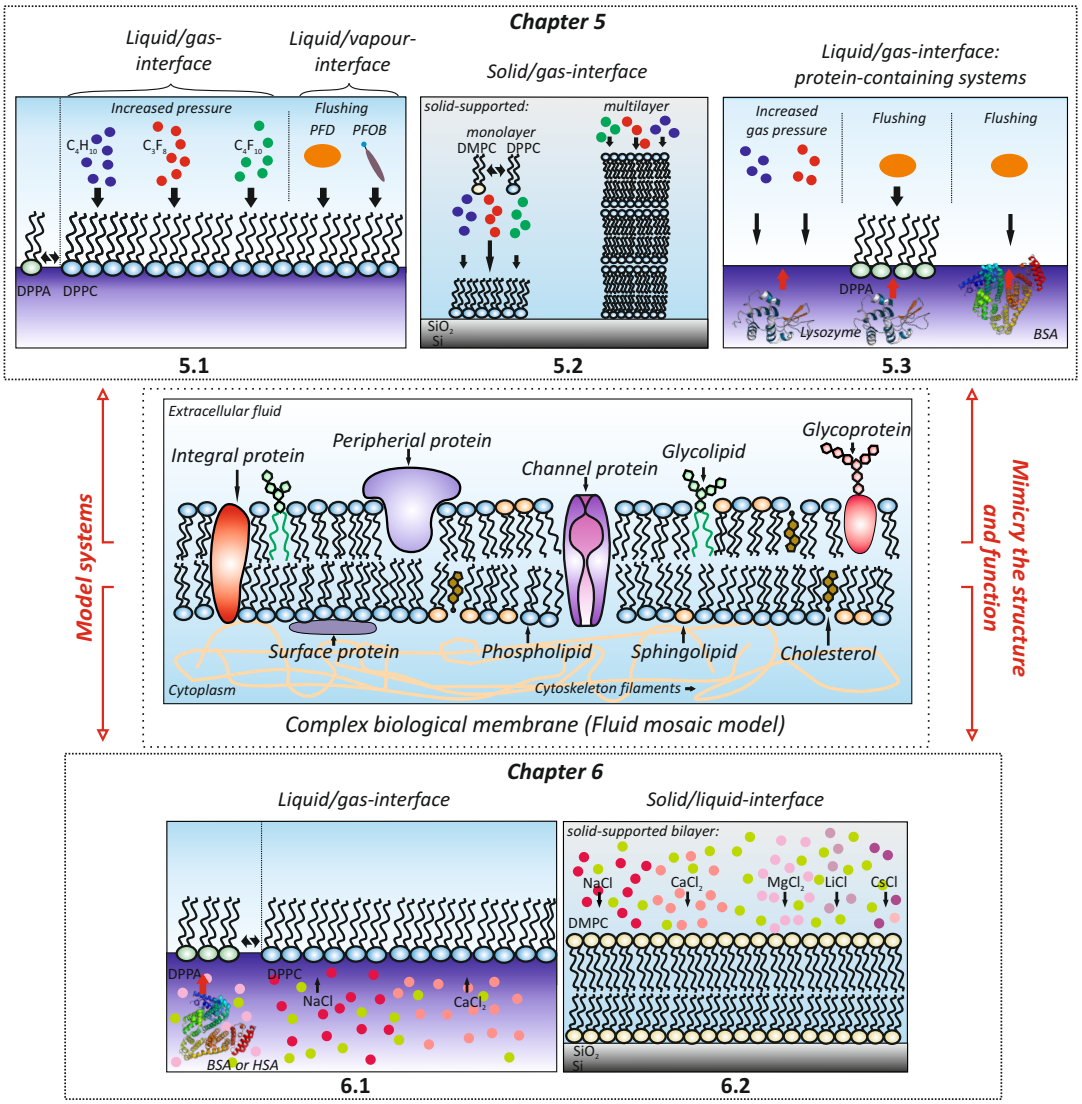

Figure 4.1: Graphical representation of a complex biological membrane (plasma membrane) based on the fluid mosaic model consisting of different proteins and lipids (center). In **chapter 5** (top) the interaction between different gases or vaporised FC molecules at the liquid/- and solid/gas-interface is examined. For this purpose, Langmuir films (left) and solid-supported lipid layers on silicon substrates (center) are applied. The influence of gFCs and vFCs on proteins and protein/lipid-interactions is studied at the liquid/gas-interface (right) (lysozyme, PDB entry 1GXV [785], BSA, PDB entry 3V03 [851]). In **chapter 6** (bottom) the interaction between DPPA and DPPC Langmuir films (left) or solid-supported DMPC bilayers (right) with different physiological important ions is studied. To test the influence of the microenvironment on protein adsorption, the effect of $MgCl_2$ has been examined in pH-dependent measurements of DPPA/BSA- and DPPA/HSA-systems, respectively. By substituting the lipids, e.g. DPPC with DPPA, it is possible to analyse the influence of electrostatic interactions, since DPPA has pH-dependent switchable charges and DPPC is zwitterionic in a wide pH-range.

4.1 Sample systems

Well-defined *in-vitro* models of complex *in-vivo* membranes allow the investigation of membrane-associated interfacial phenomena in controlled environment. This section describes the components used to create *in-vitro* biomimicry model systems, such as Langmuir films on water or buffer subphases and solid-supported lipid layers on silicon wafers.

Lipids Two different phosphatidylcholines (PCs) and a phosphatidic acid (PA) were investigated. In total, the most remarkable characteristic of the lung surfactant formulation compared to other mammalian membranes is the high DPPC level ($\sim 50\,\%$) and the presence of anionic phospholipids (~ 8 - $15\,\%$ PG and/or PI) [311, 312]. PCs have the highest fraction in cell membranes, especially in the extracellular outer leaflet, and are the most important membrane-structuring components [12, 953–956]. The PCs DPPC and DMPC are highly suitable model lipids and are widely studied. All lipids were purchased from Avanti Polar Lipids (Alabaster, USA).

1,2-dipalmitoyl-*sn*-glycero-3-phosphocholine (DPPC, CAS number 63-89-8) Figure 4.2 shows the molecule structure of the lipid. This lipid consists of two saturated palmitic acids (C16:0). The chains are attached to the zwitterionic phosphatidylcholine headgroup. The molecular formula is $C_{40}H_{80}NO_8P$. The molecular weight is $734.053\,\mathrm{g{\cdot}mol^{-1}}$.

The main phase transition temperature of DPPC in the lyotropic system lies between 313.65 K and 314.95 K (40.5 °C - 41.8 °C) [164, 957, 958]. DPPC membranes are a perfectly fitting *in-vitro* biomimetic model to study the lipid fraction of the pulmonary surfactant (see section 2.2), because about ~ 70 - $80\,\%$ of the lung surfactant molecules are phosphatidylcholines and about ~ 40 - $55\,\%$ are DPPC [295, 311, 959, 960]. The main element responsible for the near-zero surface tension of lung surfactant is DPPC [310, 961, 962]. The saturated nature of the alkyl chains in DPPC allows a high packing density causing an effective exclusion of water molecules [306, 332]. Furthermore, the DPPC content is high in brain myelin and erythrocyte membranes with about 10 - $20\,\%$ [963, 964].

1,2-dimyristoyl-*sn*-glycero-3-phosphocholine (DMPC, CAS number 18194-24-6) The molecular formula for DMPC is $C_{36}H_{72}NO_8P$, the molecular weight is $677.95\,\mathrm{g{\cdot}mol^{-1}}$.

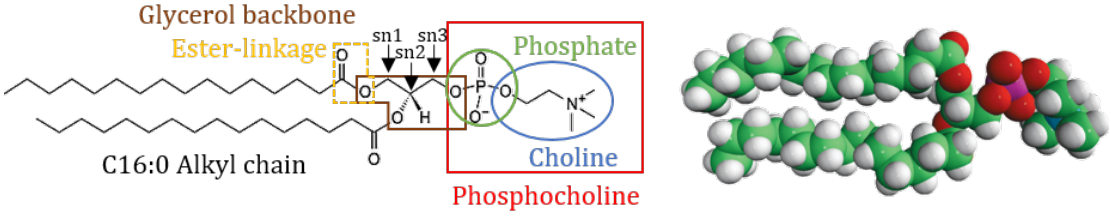

Figure 4.2: Molecule structure (left) with marked components and 3D structure (right) of the zwitterionic 1,2-dipalmitoyl-*sn*-glycero-3-phosphocholine (DPPC).

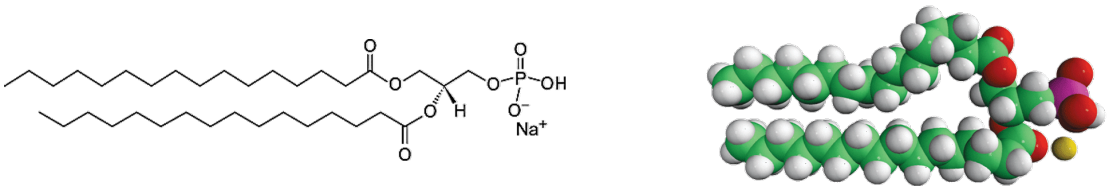

Figure 4.3: Structural formula (left) and 3D structure (right) of the singly negatively charged 1,2-dipalmitoyl-*sn*-glycero-3-phosphate (sodium salt) (DPPA).

This lipid is also a saturated phosphatidylcholine containing two myristoyl groups (C14:0). The main phase transition temperature of DMPC in lyotropic systems is 298.15 K (24 °C) [132, 164]. The phospholipid DMPC is often used for monolayer studies, primarily because of its low main phase transition temperature below physiologically relevant temperatures. It is very well-suited for the use in lipid bilayer studies and the preparations of stable solid-supported multilayer systems [81–84].

1,2-dipalmitoyl-*sn*-glycero-3-phosphate (sodium salt) (DPPA, CAS number 1690 51-60-9) Figure 4.3 shows the structure of DPPA. The molecular formula of the phospholipid is $C_{35}H_{68}O_8PNa$ and the molecular weight is 670.87 g·mol^{-1}. The lipid contains two saturated palmitic acids attached to a phosphoglycerol headgroup (C16:0). Pulmonary surfactant contains variable amounts of anionic acidic phospholipids, for example phosphatidylglycerol (7 - 18 %, PG) and phosphatidylinositol (2 - 4 %, PI) in adults [311, 349, 965]. To address and mimic this system DPPA was used, as it provides a corresponding negative charge.

Phosphatidic acid is a minor but important bioactive lipid. Some functions are discussed in chapter 2. The glycerophospholipid DPPA can exist as neutral, singly negatively and doubly negatively charged molecule. The two pK_a values are p$K_{a,1}$ = 3.2 - 3.8 and p$K_{a,2}$ = 10.5 for the first and second dissociation step [218, 966]. The PA recognition by proteins and substances can be described as electrostatic/hydrogen bond switch. The "switch" represents the ability of DPPA to be present in various protonation states (0, -1, -2) in dependence of the binding of positively charged residues [90, 101, 102, 967, 968] or divalent cations, such Ca^{2+} or Mg^{2+} [969–974]. This can shift the second pK_a to neutral pH-values (p$K_{a,2}$ = 7.1 - 8.5). The ionisation properties of the phosphomonoester headgroup is influenced by the competition of proton bonding and formation of an intermolecular hydrogen bond (-1 → -2) [975]. This also leads to a stronger electrostatic interaction between DPPA and its interaction partners. The switch mechanism is illustrated in figure 4.4. The main phase transition temperature (T_m) and the structure of DPPA containing membrane is strongly dependent on the degree of dissociation (α). The main phase transition temperature in the singly negatively state ($DPPA^-$, $\alpha = 1$) is 71 °C, this is high in contrast to other negatively charged lipids, like $DPPS^-$ which has a main phase transition temperature of 54 °C. This is explained by the intermolecular phosphate-phosphate hydrogen bonds of DPPA. The main phase transition temperature, when the membrane is completely deprotonated

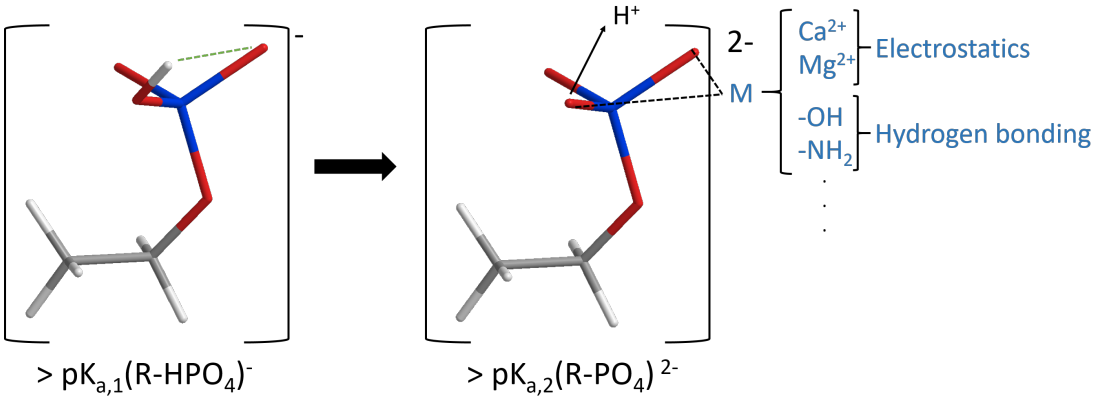

Figure 4.4: Schematic representation of the electrostatic/hydrogen bond switch of a truncated DPPA molecule (energy minimum calculated with MM2 force field using Chem3D). The green dashed line represents the intramolecular hydrogen bond of the phosphomonoester headgroup. The deprotonation is induced in the presence of divalent cations, amine or hydroxyl groups increasing its negatively charge and lowering its p$K_{a,2}$.

(DPPA^{2-}, $\alpha = 2$), is 46 °C due to the increased electrostatic repulsion, the loss of the ability to form hydrogen bonds and an increased hydration of the headgroups. As a consequence of the higher hydrodynamic radii of the headgroups, the alkyl chains tilts. This additionally reduces the van der Waals interactions. In a fully protonated state ($\alpha = 0$), the phase transition temperature T_m is approx. 62 °C. This can be attributed to the inability to form intermolecular hydrogen bonds. The addition of divalent cations generally increases the T_m due to a shielding effect [66, 133, 976, 977].

Gases Isobutane with the IUPAC name 2-methylpropane (R600a, CAS number 75-28-5, C_4H_{10}) and perfluoropropane with the preferred IUPAC name octafluoropropane (F-propane, R610, CAS number 76-19-7, C_3F_8) were purchased from Air Liquide S.A. (Paris, France). Perfluorobutane with the IUPAC name decafluorobutane (F-butane, R218, CAS: 355-25-9, C_4F_{10}) was acquired from Chemos GmbH (Altendorf, Germany). The manufacturers stated that the purities of the gases were better than 99.9 mass%. The molecular formula and some physicochemical properties are summarised in tables 4.1 and 4.7 top. The octanol-water coefficient, log P or log K_{ow}, is a measure of a compound's lipophilicity/hydrophilicity [993–996]. Log P values range typically from -3 (very hydrophilic) to +10 (extremely hydrophobic). The log P value often acts as a key descriptor for evaluating ADMET (absorption, distribution, metabolism, excretion) properties or "druglikeness", that are deduced from the chemical structure. A reliable calculation of log P is the xlog P3-AA method [990]. Perfluorination of organic compounds influences the lipophilicity (compare C_4H_{10} and C_4F_{10}). With aromatic fluorination or with perfluorination of the alkyl chains the lipophilicity increases. But it decreases with an ω-alkyl fluorination (mono fluorination) or α-fluorination (trifluoromethyl group) [997, 998].

Table 4.1: The surface tension and molecular weight are indicated with γ and M_w, respectively. Data sets for the surface tension at 294.15 K and the dipole moment (μ) are available and calculated via NIST [978, 979]. The calculated xlog P3-AA values are selected from the Pubchem database [980]. The experimental $\log P$ value for isobutane is 2.78 [981, 982]. The molecular volumes for the gFCs are extracted from Hall et al. [983]. The water solubility is selected for F-propane (at $T = 288.15$ K) from [984, 985] and F-butane (at $T = 298.15$ K) from the Pubchem database [980]. The vapour/liquid interfacial tensions (different temperature data sets) of the gFCs can be found in [986]. Water solubilities for the perfluorocarbon compounds can also be found in [987]: F-propane: 0.19 mol/m^3, F-butane: 0.021 mol/m^3 .

gas	formula	M_w / g·mol^{-1}	γ[a] / mN·m^{-1}	μ / D	V / Å^3	xlog P3-AA[b]	solubility / mg·ml^{-1}
isobutane	C_4H_{10}	58.12	10.563	0.132	83[c]	2.1	48.9
F-propane	C_3F_8	188.02	4.1676	0.014	418	3.1	5.7
F-butane	C_4F_{10}	238.03	7.5882	-	492.9	3.8	10.56

[a] Further temperature data sets are available in Lin et al. [988] for isobutane and orthobaric surface tensions for F-propane and -butane in McLure et al. [989].
[b] The calculation of the xlog P3-AA octanol-water partition coefficient is based on [990].
[c] The molecular volume is extracted from [991, 992] and calculated using Schrödinger Release 2020-1: QikProp, Schrödinger, LLC, New York, NY, 2020.

Table 4.2: The condensation pressures (p_0) at various temperatures are available via NIST [978, 979].

gas	p_0 in [bar] at T in [K]					
	288.15	294.15	297.15	309.15	313.15	323.15
isobutane	2.589	3.115	3.405	4.775	5.312	6.849
F-propane	6.562	7.779	8.443	11.545	12.748	16.18
F-butane	1.92	2.354	2.597	3.766	4.233	5.588

The perfluorocarbons display lower surface tensions in comparison to their corresponding hydrocarbon compounds. The van der Waals interaction between the fluorinated molecules are smaller than between the non-fluorinated molecules [999].

Beside measurements at N_2 atmosphere, isobutane is used as a non-perfluorinated reference. It has a globular shape and is gaseous at ambient temperature. The condensation pressures for the applied temperatures are collected in table 4.2.

Figure 4.5 shows the molecule structure as a computed 3D structure, the radius of gyration [1000, 1001] and the molecule structure of the studied gases. To study the behaviour and impact of fluorine gases at lipid monolayers, F-propane and F-butane have been selected. The fluorine gases provide a high contrast in comparison to the lipids which is essential for a detailed analysis of the structural behaviour.

vaporised perfluorocarbons (vFCs) Perfluanfene with the IUPAC name octadecafluorodecalin (F-decalin, $C_{10}F_{18}$) and perfluorooctyl bromide (F-octyl bromide,

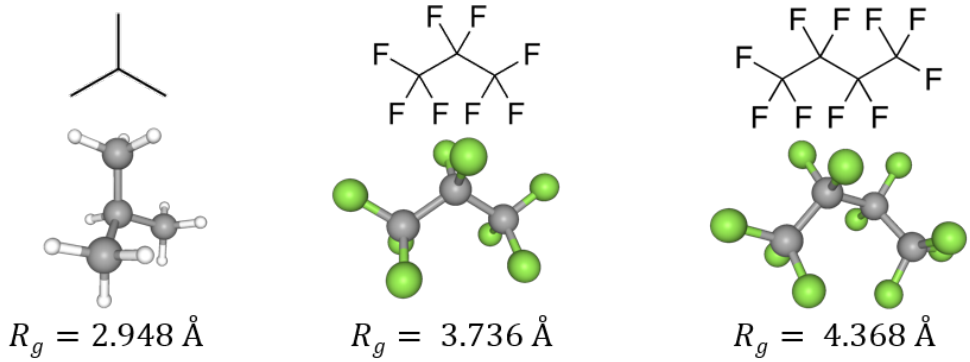

Figure 4.5: Structural formula and computed 3D molecule structures of isobutane (left), perfluoropropane (center) and perfluorobutane (right). Energy minimum calculated with MM2 force field using Chem3D. R_g indicates the gyration radius.

$C_8F_{17}Br$) were purchased from Alfa-Aeser (Haverhill, USA). F-decalin (CAS number 306-94-5) was obtained in a 50:50 *cis*:*trans*-mixture with a purity of $< 95\,\%$. The *cis*- and *trans*-isomers of F-decalin are very similar in their physicochemical properties. F-octyl bromide (CAS number 423-55-2) was received with a purity of $< 98+\,\%$. In the continuation of this work, the substances are termed F-decalin and F-octyl bromide. Some physicochemical properties are summarised and compared to water in table 4.3. The spreading coefficient s is a useful parameter for gauging wetting. For $s > 0$ the liquid wets the surface completely, for $s < 0$ partial wetting occurs[1].

The chosen gaseous and vaporised perfluorocarbons are used in medicine for various applications, frequently in combinations with lipids. Some of the specific application and the chemical nature of the substances are described in chapter 2. The calculated molecular volumes for the compounds are $204.15\,\text{Å}^3$ for F-decalin and $187.78\,\text{Å}^3$ for F-octyl bromide [1003]. They are extremely hydrophobic. The water solubility for F-decalin is about $5 \cdot 10^{-9}\,\text{M}$ and $1 \cdot 10^{-8}\,\text{M}$ for F-octyl bromide [457]. This behaviour is also reflected in the $\log P$ values. Therefore, it is expected that they insert into the hydrophobic core of a bilayer [1012–1015].

Model proteins At this point the examined model proteins, lysozyme of hen egg-white and the serum albumins of cows and humans, will be described. An overview of some structural and physicochemical properties will be given. These information are important for the data evaluation and the interpretation of the experimentally obtained results. Some physicochemical properties and structural information of the two globular model proteins are summarised in table 4.4. The adsorption behaviour will be intensely discussed in the corresponding result chapter. Detailed information and current findings in connection with these proteins are found in chapter 2 in subsection 2.4.3.

Globular proteins with a high degree of conformational stability and less flexibil-

[1]The spreading coefficient is $s = \gamma_{s,g} - (\gamma_{s,l} + \gamma_{l,g})$. In combination with the Young relation, it yields the Young-Dupré equation: $s = \gamma_{l,g}(\cos(\theta) - 1)$.

Table 4.3: Physicochemical properties of the investigated vFCs compared to water. The surface tension is indicated by γ. The vapour pressure (v.p. at $T = 310.15\,\mathrm{K}$) and oxygen solubility ($[O_2]$ /vol% at $T = 298.15\,\mathrm{K}$) were taken from Meinhardt et al. [456] and Krafft [460]. The spreading coefficients (s) are from Riess [457]. Log P values (e: experimental, c: calculated) for F-decalin are from [981, 1002], other values can be found in [1003] with empirical values of 7.97. The xlog P3-AA value is 5.6 [980]. Calculated log P for F-octyl bromide is an ACD/log P value. The method description is given in [1004]. The xlog P3-AA reveals a value of 6.9 [980]. The experimental value is extracted from [1005]. A further empirical value is 7.87 and can be found in [1003, 1006].

formula	M_w / g·mol^{-1}	γ / mN·m^{-1}	v.p. / mbar	s / mN·m^{-1}	$[O_2]$ /vol%	log P
H_2O	18	72	47	-	3	-
$C_{10}F_{18}$	462.08	19.85[a]	18.74	-1.5	24-44	6[c], 6.69[e]
$C_8F_{17}Br$	498.96	18.2[b]	13.88	+2.7	49	8.62[c], 8.82[e]

[a] The surface tension is extracted from Freire et al. [999] and
[b] from Meinhardt et al. [456], both given for $T = 293.15\,\mathrm{K}$. Surface tension at 298.15 K are 15 and 18 mN/m for a and b, respectively [479, 1007], information on the v.p can be also found there and in [1003]. Further surface tensions in dependence of the temperature can be found in the SpringerMaterials database [1008]. The interfacial tension γ_i versus saline is listed in Riess [457].

ity are regarded as rigid, or so-called "hard" proteins; they resist larger irreversible conformational changes upon adsorption at the interface. "Soft" globular proteins on the other hand are proteins with a high degree of structural flexibility and have the ability to arrange their tertiary structures upon adsorption. The foamability is a physical property indicative of protein hardness. It also correlates directly with the affinity of globular proteins for the water/air-interface. The retention time in a hydrophobic chromatography (HIC) column is an indicator for the effective surface hydrophobicity of a protein - long retention times in a HIC column indicates a high effective surface hydrophobicity (non-polar surface regions) and high affinity for amphiphilic interfaces [1016, 1017].

Lysozyme, muramidase The well-known single-chain model polypeptide lysozyme from hen egg-white consists of 129 amino acids and has a molecular mass of $M_\mathrm{w} = 14.307\,\mathrm{kDa}$. It is cross-linked with four disulfide bridges and has a high conformational stability. It is a hard protein [771, 784]. The protein was purchased from VWR International GmbH (Darmstadt, Germany) and Merck KGaA (Darmstadt, Germany).

The hen egg-white lysozyme is homologous to human lysozyme [1022–1024] and provides a convenient proxy for investigations of the protein. The tertiary structure, the protein folding pathway and the function of hen lysozyme are nearly identical to those of human lysozyme [790].

Figure 4.7 shows the solution NMR structure as ribbon diagram and the molecular surface of hen egg-white lysozyme at ambient pressures. Animal lysozymes are divided

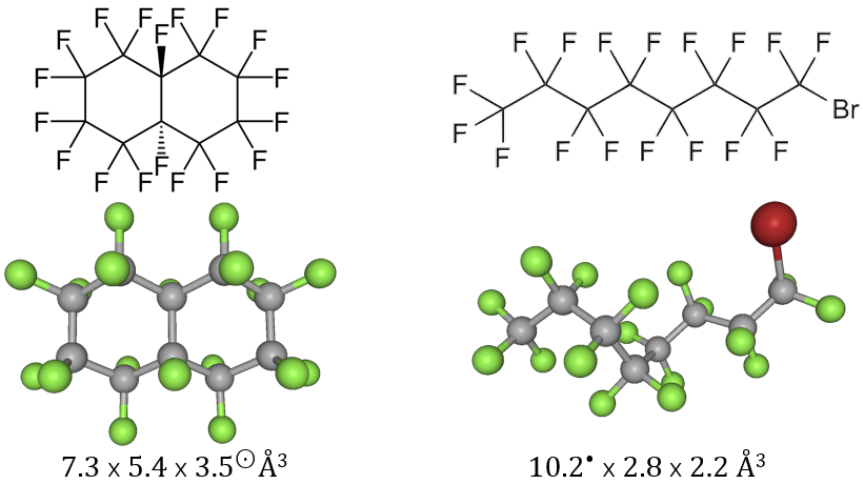

Figure 4.6: Structural formula (top) and computed 3D molecule structure (bottom) of *trans*-F-decalin (left) and F-octyl bromide (right). The sizes (l x h x d) are validated with Jmol [5, 6] and Chem3D. The specified depth value (⊙) was calculated in [1009, 1010]. End-to-end length (•) in an extended conformation is extracted from [1011] and as bulk F-octyl bromide the molecule has a length of ~ 9.99 Å.

into two domains by a large substrate-binding cleft, a larger α-helical domain containing the amino and carboxy terminus of the protein, and a smaller β-folded domain (so-called lysozyme-like folding [1025]). Since the IEP of lysozyme lies at 11.35, it is net positively charged (+7) at a pH-value of 7 with a uniform surface charge (compare figure 4.7b). Lysozyme is a small ellipsoid shaped protein with the dimensions of $30 \times 30 \times 45$ Å^3. The protein data bank [1021] in combination with eF-site (electrostatic-surface of functional site [1026, 1027]) was used to identify the hydrophobic and hydrophilic domains. As discussed in chapter 2, lysozyme is connected to a variety of diseases that are associated with interfaces, mainly the liquid/air-interface. Hence, to obtain further information about the interaction of perfluorocarbons with lysozyme at the water/air-interface in the presence and absence of lipids, experiments at different interfaces were conducted. Studies on the adsorption behaviour of lysozyme in contact with g- and vFCs under lipid monolayers or at the water surface have not yet been reported.

Serum Albumins Bovine and human serum albumin, BSA and HSA, with a molecular mass of 66.46 kDa and 66.47 kDa, respectively, were obtained from Merck KGaA (Darmstadt, Germany) with a purity of $\geqslant 97\,\%$. Serum albumin is a monomeric water-soluble and surface-active protein. It is the most abundant protein in the circulatory system.

The mature bovine serum albumin contains 583 amino acids in the primary structure, HSA contains two amino acids more. They are monomeric proteins with 35 cysteine residues, 17 internal disulfid bridges and one free thiol (-SH) group. The serum albumin molecule is structured in three homologous domains (noted as I-III). Each domain consists of two subdomains (A and B). Figure 4.8 shows a ribbon diagram of BSA

Table 4.4: Physicochemical properties of lysozyme and BSA. The IEP [821, 868, 1018–1020] and HIC [1016] indicates the isoelectric point and the experimental retention time of proteins in a hydrophobic chromatography column. The foam height is an indicator for protein hardness (5 ml protein solution shaken for 30 s) and number of S-S gives the value of disulfid bridges [1016].

protein	M_w [kDa]	IEP	net charge at pH 7	HIC [min.]	foam [mm]	no. S-S	sec.[1]	PDB entry ID
lysozyme	14.307	11.35	+7	18	0.1	4	4-α/5-β	1GXV [785] 1VDQ [1021]
BSA	66.46	4.8-5.6	-18	6.7	15	17	α(3D)	3V03 [851]

[1] Number of secondary structures determined by x-ray crystal structures. 3D = three domains.

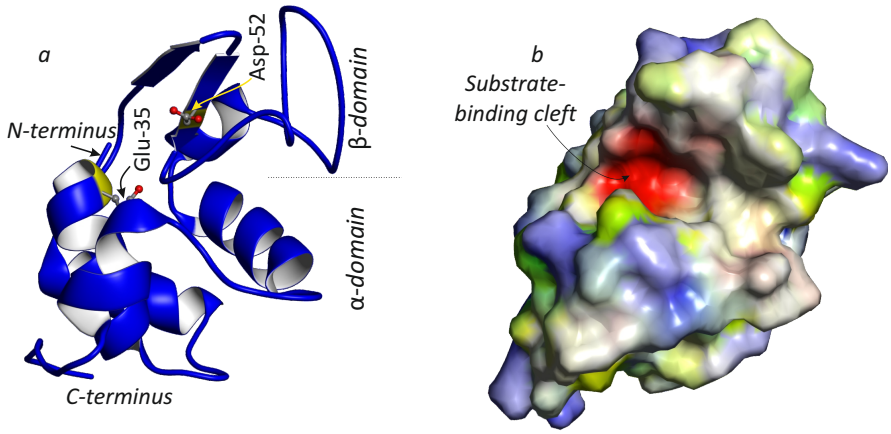

Figure 4.7: Solution NMR structure of ligand-free lysozyme from hen egg-white at ambient pressure (PDB entry 1GXV [785]) as (a) ribbon diagram with the active-site cleft (binding and catalysis) between the catalytic residues Glu-35 (highly conserved) and Asp-52 and (b) molecular surface of lysozyme, coloured according to the electrostatic potential (using eF-site [1026]).

with marked Mg^{2+} and Ca^{2+} binding sites and the molecular surface. The domains are not topologically identical, but have very similar 3D structures. The disulfid bonds stabilise the domain structures. The secondary structure of HSA and BSA is mainly α-helical (67 %). The remaining polypeptide chain occurs alternately and in extended or flexible regions between the subdomains.

The isoelectric point of the ampholytes HSA and BSA lies between the pH-values 4.6 and 5.1 [1028–1030]. BSA and HSA have an uniformly negatively charged surface at physiological pH-values (-18, -16 for BSA [821, 882] and -19 for HSA).

The conformational changes or isomerisations of BSA and HSA upon changes of the microenvironment, for example the pH-value, is described in chapter 2, subsection 2.4.3 [865]. BSA is not considered to have a high degree of structural stability and is described as a "soft" protein [821]. Due to this lack of stability, conformational changes occur upon adsorption to a surface [897]. Since the conformations of BSA and HSA are

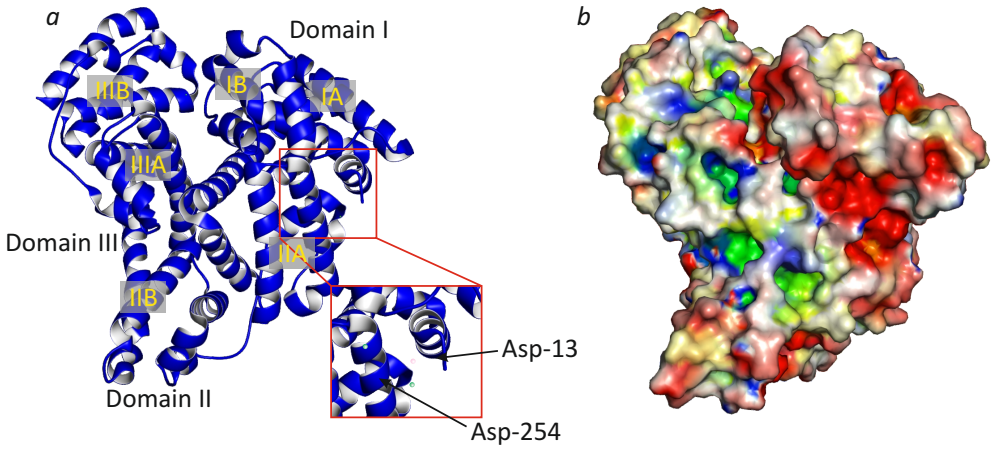

Figure 4.8: Domain and secondary structure element assignment for the crystal structure of BSA (PDB entry 3V03 [851]) as (a) ribbon diagram with bound Ca^{2+} ions, and the molecular surface (b), coloured according to the electrostatic potential (using eF-site [1026]). The zoom in (a) shows a representative binding site for a Mg^{2+} (light pink) chelate between Asp-13 and Asp-254 obtained from MD simulations [1031]. Two bound calcium ions are marked in green.

very sensitive to the microenvironment, pH-value dependent experiments in a range of 3 - 9 of the adsorption behaviour at an anionic DPPA-film with addition of $MgCl_2$ were conducted. Serum albumin is the major circulatory protein involved in the handling of Ca^{2+} and Mg^{2+} in mammals, controlling the "biologically active" levels of these metals in the blood [851]. The magnesium concentration in the blood plasma is around 1.2 mM, like Ca^{2+} around 45 % are bound to albumin. Therefore, 0.5 mM Mg^{2+} are bound to 0.6 mM circulating albumin [821, 851, 885]. The interactions between metal complexes with serum albumin can result in a disruption of the disulfide bonds, which can lead to a partial loss of α-helix conformation with the subsequent unfolding of the protein [900–903]. BSA has two metal binding sites - the N-terminal site, for example for Ni^{2+} and Cu^{2+} binding, which is marked with a red square in figure 4.8 [1032] and the multi-metal binding site that is located at the interface of domain I and domain II.

Silicon wafers The monocrystalline silicon wafers which were used as solid-support for lipid layers were purchased from Wacker Siltronic (Burghausen, Germany). The native silicon oxide layer on top with a thickness of about 10 Å reveals a roughness of 2 ± 0.5 Å. The wafers were used in combination with the well-known spin-coating technique to generate mono-, bi- and multilayers. It is possible to prepare a certain number of very homogeneous lipid bilayers and, thus, obtain multilayers. In order to produce a high quality membrane, the substrates should be hydrophilic and very smooth. To produce DMPC monolayers on the solid substrate, Langmuir-Blodgett technique was applied whereas for DPPC monolayers the spin-coating method was used.

The surface energy of the SiO_2 material is around 64 mJ/m^2. The degree of hydrophilicity and accordingly the isoelectric point depends on the number of hydroxyl

Table 4.5: Properties of the applied cations. Empirical atomic radii [1043] and calculated atomic radii in brackets [1044, 1045], ionic radii [1046], van der Waals radii [1047], hydrated radii, hydration number (number of water molecules) and the molar Gibbs energies of hydration (ΔG_{hyd}) of ions [1046].

ion	atomic radius [Å]		ionic radius [Å]	van der Waals radius [Å]	hydrated radius [Å]	hydration number[1]	ΔG_{hyd} [kJ mol^{-1}]
Cs^+	2.6	(2.98)	1.7	3.43	3.29	2.1	-250
Na^+	1.8	(1.9)	1.02	2.27	3.58	3.5	-365
Li^+	1.45	(1.67)	0.69	1.82	3.82	5.2	-475
Ca^{2+}	1.8	(1.94)	1	2.31	4.12	7.2	-1505
Mg^{2+}	1.5	(1.45)	0.72	1.73	4.28	10.6	-1830

[1] It should be noted that different measuring methods give different hydration numbers, but the trend is the same [142].

groups (silanol groups) on the surface and is around 1.9 ± 2 [1033–1036]. The ζ-potential tends to 0 below pH 3 [1037]. The Hamaker constant for silicon dioxide in water is $1.9\,k_{\mathrm{B}}T$ (at room temperature $10^{-20}\,\mathrm{J} = 2.4\,k_{\mathrm{B}}T$) [1038].

Salts and buffer For all experiments involving proteins, 10 mM Sørensen buffer with a pH-value of around 7.2 was used, which is composed of sodium hydrogen phosphate (Na_2HPO_4) and potassium dihydrogenphosphate (KH_2PO_4) [1039, 1040]. The buffer was adjusted by tuning the compound ratios and addition of phosphate acid (50 wt%) or sodium hydroxide (60 wt%). The buffer ingredients were purchased from Merck KGaA (Darmstadt, Germany). The Sørensen buffer is frequently used to achieve physiological conditions and mimics the extracellular fluid very well.

Under physiological conditions lipids in biological membranes interact with a solution of salt ions, where the exact composition depends on the respective membrane region. To study the influence, adsorption and structural response of lipid bilayers and monolayers upon salt addition at the solid/liquid- and liquid/gas-interface NaCl (CAS 7647-14-5), CsCl (CAS 7647-17-8), $CaCl_2$ (CAS 10043-52-4), $MgCl_2$ (CAS 7786-30-3) and LiCl (CAS 16712-20-2) were purchased with a purity of $< 99.9\,\%$ from Merck KGaA (Darmstadt, Germany). Lithium was chosen because of its anomalous behaviour. In fact, Li^+ is the most charge-dense cation of the Group I metals, but does not exhibit the expected salting-out effect. Lithium behave more like a large metal cation [1041, 1042]. Moreover, the effect of Li^+ has not been studied widely in this research field. Some properties of the used ions are given in table 4.5.

The biological relevance and further information on the current state of research in this field can be found in chapter 2 in the subsection 2.3. The Hofmeister classification of the cations used in the framework of this thesis is:

$$\underset{\text{kosmotrope}}{Cs^+} > Na^+ > Li^+ > Mg^{2+} > \underset{\text{chaotrope}}{Ca^{2+}}.$$

4.2 Sample cells

Liquid/gas-interfaces The custom-build stainless steel cell shown in figure 4.9 is certified for pressures up to 5 bar (tested by TÜV Germany) with an appropriate safety factor [1048, 1049].

The components mentioned in the following are sketch in figure 4.9. The L-shaped Kapton windows allow XRR and GIXD measurements. A Wilhelmy balance with a customised control unit was used to measure the surface pressure. Both were purchased from Riegler & Kirstein GmbH (Potsdam, Germany). The sensitivity of the balance is $< 0.1\,\mathrm{mN{\cdot}m^{-1}}$, the stability is better than $0.2\,\mathrm{mN{\cdot}m^{-1}}$. The microbalance allows the monitoring of the preparation process and the stability during the measurements. The gas pressure of the sample cell can be regulated by a gas in- and outlet system. The pressure is maintained by two shut-off valves and measured by a LEO 3 manometer from Keller AG (Winterthur, Switzerland) with an error of 0.05 % FullScale [1050]. The sample temperature can be controlled by a system consisting of a water cooling and a Minco heating foil (Minneapolis, USA) below the cell. Two Pt100 sensors measure the temperature ($\Delta T = \pm 0.02\,\mathrm{K}$) in the liquid and in the gaseous phase. The heating foil and the Pt100 sensors can be connected to a Lakeshore (Westerville, USA) temperature controller. The used circular sample plate (PTFE (polytetrafluorethylene)) has a diameter of 120 mm to minimise the influence of the meniscus, which is formed at the edge. The sample plate can be filled with maximum 40 ml buffer volume. The pressure cell was used for the measurements where g- and vFCs were analysed at liquid surfaces and for the investigation of proteins in interaction with membranes under FC saturated atmosphere.

Further experiments were conducted utilising a Langmuir through with one motor-driven moveable barrier, a Wilhelmy balance and control segments for XRR measurements purchased from Riegler & Kirstein GmbH (Potsdam, Germany). The Langmuir through can be filled with a maximum water volume of 250 ml. This setup was applied to investigate the behaviour of ions in contact with charged and zwitterionic lipid monolayers and BSA or HSA adsorption on DPPA-films. The Langmuir through can

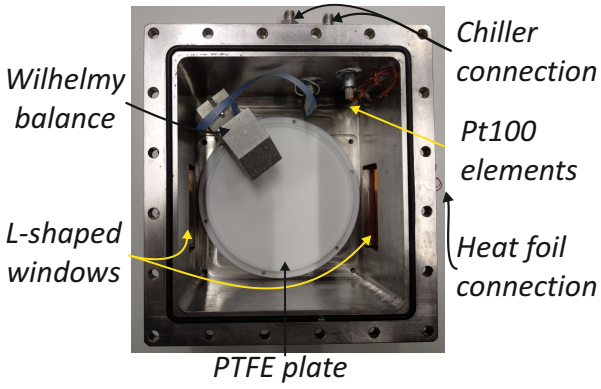

Figure 4.9: Custom-made stainless steel sample cell for *in-situ* XRR and GIXD measurements under elevated gas pressures. Open sample cell from above with marked modules and circular PTFE sample plate.

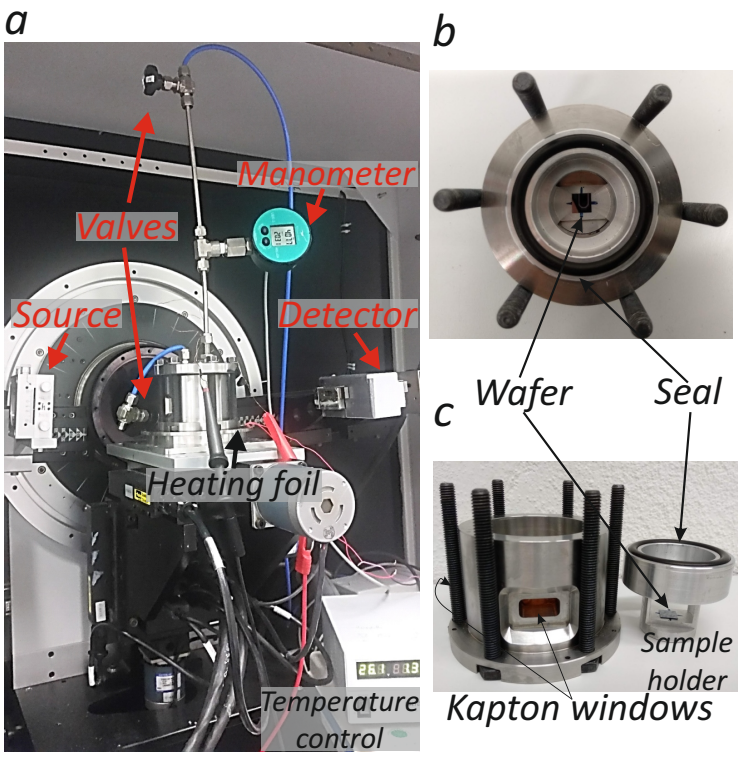

Figure 4.10: (a) Custom-made stainless steel gas pressure sample cell mounted in the laboratory diffractometer D8 for temperature-dependent measurements at the solid/gas-interface. Various components used for temperature and gas pressure control are marked. (b) Opened pressure cell with a coated wafer in the middle. (c) Side view of the sample cell with inner wafer holder.

be covered with a Kapton spanned box to prevent contaminations and evaporation. The sample plates were successively cleaned with ether and ultra-pure Milli-Q water at each use to prevent contamination of the sample system. The purity of the subphase (buffer or water) in the Langmuir through which can hold 250 ml sample volume can be checked by a Π-A isotherm. The surface pressure should not change by more than $2\,\mathrm{mN{\cdot}m^{-1}}$ for reliably cleaned components. The compression speed for a monolayer can be adjusted. A speed of 5 mm per minute was chosen. The Wilhelmy plate and the Langmuir film were freshly prepared for each surface pressure and protein measurement.

Solid/gas-interfaces For measurements at the solid/gas-interface a new gas pressure sample cell, shown in figure 4.10, with a wafer holder was designed and built. The sample cell was built as part of Christian Albers' master thesis [1051]. The pressure cell is certified for pressures up to 5 bar. The technical drawings are shown in the appendix B. The inner wafer holder has a diameter of 34 mm. The cell allows angles of incidence of more than 10°, which is sufficient for XRR measurements. The cell can be tempered with a Minco heating foil or a recirculating chiller.

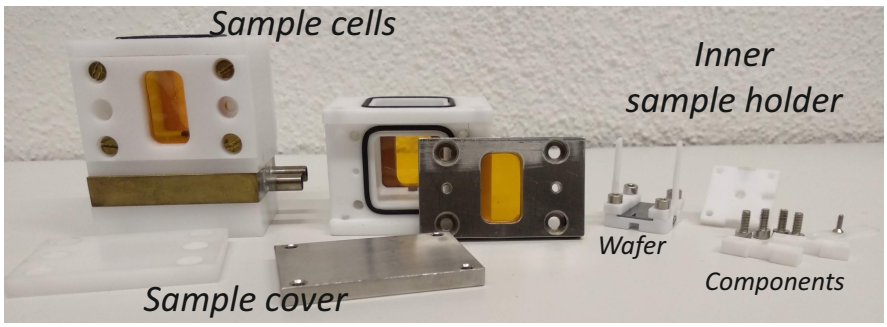

Figure 4.11: Custom-made PTFE sample cells for *in-situ* XRR measurements at solid/liquid-interfaces. From left to right: Sample cells with PTFE body and different windows (PTFE left and steel on the right), heating plate with PTFE adapter plate for installation at beamline 9 at DELTA. Inner sample holder with a silicon wafer and the individual components of the wafer holder.

Solid/liquid-interfaces The sample cell for measurements at solid/liquid-interfaces is pictured in figure 4.11. In experiments involving salt solutions, the sample cell presented by Forov [1052] was applied. This sample cell consists mostly of PTFE parts. The chemical inertness of this material is important for the suppression of undesired interactions of salt ions and the sample cell. The sample cell consists of a PTFE cell body, Kapton spanned stainless steel windows and a PTFE wafer holder. The wafer can be placed and fixed under PTFE plates which are tightened with small screws. With a fitting pin inside the PTFE sample cell, the sample holder can be fixed inside the cell to avoid movements. The sample cell can be filled with a maximum volume of 10 ml. To perform XRR experiments 4 ml sample volume is sufficient. If required, a heat exchange plate can be mounted below the sample cell. For the presented measurements a recirculating chiller was used to perform XRR measurements at a temperature of 36 °C (309.15 K).

4.3 Experimental Facilities

In this subsection the different experimental end-stations are introduced. As previously discussed in chapter 3.1, the experiments had to be implemented under shallow angles for the incoming x-ray beam to archive surface-sensitivity [930, 931]. For GIXD measurements, a constant incidence angle is utilised, while for XRR measurements the incident angle has to be changed steadily to fulfil the conditions for specular reflection. For the detection of x-rays, different two-dimensional position sensitive detectors (PSD) were used. For the liquid/gas-measurements a liquid surface reflectometer is needed to bend the x-ray beam down on the surface [1053–1056]. The experiments shown in the framework of this thesis were performed at third generation synchrotron radiation facilities since high brilliance and high photon flux even through aqueous and dense gas phases is needed. XRR experiments were also performed at the D8 laboratory diffractometer.

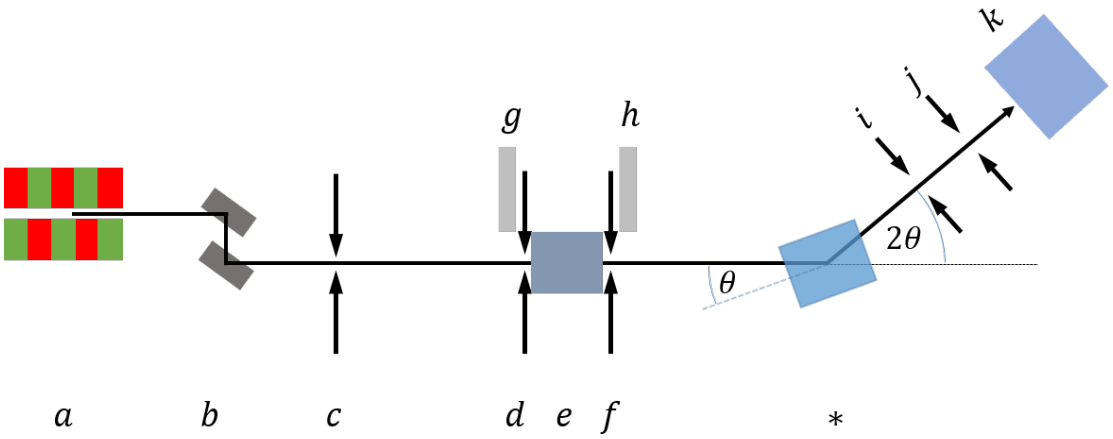

Figure 4.12: Schematic sketch of the setup and the components at beamline BL9 at DELTA based on [1057]. *a*: source SAW; *b*: Si-(311) double-crystal monochromator; *c*, *d*, *f*, *i*, *j*: slit systems; *g*, *h*: flux detector before and behind *e*: auto-absorber and fast-shutter system with absorber foils. *k*: detector, here a Pilatus 100K area detector. The star ∗ indicates the sample cell.

Beamline BL9, DELTA At the beamline BL9 [1057] located at the synchrotron light source DELTA (**D**ortmund **EL**ec**t**ron **A**ccelerator) in Dortmund (Germany), XRR experiments have been performed with a photon energy of 27 keV at solid/gas- and solid/liquid-interfaces. This beamline is described in more detail, since most of the data presented in this thesis were collected at this synchrotron light source. The storage ring operates with an electron energy of 1.5 GeV and the electrons are stored with a maximal electron current of 130 mA with an averaged lifetime of around 10 h [1058, 1059]. A schematic sketch of the components of the beamline is given in figure 4.12. For further information see also [1060–1062]. The photon source of beamline BL9 is a superconducting asymmetric wiggler (SAW, *a*). The wiggler has a critical energy of 7.9 keV. The beamline BL9 possesses optical elements optimised to operate up to a photon energy of 27 keV. A silicon-(311) double-crystal monochromator is applied to obtain monochromatic x-ray radiation (4.12 *b*). Energies from 7 up to 30 keV with an energy resolution of $\Delta E/E \simeq 10^{-4}$ can be used. The lateral focusing is achieved by the second monochromator crystal. Two of the three slit systems (*c*, *d*) collimate the beam and the third (*f*) defines the vertically beam size. It was adjusted for solid/liquid-interfaces to 0.2 mm and for solid/gas-interfaces to 0.1 mm, while the horizontally beam width was approximately 1 mm. The auto-absorber (*e*) limits the photon flux. The NaI detectors (*g*, *h*), which enclose the auto-absorber, monitors the incoming photon flux. The sample cell is located at (∗). For high-energy x-ray reflectivity measurements at 27 keV with a wavelength of $\lambda = 0.459$ Å a photon flux of $7 \cdot 10^8$ photons $\mathrm{s}^{-1}\,\mathrm{mm}^{-2}$ is received at 100 mA storage ring current. The energy range around 25 keV represents an optimum compromise between photon flux, sample transmission and radiation damage [1063, 1064]. Radiation damage to biological materials is caused by incoherent scattering

processes. Thus, the coherent scattering cross section of the sample should be high. To avoid radiation damage, the sample was continuously shifted between the scans and the reproducibility of the measured data was routinely verified. The Huber six-circle diffractometer for the adjustment of the sample cell ($\theta = \alpha_\mathrm{i}$) and the detector ($2\theta = 2\alpha_\mathrm{f}$) was used as end-station [1061]. A Pilatus 100K area detector (k) was used to capture the reflectivity. Behind the sample, the x-ray beam passes the slit system i which reduces the background radiation and the detector slit j which determines the angular resolution of the detector.

Incident angles of up to 1.2° were used with an angular resolution of 0.002°. To test the stability of the solid-supported lipid stacks, consecutive measurements of the reference were recorded. A reflectivity measurement took around 35 min. The temperature was set to 309.15 K for the solid/liquid-interfaces and to 294.15 K, 313.15 K and 328.15 K for the measurements at solid/gas-interfaces.

Beamline P08, PETRA III, DESY Some of the presented experiments at the liquid/gas-interface were performed at the high resolution diffraction beamline P08 of PETRA III (**P**ositron-**E**lectron-**T**andem-**R**ing-**A**ccelerator) located at DESY (**D**eutsches **E**lektronen-**SY**nchrotron) in Hamburg (Germany) utilising the **L**iquid **I**nterface **S**cattering **A**pparatus LISA as end-station and the Dectris Eiger-1M pixel detector to measure the scattered intensity [1065]. The beamline P08 uses x-rays emitted by two 2 m long undulators. The liquid diffractometer LISA was constructed for reflectivity and grazing-incidence diffraction measurements and it operates by means of an asymmetric tilting Si-(111) Si-(220) double-crystal monochromator in Bragg geometry [1056, 1066]. The maximal flux on the sample is $2 \cdot 10^{12}\,\mathrm{photons\,s^{-1}}$ at 8.4 keV and a spot size of $30\,\mathrm{x}\,2\,\mu\mathrm{m}^2$. An incident photon energy of 25 keV was used to obtain a sufficient scattering intensity at the detector after passing the absorbing gas phase. The beam size was adjusted by a slit system to $0.05\,\mathrm{x}\,0.1\,\mathrm{mm}^2$ (v x h). The temperature was set to 297.8 K and stabilised via a Lakeshore temperature controller. Here, the custom-made stainless steel gas pressure cell was applied with a Wilhelmy balance [1048].

Laboratory diffractometer D8 Further x-ray reflectivity measurements at the liquid/gas-interface and solid/gas-interface were performed using the x-ray diffractometer D8 Advanced (Bruker-AXS, Karlsruhe, Germany) specialised for XRR measurements. The laboratory diffractometer generates x-rays via a copper anode with a photon energy of 8.048 keV which corresponds to a wavelength of 1.54 Å ($\mathrm{Cu-K_\alpha}$). The x-ray tube operates with a voltage of 40 kV and a current of 40 mA. No radiation damage is expected at a quite low photon intensity at the sample location of around $5 \cdot 10^5\,\mathrm{photons\,s^{-1}}$ and a large beam size that is defined by a slit system to a spot size of $0.1\,\mathrm{x}\,10\,\mathrm{mm}^2$ (v x h). This was proven by control measurements. A Göbel mirror with parabolic curved layers is utilised for monochromatisation and parallelisation of the x-ray beam. The diffractometer is equipped with a NaI(Ti) scintillation detector, whereby a slit defines the diffractometer resolution with a vertical opening of 0.2 mm. The absorber with a maximum attenuation factor of 10450 protects the detector from excessive exposure. A reflectivity scan including a longitudinal diffuse scan for back-

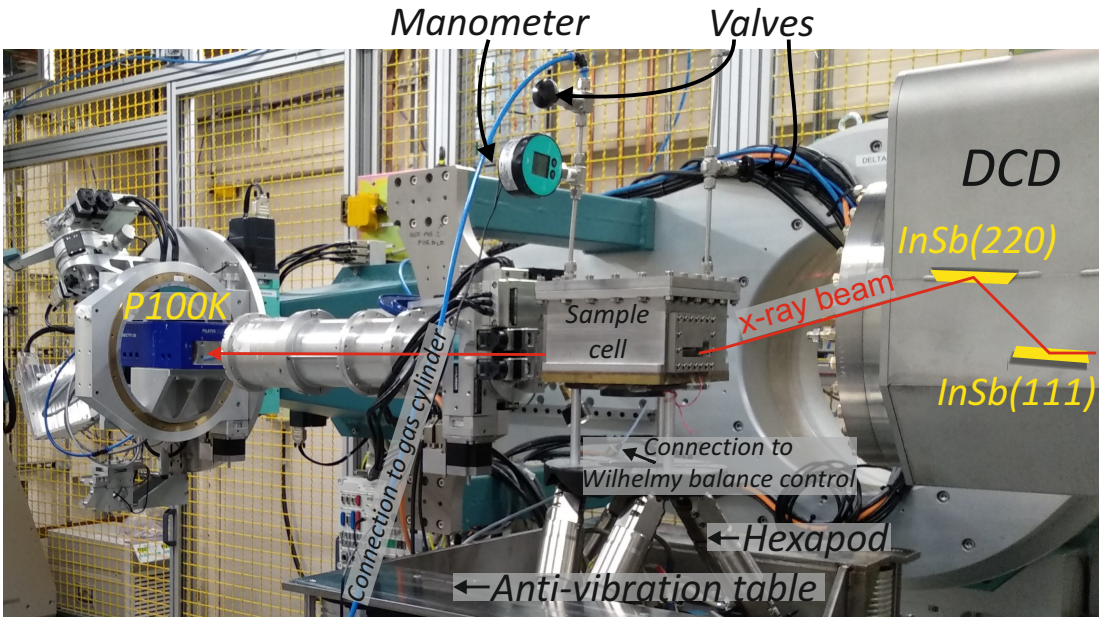

Figure 4.13: Custom-made stainless steel gas pressure cell mounted on a hexapod at I07 at DIAMOND. The DCD (Double-Crystal-Deflector) and some components of the beamline are shown. The x-ray beam path is marked in red and is detected by a Pilatus 100K (P100K) detector. The surface pressure control unit and the gas cylinder are placed behind and are not shown in the picture.

ground determination (offset scan) takes about 90 min.

Beamline I07, DIAMOND Light Source At the beamline I07 of the synchrotron radiation source **D**IAMOND **L**ight **S**ource (DLS) in Oxfordshire (England) the GIXD data were collected. The light source operates at a ring energy of 3 GeV and a current of 300 mA. The hard x-ray (8 - 30 keV) high-resolution diffraction beamline I07 is sourced by a 2 m long undulator (U23) as insertion device [1067]. Figure 4.13 shows the gas pressure cell mounted on the hexapod at beamline I07 at DIAMOND.

The Double-Crystal Deflector (DCD) end-station in hutch EH1 was used to perform experiments at the liquid surface. The system is similar to LISA at DESY. It uses two different crystals, InSb(111) and InSb(220), to reach an overall beam deflection [1055, 1068]. The photon flux at the sample with a spot size of $100 \times 300\,\mu m^2$ at 10 keV is roughly 10^{14} photons s^{-1}. A photon energy of 24 keV with a corresponding wavelength of 0.516 Å was applied to ensure, that the perfluorocarbon atmosphere can be passed. The vertical beam size was adjusted to 0.15 mm. The beam size was finally set to $0.15 \times 0.5\,mm^2$ (v x h). A Pilatus 100K area detector was used as detector. The beamline is equipped with a fast-shutter to reduce beam damage through unnecessary exposure during motor movements.

4.4 Surface preparation

In this section the preparation of stable Langmuir films and substrate-bound lipid membranes via spin-coating and Langmuir-Blodgett technique is presented. Additionally, the preparation and performance of the Π-A isotherms are explained.

All glassware and tools for the preparation of the samples were cleaned with ether and water. For all preparations with water, ultra-pure Milli-Q water with a specific resistance of $18.2\,\mathrm{M}\,\Omega \cdot \mathrm{cm}^{-1}$ and a pH-value of 6.99 were used.

Langmuir films The Langmuir films, which were used as biomimetic system for lung surfactant or as a mimicry for bilayers, were produced using two different techniques. The compression method and the dropping method. Both sample cells utilised, the custom-build gas pressure cell and the Langmuir through, are equipped with a Wilhelmy balance to measure the surface pressure during the measurements.

For every measurement a small stripe of filter paper was applied as Wilhelmy plate. To obtain reliable data, contamination of all used materials in monolayer experiments have to be avoided, especially by surface-active substances. It is important to clean the PTFE sample plate, the Langmuir trough with its barrier and the working tools with ether and ultra-pure water in order to remove organic and water soluble impurities. The lipid stock solutions were prepared freshly right before each measurement. The interfaces were created by using ultra-pure Milli-Q water ($18.2\,\mathrm{M}\,\Omega \cdot \mathrm{cm}^{-1}$, specific resistivity) or phosphate buffer solution (Sørensen buffer). The Wilhelmy balance was calibrated to the water surface tension at air (72 mN/m). The lipids were dissolved in appropriate solvents. DPPC and DMPC were dissolved in chloroform or isopropanol yielding a concentration of c = 1 mg/ml, respectively. A 9:1 chloroform:methanol (v:v) mixture was used for the production of the DPPA solution, yielding a concentration of c = 1 mg/ml. Before spreading of the lipids, the through was checked for cleanliness by a compression-expansion cycle. The lipids were then spread by dispensing the lipid stock solution with a microliter syringe (Hamilton Bonaduz) onto the subphase. To prevent injection into the volume and, thus, the formation of micelles and aggregates in or on the subphase, it is necessary to apply the lipid solution gently and slowly. The sample cell was closed to exclude impurities. The system was left for around 20 min. to evaporate the solvent and reach equilibrium. Thereby, the amphiphilic molecules orient to minimise the contact of non-polar regions with water and to maximise the water contact of polar regions. Different surface pressures can be reached by compression of the Langmuir film with a moveable barrier. The speed of the barrier was set to 5 mm/min. After reaching the target pressure a constant regulation of the surface pressure was executed with a maximum barrier speed of 1 mm/min. This guarantees a stable film with a maximum deviation of $\Delta\Pi$ = 2 mN/m from the desired surface pressure. This conditions were used for conducting the reference measurements. All subsequent measurements were performed with a constant area with the feedback control switched off yielding a constant surface coverage.

The PTFE sample plate was filled with 35 ml of subphase solution. Lipid solution was added drop wise on the subphase until the final surface pressure was reached. This

must be conducted slowly as the surface pressure changes in time while the solvent evaporates and the lipids arrange at the surface.

For the biomimicry of lung surfactant different surface pressures were generated in order to model various deficiency stages. A surface pressure of 25 mN/m was chosen for the measurements of BSA and HSA at DPPA-films. For the measurements of lysozyme at the DPPA-film, a surface pressure of 5 mN/m was chosen. The concentration in the sample cells were adjusted by addition of corresponding volumes of an immediately before prepared low concentrated protein stock solution in phosphate buffer to prevent aggregation processes. For lysozyme the concentration in the subphase was set to 0.22 mg/ml (15.29 µM) and for BSA to 0.5 mg/ml (7.52 µM). It is important to keep the influence of the monolayer to a minimum, otherwise the result can be distorted by stabbing the monolayer for adding the proteins under the Langmuir layer.

Gas washing bottles from Lenz Laborglas GmbH & Co. KG (Wertheim, Germany), so-called "bubblers" were connected to the valves of the sample system in order to vaporise the perfluorocarbons for the adsorption at the Langmuir film. Nitrogen or helium gas were saturated with the perfluorocarbons and transferred to the sample environment which is located in a gas-tight box to perform experiments under vFC atmosphere. The flow rates of the gas phase was set to approx. 1.2 L/min. The resulting evaporation rates of the FCs are around 6 ml per hour.

The salts were dissolved in ultra-pure Milli-Q water to prepare salts stock solutions. The required amount of stock solution was then incrementally added to the sample solution reaching the selected concentration without exchanging the whole sample system.

Π-A isotherms The Π-A isotherms were recorded using the KSV-NIMA KN1003 (KSV-Nima, Bioloin Scientific, Stockholm, Sweden) Langmuir trough from the CCB chair at TU Dortmund at a temperature of 294.15 K. A volume of 200 ml ultra-pure water was used as subphase. Around 20 µl of lipid solution was spread onto the water subphase and after a waiting time of 20 min. the barrier speed was set to 3 mm/min., and the isotherm was recorded.

Spin-coating Spin-coating was used as a simple and fast preparation technique to produce highly ordered lipid bilayer stacks suitable for x-ray diffraction experiments. In the following, the process for the production of substrate-bound membranes by spin-coating is explained [1069–1072]. As a first step, the wafers were cut in $10 \times 10\,mm^2$, $10 \times 18\,mm^2$ or $7.8 \times 7.8\,mm^2$ for different setups. Table 4.6 gives an overview of the wafer usage. The wafers were cleaned successively for 15 min. in acetone, isopropanol and chloroform in a supersonic bath at room temperature to remove organic impurities and other contaminations. The solvents were purchased from Merck KGaA (Darmstadt, Germany) in analytical grade. Commercially available silicon wafers might have phase boundary defects or their atoms can be substituted [1073]. In the next step, organic matter was removed from the silicon substrate and the surface was hydrophilised using the Piranha etch procedure. Polar -OH groups form at the surface on which the headgroups of the lipids attach by a self-assembly processes and multilayer formation is subsequently possible. The Piranha solution is a strong oxidising agent. When treat-

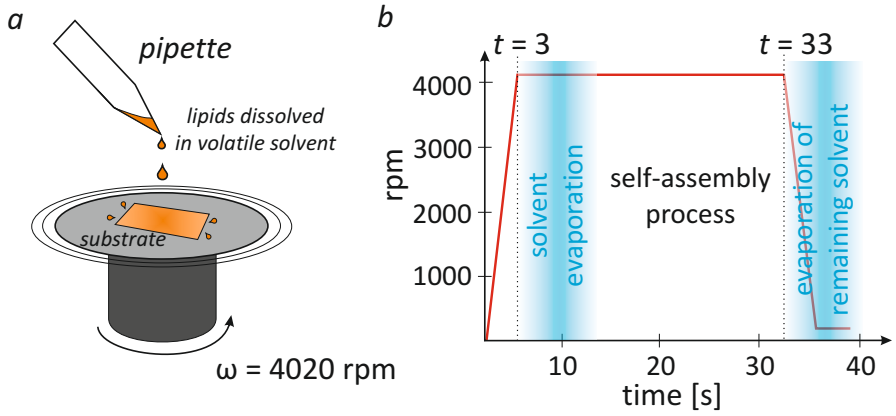

Figure 4.14: (a) Schematic representation of the spin-coating process: A lipid solution is dropped onto a freshly cleaned and hydrophilisied silicon wafer. The wafer is positioned on the moveable part of the spin-coater device. (b) Graphically abstracted spin-coating parameters used in this thesis. After placement of a defined volume of lipid solution, the wafer is accelerated for the displayed ramp. For $t < 3\,\mathrm{s}$ the solution is distributed uniformly on the wafer. For $t > 3\,\mathrm{s}$ the solvent is evaporated and the self-assembly process at a rotation speed of $\omega = 4020\,\mathrm{rpm}$ takes place and highly ordered bilayer stacks are build. At $t = 33\,\mathrm{s}$ a second ramp of 3 s to a rotation speed of 60 rpm that runs for the next 3 s follows. The figure is inspired by Reich [1077].

ing silicon surfaces with Piranha solution, covalently bonded oxygen atoms and other phase boundary defects are dissolved and replaced by hydrophilic hydroxyl groups in an acid-catalysed hydroxylation reaction [1074–1076]. The oxidation of silicon is a diffusion-dependent solid state reaction and takes place at room temperature. After the treatment in Piranha solution (1:3, H_2O_2 (J. T. Baker, USA) and H_2SO_4 (CHEMSOLUTE, Th. Geyer, Berlin, Germany) 1:3) for 40 min., the wafers were cleaned in three ultra-pure water baths to remove acid residues and are stored in ultra-pure water to avoid contamination and further chemical reactions. The sample surface always has to be covered with water to preserve the silanol groups.

To coat the hydrophilised wafers with lipid layers, lipids were dissolved in a solvent (see table 4.6). After the cleaning and subsequently piranha etch precess, the wafers were placed in the SCC-200 spin-coater from Novocontrol Technologies (Montabauer, Germany). The device was coupled with a small vacuum pump to generate a vacuum below the wafer which prevents its moving. The wafers are removed from the water bath and dried in a high purity nitrogen stream. This step should be processed rapidly. A defined volume of lipid solution is then applied onto the wafer and the spin-coater rotates at a defined speed. The spin-coating parameters were set to 67 rps (rounds per second) for 30 s with a 3 s ramp-up and 1 rps for 3 s with a ramp-down with 3 s. The preparation process with the spin-coating technique is depicted in figure 4.14.

The wafers were stored in cleaned plastic sample containers after production and were kept in a vacuum desiccator until use. The used lipids, solvents, wafer sizes and amount of dropped lipid solution are given in table 4.6. A certain number of layers remain on the surface due to the self-assembly processes of the lipids. There is an

Table 4.6: Overview of the used lipids, solvents, wafer sizes, lipid concentrations and solution volumes as well as the resulting solid-supported lipid membrane systems (ssm) and the final sample environment for the measurement.

lipid	solvent	wafer size / mm^2	c / $\frac{mg}{ml}$	amount / µl	ssm	sample environment
DPPC	chloroform	10 x 10	1	70	monolayer	dry
DPPC	chloroform	7.8 x 7.8	10	40	multilayer	dry
DMPC	isopropanol	7.8 x 7.8	10	40	multilayer	dry
DMPC	isopropanol	10 x 18	1	100	monolayer[a]	dry
DMPC	isopropanol	10 x 10	1	70	bilayer[b]	hydrated

[a] Prepared with the Langmuir-Blodgett technique at a surface pressure of 35 mN/m on a water surface.

[b] This is the state at fully hydration conditions. At dry conditions, the solid-supported lipid system consists of a bilayer and a terminating monolayer.

approximately linear relationship between the concentration of dissolved lipid and the number of layers [82, 1078]. By varying the production parameters the system can be adapted to the specific requirements. The spin-coating procedure offers the advantage that the high lipid density prevents the formation of defects and holes and achieves a homogeneous morphology [82, 83, 246, 259, 1078–1080]. A semi-empirical quantitative description for the final film thickness is given by Meyerhofer (1978) [1072, 1081].

Langmuir-Blodgett films Since it was not possible to prepare DMPC monolayers on the solid substrate by the spin-coating procedure, the Langmuir-Blodgett method was applied. With the Langmuir-Blodgett technique, molecular films from the liquid/air-interface can be transferred to a solid support [208, 213, 240, 1082–1084]. For this purpose, the KSV-NIMA KN1003 Langmuir trough with a deep basin from the chair CCB at the TU Dortmund was used. The Langmuir through was filled with 200 ml ultra-pure Milli-Q water. The clean hydrophilic substrates were attached to a motorised sample holder clip which allows to move the wafer vertically with a defined speed. The wafer were then transferred in the water subphase. Subsequently, the DMPC lipid solution were spread drop wise onto the water surface and after a waiting period of around 20 min., the lipid monolayer was compressed with a speed of 3 mm/min. until a surface pressure of 35 mN/m was reached. The wafers were vertically pulled out of the water with a speed of 1 mm/min. allowing the formation of the monolayer on the silicon wafer. During this process, the surface pressure was kept constant, the feedback regulation of the barrier was set to a maximum speed of 10 mm/min. The freshly prepared films were stored in a vacuum desiccator for 12 hours and afterwards in cleaned sample boxes until usage. For further information on Langmuir-Blodgett films, see [213, 1083–1086].

4.5 Data handling

XRR data First, a background is subtracted from the captured XRR raw data and the measured intensity is normalised to the incoming intensity. A high background originates from the scattering of the compressed gases in these experiments. In the case of laboratory diffractometer data, the intensity of the diffuse longitudinal scan was subtracted from the specular scan. In the case of 2D detectors, the lateral background scattering was measured simultaneously and can be subtracted directly. For the analysis of the obtained XRR data the program LSFit [927] was applied which uses the Parratt algorithm [920] in combination with the effective-density model [907] to account for interfacial roughness (see section 3.2).

The reflectivity curves in this thesis will be shown in the Fresnel normalised representation to take the strong intensity decay into account and to highlight slight changes in the data. Moreover, the reflectivity curves were shifted vertically for a better graphical visibility. The increase of intensity before reaching the critical angle (α_c) which typically occurs in the reflectivity curves can be attributed to the geometry angle. The geometry angle (α_{ga}) describes the smallest angle at which the whole footprint of the incoming beam hits the sample surface. Below the angle primary beam only partially reaches the sample surface. The geometric angle can be calculated by

$$\sin(\alpha_{ga}) = \frac{h}{l} \tag{4.1}$$

with the beam height h and the sample length l. For angles $\alpha_i < \alpha_{ga}$ the reflected intensity reduces by the factor $l \sin(\alpha_{ga})/h$.

To gain information about the present sample system, an initial guess of the electron density profile is assumed. The model of the electron density profile is determined by variable parameters and can, therefore, be further adapted to the measured data in an iterative process. Each layer contains a set of three changeable parameters, the dispersion δ, the thickness of the layer d and the roughness σ. These "box models" provide a simple, intuitive approach to data analysis and interpretation [335, 911, 940]. One further parameter that is not varied during the fitting procedure is the absorption β.

In the refinement process, the parameter set is optimised by applying the Levenberg-Marquardt algorithm. The deviation between theoretical and measured reflectivity curves can be used as a quality feature of the adaptation of an assumed model with

$$\chi^2 = \frac{1}{N} \sum_{i=1}^{N} (\log R(q_{cal,i}) - \log(R(q_{exp,i}))^2. \tag{4.2}$$

Here, N is the sum of the data points and $R(q_{cal,i})$ and $R(q_{exp,i})$ the calculated and experimental measured data at the i-th data point.

In the framework of this thesis different systems were used. The Langmuir monolayers can be modelled sufficiently by a two-layer parameter set, see figure 4.15a. The first layer represents the headgroup and the second the tailgroup. If adsorption is observed

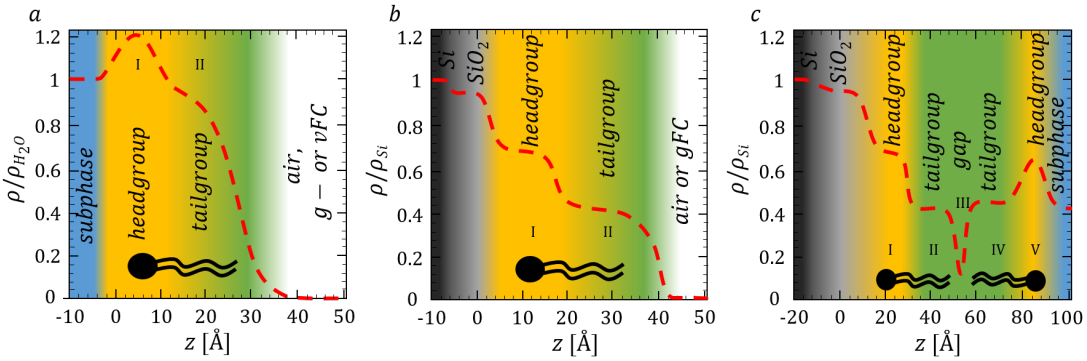

Figure 4.15: Sketch of normalised electron density profiles originating from a Langmuir layer on a subphase (a), from a solid-supported lipid monolayer in air or gFC atmosphere (b) and a lipid bilayer on silicon wafer in a subphase, e.g. salt solution or water (c).

at the film, the system is expanded by an additional layer on top (g- or vFC adsorption) or underneath the headgroup (e.g. protein or ion adsorption). Furthermore, penetration and insertion into the films (head- or tailgroup) are expected. These effects can be modelled by changing the present layers. The dispersion is proportional to the electron density and adsorbed amount of matter.

In the fitting routine, first, the layer thicknesses and dispersions were adjusted and, in the next step, the roughnesses and the whole layer system were optimised. For the samples, where adsorbate layers are expected, the results of the corresponding reference measurements were used as initial guess. For the substrate (water or buffer) the parameter δ were calculated via Davis et al. [1087]. According to the capillary wave model, the roughness of the water surface was set to approx. $\sigma_{\mathrm{D8}} = 3.2$ Å [907].

The mass densities, electron densities and absorption values for the gaseous and fluid phase of the used gases and the vFCs are given in table 4.7. The electron densities can be calculated from the mass density in the table, the molecular weight which are listed in table 4.1 and table 4.3 and the Avogadro constant. The gyration radii of the gases are summarised in figure 4.5 and size information for the vFCs are given in figure 4.6.

In the last decade, studies on silicon and silicon dioxide interfaces were in the focus of research, see also [1036, 1090–1094]. For the fitting routine of SiO_2 layers the model of Tidswell et al. [1090] was selected. A bulk silicon layer and a homogeneous layer with reduced electron density for the silicon dioxide layer is presumed, the thickness of the dioxide layer is around 10 - 15 Å.

The values for the dispersion and absorption of silicon, silicon dioxide and water were calculated via Davis et al. [1087] and are summarised in table 4.8. The solid-supported monolayers were fitted as two-layer systems (see figure 4.15b) and as systems with five layers in the bilayer case (figure 4.15c). The multilayer stacks were refined using six sublayers, consisting of periodically arranged bilayer stacks as shown in figure 4.15c and an additional gap that was postulated between the headgroups. Furthermore, to compensate and consider the substrate influence, a supplementary layer was inserted

Table 4.7: The gaseous phase densities, the values for the (liquid) FC-vapour components (vFCs) and the absorption values are calculated for ambient pressure at 293.15 K via [978, 979] and [1087]. The fluid gaseous phases are listed for 293.15 K [1088, 1089].

gas	density / $g \cdot cm^{-3}$		electron density / $e^- \cdot Å^{-3}$		absorption / $\beta \cdot 10^6$	
	gaseous	fluid	gaseous	fluid	8.048 keV	27 keV
C_4H_{10}	$2.705 \cdot 10^{-3}$	0.559	$9.529 \cdot 10^{-4}$	0.2092	$9.762 \cdot 10^{-3}$	$2.076 \cdot 10^{-4}$
C_3F_8	$7.89 \cdot 10^{-3}$	1.35	$2.3 \cdot 10^{-3}$	0.3891	$3.543 \cdot 10^{-2}$	$3.415 \cdot 10^{-4}$
C_4F_{10}	0.0123	1.517	$3.5 \cdot 10^{-3}$	0.4375	$3.513 \cdot 10^{-2}$	$3.396 \cdot 10^{-4}$
vFC	density / $g \cdot cm^{-3}$		electron density / $e^- \cdot Å^{-3}$		absorption / $\beta \cdot 10^6$	
	fluid		fluid		8.048 keV	
$C_{10}F_{18}$	1.916		0.554		$3.342 \cdot 10^{-2}$	
$C_8F_{17}Br$	1.931		0.571		$6.308 \cdot 10^{-2}$	

Table 4.8: Constants of different elements and molecules at different energies. The dispersion and absorption constants were calculated via [1087]. *Depends on the modification [1095].

compound	density / $g \cdot cm^{-3}$	dispersion / $\delta \cdot 10^6$		absorption / $\beta \cdot 10^6$	
	293.15 K	8.048 keV	27 keV	8.048 keV	27 keV
H_2O	0.998	3.57	0.316	0.0121	$1.385 \cdot 10^{-4}$
Si	2.336	7.581	0.663	0.173	$1.473 \cdot 10^{-3}$
SiO_2	2.19-2.66*	7.12	0.6264	0.0923	$8.14 \cdot 10^{-4}$
Br	3.12	8.591	0.785	0.332	0.268
F	$1.695 \cdot 10^{-3}$	$5.193 \cdot 10^{-3}$	$0.457 \cdot 10^{-3}$	$3.167 \cdot 10^{-5}$	$2.908 \cdot 10^{-7}$

between the SiO_2 layer and the first headgroup.

The solid-supported multilayer systems were only used in the non-hydrated state. The multilayer thickness can be estimated via the minima of the Kiessig fringes between the Bragg reflections. A remarkable feature of XRR curves for lipid multilayers is the occurrence of sharp Bragg reflections up to the fourth order. These peaks are caused by the highly oriented multilayers parallel to the substrate. A way to calculate the layer thickness and number of bilayers in the multilayer system is fitting a Gaussian distribution to the first Bragg reflection of the Fresnel normalised curve. The total multilayer thickness L_a is inversely proportional to the peak width Δq_z and can be calculated using the Scherrer equation

$$L_a = \frac{2\pi K}{\Delta q_z} = \frac{2\pi K}{\mathrm{FWHM}}. \tag{4.3}$$

The Scherrer constant again is denoted as K. This constant is a shape factor and common values in literature are between 0.88 and 1 depending on the lipid systems [82,

243]. The multilayer spacing d can be calculated via

$$d = \frac{2\pi}{q_{z,\mathrm{Bragg}}}. \tag{4.4}$$

The number of bilayers m in a multilayer system can then be estimated with $m = L_a/d$.

For the analysis of the protein adsorption at Langmuir films and at water/air-interfaces, some important data of the proteins are presented in table 4.9. The molar volume can be calculated using the mass density and the molecular weight of the considered protein. The molecular volume for lysozyme is 10075 cm^3/mol, for BSA a value of 50616 cm^3/mol or 48724 cm^3/mol is reached depending on the two different electron densities given in table 4.9. From the x-ray reflectivity data and the obtained electron density profiles, the volume fraction profile $\phi(z)$ along the surface normal can be calculated [1036, 1096, 1097]. The volume fraction profile is defined by subtracting the electron density profile without protein adsorbate, $\rho_{\mathrm{ref}}(z)$, from the electron density profile with protein adsorbate, $\rho(z)$, and dividing this difference by the contrast between protein and reference medium

$$\phi(z) = \frac{\rho(z) - \rho_{\mathrm{ref}}(z)}{\rho_{\mathrm{protein}} - \rho_{\mathrm{ref}}(z)}. \tag{4.5}$$

Here, ρ_{protein} is the electron density of the protein (see table 4.9). The total adsorbed amount (or surface excess) of proteins Γ can be found with[2]

$$\Gamma = \frac{m}{v} \int \phi(z)\mathrm{d}z \tag{4.6}$$

with the molar mass m and the molar volume v. This approach can only be applied if the protein is completely embedded in the homogeneous subphase $\rho(z)$ [1036, 1096, 1097]. For more complex systems, for example proteins that partially penetrate the Langmuir film or break through the liquid/gas-interface, ρ_{ref} is non-determinable and the integration on equation (4.6) can solely be used for the region where the protein is embedded in the subphase.

For HSA, the electron density of BSA is used. The human serum albumin constitutes of 35510 electrons ($C_{2936}H_{4624}N_{786}O_{889}S_{41}$).

GIXD data For the GIXD measurements an incident angle smaller than the critical angle is used. The incident angle was set to $\alpha_{\mathrm{i}} = 0.036°$ (70 % of the critical angle $\alpha_{\mathrm{c}} = 0.051°$). The GIXD pattern were collected via a position-sensitive detector. The intensity distributions of the GIXD scans were further integrated vertically in a small q_z range to determine the position and width of the lateral Bragg reflections. The data was corrected by subtracting a linear background which was scaled based on the intensity distribution in an area of the pattern where no reflection was observed. For the analysis, the measured data are plotted as a function of the wave vector transfer (see

[2]The total adsorbed amount can also be calculated with the reciprocal value of the mass density, the specific volume v_{spez} in cm^3/g with $\Gamma = \frac{1}{v_{\mathrm{spez}}} \int \phi(z)\mathrm{d}z$.

Table 4.9: Summarised key properties for lysozyme and BSA. Conformational stability, size, number of electrons (N_e), mass density (of dry protein) and electron density. [1][1097–1099], calculated with the mass density from [2][1100, 1101] and [3][1036, 1098, 1099, 1102, 1103].

protein	conformational stability	size [Å^3]	N_e	mass density [g/cm^3]	electron density [e$^-$/Å^3]
lysozyme	"hard"	30 x 30 x 45	7628[a]	1.42	0.4558[1]
BSA	"soft"	80 x 80 x 30[b]	35486[a]	1.313 1.364	0.4228[2] 0.4387[3]

[a] Calculated using the FASTA sequence P00698 for lysozyme, the molecular formula $C_{613}H_{959}N_{193}O_{185}S_{10}$ and the FASTA sequence P02769 for BSA with the molecular formula $C_{2934}H_{4615}N_{781}O_{897}S_{39}$, with Protpi.ch. Both without the signal sequence (129 aa and 583 aa).
[b] Depends intensely on the microenvironment.

Table 4.10: Formulas for the calculation of the unit cell size and lattice constant of a hexagonal lattice.

hexagonal lattice	parameter	formula
lattice constant	a	$\frac{2}{\sqrt{3}}d$
unit cell size	A_{xy}	$\frac{\sqrt{3}}{2}a^2$
molecules per unit cell	-	1
area per molecule	A_0	$\frac{\sqrt{3}}{2}a^2$

equation (3.4)). For a quantitative analysis Voigt profiles were fitted to the detected Bragg reflections. These profiles are obtained by convolution of a Gaussian profile and a Lorentzian profile. In a GIXD experiment, different effects can cause a broadening of the Bragg reflections. A broadening due to the experimental resolution has a Gaussian nature, on the contrary, the widening due to a finite crystalline domain size has a Lorentzian shape [1104]. Consequently, by applying the Voigt function, the effects can be distinguished from each other. There is no analytical expression for the Voigt profile which requires the utilisation of numerical or analytical approximations [1105]. In the beginning of the experiment the primary beam was scanned parallel to the sample surface. Thus, a Gaussian function can be fitted to the obtained beam profile to estimate the peak broadening which originates from the instrumental resolution. The calculated width defines the parameter of the Gaussian function in the Voigt profile. At high surface pressures one single Bragg reflection is expected, indicating a hexagonal packing with the unit cell parameters $a = b$, $\gamma = 120°$ of the aliphatic chains. From the position of $q_\parallel$ of the Bragg reflection the lattice plane distances $d_{h,k}$, lattice constant a and unit cell area A_0 can be calculated under consideration of equation (3.30) and (3.37). The size of the crystalline domains L can be determined with the equations (3.45) and (3.46).

Since no tilt of the lipid tails is detectable due to the resolution of the apparatus (q_z dependency of the Bragg rods), an analysis of Bragg rods and, therefore, tilt angles in the framework of this thesis is not possible. Above surface pressures of around 15 mN/m DPPA-films on water have tilt angles of nearly zero [109, 933, 1106]. Isotherm experiments reveal similar results [635, 933, 1107].

Error analysis The error handling especially of XRR data evaluated with the effective-density model is not trivial. It is possible to estimate errors by reproduced measurements. Depending on the data quality and the complexity of the sample system different error ranges can be determined. The errors can further be calculated by the variation of refinement parameters around the best fit with the lowest χ^2. It seems to be common, to allow a variation of around 5 % from χ^2 of the best fit [1036, 1096, 1099].

Chapter 5

Surface/gas-interactions

The following chapter presents the results of the investigation of the interaction of perfluorocarbons (g- and vFCs) with different lipid layer systems.

The linear perfluorocarbon gases were examined systematically in terms of size and shape. They are devoid of amphiphilicy and are highly hydrophobic. Perfluorocarbon-containing microbubbles and droplet emulsions have various biomedical applications, such as in molecular imaging and diagnostics, as artificial blood substitutes and in (targeted) drug and gene delivery. The bubble and droplet walls are in general monolayers composed of phospholipids that, thus, interact with the gaseous or liquid perfluorocarbon phase. This interaction has so far not been studied in detail [4]. Moreover, two perfluorocarbons for vaporisation that were selected are promising candidates for biomedical usage, especially for *in-vivo* oxygen delivery and ventilation (F-decalin and F-octyl bromide) and also for synthetic lung surfactant compositions. In ventilation with perfluorocarbons, the lung surfactant or alveolar lining fluid comes into direct contact with the substances. They have different molecular structures. F-decalin is a bicyclic molecule with a globular shape. In contrast, F-octyl bromide is linear with an exposed and polariseable bromide atom. It is slightly more lipophilic than F-decalin. In order to learn more about their influence on lipid phases, different initial surface pressures were used. These can also be seen as models for different degrees of lung surfactant absence, impairment and damage in respiratory diseases.

In the light of the aforementioned, it is crucial to understand the effect of perfluorocarbon-enriched gases on lipid systems. Thus, the fundamental aim of this study is to gain knowledge on the structural response of lipid model systems induced by gaseous and vaporised perfluorocarbons from the gas phase.

This chapter is subdivided into three sections. In the first section (5.1) of this chapter the XRR and GIXD results of the influence of gFCs and vFCs on DPPC- and DPPA-films with various initial surface pressures are presented. In the next section (5.2), the solid/gas-interface is discussed, where the influence of gases on spin-coated solid-supported lipid layer systems was studied. These systems offer the possibility to investigate whether the gas molecules penetrate a dense multilayer layer. The last section (5.3) deals with protein-containing systems at liquid/gas-interfaces. First, the

adsorption of lysozyme at DPPA-films under a vFC atmosphere is investigated. Then the interaction of lysozyme with g- and vFCs at the bare water/air-interface is considered. The chapter is closed with the study on the interaction between BSA and vFCs at a water surface. The serum protein is a surface-active protein which can compete with lung surfactant lipids for the adsorption at the alveolus/air-interface. With the saturation of the gaseous phase with vFCs a promotion of the re-spreading of DPPC monolayers at the interface in the presence of BSA were reported [2, 305, 442, 443, 1108]. However, not much is known about how g- and vFCs influence the protein adsorption process and resulting protein layers at the interface.

The effect of the selected g- and vFCs on the lipid systems with the chosen experimental setup and surface-sensitive x-ray scattering techniques has not been studied yet. Especially the effect of gFCs, such as C_3F_8 and C_4F_{10} on Langmuir monolayers composed of DPPC and DPPA has not been elucidated. In general, studies aiming a better understanding of the impact of non-polar and non-amphiphilic fluorocarbons on the structure of phospholipid systems are scarce [4, 497].

5.1 Liquid/gas-interfaces

This section presents the results of the interaction studies of perfluorocarbons (g- and vFCs) and an alkane with DPPC- and DPPA-films on water surfaces at different surface pressures. From XRR, GIXD and surface tension measurements the accumulation and adsorption of perfluorocarbon molecules at the liquid/gas-interface was examined.

Previous studies show that incooperated FC molecules from the gas phase drastically change the phase behaviour of lipid monolayers and lead to a fluidisation of Langmuir films. The fluorocarbon gases inhibit the formation of the liquid-condensed phase in Langmuir monolayers of DPPC or lung surfactant substitutes that instead remain in the liquid-expanded phase [1, 440, 441, 1108]. Moreover, the lipid shell can be stabilised externally via vFCs of higher molecular weight [4, 497, 505, 1109]. However, these experiments were performed at constant surface pressure meaning that the surface area increases once molecules penetrate the lipid film from the gas phase. If a fluidisation and reduction of the crystalline order also occurs at limited space is not known. Therefore, the experiments in this thesis were conducted at constant surface area. It was found, that alkane gases (*n*-butane and isobutane) significantly affect stearic acid monolayers on water [1048]. The effect of isobutane is studied on DPPA and DPPC Langmuir films with different surface pressures.

5.1.1 Experimental details

The XRR experiments were performed mainly at the laboratory diffractometer D8 of the chair E1a at TU Dortmund and P08 at PETRA III utilising the end-station LISA [1056, 1065, 1066]. The GIXD measurements were performed at beamline I07 of DLS using the DCD end-station [1055, 1067, 1068]. The two surface-sensitive techniques reveal a comprehensive picture of the sample system. Apart from the measurements at PETRA III, where the temperature was set to 297.8 K, data were collected at a temperature of

294.15 K. The samples were prepared as explained in chapter 4. For the measurements under elevated pressure with the gaseous perfluorocarbons and the alkane isobutane, the custom-build gas pressure cell in combination with the round PTFE plate (see section 4.1) equipped with an installed Wilhelmy balance was applied. The gas pressures of C_4H_{10}, C_3F_8 and C_4F_{10} were varied between 1 bar and the condensation pressure or the maximum pressure the custom-made pressure cell (5 bar) is certified for. The scans were performed 5 min. after filling the gas into the cell or increasing the pressure. The first measurement at ambient pressure was conducted after flushing the cell with the selected gas. In addition, scans at air before and after gas treatment were recorded to get references of the system and to test the stability of the film after it was exposed to gas for a longer period. And to study the reversibility of the observed effects. The applied gas pressures are given as dimensionless value p/p_0, normalised to the condensation pressure of the considered gas.

The accuracy of the parameters extracted from the XRR experiments is estimated to be about 0.5 - 1 Å for the thickness of the head- and tailgroups and 0.3 - 0.5 Å for the roughness.

5.1.2 gFC and vFC adsorption on Langmuir films

Lipid bilayers of biological membranes consists of two weakly coupled lipid monolayers. Langmuir layers therefore represent an interesting, simple and proofed model system mimicking a membrane interface [215, 225, 1110, 1111]. Especially adsorption phenomena have been studied successfully based on these systems. Since monolayers reflect half of a membrane, they are rather restricted for the analysis of transmembrane processes, but they are well-suited models for the analysis of processes at the membrane surface [1112]. Since the native lung surfactant is a complex mixture of lipids and proteins which form a monolayer at the alveolus/air-interface of mammalian species, the Langmuir film model is highly suitable to mimic these systems accurately [337]. The major components of lung surfactant are mostly saturated phosphatidylcholines, DPPC is present with around 40 %. For further information on lung surfactant and DPPC, please refer to chapter 2 section 2.2. An important role of lung surfactant is to reduce surface tension upon compression (= while expiration, $\gamma < 2$ mN/m) and to rapidly re-spread again on expansion (= while inspiration, $\gamma \approx 20$ mN/m) [1, 331, 332, 1113].

Figure 5.1 shows the Π-A isotherms of DPPA and DPPC on a water surface at a temperature of 294.15 K. The red arrows indicate the initial surface pressures where XRR measurements were conducted. The measured Π-A isotherms are similar to those presented in the literature [635, 933, 1114, 1115]. The course of the DPPA isotherm is typical for lipids with small headgroups with strong van der Waals attractions and hydrogen bonding of the phosphate headgroups. When the cross-sectional area of the polar head is small, the interaction of the lipids is dominated by van der Waals forces and hydrophobic interactions of the alkyl chains. Therefore, DPPA forms highly ordered structures already at low surface pressures and no distinct liquid-expanded regime is observed at room temperature [1116, 1117]. The lift-off area on a water subphase is at around 48 Å^2/molecule. A phase transition is indicated by a slight kink of the

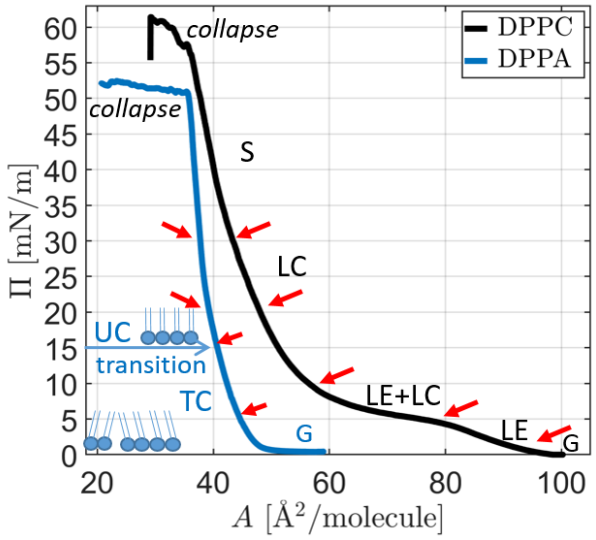

Figure 5.1: Π-A isotherms of DPPC and DPPA on a ultra-pure water subphase a pH-value of 7 at $T = 294.15\,\mathrm{K}$. G: gaseous, LE: liquid-expanded, LC: liquid-condensed, TC: tilted-LC, UC: untilted-LC phase. The red arrows indicate the initial surface pressures where XRR measurements were performed.

isotherm at a surface pressure of around 15 mN/m (41 Å^2/molecule) from the tilted-condensed to the untilted-condensed phase. The constant pressure regime at 52 mN/m (35 Å^2/molecule) indicates a film collapse. Similar values can be found in literature [635]. X-ray diffraction studies show that DPPA changes with increasing surface pressure from an oblique to rectangular to hexagonal packing lattice [933, 1118].

For DPPC a lift-off area of around 100 Å^2/molecule and collapse area of 34 Å^2/molecule at a surface pressure of 60 mN/m was observed in good agreement with the literature [1115, 1119]. The liquid-expanded to liquid-condensed phase transition occurs between 3.6 mN/m and 5.6 mN/m. This is not a real first-order transition as the surface pressure is not entirely constant in the coexistence region. Neither can it be interpreted as a second-order phase transition which is characterised by a kink in the Π-A isotherm. The slight pressure increase during the transition may result from a not sufficiently slow compression to guarantee equilibrium at any point. The surface pressure change during the transition agrees with values found in literature ($\Pi_t = 3.5 - 3.7\,\mathrm{mN/m}$ and $\Pi_t = 4.3 - 5.6\,\mathrm{mN/m}$) [1120, 1121].

The XRR and GIXD measurements were recorded with monolayers that were prepared by the dropping method. The dropping method reveals isotherms that are slightly shifted in horizontal direction to higher area per molecule (take-off at higher A) and a vertical shift to higher surface pressures (higher Π at the same A). Furthermore, they show a gradual transition compared to the sharp transitions in the compression isotherms [1122, 1123]. However, the reference measurements and the corresponding structural parameters within the refinements (thickness, roughness and electron densities) of DPPA and DPPC reveal similar results for dropped and compressed Langmuir films. Therefore, the results determined with the different preparation methods can be compared to each other.

The experimentally obtained XRR results on the response of DPPC- and DPPA-films under increasing gas pressure are presented in the following. First, Langmuir layers

composed of DPPC and then DPPA-films with different initial surface pressures are discussed. The notation "N_2" means measurements at air atmosphere after flushing the sample with nitrogen. The gaseous compounds can be classified in the following series:

$$\begin{aligned} \textbf{log } \boldsymbol{P}\textbf{, } \boldsymbol{V} \textbf{ and } \boldsymbol{R_g}: &\quad C_4H_{10} < C_3F_8 < C_4F_{10} \qquad \text{and} \\ \textbf{cohesivity, hydrophilicity, } \boldsymbol{\gamma}: &\quad C_4H_{10} > C_3F_8 > C_4F_{10}. \end{aligned}$$

Here, V, R_g and $\log P$ are the volume, the gyration radius and the logarithm of the partition coefficient, respectively. The used hydrocarbon and gaseous perfluorinated compounds are non-polar. The fluorocarbon liquids have low cohesive energy densities in comparison to hydrocarbons and, therefore, exhibit lower surface energies than the corresponding hydrocarbon. Moreover, perfluorocarbons are significantly more hydrophobic than hydrocarbons in aqueous medium. This is also reflected in lower water solubility of fluorocarbon gases compared to hydrocarbon gases [1124].

DPPC-films in interaction with different gases First, the effects of isobutane on DPPC Langmuir films with different initial surface pressures are shown. At a temperature of 294.15 K, isobutane has a condensation pressure of $p_0 = 3.115$ bar. The electron density of the non-polar hydrocarbon in its fluid phase is $0.2092\,e^-/Å^3$ ($0.622 \cdot \rho_{H_2O}$). Isobutane has a globular shape with a gyration radius of 2.948 Å. It is the smallest gas molecule that was applied to the Langmuir films.

Figure 5.2 shows the Fresnel normalised XRR curves of DPPC-films on a water subphase under increasing isobutane gas pressures on the left-hand side. The solid black lines represent the refinements to the data. The corresponding normalised electron density profiles are presented on the right-hand side of the figure. The initial surface pressures of the DPPC Langmuir films are $\Pi_{ini} = 5, 10$ and $30\,mN/m$. The x-ray reflectivity curves were measured at the laboratory diffractometer D8 up to a wave vector transfer of $q_z = 0.45\,Å^{-1}$. As explained in the section 4.5 the data were background corrected and refined by using a two-layer model applying the Parratt algorithm in combination with the effective-density model. The polar headgroups and the alkyl chains of the DPPC molecules can be well distinguished at every reference measurement. A reflectivity of the bare water/air-interface is also given in grey. The obtained electron density of the water subphase (ρ_{H_2O}) was calculated to $0.3359\,e^-/Å^3$ with a roughness of around $\sigma_{H_2O} = 3.48$ Å. These values are in accordance with the literature data [907, 1125]. The calculated reference values of the lipid monolayer at the given initial surface pressure were used for the subsequent fits. The best-fit values of the reference measurements at air are given in table 5.1. The obtained reference profiles are in accordance to the values found in literature [1126–1128].

The selected surface pressures of 5, 10 and $30\,mN/m$ correspond to the liquid-expanded and liquid-condensed co-existence phase, the tilted liquid-condensed and a less tilted liquid-condensed phase of the DPPC Langmuir film. As can be seen on the left-hand side of the figure, the minimum of the oscillation of the reference measurements at air shifts to the left, towards smaller q_z values, with increased Π_{ini} indicating a higher DPPC layer thickness due to the higher compression. At an initial surface

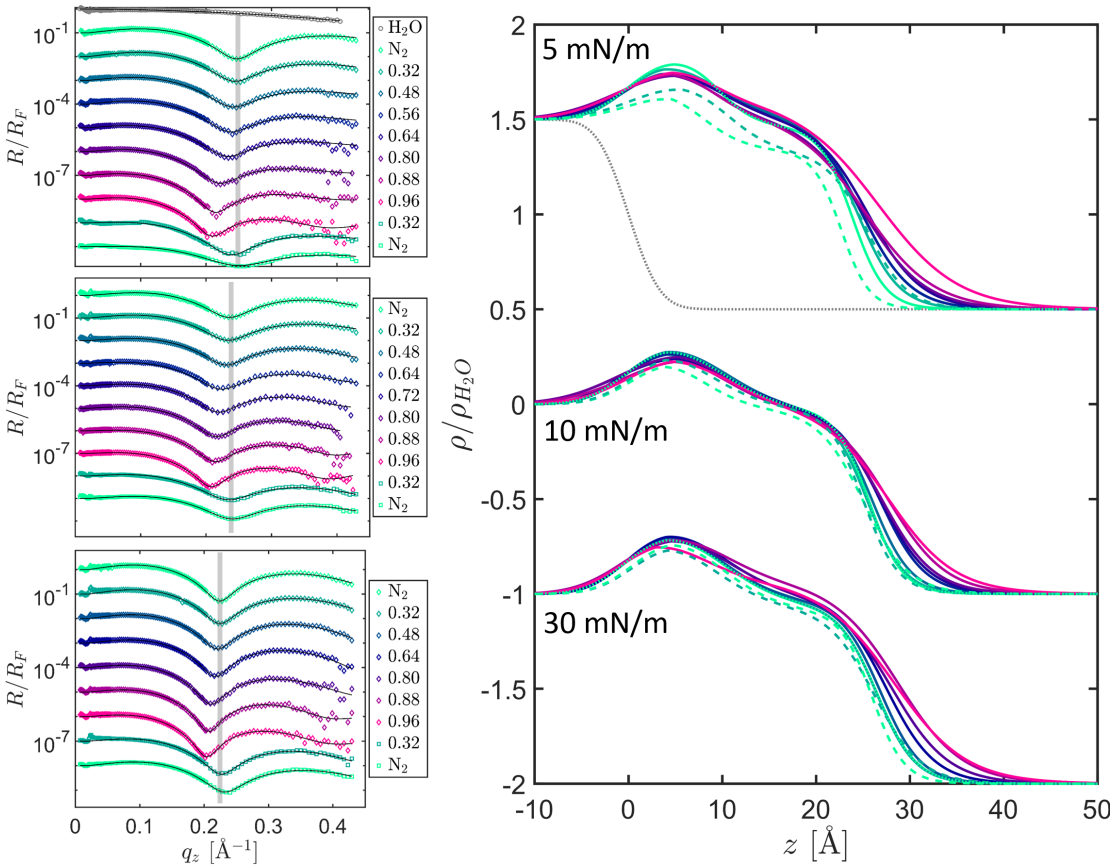

Figure 5.2: Left: Fresnel normalised XRR data of DPPC on a water subphase with different initial surface pressures and successively increasing isobutane gas pressures. Diamonds: data, solid lines: fits, squares: decreasing gas pressure, grey: water/air-interface. From top to bottom: 5, 10 and 30 mN/m. Right: Electron density profiles obtained from the refinement of the reflectivity data on the left. The density profiles are normalised to the bulk water density. The reflectivity curves and electron density profiles are shifted vertically for better visibility.

pressure $\Pi_{\text{ini}} = 10\,\text{mN/m}$, the DPPC-film already passed the co-existence region and is in a liquid-condensed phase. However, the liquid-condensed domains are still embedded in liquid-expanded-like areas due to packing defects and finite crystalline sizes. At an initial surface pressure of $\Pi_{\text{ini}} = 30\,\text{mN/m}$, the DPPC-film is denser packed and the tilt angle is reduced indicated by an increase of the thickness and electron densities. The tail chain length of 16.3 Å is in accordance with [1129]. The headgroups can adopt different configurations depending on the surface pressure (5 - 12.7 Å). The observed values are in accordance with literature data [1128–1131]. The maximal tail length of an alipathic chain with n CH_2 groups ($n = 14$) in an all-*trans* configuration is $d_{\text{max}} = 1.5 + n \cdot 1.265\,\text{Å} = 19.2\,\text{Å}$ for DPPC [1130]. With no water molecules intercalating to the headgroups of the monolayer, the Tanford length is calculated to 20.5 Å [140, 1129]. It is commonly observed, that the lipid tail thickness of lipid monolayers at

Table 5.1: The best-fit parameters of the reference measurements at air for different initial surface pressures of a DPPC-film. The water roughness was set to 3.48 Å. The water density is $0.3359\,e^-/Å^3$. The tilt angle is calculated via $\cos(\beta) = d_{t,max}/19.2\,Å$. ρ_{norm} is the normalised electron density to the water electron density.

	5 mN/m		10 mN/m		30 mN/m	
parameter	head	tail	head	tail	head	tail
ρ_{norm}	1.345	0.965	1.359	0.967	1.373	0.941
σ / Å	3.538	3.148	5.715	3.229	5.678	3.761
d / Å	9.42	14.24	10	15.64	10.18	16.33
tilt angle / °	-	42.13	-	35.45	-	31.73

the water/air-interface increases as a result of an increase of the surface pressure. It is known, that the phosphatidylcholine moiety of the polar headgroup of DPPC can adopt different configurations and thus exhibits different thicknesses and an "untilting" at higher surface pressures [1130]. Furthermore, it is known, that the headgroup of DPPC is oriented horizontally to the water interface at low surface pressures.

Previous experiments at the water/gas-interface showed a complete wetting adsorption for isobutane with a negative effective Hamaker constant [526, 527]. Isobutane has a very low water solubility at 293.15 K with about 49 mg/l and is practically insoluble in water. The measurements of DPPC at different initial surface pressures show a similar behaviour at increasing isobutane gas pressures. As it can be seen in the XRR curves in figure 5.2, by increasing the gas pressure the minimum of the oscillation shifts to lower q_z values, indicating an increasing layer thickness. At pressures near to the condensation pressure of isobutane, the shift of the oscillation becomes more pronounced.

Replacing air by isobutane causes an increased tailgroup thickness and roughness and, moreover, an increased roughness between the head- and tailgroups. This can be observed for all investigated initial surface pressures. At a low surface pressure of 5 mN/m a surface pressure increase to around 19.8 mN/m at $p/p_0 = 0.96$ is observed. At initial surface pressures of 10 mN/m and 30 mN/m an increase to 29.6 mN/m and 35.9 mN/m were observed at $p/p_0 = 0.96$, respectively. The surface pressure increases mostly due to the adsorption of gas molecules at the free water surface. The gas molecules presumably cluster at the interface and form islands between the lipid molecules, this leads to a compression of the film and a reduction of the tilt angle of the alkyl chains.

The lipid tails are not fully stretched at the highest gas pressure applied at the lowest initial surface pressure of 5 mN/m. In contrast, at the highest initial surface pressure of 30 mN/m, the thickness of the tailgroup at the highest gas pressure is about 21.4 Å. This value is slightly higher than the maximum tail length of DPPC. This could be due to a vertical displacement of the lipids or adsorption of gas molecules on top of the lipid chains. However, no improvement of the fit was reached by adding a third layer to the model which represents an adsorbate layer with a freely adjustable electron density.

Since isobutane has the smallest gyration radius, it can penetrate the alkyl chains

at some places and cause a compression even at high lipid coverage of the surface. The gas molecules adsorb via van der Waals interactions at the bare water surface and can interact via hydrophobic forces with the lipid tailgroups. It seems that the hydrophobic region of the lipid layer is packed with gas molecules at high gas pressures. The headgroups are also affected. They expand upon adsorption of gas molecules and the electron density decreases. This may indicate a change of the headgroup configuration.

The re-spreading ability after compression via the gas molecules and the de-lipidation of the surface were tested by reducing the gas pressure after a measurement series and replacing the gas atmosphere by air. The re-spreading ability of DPPC is generally not very good after a compression-cycle. After releasing gas from the pressure cell to $p/p_0 = 0.32$ the Langmuir layer structure remains stable. But after flushing the cell with nitrogen, the averaged over-all electron density decreases. This can be explained by dissolution of lipid molecules in the adsorbed alkane layer. This is most likely due to the higher alkane to lipid molecule ratio at the interface at high gas pressures. The effect becomes less pronounced at higher initial surface pressures of the Langmuir layer.

Giebel et al. found for stearic acid films a deep penetration of butane molecules and a preferred adsorption site near the headgroups [1048]. This is in good agreement with the observation that the roughness between the head- and tailgroups of DPPC are increased with increasing gas pressure at all initial surface pressures. However, while the stearic acid films were totally dissolved, for DPPC the monolayer structure consisting of a distinctive head- and tailgroup maintained at all pressures and a total dissolution did not occur.

The Langmuir film consisting of DPPC molecules is more stable than the Langmuir films of single chain fatty acids. The stability results from the enhanced hydrophilic/hydrophilic-interaction of the headgroups but also from the hydrophobic/hydrophobic-interaction of the tailgroups. These stabilise the Langmuir film against dissolution by isobutane, even near the condensation pressure. It is known that monolayers which exhibit co-existing phases have significantly different physical properties compared to single-phase lipids like stearic acid [336, 362, 1132].

In the following the results of the response of DPPC-films at different initial surface pressures under increasing F-propane gas pressures are presented. At a temperature of 294.15 K, F-propane has a condensation pressure of $p_0 = 7.779$ bar. It has a stretched shape. It exhibits a lower water solubility with about 5.7 mg/l at 15 °C and has a larger gyration radius of 3.736 Åcompared to isobutane. The electron density of fluid F-propane is $0.3891\,\mathrm{e}^-/\mathrm{Å}^3$ ($1.1583 \cdot \rho_{\mathrm{H_2O}}$). Figure 5.3 illustrates the XRR data of DPPC-films under elevated gas pressures of F-propane. The Fresnel normalised XRR curves of the data series are shown on the left-hand side of the figure. The black solid lines are the refinements to the measured XRR curves. The right-hand side depicts the obtained electron density profiles normalised to the bulk water electron density. Here, also the gaseous phase of DPPC was investigated at a surface pressure of 2 mN/m and an area of 95 $\mathrm{Å}^2$ per molecule. It was possible to refine the data with a one-layer model with a layer thickness of 16 Å, where head- and tailgroups are not separated. This model is in accordance with literature data [109, 1133]. The measurements were conducted at initial surfaces pressures of 2, 10, 18 and 30 mN/m. The best-fit values for the

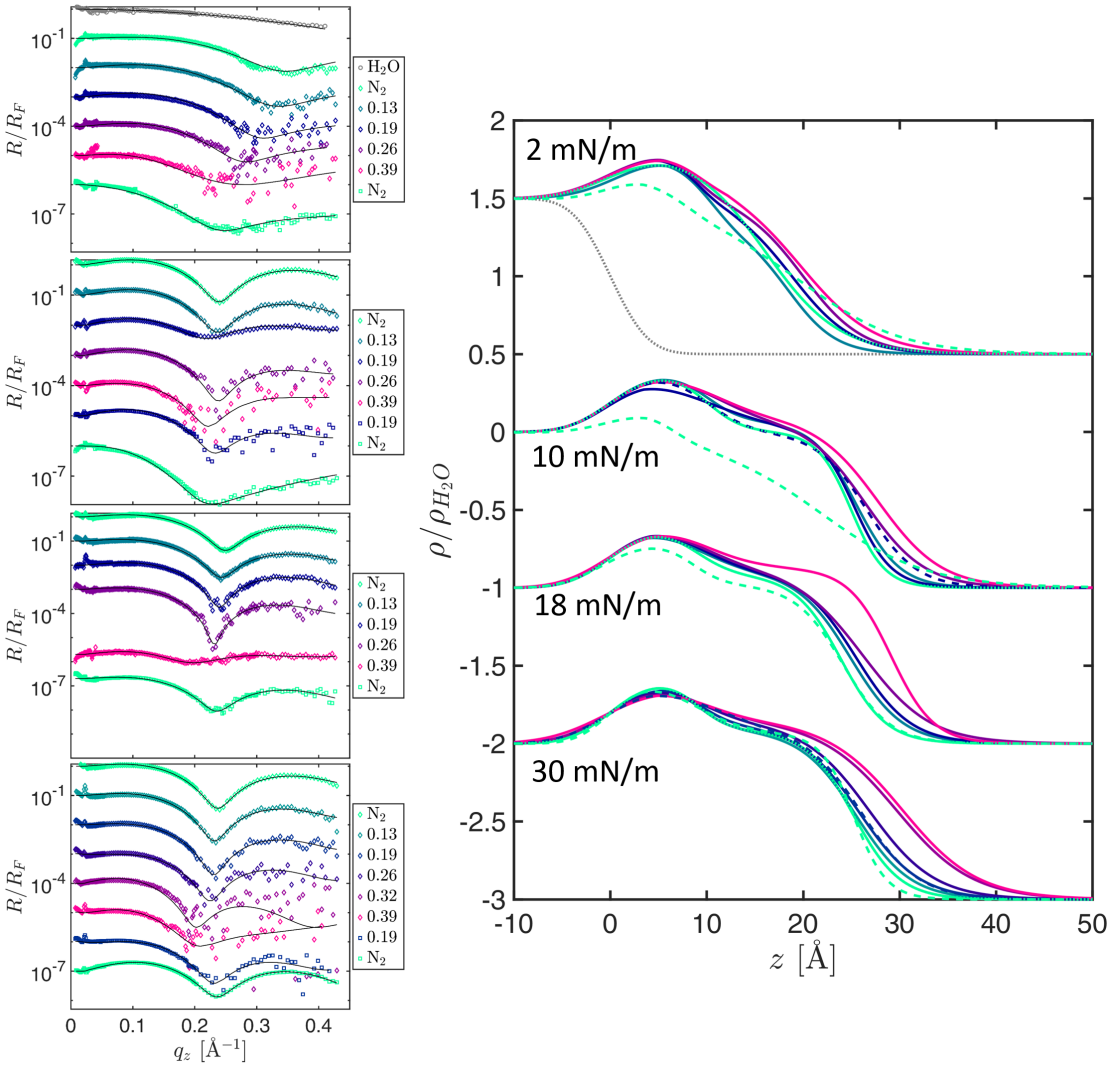

Figure 5.3: Left: Fresnel normalised XRR data of DPPC on a water subphase with different initial surface pressures and successively increasing F-propane gas pressures. From top to bottom: 2, 10, 18 and 30 mN/m. Diamonds: data, solid lines: fits, squares: decreasing gas pressure, grey: water/air-interface. Right: Electron density profiles obtained from the refinement of the reflectivity data on the left. The density profiles are normalised to the bulk water density. The reflectivity curves and electron density profiles are shifted vertically for better visibility.

reference measurements are summarised in table 5.2. By increasing the gas pressure, the detectable q_z range decreases due to a strong absorption of the incoming x-ray beam by the dense gas atmosphere, this is accompanied by an increased background.

For all initial surface pressures, an accumulation of the gas molecules at the water interface between the transition from head- to tailgroup can be observed. Furthermore, it was necessary to apply a two-layer model to refine the data of the 2 mN/m measure-

Table 5.2: The best-fit parameters of the reference measurements at air for different initial surface pressures of the DPPC-film. The water roughness was set between 3.48 and 3.8 Å. The water density is 0.3359 $e^-/Å^3$. The tilt angle is calculated via $\cos(\beta) = d_{t,max}/19.2\,Å$. ρ_{norm} is the normalised electron density to the water electron density.

	2 mN/m	10 mN/m		18 mN/m		30 mN/m	
parameter	layer	head	tail	head	tail	head	tail
ρ_{norm}	1.313	1.38	1.0	1.392	1.07	1.4062	1.08
σ / Å	6.933	3.31	3.197	3.591	4.281	2.932	4.408
d / Å	16.1	10.08	14.88	8.91	15.02	9.10	16.09
tilt angle / °	-	-	39.19	-	38.53	-	33.07

ment after increasing the gas pressure to about $p/p_0 = 0.13$. A reduction of the gas pressure leads to a substantial change of the lipid film at the low initial surface pressure and seems to destroy the vertical lipid structure. The surface pressures increase at $p/p_0 = 0.39$ to 13.2, 18.5, 26.3 and 36.3 mN/m for the initial surface pressures of 2, 10, 18 and 30 mN/m, respectively.

Figure 5.4 presents the results of the measurements of DPPC-films in contact with F-butane. The Fresnel normalised XRR curves are shown on the left-hand side. The solid black lines are the refinements to the data. The right-hand side of the figure depicts the corresponding electron density profiles. At the applied temperature of 297.8 K F-butane has a condensation pressure of 2.652 bar. The water solubility of F-butane is 10.56 mg/ml at 298.15 K. The data were collected at the beamline P08 at PETRA III with the LISA end-station.

The best-fit parameters are given in table 5.3. The surface pressures increase at $p/p_0 = 0.93$ to 17.2, 17.7, 25.2, 32.6 and 36 mN/m for the initial surface pressures of 2, 5, 10, 18 and 30 mN/m, respectively.

The film with the lowest surface pressure of 2 mN/m can again be fitted by a one-layer model. In contact with F-butane a two-layer model is needed, similar to the case of a 2 mN/m DPPC-film under a F-propane atmosphere. After formation of the two separated layers, the electron density and thickness of the tailgroups increase. This can be explained by a gas pressure-dependent untilting of the alkyl chains due to a compression of the film by adsorbed gas molecules.

At the initial surface pressures of 5 and 10 mN/m the layer is separated into two well distinguishable layers. The headgroups seem to change their conformation during the treatment with F-butane. The tailgroups are compressed by F-butane and the thickness increases. The electron density increase indicates a gas molecule penetration into the alkyl chains, which becomes more intense with increasing gas pressures. The roughness of the tailgroups and between the head- and tailgroups is also increased.

A completely different behaviour is found at the initial surface pressures of 18 and 30 mN/m. At these surface pressures the DPPC-films are in a tilted liquid-condensed phase. Already at the lowest gas pressure the headgroup thickness increases to over 13 Å and 15.3 Å at an initial surface pressure of 18 mN/m and 30 mN/m at $p/p_0 = 0.38$,

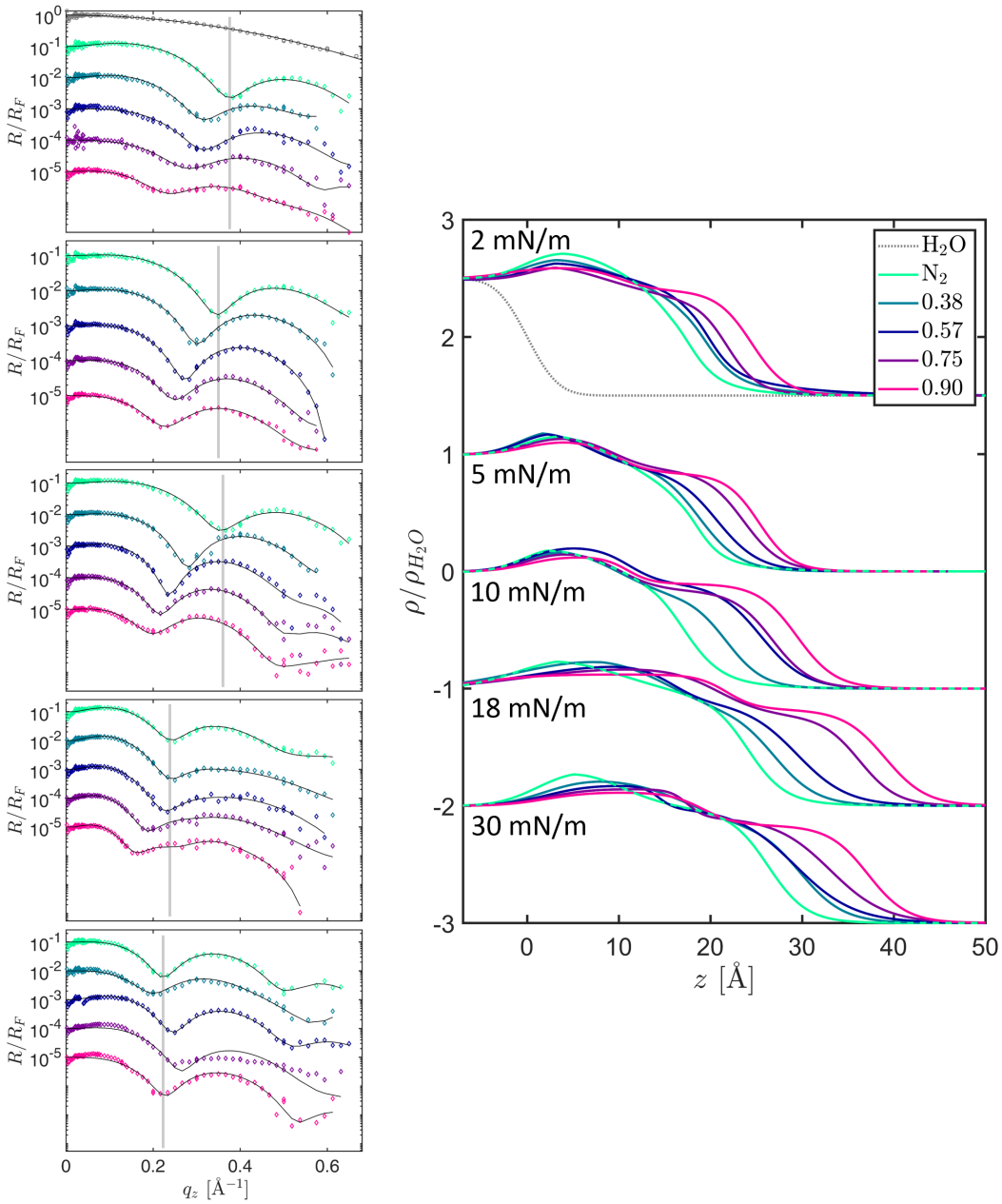

Figure 5.4: Left: Fresnel normalised XRR data of DPPC on a water subphase with different initial surface pressures and successively increasing F-butane gas pressures. From top to bottom: 2, 5, 10, 18 and 30 mN/m. Diamonds: data, solid lines: fits, squares: decreasing gas pressure, grey: water/air-interface. Right: Electron density profiles obtained from the refinement of the reflectivity data on the left. The density profiles are normalised to the bulk water density. The reflectivity curves and electron density profiles are shifted horizontally or vertically for better visibility.

Table 5.3: The best-fit parameters of the reference measurements at air for different initial surface pressures of the DPPC-film. The water roughness was set between 3.3 and 3.48 Å. The water density is 0.3359 $e^-/Å^3$. The tilt angle is calculated via $\cos(\beta) = d_{t,max}/19.2\,Å$. ρ_{norm} is the normalised electron density to the water electron density.

	2 mN/m	5 mN/m		10 mN/m	
parameter	layer	head	tail	head	tail
ρ_{norm}	1.2013	1.2021	0.5741	1.2387	0.8091
σ / Å	8	7.112	2.569	8.644	3.572
d / Å	17.01	10.21	7.76	7.35	9.51
tilt angle / °	-	-	66	-	60
	18 mN/m		30 mN/m		
parameter	head	tail	head	tail	
ρ_{norm}	1.3232	0.8405	1.3235	0.889	
σ / Å	9.038	3.66	6.019	3.806	
d / Å	8.47	15.52	7.4	16.90	
tilt angle / °	-	36.1	-	28.33	

respectively. At the highest gas pressure of $p/p_0 = 0.90$ the headgroup layer thickness increases to 27.7 Å at 18 mN/m and 17.1 Å at 30 mN/m. The tailgroup thickness of lipids also increases steadily, but the maximum increase is only 2.5 Å for both surface pressures. The contrast between head- and tailgroup is reduced. The total layer thickness is drastically increased, which is particularly noticeable at an initial surface pressure of 18 mN/m. The resulting layer thicknesses exceed the length of fully stretched DPPC molecules and, therefore, the formation of a broad film of adsorbed gas molecules at the interface can be concluded. The headgroups cannot be distinguished from the water/F-butane film, whilst the tailgroups are still visible. The lipid molecules are probably located on a water/F-butane mixture. It was not possible to improve the fit by applying a three-layer model with an adsorbate layer on top of the tails. However, a complete dissolution of the lipids in the adsorbed gas film is not observed, the tailgroups of the lipids are still clearly visible and after gas release the surface pressure assumes slightly lower values than the initial value. Although F-butane is strongly non-polar, it adsorbs via van der Waals interactions at the water interface and between the lipid headgroups. The thermodynamically favoured and stable structure of the Langmuir film is affected but not completely destroyed. The more densely packed film at 30 mN/m seems to suppress the penetration of high amounts of gas molecules as the expansion of the layer system is less pronounced compared to the 18 mN/m measurement.

DPPC Langmuir films appear to be stable enough not to be dissolved by isobutane molecules, but it is possible to damage the Langmuir film with larger gas molecules, such as F-butane. In order to compare the adsorption effects of different gases on DPPC-films, the total layer thicknesses were determined as: $d_t + d_h + \sigma_0 + \sigma_t$. Here, d_t is the layer thickness of the tailgroup and d_h is the layer thickness of the headgroup. The

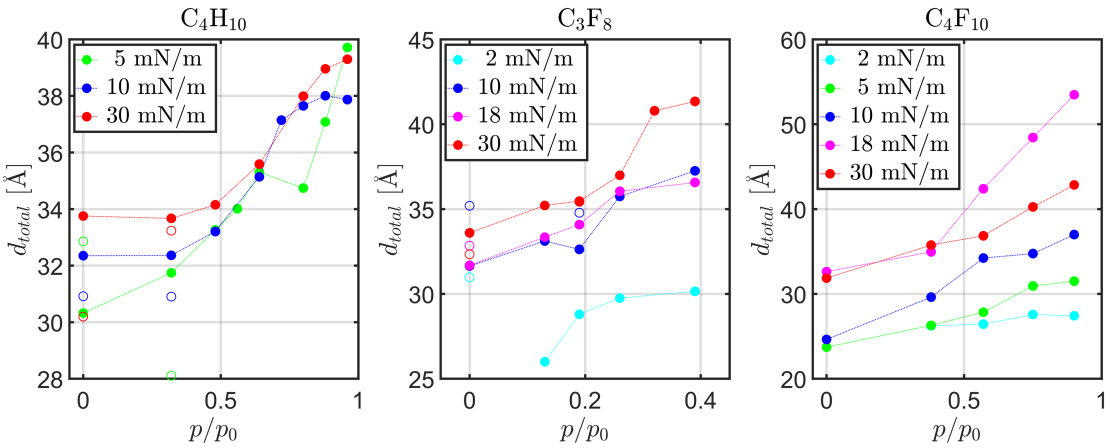

Figure 5.5: Gas pressure-dependent change of the total DPPC Langmuir layer thickness. The gas pressure is normalised to the condensation pressure. From left to right: C_4H_{10}, C_3F_8 and C_4F_{10}. The open empty markers represent the values after reduction of the gas pressure.

roughness of the substrate and the tailgroup are σ_0 and σ_t. Figure 5.5 shows the gas pressure-dependent changes of the total thickness of DPPC-films. The diagrams are sorted in ascending order from left to right according to the size of the gas molecules. It can be seen, larger gas molecules have a stronger influence on the total layer thickness.

At low initial surface pressures of DPPC-films, the gases can penetrate the layer more easily and also accumulate at the water surface. This causes a compression of the film. At high initial surface pressures an incorporation into the film is also observed. This leads to a substantial change of the Langmuir layer in case of F-butane.

DPPA-films in interaction with different gases The phospholipids DPPA and DPPC share the same alkyl chain configuration and length. But they exhibit different packing parameter p [137]. For the PC p is smaller or close to one, since the headgroup is relatively large with a slightly conical or nearly cylindrical shape. The DPPA headgroup is small and the packing parameter is higher than one [137, 1134]. DPPA has a small headgroup with a phosphatidic acid moiety. Several studies have shown, that DPPA is sensitive to hydrogen bonding, electrostatic interactions and the pH-value. DPPA can vary its phosphate group protonation from neutral to a doubly negative ionisation state in dependence of the pH-value and interaction partners. At a pH-value of 7, DPPA is singly negatively charged and can form intermolecular hydrogen bonds (phosphate-phosphate). The maximal chain thickness is the same as for DPPC. DPPA-films are more densely packed and have higher condensed order. The hydrophilic phosphate headgroup, which bears no further moieties, has smaller cross-sectional area than DPPC. Due to the smaller headgroup, the DPPA alkyl chains are oriented nearly perpendicular to the water/air-interface [1134, 1135]. In the following, the results of the adsorption of isobutane on DPPA-films will be presented.

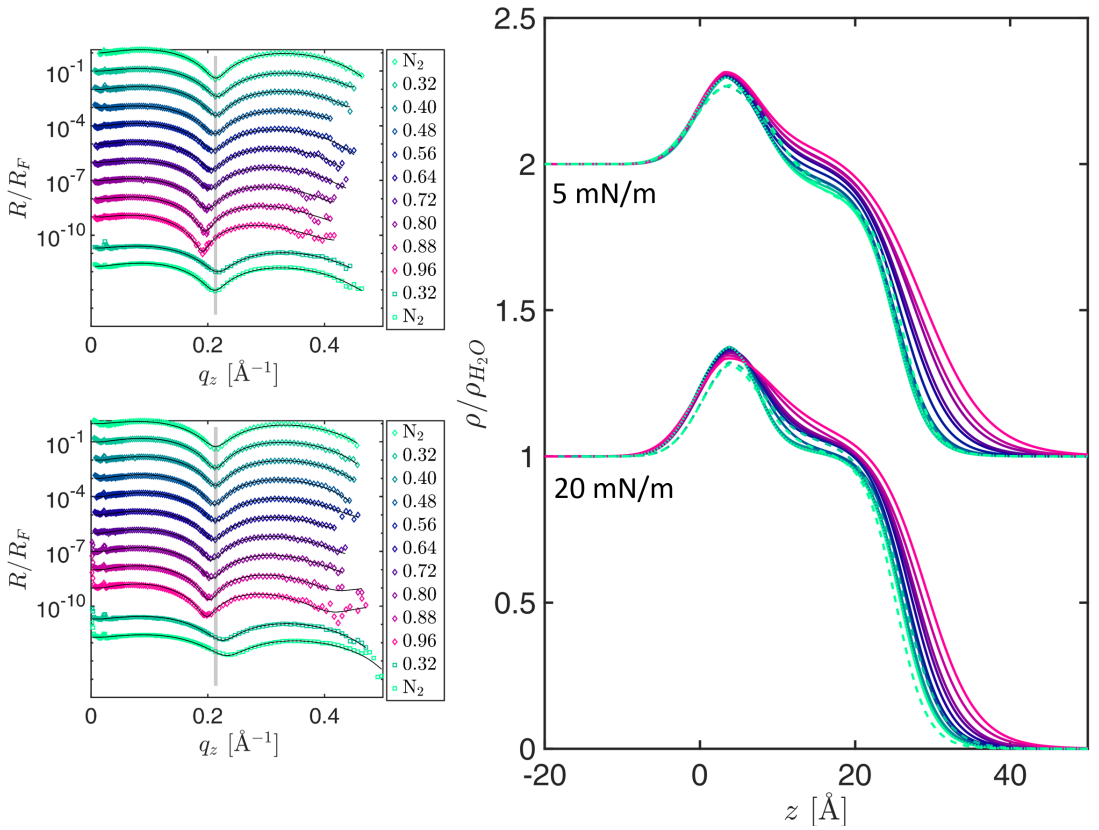

Figure 5.6: Left: Fresnel normalised XRR data of DPPA on a water subphase with different initial surface pressures and successively increasing isobutane gas pressures. From top to bottom: 5, 20 mN/m. Diamonds: data, solid lines: fits, squares: decreasing gas pressure. Right: Electron density profiles obtained from the refinement of the reflectivity data on the left. The density profiles are normalised to the bulk water electron density. The reflectivity curves and electron density profiles are shifted vertically for better visibility.

Figure 5.6 visualises the results of the isobutane pressure-dependent measurements on the behaviour of DPPA-films at two different initial surface pressures Π_{ini}. The data were recorded at a pH-value of 7. As can be seen on the left side of the figure, the reflectivity curves shift to smaller q_z values with increasing gas pressure indicating an increasing thickness of the film. Moreover, the oscillations become more pronounced. Table 5.4 summarises the results of the reference measurements at the different initial surface pressures. The reference values are in accordance to values found in literature [1136]. The effects of isobutane on the DPPA-film are similar for both investigated initial surface pressures. The initial surface pressures of 5 mN/m and 20 mN/m reflects the tilted and untilted liquid-condensed phase of DPPA, respectively. After the exchange of air by isobutane, it can be observed that especially the roughness of the headgroups and the electron density between head- and tailgroup increase. This indicates an adsorption of gas molecules at this location. At higher gas pressures the electron density increase

Table 5.4: The best-fit parameters of the reference measurements at air for different initial surface pressures of a DPPA-film. The water roughness was set to 3.4 Å for all reference measurements. The water density is 0.3359 $e^-/Å^3$. Tilt angle calculated via $\cos(\beta) = d_{t,max}/19.2\,Å$. ρ_{norm} is the electron density normalised to the water electron density.

	5 mN/m		20 mN/m	
parameter	head	tail	head	tail
ρ_{norm}	0.4811	0.308	0.498	0.4082
σ / Å	4.381	3.920	3.215	3.884
d / Å	7.73	17.52	7.11	18.71
tilt angle / °	-	24.15	-	12.97

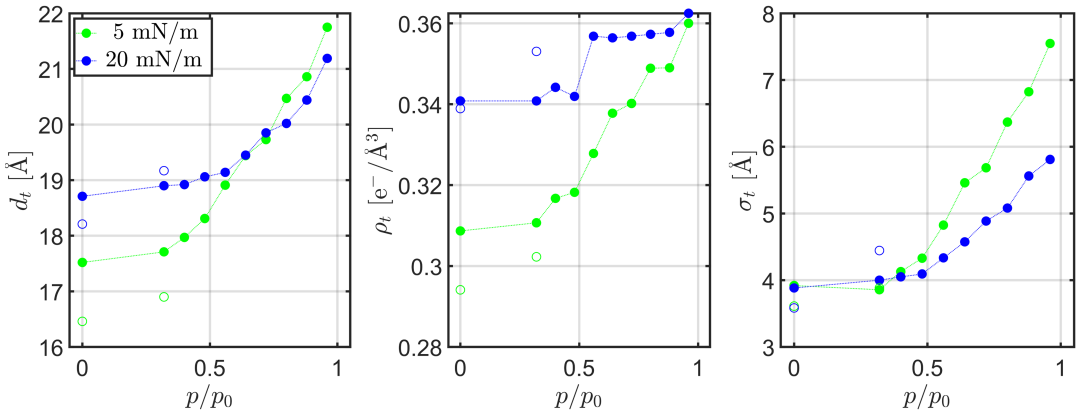

Figure 5.7: Isobutane gas pressure-dependent change of the tailgroup thickness d_t, the electron density ρ_t and the roughness σ_t of DPPA-films with initial surface pressures of 5 and 20 mN/m. The open empty markers represent the values after reduction of the gas pressure.

of the tailgroups shows that this region is filled with isobutane molecules. Even at high pressures, close to the condensation pressure, the Langmuir layer seems to be intact. Furthermore, in contrast to DPPC, the headgroups are not influenced by the gas molecules. The tailgroups are stretched during gas treatment, so that the monolayer can transform into a more compressed state. In contrast to DPPC, after reduction of the gas pressure and subsequent flushing with nitrogen the initial film structure is restored.

Since only the tailgroups of DPPA are affected by isobutane, the layer thicknesses, roughnesses and electron densities can be compared to analyse the adsorption process. Figure 5.7 shows the gas pressure-dependent change of these values. As can be seen, the thickness, electron density and roughness increase with gas pressure. Since the maximum value of the tailgroup layer thickness is exceeded, one could assume an accumulation above the Langmuir film. However, it was not possible to refine the system with a three-layer model. The response to the increased gas pressures is higher at low initial surface pressures. At a surface pressure of 5 mN/m the DPPA-film is in a tilted liquid-condensed phase. This Langmuir film structure and phase is comparable

Table 5.5: The best-fit parameters of the reference measurements at air for different initial surface pressures of a DPPA-film. The water roughness was set to 3.4 Å for all reference measurements. The water density is $0.3359\,e^-/Å^3$. Tilt angle calculated via $\cos(\beta) = d_{t,max}/19.2\,Å$. ρ_{norm} is the electron density normalised to the water electron density.

	5 mN/m		15 mN/m		28 mN/m	
parameter	head	tail	head	tail	head	tail
ρ_{norm}	1.4324	0.919	1.4482	0.98	1.3819	1.0137
σ / Å	4.381	3.92	3.22	4.033	2.637	4.542
d / Å	7.73	17.52	7.59	19.14	6.75	19.64
tilt angle / °	-	24.15	-	4.53	-	0

to stearic acid at a surface pressure of 15 mN/m and, thus, the results can be compared with those of Giebel et al. [1048]. Stearic acid has a small headgroup, which can form hydrogen bonds such as DPPA. The stability of the Langmuir layers containing DPPA or DPPC can be traced back to the higher alkyl chain content. Stearic acid has only one 17-carbon chain which is bonded to a carboxylic acid, so that the van der Waals attraction between the molecules is less pronounced. The number of alkyl chains of the lipid, therefore, seems to have a great influence on the dissolving effect. The surface pressure at $p/p_0 = 0.96$ increase to 21 and 34 mN/m for the initial surface pressures of 5 and 20 mN/m, respectively. The values are restored after the gas is released.

Figure 5.8 shows the results of the gas pressure-dependent measurements of F-propane on DPPA-films at initial surface pressures of $\Pi_{ini} = 5$, 15 and 28 mN/m. The Fresnel normalised XRR curves are shown on the left-hand side of the figure. The solid black lines represent the refinements to the data. The corresponding electron density profiles are given on the right-hand side. At an initial surface pressure of 5 mN/m the DPPA-film is in the tilted liquid-condensed phase, the initial surface pressure of 15 mN/m reflects the transition point from tilted to untilted liquid-condensed phase and at 20 mN/m the untilted liquid-condensed phase of DPPA is reached. The best-fit values of the reference measurements are given in table 5.5. As can be seen, by replacing nitrogen by F-propane, the minimum of the oscillation shifts to lower q_z values indicating a thickening of the layer. Again, the changes in the lipid films are similar for different initial surface pressures. The DPPA headgroup is not strongly influenced by the gas. The roughness and also the electron density of the tailgroup and between head- and tailgroup increase with gas pressure. This indicates a penetration of the gas molecules between the head- and tailgroups on the water surface and between the chains. Figure 5.9 shows the gas pressure-dependent change of the layer thickness, the electron density and the roughness of the tailgroups. The reduction of the gas pressure and measurement under nitrogen atmosphere reveal a stable and defined Langmuir layer. The re-spreading ability is better than detected for DPPC. The headgroup of DPPA seems to stabilise the structure of the Langmuir layer. This can be explained by the intermolecular bonds of DPPA. Furthermore, DPPA-films offer less accessible free water surface for the gas molecules, since it is tightly packed, even at low surface

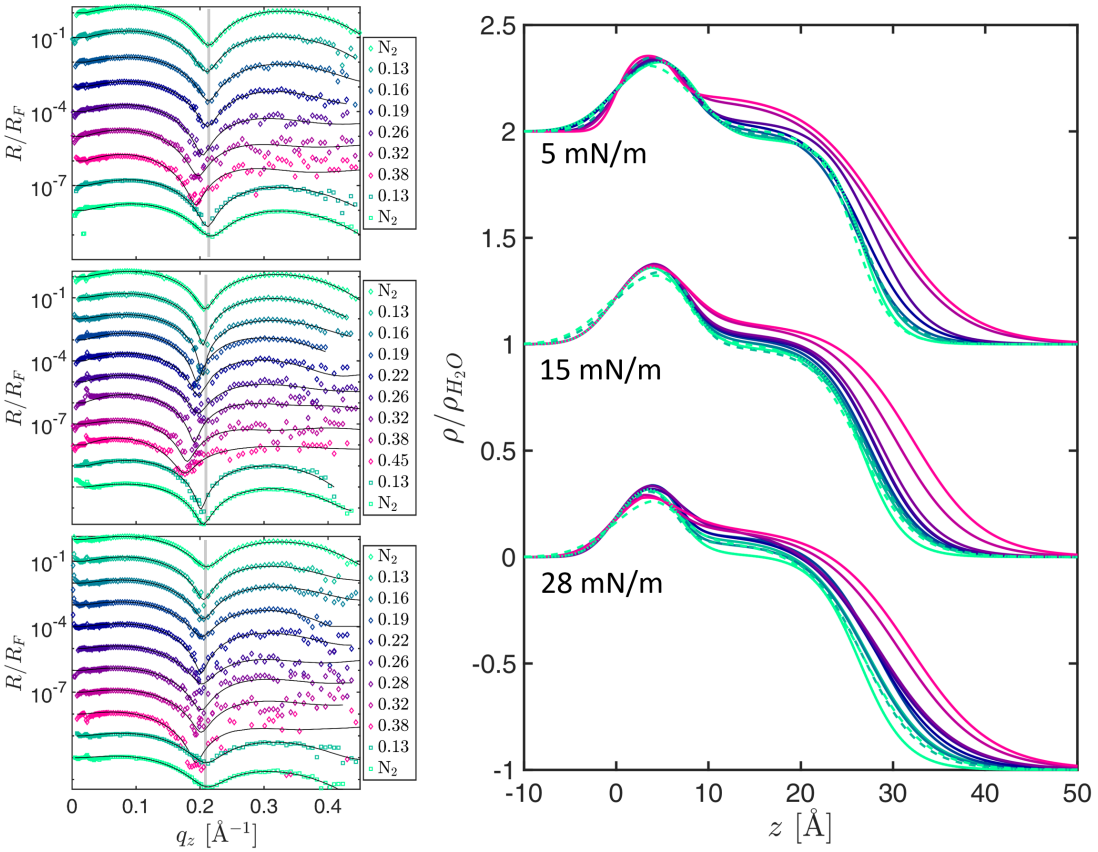

Figure 5.8: Left: Fresnel normalised XRR data of DPPA on a water subphase with different initial surface pressures and successively increasing F-propane gas pressures. From top to bottom: 5, 15 and 28 mN/m. Diamonds: data, solid lines: fits, squares: decreasing gas pressure. Right: Electron density profiles obtained from the refinement of the reflectivity data on the left. The density profiles are normalised to the bulk water density. The reflectivity curves and electron density profiles are shifted vertically for better visibility.

pressures.

In the following, the largest gas molecule with a gyration radius of 4.368 Å, F-butane, and its influence on DPPA-films will be presented. Figure 5.10 illustrates the Fresnel normalised XRR curves and the refinement to the data on the left-hand side. The right-hand side shows the corresponding electron density profiles. In this case, initial surface pressures of 5, 15 and 26 mN/m were examined. By replacing air with F-butane, the XRR curves constantly shifts to lower q_z values, indicating a thickening of the film. The best-fit parameters are summarised in table 5.6. For each surface pressure studied, it can be seen that the electron density profiles change in the same way, the electron density between head- and tailgroup and of the tailgroup increases. The roughness increases as well. The gas molecules still seem to penetrate the Langmuir layer even at

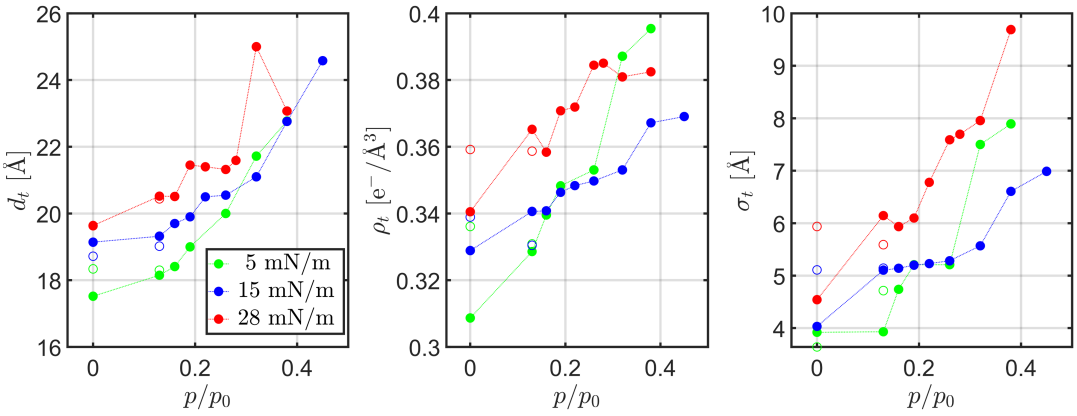

Figure 5.9: F-propane gas pressure-dependent change of the tailgroup thickness d_t, the electron density ρ_t and the roughness σ_t of DPPA-films with different initial surface pressures. The open empty markers represent the values after reduction of the gas pressure.

Table 5.6: The best-fit parameters of the reference measurements at air for different initial surface pressures of a DPPA-film. The water roughness was set to 3.4 Å for all reference measurements. The water density is 0.3359 e$^-$/Å^3. Tilt angle calculated via $\cos(\beta) = d_{\mathrm{t,max}}/19.2\,\text{Å}$. ρ_norm is the electron density normalised to the water electron density.

	5 mN/m		15 mN/m		26 mN/m	
parameter	head	tail	head	tail	head	tail
ρ_norm	1.4551	1.0325	1.4306	0.9964	1.4572	1.0169
σ / Å	3.375	3.943	3.39	4.451	3.407	4.51
d / Å	7	17.36	7.78	18.53	7	19.41
tilt angle / °	-	25.29	-	15.18	-	0

the highest surface pressure.

In contrast to DPPC-films, no F-butane adsorbate layer can be observed. The DPPA-film structure is stable and very densely packed, so that it is not possible to dissolve large amounts of F-butane at the interface. Again, the headgroups of the DPPA-film are not affected. The subsequent reduction of the gas pressure was also studied. It can be observed that gas molecules still remain in the layer. After flushing with nitrogen the profiles do not return to the initial structure. The effect becomes less pronounced the higher the initial surface pressure of the DPPA-film is. Figure 5.11 illustrates the variation of the tailgroups of DPPA-films at different initial surface pressures as a function of the reduced gas pressure. As observed with the other gases, the tailgroup expands continuously as a function of the gas pressure. It is remarkable that the tailgroup exceeds the value of maximum extension of DPPA. Since no three-layer system could be fitted to these curves, a layer with similar electron density seems to form above the Langmuir film. The deposition of perfluorocarbon molecules above a Langmuir film was also observed in other studies [1, 1048].

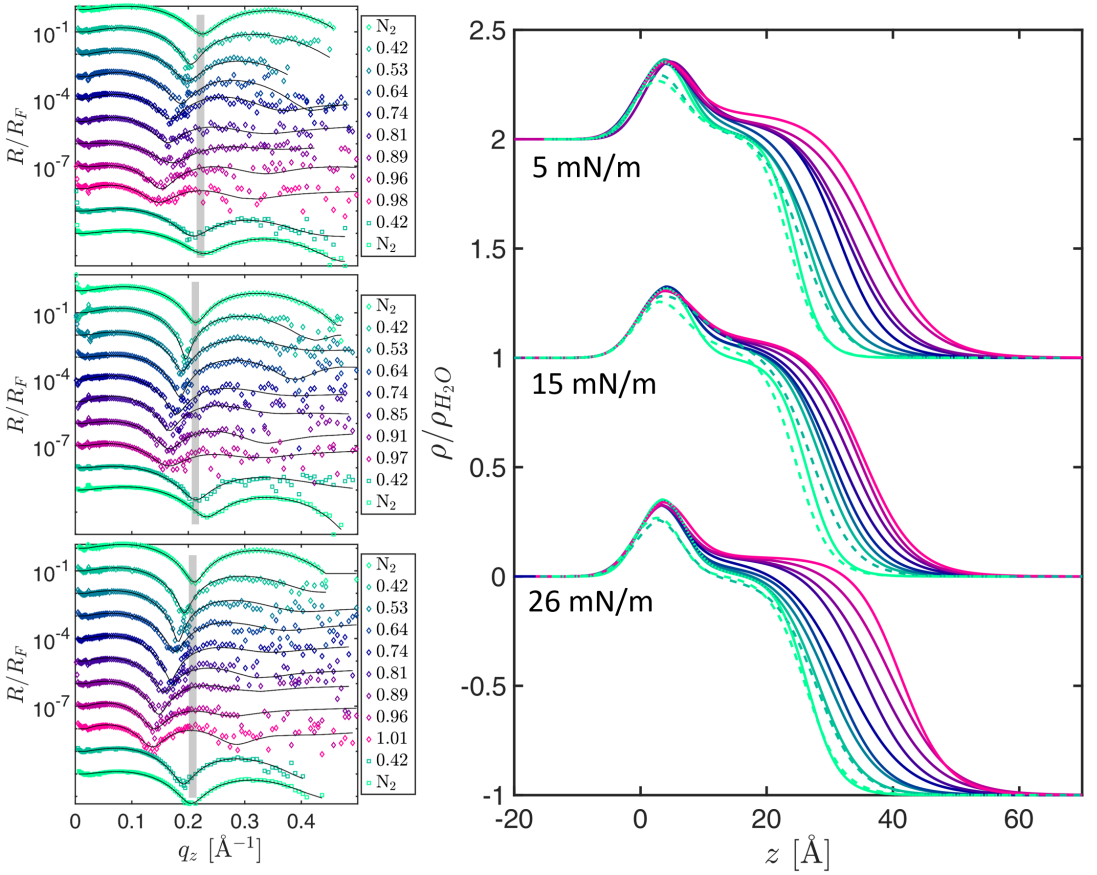

Figure 5.10: Left: Fresnel normalised XRR data of DPPA on a water subphase with different initial surface pressures and successively increasing F-butane gas pressures. Diamonds: data, solid lines: fits, squares: decreasing gas pressure. From top to bottom: 5, 18 and 26 mN/m. Right: Electron density profiles obtained from the refinement of the reflectivity data on the left. The density profiles are normalised to the bulk water density. The reflectivity curves and electron density profiles are shifted vertically for better visibility.

For DPPA it can be assumed that the adsorbed mass is proportional to $\Delta(\rho_t \cdot d_t) = \rho_{t,x} \cdot d_{t,x} - \rho_{t,ini} \cdot d_{t,ini}$ at each surface pressure. Here, $d_{t,x}$ describes the thickness of the tailgroup and $\rho_{t,x}$ the electron density of the tailgroup at a corresponding gas pressure x. The index "ini" indicates the values of the reference measurement. In order to obtain comparable data, the values for the calculation were selected at approx. 40 % of the condensation pressure for each gas. For isobutane, the values for the calculation were taken at $p/p_0 = 0.4$, for F-propane the values were taken at $p/p_0 = 0.38$ and for F-butane the values were taken at $p/p_0 = 0.42$. According to the figure 5.12, the increase is particularly high at low surface pressures, i.e. lower surface coverage. This is especially the case for F-propane and isobutane. The molecules possess different numbers of

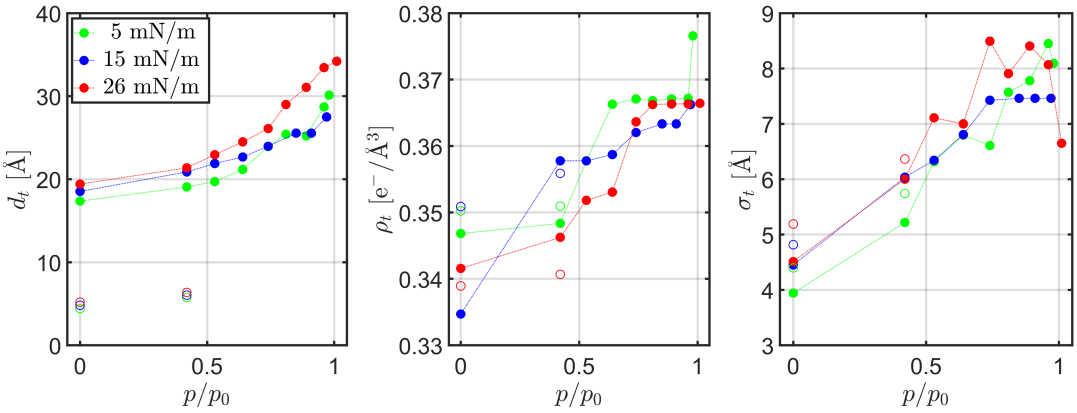

Figure 5.11: F-butane gas pressure-dependent change of the tailgroup thickness d_t, the electron density ρ_t and the roughness σ_t of DPPA-films with different initial surface pressures. The open empty markers represent the values after reduction of the gas pressure.

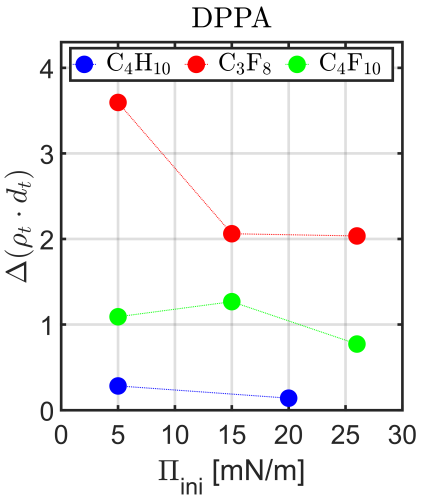

Figure 5.12: Variation of $\Delta(\rho_t \cdot d_t)$ of the investigated gases in dependence of the initial surface pressure. The values for the calculation were selected at approx. $p/p_0 = 0.4$ for the gases. Isobutane (C_4H_{10}, blue): $p/p_0 = 0.4$, F-propane (C_3F_8, red): $p/p_0 = 0.38$ and F-butane (C_4F_{10}, green): $p/p_0 = 0.42$.

electrons. For comparison: isobutane contains 34 electrons, F-propane 90 electrons and F-butane 114 electrons. The gas molecules adsorb via van der Waals interactions at the water surface, but also penetrate and accumulate within the layer at the tailgroups and interact via hydrophobic interactions.

vFC adsorption on Langmuir films In the following the interaction of vaporised perfluorocarbons with Langmuir films composed of DPPC and DPPA will be discussed. The experiments were performed with a Langmuir trough and a gas-tight box for experiments in vaporised FC atmosphere. The measurements with F-octyl bromide and F-decalin were performed with GIXD applying the gas pressure cell. Figure 5.13 shows XRR data of a DPPC-film spread on a water subphase with an initial surface pressure of 5 mN/m before, while and after flushing the cell with F-decalin saturated nitrogen. The

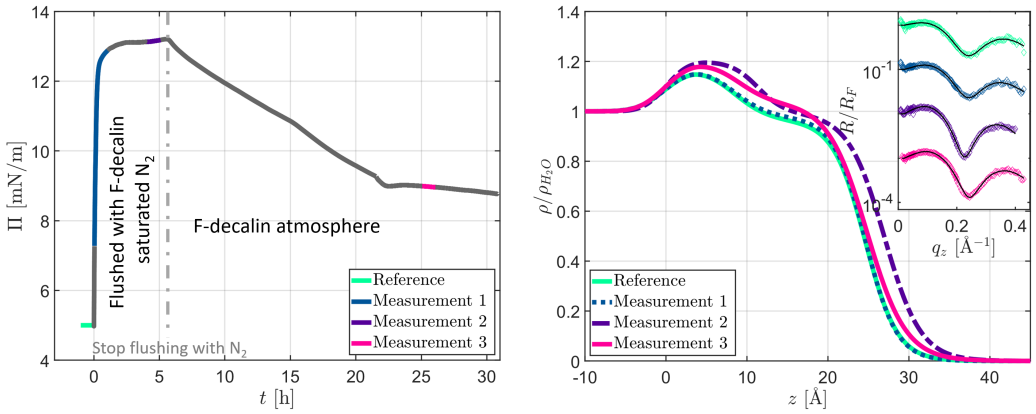

Figure 5.13: Left: Variation of the surface pressure Π of a DPPC monolayer at an initial surface pressure of 5 mN/m during flushing the Langmuir trough box with F-decalin saturated nitrogen with time t. Right: Electron density profiles obtained from the refinement of the XRR data which are shown in the inset as Fresnel normalised curves. Nitrogen flow: 1.2 L per minutes.

experiments were conducted at constant surface area. By replacing air with F-decalin saturated nitrogen, the surface pressure increases to 13 mN/m after 1.5 h of flushing. F-decalin interacts with the free water surface. As it can be seen, the electron density profile does not change immediately when flushing the cell (blue). After reaching the highest surface pressure of 13.1 mN/m (after 5 hours, purple) and detection of a plateau of the surface pressure, the second measurement reveals an increase of the electron density between the head- and tailgroups and in the tailgroups. These observations indicate an insertion of F-decalin into the alkyl chains and an adsorption at the free water surface. It seems to be a cooperative adsorption, since the surface pressure increases very fast. The flushing with F-decalin saturated nitrogen was stopped and a further measurement was conducted after reaching a second plateau-like pressure of 9 mN/m. After 24 hours the Langmuir layer reaches equilibrium. F-decalin molecules seem to desorb from the surface (pink profile). The surface pressure does not reach the initial surface pressure of 5 mN/m indicating that F-decalin molecules remain in the tailgroup area. Probably the F-decalin molecules adsorb with the shorter side pointing toward the water. The F-decalin molecules most likely accumulate in less dense liquid-expanded areas. The headgroups slightly enlarge due to the F-decalin treatment. Since the water solubility is not zero, some molecules can be dissolved in the subphase and remain at the interface. The alkyl chains of DPPC seem to be further compressed. The electron density of fluid F-decalin is not reached. The desorption is slow with 4.1 mN/m over a time span of 16.4 hours.

To study the insertion and penetration ability of F-decalin into more densely packed DPPC-films, an initial surface pressure of 10 mN/m and 20 mN/m was applied. The results are depicted in figure 5.14 and 5.15. In the liquid-condensed phase of the DPPC-films an insertion of F-decalin is monitored with XRR over different states of the flushing activity. As can be seen on the left of the figure 5.14, the flushing with F-decalin satu-

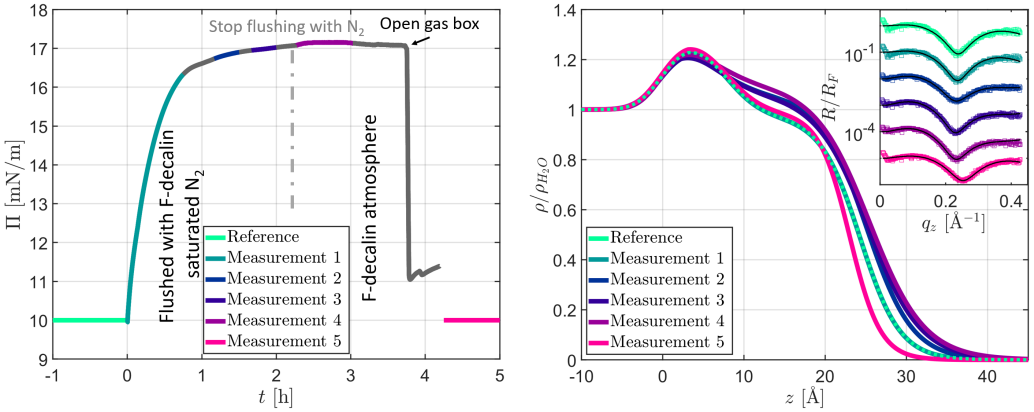

Figure 5.14: Left: Variation of the surface pressure Π of a DPPC monolayer at an initial surface pressure of 10 mN/m during flushing the Langmuir trough box with F-decalin saturated nitrogen with time t. Right: Electron density profiles obtained from the refinement of the XRR data which are shown in the inset as Fresnel normalised curves. Nitrogen flow: 1.2 L per minutes.

rated nitrogen over a time of around 1.5 h leads to an increase of the surface pressure to 16.9 mN/m. The first measurement (dark green) during the flushing, shows no change of the monolayer. The second and third measurement, shown in blue and dark blue, were taken after 1 and 2 hours. Here, the electron density of the headgroup remains the same while the thickness, the roughness and the electron density of the tailgroups as well as the area between the headgroups and alkyl chains increase. The F-decalin molecules tend to minimise the contact zone with the water and to persist in the hydrophobic alkyl chains due to their hydrophobicity. After reaching 17 mN/m, the nitrogen flow was stopped. Here, the surface seems to be in an equilibrium. The surface pressure is stable at 17.2 mN/m. The electron density profiles only change in the region between the head- and tailgroups. One can assume that this results from a reorganisation process within the layer. The XRR curve of the measurement at air after the F-decalin treatment reveals a reduction of the tailgroup thickness and an increase of the electron density compared to the reference measurement of DPPC at 10 mN/m. This might be an evidence for a conformational rearrangement of the Langmuir layer, including an increase of the tilt angle. The fluidisation effect described in chapter 2 is attributed to a reduction of the repulsive interaction between the tailgroups and allows denser packing.

Figure 5.15 shows the XRR data of the interaction between F-decalin and a DPPC-film at an initial surface pressure of 20 mN/m on the left and at a water surface on the right side of the figure. As can be seen, the insertion ability of F-decalin is reduced at films with higher surface coverage and less expanded areas. Through the globular shape it is not possible for F-decalin to penetrate in high quantities into the layer. However, an insertion can be monitored via XRR as a slight increase of the electron density and thickness of the tails is observed. Interestingly, an in- and decrease of around 2.5 mN/m of the surface pressure was observed in several measurements.

The right side of the figure 5.15 shows the XRR data of the adsorption of F-decalin

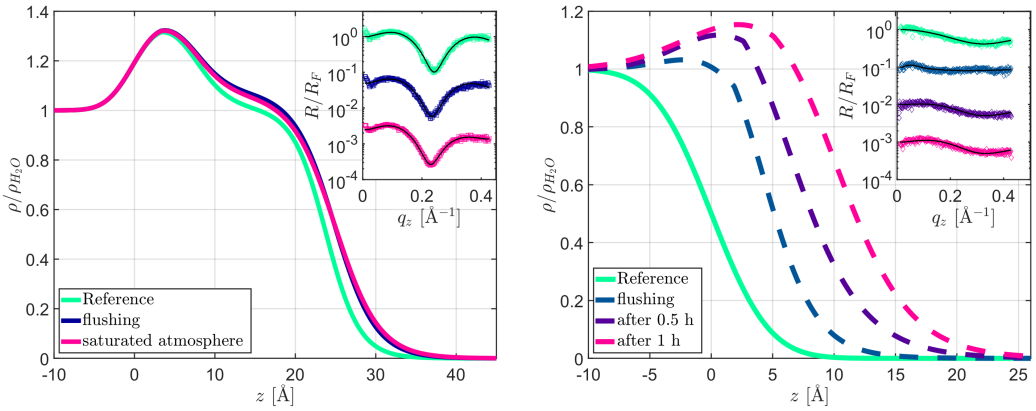

Figure 5.15: Left: Electron density profiles of a DPPC-film with an initial surface pressure of 20 mN/m, while flushing and under F-decalin atmosphere, obtained from the refinement of the XRR data which is shown in the inset as Fresnel normalised curves. Right: Electron density profiles of the adsorption of F-decalin on a bare water subphase, obtained from the refinement of the XRR data. The XRR data is shown as Fresnel normalised curves in the inset. Nitrogen flow: 1.2 L per minutes.

on a free water surface. The electron density of F-decalin which is $1.65 \cdot \rho_{H_2O}$ is not reached. It can be concluded, that F-decalin adsorbed during flushing. The thickness increase from 5.2 Å to around 11.6 Å after 1 hour of constant flushing with F-decalin saturated nitrogen. The dimensions of one F-decalin molecule is about $7.3 \times 5.4 \times 3.5$ Å^3. Moreover, with the calculated volume fraction profiles and extracted excess electrons per area it is possible to compute the area density of F-decalin molecules on the water surface. This yields 0.2 molecules/nm^2 during flushing with F-decalin saturated nitrogen, 1.2 molecules/nm^2 after 0.5 hours and 1.5 molecules/nm^2 after 1 hour of flushing.

The adsorption and insertion ability of F-decalin at DPPA-films at different surface pressures were also investigated. F-decalin saturated nitrogen was flushed over a DPPA-film with initial surface pressures of 5 mN/m and 20 mN/m. The results are shown in the appendix A, figure A.1 and figure A.2. No significant influence or penetration of F-decalin into the DPPA-layer was observed. In contrast to the penetration ability of F-decalin into a DPPC Langmuir film at sufficiently low surface coverage and surface pressure, it is not possible for F-decalin to insert into a tighter packed Langmuir film composed of DPPA.

F-decalin is lipophobic and hydrophobic as well and the observed intercalating process and adsorption is intuitively contradictory. Moreover, it displays a negative spreading coefficient. The results in general show an interaction of FCs with the tailgroups of the lipids. Linear g- and vFCs induce stronger changes of the lipid monolayer suggesting a penetration between the alkyl chains.

The interaction of DPPC and DPPA Langmuir films with gaseous perfluorocarbons was investigated with XRR. The gas molecules, including isobutane, cause strong alterations of the lipid films, even at low percentages of the condensation pressure. The

initial surface pressure plays a key role, since the penetration is hindered at high surface coverage. Moreover, the effect is smaller in the case of DPPA, as DPPA is more stable due to the hydrogen bonds that stabilise the headgroups. Since DPPA creates more compact layers even at low surface pressures compared to DPPC, the insertion of bicyclic globular shaped F-decalin is more hindered. Furthermore, the larger the gas molecule, the stronger the effect on the tailgroups. The boundary between head- and tailgroup seems to be a favourable adsorption site.

It is remarkable that the gaseous perfluorocarbons and the vaporised F-decalin can cause such a significant change of surface pressure, since the molecules are not amphiphilic but behave like co-surfactants.

To study the effect on crystalline domains of a Langmuir film composed of DPPA, the interaction at different surface pressures and, hence, coverage with the gFCs F-propane (C_3F_8) and F-butane (C_4F_{10}) and with the vFCs F-octyl bromide and F-decalin was investigated with GIXD. The results are presented in the following section.

5.1.3 GIXD data of DPPA-films under gFCs and vFCs

The GIXD data provide information about the change of the crystalline structure of the DPPA Langmuir layers caused by gas treatment. The experiments were performed at beamline I07 of the DLS. As previously described, the raw GIXD data were integrated along the q_z direction and refined with a Voigt function. The Gaussian contribution was kept constant through all measurements, since it considers the apparatus resolution. From the position of the maxima of the Bragg reflection it is possible to calculate the lattice constant a. The *in-plane* coherence length L, which represents the size of the crystalline domains, can be calculated from the full width at half maximum (FWHM) value of the refined Lorentzian part of the Voigt function. Unfortunately, due to the resolution of the apparatus, the tilt angle cannot be determined.

The GIXD data for a DPPA-film with an initial surface pressure of 5 mN/m with elevated gas pressures of F-propane (C_3F_8) up to $p/p_0 = 0.26$ is shown in figure 5.16 as a function of the wave vector transfer parallel to the surface $q_{\|}$. The plot on the right of the figure shows the determined parameters L and a. The data were collected after the surface pressure had reached equilibrium, typically, after 5 min. waiting time. Table 5.7 summarises the parameters from the fitted Voigt functions. The parameter Π_{max} gives the maximum measured surface pressure at the corresponding C_3F_8 gas pressure. The reference measurements at air reveals no detectable lateral order of the DPPA Langmuir film. The surface pressure rises from 5 mN/m up to 7.5 mN/m during the gas pressure increase. A Bragg reflection was formed and vanished again at the highest gas pressure.

The treatment of a disordered DPPA Langmuir layer with F-propane leads to a higher ordered structure. With rising gas pressure, the lattice constant increases. The appearance of the Bragg reflection leads to the assumption that the DPPA-film is compressed due to the adsorption of gas molecules between the alkyl chains at the water surface. At higher pressures the lateral crystalline domain size decreases whilst the lattice constant increases, indicating a looser structure of the Langmuir film. A dissolution is not probable since the XRR data do not indicate a significant loss of matter from

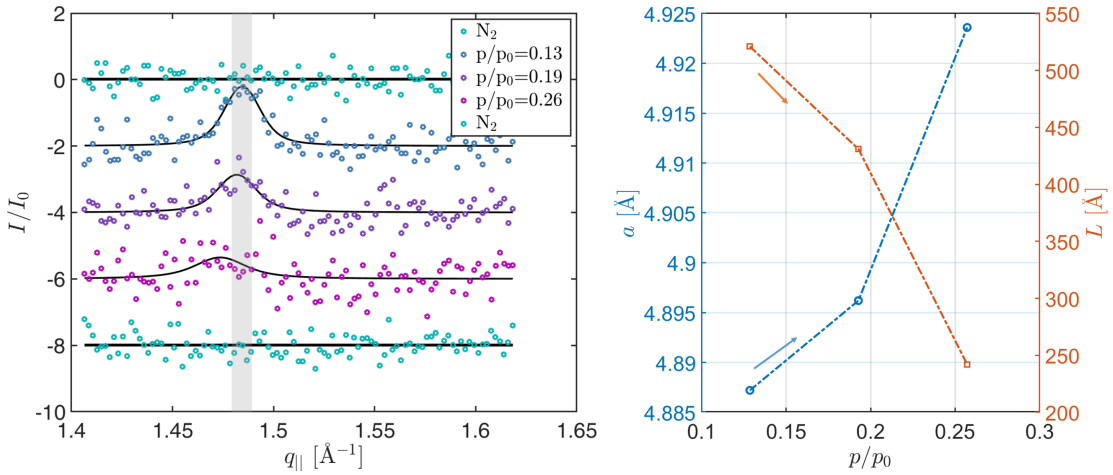

Figure 5.16: Left: GIXD scans of a DPPA monolayer at 5 mN/m under different C_3F_8 pressures up to $p/p_0 = 0.26$. The refinements of the data are shown as black solid lines. The scans are shifted vertically for clarity. Right: Crystalline domain size L (orange) and lattice constant a (blue) as a function of the reduced gas pressure. The arrows indicate the temporal sequence.

Table 5.7: Crystallographic data of a DPPA Langmuir film with an initial surface pressure of 5 mN/m. Calculated parameters by evaluation of the GIXD data of DPPA-films under different pressures of F-propane with a condensation pressure of $p_0 = 7.779$ bar at 294.15 K. The development of the surface pressure is also given.

Π_{ini} / $\frac{mN}{m}$		C_3F_8 / $\frac{p}{p_0}$				
		N_2	0.13	0.19	0.26	N_2
5	a/Å	-	4.8872	4.8962	4.9236	-
	$q_\parallel$/Å^{-1}	-	1.4845	1.4818	1.4735	-
	L/Å	-	521	431	242	-
	$\Pi_{max}/\frac{mN}{m}$	5	5.8	6.3	7.5	-

the surface. The XRR data of DPPA-films with C_3F_8 revealed an untilting and density increase of the tailgroups. This is in contrast to the results obtained with stearic acid and butane [1048].

Another indication for a C_3F_8 induced compression is that the XRR data of DPPC-film measurements at a surface pressure of 2 mN/m at which the Langmuir layer is in the gaseous phase could be fitted with a two-layer model after treatment with 1 bar F-propane. Moreover, the lattice constant a at $p/p_0 = 0.13$ is similar to the values of the reference measurements at an initial surface pressure of 15 mN/m. After removing the gas and replacing it by air, a displacement of the gas molecules from the monolayer occurs and the Bragg reflection vanishes again.

Figure 5.17 and figure 5.18 show on the left the development of a DPPA-film under increasing F-propane (C_3F_8) gas pressures starting from different initial surface pressures of 15 mN/m and 30 mN/m, respectively. The measurements were conducted up to

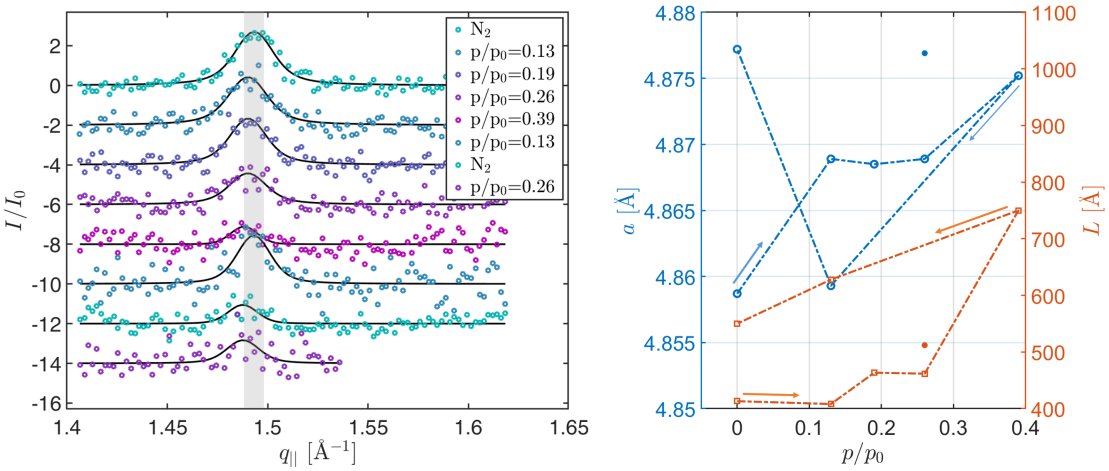

Figure 5.17: Left: GIXD scans of a DPPA monolayer at 15 mN/m under different C_3F_8 gas pressures up to $p/p_0 = 0.39$. The refinements of the data are shown as black solid lines. The scans are shifted vertically for clarity. Right: Crystalline domain size L (orange) and the corresponding lattice constant a (blue) in dependence of the reduced gas pressure. The blue and the red dot mark the parameters subsequent to the gas pressure increase after opening the cell. The arrows indicate the temporal sequence.

a maximum pressure of $p/p_0 = 0.39$. At 15 mN/m, after the final measurement at air, the cell was closed again and an additional measurement at $p/p_0 = 0.26$ was performed. The GIXD scans at higher initial surface pressures reveal higher scattered intensity due to the more ordered lipid phase. The reference measurements are in accordance with the literature [109, 933] and the data is consistent throughout the individual measurement series (higher surface pressure leads to smaller a and higher L). As can be seen in the figures 5.17 and 5.18, the Bragg reflections shift to lower angles which results in higher lattice constants. DPPA has only one reflection, indicating a hexagonal packing of the tails. Table 5.8 summarises the parameters obtained from the refinement of the GIXD scans (top: $\Pi_{ini} = 15$ mN/m, bottom: $\Pi_{ini} = 30$ mN/m). Both data series show a similar behaviour. The lattice constant a and the crystalline domain size L increase after rise of the gas pressure. It is possible that adsorbed F-propane molecules form small clusters or islets which compress the layer. Presumably, this occurs at more expanded areas, where the gas molecules can penetrate the monolayer. Due to the larger lattice constant also a penetration into the crystalline (liquid-condensed) domains occurs. Since the F-propane molecules are hydrophobic and lipophobic as well, they penetrate the hydrophobic alkyl chains of the lipids and can accumulate at a free water surface. The surface pressure which was measured separately also increases. This also suggests an incooperaton of gas molecules into the layer and an adsorption at the water interface.

After removing the gas phase, the measurements at air reveal values of a and L that are different from the initial ones. The lattice constants are higher than the initial values, which means that the lipid film is in a looser state. Moreover, also the surface pressures are lower after the treatment with gas. A repeated increase of the gas pres-

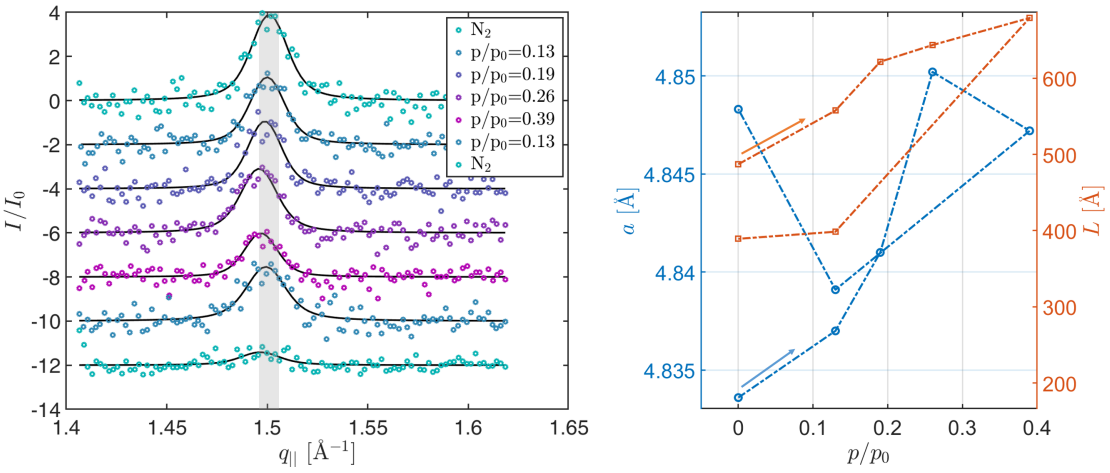

Figure 5.18: Left: GIXD scans of a DPPA monolayer at 30 mN/m under different C_3F_8 gas pressures up to $p/p_0 = 0.39$. The refinements of the data are shown as black solid lines. The scans are shifted vertically for clarity. Right: Crystalline domain size L (orange) and the corresponding lattice constant a (blue) as a function of the reduced gas pressure. The arrows indicate the temporal sequence.

sure to about $p/p_0 = 0.26$ has no significant effect (compare figure 5.17). The Bragg reflection vanishes gradually with increasing gas pressure. As can be seen in the XRR measurements even the highest pressure ($p/p_0 = 0.45$ at $\Pi_{ini} = 15$ mN/m or $p/p_0 = 0.38$ at $\Pi_{ini} = 5$ mN/m, compare figure 5.8) the Langmuir layer has a vertical order and is not destroyed. Meaning that the intensity loss is not caused by the dissolution of lipids in F-propane islets.

The GIXD scans of a measurement series with DPPA Langmuir films at an initial surface pressure of 20 mN/m under increasing gas pressures of F-butane (C_4F_{10}) are shown in figure 5.19. The parameters of the Voigt functions are summarised in table 5.9. The refinement of the reference measurement is in accordance with the literature. As can be seen, the Bragg reflection shifts to lower $q_\parallel$ at $p/p_0 = 0.42$ indicating a higher lattice constant. The crystalline domain size also increases. This effect may suggest penetration into the liquid-condensed (crystalline) domains as well as compression of the layer via interaction with the liquid-expanded lipid phases.

The position of the Bragg reflection at $p/p_0 = 0.85$ remains nearly the same. With reducing the gas pressure again to $p/p_0 = 0.42$, the Bragg reflection is not observable. But by replacing the gas phase with nitrogen again, the Langmuir layer seems to be stable again with a broader Bragg reflection at smaller $q_\parallel$ indicating a larger lattice constant and a smaller domain size. Comparing the change of the lattice constant and crystalline domain size with F-propane, the smaller F-propane with a gyration radius of 3.736 Å has a stronger influence on the Langmuir layer than the larger F-butane with a gyration radius of 4.368 Å. The smaller F-propane molecules can penetrate the denser packed layer easier at higher surface pressures.

To study the response of a DPPA-film to vFCs, GIXD experiments were performed

Table 5.8: Crystallographic data of the DPPA Langmuir films. Calculated parameters of the GIXD data of DPPA-films with an initial surface pressure of 15 mN/m (top) and 30 mN/m (bottom) under different pressures of F-propane. The development of the surface pressure is also given.

		C_3F_8 / $\frac{p}{p_0}$						C_3F_8 / $\frac{p}{p_0}$
	N_2	0.13	0.19	0.26	0.39	0.13	N_2	0.26
a/Å	4.8587	4.8689	4.8685	4.8689	4.8752	4.8593	4.8772	4.8769
$q_\parallel$/Å^{-1}	1.4932	1.4901	1.4902	1.4901	1.4882	1.4931	1.4876	1.4877
L/Å	413.1	408.1	463.4	461.7	750*	627	550	512
$\Pi_{max}/\frac{mN}{m}$	15	15.6	17.1	17.6	18.3	15	13.5	16
a/Å	4.8336	4.8370	4.8410	4.8502	4.8472	4.8391	4.8483	-
$q_\parallel$/Å^{-1}	1.5010	1.4999	1.4987	1.4958	1.4968	1.4993	1.4964	-
L/Å	487.07	557.48	621.56	643.47	679.03	398.52	389.21	-
$\Pi_{max}/\frac{mN}{m}$	30.5	31.5	32.8	34.2	36.1	32	29.8	-

Table 5.9: Crystallographic data of the DPPA Langmuir films. Calculated parameters of the Voigt functions fitted to the GIXD data of DPPA-films with an initial surface pressure of 20 mN/m under different pressures of F-butane with a condensation pressure of $p_0 = 2.345$ bar at 294.15 K.

Π_{ini} / $\frac{mN}{m}$		C_4F_{10} / $\frac{p}{p_0}$				
		N_2	0.42	0.85	0.42	N_2
20	a/Å	4.8407	4.825	4.8495	-	4.8851
	$q_\parallel$/Å^{-1}	1.4988	1.4952	1.4961	-	1.4852
	L/Å	410	332	750	-	684
	$\Pi_{max}/\frac{mN}{m}$	20	20.8	22.2	17	15.4

at perfluorodecalin (F-decalin, $C_{10}F_{18}$) and perfluorooctyl bromide (F-octyl bromide, $C_8F_{17}Br$) atmosphere. For this purpose, helium was flushed through a gas washing bottle and the F-decalin or F-octyl bromide saturated helium was then passed to the sample cell. The gas pressure cell was flushed with F-decalin saturated helium with a flow rate of approx. 1.2 L/minutes. Figure 5.20 shows the background subtracted, normalised and with Voigt functions refined GIXD data at N_2 atmosphere and under F-decalin saturated helium atmosphere. The experiments were performed at an initial surface pressure of 10 mN/m. The DPPA-film is then in the tilted phase, which was chosen to investigate the insertion of the vFCs and to produce a lower coverage of surfactant to simulate the situation of a lung surfactant failure or absence. After flushing the sample cell for 200 minutes the scans were started. The Bragg reflection of the crystalline domains does not change significantly when vaporised F-decalin is introduced into the sample cell. This indicates a stable DPPA monolayer with a high lateral order.

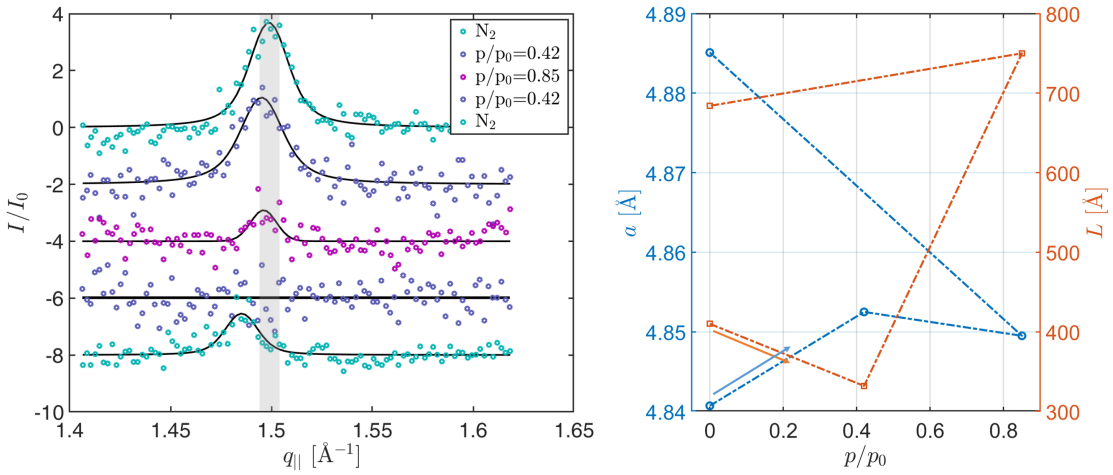

Figure 5.19: Left: Integrated GIXD scans of a DPPA monolayer at 20 mN/m under different C_4F_{10} gas pressures up $p/p_0 = 0.85$. The refinements of the data are shown as black solid lines. The scans are shifted vertically for clarity. Right: Crystalline domain size L (orange) and the corresponding lattice constant a (blue) in dependence of the reduced gas pressure.

As already mentioned, the low interactions between F-decalin and DPPA-films can be explained by the globular shape of F-decalin. It is not possible to incooperate into the monolayer and an insertion is more unfavourable than for linear shaped perfluorocarbon molecules of e.g F-octyl bromide. Also no effect has been observed by XRR, shown in the appendix A (compare figures A.1 and A.2).

Figure 5.21 shows the same DPPA-film as in figure 5.20. However, at t_2 the F-decalin atmosphere was replaced by F-octyl bromide. The parameters of the refinements are given in table 5.10. As can be seen in the figure, the vFC F-octyl bromide has a significant effect on the DPPA Langmuir film. Compared to the globular shaped F-decalin, F-octyl bromide has a linear shape and an exposed hydrophilic and terminal bromide entity, so that intercalation into the lipid layer is easier and more favourable. Moreover, the molecule has a positive spreading coefficient and is more lipophilic than F-decalin. F-octyl bromide shifts the Bragg reflections into the direction of higher angles which indicates a smaller lattice constant a. The lattice constant at t_3 is nearly similar to those of a DPPA-film which is compressed to 30 mN/m. At t_3 the Bragg reflection widens, indicating a decrease of the crystalline domain size L. Since the lattice constant is smaller at t_3, the smaller crystalline domains which are spread over the area are more tighten or denser. From t_2 to t_3 the lattice constant of the Langmuir layer with incooperated F-octyl bromide does not change significantly but the crystalline domain size is drastically reduced.

The influence of F-octyl bromide on a freshly prepared Langmuir layer was tested afterwards. Figure 5.22 illustrates the results of the refinement of the GIXD scans. The evaluated parameters of the film are summarised in table 5.11.

As can be seen, flushing the sample with F-octyl bromide, the Bragg reflections shift to higher $q_{||}$ and widen. In comparison to the results with F-decalin, the decrease of the

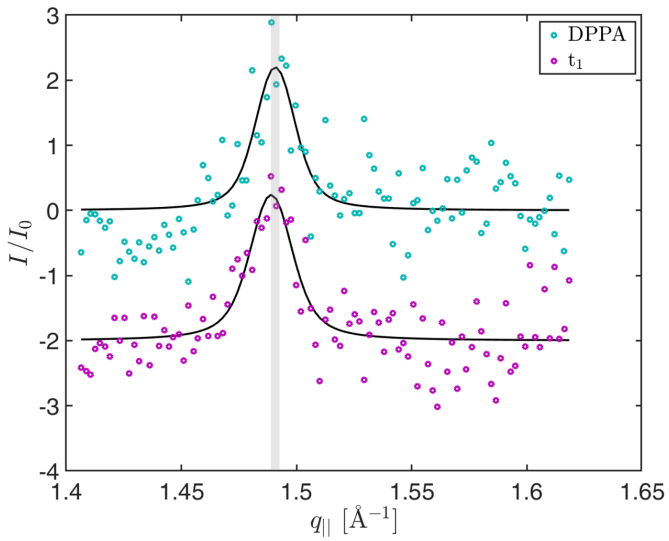

Figure 5.20: Integrated GIXD scans of a DPPA monolayer at 10 mN/m under N_2 atmosphere and while flushing the sample cell with F-decalin saturated helium. The refinements of the data are shown as black solid lines. The scans are shifted vertically for clarity, $t_1 = 200$ min.

Table 5.10: Properties of the DPPA Langmuir film at an initial surface pressure of 10 mN/m and treatment with F-decalin (PFD) and F-octyl bromide (PFOB) saturated helium.

Π_{ini} / $\frac{mN}{m}$			PFD	PFOB	
		N_2	t_1	t_2	t_3
10	a/Å	4.8667	4.8726	4.8407	4.8356
	$q_{\|\|}$/Å^{-1}	1.4908	1.4890	1.4988	1.5004
	L/Å	576.5	464	620.29	229.05
	$\Pi_{max}/\frac{mN}{m}$	10	11.2	13.5	14.8

lattice vector length begins immediately. It seems, that the insertion of F-octyl bromide into the DPPA-layer is reaching a maximum at t_2. The decrease of the lattice constant and the crystalline domain size indicates the formation of tightly packed lipid patches in the shrinking crystalline domains.

Based on the GIXD data it can be summarised that the gFCs (F-propane and F-butane) increase the lattice constant and thus the distance between the lipids within the crystalline domains. This remains when the gas is replaced by air. Interestingly, the crystalline domains also increase in size, which suggests that there is a compression effect by the gases that accumulate on the surface. Compression occurs due to the adsorption into less condensed lipid phases (liquid-expanded), because at low surface pressures the gases can trigger the formation of Bragg reflections. In general, it can be stated that the perfluorocarbon gases loosen the crystalline structures of the film and at the same time increase their long-range order. A penetration into crystalline and

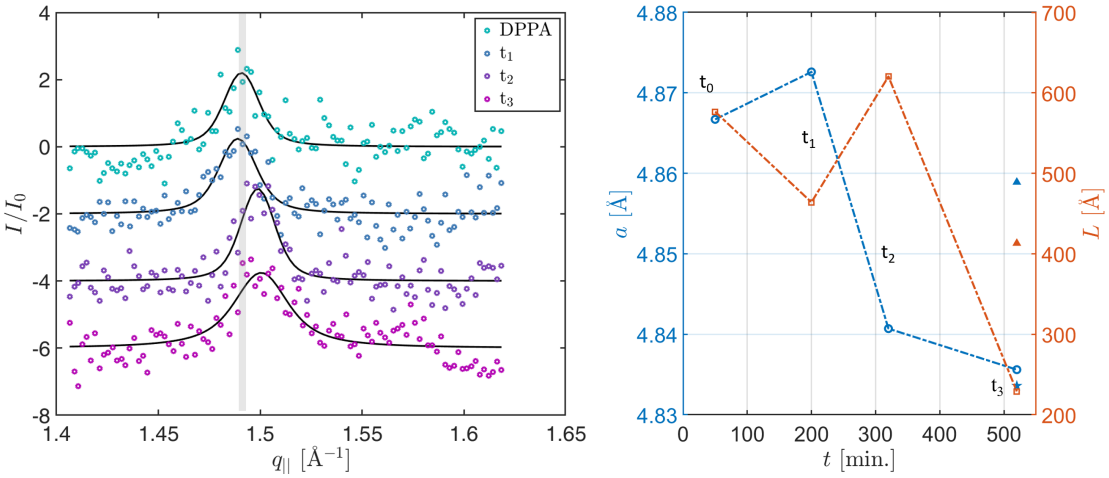

Figure 5.21: Left: GIXD scans of a DPPA monolayer at 10 mN/m under N_2 atmosphere and while flushing the sample cell with F-decalin saturated helium and afterwards with F-octyl bromide. The refinements of the data are shown as black solid lines. The scans are shifted vertically for better visualisation. $t_0 = 50$, $t_1 = 200$, $t_2 = 320$, $t_3 = 520$ min. Right: Changes of the crystalline domain size L (orange) and the corresponding lattice constant a (blue) in time. Additional parameters of a DPPA-film at 15 mN/m (triangles) and 30 mN/m (star) are given for comparison.

expanded regions can therefore be assumed.

When vaporised F-decalin and F-octyl bromide were used, it was shown that F-decalin has no effect on the DPPA monolayers even at low surface pressures. This can be attributed to its bicyclic, globular structure and very high lipophobicity. It also has a negative spreading coefficient in contrast to F-octyl bromide. F-octyl bromide primarily causes a decrease in both, crystalline domain size and lattice constant, which suggests that it is deposited in the less crystalline regions of the lipid phase. As the crystalline domains also become smaller, fluidisation seems to occur. Thus, F-octyl bromide has the ability to compress the liquid-condensed regions while reducing the crystallinity of the DPPA-film.

At a constant surface pressure of 20 mN/m of DPPC, it was observed by Gerber et

Table 5.11: Properties of the DPPA Langmuir film at an initial surface pressure of 10 mN/m and treatment with F-octyl bromide (PFOB) saturated helium.

Π_{ini} / $\frac{mN}{m}$			PFOB		
		N_2	t_1	t_2	t_3
10	a/Å	4.8604	4.8486	4.8383	4.8419
	$q_{\|\|}$/Å^{-1}	1.4927	1.4964	1.4995	1.4984
	L/Å	566.37	582.12	604.6	404
	$\Pi_{max}/\frac{mN}{m}$	10	12.2	15.7	16.6

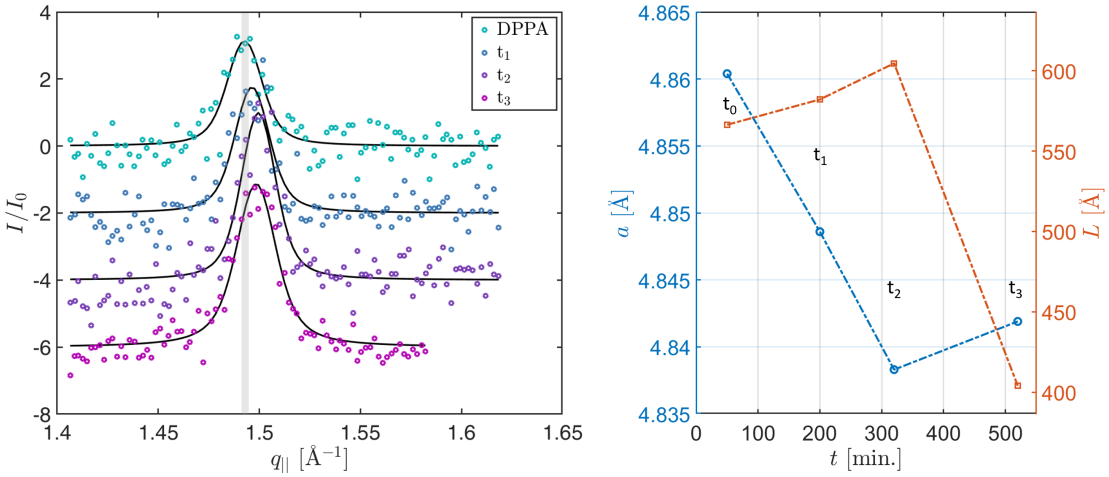

Figure 5.22: Left: GIXD scans of a DPPA monolayer at 10 mN/m under N_2 atmosphere and while flushing the sample cell with F-octyl bromide saturated helium. The refinements of the data are shown as black solid lines. The scans are shifted vertically for better visualisation. $t_0 = 50$, $t_1 = 200$, $t_2 = 320$, $t_3 = 520$ min., t_0 indicates the DPPA-film under air atmosphere. Right: Changes of the crystalline domain size L (orange) and the corresponding lattice constant a (blue) in time.

al. that F-octyl bromide caused a loss of crystallinity [1, 441]. The differences in the results of the work compared to the referenced work can be explained by the fact that the experiments were conducted at constant surface area and not at constant surface pressure. Therefore, the lateral displacement of lipids is limited. The structure and the physicochemical properties of the perfluorocarbons but also the lipid phase seems to play a key role for the effect on a Langmuir film.

In summary, the GIXD experiments demonstrate that FC molecules interact with different lipid phases of the Langmuir film and induce the formation of looser and smaller crystalline domains at constant area of the DPPA Langmuir film. The lateral and the vertical structure of the Langmuir films are affected by the treatment with FCs due to the incoopertaion and penetration between the tailgroups. Although these molecules have no amphiphilic character, the studied perfluorocarbons act like pseudo-surfactants or co-surfactants without destroying the DPPA Langmuir film. The observations reported here are significant, as they suggest that the mixture of gFCs and phospholipids could be a synthetic new approach for the treatment of lung diseases, since the fluidisation effect can also be observed at constant area of the Langmuir film. The fluidisation effect of the FCs on DPPC Langmuir films is explained by the reduction of the mutual van der Waals interaction energy between the lipid molecules upon FC adsorption [3, 305, 1137]. This was primarily theoretically modelled and calculated for DPPC and may also apply for DPPA.

In all cases, the investigated gFCs and the vFCs generate higher surface pressures and consequently lower the surface tension of the Langmuir films, which is important for the design of replacement formulas for the treatment of lung diseases which are related

to lung surfactant failure. Moreover, the surface tension lowering is most pronounced for DPPC, which is one of the most used phospholipids for microbubble or droplet shell composition used in CEUS and ^{19}F-MRI, and is the main component of lung surfactant. The results obtained might be useful for the development and construction of emulsions and microbubbles with FC compounds, for example for microbubbles which are composed of a phospholipid shell structure and additional fluorocarbon vapour, which increase the shell resistance and stabilises the surrounding medium [4, 497, 511, 1138]. Beside molecular imaging and lung surfactant replacement compositions, the results may be useful for the design of lipid-PFC emulsions for *in-vivo* oxygen delivery (artificial blood replacements) [469] or organ and cell preservation [1139].

5.2 Solid/gas-interfaces

So far, only aqueous subphases have been applied as substrates. In order to obtain information, the next step will be the investigation of gFCs at solid-supported lipid systems such as mono- and multilayers on silicon/silicon dioxide substrates.

5.2.1 Experimental details

This section deals with solid-supported lipid systems under elevated gas pressures. For this purpose, DPPC and DMPC mono- and multilayers were examined. DPPC monolayers and DMPC multilayers were produced via spin-coating. To obtain reproducible solid-supported DMPC monolayers the Langmuir Blodgett technique was applied. It is not possible to obtain DMPC monolayer with the spin-coating method.

The DPPC monolayers were investigated exclusively with the laboratory diffractometer D8 of the E1a chair at TU Dortmund. The DMPC mono- and multilayers were examined at beamline 9 of DELTA. The gases were tested for penetration into multilayers. The multilayers were measured at room temperature. For the monolayers the temperature was varied to investigate the influence of the lipid phase.

To suppress radiation damage at BL9, the sample was shifted laterally after each scan. Stability was nevertheless ensured by repeated measurements at one position. Table 5.12 provides an overview of the investigated sample systems. One XRR scan at the laboratory diffractometer D8 took about 2.5 hours including the diffuse scan and 45 minutes at DELTA. Further information on setup and experimental procedure as well as sample preparation is given in section 4.2 and 4.4.

5.2.2 gFC adsorption on solid-supported lipid mono- and multilayers

Under quasi-physiological conditions it is possible to determine different parameters associated with the structure and function of membranes with biomimicking solid-supported lipid bilayer systems [199, 1080].

In contrast to the finding that the selected gases do not penetrate hydrophobic OTS- (octadecyltrichlorosilane) layer systems [1051], they induce a significant change at solid-supported lipid layer systems. Figure 5.23 shows the electron density profiles

Table 5.12: Overview of the investigated lipid systems with applied gases and thermodynamic parameters.

lipid system	T / [K]	gas	p_0 / [bar]	$p_{\max}$ / [bar]	lipid
monolayer	323.15	C_3F_8	16.18	4.5	DPPC
	323.15	C_4F_{10}	5.588	2.3	DPPC
	313.15	C_4F_{10}	4.233	2.3	DPPC
	294.15	C_4F_{10}	2.354	2.0	DMPC
multilayer	294.15	C_4F_{10}	2.354	2.3	DMPC
	294.15	C_4F_{10}	2.354	2.3	DPPC
	294.15	C_4H_{10}	3.115	3	DMPC

with a schematic sketch of the model system (left) and the Fresnel normalised XRR curves (right) of a solid-supported DPPC monolayer on a silicon/silicon dioxide wafer at $T = 323.15\,\mathrm{K}$ under F-propane. Although the temperature is higher than the main phase transition temperature of DPPC, the monolayer might not be fully in the fluid phase, since the substrate has a significant influence on T_m. The L_α phase is the biological relevant phase. Biological membranes are usually fully hydrated. This is neglected here, since a controlled humidity degree in the pressure cell is not possible so far. The dispersion values for the silicon substrate and the silicon dioxide layer was assigned to the theoretical values, taken from [1087], see section 4.5. The silicon substrates were refined with a roughness of around 1 Å and the native silicon dioxide layer with a layer thickness between 10 and 15 Å. It is possible to calculate the area per lipid molecule from the difference of the lipid electron density profile and the bare silicon/silicon dioxide substrate. The integration over the resulting volume fraction profile yields the number of electrons per area. Considering the number of electrons of DPPC the area per lipid molecule can be determined. One DPPC lipid contains 406 electrons. This yields an area per lipid of $60.9 \pm 0.25\,\mathrm{Å}^2$. The value is in accordance with fluid phase data found in the literature [1140–1142]. The temperature seems sufficient to overcome the influence of the substrate, in this regard.

The phospholipid DPPC is a zwitterionic molecule with a phosphatidyl group. The headgroup is attached in an extended conformation on the silicon wafer with a layer thickness of $9.85 \pm 0.2\,\mathrm{Å}$. This is presumably due to the repulsion forces between the negatively charged silicon dioxide surface and the equally charged phosphate group. The thickness of the tailgroup is $12 \pm 0.3\,\mathrm{Å}$. This value is smaller than observed in the L_α phase in lipid bilayers. This might be caused by a restricted mobility of the substrate-bound lipids.

In contrast to the liquid/gas-interface at low initial surface pressures, the measurements after removing the gas reveal that the adsorbed gas does not cause a loss of lipid material due to a dissolving processes. Here, the C_3F_8 molecules penetrate the solid-supported monolayer and adsorb between the head- and tailgroups during pressure

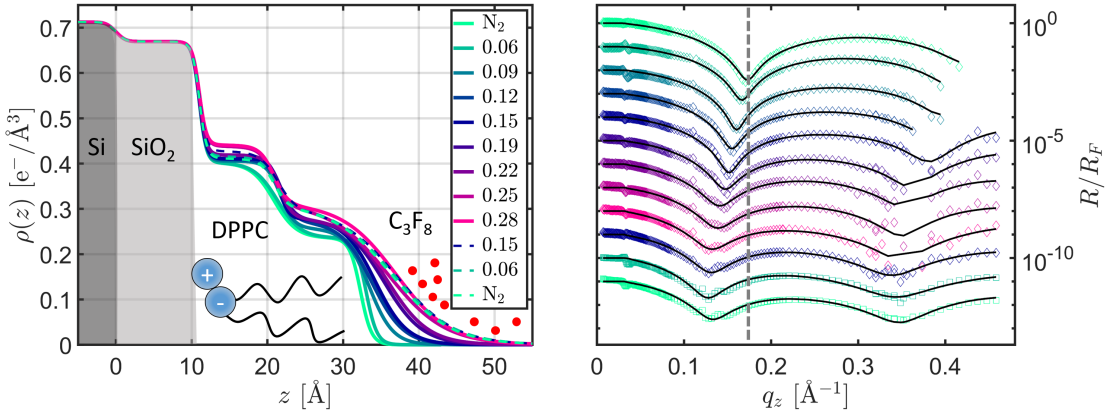

Figure 5.23: Left: Electron density profiles corresponding to the refinements with a sketch of the underlying model. Right: Fresnel normalised XRR curves of the measurement of a solid-supported DPPC monolayer at a temperature of 323.15 K and at increasing F-propane gas pressures. Diamonds: data, solid lines: fits, squares: decreasing gas pressure.

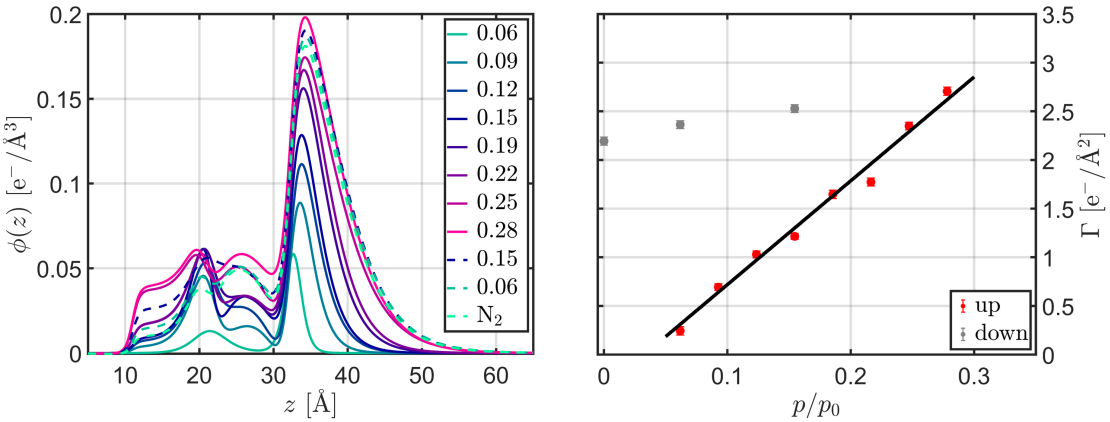

Figure 5.24: Left: Volume fraction profiles after subtraction of the F-propane treated solid-supported monolayer system and the reference system. Dotted lines: decreasing pressure. Right: Excess electrons per area as a function of the reduced gas pressure. Grey squares: decreasing pressure. Temperature was 323.15 K.

increase as the electron density increases in both sublayers and remain in the monolayer after pressure release. Beside the electron density also the thickness of the monolayer and the roughness of the tailgroup increases. This could be due to a stretching of the alkyl chains or the formation of an adsorbate on top of the lipids. The adsorbed electrons per volume can be determined from volume fraction profiles ($\rho(z)_{\text{gas treated}} - \rho(z)_{\text{reference}}$). The extracted volume fraction profiles $\phi(z)$ are shown in figure 5.24 on the left side. The right side of the figure depicts the integration of $\phi(z)$ and therefore the excess electrons per area. The error bars are obtained via the variation of the refinement pa-

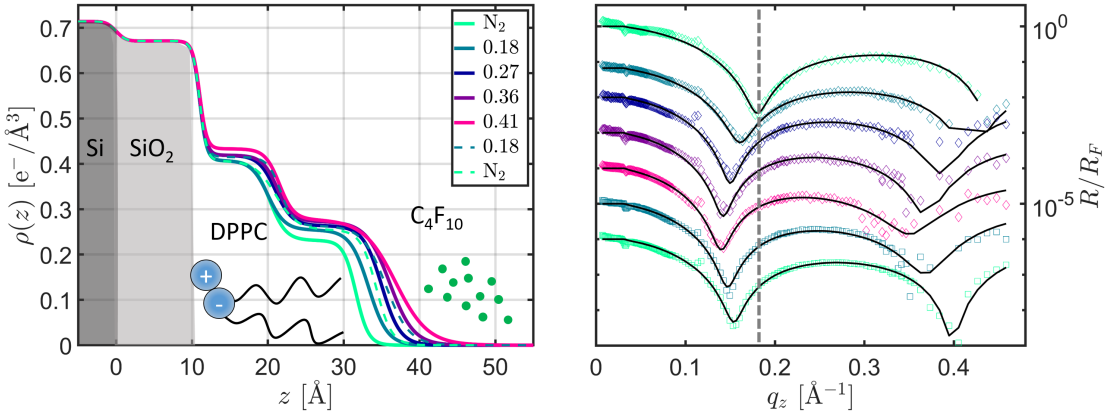

Figure 5.25: Left: Electron density profiles corresponding to the refinements with a sketch of the underlying model. Right: Fresnel normalised XRR curves of the measurement of a solid-supported DPPC monolayer at a temperature of 323.15 K and at increasing F-butane gas pressures. Diamonds: data, solid lines: fits, squares: decreasing gas pressure.

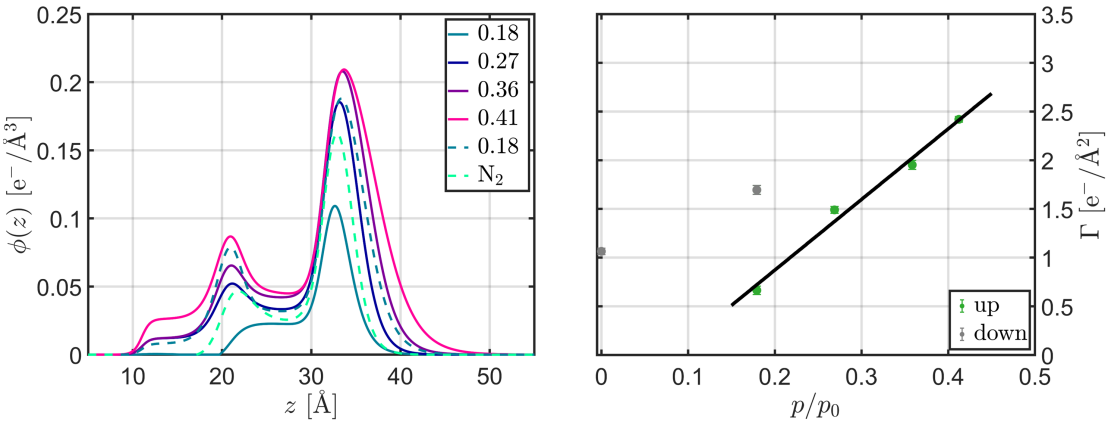

Figure 5.26: Left: Volume fraction profiles after subtraction of the F-butane treated solid-supported monolayer system and the reference system. Dotted lines: decreasing pressure. Right: Excess electrons per area as a function of the reduced gas pressure. Grey squares: decreasing pressure. Temperature was 323.15 K.

rameters. The persistence of the gas molecules, which remain in the layer even after the gas pressure has been reduced, is shown in grey on the right and as dashed lines on the left.

Further experiments with DPPC monolayers were conducted to investigate the influence of F-butane. The results are presented in figure 5.25. The area per DPPC lipid molecule is $63.4 \pm 0.2\,\text{Å}^2$. The lipid layer can be refined with similar fitting parameters as before. This confirms the reproducibility of the solid-supported membranes by spin-coating. The electron density profiles change in the same way as before with F-propane.

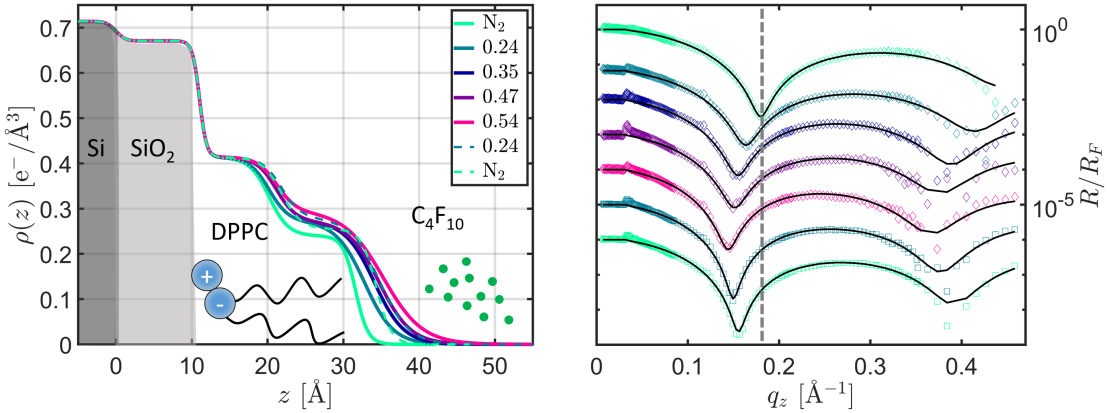

Figure 5.27: Left: Electron density profiles corresponding to the refinements with a sketch of the underlying model. Right: Fresnel normalised XRR curves of the measurement of a solid-supported DPPC monolayer at a temperature of 313.15 K and at increasing F-butane gas pressures. Diamonds: data, solid lines: fits, squares: decreasing gas pressure.

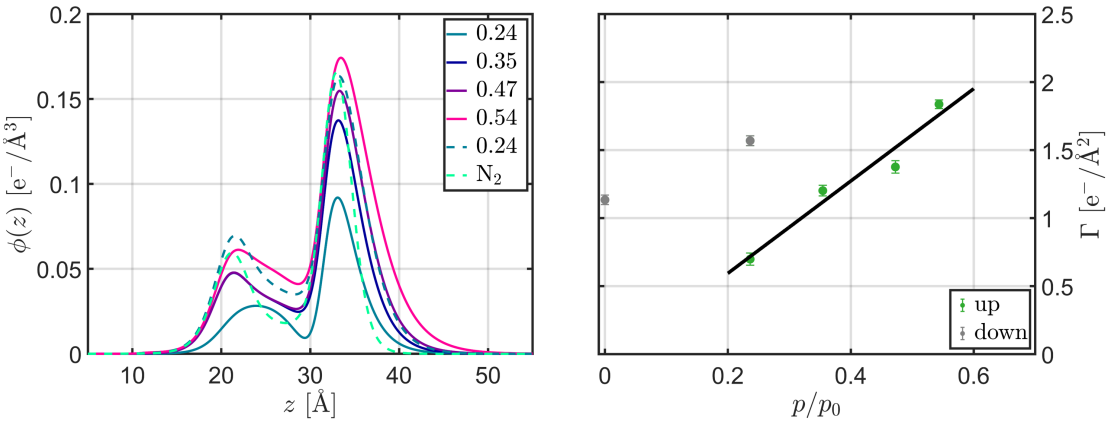

Figure 5.28: Left: Volume fraction profiles after subtraction of the F-butane treated solid-supported monolayer system and the reference system. Dotted lines: decreasing pressure. Right: Excess electrons per area as a function of the reduced gas pressure. Grey squares: decreasing pressure. Temperature was 313.15 K.

F-butane also inserts deep into the monolayer and remains in it after the gas is replaced by nitrogen. Figure 5.26 depicts the volume fraction profiles and the excess electrons per area. The adsorbed amount of F-butane seems to be lower than for the smaller F-propane gas molecule. The large molecular volume seems to cause a faster saturation in the lipid layer.

In order to investigate the influence of the lipid phase on the F-butane intercalation, the temperature of the system was reduced to 315.15 K, closely below the main phase transition of DPPC. The electron density profiles are shown on the left of figure 5.27

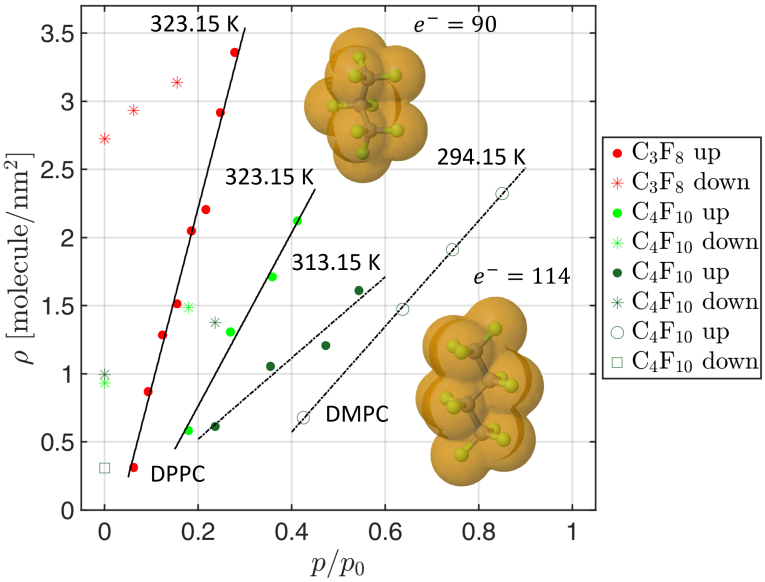

Figure 5.29: Surface density of the adsorbed molecules as a function of the reduced gas pressure on DPPC (filled symbols) and DMPC (open symbols) monolayers. The molecules of C_3F_8 (on the left) and C_4F_{10} (on the right) were visualised via Jmol [5, 6].

and the Fresnel normalised XRR curves and refinements are depicted on the right. The gel phase of the DPPC monolayer hinders the gas molecules from penetrating the headgroups (see also the volume fraction profiles in figure 5.28). At these temperatures the lipid system is less flexible. It can be seen that the amount of electrons per area is lower even at high F-butane gas pressures. The volume fraction profiles reveal a penetration and adsorption of the gas molecules mainly between the tailgroups. In every case, the gas molecules cause a higher thickness and electron density of the tailgroups. This consequently leads to the assumption that the gas molecules intercalate between the lipid molecules and cause an untilting of the tailgroups.

Considering the number of electrons per molecule it is possible to calculate the number of adsorbed gas molecules per area (ρ [e$^-$/nm^2]). F-propane possesses 90 electrons and F-butane 114 electrons. Figure 5.29 gives an overview of the adsorbed gas molecules. The solid support seems to influence the release of the gas molecules from the lipid layer, especially in the region of the tailgroups. It can be concluded that smaller gas molecules, like F-propane can penetrate and accumulate easier in the lipid layer. Furthermore, the lipid phase is important for the incooperation of the gas molecules. The rigidity of the lipid tails prevents the penetration of the molecules from the gas phase below the main phase transition temperature. To test a different phosphatidylcholine, DMPC with a C14:0 configuration was prepared by the Langmuir-Blodgett technique. The measurements were conducted at a temperature of 294.15 K and the response to F-butane has been examined. The calculated additional molecules per area are also implemented in

the figure 5.29 as open symbols. The XRR curves, electron density profiles and volume fraction profiles as well as the excess electrons per area are shown in the appendix A in figure A.3 and A.4.

gFC adsorption on solid-supported DMPC multilayers To investigate the influence of the solid substrate on the adsorption behaviour of the gases on the lipid films, solid-supported multilayers were prepared by spin-coating. It is known that the influence of the substrate becomes weaker with increasing distance between the solid support and the lipid layers. Above 10 bilayers the interaction between the substrate and the lipid film can be neglected.

Figure 5.30 top shows the collected XRR curves of a DMPC multilayer on a silicon/silicon dioxide solid support at air and with increasing gas pressures of F-butane. For the refinement of the reference XRR curve at ambient environment a three-box model was used. The silicon dioxide ($\sigma = 1.84\,\text{Å}$, $d = 14\,\text{Å}$) is the first layer. The second layer is used to simulate the transition between the first lipid layer and the solid support ($\sigma = 5.79\,\text{Å}$). The last box contains a periodically repeating set of six sublayers. Each set represents one bilayer. The system is sketched schematically in the bottom of figure 5.30. A remarkable feature of the XRR curves of the DMPC multilayer is the occurrence of sharp Bragg reflections up to the fourth order of diffraction. These reflections are due to the diffraction by the highly ordered bilayers forming periodically arranged planes parallel to the substrate. The refinement of the reference measurement with the Parratt algorithm in combination with the effective-density model yields 13.5 bilayers and a total multilayer thickness L_a of 705.64 Å.

As can be seen in the XRR curves, the Bragg reflections do not shift upon gas treatment indicating that no structural changes occur that affect the entire multilayer. However, modification of the upper layer cannot be excluded. The calculation of the bilayer thickness for the measurement at air yields a thickness of 54.28 Å. This is in accordance with the literature for non-hydrated DMPC multilayers on a solid substrate [81, 82, 84, 1079, 1143]. The obtained headgroup thickness of 9.8 Å and tailgroup thickness of 15.35 Å are also in accordance with reported values.

A significant feature in the XRR curve of the measurement of the solid-supported multilayer stacks at air are the “negative” peaks. These are marked with black arrows in figure 5.30 and are shown magnified in figure 5.31 top. These negative peaks are due to the relaxation of the terminating monolayer at the lipid film/air-interface [243, 1078]. Salditt et al. observed this effect also for OPPC [1078], the negative peak vanishes by hydrating the stacks. With hydrating the solid-supported multilayer, the terminating monolayer disappears and the bilayers within the multilayer swells due to the hydration process. The total thickness of the multilayer increases and the negative peak disappears [243, 1079, 1144]. In figure 5.31 top it can be seen, that the negative peak decreases and disappears with the application of the gas and appears again after removing the gas out of the sample cell. This implies that, like in the hydration process, structural changes occur at the terminal monolayer. Unfortunately, it is difficult to model uneven changes in individual layers of a multilayer, because the results become less distinct as the number of independent parameters increases. Therefore, the data will only be

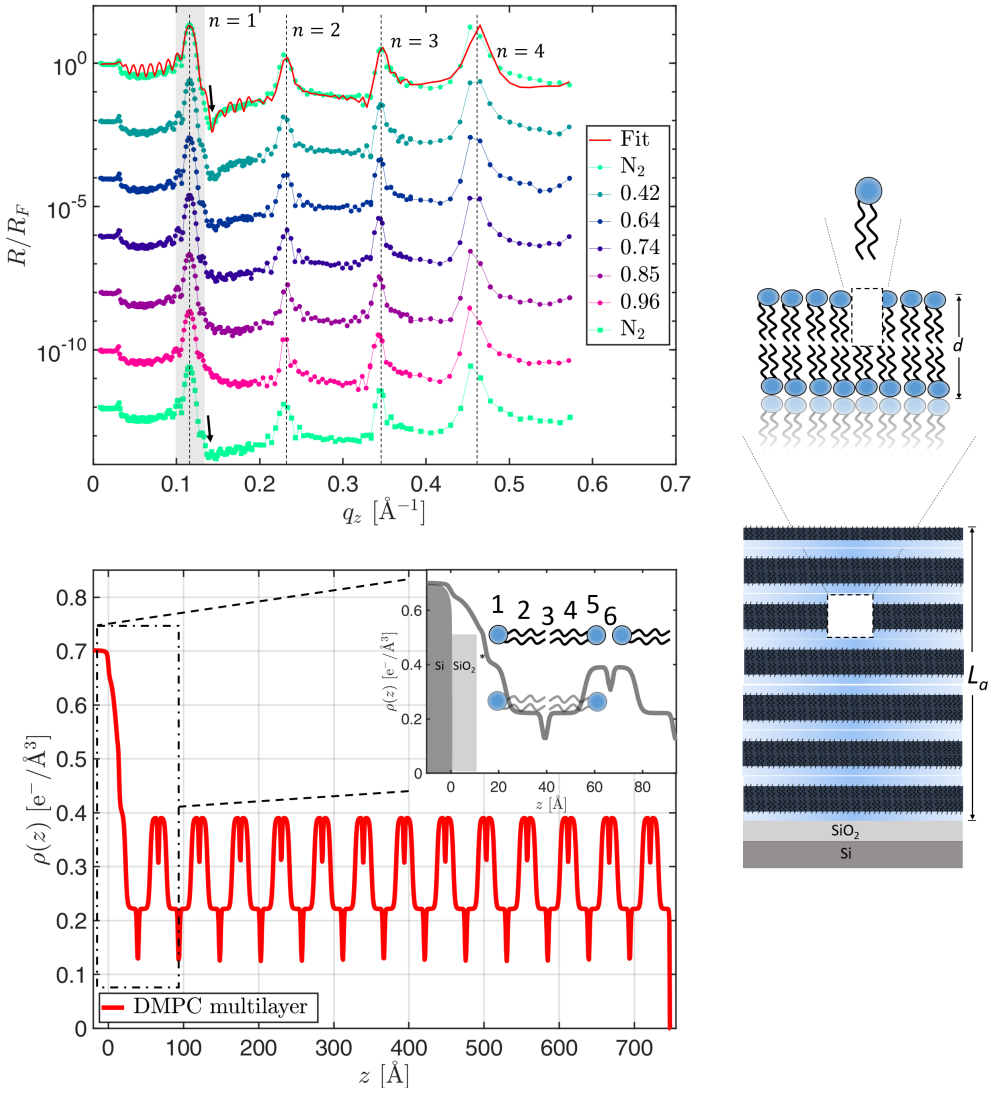

Figure 5.30: Top: Fresnel normalised XRR curves, shifted vertically for clarity, of solid-supported DMPC multilayers on previously hydrophilised silicon/silicon dioxide wafers collected at a temperature of 294.15 K at air and with increasing F-butane gas pressures. Squares: measurement at air after gas release, red solid line: fit. The black dotted lines highlight the unchanged Bragg reflection positions. The arrows indicate the negative peaks. Bottom: Reference electron density profile. The inset shows a zoom on the first 95 Å of the profile and the underlying six-sublayer system of the model. The additional layer that considers the influence of the substrate on the first lipid layer is marked by a star (*). The sketch on the right shows a schematic depiction of a DMPC multilayer film consisting of stacked DMPC bilayers with a spacing d. The coherence length L_a is calculated from the analysis of the broadening of the Bragg peaks (FWHM, Δq_z) considering the Scherrer equation.

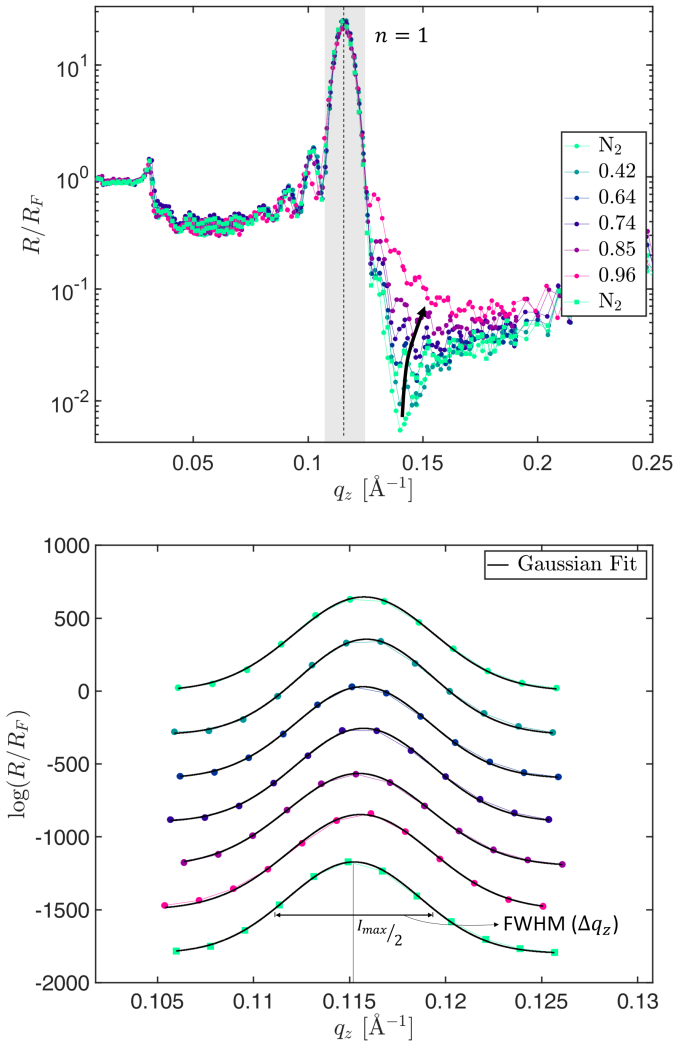

Figure 5.31: Top: Region around the first order Bragg reflection of the XRR curves from figure 5.30 to highlight the modification of the negative peak of the reference XRR curve by applying F-butane gas into the sample cell. The arrow marks the disappearance of the negative peak. Bottom: The first order Bragg maxima and the fitted Gaussian curves (black solid lines). The colours corresponds to the top plot.

discussed with regard to the Bragg reflection positions and widths and the vanishing of the negative peak.

The Bragg reflections were analysed by fitting a Gaussian to the first order maximum. With the resulting value for the reference measurement and the L_a from LSFit it is possible to calculate the Scherrer constant K via equation (4.3). However, it must be emphasised, that no resolution effects were taken into account and, therefore, the calculated factor is not a universally valid but suitable to compare the data from this

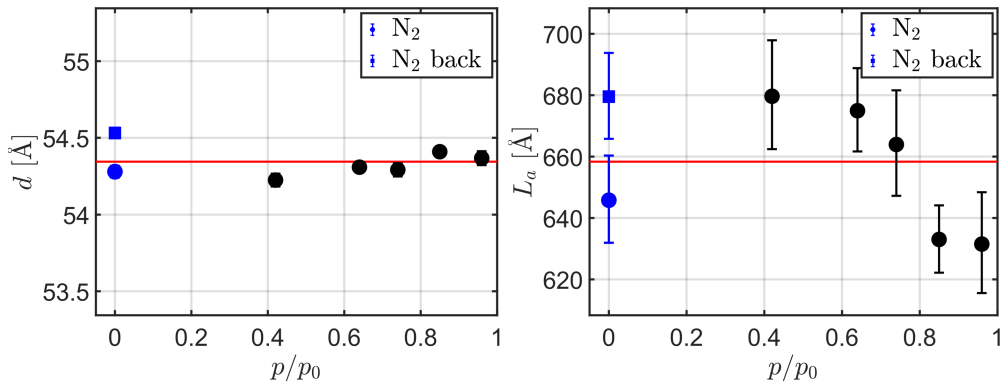

Figure 5.32: Left: Extracted bilayer thicknesses of the DMPC multilayers (via equation (4.4)) in dependence of the reduced F-butane gas pressure. The error bars are calculated from the Gaussian fit to the Bragg reflex position and are smaller than the marker size. The bilayer thickness as a function of the reduced condensation pressure was fitted by a constant (red line) resulting in a mean thickness of 54.35 Å. Right: Extracted multilayer thicknesses L_a of the system using equation (4.3). The error bars are calculated from the error of the Gaussian fit of the Bragg maxima.

experiment. The calculated value of 0.96 is used for the further calculations. The determined value is in the range of the Scherrer constants described in the literature (0.88 - 1 [82, 243]).

The Bragg reflection positions of the measurements at air and during gas application do not change. The Gaussian fits can be seen in figure 5.31 bottom. It is likely, that the gas molecules penetrate the terminating monolayer and adsorbs on top of it, similar to the solid-supported DMPC monolayer systems as the negative peak disappears. However, since no shift of the Bragg peaks is visible, a penetration deep into the multilayer stack is not probable. After removing the gas, the negative peak is not as deep as in the reference measurement at air. Some molecules seem to persist in the terminating layer. It can therefore be assumed that like in case of solid-supported monolayers molecules remain in the layer after removing the gas. The calculated multilayer and bilayer thicknesses in dependence of the reduced gas pressure p/p_0 of F-butane is shown in figure 5.32. As can be seen in the figure the bilayer thickness remains the same during gas application, while the multilayer thickness seems to decrease. This effect is, however, smaller than the thickness of one single bilayer and also small against the error bars. The slight decrease is most likely caused by the changes of the top layer that reduce the coherence of the stack but not the actual thickness. Similar observations were obtained when examining DPPC solid-supported multilayers under F-butane. The results are depicted in the appendix A in figure A.5 and A.6. The detected bilayer and multilayer thicknesses are plotted against the reduced gas pressure in figure A.7.

Since the melting point of DPPC is higher than for DMPC, the disappearance of the negative peak can be observed with DPPC only at higher gas pressures near to the condensation pressure. This is due to the lower flexibility of DPPC at the same temperature. The gas molecules cannot penetrate the terminating DPPC monolayer

as effectively as at the DMPC monolayer structure. The measurements with isobutane at solid-supported DMPC multilayers reveal no changes of the Bragg peak positions or broadening of the maxima. The XRR curves at air and under isobutane in comparison remain the same and can be seen in figure A.8. The fitted Gaussians are shown in figure A.9. The negative peak also persists. The fluorinated compounds have the advantage that they have a higher electron density contrast and, therefore, the adsorption can be detected more accurately.

To gain further insight into the influence of a smaller gFC, additional experiments with F-propane were conducted with DPPC and DMPC solid-supported multilayers at room temperature and at a temperature of 313.15 K for DMPC and 328.15 K for DPPC. The analysis of the results has shown that the curves do not change significantly (data not shown).

5.3 Liquid/gas-interfaces: protein-containing systems

In order to investigate the influence of perfluorinated molecules on the adsorption behaviour of proteins, several studies were carried out and are presented in the following. Two well-known globular and surface-active proteins, lysozyme and BSA, were investigated.

In the first section 5.3.2 the influence of F-decalin on the adsorption behaviour of lysozyme at DPPA-films is presented, the following section 5.3.3 deals with the lysozyme adsorption at the water/gFC-interface. The last section 5.3.4 discusses the results of BSA measurements at the water interface and the influence of F-decalin.

5.3.1 Experimental details

The studies presented in subsection 5.3.3 and 5.3.4 were conducted in the framework of the bachelor's theses by Isabel Maria Gernhold and Canan Orak [1145, 1146].

The measurements of lysozyme at a DPPA monolayer were performed with the injection method, where the protein is introduced underneath the Langmuir film. The required amount was taken from a stock solution and the volume necessary to achieve a final concentration of 0.22 mg/ml (15.29 µM) in the sample system was added. The surface pressure of the Langmuir film was initially set to 5 mN/m. This corresponds to the tilted liquid-condensed phase of the lipid. Rinsing with F-decalin was performed using a gas washing bottle and a nitrogen stream and started 2 hours after injecting lysozyme.

The measurements under elevated gas pressures at the water/air-interface were performed with identical lysozyme concentrations. The temperature was set to 294.15 K for the measurements with F-propane and 288.15 K for the measurements with isobutane. For the investigation of the BSA adsorption at the water surface, a protein concentration of 0.5 mg/ml (7.52 µM) was chosen. The flushing with F-decalin was started at different times after the injection of BSA into the subphase. For all measurements a 10 mM phosphate buffer at pH 7 was applied. The experiments were performed at a constant area in the gas pressure sample cell with the circular PTFE sample plate.

5.3.2 Lysozyme adsorption at the DPPA-film/vFC-interface

The lipid DPPA carries one negative charge at physiological pH-value in the absence of divalent cations [102, 967, 1147]. By the binding of proteins with basic amino residues, like arginine or lysine, the negative charge increases by switching to the doubly deprotonation state. Lysozyme is an ellipsoidal shaped protein with an isoelectric point at pH 11.35. Therefore, it is positively charged at pH 7. It has furthermore an uniform surface charge. Investigations of the influence of vFC and gFC atmospheres on the adsorption and penetration behaviour of lysozyme at lipid films but also at water/gas-interfaces are not available. Although the F-decalin molecule itself cannot penetrate and incooperate into DPPA-films (compare results of the GIXD and XRR experiments), an interaction between F-decalin and a lysozyme adsorbate at a DPPA monolayer could be triggered by a lysozyme-induced loosening of the film structure. The adsorption, insertion and penetration of lysozyme into lipid films was shown in several studies [1097, 1126, 1148, 1149]. Lysozyme is an amyloidogenic and aggregation-prone protein, which can form insoluble amyloid fibrils [801, 1150]. The fibril formation can often be promoted by lipids under certain conditions [795]. The mechanism of membrane interaction and penetration into lipid membranes is not fully understood. For example, the clinical dry eye condition is caused by lysozyme penetration into the outer layer of the tear lipid film (ocular surface tear film). The necessary low surface tension is disturbed by this process.

Figure 5.33 and figure 5.35 show the electron density profiles of DPPA-films at an initial surface pressure of 5 mN/m and further measurements of the adsorption of lysozyme under the influence of a F-decalin flow. Due to the large number of profiles, the results are subdivided in two figures. Figure 5.33 depicts the behaviour of the lysozyme adsorption under a F-decalin atmosphere. Figure 5.35 presents the results after replacing F-decalin with a nitrogen atmosphere. The colours of the density profiles corresponds to the Fresnel normalised XRR curves shown on the right side of each figure. Before flushing F-decalin saturated nitrogen into the sample cell, the reflectivity exhibits a single oscillation, even after lysozyme was added to the subphase. The protein adsorbs by penetrating into the monolayer headgroups. That can be seen in the corresponding electron density profiles (solid and dotted black line) on the left-hand side of the figure. The surface pressure increases due to the penetration of the protein. The thickness of the protein layer underneath the lipid film is around $d_{\mathrm{lys}} = 28 \pm 0.5\,\text{Å}$. The adsorption of lysozyme is time-dependent. Since it is a hard protein, the arrangement processes at the surface require a certain time until a stable adsorbate film is developed. However, the second measurement after a waiting time of 2 h shows no changes of the electron density profile. The protein and the DPPA-film are oppositely charged at these conditions. Thus, the main driving force of the interaction are of electrostatic nature. Lysozyme prefers probably a special orientation, since it is relative high negatively charged on one side of the surface, in fact at the substrate-binding cleft. The surface properties of the protein is illustrated in figure 5.34 in different orientations. The hydrophilic positively and negatively charged domains are coloured in blue and red, respectively. The hydrophobic residues are shown in green to yellow. The ratio

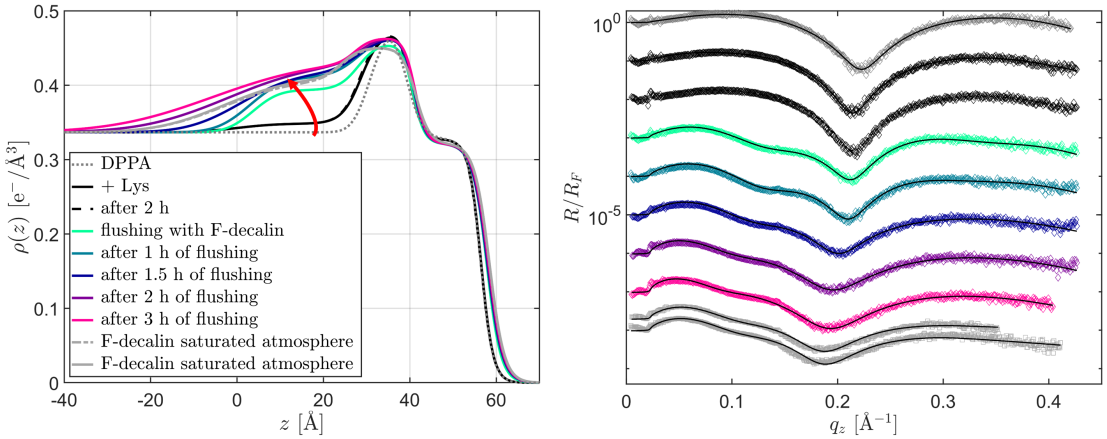

Figure 5.33: Left: Electron density profiles of lysozyme adsorption (c = 15.29 µM) to a DPPA-film (5 mN/m) before, while and after flushing F-decalin into the sample cell. Right: Vertically shifted Fresnel normalised reflectivity curves. The refinements are shown as solid black lines.

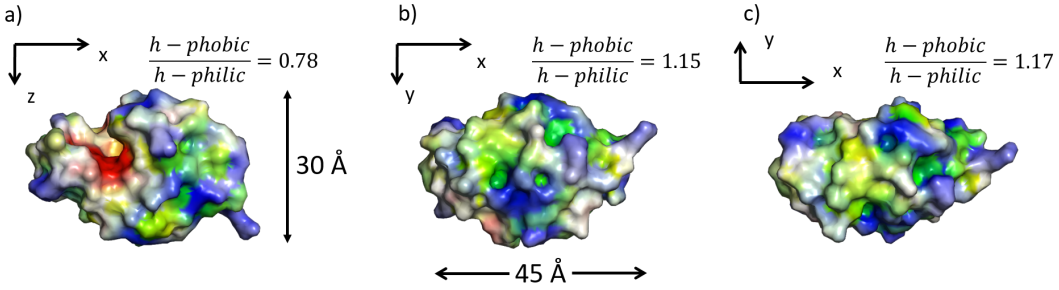

Figure 5.34: Lysozyme in different orientations (PDB file 1VDQ [1152]). The hydrophobic, positively, and negatively charged regions are coloured in green (to yellow), blue and red, respectively. The protein data bank [1021] using eF-site (electrostatic-surface of functional site [1026, 1027]) were utilised to identify the hydrophobic and hydrophilic domains. The hydrophobicity/hydrophilicity ratio that corresponds to the shown coloured areas are adapted from [1151].

of hydrophobicity/hydrophilicity of lysozyme in the different orientations are also given in the figure and were selected from [1151]. They corresponds to the shown coloured regions. The surface is to a large extend hydrophobic. The negative charges are primarily located at the side which is shown in part a) of the figure. This cannot be the initial adsorption site of lysozyme to the DPPA-film. The protein seems to adsorb with the long axis parallel to the DPPA surface, since the thickness of the layer matches this dimensions. The globular dimensions of lysozyme in the crystalline state are 30 x 30 x 45 Å^3. A sideways-on orientation with a slight denaturation of the structure due to the water/air-interface contact is likely. The lysozyme adsorbate seems to be structurally stable up to the point where F-decalin saturated nitrogen is flushed over the protein/lipid-interface. Upon flushing with F-decalin, the reflectivity curves show a superposition of several oscillations.

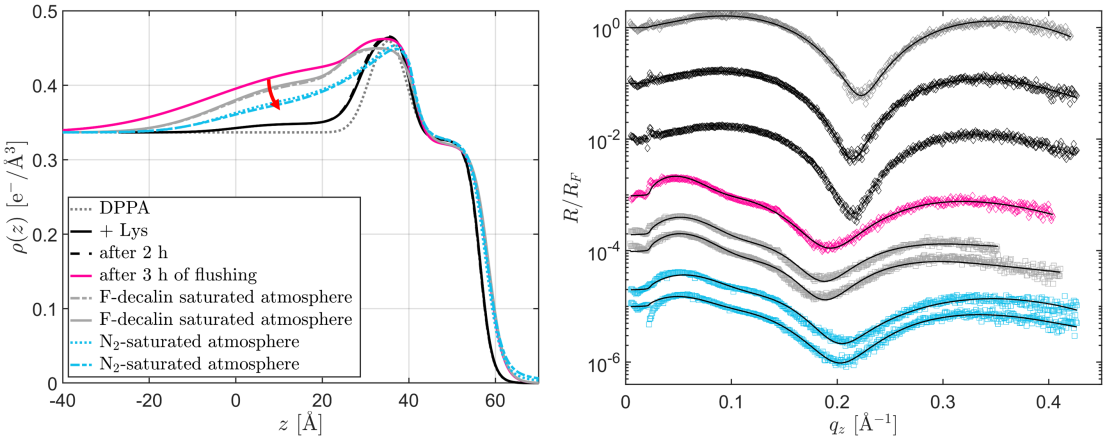

Figure 5.35: Left: Electron density profiles of lysozyme adsorption (c = 15.29 µM) to a DPPA-film (5 mN/m) showing the structural changes after the release of F-decalin from the sample cell. Right: Vertically shifted Fresnel normalised reflectivity curves. The refinements are shown as solid black lines.

The electron density profiles change during the F-decalin flow. Although the tail-groups are barely affected. The electron density of the protein adsorbate increases indicating that more proteins attach to the surface. Moreover, the protein layer thickness ranges from 24.35 Å at the beginning of the flushing, up to 30.5 Å after 3 h of F-decalin flow. Since the roughness also increases strongly (up to 15 Å), the actual adsorbate is expected to be even thicker. It can be concluded that an additional protein adsorbate, which is presumably in a non-native partially unfolded or denaturated state, attached to the initial protein layer. Since it was not necessary to use an additional layer to fit the data resulting in a levelly electron density profile of the adsorbate, a reorientation of the protein film is also possible. Besides changes of the orientation and amount of lysozyme, also an insertion of F-decalin into the protein layer might contribute to the resulting electron density profiles. Figure 5.35 shows on the left-hand side the electron density profiles obtained from the refinements of the reflectivity curves which are shown on the right-hand side. After stopping the F-decalin flow and measuring at a saturated F-decalin atmosphere, the profiles reveal a slightly decreased electron density accompanied with a reduction of the thickness of the adsorbed protein layer (grey dashed and solid line). When replacing the F-decalin atmosphere with nitrogen, shown as light blue dashed and dotted lines, the electron density of the protein film still decreases indicating a desorption of lysozyme from the DPPA-film. Only the adsorbed amount changes, not the thickness of the protein layer.

Additional time-dependent measurements of the development of the surface pressure of the DPPA-film with lysozyme were recorded. The Π-t curve is shown in figure 5.36. The first lysozyme measurement was conducted at a surface pressure of around 10 mN/m, the second measurement at a surface pressure of 15 mN/m. The sample was left over night and the surface pressure did not change significantly and remained at approx. 30 mN/m. By opening the sample cell and flushing gently with pure nitrogen,

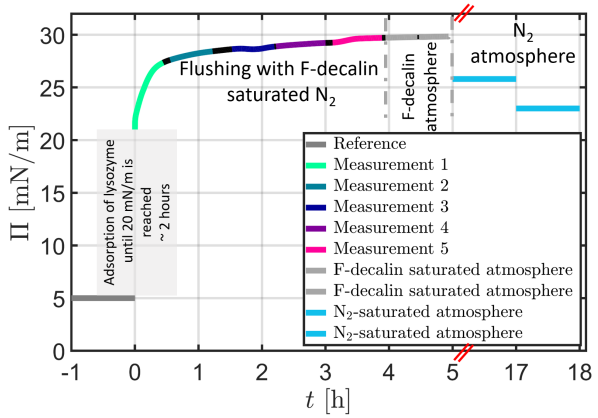

Figure 5.36: Time-dependent change of the surface pressure (Π-t curve) while flushing the sample cell with F-decalin saturated nitrogen. The colours correspond to those from figures 5.33 and 5.35.

the surface pressure decreased in the first 30 min. to around 25.8 mN/m and in the further hour to 23 mN/m and stayed stable for the last two hours.

A desorption process of adsorbed lysozyme like it was observed after F-decalin treatment in the present experiments is very unusual. The molecular reorganisation of lysozyme at a surface after adsorption is not reversible and insoluble aggregates form [794, 1017, 1148, 1151, 1153]. This seems to be inhibited by F-decalin. How F-decalin manages to interact with lysozyme despite the presence of a condensed DPPA-film at the interface remains unclear as there are no indications of a lysozyme-induced incooperation of F-decalin into the lipid layer. Nevertheless, F-decalin seems to have a unique effect on the desorption ability and thus the folding of the protein film. Presumably F-decalin inserts through loosely packed areas of the DPPA-film into the hydrophobic sites of the protein layer, which results in a merged lysozyme-F-decalin layer at the interface. F-decalin promotes to the hydrophobicity of the interface. This could explain the progressive accumulation of lysozyme at the interface and the increase of the surface pressure as well. Since the protein desorption is associated with the removal of F-decalin, an interaction cannot be excluded.

Effects on the protein/lipid-interaction by perfluorocarbons were also observed for serum albumins and DPPC in presence of F-octyl bromide and F-hexane [305, 440]. It is assumed that hydrophobic patches of the protein interact with the perfluorocarbons and that unfolding of the protein leads to an expulsion into the subphase [442, 443].

5.3.3 Lysozyme adsorption at the water/gFC-interface

The adsorption of lysozyme and the influence of the gFC C_3F_8 at different gas pressures are shown in figure 5.37. Since a very low concentrated buffer solution (10 mM) was used, the water electron density was utilised to refine the data [1154].

The surface of lysozyme is widely hydrophobic (see illustration of the protein surface in figure 5.34). If lysozyme is present in the buffer subphase, a protein film at the interface can be observed. The interfacial structure of the lysozyme adsorbate can be refined by a two-layer model: a more diffuse lower layer and a denser layer which is

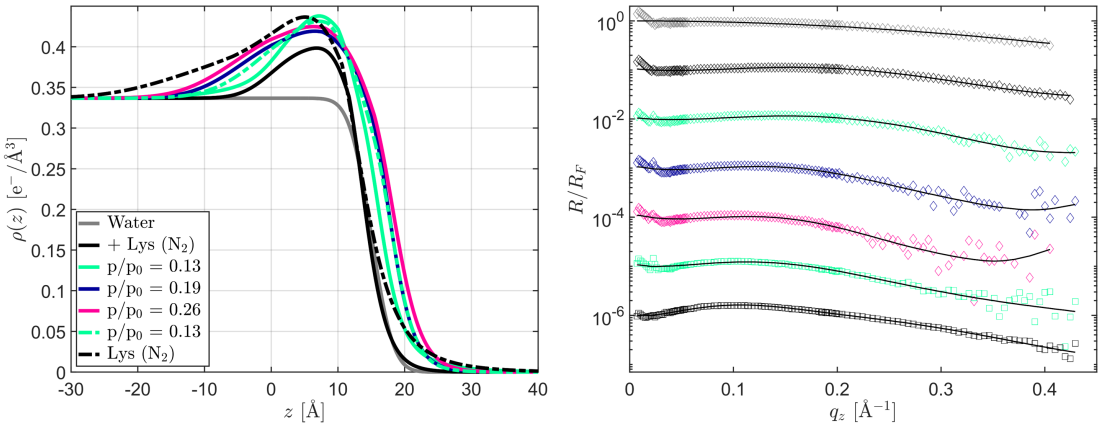

Figure 5.37: Left: Electron density profiles of the bare water interface, the adsorbed lysozyme layer and the influence of F-propane on the structure. The dashed lines highlight the measurements when the gas pressure is lowered or the measurement after gas treatment at air (N_2). Right: Fresnel normalised XRR curves shifted vertically for better visibility. The colours in the left plot correspond to those from right. Measurements were taken at a temperature of 294.15 K, $[c_{protein}] = 15.29\,\mu M$.

directly attached to the interface. The over-all thickness of the protein adsorbate can be calculated via: $d_{lys} = d_1 + d_2 + \sigma_0 + \sigma_2$ [1096]. The thickness of the initially adsorbed lysozyme without gas treatment is between 19.5 - 20.5 Å for each shown measurement. This thickness does not match any dimension of lysozyme in a native state. The values are lower than the dimensions of the crystalline state. It can be assumed that two different volume fractions are formed by a partial unfolding of the protein [1155–1158]. The partial unfolding occurs since disulfid bridges and β-sheet (5 folds) secondary structures are still present and prevent a complete unfolding at the surface [1156].

The treatment of the lysozyme adsorbate with increasing F-propane gas pressures at the water interface cause changes in the electron density profiles and, thus, influences the adsorption process of the protein. The protein film thickness and electron density increase constantly with rising gas pressure. After replacing the air atmosphere with the gFC, the electron density profiles have to be modelled by a three-box model. The gas adsorbs at the surface and with increasing gas pressure the layer on top growth and simultaneously the lysozyme film changes. Especially the part which is directly affiliated to the water surface expands. This can be induced by insertion of gas molecules and further unfolding of the protein. Presumably also more protein adsorbs at the surface.

The lysozyme adsorbate transform into a different structure after the gas pressure treatment. The thickness of the resulting layer is with about 42.3 Å much larger as the reference value. The very high hydrophobicity of the gas should be taken into account. It can be expected that the gas increases the probability of hydrophobic interactions at the interface and thus contributes to further unfolding of the protein. Since it is not possible to determine the exact position of the water surface, a calculation of volume fraction profiles is not possible. The electron densities of the gas layers are much higher

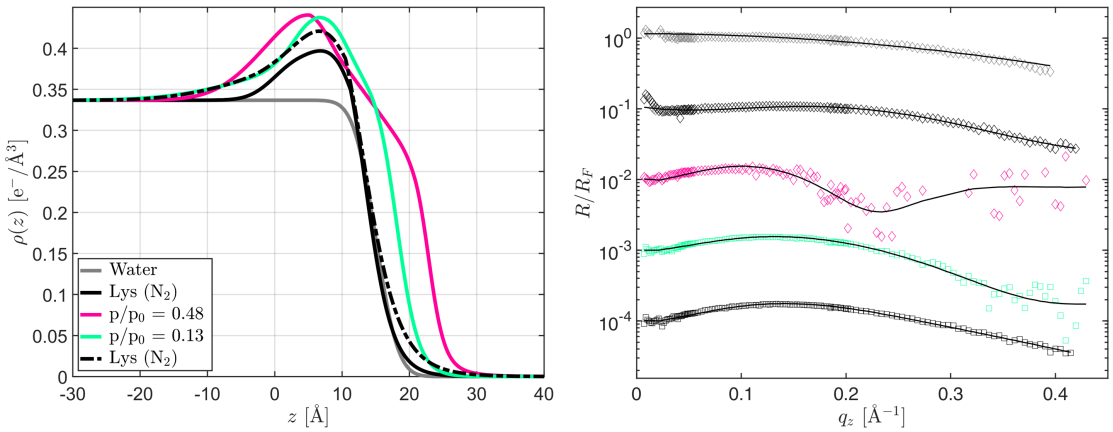

Figure 5.38: Left: Electron density profiles of the bare water interface, the adsorbed lysozyme layer and the influence of a strong gas pressure increase of F-propane to the structure. The dashed lines highlight the measurements when the gas pressure is lowered or the measurement after gas treatment at air (N_2). Right: Fresnel normalised XRR curves shifted vertically for better visibility. The colours in the left plot correspond to those from right. Measurements were taken at a temperature of 294.15 K, $[c_{protein}] = 15.29\,\mu M$.

than those of the reference system without protein [1049]. This indicates an affinity of F-propane to the protein-rich surface. Presumably, some of the adsorbed gas molecules also merge with the protein adsorbate at the interface.

To test a strong gas pressure increase onto the protein adsorbate, further measurements were performed on a freshly prepared sample system. The results are shown in figure 5.38. The initial electron density profile of the lysozyme film is similar to those from figure 5.37. By increasing the gas pressure rapidly to $p/p_0 = 0.5$, the structure at the interface changes significantly. The results show a gas film with a thickness of 7.5 Å. Unfortunately, due to the increased x-ray absorption by the denser gas phase, it is not possible to completely resolve the oscillation of the XRR curve. By decreasing the gas pressure again to about $p/p_0 = 0.13$, the obtained density profile is similar, but not identical to the above measured. A strong increase of the gas pressure leads to different electron density profiles of the remaining protein adsorbate after opening and flushing the cell with nitrogen. However, the effects are similar. In general, the interaction of F-propane (C_3F_8) and the surface system leads to a non-reversible increase of the protein adsorption at the interface.

Figure 5.39 shows the results of isobutane (C_4H_{10}) gas pressure-dependent measurements of the adsorption of lysozyme at a temperature of 288.15 K. At this temperature, the condensation pressure of isobutane is 2.589 bar. A comparison of the initially adsorbed lysozyme film with the before shown measurements reveals a quite similar interfacial structure as the electron density profiles are almost identical. The thickness of the protein layer is about 19.5 Å.

At low gas pressures, isobutane has almost no effect on the interfacial structure and no gas adsorbate layer form. This changes with increasing pressures as the electron

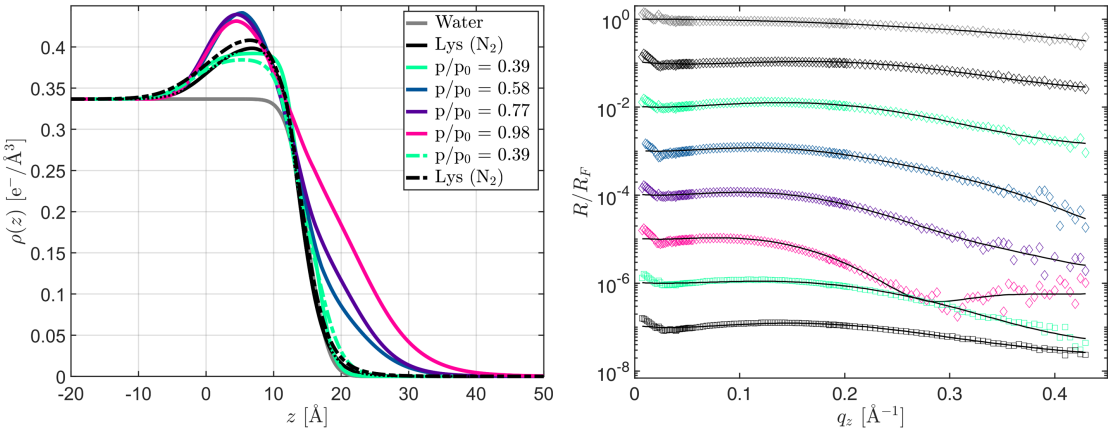

Figure 5.39: Left: Electron density profiles of the bare water interface, the adsorbed lysozyme layer and the influence of increasing isobutane gas pressure to the structure. The dashed lines highlight the measurements when the gas pressure is lowered or the measurement after gas treatment at air (N_2). Right: Fresnel normalised XRR curves shifted vertically for better visibility. The colours in the left plot correspond to those from right. Measurements were performed at a temperature of 288.15 K, $[c_{protein}] = 15.29\,\mu M$.

density of the protein layer increases and an additional layer above the surface forms. However, the thickness of the protein film is almost constant, in contrast to the effect of F-propane. The increase of the electron density and thickness of the additional layer with increasing gas pressure can be attributed to the accumulation of isobutane at the surface. The increase of the density of the protein layer might be caused by the adsorption of more lysozyme or by the penetration of gas molecules.

In contrast to the results of the gFC treatment, isobutane does not change the structural conformation of the lysozyme adsorbate at the surface. The lysozyme film can be modelled with similar parameters at higher gas pressures, only the gas layer changed progressively. To further study the influence of a strong increase of the isobutane gas pressure on the lysozyme film, a data series with freshly prepared samples were measured. Figure 5.40 shows the obtained XRR data. As can be seen in the figure, by increasing the gas pressure immediately to $p/p_0 = 0.58$, the refinement of the XRR curves reveals similar electron density profiles as observed before (compare figure 5.39). The gas pressure decrease and the replacement of the isobutane gas phase with nitrogen yield also very similar profiles as obtained during the measurements where the gas pressure was slowly increased. In comparison to the reference measurement of lysozyme, the adsorbed amount at the surface is increased, but the thickness remains the same.

In order to be able to correctly classify the results shown above, additional time-dependent experiments on the adsorption of the protein were conducted under the same experimental conditions, but without the influence of the gases.

The first presented measurements of the time-dependent adsorption process of lysozyme at the water/air-interface were recorded within 22 hours. Figure 5.41 shows the electron density profiles on the left and the Fresnel normalised XRR curves on the right.

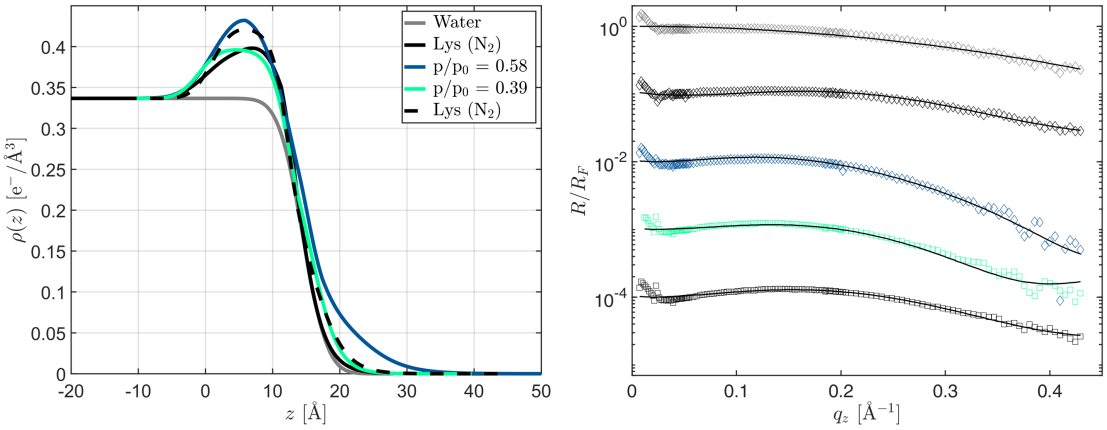

Figure 5.40: Left: Electron density profiles of the bare water interface, the adsorbed lysozyme layer and the influence of a sharp increase of isobutane gas pressure to the structure. The dashed lines highlight the measurements when the gas pressure is lowered or the measurement after gas treatment at air (N_2). Right: Fresnel normalised XRR curves shifted vertically for better visibility. The colours in the left plot correspond to those from right. Measurements were performed at a temperature of 288.15 K, $[c_{protein}] = 15.29\,\mu M$.

The data set was recorded at 288.15 K. As the temperature can alter and modify the adsorption behaviour of lysozyme [1159], additional experiments at a temperature of 294.15 K were conducted, these are shown hereafter. As can be seen, the electron density changes over time. The initial total layer thickness of around 20.5 Å, which is a value less than the minimal size of the protein, indicates again an altered lysozyme structure at the surface. The initial maximum electron density is $0.41\,e^-/Å^3$. The adsorbed amount of lysozyme increases accompanied by a rearrangement of the adsorbate, which is most pronounced after the 6 h measurement. The total layer thickness then rises up to 31.5 Å with a maximum electron density of $0.46\,e^-/Å^3$. This values match the dimensions of the lysozyme molecule in a sideways-on orientation. It seems, that the native globular structure unfolds at the interface with time.

For comparison of the data set with the gFC, the measurements of lysozyme at the water/air-interface were conducted additionally at a temperature of 294.15 K. Here, lysozyme from the company Merck KGaA were purchased and used for the measurements. The right-hand side of the figure 5.42 shows the obtained XRR curves in Fresnel normalised illustration and the refinements to the data as solid lines. The corresponding electron density profiles are shown on the left-hand side of the figure. As can be seen, a similar behaviour and electron density profiles can be observed. After 19 h, the temperature was changed to 288.15 K in order to test the structural rearrangement upon temperature change of the non-native species at the interface. The temperature has no effect on the lysozyme adsorbate.

By the calculation of the volume fraction profiles and consideration of the protein electron density, it is possible to obtain the adsorbed amount of protein (Γ) at the interface by integration of the resulting volume fraction profiles. The time-dependence

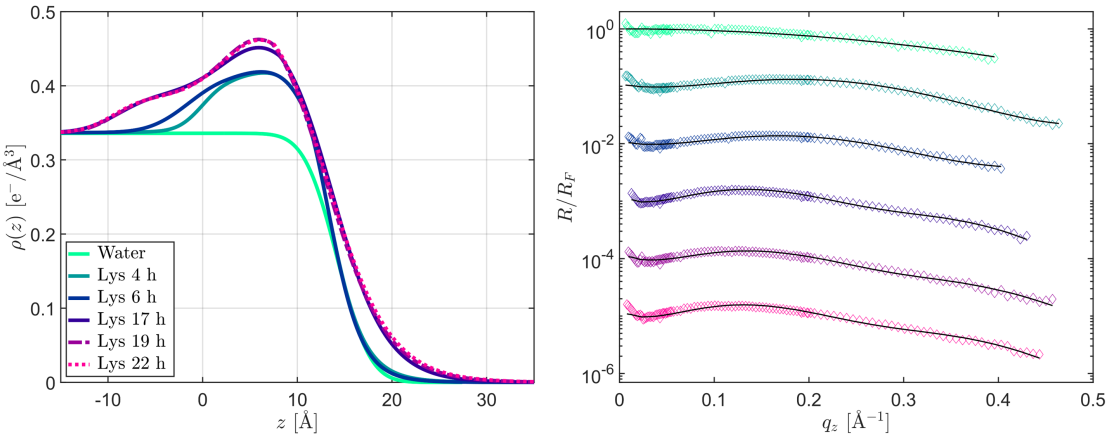

Figure 5.41: Left: Electron density profiles obtained from the refinements. Right: Fresnel normalised XRR curves of the time-dependent adsorption process of lysozyme at a temperature of 288.15 K. The initial protein concentration was 0.22 mg/ml (15.29 µM) in 10 mM phosphate buffer. The solid lines are the fits to the data.

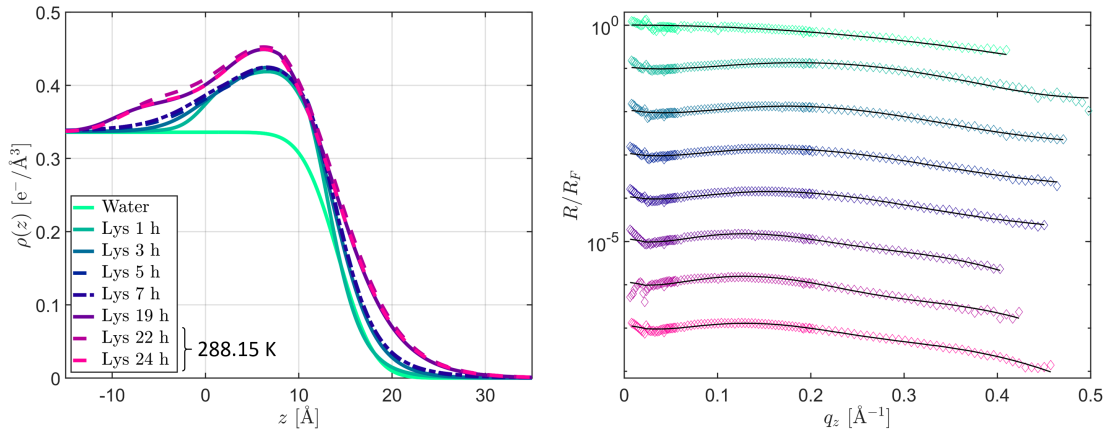

Figure 5.42: Left: Electron density profiles obtained from the refinements. The temperature was changed at 22 h to 288.15 K. Right: Fresnel normalised XRR curves of the time-dependent adsorption process of lysozyme at a temperature of 294.15 K. The initial protein concentration was 0.22 mg/ml (15.29 µM) in 10 mM phosphate buffer. The solid lines are the fits to the data.

of the adsorbed amount of lysozyme as a function of time is shown in figure 5.43 on the right for both temperatures. The surface pressure was recorded during the XRR measurements (see figure 5.42). The coloured regions corresponds to the XRR data.

With the assumption that lysozyme forms a monolayer, the corresponding occupied area per molecule can be calculated. The results are plotted as asterisks in the figure 5.43. The molar mass of lysozyme is 14307 g/mol, the area per molecule ranges over time between $\approx 19\,\mathrm{nm}^2$ (non-saturated conditions, averaged value over the first 7 h) and $\approx 12\,\mathrm{nm}^2$ (constant region). The area of a natively folded lysozyme protein is $13.5\,\mathrm{nm}^2$ and $9\,\mathrm{nm}^2$ in a sideways-on (adsorption with the long axis parallel to the surface) or

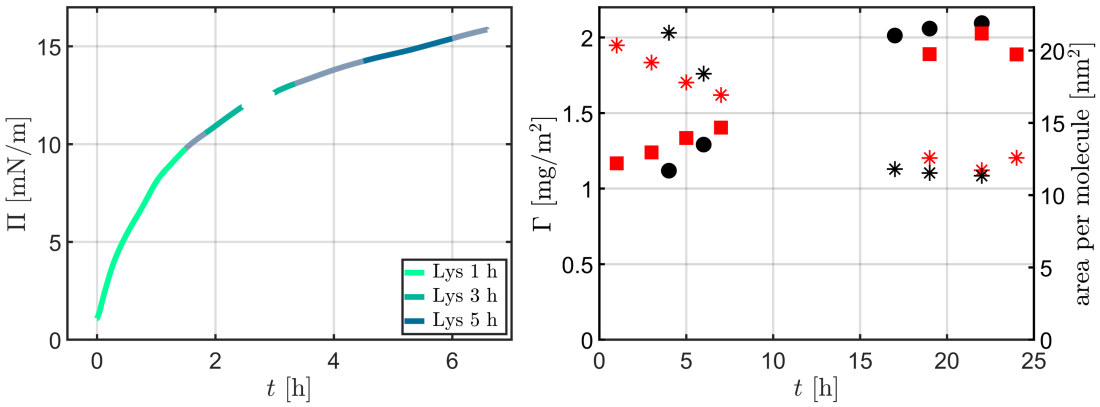

Figure 5.43: Left: Time-dependence of the surface pressure for lysozyme at a pH-value of 7.2 and a concentration of 0.22 mg/ml (15.29 µM) in a 10 mM phosphate buffer. The coloured regions correspond to those from figure 5.42. Right: Adsorbed mass per area as a function of time. Black dot symbols correspond to the data shown in 5.41, red square markers correspond to the data shown in 5.42. The area occupied per molecule is given in the same colours by asterisks. The error of the adsorbed mass is between 0.11 and 0.25 mg/m^2, estimated via variation of the refinement parameter.

headways-on (adsorption with the short axis parallel to the surface) orientation, respectively. The area of 12 mm^2 is little below the required area in the sideways-on orientation. The structural rearrangements lead in particular to a higher adsorbed amount and a thicker adsorbate layer with a more compact conformation of the lyosozyme molecules at the interface.

Possibly, a two-step surface-induced denaturation process occurs. First, the lysozyme adsorbs via van der Waals interaction at the surface and, then, denatures with time due to the additional hydrophobic patches which are exposed to the water/gas-interface. Hydrophobic residues are commonly buried in the core of a protein. A structural rearrangement and due to the newly created interaction sites of the proteins at the interface itself, it is possible, that more protein from the bulk solution can interact with the hydrophobic regions as interaction sites. Partially unfolding occurs already at the initial adsorption process by hydrophobic interactions at the water/air-interface which yields in the observed partially unfolded state.

The effects observed in the measurements of lysozyme adsorption under gas pressure cannot be attributed to a time effect. Surprisingly, the solvent isobutane seems to have a stabilising effect on the initial conformation of the lysozyme at the interface and inhibits the further rearrangements which occur over time. The perfluorinated gas in the atmosphere, on the other hand, has an “attracting” effect on the protein molecules and the adsorbed amount but also the thickness of the layer increases. However, the resulting layers seem to differ significantly from those observed in time-dependent measurements. In general, the affinity of the examined gases are high for protein-rich surfaces.

5.3.4 Bovine serum albumin adsorption at the water/vFC-interface

In order to investigate another well-established model protein under a vFC atmosphere, bovine serum albumin (BSA) was selected and its adsorption behaviour as well as its interaction with F-decalin at the water/air-interface was studied.

The pulmonary surfactant or lung surfactant is a complex mixture of proteins and lipids at the alveolar-interface and stabilises the lungs by reducing the surface tension at the alveolar lining fluid. Blood proteins such as serum albumins which leak into the lungs due to injuries or diseases are capable to inactivate the lung surfactant and have the ability to disturb the surface tension and proper function of the surfactant at the alveolus/air-interface. In 1965 Tierney and Johnson found that the pulmonary surfactant can be inhibited by blood plasma leakage in the alveolar lining layer [380].

The soluble proteins interfere with surfactant and prevent the *de-novo* surfactant phospholipid adsorption. The (insoluble) phospholipids of the native lung surfactant are present in large aggregate structures. The large molecular structures reach the surface via cooperative diffusion, adsorb and spread slowly at the alveolar lining fluid interface by unzipping mechanisms. The proteins which leak into the alveolar space are surface-active. The large amphiphilic proteins reach the surface rapidly via molecular diffusion processes and adsorb spontaneously at the surface. Consequently, the proteins can adsorb faster at the alveolar/gas-interface than the surfactant aggregates. The proteins hinder the access of lung surfactant to the alveolar interface by competitive adsorption. After adsorption, the protein film prevents the lipids from penetrating the interface by generating a steric and/or electrostatic energy barrier [285, 1160, 1161]. The exogenous surfactant preparations are inhibited by the proteins, alternative and novel approaches for the treatment are necessary. A more recent approach is the use of perfluorocarbons that were investigated for partial liquid ventilation and ventilation of aerolised and vaporised perfluorocarbons. A perfluorocarbon that was intensively studied for biomedical applications is F-decalin ($C_{10}F_{18}$). It was selected to investigate the interaction of PFCs and bovine serum albumin at the buffer/air-interface and their influence on the adsorption behaviour of the proteins.

The adsorption of BSA and the effect of F-decalin were investigated time-dependently in three different experimental procedures. The time of the addition, respectively the starting point of the flushing with F-decalin saturated nitrogen was varied. At higher concentrations of around 1 mg/ml it took about one hour to reach adsorption equilibrium [1162]. For lower concentrations, which were also used in this work, the equilibrium is reached after 5 hours [1163–1165]. Based on this, different times were chosen to investigate the various stages of the adsorption path and the influence of F-decalin on the adsorption behaviour. For this purpose, also faster XRR measurements were conducted, where one measurement took about 30 minutes.

Figure 5.44 shows schematically the design of the experiment. To exclude a time effect of the adsorption process of BSA, XRR curves were also recorded 12 hours after addition of the protein. First, the reference measurements of F-decalin at the free water surface are presented. Figure 5.45 shows the electron density profiles on the left obtained from the refinements of the XRR curves shown right. The spreading coefficient of F-

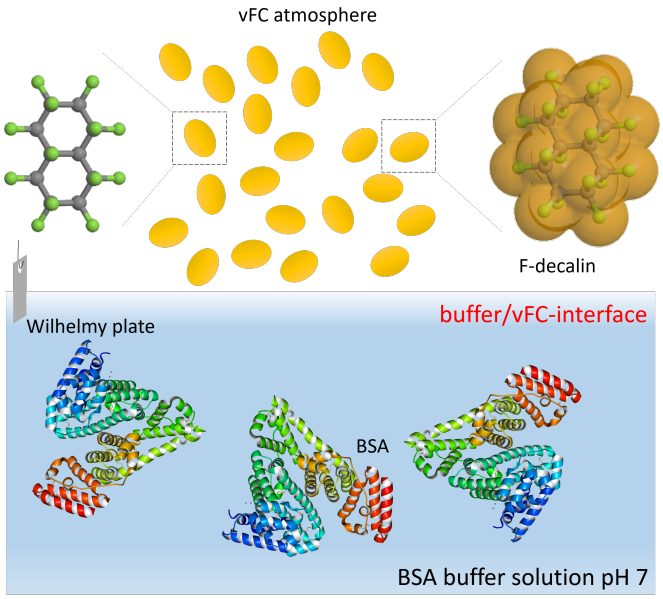

Figure 5.44: Schematic illustration of the sample system.

decalin is negative and it is a highly hydrophobic and non-polar molecule. However, an adsorption of the perfluorocarbon compound can be observed. As can be seen in the figure, by replacing air with F-decalin saturated nitrogen, the XRR curves develop a slight oscillation. The maximal surface pressure during the flow of the vapour was 2.5 mN/m. The thickness of the adsorbed F-dacalin layer increases during the flow of the vFC from 15.8 Å to about 20 Å. Also, the electron density in the near-surface region increases. The bulk electron density of fluid F-decalin ($\rho = 0.554\,e^-/Å^3$) is not reached. The measurements under vFC atmosphere without gas flow reveal a decreasing electron density and thickness of the layer in time (labelled as "PFD atm" in the figure). The surface pressure decreases to 1.3 mN/m indicating a desorption of molecules from the interface. When the sample cell is opened, the electron density profile does not change to the profile expected for a free water surface. Some adsorbed molecules are detectable on the surface within the timescale of the experiment. The surface pressure is around 1 mN/m.

The reduction of the surface tension in the presence of the vFC is explained by the formation of a thin PFC layer on the free water surface. Since F-decalin in general has a low water solubility, it is a reasonable approach to calculate volume fraction profiles assuming adsorbate layer consists exclusively of F-decalin and incooperates no water molecules. The volume fraction profiles are shown in figure 5.46 with the corresponding calculated molecules per area in e^-/nm^2 and the thicknesses of the observed F-decalin layer. The layer thicknesses were determined by taking the roughness of the substrate and of the adsorbed layer into account.

Figure 5.47 presents the results of the measurements of the adsorption of BSA in a

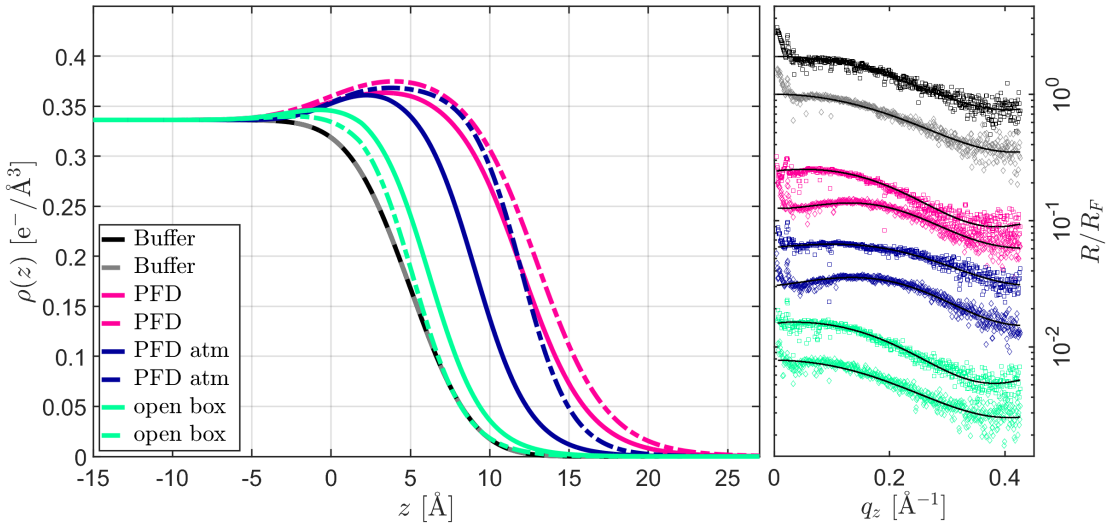

Figure 5.45: XRR data of F-decalin adsorption at the water surface. Left: Electron density profiles. The continuous flow of the vFC is labelled as "PFD", the measurements at F-decalin atmosphere without gas flow as "PFD atm". Right: Fresnel normalised XRR curves vertically shifted for clarity. The fits to the data are shown as solid black lines.

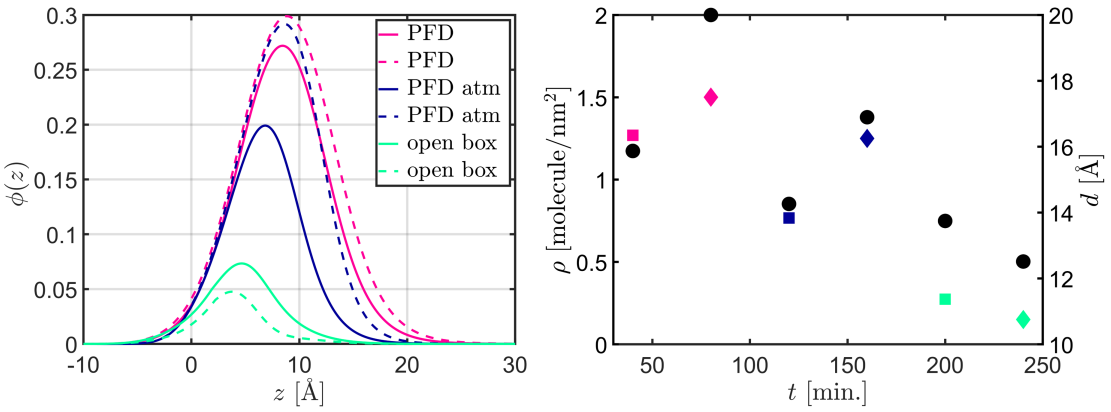

Figure 5.46: Left: Volume fraction profiles for F-deaclin at the water/air-interface. Right: Variation of the adsorbed molecules per area, coloured in the same code as shown in the volume fraction profiles. The first measurement of one condition ("PFD, PFD atm, open box") is marked as square and the following one as diamond. The thicknesses are shown as black circles.

phosphate buffer solution with a pH-value of 7 at a concentration of 0.5 mg/ml (7.52 µM). The flushing with F-decalin was started immediately after the first reflectivity curve with protein-containing subphase was taken. At the applied concentration and pH-value BSA (IEP ∼4.5 - 5[1]) is monomeric [1016] and negatively charged with -10 in the N-terminal

[1]The isoelectric point is calculated by using the FASTA sequence of BSA (P02769 Bos taurus

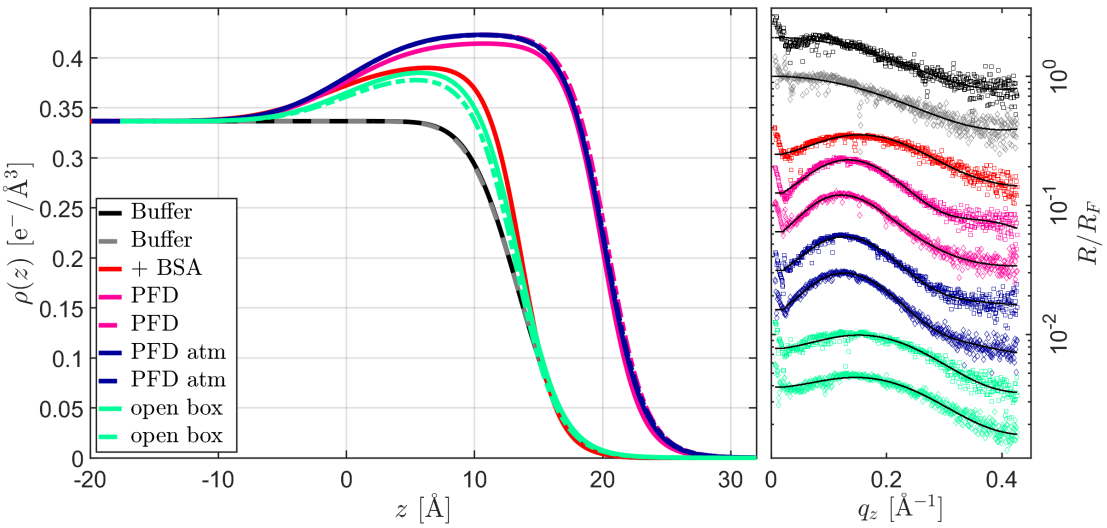

Figure 5.47: XRR data of the measurements of the adsorption of BSA at the water/air-interface before, while and after flushing with F-decalin saturated nitrogen. Left: Electron density profiles. "+ BSA" marks the measurement immediately after preparation. The continuous flow of the vFC is labelled as "PFD", the measurements at F-decalin atmosphere, without gas flow as "PFD atm". Right: Fresnel normalised XRR curves vertically shifted for clarity. The fits to the data are shown as solid black lines.

domain I, -8 in the middle domain II and 0 in the C-terminal domain III. The net charge is -10 [887, 888, 1162, 1169]. The maximum electron density of the BSA adsorbate layer that form before F-decalin is introduced is 0.39 e$^-$/Å^3. This value is less than the electron density of the protein in the native conformation. The thickness of the BSA layer is 22.2 Å. After replacing the air by F-decalin saturated nitrogen the oscillation of the XRR curve is more pronounced. The precise measurement of the adsorbed amount and layer thickness together with the known dimensions of the spherical structure of BSA allow to derive information about the adsorption state of the protein within the film. The protein BSA is in its N-form at these microenvironment and experimental conditions. The triangular shaped conformer has dimensions of 80 Å x 80 Å x 80 Å x 30 Å. It is described as an equilateral triangle with a side length of 80 Å. The obtained thickness of the protein film is lower than the dimensions for the short side of the crystalline state. It seems, that the protein unfolds by adsorption at the extreme hydrophobic water/air-interface. BSA has a high conformational flexibility and the structure is intensively altered upon adsorption at the water/air-interface [1017, 1151, 1170]. However, it is known that the α-helical secondary structure is only lost under high concentrations of denaturants in the solution [1170]. Moreover, the numerous disulfid bridges stabilise the structure and limit the maximum elongation of BSA. Thus, the protein film can

(Bovine)) without the signal sequence and the PepCalc.com - Innovagen peptide property calculator [1166]. Note, that the calculated isoelectric point differs from the experimental obtained. There is no consensus about the correct isoelectric point of BSA [1019, 1167, 1168].

be composed of alternated and unfolded N-forms of BSA with hydrophobic regions and residues oriented to the interface. The so-called E-(extended) shape, which is usually present at pH-values lower than 4, is the most elongated structure and nevertheless exhibits a high content of α-helical regions. The elongated structure dimensions are 250 x 21 x 21 Å^3 (crystallography study [875]). The short side matches to the thickness which is observed here. The attachment takes place with the hydrophobic residues of the α-sheets which are usually buried in and folded towards the core of the protein.

The aliphatic α-helices can be displaced with the hydrophobic side chains towards the interface. Unfolding does not necessarily mean that the protein is denatured, the secondary structure can remain unchanged. Therefore, an adsorption of BSA at the interface can be explained by a spreading of the homologous three-domain structure, while retaining the secondary structure. The globular BSA has a low effective surface hydrophobicity, the HIC retention time is around 6.7 minutes [1016, 1151]. Figure 5.48 shows the molecular surface of BSA in three different orientations. The colour code is the same as before, green to yellow indicates the hydrophobic patches, the positively and negatively charged residues are shown in blue and red, respectively. The hydrophobic area of BSA is much lower than those of lysozyme (compare figure 5.34).

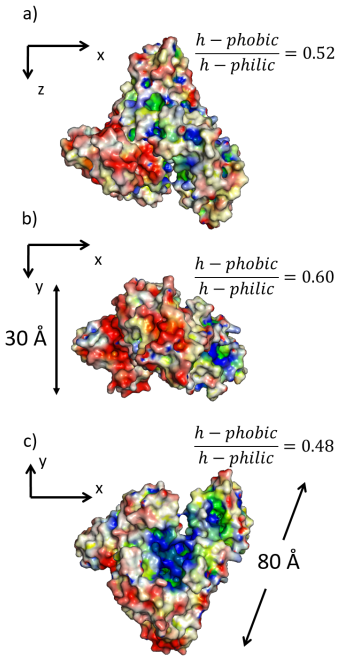

Figure 5.48: Different orientations of the molecular surface of the heart-shaped structure (N-form) of BSA of the PDB file 3V03. The hydrophobic, positively, and negatively charged regions are coloured in green, blue and red, respectively. The hydrophobicity/hydrophilicity ratio that corresponds to the shown coloured areas are adapted from [1151].

As can be seen, the thickness and electron density first increase with replacing nitrogen with vaporised F-decalin. It was not necessary to refine the data with an additional layer for F-decalin. The exact position of the water surface of the complex is therefore not exactly known and it is not possible to calculate the volume fraction profiles. Nevertheless, the adsorbed mass can be determined for the system in absence of F-decalin. The electron density of BSA can be computed with the number of 35486 electrons (estimated via the primary sequence of the protein and the amino acids[2]). The bulk density of BSA at pH 7 is 1.313 g/cm^3 [1100, 1101] (calculated with the partial specific, molar volume) and the molecular mass is 66.463 kDa (66463 g/mol). By considering the Avogadro constant it is possible to calculate the electron density yielding 0.4228 e$^-$/Å^3. The surface excess Γ [mg/m^2] can be calculated by integration of the volume fraction profiles. The corresponding volume fraction profiles which are used to calculate the surface

[2]The molecular formula ($C_{2934}H_{4615}N_{781}O_{897}S_{39}$) is calculated via the FASTA sequence of BSA (P02769) without the signal sequence yielding 583 aa and computed using Protpi.ch.

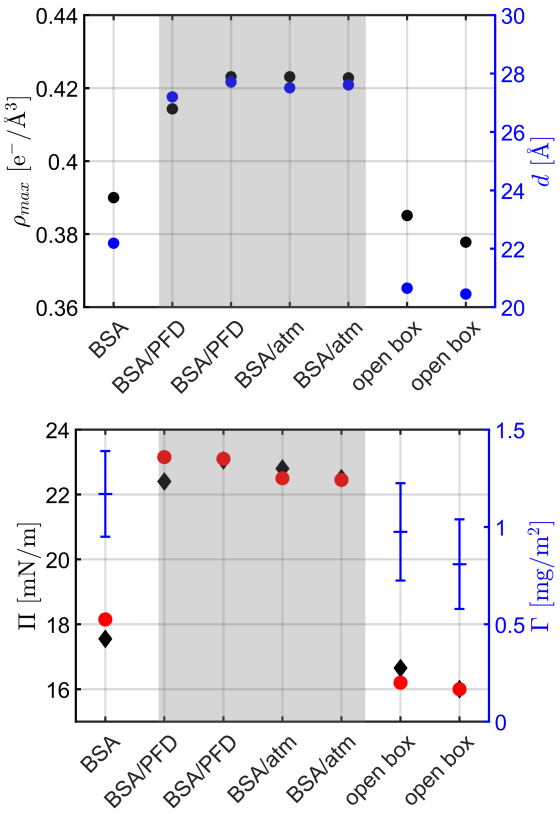

Figure 5.49: Top: Maximum electron densities and thicknesses of the interfacial film over time and in the presence and absence of F-decalin. The grey box highlights the presence of F-decalin. Bottom: Variation of the surface pressure over time and calculated adsorbed amount of BSA in the absence of F-decalin. The errors are estimated via variation of the refinement parameters.

excess are shown in the appendix A in figure A.10. The corresponding area of the adsorbed mass at the initial stage (first measurement) is 88.5 Å^2. The required area for one BSA molecule in a native state is about 27.7 Å^2. This suggests also an unfolding at the water/air-interface. The figure 5.49 bottom depicts the adsorbed mass of the protein film (blue crosses). The surface pressure at the beginning (black diamonds) and end (red diamonds) of each measurement is presented in the bottom. Figure 5.49 shows the maximum electron density (black circles) and the adsorbate layer thickness (blue circles) obtained from the data in figure 5.47.

It seems, that the affinity of F-decalin for the protein adsorbate at the interface is higher as for the free water surface since the surface pressure increases to much higher values. The course of the surface pressure change corresponds to the course of the layer thickness and of the electron density variation. The adsorbed amount of the protein does not change after F-decalin treatment. As can be seen at the bottom of the figure, the adsorbed mass of BSA is in the range of the error bars.

Due to the unfolding of BSA at the water/air-interface, the hydrophobic regions and

residues of the protein (mainly located in the sub-domains IIA and IIIA) are directed to the interfacial region, whilst the polar regions are submerged in the subphase. The F-decalin molecules can interact with the hydrophobic cavities of the protein structure since the perfluorinated compound is extremely hydrophobic. These interactions and the formation of merged BSA-F-decalin structures cause the detected electron density profiles under F-decalin flow and atmosphere (without gas flushing). In addition, under F-decalin flow and atmosphere more protein is attracted to the surface, the perfluorinated compound "mobilises" BSA. But after removal of the F-decalin atmosphere it is also expelled again into the subphase. As it has been shown that fluorinated anaesthetics and perfluoroalkylated amphiphiles do indeed bind to BSA in solution, the interaction at the interface seems to be the explanation for the resulting structure [1171, 1172]. It was also reported that F-hexane adsorbs, induces the unfolding of BSA [305, 442, 443] and accelerates the adsorption of DPPC from solution. One process that was proposed is the rapid adsorption of F-hexane at the water/air-interface and incorporation into the hydrophobic sites of the serum albumin. This mechanism promotes its unfolding and, thus, facilitates expulsion into the aqueous phase. This process is not initiated by F-decalin. The process at the water/F-decalin-interface is entirely reversible and non-destructive.

To gain more insight into the interaction and to investigate the effect of F-decalin on older adsorbates of BSA the measurements of the interaction of BSA and F-decalin at the water/air-interface have been reproduced with equilibration times for the BSA adsorption before the addition of F-decalin of 2 hours and 12 hours. It was found, that the BSA layer does not change on this timescale and also the effect of F-decalin was the same. The data are shown in the appendix A. The XRR data of 2 hours incubated BSA under F-decalin are shown in figures A.11, A.12 and A.13 and the XRR data of over night incubated BSA under F-decalin are shown in figures A.14, A.15 and A.16.

F-decalin is not an efficient promoter of the displacement of the adsorbed BSA structures at the water/air-interface, but does not lead to any significant changes in protein structure or aggregation after treatment. Nevertheless, the results demonstrate the bio-inertness of F-decalin on serum albumin structures and may have implications for the partial ventilation or ventilation with aerolised and vaporised perfluorocarbons in lung conditions as a consequence of lung immaturity. Synthetic components for the lung surfactant replacement therapy are necessary. These have a lower risk than animal derived surfactant preparations (disease transmission, lesser immunological rejection and defined formulations with adjusted and matched biophysical properties, no batch-to-batch variation). F-decalin leads to a strong decrease in surface tension and could also serve as a vehicle for DPPC in surfactant replacement formulations. DPPC could be more effective at the surface, since when it is introduced over an adsorbed layer of BSA it controls the surface tension and is not interfered by BSA [395]. The surface-activity of F-decalin is not impaired by BSA.

Furthermore, it is necessary to know how artificial oxygen carriers or blood substitutions and other injected emulsions for molecular imaging with F-decalin core influence plasma proteins such as serum albumin. In adsorbed serum proteins, F-decalin appears to interfere with but not damage the serum proteins.

In summary, F-decalin causes a growth of the BSA adsorbate at the surface and allows a displacement of the protein from the surface again after the interaction without any induction of any structural changes. The interaction process is completely reversible, also after long equilibration times. This observation is quite similar to the results obtained for lysozyme adsorption on DPPA-films under F-decalin which suggested that F-decalin acts locally on lysozyme through the lipid layer at more loosened DPPA-film regions. Probably, F-decalin also merged in the hydrophobic structures of lysozyme. After the F-decalin atmosphere has been removed the protein is released into the subphase again. However, in this case the effect was not entirely reversible. In general, F-decalin has an affinity for a protein-rich interfaces and attracts more proteins to the surface. The interaction causes the formation of a mixed protein-F-decalin layer.

5.4 Summary and general conclusions

In this chapter results on the influence of different gas and vaporised perfluorocarbon atmospheres on model lipid systems and protein adsorbates were presented. The surface sensitive x-ray scattering methods XRR and GIXD were used to investigate the influence of the perfluorocarbon compounds with sub-angstrom resolution at *in-situ* conditions.

In the first section the liquid/gas-interface was considered. To evaluate the effects of the non-polar, non-amphiphilic and hydrophobic perfluorocarbon molecules on lipid systems that mimic the lung surfactant, the first subsection examined DPPA- and DPPC-films on aqueous subphases with different initial surface pressures. The data reveal that the non-polar gas molecules of isobutane and perfluorinated gases have an affinity to the lipid monolayers. The gas molecules adsorb at the water interface and accumulate after penetration between the tailgroups. The XRR data indicate that for DPPC-films the headgroup is influenced by the intercalation and accumulation of the gas molecules and changes its configuration to an untilted state. However, with DPPA a change of the headgroup is not observed. In addition, DPPC-films are partially dissolved in F-butane in the presence of sufficient lipid coverage. This was also not observed for DPPA-films. The gases lower the interfacial tension of a bare water interface and in presence of DPPA- and DPPC-films. The adsorption of the gFCs occurs in crystalline regions of the DPPA-film, but also in more expanded regions of the lipid structure. It was found that F-propane causes compression of the film at low gas and surface pressures and can lead to a crystalline structure of the film. The gas application leads to a compression of the lipid films. The gas effects on Langmuir films depend on the size of the gas and also on the packing conditions of the monolayer. The observed effects are stronger for the less densely packed DPPC-films. The properties of the Langmuir films are modified by co-adsorbed gas molecules. For F-decalin it was shown, that the spherical and bicyclic molecule can penetrate DPPC-films at low surface pressures, but does not affect DPPC- and DPPA-films at high initial surface pressures. The application of vaporised F-decalin has no effect on DPPA-films in GIXD scans. In contrast, the more lipophilic F-octyl bromide indicates a fluidisation of the DPPA monolayer by causing compression and simultaneous dissolution of crystalline domains by adsorption

into less compressed areas. The fluidisation effect on DPPC-films is explained by the reduction of the interaction energy between the DPPC molecules upon perfluorocarbon intercalation and interaction with DPPC [3, 305, 1137]. Considering the results of this work, this also applies for the interaction of DPPA monolayers and F-octyl bromide.

In summary, it can be concluded that the hydrocarbon gas and also the perfluorinated gases and vapours have an influence on DPPA and DPPC monolayers. Decisive for the extent of the effect is the packing density of the lipids, but also the size of the molecules from the gas phase. The perfluorocarbons under investigation behave like co-surfactants as they intercalate the Langmuir films and contribute to the reduction of surface tension, whereby they do not possess any amphiphilic character.

In the next section the results of the solid/gas-interface were presented. DPPC and DMPC mono- and multilayers were prepared on silicon substrates by spin-coating or Langmuir-Blodgett technique and the lipid layer structures were investigated under gas atmosphere. A gas pressure-dependent accumulation of F-propane and F-butane gas molecules in the lipid monolayers were detected. The influence of the gases on the lipid structure depends on the flexibility of the lipids. The lower the rigidity the more gas molecules can intercalate into the layer. Furthermore, when reducing the gas pressure and replacing the gas phase by air, it was found that gas molecules remain in the lipid layer. This might be attributed to a substrate-dependent effect. In order to gain more insight into the persistence and substrate influence, solid-supported multilayers were investigated under different gas atmospheres and temperatures. It was found that the gases have no influence on the bilayer thicknesses of the multilayer stacks and only the negative peak under F-butane is influenced. The negative peak is a feature that is closely connected to the structure of the terminal monolayer. The negative peak vanishes or disappears at high pressures of F-butane. After lowering the gas pressure and measuring at air, it can be seen that the depth of the negative peak does not return to the previous position, which is an indication of remaining gas molecules in the terminal monolayer. It can be assumed that the intercalation of gas into the terminal monolayer of the multilayer stacks is comparable to those occurring in the solid-supported monolayers, while the bilayers below are widely unaffected.

In the last section, the influence of perfluorinated substances on the adsorption behaviour of lysozyme at DPPA-films and at the bare buffer/gas-interface was investigated. Furthermore, the adsorption behaviour of BSA at the water surface and the reaction of the structure to an overlying F-decalin atmosphere was studied. The hard protein lysozyme adsorbs to the DPPA-film by attractive electrostatic interactions. An additional protein layer below the lipid film and penetration into the headgroup is observed. After treatment with F-decalin, the thickness and density of the protein film is reduced. Since previous studies showed that lysozyme adsorbs irreversibly on the lipid film, this can be assigned to the influence of F-decalin. However, the remaining structure is modified. F-decalin probably acts very locally on the structure of lysozyme via hydrophobic interactions.

The adsorption of lysozyme has also been studied at the water surface and under different isobutane and F-propane gas pressures. The resulting protein films are not comparable to the resulting protein films of the reference measurements of lysozyme

at air. The gases seem to have a significant influence on the adsorbate structure of lysozyme. In contrast to isobutane which probably stabilises the initial structure and leads to more protein at the surface, F-propane seems to cause denser and thicker protein structures at the surface. An additional layer which reflects the gas films on the protein-rich surface could also be observed. After replacing the gas phases with air, the resulting structures are different to the initially observed ones and in comparison of the gases. The interaction process and the induced structural changes are not reversible. It is very likely that the gases hydrophobise the interface. This changes the interface chemistry and, thus, can influence the protein adsorption. The investigation of the interaction of BSA and F-decalin at the buffer/gas-interface suggests that the protein, especially the hydrophobic sites, interact with F-decalin and this interaction attracts more protein to the interface. The interaction process is completely reversible and the initially observed profiles are detectable again after F-decalin removal. F-decalin mobilises serum albumin to and from the surface and upon F-decalin flow and atmosphere merged BSA-F-decalin structures are formed.

Chapter 6

Ion adsorption at model membranes

This chapter presents the results of the ion adsorption experiments at model membranes. Ions at cell membranes can affect the function and properties of the nearby molecules and of the membrane, and thus play an important role in various processes [156, 643]. The local concentration of ions influences the protein function in the vicinity and the protein binding to membranes in general. Furthermore, ions contribute to membrane stability and the induction of curvature, e.g. in fusion processes.

It is known, that divalent cations interact strongly with negatively charged and moderately with zwitterionic lipid membranes [156]. The interaction of divalent cations with anionic lipids is remarkably. The glycerophospholipid DPPA for instance, an important signalling lipid molecule which is involved in practically all signalling pathways across the cell membrane, bears unique biophysical properties and its protonation state can be affected by divalent cations. Indeed, even more abundant phospholipids such as phosphatidylcholines (DPPC and DMPC) can be involved in the signalling pathways. Monovalent cations also interact with anionic lipids. However, currently there is no consensus on the interaction of monovalent ions, especially sodium cations, with zwitterionic lipid membranes. Generally, the effect of salts and charge are under debate and the mechanism of ion adsorption is not fully understood. In particular, there are open questions regarding the binding affinity of sodium to zwitterionic membranes and how membranes respond to direct calcium cation adsorption [620, 626–628, 1173]. A lack of well-defined membrane systems is one of the difficulties [1173]. Within this thesis a stable solid-supported lipid bilayer system was developed and tested. This is explained in more detail in section 6.2. Most studies focus on the changes of the dynamical properties and subsequently induced structural conformation alterations caused by the binding of ions. Common techniques used to characterise the interaction of calcium ions with membranes are differential scanning calorimetry, microelectrophoresis, spectroscopic techniques and x-ray scattering. In this work the surface-sensitive x-ray reflectivity technique was applied for the structural characterisation and investigation of ion adsorption processes at lipid films on aqueous subphases *in-situ* on the sub-angstrom

length scale.

Pure lipid membranes are well-established model systems to study mechanical, thermodynamic and structural properties related to natural biological membranes. The present study attempts to gain further insights into the interaction of chloride salts with negatively charged and zwitterionic lipid membranes. The adsorption or binding process is studied using two different model membrane systems, Langmuir films and solid-supported bilayers. To analyse the interaction of cations with anionic and zwitterionic Langmuir films the metal chlorides NaCl and $CaCl_2$ and the phospholipids DPPA and DPPC were chosen. For the study of the interactions of mono- and divalent cations with DMPC bilayers, the salts NaCl, LiCl, $MgCl_2$ and $CaCl_2$, listed in ascending order of their chaotropic effect, were used. The results of the first presented study "Mono- and divalent cation interactions with DPPA- or DPPC monolayers" in section 6.1.2 and 6.1.3 were recorded within the framework of Melina Helfrich's bachelor thesis [1174]. The section 6.1.4 presents findings on the "Influence of the microenvironment on the adsorption of serum albumins at DPPA monolayers" from the bachelor thesis of Carolin Olbrisch [1175]. The results concerning the interaction of NaCl and $CaCl_2$ with zwitterionic solid-supported DMPC bilayers in section 6.2 "Ions at solid-supported membranes" were obtained in cooperation with the University of Helsinki. In the framework of this cooperation the experimental data presented here will be compared with state-of-the-art all-atom molecular dynamic simulations [669].

Studies have shown that chloride Cl^- co-ions have no affinity to lipid headgroups. Therefore, the effect of these anions can be neglected [635, 646, 971]. However, charge densities of adsorbed cations are assumed to be counterbalanced by a layer of chloride ions which remain in the water phase and create an electrical double layer [54, 627, 646, 656, 971, 1176–1178]. In x-ray fluorescence and x-ray reflectivity experiments with $CaCl_2$, $BaCl_2$ and CaI_2 at DMPA Langmuir films an accumulation of chloride anions due to a charge inversion was not detected [970, 971]. Furthermore, chloride ions may be oxidised to chlorine gas in solution [689]. Therefore, chloride ions are not further considered.

For the monovalent Na^+ cations the intracellular concentration in eukaryotic cells is around 150 mM, for divalent Ca^{2+} cations the extracellular concentration is in resting cells about 1 - 2 mM. However, the local concentration of divalent cations can be temporally enhanced due to transient signal responses to external stimuli, for example the signal transmission in neurons [610, 611] and the induction of Ca^{2+} waves for a proper signal transduction. Therefore, also higher divalent cation concentrations are physiologically important and also investigated here. Since there seem to be controversies about how lipid membranes responds to salt addition, non-invasive and tracer-free *in-situ* XRR measurements were conducted.

Additional information A phosphate buffer precipitates in the presence of calcium ions and therefore the measurements were conducted in ultra-pure Milli-Q water. The net charge of DPPC Langmuir films and the solid-supported DMPC bilayers are not affected by pH-value changes upon salt addition. The experiments were conducted without a buffering solution, to prevent cross interactions of the molecules inside the buffer solution. For example, a phosphate buffer could provide three different species

of the phosphoric acid: the phosphoric acid $[PO_4]^{3-}$, the hydrogenphosphate $[HPO_4]^{2-}$ and the dihydrogenphosphate ion $[H_2PO_4]^-$. These anions have a rising chaotrope effect in the order in which they were listed and can influence the mono- or bilayer itself.

Although the applied salts calcium chloride, magnesium chloride and lithium chloride usually react neutrally, their addition to the sample solution causes a pH increase. This is due to contaminations with oxides of the anhydrous salts. In the following the reaction pathway is described for calcium chloride. Calcium chloride first dissolves to form hydrated calcium cations and chloride anions with

$$\mathrm{CaCl_{2\,(s)}} \xrightarrow[\Delta T(^\circ\mathrm{C})\uparrow]{+\mathrm{H_2O}} \mathrm{Ca^{2+}{}_{(aq)}} + 2\,\mathrm{Cl^-{}_{(aq)}} \tag{6.1}$$

and the calcium oxide that is present in the salt preparations reacts with water to calcium hydroxide

$$\mathrm{CaO_{(s)}} \xrightarrow[\Delta \mathrm{H_R} = -65\,\mathrm{kJ/mol}]{+\mathrm{H_2O}} \mathrm{Ca(OH)_{2\,(s)}} \tag{6.2}$$

and increases the pH-value due to the following reaction

$$\mathrm{Ca(OH)_{2\,(s)}} \xrightarrow{+\mathrm{H_2O}} \mathrm{Ca^{2+}{}_{(aq)}} + 2\,\mathrm{OH^-}. \tag{6.3}$$

With increasing the ionic strength of a solution the pH-value increases. This affects the used lipid DPPA, since the second $pK_{a,2}$ (10.5) lies in the alkaline pH regime. Between the first and the second acid constant DPPA is singly negatively charged. Above the $pK_{a,2}$ the phosphomonoester moiety is doubly deprotonated and therefore twice negatively charged. It has to be noticed that the pH-value is lower in the near-surface area than it is in the bulk, since a negatively charged surface attracts more excess protons [635, 969]. It is known, that divalent and trivalent cations affect the protonation state and that DPPA is doubly deprotonated at physiological pH-values [970, 971, 1178, 1179]. This is not in accordance with measured and calculated pK_a values stated above [90, 969]. The $pK_{a,1}$ for phosphatidic acid is 3.0 - 3.8 and $pK_{a,2}$ is about 7.1 - 8.5 in aqueous dispersions and monolayers in presence of divalent cations [90, 969]. Divalent cations thus reduce the $pK_{a,2}$ by binding to and deprotonation of the phosphomonoester headgroup of DPPA [973]. By addition of alkaline reacting salts, the process of deprotonation and cation adsorption is self-amplifying. In contrast, the behaviour of DPPC and DMPC are pH-independent. The variation of the pH-value with increasing salt concentration is shown in figure 6.1. The pH-value is a good parameter to monitor the oxide content of commercially available salts. Impurities and also environmental conditions can affect the measurements and thus, leads depending on their origin, to own influence [1180].

Another point to consider is the purity of the salts used. It is strongly recommended, especially in the studies related to alkali/carboxylate-interactions to use ultrapure (UP) grade salts. The changes, for example in a vibrational sum frequency generation spectroscopy study of the interaction of palmitic acid monolayer with sodium chloride of ACS grade, are largely due to the the trace metal impurities, that strengthen the cation-carboxylate binding. It is still unknown, whether the salt purity effect affects the interactions between monovalent cations and negatively charged units such as the phosphate group in phospholipids [1181].

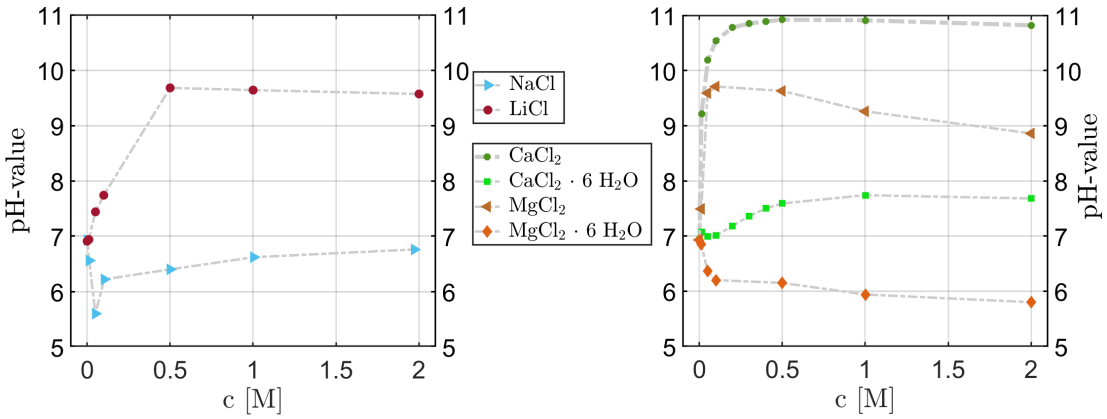

Figure 6.1: Change of the pH-value depending on the chloride salt concentration in ultra-pure water. Measured with S220 from Mettler Toledo. The error is around ±0.002 as stated from the manufacturer.

6.1 Ions at Langmuir films

In this section, the results of the study on DPPA and DPPC Langmuir films and their response to the addition of NaCl and $CaCl_2$ are presented. Moreover, the XRR data on the influence of the pH-value and $MgCl_2$ addition on the adsorption behaviour of BSA and HSA at DPPA-films will be shown. First, the experimental details will be introduced.

6.1.1 Experimental details

The experiments presented in the next three subsections were conducted at the laboratory diffractometer D8 at the E1a chair of TU Dortmund. The sample and surface preparation is introduced in section 4.4. Before DPPA or DPPC was spread onto the water surface, the setup was checked for cleanliness. After the spreading and 20 min. equilibration time, the target surface pressure of 15 mN/m was adjusted with the moveable barrier by compression. The area of the Langmuir trough was kept constant after reaching the target pressure and during the measurements. This is the initial state in which the reference measurements were conducted. For the concentration-dependent experiments, stock solutions of $CaCl_2$ and NaCl were prepared in ultra-pure Milli-Q water with a concentration of around 5 M. For the following measurements with consecutively increasing concentrations of salt, a previously calculated amount of salt solution was added. The salt concentration was varied between 0 M and 1 M and the influence on the Langmuir layer were measured by means of XRR. At a surface pressure of 15 mN/m DPPA is at the transition point between the tilted liquid-condensed and untilted liquid-condensed phase. The phospholipid DPPC is in the liquid-condensed phase.

The measurements of the adsorption behaviour of BSA or HSA at DPPA-films were also conducted with the Langmuir through. Here, a surface pressure of 25 mN/m was

used to generate a closed untilted and condensed DPPA monolayer. A concentration of 0.5 mg/ml or 7.52 µM (0.125 g of BSA) of the protein was used. The serum albumins were added by injecting stock solution into the subphase under the equilibrated Langmuir film. The injection under the pre-compressed Langmuir film is necessary for the imitation of the physiological conditions [1182]. In the next step, the concentration of magnesium chloride in the subphase was set to 20 mM by the removal of solution and refill with salt solution yielding the final subphase concentration. The area of the interface was kept constant during the measurements. One measurement took around 30 minutes. Between the measurements, the correct adjustment was checked. The magnesium chloride and protein stock solutions were prepared in the respective pH-value buffer solutions. Furthermore, at pH 3 experiments were conducted in the contrary way. For this purpose, the DPPA-film was spread onto a magnesium chloride containing buffer subphase and BSA was injected afterwards under the equilibrated and compressed DPPA Langmuir film. All measurements were conducted at room temperature, thus, below the (pH-dependent) denaturation temperature (at pH 3.5, 46.8 °C [1183]).

6.1.2 Mono- and divalent cation interactions with DPPA monolayers

In this subsection the results of the concentration-dependent study of the interactions between mono- and divalent cations with DPPA-films are presented.

Figure 6.2 shows the Fresnel normalised reflectivities of DPPA monolayers spread on pure water at increasing NaCl concentrations in the subphase. The reflectivities are displayed separately on linear and semilogarithmic scales to highlight different details. The amplitude of the observed oscillations which is correlated with the excess electron density at the surface with regard to the subphase is best seen on the linear scale. The semilogarithmic scale gives the best view on the q_z value of the minimum which is inversely proportional to the surface layer thickness. The reference measurement of DPPA at a surface pressure of 15 mN/m on pure water (green) is in accordance with literature and the electron densities and thicknesses are comparable to those in chapter 5. The bulk electron density was set to $\rho_{\mathrm{sub}} = 0.334\,\mathrm{e}^-/\text{Å}$ for both, chloride salt containing and salt-free water subphase [1184]. The left panel of the figure shows the linear scale visualisation of the normalised reflectivities for the DPPA-film on NaCl solution. The middle panel of the figure shows the normalised reflectivities on a logarithmic scale. The minima of the reflectivity data show a slight shift to higher q_z values with increasing NaCl concentrations in the solution. The electron density profiles are shown in the right panel of the figure. It can be seen that the monolayer thickness decreases. The pH-value within the measurements remains in the range where the single deprotonated state of DPPA is assumed, see also figure 6.1.

The change of the electron density profiles and also the shift of the minima to higher wave vector transfers is systematically and was reproduced. The electron density profiles consistently indicate a broadening of the headgroups of 2 Å, but also an increase of the tilting of the tailgroups as their thickness reduces by 2.5 Å. Figure 6.3 shows the change of the surface pressure (blue circles) and the total layer thickness (as black squares) of

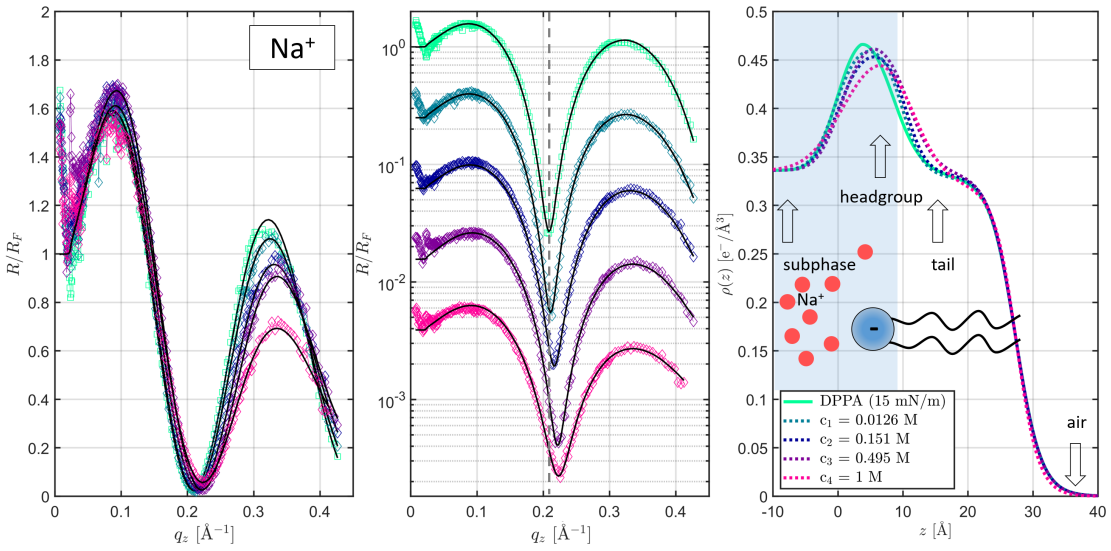

Figure 6.2: Measured Fresnel normalised reflectivities of DPPA Langmuir films with increasing NaCl concentration on linear and semilogarithmic scale (left and middle). The semilogarithmic presented XRR curves are shifted vertically for clarity. The solid black lines represent the refinements to the data. The corresponding electron density profiles are shown in the right panel.

the monolayer in dependence of the NaCl subphase concentration. The inset illustrates the change of the maximal electron density as black triangles.

An accumulation of sodium cations at the DPPA-film cannot clearly be seen within the XRR data. One possible explanation is the poor contrast as sodium cations (10 electrons) replace water molecules (10 electrons). Indeed, sodium cations are smaller (van der Waals radius 2.27 Å) than water molecules (2.82 Å [1185]) but as the hydration state of the sodium cations (hydrated radius 3.58 Å) and the DPPA headgroups before and after a possible adsorption process also contributes to the final electron density, it cannot be excluded that an accumulation of sodium cations at DPPA monolayers is not detectable with XRR.

In general, the sodium cations are attracted via electrostatic forces to the negatively charged DPPA-film and via charge screening effects it is possible to shield the phosphate charge and reduce the repulsion of the headgroups (loosening), which is then reflected in slightly lower surface pressures especially at lower concentrations.

A sketch of the assumed structural changes from the obtained data is shown in the bottom of figure 6.3. However, a deprotonation or binding and adsorption mechanism or localisation cannot be derived directly from the data for sodium chloride. Additional experiments, especially to resolve the lateral structure are necessary to determine the domain structure changes. Brewster angle microscopy and grazing-incidence x-ray diffraction are suitable methods to study the film morphology and crystal structure. Experiments at constant concentrations and different constant pH-values (pH 5, 7 and 10) are planned to test the effect of monovalent sodium and divalent calcium cations on

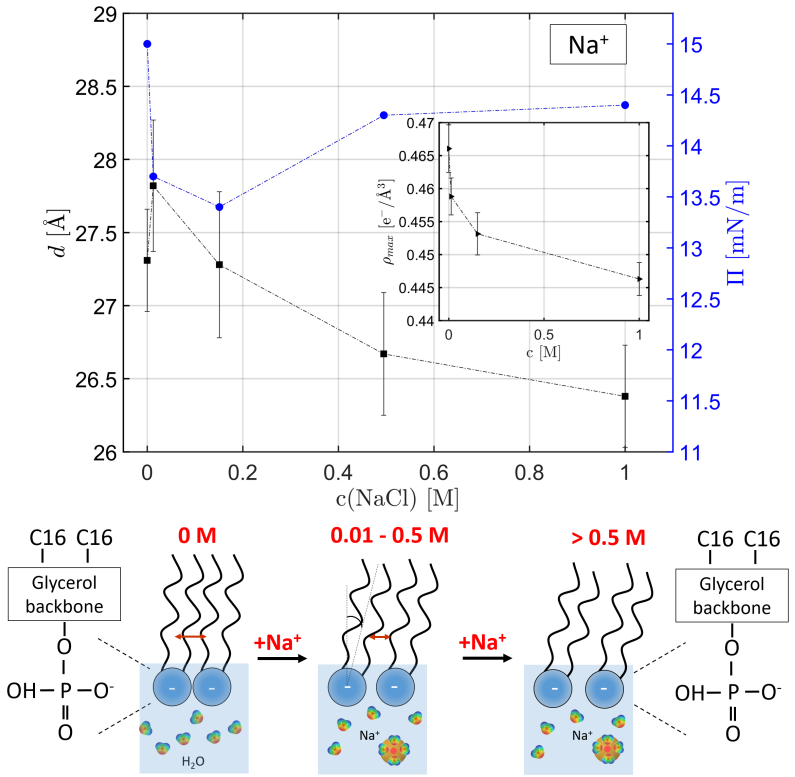

Figure 6.3: Extracted total layer thicknesses of the DPPA-film and change of the surface pressure upon increased NaCl concentration. The inset shows the maximum electron density of the headgroup. The error bars are estimated by variation of the refinement parameters. The bottom shows schematically the system and assumed changes of the lipid system.

the deprotonation state of DPPA.

The interaction of DPPA-films with calcium chloride on the contrary shows a complete different effect. For the measurements anhydrous calcium chloride was used. The concentration-dependent change of the subphase pH-value upon calcium chloride addition is shown in figure 6.1. It should be noticed that the pH-value can also vary due to the deprotonation process of DPPA which is also pH-dependent and can be triggered by calcium binding [973].

The left and middle panel of figure 6.4 show the linear and semilogarithmic scale plots of the Fresnel normalised reflectivity curves of a DPPA monolayer on water and at increasing $CaCl_2$ concentration in the subphase at an initial surface pressure of 15 mN/m at constant area. As can be seen in the left plot, the addition of $CaCl_2$ increases the reflectivity in a concentration-dependent manner indicating an accumulation of ions at the interface. The first minimum that can be seen in the middle panel shifts slightly to lower wave vector transfers indicating an increase of the total layer thickness. Furthermore, the minimum becomes sharper and deeper with increasing concentration. The

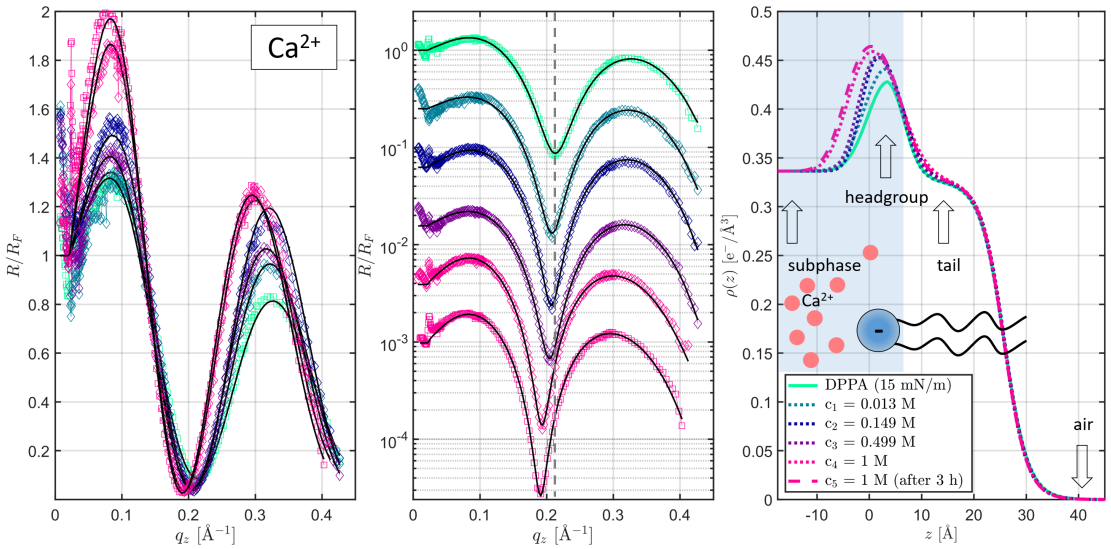

Figure 6.4: Measured Fresnel normalised reflectivities of DPPA Langmuir films with increasing $CaCl_2$ concentration on linear and semilogarithmic scale (left and middle). The semilogarithmic presented XRR curves are shifted vertically for clarity. The solid black lines represent the refinements to the data. The corresponding electron density profiles are shown in the right panel.

electron density profile in the right panel shows an increase of the electron density in the area of the headgroups upon salt addition. Furthermore, an enlargement of the headgroups can be observed. Both can be assigned to the binding of Ca^{2+} ions.

The concentration-dependent accumulation of Ca^{2+} ions at the DPPA-film is reported in the literature [969, 1186–1188]. The increase of the electron density in the headgroup region can be explained by the penetration and lateral intercalation of Ca^{2+} cations among the lipid headgroups. The increasing thickness of the headgroups also indicates an adsorption slightly below the phosphate moiety, as can be seen in the electron density profiles. The surface excess electrons can be calculated via the integration of the volume fraction profiles calculated from the difference of the electron density profiles of DPPA-films on calcium chloride solutions and the DPPA-film reference measurement ($\Delta\Gamma^e$). The calculation yields the additional electrons per area (Γ^e) which then can be used to compute the number of Ca^{2+} ions per headgroup moiety. The area that is occupied by one lipid molecule at a surface pressure of 15 mN/m is taken from the Π-A isotherm (figure 5.1) and is about $A = 40.7\,\text{Å}^2$ for DPPA. The product of the surface excess electron density and the molecular area of one DPPA molecule yields the surface excess electrons per DPPA molecule. A Ca^{2+} ion can exist in its hydrated state in aqueous solution in the form $[Ca(H_2O)x]^{2+}$ as complex with $x = 4$ or $x = 6$ coordinated water molecules in the first hydration shell [1189–1191]. The calcium ion with a partial dehydrated shell, a $[Ca(H_2O)_4]^{2+}$ octahedron, can form a bridge between two charged moieties [1192, 1193] and the fully hydrated calcium ion, a $[Ca(H_2O)_6]^{2+}$ octahedron, reaches the surface without loosing its hydration shell. Taking this and the replacement

of subphase water into account, the assumption that the volume of each bound water molecule is V'_{H_2O} with $m_{H_2O} = n_{ion} \cdot x$ associated with a calcium cation that binds to each DPPA moiety is made. Beside the volume constraints, the assumption that co-ions (Cl^-) do not penetrate the headgroup region applies. The number of surface excess electrons with respect to the reference and, thus, the number of bound ions per molecule upon salt addition can then be calculated using [969, 970]

$$n_{ion} = \frac{\Delta(A \cdot \Gamma^e)}{x(N^e_{H_2O} - \rho_{sub} V'_{H_2O}) + (N^e_{ion} - \rho_{sub} V_{ion})}. \tag{6.4}$$

Here, x is the coordination number or the number of bound water molecules of the hydration shell of the calcium ion. $N^e_{H_2O}$ is the electron number of one water molecule (10 electrons) and N^e_{ion} is the number of electrons possessed by one calcium cation (18 electrons). V_{ion} is the volume of one single calcium cation without a hydration shell ($\approx 4\,Å^3$). Three different cases were examined. First, Ca^{2+} ions bind to the headgroup moiety as bare cations without a hydration shell, i.e. $m_{H_2O} = 0$. Second, a Ca^{2+} binds to a phosphate moiety with a fully hydrated first shell consisting 6 water molecules, i.e. $m_{H_2O} = 6n_{ion}$. Here, the calcium ion is in the middle of an octahedron and water molecules are placed at the vertex. Finally, a Ca^{2+} ion binds to the headgroup where two water molecules of $[Ca(H_2O)_6]^{2+}$ are replaced by the binding to one phosphate moiety with both sites, or complexing two phosphate molecules, i.e. $m_{H_2O} = 4n_{ion}$ yielding $[Ca(H_2O)_4]^{2+}$. The radius of an octahedron or fully hydrated cation ($[Ca(H_2O)_6]^{2+}$) is about $\sim 3\,Å$ with an estimated volume of $113\,Å^3$. Therefore, V'_{H_2O} leads to $\approx 19\,Å^3$ [969]. The determination is thus based on the selected hydration state of the bound Ca^{2+} ions. Figure 6.5 shows the calculated fractions of Ca^{2+} ions per DPPA lipid molecule for the mentioned cases as a function of the $CaCl_2$ concentration of the solution. Furthermore, it shows the variation in surface pressure on the right with the total layer thickness change of the film. The bare, dehydrated Ca^{2+} ion selection gives the upper limit of the number of calcium ions per lipid molecule, while the fully hydrated $[Ca(H_2O)_6]^{2+}$ complex gives the lower limit.

It is very improbable that a fully hydrated $[Ca(H_2O)_6]^{2+}$ binds to a DPPA moiety without partially loosing water molecules of the hydration shell [1178]. Calcium ions have a high binding affinity to the phosphate group (in comparison for example to Mg^{2+} [1046]) and forms inner-sphere complexes with a partial loosing of the hydration shell. It is strongly suggested that solvated ions shed their hydrate shell partly upon binding inducing also a dehydration of the headgroup. In the present case it can be assumed that partially solvated calcium ions in the form $[Ca(H_2O)_4]^{2+}$ bind to the headgroups.

As can be seen in figure 6.5 on the left side, by increasing the $CaCl_2$ concentration complexes of $[Ca(H_2O)_4]^{2+}$/DPPA are first 1:2, indicating one calcium cation bridges two DPPA lipid head moieties. With increased amount of salt, the partial hydrated Ca^{2+} ions bind to single DPPA headgroups due to a deprotonation and complexes of 1:1 are formed. The stoichiometric ratio changes from 1:2 $[Ca(H_2O)_4]^{2+}$ ion per DPPA molecule to 1:1 $[Ca(H_2O)_4]^{2+}$ ion per DPPA. This occurs above 0.5 M. It seems that it is energetically favourable to complex two DPPA molecules and by increased

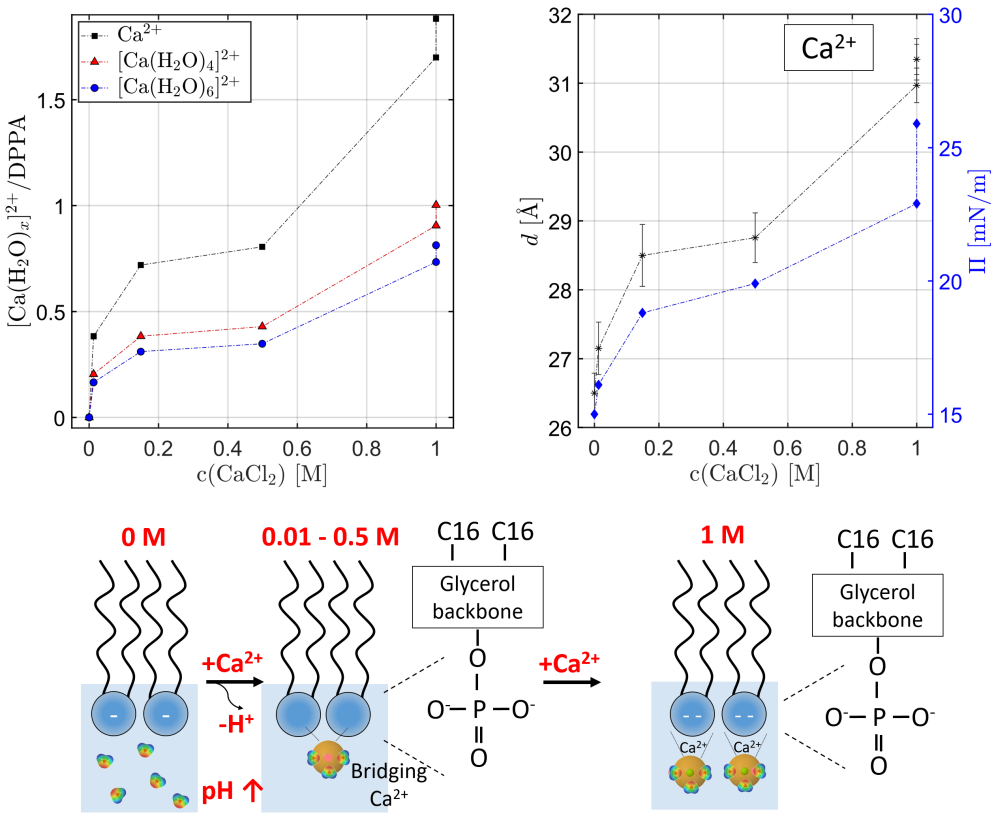

Figure 6.5: The left plot presents the numbers or the stoichiometric ratio of surface bound Ca^{2+} ion per lipid moiety at different concentrations calculated from the best fit of the reflectivity data. Black squares present the bare and dehydrated Ca^{2+} ion, red triangles the partial dehydrated $[Ca(H_2O)_4]^{2+}$ bridging of two charges at the surface and blue circles the fully hydrated $[Ca(H_2O)_6]^{2+}$ octahedron. The right side shows the change of the total layer thickness as black stars and the surface pressure change as blue diamonds. The error bars are estimated by variation of the refinement parameters. The higher values at 1 M correspond to the measurements after 3 hours. The error of the electron density can be estimated as $\pm 0.01\,e^-/Å^3$ by variation of refinement parameters.

concentrations to bind one single DPPA molecule. The sketch illustrated at the bottom of the figure shows the binding process. A further intercalating to the headgroups does not appear after 3 hours at higher (> 0.5 M) concentrations, because the increase of the electron density of the headgroup at the phosphate moiety does not develop further. Whether the carbonyl or diester groups of the DPPA molecules are involved in calcium binding cannot be assessed.

In general, the calcium cations screen the DPPA charge and lead to lower repulsion between the headgroups due to a bridgening and shielding of the DPPA charge and, thus, yield a more tightly packed layer. This condensation effect due to complexation of the headgroups is well-known and is usually accompanied by a reduction of the surface

pressure at constant pH-values [109, 113, 625, 973, 1178, 1194, 1195]. Nevertheless, here, the surface pressure increases and contraindicates a condensation effect. The dominating effect seems to be enhanced repulsion forces between the headgroups, which is reflected in the increase of the surface pressure.

Above a pH-value of around 9, the DPPA monolayer exhibits elevated surface pressures due to decreased hydrogen bonds between the phosphate groups and higher electrostatic repulsion to around 27 mN/m [1194]. In the present experiment, the pH-value is alkaline due to the addition of calcium chloride solution even at the lowest concentration (see figure 6.1). This surface pressure value is only reached at the highest calcium concentration, therefore, it can be assumed that at low calcium chloride concentrations a sufficient complexation of the headgroups appears, which countered the repulsion of the phosphate charges. For example, Laroche et al. reports a 1:2 complex at low concentrations using ^{2}H-NMR, Raman and infrared spectroscopy techniques to investigate the complex building and the interaction of calcium ions with DMPA [1192]. With elevated calcium concentration the surface pressure increases indicating an intercalation and expanding effect of calcium cations. The surface area change is attributed to the area of one calcium ion ($\sim 4\,\text{Å}^2$) [1196]. To verify this for the present measurements, surface pressure isotherms at basic pH-values are necessary.

Furthermore, it is reported that the stoichiometric ratio of calcium cations that bind to lipid headgroups (1:2 to 1:1) depends on the calcium concentration [644, 674]. This can be concluded here as well since the pH-value of the subphase at the lowest concentration was already above the second dissociation constant of DPPA, and would have allowed a 1:1 complex. To elucidate the exact concentration where the switch of the stoichiometric ratio (or binding mode) takes place, more closely meshed concentration-dependent measurements are required, particularly between 0.5 M and 1 M.

Wang et al. investigated DMPA monolayers with increasing pH-values at constant calcium chloride concentrations [969]. They observed an enhanced calcium accumulation and building of 1:1 Ca^{2+}-DPPA complexes with increasing pH-values from 3.4 to 7.8. They also stated that free Ca^{2+} ions and partial dehydrated calcium $[Ca(H_2O)_4]^{2+}$ clusters can bind to the DMPA headgroup. The binding nearby the headgroups were also reported in Bu et al. with DMPA by XRR measurements [971]. Reports with other measurement techniques for the complex building and bound fractions can be found in [635, 969, 973, 1178, 1197–1199].

Calcium ions are bound very strongly to the interface and desorption events are rare [620]. The results might have implications for phosphoinositides, as these molecules also bear phosphomonoester groups and are highly negatively charged. They are also important for intracellular signalling [1200, 1201]. *In-vivo* studies have shown, that DPPA or PAs act as pH-biosensors [94, 95].

6.1.3 Mono- and divalent cation interactions with DPPC monolayers

In contrast to the DPPA-films on water at a surface pressure of 15 mN/m, the DPPC-films are not in the vicinity to a phase transition and in a liquid-condensed phase. In addition, the DPPC tailgroups are more tilted and therefore exhibit a reduced length.

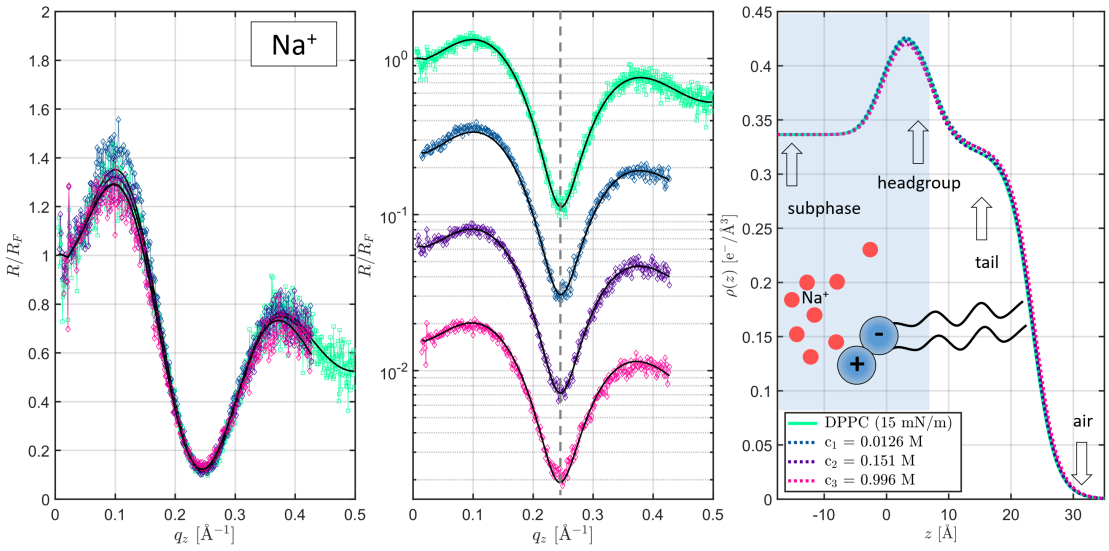

Figure 6.6: Measured Fresnel normalised reflectivities of DPPC Langmuir films with increasing NaCl concentration on linear and semilogarithmic scale (left and middle). The semilogarithmic presented XRR curves are shifted vertically for clarity. The solid black lines represent the refinements to the data. The corresponding electron density profiles are shown in the right panel.

A difference of the total layer thickness of around 5 Å could be determined compared to DPPA-films at the same surface pressure. Since the DPPA lipid headgroups can be packed more densely due to their small size, the electron density at the DPPA head- and tailgroups is slightly higher. Moreover, DPPC is not affected by the pH-value.

Figure 6.6 illustrates the XRR results of DPPC-films in the presence of NaCl. The left panel shows the linear scale presentation of the Fresnel normalised data and the middle plot presents the semilogarithmic scale with vertically shifted curves. The electron density profiles obtained from the refinement of the XRR curves are presented in the right panel. As can be seen, the electron density profiles indicate no difference and the XRR curves are very similar. An ion accumulation cannot be observed. The DPPC-film is stable over the whole time at all NaCl concentration. The thickness of the layer, which is about 23.5 ± 0.5 Å, and the surface pressure, that ranges between 15 and 15.5 mN/m during the measurements, does not changed significantly. Sodium ions show no effect on DPPC-films. This is in accordance with previously reported studies [156, 626, 628, 649].

Figure 6.7 depicts the Fresnel normalised XRR curves and the corresponding electron density profiles of a DPPC-film with increasing $CaCl_2$ concentration in the subphase. The linear and semilogarithmic scaled reflectivities show a slight shift to lower q_z at the highest $CaCl_2$ concentration indicating a thickening and probably an accumulation of ions.

It is well-known that divalent cations interact strongly with negatively charged lipids, but interact only weak with zwitterionic lipids [649, 1202]. As figure 6.7 shows, the

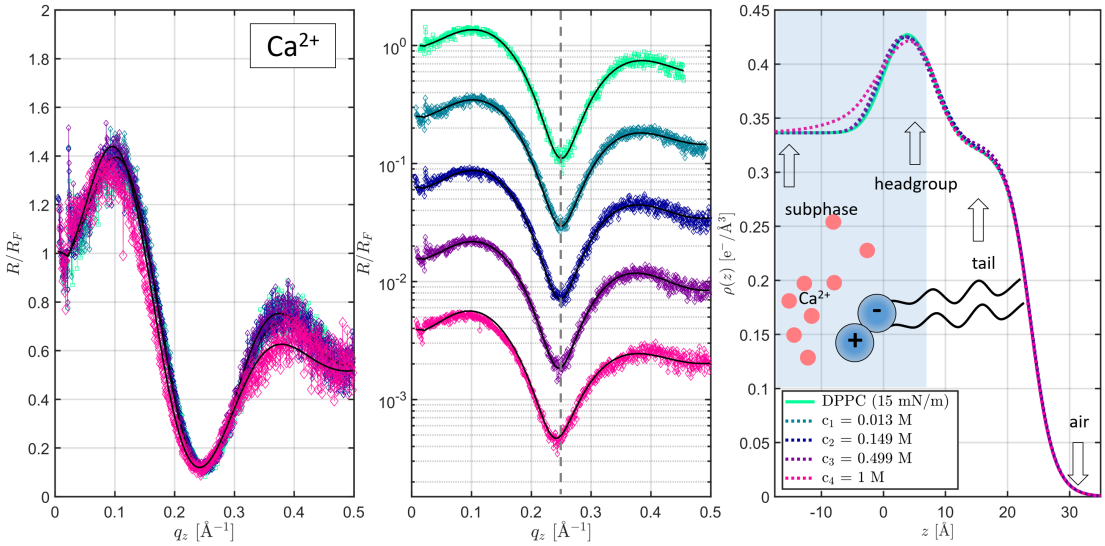

Figure 6.7: Measured Fresnel normalised reflectivities of DPPC Langmuir films with increasing $CaCl_2$ concentration on linear and semilogarithmic scale (left and middle). The semilogarithmic presented XRR curves are shifted vertically for clarity. The solid black lines represent the refinements to the data. The corresponding electron density profiles are shown in the right panel.

DPPC-film is not significantly altered.

It was reported that the lipid phase is important for the binding of calcium ions [256, 661, 1196, 1203, 1204]. The formation of 2:1 complexes is observed at surface pressures above 16 mN/m [661, 1196, 1204]. It is assumed that the ion binding enhances the lipid/lipid-interaction that yields in a compression of the monolayer. However, the measured data do not show this effect, which may also be due to the resolution limit of the laboratory diffractometer. Indeed, an influence of Ca^{2+} on zwitterionic DMPC bilayer could be reported within this work and the results can be found in section 6.2. The surface pressure of the DPPC Langmuir film decreases to values of 12 mN/m at the highest $CaCl_2$ concentration. This might be an indication for the complexation of headgroups and resulting decreased repulsion forces (condensation effect).

To study the effect of cations on zwitterionic and negatively charged lipids, it is necessary to apply complementary techniques. Therefore, in addition to XRR measurements, other methods that resolve the lateral structure are useful to obtain a comprehensive overview of the molecular processes. Furthermore, the consideration of the surface pressure and pH-value is important to validate and separate the observed effects.

6.1.4 Influence of the microenvironment on the adsorption of serum albumins at DPPA monolayers

In this subsection, the objective is to investigate and gain more information on the interaction between (bovine and human) serum albumin (BSA, HSA) and the pH-sensitive

DPPA Langmuir films. Moreover, magnesium chloride, a BSA ligand, was added to examine the ligand-dependent adsorption behaviour. BSA has the feature to bind reversibly negatively charged substances and fatty acids [1205]. DPPA is in the examined pH-range mostly negatively charged. A publication from Liu et al. (2020) reports that magnesium ions enhance the stability of the secondary structure of BSA monomers and inhibit the aggregation into large structures [1031]. In consideration of the ubiquity of serum proteins and magnesium ions, the study is justified. Furthermore, the pH-switch triggered interactions and induced structural changes are important in biology [1206–1212].

The properties of BSA in different microenvironments are not entirely understood. BSA is an aggregation-prone protein that shows a tendency for the assembly in large macromolecular (oligomeric structure and cross-β-sheet) structures [1213–1215]. It is known that the presence of membranes can enhance aggregation. Metal ions and their effect on the aggregation of peptides and proteins have been investigated and it was found that they can act as aggregation promoter or inhibitor [1213, 1216–1220]. Metal ions are associated with protein aggregation processes in various neurodegenerative pathologies and BSA is homologeous to the human variant and can serve as model protein for aggregation and amyloidogenic pathways. The fact that over-all α-helical proteins such as BSA and HSA can form β-rich amyloid-like structures has aroused great interest in recent years [840, 1215, 1221–1223]. The oligomeric variants are proposed to be the toxic species that can lead to permeabilisation of cell membranes. The measurements were conducted between the pH-values 3 and 9, including the well-recognised reversible pH-dependent conformational changes of BSA, see also subsection 2.4.3. The adsorption behaviour was compared with HSA at the pH-values 3 and 9. The influence of the solvent on the protein can induce solvent-dependent and -adapted structural responses on the aggregation mechanism. In detail, the significance of electrostatic interactions in the development of amyloid fibrils [1224–1226] and the importance of the total net charge of the protein for the tendency to form fibrils was emphasised [1225–1227].

The isoelectric point (IEP) of BSA is between 4.5 and 5.0 [1169] (and 4.7 - 4.8 [821]). Seven pH-values were chosen to test the positive (at pH-values 3 and 4) and negative (at pH-values 6, 7, 8 and 9) net charge as well as the neutral one (at pH-value 5). Table 6.1 summarises some effective and net charges of BSA in solutions with different pH-values.

Moreover, it has been reported that the hydrophobicity of BSA depends on the microenvironment. Since proteins such as BSA display pH-dependent surface hydrophobicity, different studies were carried out to characterise these property. Alizadeh et al. reported that BSA is lesser hydrophobic in acidic pH conditions (pH-value 3 - 4) in comparison to neutral (≈ 7) or basic environments (≈ 9) [1228] and measurements with DMPA at different pH-values verified and confirmed these findings [889, 1229]. However, by consideration of the different isoforms present at various pH-values, the F-isoform in the low acidic pH-region has an extended conformation and exposes the most hydrophobic residues to the solution [1230–1232]. Hence, the protein surface hydrophobicity becomes less with increasing pH-value of the subphase [1232, 1233], this is the opposite effect to that described above. The pH-value can therefore generate different structural changes when BSA is incorporated into a bi- or monolayer. Changes

Table 6.1: Effective charge, net charge and theoretically calculated net charge accounting for over-all charges of BSA [1234–1236].

pH-value	effective charge	net charge	calculated charge
2.4	$+21.1 \pm 1.2$	+65	$\sim +100$
4.6-5.1	0	0	0
6	-3.18	-	-10
6.8	-8.4 ± 0.3	-11	-13
10.5	-17.2 ± 0.6	-39	-80

in the used concentrations and different conditions, such as ionic strength can indeed lead to different results.

The IEP is within the N $\rightarrow$ F transition and the charge of the protein changes from -16 at a pH-value of 7.4 to +100 at a pH-value of 3.5 [885, 886]. At the IEP, the protein solubility is greatly reduced, since charged residues increase the dissolution of proteins in solution [885, 1232]. The subphase pH-value is a key variable, since it affects the adsorption behaviour through changing the acting (electrostatic) forces and could influence the structure of the adsorbed pattern due to the reversible conformational transitions.

In the following, the XRR curves and electron density profiles of the pH-dependent adsorption behaviour of BSA at DPPA-films will be presented in ascending pH-values of the subphase. A two-layer model similar to those in the previously discussed subsection 6.1.2 was used to model the reference DPPA-films. A three-layer model was used to describe the resulting data after BSA or HSA adsorption at pH 3. The obtained reflectivity data is shown together with the corresponding electron density profiles in figure 6.8. In a), the BSA adsorption with addition of salt into the subphase, in b) the BSA adsorption in already magnesium chloride containing buffer and in c) of the figure the HSA adsorption at DPPA-films with subsequent application of salt is shown. Several reflectivities were recorded consecutively to investigate time effects of the adsorption and the resulting structures.

At a pH-value of 3, BSA and HSA are in the F-isoform and highly positively charged with dimensions of $140 \times 40 \times 35$ Å^3. The proteins are attracted via electrostatic forces to the DPPA-film. The surface is probably very slightly negatively charged, since the pH-value is in the region of the first dissociation constant of the phosphomonoester moiety. Otherwise, non-electrostatic forces such as hydrophobic interactions can play a major role, since the surface pressure increased by $\Delta 13$ mN/m to approximately 38 mN/m. This occurs with both preparation methods, when salt is added or when the buffer was previously prepared with magnesium chloride. The changes of the surface pressure upon BSA or HSA and magnesium chloride addition at the different pH-values of the subphase are presented in figure 6.12.

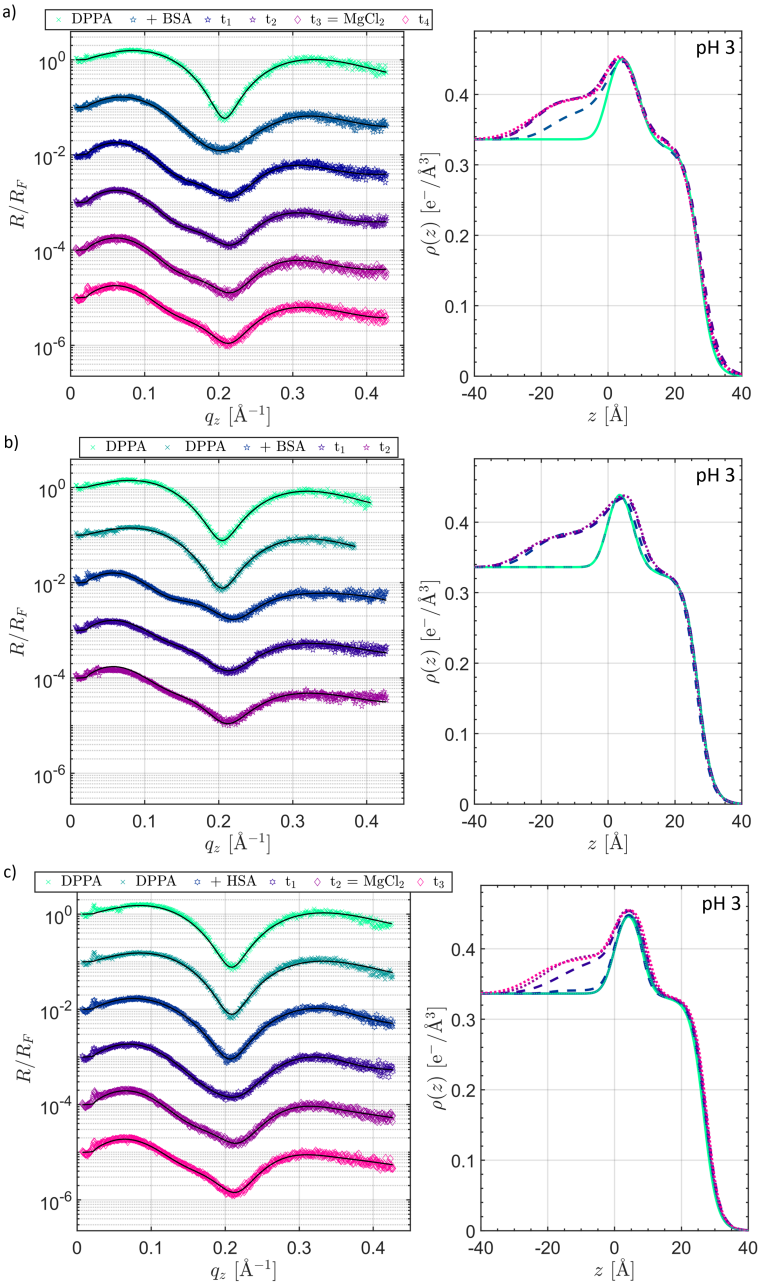

Figure 6.8: XRR data of BSA adsorption a) in buffer with further salt addition and b) in salt containing buffer. c) HSA under a DPPA-film at a pH-value of 3 with further salt addition. Left: Fresnel normalised XRR data and refinement curves. The crosses correspond to the reference measurements, stars to the measurements with BSA and diamonds to the addition of magnesium chloride. The refinements are shown as black solid lines. Right: Electron density profiles obtained by the refinement to the data. The colour code of the XRR data applies. Dashed lines correspond to the protein containing system, dotted lines to the magnesium chloride addition into the subphase. $[c_{protein}] = 7.52\,\mu M$ and $[c_{MgCl_2}] = 20\,mM$.

In figure 6.8 the first protein containing measurements performed directly after preparation are designated as "+ BSA" or "+ HSA". The designation t_i indicates repeat measurements to analyse time effects. The scans were conducted in immediate succession. A measurement takes about 30 minutes, including calibration about 40 minutes. The XRR curves change with addition of the protein and a short oscillation occurs that is superimposed with the wide oscillations of DPPA. In the electron density profiles in a), the formation of a BSA adsorbate film underneath the DPPA-film can be observed in the first measurement conducted directly after preparation. It can be determined that the density and thickness of the protein film increases over time (compare "+BSA" and t_1) but reaches equilibrium after the first scan as the structure is the same at t_1 and t_2. Moreover, the resulting structure is not affected by the addition of magnesium chloride salt. In the study of HSA shown in c) a slow formation of a protein layer can be observed and the addition of magnesium chloride appears to result in the formation of a denser film. However, it should be noted that only two consecutive measurements were recorded using HSA and it is likely that the growth of the protein layer after the addition of magnesium chloride is only a time effect, especially as the final structure is similar to BSA at a DPPA-film in absence of magnesium chloride. Compared to BSA in a), the adsorption of HSA seems to be slower, since at t_1 the BSA layer is already at its full extent. In both cases, intermediate steps can be observed. When using a buffer solution containing magnesium chloride, the BSA adsorption results directly in an increased adsorbed amount of protein, (see part b)) no intermediate step is observed in comparison to a) and, therefore, takes place more quickly. The presence of salt seems to have a significant influence on the adsorption kinetics and accelerates the binding. However, the temporal resolution of this study is of course not sufficient to examine dynamics in detail.

Due to the hydrophobicity of BSA in the F-form and the observed increase in surface pressure, it is very likely that there will be also an approach to the water/air-interface in less condensed areas of the film. But also an attachment to the headgroups which affects their packing density can generate higher surface pressures. GIXD data indicate a complex influence of HSA on DPPA-films at pH 3.8 with reduction of the headgroup repulsion, as observed here in the surface pressures measurements, and changing of the lipid arrangement [1118]. However, a direct insertion and penetration into the headgroups cannot be observed in the electron density profiles.

The DPPA Langmuir film without the repulsion of the headgroups generated by the deprotonation (above $pK_{a,1}$) is very dense and tightly packed, because the distance is limited only by the repulsion of the tailgroups and sterical hindrance. However, such a film has a certain degree of instability. The effective thickness ($\sigma_{\text{subphase}} + d_{\text{protein}} + \frac{1}{2}\,\sigma_{\text{protein}}$) of the adsorbed layer is 25.1 - 27.7 Å for the less dense protein layer (intermediate step), and 32.9 - 35.7 Å in the case of the dense protein packing. This is in accordance with the assumption of an adsorption with the long axis of the F-form and hence orientation parallel to the surface. The lower thickness could arise due to the interaction with the film and alterations of the protein structure. The minimum layer thickness that BSA or HSA can adopt under the given non-reducing conditions is 21 Å, this is the thickness allowed by the (17) disulfid bonds.

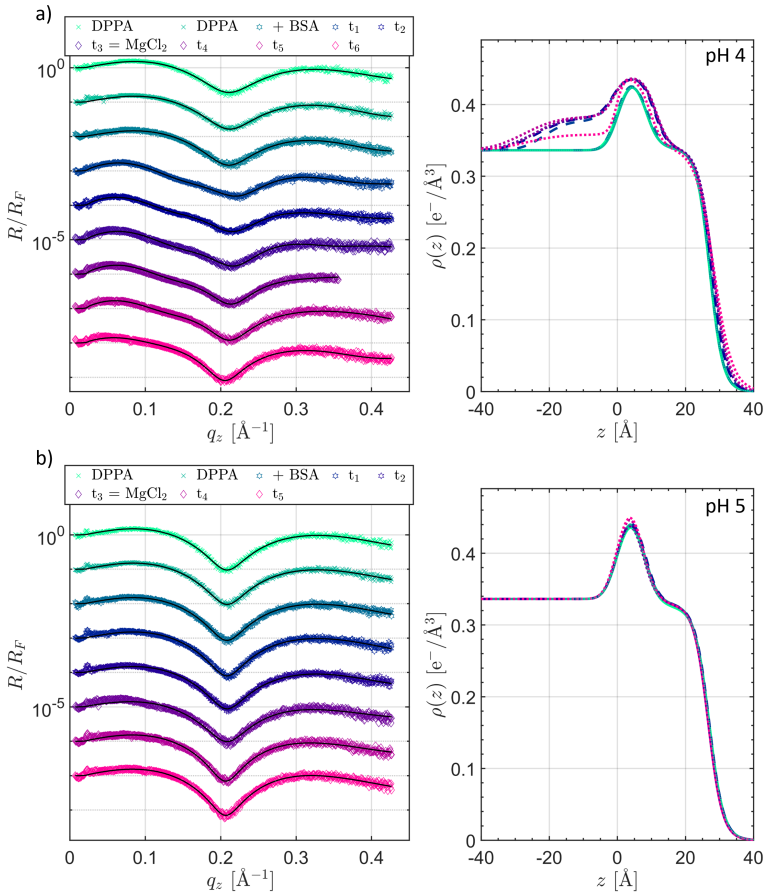

Figure 6.9: XRR data of BSA adsorption at a DPPA-film at a pH-value of a) 4 and b) 5 with subsequent addition of magnesium chloride. Left: Fresnel normalised XRR data and refinement curves. The crosses correspond to the reference measurements, stars to the measurements with BSA and diamonds to the addition of magnesium chloride. The refinements are shown as black solid lines. Right: Electron density profiles obtained by the refinement to the data. The colour code of the XRR data applies. Dashed lines correspond to the protein containing system, dotted lines to the magnesium chloride addition into the subphase. $[c_{protein}] = 7.52\,\mu M$ and $[c_{MgCl_2}] = 20\,mM$.

Figure 6.9 illustrates the XRR data of the adsorption of BSA at a DPPA-film with a subphase pH-value of a) 4 and b) 5. The pH-value of 4 is still under the isoelectric point of BSA and, hence, the protein is positively charged and still in the F-isoform. In this pH-region, the $pK_{a,1}$ value of the DPPA molecules is exceeded and therefore DPPA is present in the singly negatively charged state and is able to form hydrogen bonds or phosphate-phosphate bridges which stabilise the film. This also leads to a decreased electron density due to the increased electrostatic repulsion between the headgroups. As can be seen in the electron density profiles, BSA does not immediately adsorb at a pH-value of 4. The adsorption underneath the film and also penetration between

the headgroups can be observed at t_1 for the first time. The tailgroups of the film are not affected by the insertion. BSA is attracted through electrostatic forces to the surface. In contrast to pH 3, only a small influence on the surface pressure can be detected here. Possibly this results from the predominant electrostatic forces exceeding the hydrophobic interactions. The thickness of the BSA layer changes from 26.9 Å at t_1 to 31.5 Å at t_2 and increases with magnesium chloride to about 35.6 Å. The error of the thicknesses is between 0.5 Å and 1 Å. Surprisingly, at t_6, the last measurement with salt, the density of the protein film is significantly reduced, while the thickness of the protein film is maintained. The variation of the thickness can be attributed to conformational changes of the flexible protein upon initial adsorption at a surface, several molecular reorganisation processes can follow [887, 1237]. An intact tertiary structure can be assumed for the pH-region of 3 and 4.

It seems that magnesium chloride on the one hand improves the adsorption and on the other hand leads to a desorption of protein. One explanation could be that binding sites on the DPPA-film are occupied by magnesium chloride and it is subsequently not possible that BSA is adsorbed due to the increased repulsion. Divalent cations have a high affinity to anionic lipid headgroups, as already shown. To test this behaviour in detail, replacement experiments with different divalent cations and predominantly magnesium chloride at DPPA-films with subsequent BSA addition might be useful.

At a pH-value of 5 the IEP of BSA and, thus, the transition point into the N-isoform is reached and, therefore, the solubility is greatly reduced [885]. At the isoelectric point the protein molecules do not have repulsion among each other and can pack closely together at an interface. However, a BSA assembly can also take place in the subphase. The electron density profiles show that the zero-net charged proteins exhibit no affinity to the negatively charged DPPA layer. No protein layer or change of the lipid film could be detected. The measurements at pH 5 are exemplary for the pH-values 6 and 7. No protein film formation or adsorption was observed here either. Above a pH-value of 5, BSA is negatively charged and electrostatic repulsion hinders the protein to adsorb at the DPPA-film. At a pH-value of 6 no significant change of the surface pressure can be detected, but at a pH-value of 7 the surface pressure decreased clearly. BSA is slightly negative at a pH-value of 6, but the binding of magnesium chloride is not sufficient to allow a charge inversion and adsorption at the DPPA-film. At pH 7 this can be different. The protein does not adsorb directly to the surface, but rather binds lipids and BSA-lipid complexes that are formed and submerged in the subphase. The carriage of lipids into the subphase was reported in the literature and is discussed further below. At the physiological pH-value, condensation of the DPPA-film can be assumed when magnesium chloride is added, as the surface pressure decreases further (see figure 6.12).

Above the isoelectric point the protein and the DPPA Langmuir film are both negatively charged and hence other interaction forces such as hydrophobic interactions are necessary to overcome the repulsive electrostatic barrier. Between pH 4.3 and 7 BSA is in the most stable form which is the triangluar or heart-like shaped N-conformer [820, 876].

At alkaline conditions (pH-values above 7) BSA undergoes gradual molecular conformational transitions into the B-form ($\mathrm{N} \rightarrow \mathrm{B}$ transition). This conformational change

particularly involves the N-terminal region and consequently influences the ligand binding capacity [1238, 1239]. The B-form is characterised by a loss of rigidity and loosening of the structure [885]. Similar to the acid-induced transformations, the more gradual N $\rightarrow$ B transition has been proposed to have physiological importance [876, 885]. The B- and A-form are structurally not sufficiently described [1232, 1240]. The only available structural information is that the α-helical content is reduced and that the volume increase during the N $\rightarrow$ B transition is generally not as significant as during the transition from N- to F-isoform.

In figure 6.10, the XRR results of the adsorption of BSA at a pH-value of a) 8, b) 9 and c) the HSA adsorption at pH 9 at a DPPA-film are shown. The DPPA-film is presumably partly in a doubly deprotonated state and generates a non-zero zeta-potential surface which is strongly negatively charged. At these pH-values the surface pressure decreases rapidly upon addition of the serum albumins. The hydrophobic interactions can overcome the electrostatic repulsion and an uptake of lipid material at less crystalline regions of the film is possible. However, a directly observed alteration of the film in the XRR curves with the proteins is not observed at all pH-values. After adding magnesium chloride to the subphase, the DPPA-film is penetrated by the proteins. The electron density and thickness of both, the head- and tailgroup region, increase indicating an insertion and penetration of BSA and HSA into the lipid film. It seems that the Mg^{2+} ions bridge the equal charged protein and DPPA Langmuir film surface by a counterion or charge inversion effect. It cannot be distinguished, where the Mg^{2+} cations bind first, as BSA and the DPPA-film attract the cations via electrostatic forces. At pH 8 in the last measurement at t_6 the electron density profile indicates a disruption of the DPPA-film. Another remarkable effect is observed for the adsorption of BSA or HSA on DPPA-films with a subphase pH of 9 and incubation with magnesium chloride. As can be seen, at t_5 for BSA and t_4 for HSA a very dense and thick layer with a thickness of about 100 - 110 Å is formed. The N-conformer (triangular shape) of BSA has dimensions of 80 Å x 80 Å x 80 Å x 30 Å which are being loosened during the transition to the B-form. An embedding with the long axis perpendicular to the surface, as well as cross-linking between the BSA molecules via magnesium cations is possible. However, several layers of BSA are present at the interface. For HSA, the measurement at t_3 indicates a partial penetration of the protein and might be an intermediate step to the oligomeric structures.

The self-assembly and formation of irreversible hydrophobic coagulates and aggregation of BSA is normally observed in the low acidic pH-region (pH 3 - 3.7) with different additives and upon heating [886, 1215, 1241–1243]. Therefore, this observation of a Bragg-like structure peak in the low part of the wave vector transfer at alkaline conditions is noteworthy. It seems, that BSA and HSA undergo a complex process of protein aggregation. This includes different and simultaneous steps, such as a partial unfolding and formation of molten globules or intermediate states and the further formation of pre-aggregates which expose hydrophobic patches as templates for continuing aggregation and self-assembly.

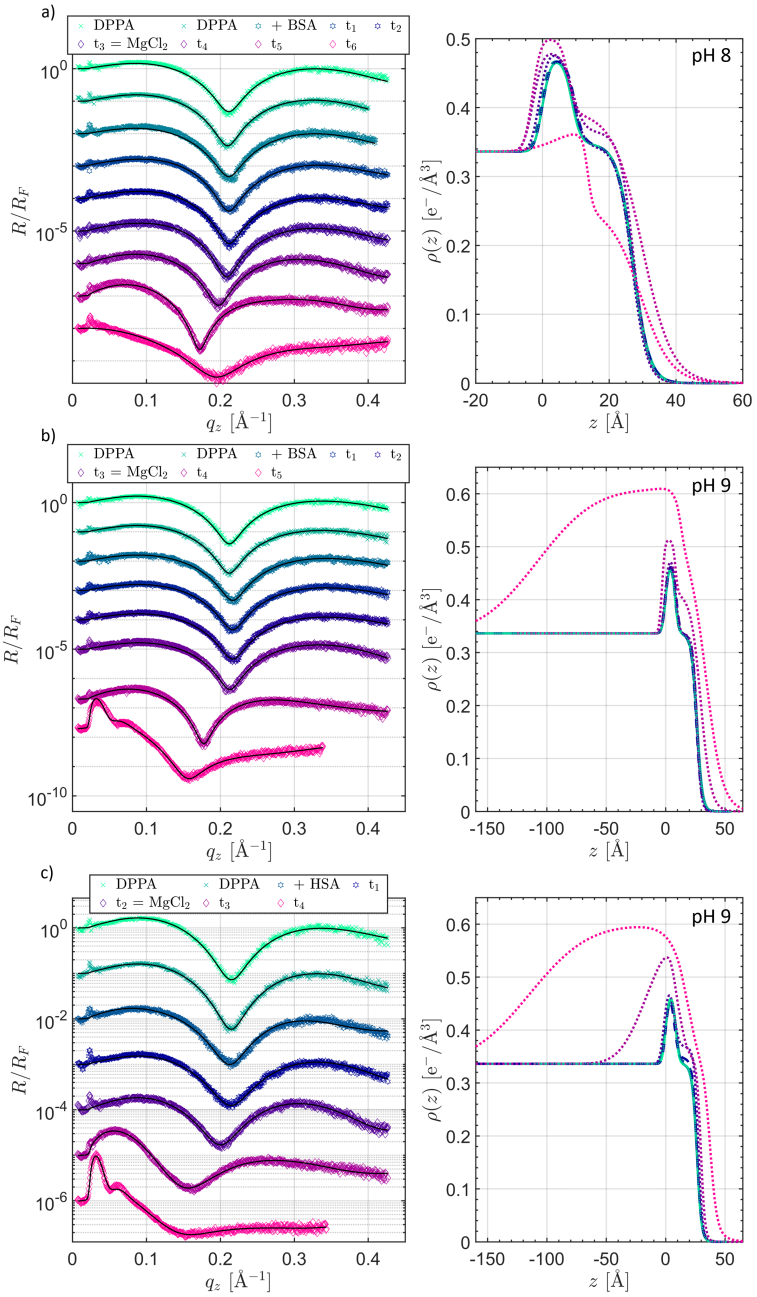

Figure 6.10: XRR data of BSA adsorption at a pH-value of a) 8 and b) 9 and c) HSA adsorption at a pH-value of 9 to a DPPA-film with subsequently addition of salt. Left: Fresnel normalised XRR data and refinement curves. The crosses correspond to the reference measurements, stars to the measurements with protein and diamonds to the addition of magnesium chloride. The refinements are shown as black solid lines. Right: Electron density profiles obtained by the refinement to the data. The colour code of the XRR data applies. Dashed lines correspond to the serum albumin containing system, dotted lines to the subsequent magnesium chloride addition into the subphase. $[c_{protein}] = 7.52\,\mu M$ and $[c_{MgCl_2}] = 20\,mM$.

The conformational solubility is B > N > F [1232] and the B-conformer in general exposes fewer hydrophobic residues to the solvent [1244]. However, here it seems that the B-conformer acts more hydrophobic since it penetrates deeply into the monolayer and interacts also with the tailgroups.

The observed decrease of the surface pressure, above pH 7 in the presence of the serum albumin, but without addition of the salt, can be attributed to the electrostatic repulsion and thus hindrance of protein adsorption, but change of orientation of the DPPA molecules at the interface, which leads to condensation [1244]. A lipid uptake and solubilisation into the subphase is also likely.

Xu et al. observed a decrease in the collapse pressure of anionic DPPG monolayers in Π-A isotherms in the presence of BSA and Π-t measurements also revealed a decrease in surface pressure as well. This was attributed to the carriage of negatively charged DPPG molecules into the subphase during BSA desorption [1244]. BSA displays a strong binding ability to DPPG molecules, the same could apply for DPPA. At anionic arachidic acid and cationic pH-independent DOTAP Langmuir films similar trends of the surface pressure change and uptake of lipids by BSA were detected [1232, 1233]. De Souza et al. [1245] investigated DMPA-films in contact with BSA at a pH near the IEP (5.7), no uptake or significant loss of lipid matter was found, similar to the results here at pH 5 and 6. The uptake process would have to take place very quickly, as there is no accumulation of protein or significant modification in the XRR curves and density profiles with time. The XRR data for all pH-values above (excluding) pH 6 only show a small shift of the minimum in the direction of high wave vector transfers, which can be explained by a reduction of the lipid film thickness and possibly an increase of the tilt angle. Probably only small amounts of lipids are removed from the interface, as the electron densities remain almost constant. However, even small changes in the surface coverage can cause large differences in surface pressure.

A distinction between the protein and lipid layer is possible at pH 3 and 4. With the consideration of equation (4.5) and equation (4.6) it is possible to obtain the adsorbed amount Γ of protein at the surface as shown in figure 6.11 (left). The integration was only performed in the region below $z = 0$ and the protein layer was merely considered. For the calculation of the volume fraction profiles the tailgroups were precisely aligned to each other in one measurement set. The electron density of BSA in the N-form was used ($0.4228\,e^-/Å^3$). The diagram shows that the adsorbed mass of BSA and HSA (in buffer without salt) increases over time. The surface excess is not affected by the addition of magnesium chloride. The amount of adsorbed BSA in the system with magnesium chloride already shows higher values at the first measurement. Furthermore, the desorption process at pH 4 can be seen.

It is not possible to differentiate between the protein and the DPPA-film at the alkaline pH-values, since the serum albumin is located within the layer. The additional electrons per area were calculated from the electron density profiles, see figure 6.11 (right). For this purpose, the headgroups were shifted and aligned to overlap each other. As the figure clearly displays, the number of electrons per area increases with the addition and incubation of magnesium chloride in the system. The variation of the surface pressure for each pH-value and after addition of serum albumin or magnesium

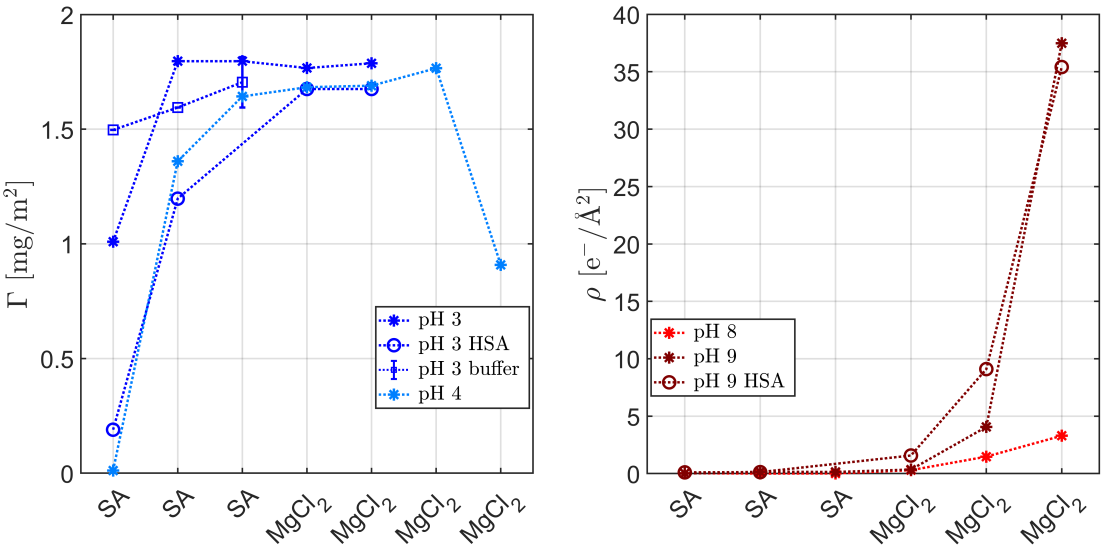

Figure 6.11: Left: Magnesium chloride and time-dependent adsorbed mass calculated from the XRR data of BSA and HSA at a DPPA-film for the pH-values 3 and 4. The error can be estimated with the calculation of the difference of the obtained amount by using the best fit and the calculated amount via variation of the parameter set. It is between 0.08 and 0.12 mg/m^2. Right: Calculated additional electrons per area. The dotted lines are guides to the eye.

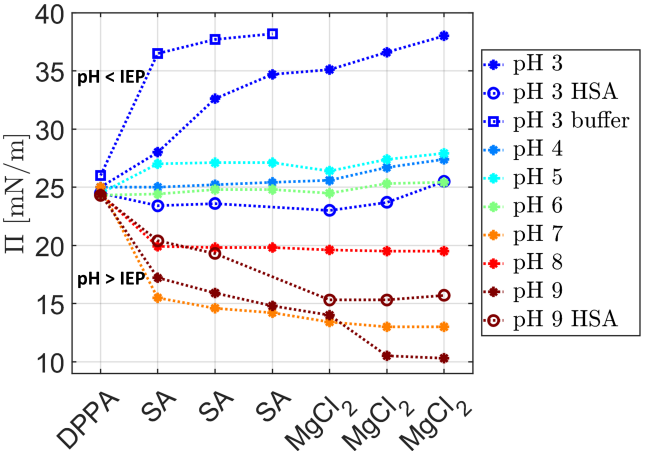

Figure 6.12: Surface pressure (Π) variation of DPPA Langmuir films at different subphase pH-values and addition of serum albumin and $MgCl_2$. The measurement "pH 3 buffer" corresponds to the salt containing buffer measurement in figure 6.8 b). In the previously shown XRR data the first and directly after injection of the protein performed measurements are designated as "+ BSA" or "+ HSA". The data points in this figure are shown in the chronological order.

chloride is depicted in figure 6.12. A trend can be derived. Below the IEP of BSA and the first dissociation constant of DPPA, the surface pressure increases strongly. Within the IEP of BSA and above the first dissociation constant of DPPA this effect becomes less and above the dissociation constant of DPPA the surface pressure decreases drastically.

The most important results obtained in the study of the pH-dependent adsorption behaviour of BSA, which undergoes pH-dependent structural changes, is sketched in figure 6.13.

The XRR analysis shows that it is possible to trigger the adsorption at high alkaline

pH-values by recharging the protein or the surface or by bridging by a divalent cation which enables pronounced hydrophobic interactions. In the low acidic pH-region it is possible to influence the initial adsorption of the serum albumins. Moreover, mainly hydrophobic forces could be involved in the adsorption process at pH 3, whereas at pH 4 electrostatic attraction become more important. The results show that the microenvironment, namely ionic strength and pH-value, plays an important role in the adsorption behaviour of globular soft proteins.

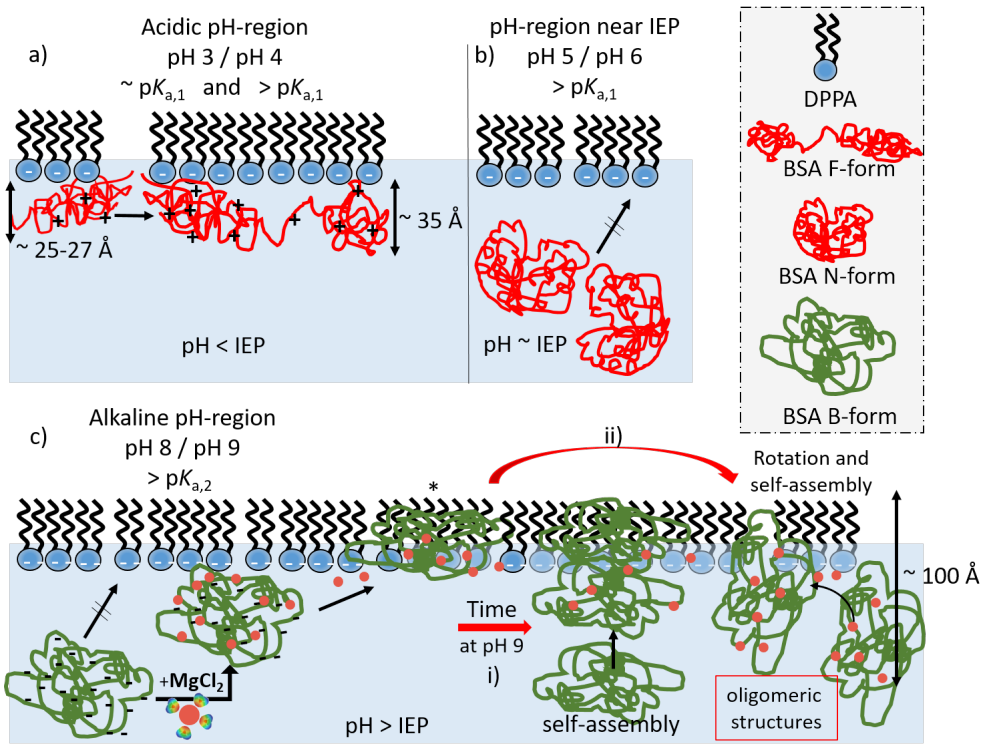

Figure 6.13: Schematic illustration of the assumed adsorption processes of BSA to the DPPA-film at different pH-values derived from XRR measurements. In the acidic pH-region, shown in a), the F-form of BSA adsorbs with the long axis parallel to the surface (35 Å). The measurements conducted directly after the injection of BSA indicate structural molecular reorganisations since the obtained thicknesses are smaller. This can be caused by the initial interaction with the lipid layer. In the pH-regime near the IEP, visualised in b), BSA has the lowest solubility and tends to self-assembly in the subphase due to minimised repulsion forces between the protein molecules. In the neutral and alkaline pH-regions, BSA presumably binds and solubilises lipid matter and a carriage into the buffer phase occurs. This leads to the formation of BSA-DPPA lipid complexes. This process is not shown and is indicated by surface pressure measurements. Moreover, BSA has an intrinsic binding affinity for negatively charged substances. An alteration in the absence of magnesium chloride cannot be observed. In presence of the salt at pH 9 and after incubation, very dense and thick layers at the interface can be observed, for both HSA and BSA, illustrated in part c). This indicates a formation of oligomeric structures by self-assembly within and underneath the DPPA-film. The interaction between equally charged protein surface and DPPA-film can be established by charge screening effects and bridging via the divalent Mg^{2+} cations. A charge inversion caused by cation binding of BSA is possible, since the protein displays a high affinity and possesses binding sites for metal cations. First, the protein molecules penetrate completely into the DPPA-film (marked by a star (*)), presumably embedded with the short axis parallel to the surface (> 30 Å). The dense protein layers are then archived either via self-assembly to the long axis i) or by rotation and lateral assembly ii). Presumably the protein is altered by the interaction with the lipid layer and at the water surface in such a way that hydrophobic patches are released and an attachment via hydrophobic interactions with further BSA proteins is possible.

6.2 Ions at solid-supported membranes

A biological membrane is surrounded by an aqueous environment that contains different mono- and divalent ions, such as Na^+, Ca^{2+}, Mg^{2+} or Li^+. These biological interfaces are susceptible to perturbations by ions that typically bind to membranes via interactions with the polar headgroups. The physical origin of and the diverse structural changes induced by specific ion effects on lipid bilayers are not well understood. Despite the vast amount of experimental and theoretical studies on the interaction of cations with zwitterionic phospholipid bilayers, the role of the interaction and the quantitative affinity as well as the binding locations are mostly uncharted and highly controversial.

This subsection focuses on the results of the experiments on the interaction of high Z-cations and cations of the Hofmeister series with solid-supported DMPC bilayers in the L_α phase. The aim of the study was to contribute to the elucidation of the structural changes induced by ion-specific interactions with membranes. By using solid-supported bilayers, a realistic biological bilayer system can be imitated more accurately than with Langmuir films [199]. The results concerning NaCl and $CaCl_2$ were obtained in cooperation with Dr. Simo Huotari from the University of Helsinki. In the framework of this cooperation the experimental received data and results will be compared with state-of-the-art all-atom molecular dynamic simulations in the future [669, 1246].

6.2.1 Experimental details

The experiments were conducted at the beamline BL9 of the synchrotron radiation facility DELTA (Dortmund, Germany) using an incident photon energy of 27 keV. The measurements were performed at low and high salt concentrations, ranging from 0 M to 1 M. The high salt concentrations were used to isolate the van der Waals interactions. Any possible electrostatic interactions are screened.

For all samples, free-salt reference scans were recorded to determine the structure of the substrate-bound DMPC bilayer system and as a quality check. The resulting parameters of the substrate (silicon/silicon dioxide) were used for the fit of the additional salt measurements. In order to minimise the x-ray radiation damage, the sample was shifted laterally. The radiation damage and the stability in water was checked before (see figure 6.15). Each measurement at a defined salt concentration was performed twice to monitor time effects. The measurements with NaCl and $CaCl_2$ were reproduced three and four times, respectively.

The structure of the solid-supported DMPC bilayers are not affected by pH-value changes. The experiments were conducted without a buffering solution to prevent cross interactions with molecules of the buffer solution. Further, a phosphate buffer, which generally is the most suitable system, can precipitate in presence of calcium cations.

The spin-coating technique has been utilised as a fast and simple preparation method to generate highly ordered and defect-free bilayers. The exact implementation is given in section 4.4. To remove any traces of remaining solvent, the lipid coated wafers were treated in a vacuum desiccator for around two hours prior to the measurements. The hydrophilicity of the Piranha etch treated wafers were characterised by contact angle

measurements which reveal angles less than 10°. The coated wafers were fixed in the inner sample holder and transferred into the sample cell, which was filled afterwards with degassed ultra-pure water. The salt concentration was successively increased by adding previously calculated quantities from the salt stock solution. The salt solutions were also prepared with degassed ultra-pure water. The measurements were conducted at a temperature of 309.15 K after a waiting time of 30 minutes to allow the sample to reach the temperature in the fully hydrated state. The chosen temperature was above the main phase transition temperature of the lyotropic bulk system of DMPC ($T > T_m$, $T_m = 23\text{-}24\,°C$) [81, 84, 282, 1247–1249]. The ripple phase ($P_{\beta'}$) of a solid-supported single bilayer system is suppressed by the substrate via minimisation of the undulation forces of the bilayer (lateral stress, sterical hindrance) [81, 83, 279, 1250, 1251].

For the silicon dioxide film typical values of 10 - 15 Å thickness, a roughness of about 1.5 - 3 Å and an electron density of around 95 - 97 % of the electron density of the bulk silicon were used. The interfacial roughness between the silicon and the silicon dioxide was kept constant within one data set, values between 1 Å and 1.5 Å were used. In order to investigate to what extent the corresponding cations of different (earth) alkali metal chloride salts influence a DMPC bilayer, two studies are presented in this section. First, in subsection 6.2.3 the influence of monovalent cations, namely Na^+, Cs^+ and Li^+, is discussed. Then, the results of the interaction of divalent cations, Ca^{2+} and Mg^{2+}, with solid-supported DMPC bilayers are shown in the subsection 6.2.4.

As described in the previous section, the effect of the Cl^- co-ions can be neglected. With XRR it is possible to investigate the interaction process and structural change during adsorption and binding.

6.2.2 Characterisation of solid-supported bilayers

To characterise and test the reproducibility of the solid-supported DMPC bilayers on silicon/silicon dioxide wafers, XRR measurements using the laboratory diffractometer D8 at air were conducted. The XRR data collected from the as-prepared samples at room temperature and ambient relative humidity in air are depicted in figure 6.14 on the left, the corresponding electron density profiles are shown on the right.

The reflectivity curves were background corrected and show well-pronounced Kiessig oscillations in the Fresnel normalised presentation. The curves do not exhibit Bragg peaks from multilamellar structures on the surface. The density profiles of the data allow the assumption that this samples consist less than two bilayers. At the used preparation parameters and the concentration of 1 mg/ml a complete DMPC bilayer forms on the solid substrate with an additional monolayer on top, as also reported in [82, 1080]. By full hydration of the samples in excess water and tempering over 30 °C, the terminating monolayer will be immediately removed, so that a well-reproducible highly oriented and homogeneous solid-supported DMPC bilayer remains [246].

The dry spin-coated lipid film sample system appears to have a high lipid density that allows a hydration without loss of lipid matter from the bilayer and equilibration without formation of holes. For the first sample, shown in red, a total thickness of 85.9 Å (silicon dioxide layer included) and for the second sample, shown in blue, a total

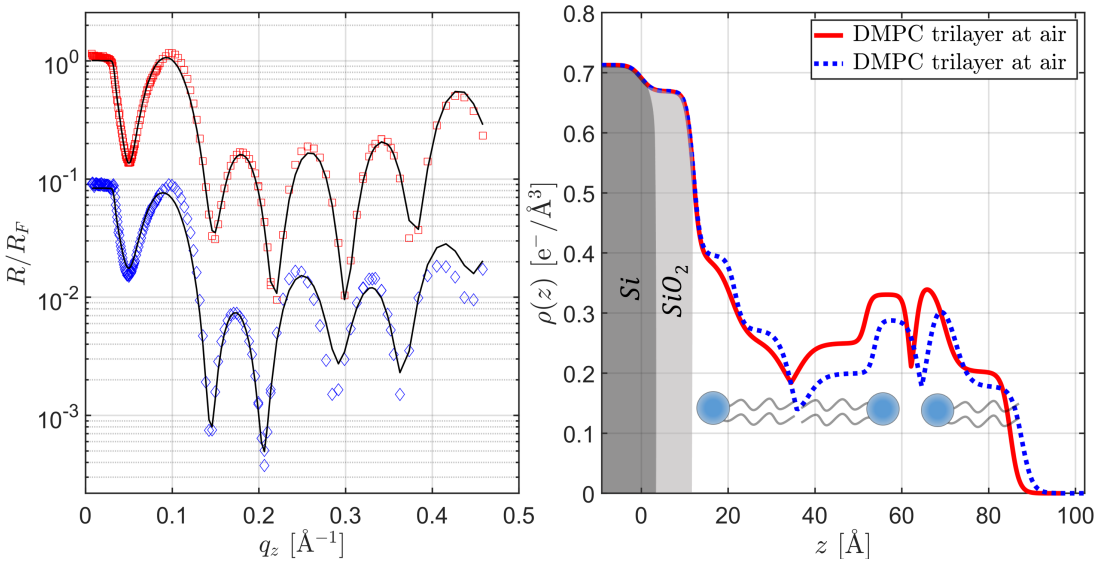

Figure 6.14: XRR data of as-prepared solid-supported DMPC samples. Left: Fresnel normalised XRR data of a spin-coated solid-supported DMPC bi- and terminating monolayer at ambient pressure and temperature. Solid black lines are the best fits to the data. Right: Electron density profiles obtained from the refinement of the corresponding XRR curves.

thickness of 87.6 Å could be calculated by refinement of the XRR curves. The refinement of the data exhibits a trilayer system, consisting a bilayer and one monolayer presumably in a gel phase.

To test the stability, structural properties and homogeneity of the fully hydrated DMPC bilayer and a possible temporal detachment of the lipids from the solid support, the samples of the DMPC bilayers were measured three times in a row. The investigated sample is the same as in the measurements shown in figure 6.14 in red. Figure 6.15 shows the measured Fresnel normalised XRR curves with a vertical offset for clarity, from top to bottom in time. The first measurement is denoted as t_1, the second measurement as t_2 and so on. Furthermore, XRR data of a bare hydrophilised silicon wafer in water at pH 7 is shown in green. The reflectivity data of the spin-coated samples show characteristic Kiessig oscillations that indicate the presence of a substrate-associated lipid layer. The right side of the figure shows the obtained whole electron density profiles (top) and substrate-subtracted profiles (bottom) obtained from the refinement of the XRR curves. The shape of the curves remained unchanged during time. No detachment of lipids and change of the underlying density profiles could be observed - the system is stable over several hours immersed in water.

In order to test the stability of the fitted model, different layer systems were suggested and tested over a number of reference measurements. First, the electron density profile of the lipid bilayer was modelled using a simple three-layer system (head-tail-head). The dotted light grey curve in figure 6.15 shows the best fit of the three-layer model that yields a χ^2 of 0.52 after further refinement. The dashed dark grey refinement

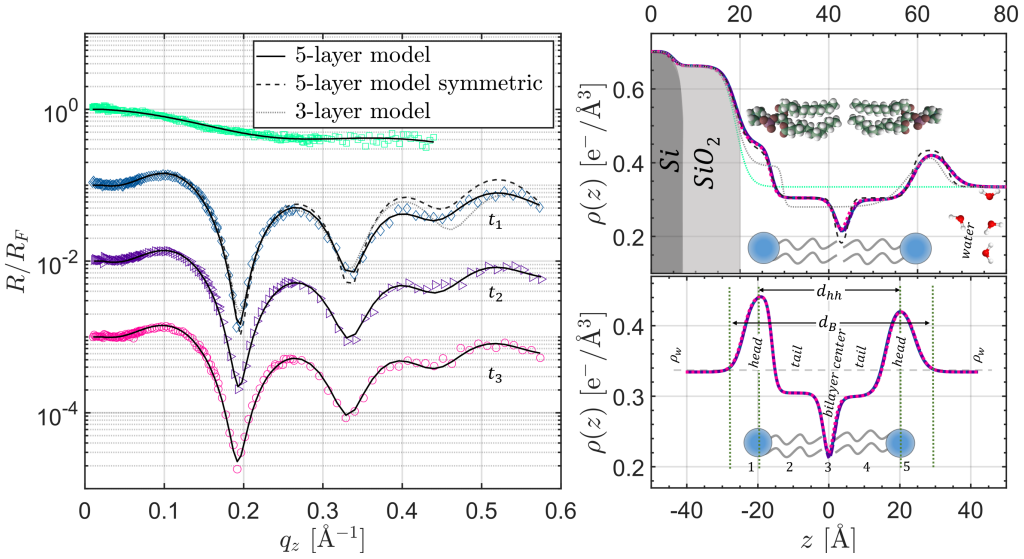

Figure 6.15: XRR data of a fully hydrated solid-supported DMPC sample at different times fitted with different refinement models. Left: Reflectivity of an immersed solid-supported (Si/SiO_2) DMPC bilayer prepared with spin-coating in excess water. The data is background, attenuation and footprint corrected and shifted vertically for clarity. Right: Electron density profiles obtained from the refinement of the corresponding XRR curves. To test the stability of the fit, different models were tested (see text). The schematic drawing below illustrates the physical composition of the layers.

has a χ^2 of 0.9 and corresponds to a symmetric five-layer model that can be seen in the top electron density profile map in the same colour. It was not possible to fit a symmetric bilayer by further refinement. An asymmetric bilayer model yields for the best fit to the data. A further not shown possibility to refine the data is the assumption of a water layer between the substrate and the inner headgroup. It is currently being discussed whether the fluidity of the supported lipid bilayer is based on the presence of a very thin layer of water at the solid support surface [279, 915, 1063, 1064, 1252, 1253]. However, it was not possible to implement and resolve such a layer of water to adequately reproduce the data. This implies that the water layer must be smaller as 3 Å if present at all. The first leaflet seems to be attached directly at the substrate. Indeed, other studies also imply that a water layer is not necessary to adequately describe the results and maintain the fluidity of a bilayer [281, 915, 1254], also with the spin-coating technique [81, 84, 246, 258, 259, 281, 282].

The calculated reflectivity of an asymmetric five-layer model reproduces the data accurately with a χ^2 of 0.13 and was further used. The bilayer structure is distinguished by five different domains: the inner headgroup (choline and phosphate) directed to the substrate, the inner tailgroup which is separated by a small gap (terminating methyl groups) from the dense outer tailgroup and the outer headgroup. The solid-supported bilayer is asymmetric, the outer headgroup shows a lower electron density. The electron density profile shows a typical shape of a bilayer.

The vertical head-to-head distances d_{hh} can be calculated by consideration of the electron density profiles and fitting of two Gaussian to the headgroups, to locate the position of the headgroup maxima of the upper and lower leaflet. Another possibility is the determination of the area underneath the headgroup region and calculation of the position, which divides the area in half. To get comparable and consistent calculations, the d_{hh} distance is calculated via Gaussian fitting or via visual judgement if the shape of the profile does not allow a Gaussian fit. The layer thicknesses calculated from the electron density profiles were used for comparison with literature values (d_{hh} and total bilayer thickness d_{B}). The head-to-head (phosphate-phosphate) distance, was found to be 37.5 Å. The total bilayer thickness d_{B} of the solid-supported DMPC bilayer can be calculated to 47 Å. The length scales extracted from the electron density profiles are illustrated in figure 6.15. The error of the thicknesses can be estimated to $\pm$ 0.5 - 1 Å for each layer by a variation of the parameters. The area occupied per lipid molecule can be calculated via integration of the electron density between the centres of the headgroups [167, 1255]. Dividing the electrons per two DMPC molecules (374 electrons each) by the resulting value yields the area per lipid molecule. The obtained area of 59.5 $\pm$1.5 Å^2 is in good agreement with literature values (59.7 Å^2 [1255], 59.5 Å^2 [1256]) for the L_α phase.

When comparing the data with literature values, it is crucial that different definitions of bilayer thickness exist, depending on the sensitivity of the technique used [167, 174, 1255, 1257]. The modelling of the bilayer system with the five-layer system (SiO_2 and five lipid sublayers) is widely accepted and also used in MD simulations [81, 84, 258, 1078, 1250, 1253, 1258, 1259]. For the L_α phase of DMPC d_{hh} values between 34 Å and 35.5 Å were reported [83, 1255, 1258, 1260]. With solid-supported DMPC bilayers in the liquid-crystalline phase, Nowak et al. reported thicknesses d_{B} of about 44.5 Å [81], similar to those found elsewhere (43 Å, 44.2 Å) [279, 1255]. However, there are not many d_{B} values for solid-supported DMPC bilayer systems. The vast majority are lamellar thicknesses, that also include the water layer of a stack system (e.g. 55 Å [1078] or 53.9 Å [83] found for lamellar (L_α) DMPC thicknesses).

For comparison with the literature data the obtained values d_{hh} and d_{B} are used. Both obtained thicknesses, the head-to-head thickness and total bilayer thickness, show higher values than described in the literature for liquid-crystalline DMPC phases. The observed thicknesses are between those of a liquid-crystalline and a gel phase bilayer. It can be assumed that the solid-supported DMPC bilayer under consideration does not completely migrate into the liquid phase. Some regions of the bilayer seem to remain in a gel phase. The broadening of the phase transition region and the temperature width is discussed in the following. Further, a small variation of the thicknesses of the reference measurements are expected since near the main phase transition temperature fluctuations occur which have an enhanced temperature sensitivity [1140, 1247, 1261].

It is known that different substrates and preparation techniques can influence the lipid diffusion and the phase behaviour in solid-supported lipid systems [262, 268, 1262–1264]. The temperature-dependent phase behaviour of solid-supported DMPC bilayers prepared by spin-coating is not known exactly. Atomic force microscopy studies reported a broader T_{m} range for DMPC with a width of $\sim$ 10 °C on mica for the $L_\beta \rightarrow L_\alpha$ transition

[263, 1265, 1266]. The same behaviour was found for DPPC [1267]. In this range, gel and liquid-crystalline phases coexists on the surface. Some main phase transition temperatures and temperature widths of DMPC and DPPC for different systems can be found in [1263, 1266]. In general, the phase behaviour of solid-supported DMPC bilayer stacks and vesicles in bulk can be compared and are quite similar [84]. Thus, the main influence seems to be the solid support.

Mica-supported PC bilayers show two transition temperatures, where the first transition is 2 °C higher than the main phase transition in lamellar DPPC bilayers [1264]. This behaviour can be explained by a strong lipid/substrate-interaction which could be stronger than the interaction between the leaflets [1268]. However, a coupled phase transition for silicon dioxide surfaces could be observed [262], this effect was attributed to the higher roughness of the silicon dioxide surface. But, it should be also considered, that the Hamaker constant of silicon dioxide is smaller than for mica and the substrate coupling is thus lower. Mouritsen et al. obtained two phase transitions and attributed the lower phase transition temperature to the distal (outer) leaflet and the higher phase transition temperature to the proximal (inner) leaflet. They concluded, that the distal leaflet is minimal affected by the solid-support [263]. Tokumasu et al. describe that the increased temperature range for the main phase transition on a solid support is caused by the reduced cooperativity within the bilayer during the transition [1269, 1270]. The cooperativity seems to be more affected on mica than on silicon dioxide substrates due to the reduced coupling with silicon dioxide substrates and enhanced coupling between the leaflets, as already mentioned. The general explanation for the higher main transition temperature is the loss of entropy.

As can be seen in figure 6.15, the inner leaflet is more condensed and compressed ($0.441\,e^-/Å^3$ (proximal) and $0.42\,e^-/Å^3$ (distal)). This was already reported in literature [281, 915, 1063, 1064, 1254]. The denser inner leaflet seems to be in a gel phase, this is consistent with the above described transition phenomena.

Nevertheless, Ghosh et al. assume that the electron density of the silicon dioxide layer plays a decisive role and contributes to the electron density of the headgroups. Due to the reduced thickness of the inner headgroup, which has been detected in many investigations, it can also be assumed that a compression of the headgroup occurs. The inner headgroup might also contain a lower water content. This finding is consistent with a reduction in the movement of internal leaflet lipids due to interactions with the solid support and a simultaneous reduction of fluctuations [1254]. Probably many factors originating from the substrate play a major role for the resulting density profile, especially the affection of the inner leaflet. The outer leaflet pointing to the subphase can be assumed to be in the liquid-crystalline phase. The electron densities and thicknesses of the head- and tailgroups as well as the values of the bilayer center, gap or the methyl groups of the alkyl chains are in accordance with the literature.

6.2.3 Influence of monovalent cations on DMPC bilayers

After considering the time-dependent stability of the DMPC bilayers, measurements and discussion of the influence of the monovalent cations of the metal chlorides NaCl,

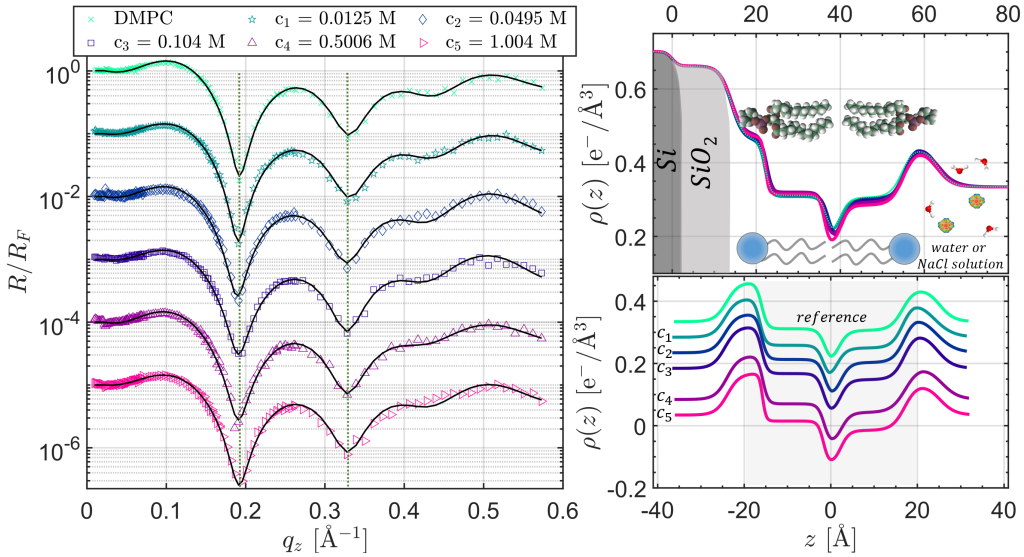

Figure 6.16: XRR data of a fully hydrated solid-supported DMPC bilayer with elevated NaCl concentration. Left: Fresnel normalised XRR curves of the DMPC bilayer with increased salt concentration. Solid lines represent the best fit to the data. Right: Electron density profiles corresponding to the refinements with complete profile (top) and extracted bilayer system (bottom).

CsCl and LiCl on these bilayers follow. Figure 6.16 on the left shows the Fresnel normalised XRR curves of the solid-supported DMPC bilayer in water, with the reference measurement (green, cross symbol) and the behaviour of the bilayer system with increasing NaCl salt concentrations. The XRR curves are shifted vertically for clarity. Corresponding electron density profiles are shown on the right. The upper plot presents the full profiles, whereas the representation at the bottom displays the profiles after subtraction of the substrate electron density.

Repetitive measurements were conducted to check for time-dependent changes. Only the last measurement at the corresponding concentration is shown here. A significant time effect could not be determined.

Two data sets are shown exemplary. The oscillations at higher wave vector transfers are more clearly visible in the second example (compare figure 6.17). As can be seen from the XRR curves and electron density profiles, the system remains almost unchanged upon addition of NaCl. There is no significant shift of a minimum or features that would imply a thickness change of the surface associated layers. However, the electron density profile changes steadily with increasing the NaCl concentration. But this effect could not be reproduced directly and the profiles presented in figure 6.17 reflect a different behaviour of the DMPC bilayer system. Therefore, it is reasonable to assume that the system is probably not altered by binding or adsorption or even an ion-specific effect of Na^+. The head-to-head thicknesses of the reference measurements were 40 ± 1 Å and 40.5 ± 1 Å. Total bilayer thicknesses of 48.4 Å and 47.5 Å were estimated, respectively.

A definite assessment about the adsorption or binding position of sodium cations

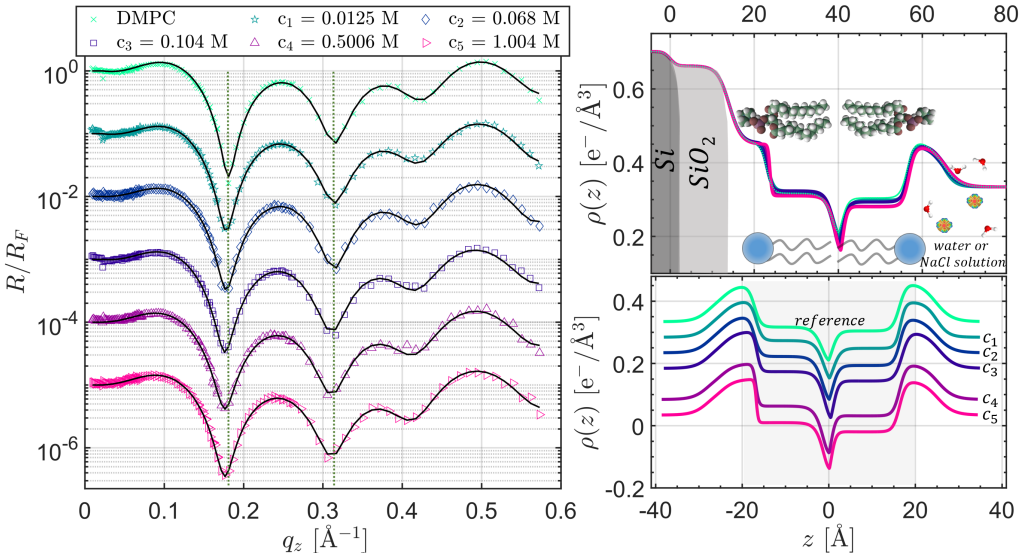

Figure 6.17: XRR data of a fully hydrated solid-supported DMPC bilayer with elevated NaCl concentration. Left: Fresnel normalised XRR curves of the DMPC bilayer with increased salt concentration. Solid lines represent the best fit to the data. Right: Electron density profiles corresponding to the refinements with complete profile (top) and extracted bilayer system (bottom).

is not possible. Further, a significant and repeatedly similar molecular reorganisation of the DMPC bilayer upon NaCl addition cannot be derived. In summary and with regard to chapter 2 (section 2.3) it can be cautiously assumed, that NaCl does not affect a zwitterionic bilayer system. The slight compression of the bilayer can be caused through fluctuations. There is a vast majority of literature that describes an interaction between NaCl and zwitterionic, mostly PC membranes. Nevertheless, the question of specificity on Na^+ is a major debate and controversial in this scientific field. Some very recent publications confirm the negligible effect of NaCl on PC membranes [156, 583, 626, 628, 644, 648, 649].

Figure 6.18 presents the results of the interaction between DMPC bilayers and CsCl in the low concentration regime at 0.05 M and LiCl in the high concentration regime at 1 M.

As can be seen, Cs^+ influences significantly the distal leaflet of the bilayer. The first minimum in the Fresnel normalised representation shifts to higher wave vector transfers and a decreased thickness of the bilayer could also be refined within the electron density profile. The electron density in the outer leaflet (head- and tailgroup) is increased. The caesium cation is weakly hydrated (ionic radius of 1.7 Å and hydrated radius of 3.29 Å) and enhances the electron density contrast, since it constitutes of 54 electrons. In the literature Cs^+ is described as a hydrophobic acting ion that can also penetrate black lipid membrane systems [700, 1271]. Already at a CsCl concentration of 0.01 M an ion transport through the membrane could be observed, whereas the Cs^+ cation exists as non-hydrated species in the lipid membrane [699, 700]. The observed deep penetration

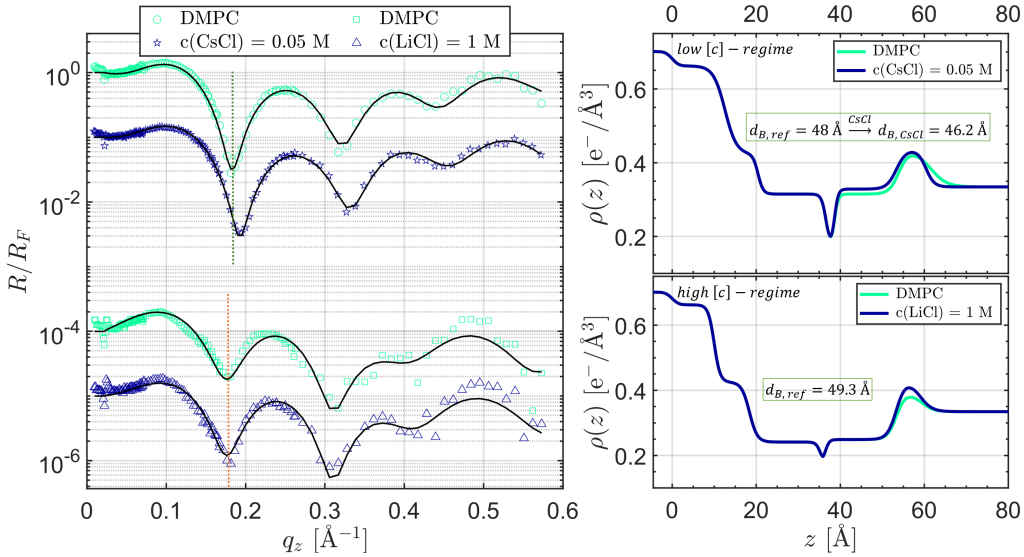

Figure 6.18: XRR data of fully hydrated solid-supported DMPC bilayers with low CsCl concentration or high LiCl concentration. Left: Fresnel normalised XRR curves of a DMPC bilayer with low CsCl concentration (top curves) and data of the interaction with LiCl in the high concentration regime (bottom curves). Solid lines represent the best fit to the data. Right: Electron density profiles corresponding to the refinements (top: CsCl, bottom: LiCl).

into the tailgroups is therefore not unreasonable. For higher concentrations a refinement of the data was not possible due to the strong absorption of the CsCl solution, further measurements are necessary.

The electron density profiles of DMPC bilayers interacting with Li^+ show that the ions bind to the distal headgroup without affecting the other sublayers. The data were recorded at a different beamtime, therefore the measurements do not provide the same quality. Although lithium offers only 2 electrons, the increase of the electron density is rather high. This indicates that a large number of binding sites are occupied. Recent studies investigate the open question if lithium induces a reorganisation of membranes or whether this effect originates from lithium-induced metabolic changes [1272]. This result is merely an indication that probably lithium does not cause a reorganisation of the membrane. Studies report that lithium cations reduce the water motion activation energy, as they show the highest degree of association with PC and PC-PG mixed membranes and have the highest affinity of the monovalent or alkali metal cations under consideration [587, 696, 697]. A deep penetration of lithium and a conformational change of the headgroup that is reported in the literature [1042] cannot be extracted from the presented data.

6.2.4 Influence of divalent cations on DMPC bilayers

The XRR results of the interaction of solid-supported DMPC bilayers with $CaCl_2$ in a concentration range from 0.0125 M to 0.5 M are shown in Figure 6.19. The reflectivity

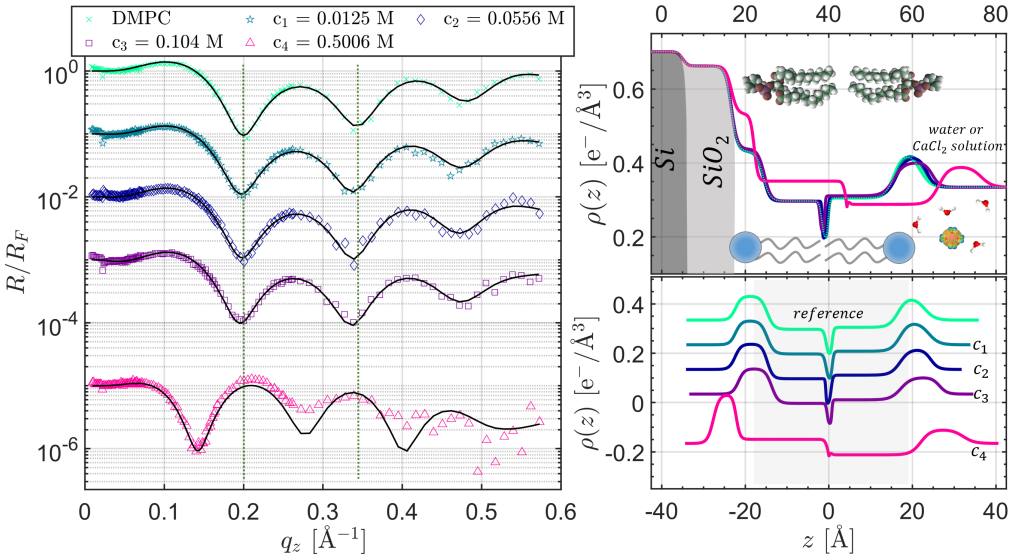

Figure 6.19: XRR data of a fully hydrated solid-supported DMPC bilayer with elevated $CaCl_2$ concentration. Left: Fresnel normalised XRR curves of the DMPC bilayer with increased salt concentration. Solid lines represent the best fit to the data. Right: Electron density profiles corresponding to the refinements with complete profile (top) and extracted bilayer system (bottom).

data were reproduced and an exemplary measurement is shown here.

The head-to-head thickness d_{hh} of the reference measurements is 38.3 Å and the total bilayer thickness d_B yields 47 Å. With increasing calcium chloride concentration, it can be seen, that the minima in the Fresnel normalised presentation shift slightly to the left, indicating a thicker layer. At the highest concentration of 0.5 M, the minima shift further to lower wave vector transfers, which is in accordance to a further thickening of the bilayer that can be seen in the corresponding electron density profiles. At low submolar concentrations, the adsorption takes place at the outer headgroup. The headgroup thickness increases while the electron density decreases. Indeed, the area beneath the headgroup and volume occupied is larger due to the binding and accumulation of Ca^{2+} ions. A complexation can be expected. The proximal leaflet appears to be slightly compressed. These effects intensify with increasing salt concentration. At the highest concentration of 0.5 M the bilayer seems to be strongly altered. The inner leaflet becomes denser and thickens while the electron density of the outer leaflet appears to be lower and also significantly enlarged. It was not possible to refine this curve accurately. However, this behaviour has been reproduced several times in this study. Furthermore, a time-dependent binding can also be observed (data not shown). A comparison with the first reflectivity shows that the adsorption process is still ongoing at the first reflectivity.

To screen the concentration range between 0.1 M and 0.5 M, measurements were taken in 100 mM steps. The results are depicted in figure 6.20.

The XRR curves and resulting electron density profiles clearly show that the reorganisation occurs at a concentration of 0.3 M. For the concentration of 0.1 M the before

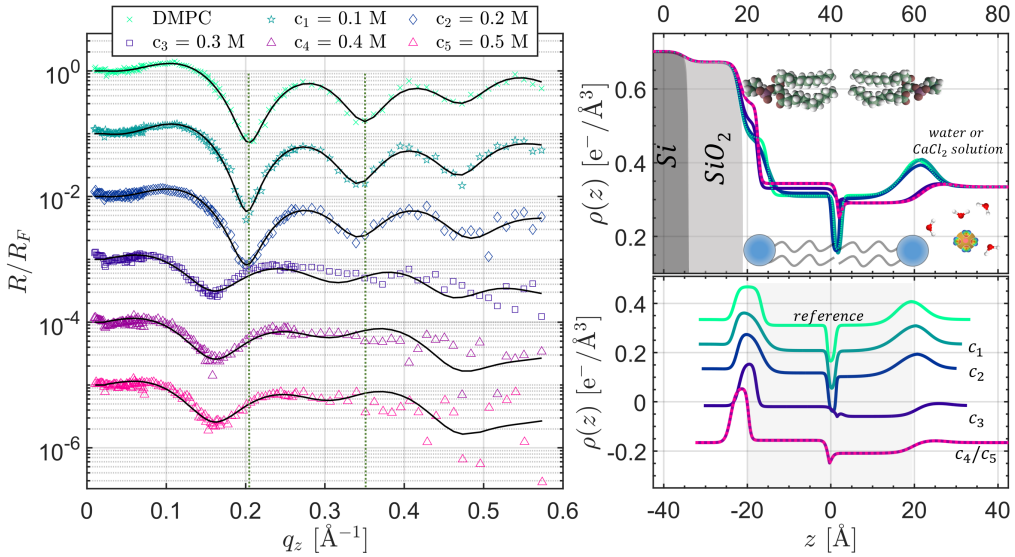

Figure 6.20: XRR data of a fully hydrated solid-supported DMPC bilayer with elevated $CaCl_2$ concentration. Left: Fresnel normalised XRR curves of the DMPC bilayer with increased salt concentration. Solid lines represent the best fit to the data. Right: Electron density profiles corresponding to the refinements with complete profile (top) and extracted bilayer system (bottom).

observed binding at the outer headgroups can be confirmed. The surface associated bilayer might be very inhomogeneous as it was not possible to refine the data accurately at high concentrations (compare figure 6.19). However, the obtained total bilayer thickness is assumed to be reliable since especially the first minimum was accurately fitted. An explanation for the observed effect might be the stretching of the hydrocarbon tails in the course of a phase transition. The maximum alkyl chain length of 19.2 Å corresponds approximately to the observed enlargement. This is probable since calcium is known to increase the phase transition temperature of DMPC. The bilayer thickness d_B yields 61.4 Å. However, this thickness cannot be attributed to the usually occurring gel phase (49 Å for gel-like DMPC phases at 20 °C) [84].

Recently published studies focus on the effect of monovalent and divalent ions on the swelling behaviour of multilamellar layers in different vesicle-derived or solid-supported model systems. The swelling effect was attributed to the interlamellar water between the headgroups of the layers, a change of the bilayers was not observed [588, 648, 687, 689]. However, these results were found at particularly high salt concentrations (> 1 M). The phenomenon observed here, above a calcium chloride concentration of 300 mM and higher seems to be a molecular reorganisation in the bilayer itself. As the physiological concentrations of calcium are naturally low, the overall membrane changes induced by their local binding and the identification of the binding sites are of high relevance. Upon binding in the outer headgroup, a conformational change can be assumed, since the headgroup undergoes detectable modifications with increasing concentrations. This was also reported in literature [625, 660, 1273]. The exact binding location within the

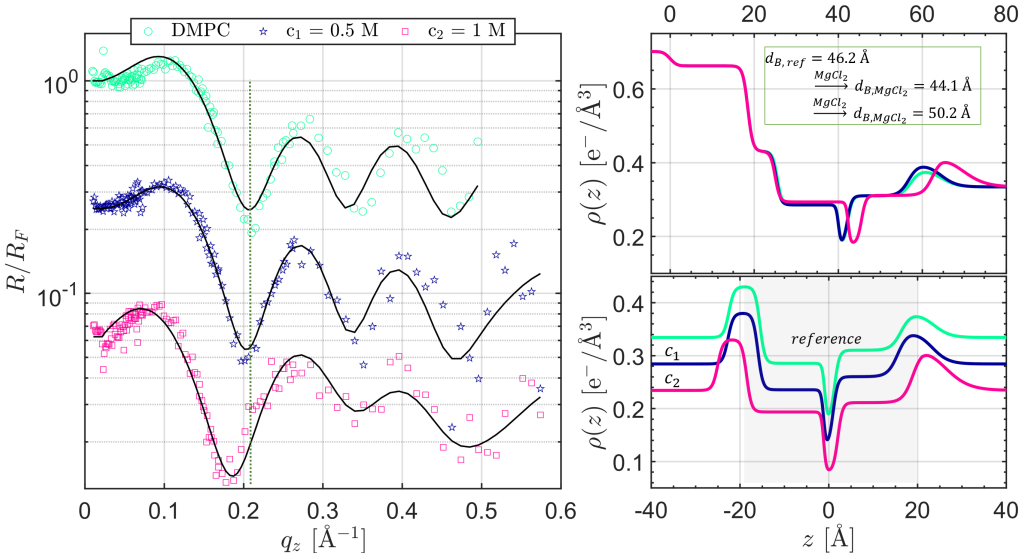

Figure 6.21: XRR data of a fully hydrated solid-supported DMPC bilayer with low and high $MgCl_2$ concentrations. Left: Fresnel normalised XRR curves of the DMPC bilayer with increased salt concentration. Solid lines represent the best fit to the data. Right: Electron density profiles to the refinements with complete profile (top) and extracted bilayer system (bottom).

headgroup cannot be identified, presumably the phosphate moieties are complexed.

The second divalent cation of a chloride salt investigated on DMPC bilayers was magnesium chloride in low and high concentrations. The Fresnel normalised XRR curves and the corresponding electron density profiles are illustrated in figure 6.21.

Unfortunately, the scan quality is not very high, particularly at high concentrations, but the first minimum is well resolved. The outer leaflet is first compressed and the whole bilayer is elongated at higher concentrations. At low concentrations a binding of Mg^{2+} could be determined in the outer headgroup. The response of the lipid DMPC bilayer to the addition of magnesium chloride is similar to that observed with calcium chloride. First, a compression is detected and with further increase of the concentration an increase of the total layer thickness follows. The resulting thickness of about 50.2 Å at a $MgCl_2$ concentration of 1 M is in the range of gel-like phases. The shift to lower q_z with higher concentration is not as pronounced as was observed with low concentrated calcium solutions. This is in accordance with the literature. Magnesium cations have a high affinity for PC membranes, but it is lower than of calcium cations [577].

6.3 Summary and general conclusions

In this chapter the results of the experiments on response of model lipid systems to the addition of salts were presented. Furthermore, the adsorption of BSA and HSA on DPPA-films was investigated in dependence of the microenvironment, namely between pH values 3 to 9 and by applying magnesium chloride to the subphase. Structural

information at the sub-angstrom scale was obtained with XRR.

In conclusion of the investigation of the interaction of mono- and divalent cations with Langmuir films, it can be stated that especially divalent cations show a high affinity for anionic phospholipid layers. When investigating DPPA and calcium cations, it is assumed that an accumulation occurs at the headgroups, whereby presumably free (bare dehydrated) and partially dehydrated calcium cations adsorb. The stoichiometric ratios are first 1:2 and at higher concentrations 1:1 of the Ca^{2+}-DPPA complex. Therefore, the binding mode depends on the concentration of calcium chloride. In contrast, sodium cations appear to affect the DPPA layer and the effect becomes continuously more intense with increasing concentration, although it is not possible to determine exactly the underlying effect. The layers are slightly compressed. Apart from the effect that presumably calcium ions only attach to the DPPC headgroups at very high concentrations (1 M), no further changes could be observed with cations at these zwitterionic Langmuir films.

To get one step closer to the *in-vivo* situation of biomembranes, solid-supported bilayer models of DMPC on silicon wafers were also applied. The sodium cation, which is physiologically very important, exhibits, similar to the Langmuir film model, no binding. Caesium and lithium cations, on the other hand, accumulate at the outer headgroup, whereby caesium, the cation that is classified as a hydrophobic ion, is also located within the outer tailgroups. The calcium cation with a moderate affinity to zwitterionic lipid membranes shows a binding at the outer headgroup area at low sub-molar concentrations. At concentrations higher than 0.3 M a calcium-induced reorganisation of the bilayer takes place. The previous compression of the membrane is followed by a swelling which shows layer thicknesses in the range of more than 60 Å. This result in particular underlines the importance of this cations with regard to membrane structure. In literature, the swelling behaviour which is triggered by divalent or monovalent cations is not attributed to the change of the bilayer structure itself but to the interlayer water regions. This can be excluded here. The bilayer does not transform into the normally observed gel-like phases. Therefore, the observed effect seems to be of calcium cation-specific origin. The second divalent cation Mg^{2+} investigated in this work shows a similar effect on the DMPC bilayer, although at very high concentrations no such distinct increase in layer thickness is observed.

The findings are in good agreement with the understanding that ions influence the interface of membranes. The order of magnitude of the structural change can be classified as follows: $Ca^{2+} > Mg^{2+} > Cs^{+} > Li^{+} > Na^{+}$. Lithium behaves like a polyvalent cation and adsorbs at high concentrations to the headgroup. It is sorted behind caesium, since the hydrophobic acting ion has an effect on the bilayer structure even at low concentrations.

Within the reference measurements, it was also found that the bilayer thickness ranges from 46.2 Å to 49.3 Å. This indicates that the temperature sensitivity of the bilayer is strong as the applied temperature is close to the main phase transition which is broadened and shifted to higher temperatures due to the solid support. Therefore, it would be desirable to study the phase behaviour of solid-supported DMPC bilayers in more detail, especially regarding differences between the inner and outer leaflet.

The most important findings obtained in the experiments of the pH-dependent adsorption behaviour of BSA, which undergoes reversible pH-dependent conformational transitions, can be summarised as followed. The results are graphically visualised in figure 6.13. In an acidic pH-range at pH 3 and 4, a protein layer formation can be observed, corresponding to the thickness of the F-conformer (cigar-shaped form). The adsorption takes place with the long axis parallel to the surface. If magnesium chloride is added to the subphase beforehand, the adsorption seems to be accelerated. The F-shape has many contact areas to the surface because it is very extended and hydrophobic. In combination with the injection of BSA, a strong surface pressure increase was observed. This is due to the interaction of BSA with the water interface or the compression and interference during the adsorption to the DPPA-film. The protein adsorbate is stable in the presence of magnesium chloride. At pH 4, electrostatic forces are increased because the $pK_{a,1}$ value of DPPA is surpassed. No adsorption is expected and detected near the isoelectric point at pH 5 and 6 where BSA is neutral and in the N-form (heart-like or triangular shape). Moreover, this conformation tends to coagulate within the subphase since the repulsion forces between the proteins are minimised and the solubility is hence reduced.

Above the isoelectric point, at pH 7, only a shift of the minimum in the XRR data is visible to larger q_z values which are also noticeable at pH-values 8 and 9 when the serum albumins were added to the subphase. This means, that lipid matter is removed from the surface and macromolecular BSA-lipid complexes are formed. However, when magnesium chloride is added in the alkaline pH-region, BSA and HSA appear to interact with the DPPA-film and even penetrate it completely. An increase of the electron density in the whole film was observed. With a sufficiently long incubation time an aggregate or oligomeric structure seems to be formed at the interface, which probably contains several BSA molecules. This is a magnesium-induced effect. Due to charge inversion effects caused by charge screening of salt or Mg^{2+} ion bridging of DPPA and protein surface, it is enabled that proteins with the charge state on the "wrong side" of the isoelectric point, can approach the equally charged surface and even penetrate it. With the initial interaction triggered by magnesium cations, a hydrophobic force can arise due to an unfolding and partial denaturation which in turn can lead to the dense protein layer (oligomeric or aggregated structures). In particular the measurements in the alkaline pH-regime show that the ionic strength can tune the protein adsorption at membranes.

Chapter 7

Conclusion and outlook

This chapter summarises the main results of this thesis and gives an outlook on future projects regarding the research areas considered.

The experiments conducted in the framework of this thesis demonstrate that gaseous and vaporised perfluorocarbons and volatile hydrocarbon solvents can influence the structure of phospholipid monolayers at the liquid/gas-interface to a considerable extent. The non-polar, non-amphiphilic and hydrophobic perfluorocarbons have a high affinity to lipid membranes but also to protein films at the liquid/gas-interface and act as co-surfactant. The results also show an influence of gFCs and vFCs on the adsorption of soft and hard proteins at the liquid/gas-interface.

The second point of emphasis was the investigation of the interaction of physiologically relevant mono- and divalent cations with zwitterionic and anionic phospholipid systems. It was found that sodium in sub-molar and high concentrations has no affinity to zwitterionic mono- and bilayers. Calcium instead induces a reorganisation of bilayers.

For these purposes, Langmuir films on aqueous subphases and solid-supported lipid membrane systems were investigated by surface-sensitive x-ray scattering techniques with regard to structural changes caused by adsorption processes from the gas and liquid phase. The XRR and GIXD techniques provide access to the vertical and lateral structure of lipid layers *in-situ*.

7.1 Conclusion

First, the results of the study on the interaction of lipid membranes with (fluorine) gases and vaporised perfluorocarbons, presented in chapter 5, are summarised. There are only limited reports on the structural properties of lipid membranes interacting with perfluorocarbons.

Towards potential biomedical applications of vaporised and aerolised perfluorocarbons as stabilisers of disturbed lung surfactant in ventilation or the treatment of a lack of lung surfactant, the influence of these substances on biomimetic phospholipid model systems was investigated in this thesis.

The influence of different gas pressures of isobutane, F-propane and F-butane on the

structure of DPPA and DPPC lipid monolayers prepared on water were investigated with XRR. GIXD measurements were performed on DPPA-films under different F-butane and F-propane gas pressures and vaporised F-decalin and F-octyl bromide atmospheres. In general, it can be stated that the gases have a significant effect on the lipid monolayers. Already at low gas pressures, the gas molecules penetrate and accumulate between the tailgroups of the lipid molecules. An adsorption and accumulation of gas molecules was also observed at the bare water interface. The structural changes induced in DPPC and DPPA monolayers were found to differ from each other. All gas molecules showed an effect on the headgroups of DPPC-films caused by the compression of the lipid film. It seems that Langmuir films composed of DPPA are generally more stable due to the hydrogen bonds of the headgroups which do not permit the dissolution by F-butane gas molecules. Furthermore, the size of the gas molecules and the packing density of the Langmuir films seem to play an important role for the strength of the impact on the interfacial structures. Moreover, gas molecules can accumulate above the lipid films without destroying them. The gas molecules tend to penetrate into more accessible, expanded areas of the lipid films. Smaller gas molecules, such as isobutane penetrate even at high initial surface pressures into the monolayers. It is found that the gas molecules have a higher affinity for DPPC than for DPPA. The gases reduce the interfacial tension of a bare water interface and also the surface tension of DPPA and DPPC Langmuir films. The gFCs also penetrate into the crystalline domains of DPPA-films at high initial surface pressures of the Langmuir film. At low initial surface pressures, where the DPPA-film exhibits no lateral order with detectable Bragg reflections, it was observed that the gas molecules compress the monolayer inducing a formation of observable crystallites on the surface. Furthermore, an influence of F-octyl bromide on DPPA Langmuir films was found. These molecules appear to fluidise the monolayer, causing a compression and simultaneous dissolution of the crystalline domains by adsorption in less compressed regions. On the contrary, F-decalin showed an effect on DPPC Langmuir films only at low surface pressures. This effect could not be observed for DPPA-films with XRR and GIXD.

In addition to Langmuir monolayer, solid-supported DMPC and DPPC mono- and multilayers were investigated at elevated pressures of isobutane, F-propane and F-butane. It was found that the lipid phase and an increased rigidity of the tailgroups can prevent the penetration of the gas molecules. Furthermore, it was observed that some gas molecules remain in the monolayer after reducing the gas pressure. This seems to be a substrate related effect. In the solid-supported monolayer systems an accumulation of gas molecules can be observed in the entire layer increasing with temperature. The situation is different for solid-supported multilayers. The layer thicknesses of the bilayers within the multilayer stacks as well as the multilayer thickness does not change at different gas pressures. Nevertheless, the vanishing of the negative peak in the XRR curves at scattering angles slightly above the first Bragg reflection that was observed for DPPC and DMPC multilayers interacting with F-butane indicates an adsorption of molecules at the terminal monolayer. Similar to the observation of remaining gas molecules in solid-supported monolayers, the depth of the negative peak does not return to the former value after reducing the gas pressure and replacing the atmosphere

by nitrogen. This is an indication of remaining gas molecules in the terminal layer. It can be assumed that the effect on the terminal monolayer at the film/gas-interface is comparable to the effect on the single solid-supported monolayers.

In order to investigate the influence of gases and vaporised perfluorocarbons on the adsorption behaviour of proteins experiments with lysozyme and BSA at the liquid/gas-interface were performed. The hard protein lysozyme adsorbs to DPPA-films by attractive electrostatic interactions. A protein layer below the lipid film and a penetration into the headgroup region was observed. F-decalin causes the mobilisation of proteins from the subphase to the interface. After treatment with F-decalin, the thickness and density of the F-decalin-protein film is reduced indicating a desorption of lysozyme. Since typically lysozyme adsorbs irreversibly at the lipid films it can be concluded that the desorption process is enabled by F-decalin. F-decalin probably adsorbs at the hydrophobic sites of the protein and, thus, facilitates expulsion into the subphase after the treatment. A similar mechanism has been proposed for F-hexane and F-octyl bromide interacting with albumins at DPPC-films [305]. Moreover, the adsorption behaviour of lysozyme at the water surface under isobutane and F-propane gas atmosphere was studied in this work. The resulting protein films have a different structure than the protein layers of lysosome at air and cannot be attributed to a time effect. The gases seem to have a significant influence on the adsorbate structure of lysozyme. In contrast to isobutane, which probably stabilises the initial structure, F-propane seems to cause denser and thicker protein structures at the interface. At higher gas pressures, the electron density of the protein film increases. The gas pressure-dependent measurements reveal, moreover, gas films above the interfacial protein film indicating that the gas molecules are not only incorporated into the protein film, but also adsorb on top of the interfacial structure. Both gases attract more protein to the surface. It is very probable that the gases hydrophobise the interface. This modifies the interface chemistry and can thus affect protein adsorption.

The study of the interaction of BSA and F-decalin at the buffer/gas-interface indicates that the protein interacts with F-decalin. F-decalin adsorbs at the interface and interacts with the hydrophobic sites of the adsorbed protein structure, so that a mixed layer of F-decalin and BSA forms at the interface. This effect of F-decalin was found to be entirely reversible. The surface-activity of F-decalin is not inhibited by BSA. In contrast to the results of the adsorption behaviour of lysozyme in contact with isobutane and F-propane, it can be shown for BSA that the interaction with F-decalin is reversible and non-destructive with regard to the secondary structure.

The gas phase interacts via van der Waals and hydrophobic interactions with the interfacial structures. The perfluorocarbons possess an affinity for lipid layers and also protein films at the interface. The surface activity of perfluorocarbons and the ability to reduce the surface tension of the interface is not inhibited by surface-active proteins. This is an important factor in the design of treatment options for lung diseases, where surface-active proteins are responsible for lung surfactant inactivation. The results may have implications for the design of perfluorocarbon-containing injectable lipid drugs such as microbubbles and the development of lung surfactant replacement therapies.

Although there are numerous theoretical and experimental studies on the interaction of cations with phospholipid membranes, especially results on the binding of sodium in sub-molar concentrations at phospholipid bilayers are highly controversial. The binding sites as well as structural changes of membranes due to cation binding or adsorption are not yet thoroughly investigated. Furthermore, the binding behaviour of the physiologically highly relevant calcium is discussed in literature with respect to the binding stoichiometry and the resulting structural change of the membrane. Therefore, the second part of the thesis (chapter 6) focused on the research of the interaction of mono- and divalent cations with anionic and zwitterionic phospholipid model systems. In order to shed more light on the binding stoichiometry of calcium to anionic lipids and to study the binding affinity of sodium to zwitterionic phospholipid bilayers, various experiments were performed. The adsorption of sodium and calcium cations was first investigated at Langmuir films consisting of DPPC or DPPA. The interaction of sodium cations with DPPA Langmuir films induce changes in the electron density profiles. However, it was not possible to quantify the adsorption. When examining DPPA Langmuir films and the binding of calcium, a stoichiometric ratio of 1:2 and 1:1 (Ca^{2+}:DPPA) depending on the concentration of the salt solution in the subphase was found. In contrast to the results obtained with the anionic DPPA-films, calcium and sodium display no affinity to zwitterionic DPPC Langmuir films and cause only minor structural changes even at high concentrations.

To study the pH-dependence of the adsorption of BSA and HSA at DPPA-films and the influence of magnesium chloride on the protein adsorbate structures, experiments in the pH-range from pH 3 to 9 were performed.

At the acidic pH-values 3 and 4, which are below the isoelectric point of HSA and BSA, the proteins are in the F-form and adsorption can be observed below the DPPA-film. At the alkaline pH-values 8 and 9, which are above the isoelectric point of BSA and HSA, no adsorption at the DPPA-film could initially be detected. After addition of magnesium chloride a complete penetration of BSA and HSA into the monolayer could be observed. The increase of the adsorption of the proteins with increasing magnesium chloride concentration is due to the screening of the DPPA headgroups and the surface charges of the protein by magnesium chloride. No adsorption could be detected in the pH-range from 5 to 7 in absence and presence of magnesium chloride. Probably the charge inversion is not sufficient upon magnesium chloride addition. Furthermore, for acidic pH-values, an orientation of BSA and HSA with the long axis parallel to the surface is preferred. The dimensions of the layer thickness correspond to the size of the F-conformer. Moreover, oligomeric structures of the protein are formed at the surface in the alkaline pH-range in the presence of magnesium chloride. This study shows that the addition of salt allows direct regulation of protein adsorption on charged membranes by tuning the electrostatic forces.

The results of the adsorption measurements of the Hofmeister series cations on zwitterionic solid-supported DMPC bilayers can be expressed as a function of the strength of the structural change in the following series: $Ca^{2+} > Mg^{2+} > Cs^{+} > Li^{+} > Na^{+}$. In contrast to the results obtained with zwitterionic Langmuir films, calcium exhibits a high affinity to zwitterionic bilayers. A calcium-induced change of the membrane structure

was observed above a concentration of 0.3 M. The bilayer thickens and the electron density of the inner leaflet increases strongly. The swelling of the layer can be attributed to a rearrangement of the tailgroups, which are extended to a fully stretched conformation. The state of the bilayer induced by calcium cannot be identified as one of the known gel-like phases. Sodium cations have no effect on the zwitterionic DMPC bilayers, even at high concentrations.

7.2 Outlook

The results of this thesis are promising for the application of vaporised perfluorocarbons in lung surfactant replacement compositions. The results concerning the stability and structural response of Langmuir films under gFC atmosphere indicate that lipids with small headgroups and the ability to form hydrogen bonds exhibit more stable structure at high gas pressures. The data presented in chapter 5 suggest that DPPA, in contrast to DPPC, is not dissolved by larger fluorine gases even at high pressures. In general, the influence of larger fluorine gases is pronounced, but not destructive for the DPPA monolayer. This finding may has implications for the design of stable microbubbles for medical applications. In fact, all experiments were conducted solely with monolayers. It would therefore be useful to perform experiments in bulk systems to test the stability and lifetime of the bubbles.

With regard to the interaction between gaseous or vaporised perfluorocarbons and proteins at an interface, further investigations are necessary. Experiments to determine whether the effects induced by the gases and vaporised perfluorocarbons on adsorbed protein layers depend on the protein in terms of stability (hard or soft) or on the type of molecules from the gas phase could provide further insight into the molecular details. To examine this question in particular the adsorption of BSA at the buffer/isobutane- or buffer/F-propane-interface and lysozyme at the buffer/F-decalin-interface should be investigated. The result and the comparison with the findings of this work will reveal whether the type of gas or the stability of the protein is responsible for the resulting observations.

Further studies are required to gain more detailed insight into the influence of gases on DPPC Langmuir films. The experiments only provide information on vertical structure and density and no conclusions can be drawn about the lateral order. Adsorption studies with different vaporised perfluorocarbons and the influence on more complex proteins reflecting the interaction of the surfactant proteins may provide further evidence for the formulation of replacement therapies. Here, GIXD and BAM measurements may reveal further details of the interaction. In a next step, the re-spreadability of DPPC from the subphase (Gibbs isotherm) can be tested in the presence of surface-active proteins and vaporised perfluorocarbons.

Apart from that, the temperature-dependent phase behaviour of DMPC bilayers on solid substrates should first be examined to find the appropriate temperature for the physiologically relevant (liquid-crystalline) fluid phase for further phase- and salt

concentration-dependent ion binding studies. The protocol for the preparation of substrate-bound DMPC bilayers by spin-coating, which was established in this thesis, is simple, fast and successful in application. Even in a fully hydrated state the layers are homogeneous and stable. They are useful for the investigation of interfacial processes on zwitterionic bilayers. Since the binding of divalent cations to zwitterionic DPPC Langmuir films is presumably surface pressure-dependent, measurements at different lipid surface coverage and salt concentrations can provide further evidence of the binding stoichiometry and induction of structural changes. In addition, DPPA monolayers can be investigated for stoichiometric ratio changes under constant pH-values and salt concentrations. For this purpose, preparation methods are suitable, whereby lipids are spread onto the salt subphase at the appropriate pH-value and salt content. By using different pH-values more can be learned about the electrostatic/hydrogen bond switch mechanism of the phosphomonoester headgroup.

Appendix A

Supplementary Information: Additional measurements

The figures A.1 and A.2 show the effect of F-decalin saturated nitrogen on a DPPA Langmuir film with an initial surface pressure of 5 mN/m and 20 mN/m, respectively. The measurements were conducted using a Langmuir through at the laboratory diffractometer D8. Figure A.3 shows the XRR data of solid-supported monolayer under

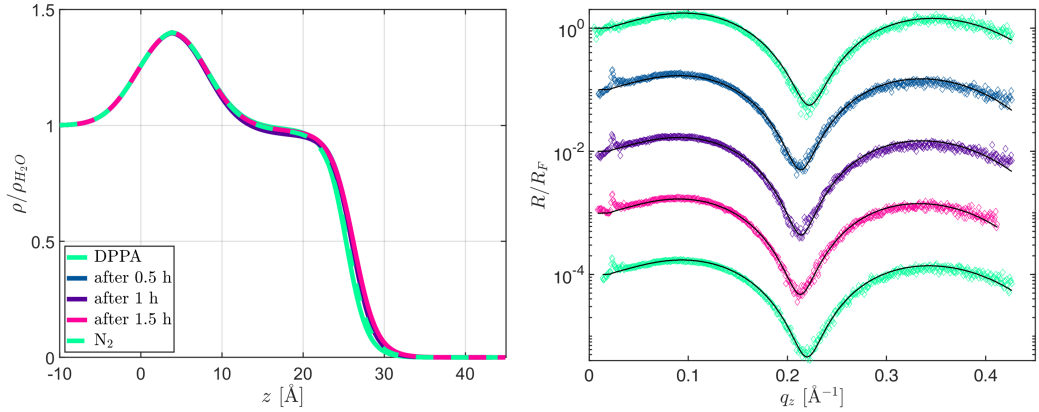

Figure A.1: Left: Electron density profiles of a DPPA-film with an initial surface pressure of 5 mN/m before, while and after flushing with F-decalin. Right: Fresnel normalised XRR data and refinements. The surface pressure increased during flushing to about 8 mN/m.

different F-butane pressures. The monolayer was prepared via Langmuir-Blodgett technique. Figure A.4 depicts the volume fraction profiles (left) and excess electrons per area (right) of the data shown in figure A.3. The calculated area of one DMPC lipid molecule is 65.7 Å^2.

Figure A.5 shows the XRR data of DPPC multilayers under different F-butane gas pressures. Figure A.6 depicts the magnified XRR curves (top) and Gaussian fits.

Figure A.7 illustrates the bi- and multilayer thicknesses of the system shown in figure

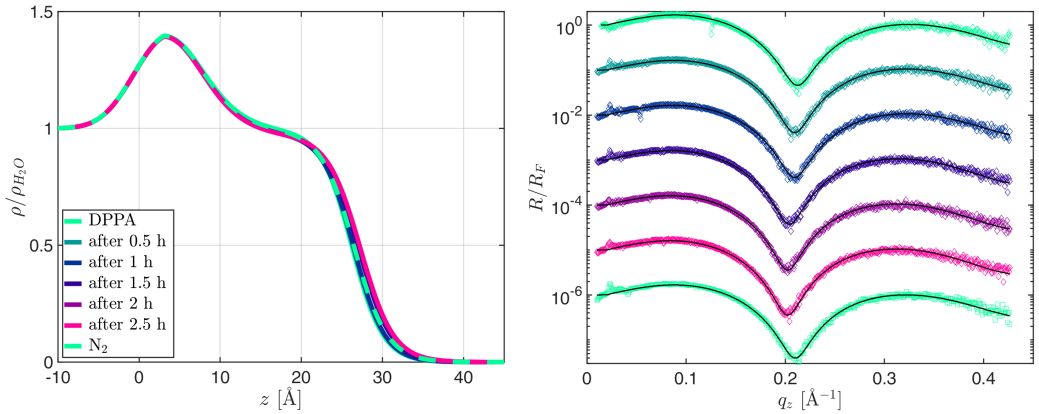

Figure A.2: Left: Obtained electron density profiles of a DPPC-film with an initial surface pressure of 20 mN/m before, while and after flushing with F-decalin. Right: Fresnel normalised XRR data and refinements. The surface pressure increased during flushing to about 21.4 mN/m.

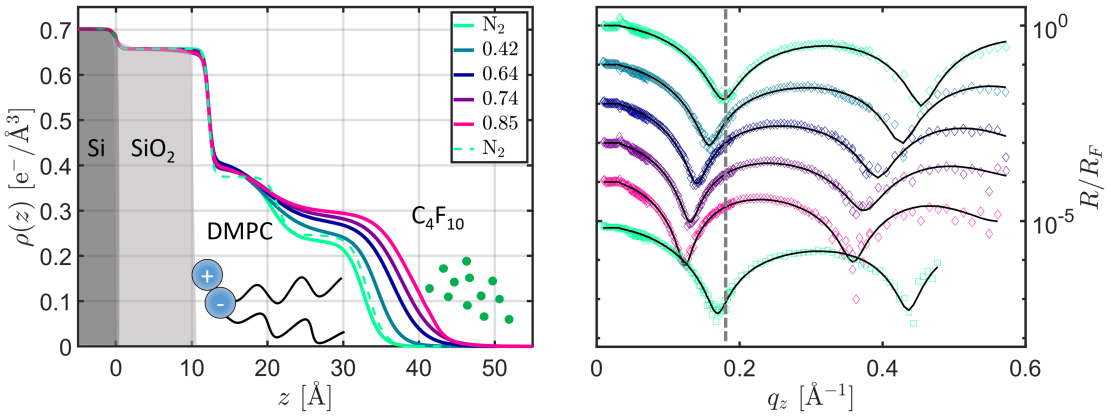

Figure A.3: Left: Electron density profiles with a schematic sketch of the underlying model. Right: Fresnel normalised x-ray reflectivity curves, shifted vertically for clarity, of the measurements of a solid-supported DMPC monolayer prepared by Langmuir-Blodgett technique on a silicon/silicon dioxide wafer at 294.15 K under different F-butane gas pressures. Diamonds: data, solid lines: fits, squares: decreasing gas pressure.

A.6. Figure A.8 shows the XRR data of DMPC multilayer under different isobutane gas pressures. Figure A.9 depicts magnified XRR curves of figure A.8 and fitted Gaussian curves.

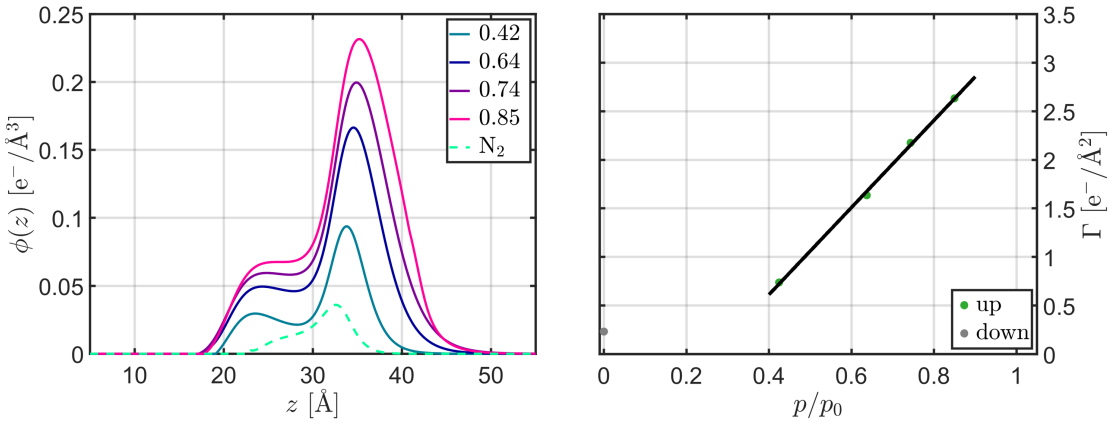

Figure A.4: Left: Volume fraction profiles. Dotted lines: after pressure release. Right: Excess electrons per area. Temperature was set to 294.15 K.

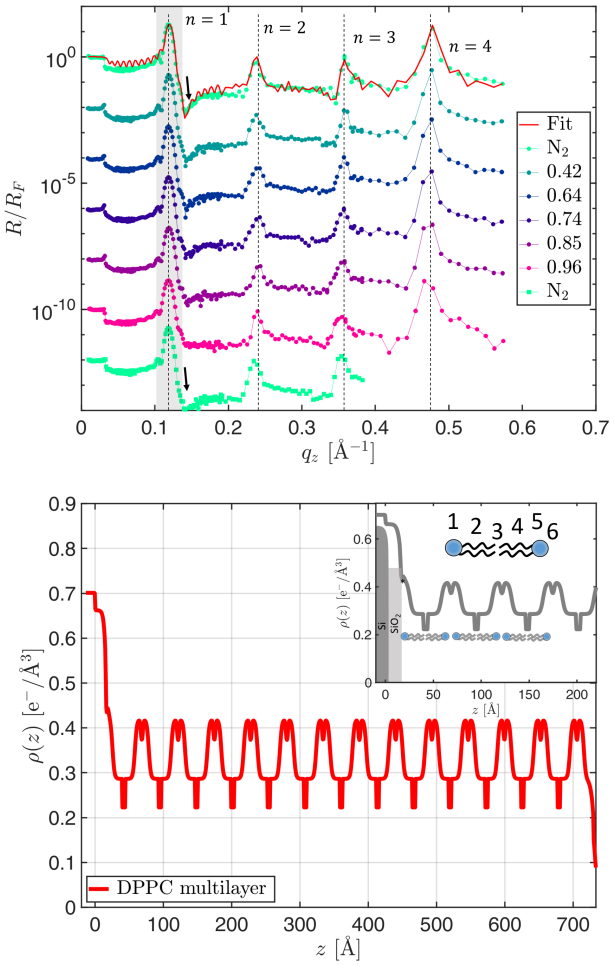

Figure A.5: Top: Fresnel normalised XRR curves (shifted vertically for clarity) of a solid-supported DPPC multilayer on previously hydrophilised silicon/silicon dioxide wafer collected at a temperature of 294.15 K under air and with increasing F-butane pressures. Squares: removing gas and measurement at air, red solid line: refinement. The black dotted lines emphasise the unchanged Bragg reflections. The arrows indicate the negative peaks. Bottom: From the refinement of the reference measurement obtained electron density profile. The inset shows a zoom of the first 220 Å of the profile and the six sublayers of the model system. The additional layer to simulate the influence of the substrate on the first layer is marked by a star (*).

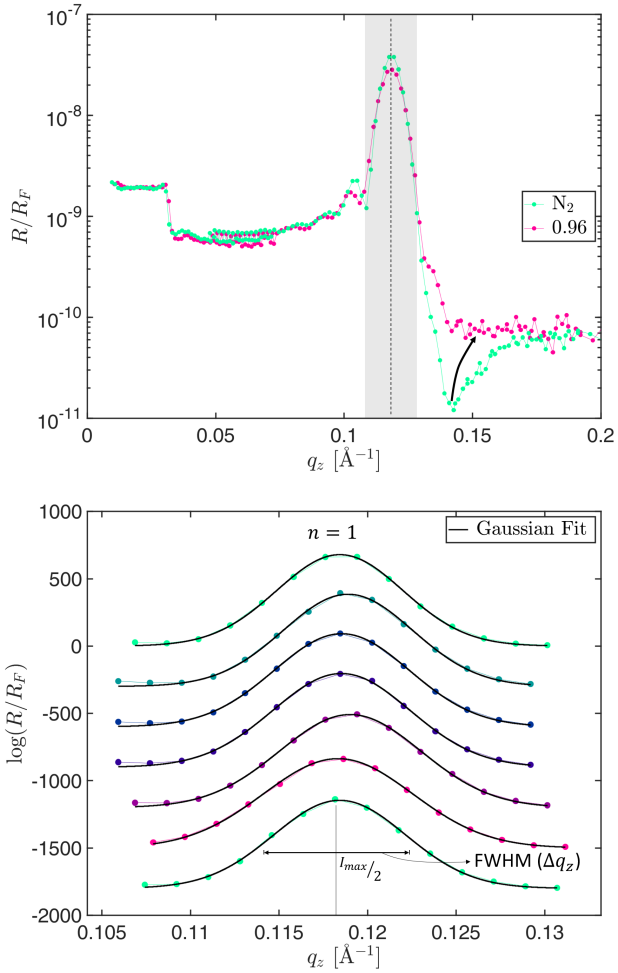

Figure A.6: Top: Region around the first order Bragg reflection of the XRR curves from figure A.5 to highlight the modification of the negative peak of the reference XRR curve by applying F-butane gas ($p/p_0 = 0.96$) into the sample cell. The arrow marks the disappearance of the negative peak. Bottom: The Bragg maxima and the fitted Gaussian curves (black solid lines). The colours corresponds to those in figure A.5.

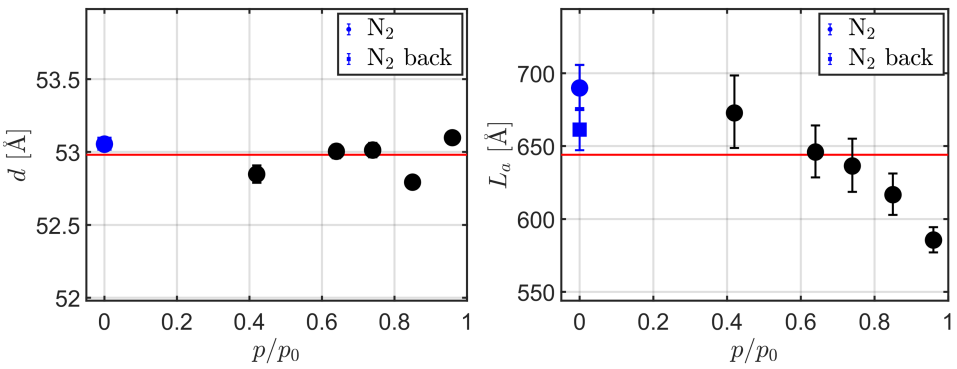

Figure A.7: Left: Extracted bilayer thicknesses from the Gaussian fits to the data from figure A.6 and the calculated thicknesses via equation (4.4) of the DPPC multilayer in dependence of the different F-butane gas pressures. The error bars are calculated from the Gaussian fit to the Bragg peak position ($q_{z,\mathrm{Bragg}}$). Right: Extracted multilayer thicknesses L_a of the system using equation (4.3) and the before calculated proportionality factor of 0.93. The error bars are calculated from the Gaussian fits.

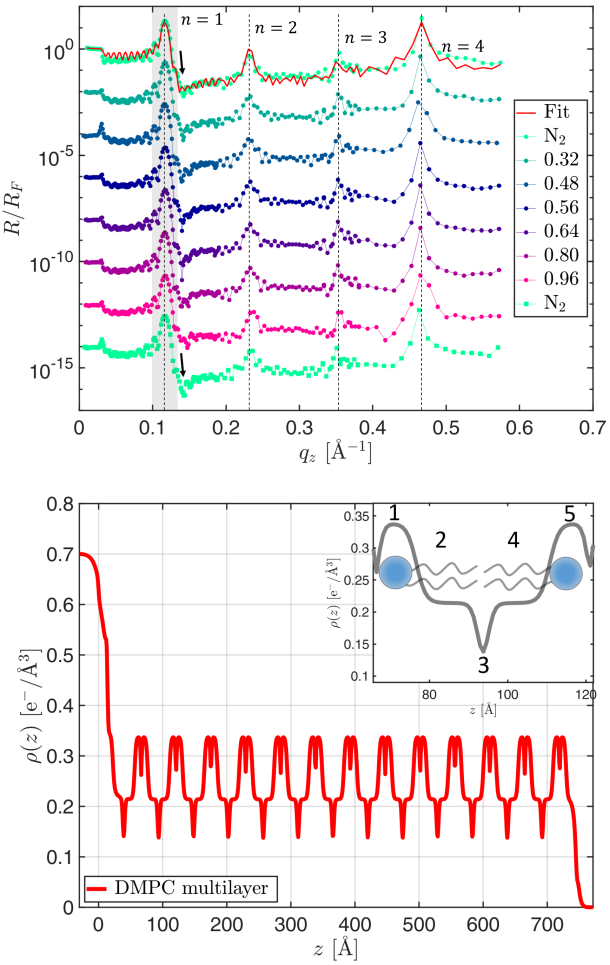

Figure A.8: Top: Fresnel normalised XRR curves (shifted vertically for clarity) for a solid-supported DMPC multilayer on previously hydrophilised silicon/silicon dioxide wafer collected at a temperature of 294.15 K under air and with increasing isobutane gas pressure. Squares: removing gas and measurement at air, red solid line: refinement. The black dotted lines highlight the unchanged Bragg peaks (position and widening). The arrows indicate the negative peaks. Bottom: Obtained reference electron density profile. The inset shows a zoom of a bilayer structure of the profile and the six sublayers of the model system. The additional layer to simulate the influence of the substrate on the first layer is marked by a star (*).

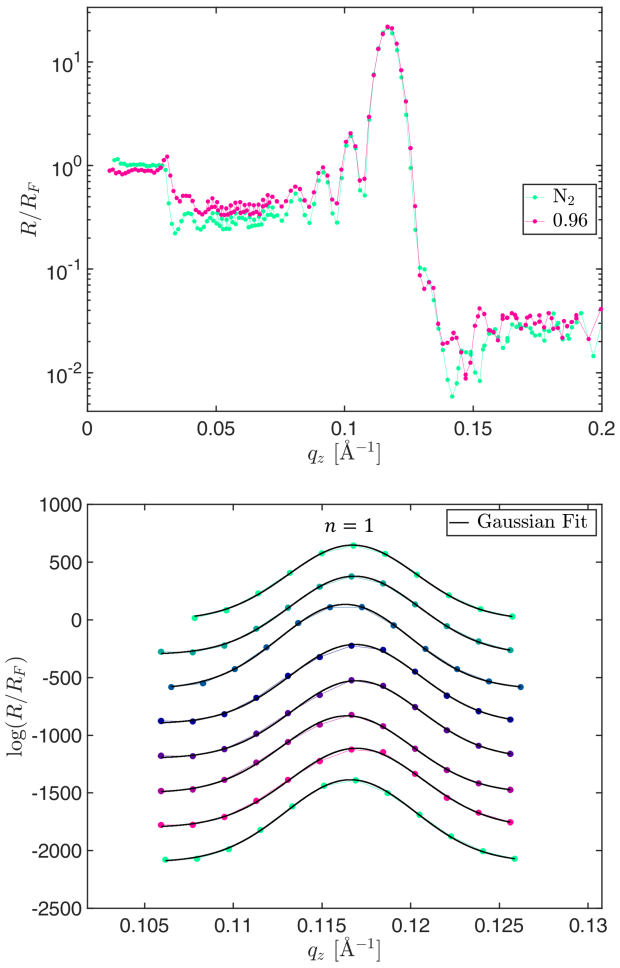

Figure A.9: Top: Region around the first order Bragg reflection of the XRR curves from figure A.8 to highlight the absent modification of the negative peak of the reference XRR curve by applying isobutane gas ($p/p_0 = 0.96$) into the sample cell. Bottom: The Bragg maxima and the fitted Gaussian curves (black solid lines). The colours corresponds to those in figure A.8.

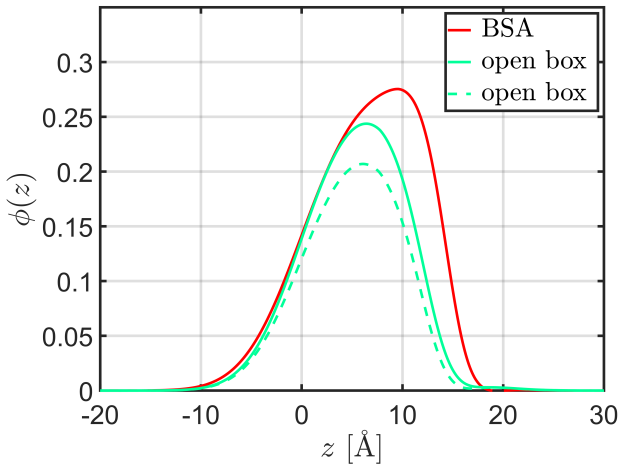

Figure A.10: Volume fraction profiles corresponding to figure 5.47.

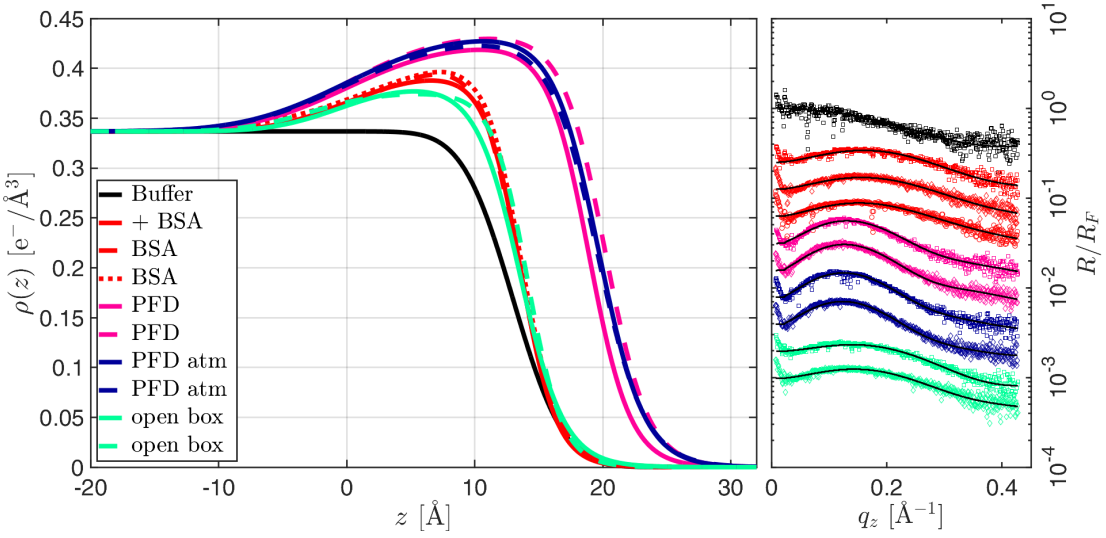

Figure A.11: XRR data of the measurements of the adsorption of BSA at the water/air-interface during flushing of F-decalin saturated nitrogen. Left: Electron density profiles corresponding to the refinements. The continuous flow of the vFC is labelled as "PFD", the measurements at F-decalin atmosphere as "PFD atm". Right: Fresnel normalised XRR curves, vertically shifted for clarity. The fits to the data are shown as solid black lines.

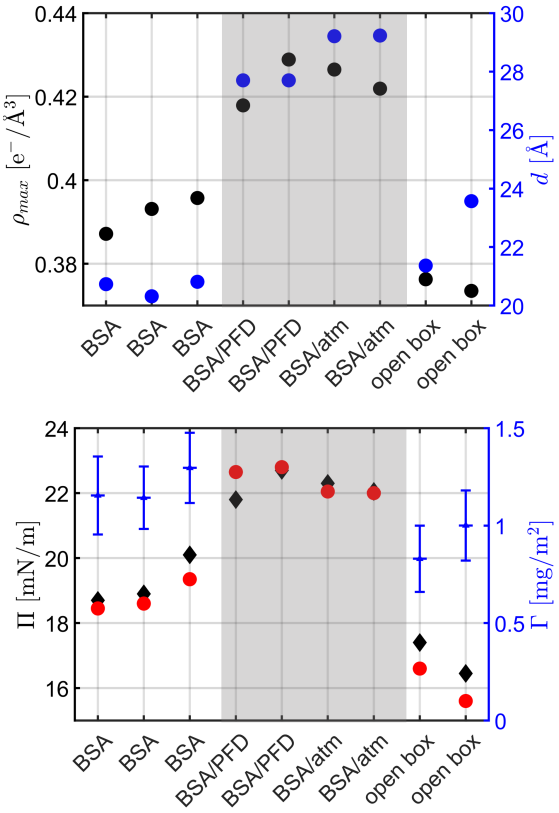

Figure A.12: Top: Maximal detected electron densities and thicknesses of the interfacial film over time and in the presence and absence of F-decalin. The grey box highlights the presence of F-decalin. Bottom: Variation of the surface pressure over time and calculated adsorbed amount of the BSA film in the absence of F-decalin. The errors are estimated by variation of the refinement parameters.

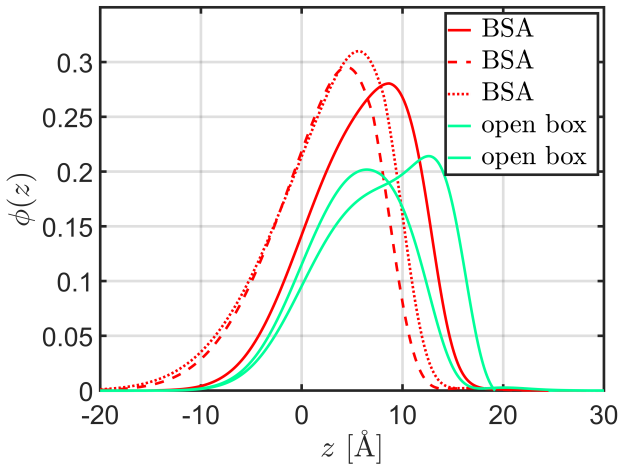

Figure A.13: Volume fraction profiles corresponding to figure A.11.

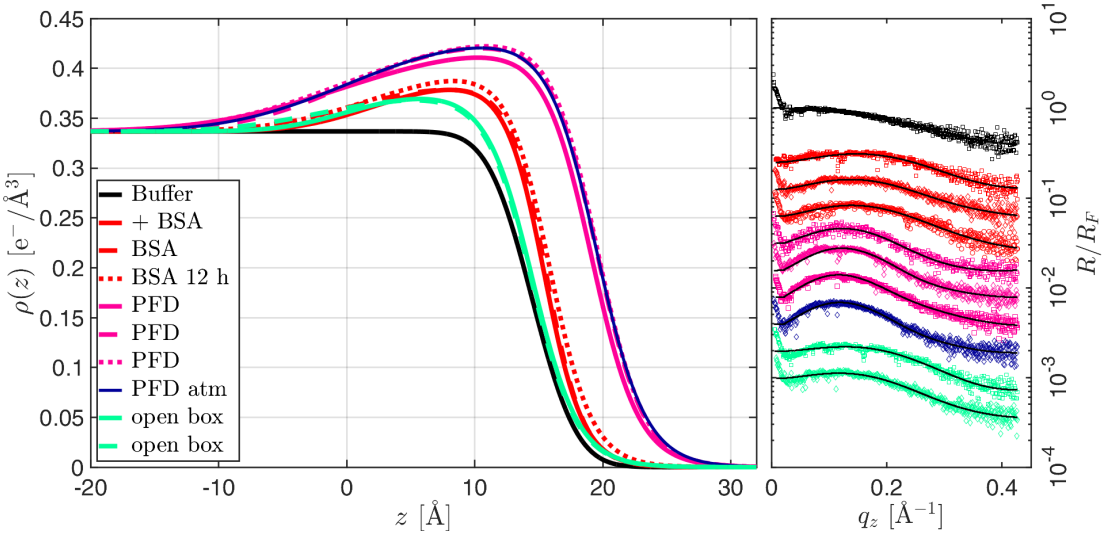

Figure A.14: XRR data of the measurements of the adsorption of BSA (for 12 hours) at the water/air-interface during flushing of F-decalin saturated nitrogen. Left: Electron density profiles corresponding to the refinements. The continuous flow of the vFC is labelled as "PFD", the measurements at F-decalin atmosphere as "PFD atm". Right: Fresnel normalised XRR curves, vertically shifted for clarity. The fits to the data are shown as solid black lines.

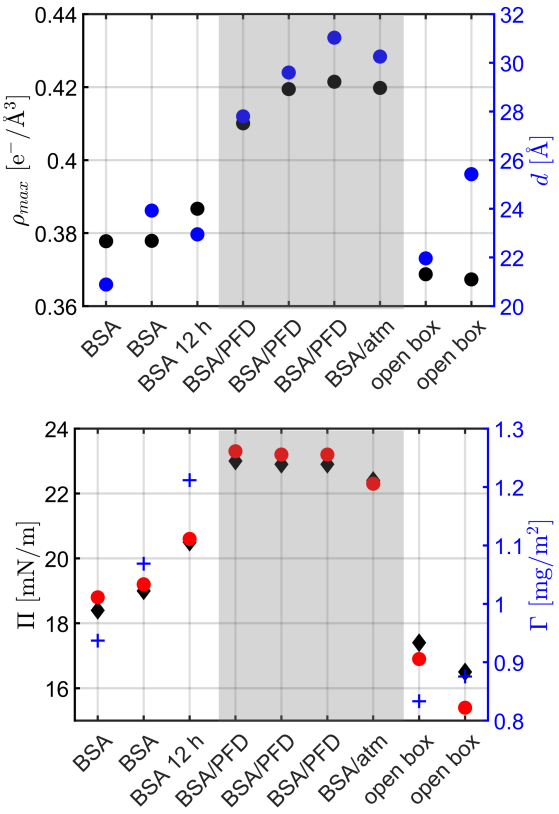

Figure A.15: Top: Maximal detected electron densities and thicknesses of the interfacial film over time and in the presence and absence of F-decalin. The grey box highlights the presence of F-decalin. Bottom: Variation of the surface pressure over time and calculated adsorbed amount of the BSA film in the absence of F-decalin.

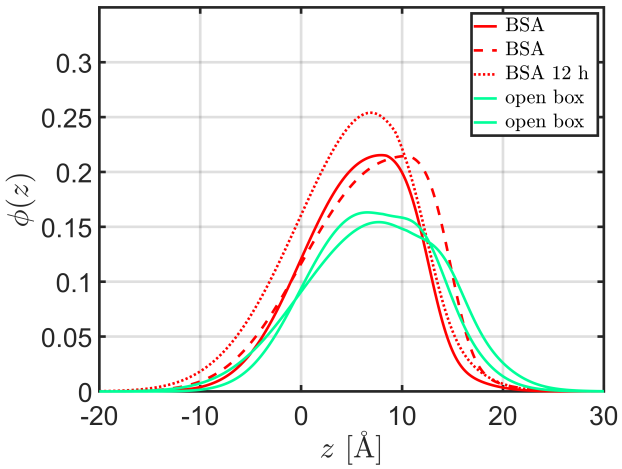

Figure A.16: Volume fraction profiles corresponding to figure A.14.

Appendix B

Supplementary Information: Technical drawings

1. Technical drawing: Gas pressure cell (Solid/gas-interface)

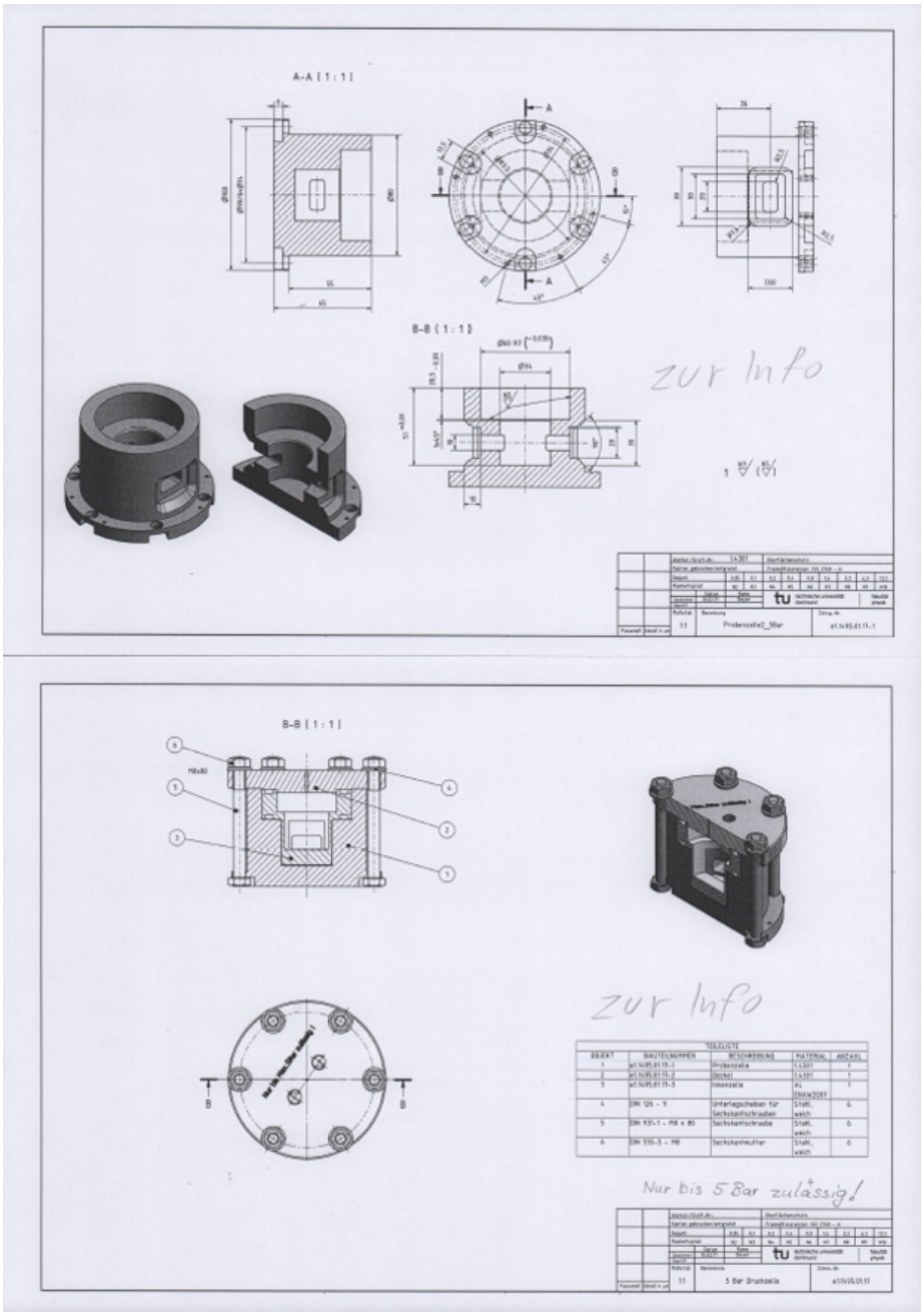

Figure B.1: Technical drawing part I of the gas pressure cell for measurements at solid/gas-interfaces.

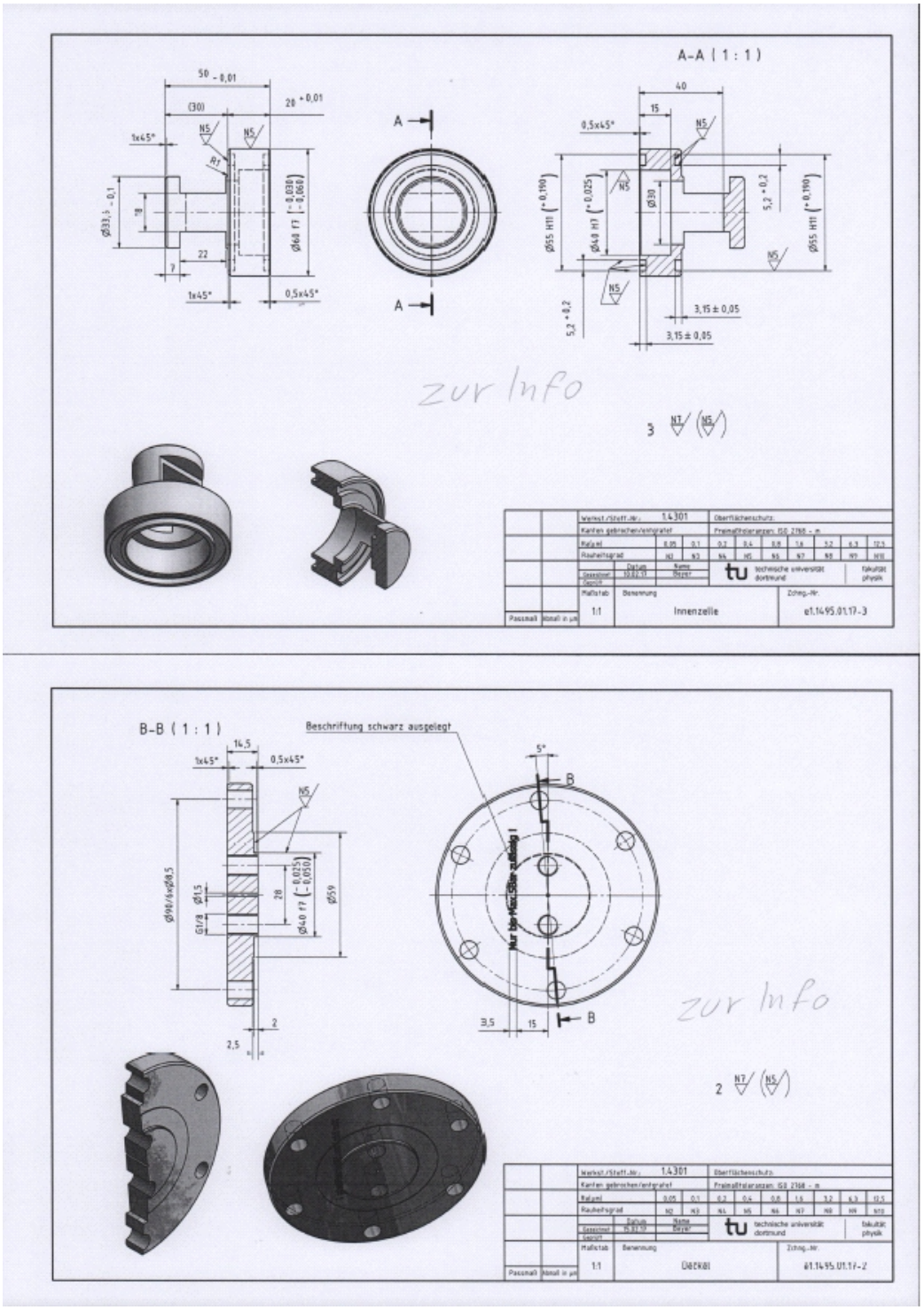

Figure B.2: Technical drawing part II of the gas pressure cell for measurements at solid/gas-interfaces.

List of Figures

List of Tables

Bibliography

[1] Frédéric Gerber et al., "Fluidization of a dipalmitoyl phosphatidylcholine monolayer by fluorocarbon gases: potential use in lung surfactant therapy", in: *Biophysical journal* 90.9 (2006), pp. 3184–3192.

[2] Frédéric Gerber, Marie Pierre Krafft, and Thierry F Vandamme, "The detrimental effect of serum albumin on the re-spreading of a dipalmitoyl phosphatidylcholine Langmuir monolayer is counteracted by a fluorocarbon gas", in: *Biochimica et Biophysica Acta (BBA)-Biomembranes* 1768.3 (2007), pp. 490–494.

[3] VB Fainerman, EV Aksenenko, and Reinhard Miller, "Influence of alkane and perfluorocarbon vapors on adsorbed surface layers and spread insoluble monolayers of surfactants, proteins and lipids", in: *Advances in colloid and interface science* 244 (2017), pp. 100–112.

[4] Da Shi et al., "Fluorocarbon Exposure Mode Markedly Affects Phospholipid Monolayer Behavior at the Gas/Liquid Interface: Impact on Size and Stability of Microbubbles", in: *Langmuir* 35.31 (2018), pp. 10025–10033.

[5] Robert M Hanson et al., "JSmol and the next-generation web-based representation of 3D molecular structure as applied to proteopedia", in: *Israel Journal of Chemistry* 53.3-4 (2013), pp. 207–216.

[6] *Jmol: an open-source browser-based HTML5 viewer and stand-alone Java viewer for chemical structures in 3D*, URL: `http://jmol.sourceforge.net/`.

[7] Matej Orešič, Virve A Hänninen, and Antonio Vidal Puig, "Lipidomics: a new window to biomedical frontiers", in: *Trends in biotechnology* 26.12 (2008), pp. 647–652.

[8] Andrew D Watson, "Thematic review series: systems biology approaches to metabolic and cardiovascular disorders. Lipidomics: a global approach to lipid analysis in biological systems", in: *Journal of lipid research* 47.10 (2006), pp. 2101–2111.

[9] Tzong-Hsien Lee et al., "Exploring molecular-biomembrane interactions with surface plasmon resonance and dual polarization interferometry technology: expanding the spotlight onto biomembrane structure", in: *Chemical reviews* 118.11 (2018), pp. 5392–5487.

[10] William A Prinz, "Lipid trafficking sans vesicles: where, why, how?", in: *Cell* 143.6 (2010), pp. 870–874.

[11] Yechezkel Barenholz, "Liposomology", in: *Progress in lipid research* 39.1 (2000), pp. 1–2.

[12] Gerrit Van Meer, Dennis R Voelker, and Gerald W Feigenson, "Membrane lipids: where they are and how they behave", in: *Nature reviews Molecular cell biology* 9.2 (2008), pp. 112–124.

[13] Evgenia Glukhov et al., "Basis for selectivity of cationic antimicrobial peptides for bacterial versus mammalian membranes", in: *Journal of Biological Chemistry* 280.40 (2005), pp. 33960–33967.

[14] Christian Sohlenkamp and Otto Geiger, "Bacterial membrane lipids: diversity in structures and pathways", in: *FEMS microbiology reviews* 40.1 (2016), pp. 133–159.

[15] Joshua B Parsons and Charles O Rock, "Bacterial lipids: metabolism and membrane homeostasis", in: *Progress in lipid research* 52.3 (2013), pp. 249–276.

[16] Zhen Huang and Erwin London, "Cholesterol lipids and cholesterol-containing lipid rafts in bacteria", in: *Chemistry and physics of lipids* 199 (2016), pp. 11–16.

[17] Laura Villanueva, Jaap S Sinninghe Damsté, and Stefan Schouten, "A re-evaluation of the archaeal membrane lipid biosynthetic pathway", in: *Nature Reviews Microbiology* 12.6 (2014), pp. 438–448.

[18] Yan Boucher, Masahiro Kamekura, and W Ford Doolittle, "Origins and evolution of isoprenoid lipid biosynthesis in archaea", in: *Molecular microbiology* 52.2 (2004), pp. 515–527.

[19] Tomáš Řezanka et al., "Lipidomic analysis: from archaea to mammals", in: *Lipids* 53.1 (2018), pp. 5–25.

[20] William Dowhan, Mikhail Bogdanov, and Eugenia Mileykovskaya, "Functional roles of lipids in membranes", in: *Biochemistry of lipids, lipoproteins and membranes*, Elsevier, 2008, pp. 1–37.

[21] William Dowhan, Mikhail Bogdanov, and Eugenia Mileykovskaya, "Functional roles of lipids in membranes", in: *Biochemistry of lipids, lipoproteins and membranes*, Elsevier, 2016, pp. 1–40.

[22] Lynn Margulis, "Symbiotic theory of the origin of eukaryotic organelles; criteria for proof.", in: *Symposia of the Society for Experimental Biology*, 29, 1975, pp. 21–38.

[23] B Franz Lang, Michael W Gray, and Gertraud Burger, "Mitochondrial genome evolution and the origin of eukaryotes", in: *Annual review of genetics* 33.1 (1999), pp. 351–397.

[24] František Baluška, "Cell-Cell Channels, Viruses, and Evolution: Via Infection, Parasitism, and Symbiosis toward Higher Levels of Biological Complexity", in: *Annals of the New York Academy of Sciences* 1178.1 (2009), pp. 106–119.

[25] Manabu T Nakamura, Barbara E Yudell, and Juan J Loor, "Regulation of energy metabolism by long-chain fatty acids", in: *Progress in lipid research* 53 (2014), pp. 124–144.

[26] Antoine-Emmanuel Saliba, Ivana Vonkova, and Anne-Claude Gavin, "The systematic analysis of protein–lipid interactions comes of age", in: *Nature Reviews Molecular Cell Biology* 16.12 (2015), pp. 753–761.

[27] Takao Shimizu, "Lipid mediators in health and disease: enzymes and receptors as therapeutic targets for the regulation of immunity and inflammation", in: *Annual review of pharmacology and toxicology* 49 (2009), pp. 123–150.

[28] Francesc-Xabier Contreras et al., "Specificity of intramembrane protein–lipid interactions", in: *Cold Spring Harbor perspectives in biology* 3.6 (2011), a004705.

[29] Arthur Laganowsky et al., "Membrane proteins bind lipids selectively to modulate their structure and function", in: *Nature* 510.7503 (2014), pp. 172–175.

[30] Takeshi Harayama and Howard Riezman, "Understanding the diversity of membrane lipid composition", in: *Nature Ecology & Evolution* (2018), pp. 1–18.

[31] Evert Gorter and FJEM Grendel, "On bimolecular layers of lipoids on the chromocytes of the blood", in: *Journal of experimental medicine* 41.4 (1925), pp. 439–443.

[32] James Frederic Danielli and Hugh Davson, "A contribution to the theory of permeability of thin films", in: *Journal of cellular and comparative physiology* 5.4 (1935), pp. 495–508.

[33] JD Robertson, "The cell membrane concept", in: *JOURNAL OF PHYSIOLOGY-LONDON*, vol. 140, 3, CAMBRIDGE UNIV PRESS 40 WEST 20TH STREET, NEW YORK, NY 10011-4211, 1958, P58–P59.

[34] S Jonathan Singer and Garth L Nicolson, "The fluid mosaic model of the structure of cell membranes", in: *Science* 175.4023 (1972), pp. 720–731.

[35] OG Mouritsen and MYER Bloom, "Mattress model of lipid-protein interactions in membranes", in: *Biophysical journal* 46.2 (1984), pp. 141–153.

[36] Ken Jacobson, Erin D Sheets, and Rudolf Simson, "Revisiting the fluid mosaic model of membranes", in: *Science* 268.5216 (1995), pp. 1441–1443.

[37] G Vereb et al., "Dynamic, yet structured: the cell membrane three decades after the Singer–Nicolson model", in: *Proceedings of the national academy of sciences* 100.14 (2003), pp. 8053–8058.

[38] Kai Simons and Elina Ikonen, "Functional rafts in cell membranes", in: *Nature* 387.6633 (1997), p. 569.

[39] Kai Simons and Derek Toomre, "Lipid rafts and signal transduction", in: *Nature reviews Molecular cell biology* 1.1 (2000), p. 31.

[40] DA Brown and E London, "Structure and origin of ordered lipid domains in biological membranes", in: *The Journal of membrane biology* 164.2 (1998), pp. 103–114.

[41] Kai Simons and Winchil LC Vaz, "Model systems, lipid rafts, and cell membranes", in: *Annu. Rev. Biophys. Biomol. Struct.* 33 (2004), pp. 269–295.

[42] PR t Cullis and B de Kruijff, "Lipid polymorphism and the functional roles of lipids in biological membranes", in: *Biochimica et Biophysica Acta (BBA)-Reviews on Biomembranes* 559.4 (1979), pp. 399–420.

[43] Leonid Chernomordik, "Non-bilayer lipids and biological fusion intermediates", in: *Chemistry and physics of lipids* 81.2 (1996), pp. 203–213.

[44] Md Rejwan Ali, Kwan Hon Cheng, and Juyang Huang, "Ceramide drives cholesterol out of the ordered lipid bilayer phase into the crystal phase in 1-palmitoyl-2-oleoyl-sn-glycero-3-phosphocholine/cholesterol/ceramide ternary mixtures", in: *Biochemistry* 45.41 (2006), pp. 12629–12638.

[45] Juyang Huang and Gerald W Feigenson, "A microscopic interaction model of maximum solubility of cholesterol in lipid bilayers", in: *Biophysical journal* 76.4 (1999), pp. 2142–2157.

[46] E Fahy et al., "A comprehensive classification system for lipids", in: *J. Lipid Res* 46 (2005), pp. 839–862.

[47] Gerrit van Meer, "Cellular lipidomics", in: *The EMBO journal* 24.18 (2005), pp. 3159–3165.

[48] John F Hancock, "Lipid rafts: contentious only from simplistic standpoints", in: *Nature Reviews Molecular Cell Biology* 7.6 (2006), p. 456.

[49] Leonard J Foster, Carmen L de Hoog, and Matthias Mann, "Unbiased quantitative proteomics of lipid rafts reveals high specificity for signaling factors", in: *Proceedings of the National Academy of Sciences* 100.10 (2003), pp. 5813–5818.

[50] Hermann-Josef Kaiser et al., "Order of lipid phases in model and plasma membranes", in: *Proceedings of the National Academy of Sciences* 106.39 (2009), pp. 16645–16650.

[51] Daniel Lingwood and Kai Simons, "Lipid rafts as a membrane-organizing principle", in: *science* 327.5961 (2010), pp. 46–50.

[52] John A Allen, Robyn A Halverson-Tamboli, and Mark M Rasenick, "Lipid raft microdomains and neurotransmitter signalling", in: *Nature reviews neuroscience* 8.2 (2007), pp. 128–140.

[53] Peter J Quinn, Dennis Chapman, and Alec D Keith, "The Dynamics Of Membrane Structur", in: *Critical Reviews in Biochemistry* 8.1 (1980), pp. 1–117.

[54] Rainer A Böckmann et al., "Effect of sodium chloride on a lipid bilayer", in: *Biophysical journal* 85.3 (2003), pp. 1647–1655.

[55] L. Stryer J. M. Berg and J. L. Tymoczko, *Biochemistry*, Springer Verlag, 2015.

[56] Wia Baron and Dick Hoekstra, "On the biogenesis of myelin membranes: sorting, trafficking and cell polarity", in: *FEBS letters* 584.9 (2010), pp. 1760–1770.

[57] William T Norton et al., "The lipid composition of isolated brain cells and axons", in: *Journal of neuroscience research* 1.1 (1975), pp. 57–75.

[58] P St Sastry, "Lipids of nervous tissue: composition and metabolism", in: *Progress in lipid research* 24.2 (1985), pp. 69–176.

[59] Victor W Rodwell et al., *Harper's illustrated biochemistry*, McGraw-Hill Education, 2015.

[60] William Stillwell, "Chapter 6 - Membrane Proteins", in: *An Introduction to Biological Membranes (Second Edition)*, ed. by William Stillwell, Second Edition, Elsevier, 2016, pp. 89–110, ISBN: 978-0-444-63772-7, DOI: https://doi.org/10.1016/B978-0-444-63772-7.00006-3, URL: http://www.sciencedirect.com/science/article/pii/B9780444637727000063.

[61] Robert B Gennis, *Biomembranes: molecular structure and function*, Springer Science & Business Media, 2013.

[62] RFS Walters and WF DeGrado, "Helix-packing motifs in membrane proteins", in: *Proceedings of the National Academy of Sciences* 103.37 (2006), pp. 13658–13663.

[63] Hayley J Sharpe, Tim J Stevens, and Sean Munro, "A comprehensive comparison of transmembrane domains reveals organelle-specific properties", in: *Cell* 142.1 (2010), pp. 158–169.

[64] Markus Sällman Almén et al., "Mapping the human membrane proteome: a majority of the human membrane proteins can be classified according to function and evolutionary origin", in: *BMC biology* 7.1 (2009), p. 50.

[65] Timothy J Stevens and Isaiah T Arkin, "Do more complex organisms have a greater proportion of membrane proteins in their genomes?", in: *Proteins: Structure, Function, and Bioinformatics* 39.4 (2000), pp. 417–420.

[66] Reinhard Lipowsky and Erich Sackmann, *Structure and dynamics of membranes: I. from cells to vesicles/II. generic and specific interactions*, Elsevier, 1995.

[67] Erick J Dufourc, "Sterols and membrane dynamics", in: *Journal of chemical biology* 1.1-4 (2008), pp. 63–77.

[68] Gerrit van Meer and Anton IPM de Kroon, "Lipid map of the mammalian cell", in: *J Cell Sci* 124.1 (2011), pp. 5–8.

[69] Kai Simons and Julio L Sampaio, "Membrane organization and lipid rafts", in: *Cold Spring Harbor perspectives in biology* 3.10 (2011), a004697.

[70] Eoin Fahy et al., "Update of the LIPID MAPS comprehensive classification system for lipids", in: *Journal of lipid research* 50.Supplement (2009), S9–S14.

[71] Wolfgang Bernhard et al., "Phosphatidylcholine molecular species in lung surfactant: composition in relation to respiratory rate and lung development", in: *American journal of respiratory cell and molecular biology* 25.6 (2001), pp. 725–731.

[72] Günther Daum, "Lipids of mitochondria", in: *Biochimica et Biophysica Acta (BBA)-Reviews on Biomembranes* 822.1 (1985), pp. 1–42.

[73] W Dowhan, "Molecular basis for membrane phospholipid diversity: why are there so many lipids?", in: *Annual review of biochemistry* 66.1 (1997), pp. 199–232.

[74] Erik Goormaghtigh et al., "Evidence of a specific complex between adriamycin and negatively-charged phospholipids", in: *Biochimica et Biophysica Acta (BBA)-Biomembranes* 597.1 (1980), pp. 1–14.

[75] Tung Ming Fong and Mark G McNamee, "Stabilization of acetylcholine receptor secondary structure by cholesterol and negatively charged phospholipids in membranes", in: *Biochemistry* 26.13 (1987), pp. 3871–3880.

[76] Piet WM Van Dijck, "Negatively charged phospholipids and their position in the cholesterol affinity sequence", in: *Biochimica et Biophysica Acta (BBA)-Biomembranes* 555.1 (1979), pp. 89–101.

[77] Sanja Pöyry and Ilpo Vattulainen, "Role of charged lipids in membrane structures—insight given by simulations", in: *Biochimica et Biophysica Acta (BBA)-Biomembranes* 1858.10 (2016), pp. 2322–2333.

[78] Bruce Alberts et al., "Molecular biology of the cell: Garland Pub", in: *Inc., London* (2002).

[79] Derek Marsh, "Lateral pressure profile, spontaneous curvature frustration, and the incorporation and conformation of proteins in membranes", in: *Biophysical journal* 93.11 (2007), pp. 3884–3899.

[80] Norbert Kučerka, Stephanie Tristram-Nagle, and John F Nagle, "Structure of fully hydrated fluid phase lipid bilayers with monounsaturated chains", in: *The Journal of membrane biology* 208.3 (2006), pp. 193–202.

[81] Benedikt Nowak et al., "Solid-supported lipid multilayers under high hydrostatic pressure", in: *Langmuir* 32.11 (2016), pp. 2638–2643.

[82] Ulrike Mennicke and Tim Salditt, "Preparation of solid-supported lipid bilayers by spin-coating", in: *Langmuir* 18.21 (2002), pp. 8172–8177.

[83] Ulrike Mennicke, Doru Constantin, and Tim Salditt, "Structure and interaction potentials in solid-supported lipid membranes studied by x-ray reflectivity at varied osmotic pressure", in: *The European Physical Journal E* 20.2 (2006), pp. 221–230.

[84] Göran Surmeier et al., "Cholesterol modulates the pressure response of DMPC membranes", in: *Biophysical Chemistry* (2019), p. 106210.

[85] Karin Athenstaedt and Günther Daum, "Phosphatidic acid, a key intermediate in lipid metabolism", in: *European Journal of Biochemistry* 266.1 (1999), pp. 1–16.

[86] Edgard M Mejia and Grant M Hatch, "Mitochondrial phospholipids: role in mitochondrial function", in: *Journal of bioenergetics and biomembranes* 48.2 (2016), pp. 99–112.

[87] Nicholas T Ktistakis et al., "Evidence that phospholipase D mediates ADP ribosylation factor-dependent formation of Golgi coated vesicles.", in: *The Journal of Cell Biology* 134.2 (1996), pp. 295–306.

[88] Ye-Guang Chen et al., "Phospholipase D stimulates release of nascent secretory vesicles from the trans-Golgi network", in: *The Journal of cell biology* 138.3 (1997), pp. 495–504.

[89] Edgar E Kooijman et al., "Modulation of membrane curvature by phosphatidic acid and lysophosphatidic acid", in: *Traffic* 4.3 (2003), pp. 162–174.

[90] Edgar E Kooijman et al., "What makes the bioactive lipids phosphatidic acid and lysophosphatidic acid so special?", in: *Biochemistry* 44.51 (2005), pp. 17007–17015.

[91] Denis English, Yi Cui, and Rafat A Siddiqui, "Messenger functions of phosphatidic acid", in: *Chemistry and physics of lipids* 80.1-2 (1996), pp. 117–132.

[92] Zachary Freyberg, Anirban Siddhanta, and Dennis Shields, "'Slip, sliding away': phospholipase D and the Golgi apparatus", in: *Trends in cell biology* 13.10 (2003), pp. 540–546.

[93] Christa Testerink and Teun Munnik, "Phosphatidic acid: a multifunctional stress signaling lipid in plants", in: *Trends in plant science* 10.8 (2005), pp. 368–375.

[94] John JH Shin and Christopher JR Loewen, "Putting the pH into phosphatidic acid signaling", in: *BMC biology* 9.1 (2011), p. 85.

[95] Barry P Young et al., "Phosphatidic acid is a pH biosensor that links membrane biogenesis to metabolism", in: *Science* 329.5995 (2010), pp. 1085–1088.

[96] Carol V Robinson, Tibor Rohacs, and Scott B Hansen, "Tools for understanding nanoscale lipid regulation of ion channels", in: *Trends in biochemical sciences* (2019).

[97] Yannick Comoglio et al., "Phospholipase D2 specifically regulates TREK potassium channels via direct interaction and local production of phosphatidic acid", in: *Proceedings of the National Academy of Sciences* 111.37 (2014), pp. 13547–13552.

[98] Christine Delon et al., "Sphingosine kinase 1 is an intracellular effector of phosphatidic acid", in: *Journal of Biological Chemistry* 279.43 (2004), pp. 44763–44774.

[99] C Limatola et al., "Phosphatidic acid activation of protein kinase C-ζ overexpressed in COS cells: comparison with other protein kinase C isotypes and other acidic lipids", in: *Biochemical Journal* 304.3 (1994), pp. 1001–1008.

[100] Philippe Gascard et al., "Asymmetric distribution of phosphoinositides and phosphatidic acid in the human erythrocyte membrane", in: *Biochimica et Biophysica Acta (BBA)-Biomembranes* 1069.1 (1991), pp. 27–36.

[101] Mikhail A Zhukovsky et al., "Phosphatidic acid in membrane rearrangements", in: *FEBS letters* 593.17 (2019), pp. 2428–2451.

[102] Jolanta Zegarlinska et al., "Phosphatidic acid–a simple phospholipid with multiple faces", in: *Acta Biochimica Polonica* 65.2 (2018), pp. 163–171.

[103] Edgar Eduard Kooijman and Koert NJ Burger, "Biophysics and function of phosphatidic acid: a molecular perspective", in: *Biochimica et Biophysica Acta (BBA)-Molecular and Cell Biology of Lipids* 1791.9 (2009), pp. 881–888.

[104] Xuemin Wang et al., "Signaling functions of phosphatidic acid", in: *Progress in lipid research* 45.3 (2006), pp. 250–278.

[105] Sergei Medvedev et al., "Phosphatidic acids mediate transport of Ca2+ and H+ through plant cell membranes", in: *Functional Plant Biology* 46.6 (2019), pp. 533–542.

[106] Jin-Hyeok Jang et al., "Understanding of the roles of phospholipase D and phosphatidic acid through their binding partners", in: *Progress in lipid research* 51.2 (2012), pp. 71–81.

[107] Catherine L Stace and Nicholas T Ktistakis, "Phosphatidic acid-and phosphatidylserine-binding proteins", in: *Biochimica et Biophysica Acta (BBA)-Molecular and Cell Biology of Lipids* 1761.8 (2006), pp. 913–926.

[108] Edgar E Kooijman et al., "Spontaneous curvature of phosphatidic acid and lysophosphatidic acid", in: *Biochemistry* 44.6 (2005), pp. 2097–2102.

[109] I Estrela-Lopis, G Brezesinski, and H Möhwald, "Miscibility of DPPC and DPPA in monolayers at the air/water interface", in: *Chemistry and physics of lipids* 131.1 (2004), pp. 71–80.

[110] M Lösche, H-P Duwe, and Helmuth Möhwald, "Quantitative analysis of surface textures in phospholipid monolayer phase transitions", in: *Journal of colloid and interface science* 126.2 (1988), pp. 432–444.

[111] Lee R Cambrea et al., "Effect of ions on the organization of phosphatidylcholine/phosphatidic acid bilayers", in: *Biophysical journal* 93.5 (2007), pp. 1630–1638.

[112] Emily R Lamberson, Lee R Cambrea, and Jennifer S Hovis, "Controlling the charge and organization of anionic lipid bilayers: effect of monovalent and divalent ions", in: *The Journal of Physical Chemistry B* 111.49 (2007), pp. 13664–13667.

[113] M Lösche and Helmuth Möhwald, "Electrostatic interactions in phospholipid membranes: II. Influence of divalent ions on monolayer structure", in: *Journal of colloid and interface science* 131.1 (1989), pp. 56–67.

[114] Gerrit van Meer and Quirine Lisman, "Sphingolipid transport: rafts and translocators", in: *Journal of Biological Chemistry* 277.29 (2002), pp. 25855–25858.

[115] Nigel M Hooper, "Detergent-insoluble glycosphingolipid/cholesterol-rich membrane domains, lipid rafts and caveolae", in: *Molecular membrane biology* 16.2 (1999), pp. 145–156.

[116] T Heimburg, *Thermal Biophysics of Membranes Wiley-VCH*, 2007.

[117] E Sackmann, "Physical basis of self-organization and function of membranes: physics of vesicles", in: *Handbook of biological physics* 1 (1995), pp. 213–304.

[118] Graham A Jamieson and David Mason Robinson, *Mammalian cell membranes: Volume 2: The diversity of membranes*, Elsevier, 2014.

[119] Peter A Leventis and Sergio Grinstein, "The distribution and function of phosphatidylserine in cellular membranes", in: *Annual review of biophysics* 39 (2010), pp. 407–427.

[120] Martin Raff et al., *Molecular Biology of the Cell 4th edition*, 2002.

[121] Mark S Bretscher, "Asymmetrical lipid bilayer structure for biological membranes", in: *Nature New Biology* 236.61 (1972), pp. 11–12.

[122] Michael Schlame, Diego Rua, and Miriam L Greenberg, "The biosynthesis and functional role of cardiolipin.", in: *Progress in lipid research* 39.3 (2000), p. 257.

[123] Helen Watson, "Biological membranes", in: *Essays in biochemistry* 59 (2015), pp. 43–69.

[124] JN Israelachvili, "Aggregation of amphiphilic molecules into micelles, bilayers, vesicles, and biological membranes", in: *Intermolecular and Surface Forces: With Applications to Colloidal and Biological Systems. Academic Press, London* (1985), pp. 60–63.

[125] Vittorio Luzzati, A_ Tardieu, and T Gulik-Krzywicki, "Polymorphism of lipids", in: *Nature* 217.5133 (1968), pp. 1028–1030.

[126] Bengt Kronberg and B Lindman, *Surfactants and polymers in aqueous solution*, John Wiley & Sons Ltd., Chichester, 2003.

[127] Wilfried Blokzijl and Jan BFN Engberts, "Hydrophobe Effekte–Ansichten und Tatsachen", in: *Angewandte Chemie* 105.11 (1993), pp. 1610–1648.

[128] VV Kumar, "Complementary molecular shapes and additivity of the packing parameter of lipids", in: *Proceedings of the National Academy of Sciences* 88.2 (1991), pp. 444–448.

[129] Himanshu Khandelia and Ilpo Vattulainen, "Lipid Organization, Aggregation, and Self-assembly", in: *Encyclopedia of Biophysics*, ed. by Gordon C. K. Roberts, Berlin, Heidelberg: Springer Berlin Heidelberg, 2013, pp. 1273–1280, ISBN: 978-3-642-16712-6, DOI: 10.1007/978-3-642-16712-6_541, URL: https://doi.org/10.1007/978-3-642-16712-6_541.

[130] Ole G Mouritsen, "Lipidology and lipidomics—-quo vadis? A new era for the physical chemistry of lipids", in: *Physical Chemistry Chemical Physics* 13.43 (2011), pp. 19195–19205.

[131] Ole G Mouritsen, "Model answers to lipid membrane questions", in: *Cold Spring Harbor perspectives in biology* 3.9 (2011), a004622.

[132] Rumiana Koynova and Martin Caffrey, "Phases and phase transitions of the phosphatidylcholines", in: *Biochimica et Biophysica Acta (BBA)-Reviews on Biomembranes* 1376.1 (1998), pp. 91–145.

[133] Roland Winter and Christoph Jeworrek, "Effect of pressure on membranes", in: *Soft Matter* 5.17 (2009), pp. 3157–3173.

[134] JN Israelachvili, "Intermolecular and surface forces: revised third edition", in: *Search PubMed* (2011), p. 704.

[135] A Anishkin, S Sukharev, and M Colombini, "Searching for the molecular arrangement of transmembrane ceramide channels", in: *Biophysical journal* 90.7 (2006), pp. 2414–2426.

[136] Stephen Hyde et al., *The language of shape: the role of curvature in condensed matter: physics, chemistry and biology*, Elsevier, 1996.

[137] JN Israelachvili, S Marčelja, and Roger G Horn, "Physical principles of membrane organization", in: *Quarterly reviews of biophysics* 13.2 (1980), pp. 121–200.

[138] Jacob N Israelachvili, D John Mitchell, and Barry W Ninham, "Theory of self-assembly of hydrocarbon amphiphiles into micelles and bilayers", in: *Journal of the Chemical Society, Faraday Transactions 2: Molecular and Chemical Physics* 72 (1976), pp. 1525–1568.

[139] Walter Kauzmann, "Some factors in the interpretation of protein denaturation", in: *Advances in protein chemistry*, vol. 14, Elsevier, 1959, pp. 1–63.

[140] Charles Tanford, *The hydrophobic effect: formation of micelles and biological membranes 2d ed*, J. Wiley., 1980.

[141] D Fennell Evans and BW Ninham, "Molecular forces in the self-organization of amphiphiles", in: *The Journal of Physical Chemistry* 90.2 (1986), pp. 226–234.

[142] Jacob N Israelachvili, *Intermolecular and surface forces*, Academic press, 2015.

[143] Robert S Cantor, "Lateral pressures in cell membranes: a mechanism for modulation of protein function", in: *The Journal of Physical Chemistry B* 101.10 (1997), pp. 1723–1725.

[144] Derek Marsh, "Protein modulation of lipids, and vice-versa, in membranes", in: *Biochimica et Biophysica Acta (BBA)-Biomembranes* 1778.7-8 (2008), pp. 1545–1575.

[145] Eduardo Perozo et al., "Physical principles underlying the transduction of bilayer deformation forces during mechanosensitive channel gating", in: *Nature structural biology* 9.9 (2002), pp. 696–703.

[146] Alba Diz-Muñoz, Daniel A Fletcher, and Orion D Weiner, "Use the force: membrane tension as an organizer of cell shape and motility", in: *Trends in cell biology* 23.2 (2013), pp. 47–53.

[147] Gary J Doherty and Harvey T McMahon, "Mediation, modulation, and consequences of membrane-cytoskeleton interactions", in: *Annu. Rev. Biophys.* 37 (2008), pp. 65–95.

[148] Barbara Hissa et al., "Membrane cholesterol removal changes mechanical properties of cells and induces secretion of a specific pool of lysosomes", in: *PloS one* 8.12 (2013).

[149] Mingzhai Sun et al., "The effect of cellular cholesterol on membrane-cytoskeleton adhesion", in: *Journal of cell science* 120.13 (2007), pp. 2223–2231.

[150] H Träuble, "Phasenumwandlungen in Lipiden mögliche Schaltprozesse in biologischen Membranen", in: *Naturwissenschaften* 58.6 (1971), pp. 277–284.

[151] P Läuger, "Künstliche Lipidfilme als Modelle biologischer Membranen", in: *Naturwissenschaften* 57.10 (1970), pp. 474–480.

[152] Tadao Tomita, "Membrane capacity and resistance of mammalian smooth muscle", in: *Journal of theoretical biology* 12.2 (1966), pp. 216–227.

[153] R Fettiplace, DM Andrews, and DA Haydon, "The thickness, composition and structure of some lipid bilayers and natural membranes", in: *The Journal of membrane biology* 5.3 (1971), pp. 277–296.

[154] Peter Schoch, David F Sargent, and Robert Schwyzer, "Capacitance and conductance as tools for the measurement of asymmetric surface potentials and energy barriers of lipid bilayer membranes", in: *The Journal of membrane biology* 46.1 (1979), pp. 71–89.

[155] Uwe Peterson et al., "Origin of membrane dipole potential: Contribution of the phospholipid fatty acid chains", in: *Chemistry and physics of lipids* 117.1-2 (2002), pp. 19–27.

[156] Gregor Cevc, "Membrane electrostatics", in: *Biochimica et Biophysica Acta (BBA)-Reviews on Biomembranes* 1031.3 (1990), pp. 311–382.

[157] David W Deamer and John Bramhall, "Permeability of lipid bilayers to water and ionic solutes", in: *Chemistry and physics of lipids* 40.2-4 (1986), pp. 167–188.

[158] J De Gier, "Permeability barriers formed by membrane lipids", in: *Bioelectrochemistry and bioenergetics* 27.1 (1992), pp. 1–10.

[159] Frank D Gunstone, *Fatty acid and lipid chemistry*, Springer, 2012.

[160] Derek Marsh, "General features of phospholipid phase transitions", in: *Chemistry and physics of lipids* 57.2-3 (1991), pp. 109–120.

[161] Winchil LC Vaz, "Lipid bilayers: properties", in: *Wiley Encyclopedia of Chemical Biology* (2007), pp. 1–15.

[162] A Tardieu, Vittorio Luzzati, and FC Reman, "Structure and polymorphism of the hydrocarbon chains of lipids: a study of lecithin-water phases", in: *Journal of molecular biology* 75.4 (1973), pp. 711–733.

[163] John F Nagle, "Theory of the main lipid bilayer phase transition", in: *Annual Review of Physical Chemistry* 31.1 (1980), pp. 157–196.

[164] R Koynova and B Tenchov, "Phase Transitions and phase behavior of lipids", in: *Encyclopedia of Biophysics. Berlin: Springer Verlag* (2013), pp. 1841–54.

[165] Ruthven NAH Lewis and Ronald N McElhaney, "Membrane lipid phase transitions and phase organization studied by Fourier transform infrared spectroscopy", in: *Biochimica et Biophysica Acta (BBA)-Biomembranes* 1828.10 (2013), pp. 2347–2358.

[166] John Katsaras et al., "Clarification of the ripple phase of lecithin bilayers using fully hydrated, aligned samples", in: *Physical Review E* 61.5 (2000), p. 5668.

[167] John F Nagle and Stephanie Tristram-Nagle, "Lipid bilayer structure", in: *Current opinion in structural biology* 10.4 (2000), pp. 474–480.

[168] Hayato Ichimori et al., "Effect of unsaturated acyl chains on the thermotropic and barotropic phase transitions of phospholipid bilayer membranes", in: *Chemistry and physics of lipids* 100.1-2 (1999), pp. 151–164.

[169] Masaki Goto et al., "Effect of hydrostatic pressure on the bilayer phase behavior of symmetric and asymmetric phospholipids with the same total chain length", in: *Biochimica et Biophysica Acta (BBA)-Biomembranes* 1778.4 (2008), pp. 1067–1078.

[170] Shoji Kaneshina et al., "Barotropic phase transitions of dioleoylphosphatidylcholine and stearoyl-oleoylphosphatidylcholine bilayer membranes", in: *Biochimica et Biophysica Acta (BBA)-Biomembranes* 1374.1-2 (1998), pp. 1–8.

[171] Hitoshi Matsuki et al., "Thermotropic and barotropic phase behavior of phosphatidylcholine bilayers", in: *International journal of molecular sciences* 14.2 (2013), pp. 2282–2302.

[172] John Katsaras and Thomas Gutberlet, *Lipid bilayers: structure and interactions*, Springer Science & Business Media, 2013.

[173] Thomas Heimburg, *Thermal biophysics of membranes*, John Wiley & Sons, 2008.

[174] John F Nagle and Stephanie Tristram-Nagle, "Structure of lipid bilayers", in: *Biochimica et Biophysica Acta (BBA)-Reviews on Biomembranes* 1469.3 (2000), pp. 159–195.

[175] Stephanie Tristram-Nagle and John F Nagle, "Lipid bilayers: thermodynamics, structure, fluctuations, and interactions", in: *Chemistry and physics of lipids* 127.1 (2004), pp. 3–14.

[176] Gregor Cevc and Derek Marsh, *Phospholipid bilayers: physical principles and models*, Wiley, 1987.

[177] Derek Marsh, *Handbook of lipid bilayers*, CRC press, 2013.

[178] PF Fahey et al., "Lateral diffusion in planar lipid bilayers", in: *Science* 195.4275 (1977), pp. 305–306.

[179] Göran Lindblom and Greger Orädd, "Lipid lateral diffusion and membrane heterogeneity", in: *Biochimica et Biophysica Acta (BBA)-Biomembranes* 1788.1 (2009), pp. 234–244.

[180] Marc Eeman and Magali Deleu, "From biological membranes to biomimetic model membranes", in: *Biotechnologie, Agronomie, Société et Environnement* 14.4 (2010), pp. 719–736.

[181] M Stelzle, R Miehlich, and E Sackmann, "Two-dimensional microelectrophoresis in supported lipid bilayers", in: *Biophysical journal* 63.5 (1992), pp. 1346–1354.

[182] Jeffery B Klauda et al., "Rotation of lipids in membranes: molecular dynamics simulation, 31P spin-lattice relaxation, and rigid-body dynamics", in: *Biophysical journal* 94.8 (2008), pp. 3074–3083.

[183] Paul Stevenson et al., "Membrane and Membrane Protein Dynamics Studied with Time-resolved Infrared Spectroscopy", PhD thesis, Massachusetts Institute of Technology, Department of Chemistry, 2017.

[184] F-Xabier Contreras et al., "Transbilayer (flip-flop) lipid motion and lipid scrambling in membranes", in: *FEBS letters* 584.9 (2010), pp. 1779–1786.

[185] Harden M McConnell and Roger D Kornberg, "Inside-outside transitions of phospholipids in vesicle membranes", in: *Biochemistry* 10.7 (1971), pp. 1111–1120.

[186] Minoru Nakano et al., "Flip-flop of phospholipids in vesicles: kinetic analysis with time-resolved small-angle neutron scattering", in: *The Journal of Physical Chemistry B* 113.19 (2009), pp. 6745–6748.

[187] WF Drew Bennett et al., "Molecular view of cholesterol flip-flop and chemical potential in different membrane environments", in: *Journal of the American Chemical Society* 131.35 (2009), pp. 12714–12720.

[188] James A Hamilton, "Fast flip-flop of cholesterol and fatty acids in membranes: implications for membrane transport proteins", in: *Current opinion in lipidology* 14.3 (2003), pp. 263–271.

[189] Iván López-Montero et al., "Rapid transbilayer movement of ceramides in phospholipid vesicles and in human erythrocytes", in: *Journal of Biological Chemistry* 280.27 (2005), pp. 25811–25819.

[190] Barry R Ganong and Robert M Bell, "Transmembrane movement of phosphatidylglycerol and diacylglycerol sulfhydryl analogs", in: *Biochemistry* 23.21 (1984), pp. 4977–4983.

[191] Theodore L Steck, Jin Ye, and Yvonne Lange, "Probing red cell membrane cholesterol movement with cyclodextrin", in: *Biophysical journal* 83.4 (2002), pp. 2118–2125.

[192] James G Stout, Peter J Sims, Therese Wiedmer, et al., "Isolation of an erythrocyte membrane protein that mediates Ca2+-dependent transbilayer movement of phospholipid", in: *Journal of Biological Chemistry* 271.29 (1996), pp. 17205–17210.

[193] Philippe F Devaux et al., "How lipid flippases can modulate membrane structure", in: *Biochimica et Biophysica Acta (BBA)-Biomembranes* 1778.7-8 (2008), pp. 1591–1600.

[194] T Pomorski and AK Menon, "Lipid flippases and their biological functions", in: *Cellular and Molecular Life Sciences CMLS* 63.24 (2006), pp. 2908–2921.

[195] David L Daleke, "Regulation of transbilayer plasma membrane phospholipid asymmetry", in: *Journal of lipid research* 44.2 (2003), pp. 233–242.

[196] Erdinc Sezgin and Petra Schwille, "Model membrane platforms to study protein-membrane interactions", in: *Molecular membrane biology* 29.5 (2012), pp. 144–154.

[197] Yee-Hung M Chan and Steven G Boxer, "Model membrane systems and their applications", in: *Current opinion in chemical biology* 11.6 (2007), pp. 581–587.

[198] Michael Edidin, "The state of lipid rafts: from model membranes to cells", in: *Annual review of biophysics and biomolecular structure* 32.1 (2003), pp. 257–283.

[199] Erich Sackmann, "Supported membranes: scientific and practical applications", in: *Science* 271.5245 (1996), pp. 43–48.

[200] Motomu Tanaka and Erich Sackmann, "Polymer-supported membranes as models of the cell surface", in: *Nature* 437.7059 (2005), pp. 656–663.

[201] Jana Jass, Torbjörn Tjärnhage, and Gertrud Puu, "From liposomes to supported, planar bilayer structures on hydrophilic and hydrophobic surfaces: an atomic force microscopy study", in: *Biophysical journal* 79.6 (2000), pp. 3153–3163.

[202] Martin Loose and Petra Schwille, "Biomimetic membrane systems to study cellular organization", in: *Journal of structural biology* 168.1 (2009), pp. 143–151.

[203] Salvatore Chiantia, Nicoletta Kahya, and Petra Schwille, "Raft domain reorganization driven by short-and long-chain ceramide: a combined AFM and FCS study", in: *Langmuir* 23.14 (2007), pp. 7659–7665.

[204] Mikkel Herholdt Jensen, Eliza J Morris, and Adam Cohen Simonsen, "Domain shapes, coarsening, and random patterns in ternary membranes", in: *Langmuir* 23.15 (2007), pp. 8135–8141.

[205] Erich Sackmann and Motomu Tanaka, "Supported membranes on soft polymer cushions: fabrication, characterization and applications", in: *Trends in biotechnology* 18.2 (2000), pp. 58–64.

[206] Ralf P Richter, Rémi Bérat, and Alain R Brisson, "Formation of solid-supported lipid bilayers: an integrated view", in: *Langmuir* 22.8 (2006), pp. 3497–3505.

[207] Garth L Nicolson, "The Fluid—Mosaic Model of Membrane Structure: Still relevant to understanding the structure, function and dynamics of biological membranes after more than 40 years", in: *Biochimica et Biophysica Acta (BBA)-Biomembranes* 1838.6 (2014), pp. 1451–1466.

[208] Irving Langmuir, "The constitution and fundamental properties of solids and liquids. II. Liquids.", in: *Journal of the American Chemical Society* 39.9 (1917), pp. 1848–1906.

[209] Wolfgang Ostwald, "Die Arbeiten von Agnes Pockels über Grenzschichten und Filme", in: *Kolloid-Zeitschrift* 58.1 (1932).

[210] Agnes Pockels, *On the relative contamination of the water-surface by equal quantities of different substances*, 1892.

[211] Agnes Pockels, "On the spreading of oil upon water", in: *Nature* 50.1288 (1894), p. 223.

[212] JF Nagle, "Theory of lipid monolayer and bilayer phase transitions: effect of headgroup interactions", in: *The Journal of membrane biology* 27.1 (1976), pp. 233–250.

[213] Michael C Petty, *Langmuir-Blodgett films: an introduction*, Cambridge University Press, 1996.

[214] Mohamed Elderdfi and Aleksander F Sikorski, "Langmuir-monolayer methodologies for characterizing protein-lipid interactions", in: *Chemistry and physics of lipids* 212 (2018), pp. 61–72.

[215] Derek Marsh, "Lateral pressure in membranes", in: *Biochimica et Biophysica Acta (BBA)-Reviews on Biomembranes* 1286.3 (1996), pp. 183–223.

[216] Derek Marsh, "Comment on Interpretation of Mechanochemical Properties of Lipid Bilayer Vesicles from the Equation of State or Pressure- Area Measurement of the Monolayer at the Air- Water or Oil- Water Interface", in: *Langmuir* 22.6 (2006), pp. 2916–2919.

[217] RA Demel et al., "Relation between various phospholipase actions on human red cell membranes and the interfacial phospholipid pressure in monolayers", in: *Biochimica et Biophysica Acta (BBA)-Biomembranes* 406.1 (1975), pp. 97–107.

[218] Alfred Blume, "A comparative study of the phase transitions of phospholipid bilayers and monolayers", in: *Biochimica et Biophysica Acta (BBA)-Biomembranes* 557.1 (1979), pp. 32–44.

[219] F Jähnig, "Lipid exchange between membranes", in: *Biophysical journal* 46.6 (1984), pp. 687–694.

[220] David WR Gruen and Joe Wolfe, "Lateral tensions and pressures in membranes and lipid monolayers", in: *Biochimica et Biophysica Acta (BBA)-Biomembranes* 688.2 (1982), pp. 572–580.

[221] George L Gaines Jr, "Thermodynamic relationships for mixed insoluble monolayers", in: *Journal of colloid and interface science* 21.3 (1966), pp. 315–319.

[222] Malcolm N Jones, Dennis Chapman, et al., *Micelles, monolayers, and biomembranes*, Wiley-Liss, 1995.

[223] George L Gaines, "Insoluble monolayers at liquid-gas interfaces", in: (1966).

[224] George L Gaines Jr, "On the use of filter paper Wilhelmy plates with insoluble monolayers", in: *Journal of Colloid and Interface Science* 62 (1977), pp. 191–192.

[225] Vladimir M Kaganer, Helmuth Möhwald, and Pulak Dutta, "Structure and phase transitions in Langmuir monolayers", in: *Reviews of Modern Physics* 71.3 (1999), p. 779.

[226] Gerold Adam, Peter Läuger, and Günther Stark, *Physikalische chemie und biophysik*, Springer-Verlag, 2009.

[227] Roland Winter and Frank Noll, *Methoden der biophysikalischen Chemie*, Springer-Verlag, 2013.

[228] M Lösche, E Sackmann, and Helmuth Möhwald, "A fluorescence microscopic study concerning the phase diagram of phospholipids", in: *Berichte der Bunsengesellschaft für physikalische Chemie* 87.10 (1983), pp. 848–852.

[229] Helmuth Möhwald, "Phospholipid monolayers", in: *Handbook of biological physics* 1 (1995), pp. 161–211.

[230] VB Fainerman, D Vollhardt, and V Melzer, "Equation of state for insoluble monolayers of aggregating amphiphilic molecules", in: *The Journal of Physical Chemistry* 100.38 (1996), pp. 15478–15482.

[231] Jacob Israelachvili, "Self-assembly in two dimensions: surface micelles and domain formation in monolayers", in: *Langmuir* 10.10 (1994), pp. 3774–3781.

[232] Ralf Richter, Anneke Mukhopadhyay, and Alain Brisson, "Pathways of lipid vesicle deposition on solid surfaces: a combined QCM-D and AFM study", in: *Biophysical journal* 85.5 (2003), pp. 3035–3047.

[233] Wolfgang Knoll et al., "Functional tethered lipid bilayers", in: *Reviews in Molecular Biotechnology* 74.3 (2000), pp. 137–158.

[234] Adrienne A Brian and Harden M McConnell, "Allogeneic stimulation of cytotoxic T cells by supported planar membranes", in: *Proceedings of the National Academy of Sciences* 81.19 (1984), pp. 6159–6163.

[235] Tania H Watts et al., "Antigen presentation by supported planar membranes containing affinity-purified I-Ad", in: *Proceedings of the National Academy of Sciences* 81.23 (1984), pp. 7564–7568.

[236] Harden M McConnell et al., "Supported planar membranes in studies of cell-cell recognition in the immune system", in: *Biochimica et biophysica acta* 864.1 (1986), pp. 95–106.

[237] Edwin Kalb, Sammy Frey, and Lukas K Tamm, "Formation of supported planar bilayers by fusion of vesicles to supported phospholipid monolayers", in: *Biochimica et Biophysica Acta (BBA)-Biomembranes* 1103.2 (1992), pp. 307–316.

[238] Steven G Boxer, "Molecular transport and organization in supported lipid membranes", in: *Current opinion in chemical biology* 4.6 (2000), pp. 704–709.

[239] R Merkel, E Sackmann, and eE Evans, "Molecular friction and epitactic coupling between monolayers in supported bilayers", in: *Journal de Physique* 50.12 (1989), pp. 1535–1555.

[240] Katharine B Blodgett, "Films built by depositing successive monomolecular layers on a solid surface", in: *Journal of the American Chemical Society* 57.6 (1935), pp. 1007–1022.

[241] Irving Langmuir and Vincent J Schaefer, "Activities of urease and pepsin monolayers", in: *Journal of the American Chemical Society* 60.6 (1938), pp. 1351–1360.

[242] H Ti Tien and Zdzislaw Salamon, "Formation of self-assembled lipid bilayers on solid substrates", in: *Journal of electroanalytical chemistry and interfacial electrochemistry* 276.3 (1989), pp. 211–218.

[243] Beatrice Sironi et al., "Structure of lipid multilayers via drop casting of aqueous liposome dispersions", in: *Soft matter* 12.17 (2016), pp. 3877–3887.

[244] Daniel J Estes and Michael Mayer, "Electroformation of giant liposomes from spin-coated films of lipids", in: *Colloids and Surfaces B: Biointerfaces* 42.2 (2005), pp. 115–123.

[245] G Pompeo et al., "AFM characterization of solid-supported lipid multilayers prepared by spin-coating", in: *Biochimica et Biophysica Acta (BBA)-Biomembranes* 1712.1 (2005), pp. 29–36.

[246] Adam Cohen Simonsen and Luis A Bagatolli, "Structure of spin-coated lipid films and domain formation in supported membranes formed by hydration", in: *Langmuir* 20.22 (2004), pp. 9720–9728.

[247] B Derjaguin, "On the repulsive forces between charged colloid particles and on the theory of slow coagulation and stability of lyophobe sols", in: *Transactions of the Faraday Society* 35 (1940), pp. 203–215.

[248] EJW Verwey and J Th G Overbeek, "Theorie der Stabilität lyophober Kolloide", in: *Kolloid-Zeitschrift* 141.1 (1955), pp. 44–45.

[249] Jacob N Israelachvili and Haakan Wennerstroem, "Entropic forces between amphiphilic surfaces in liquids", in: *The Journal of Physical Chemistry* 96.2 (1992), pp. 520–531.

[250] Hiroyuki Ohshima and Toshio Mitsui, "A theory of the effects of calcium ions on the lamellar phase of dipalmitoyl lecithin", in: *Journal of Colloid and Interface Science* 63.3 (1978), pp. 525–537.

[251] Motomu Tanaka et al., "Physical chemistry of biological interfaces: generic and specific roles of soft interlayers.", in: *Chemistry, an Asian journal* 6.7 (2011), pp. 1728–1738.

[252] W Rawicz et al., "Effect of chain length and unsaturation on elasticity of lipid bilayers", in: *Biophysical journal* 79.1 (2000), pp. 328–339.

[253] Wolfgang Helfrich, "Elastic properties of lipid bilayers: theory and possible experiments", in: *Zeitschrift für Naturforschung C* 28.11-12 (1973), pp. 693–703.

[254] Markus Deserno, "Fluid lipid membranes: From differential geometry to curvature stresses", in: *Chemistry and physics of lipids* 185 (2015), pp. 11–45.

[255] Yōji Inoko et al., "Effects of cations on dipalmitoyl phosphatidylcholine/cholesterol /water systems", in: *Biochimica et Biophysica Acta (BBA)-Biomembranes* 413.1 (1975), pp. 24–32.

[256] Johan Marra and Jacob Israelachvili, "Direct measurements of forces between phosphatidylcholine and phosphatidylethanolamine bilayers in aqueous electrolyte solutions", in: *Biochemistry* 24.17 (1985), pp. 4608–4618.

[257] Adam Cohen Simonsen, "Spatiotemporal Organization of Spin-Coated Supported Model Membranes", in: *Biomembrane Frontiers*, Springer, 2009, pp. 141–170.

[258] Tim Salditt, "Thermal fluctuations and stability of solid-supported lipid membranes", in: *Journal of Physics: Condensed Matter* 17.6 (2005), R287.

[259] Margaret R Horton et al., "Structure and dynamics of crystalline protein layers bound to supported lipid bilayers", in: *Langmuir* 23.11 (2007), pp. 6263–6269.

[260] Toshinori Motegi et al., "Substrate-induced structure and molecular dynamics in a lipid bilayer membrane", in: *Langmuir* 33.51 (2017), pp. 14748–14755.

[261] Simon Faiss et al., "Phase transition of individually addressable microstructured membranes visualized by imaging ellipsometry", in: *The Journal of Physical Chemistry B* 111.50 (2007), pp. 13979–13986.

[262] Heiko M Seeger et al., "Supported lipid bilayers on mica and silicon oxide: comparison of the main phase transition behavior", in: *The Journal of Physical Chemistry B* 114.27 (2010), pp. 8926–8933.

[263] Danielle Keller et al., "Decoupled phase transitions and grain-boundary melting in supported phospholipid bilayers", in: *Physical review letters* 94.2 (2005), p. 025701.

[264] Ralf P Richter, Nicolas Maury, and Alain R Brisson, "On the effect of the solid support on the interleaflet distribution of lipids in supported lipid bilayers", in: *Langmuir* 21.1 (2005), pp. 299–304.

[265] Travers H Anderson et al., "Formation of supported bilayers on silica substrates", in: *Langmuir* 25.12 (2009), pp. 6997–7005.

[266] S Marčelja and N Radić, "Repulsion of interfaces due to boundary water", in: *Chemical Physics Letters* 42.1 (1976), pp. 129–130.

[267] RP Rand and VA Parsegian, "Hydration forces between phospholipid bilayers", in: *Biochimica et Biophysica Acta (BBA)-Reviews on Biomembranes* 988.3 (1989), pp. 351–376.

[268] Andrea Alessandrini and Paolo Facci, "Phase transitions in supported lipid bilayers studied by AFM", in: *Soft matter* 10.37 (2014), pp. 7145–7164.

[269] Fabio L Leite et al., "Theoretical models for surface forces and adhesion and their measurement using atomic force microscopy", in: *International journal of molecular sciences* 13.10 (2012), pp. 12773–12856.

[270] Chenyue Xing and Roland Faller, "Interactions of lipid bilayers with supports: a coarse-grained molecular simulation study", in: *The Journal of Physical Chemistry B* 112.23 (2008), pp. 7086–7094.

[271] Li-Hsien Yeh et al., "Field effect control of surface charge property and electroosmotic flow in nanofluidics", in: *The Journal of Physical Chemistry C* 116.6 (2012), pp. 4209–4216.

[272] Murat Barisik et al., "Size dependent surface charge properties of silica nanoparticles", in: *The Journal of Physical Chemistry C* 118.4 (2014), pp. 1836–1842.

[273] DR Heine, AR Rammohan, and J Balakrishnan, "Atomistic simulations of the interaction between lipid bilayers and substrates", in: *Molecular Simulation* 33.4-5 (2007), pp. 391–397.

[274] Astrid F Brandner et al., "Modelling lipid systems in fluid with Lattice Boltzmann Molecular Dynamics simulations and hydrodynamics", in: *Scientific reports* 9.1 (2019), pp. 1–14.

[275] Philip L Yeagle, "Non-covalent binding of membrane lipids to membrane proteins", in: *Biochimica et Biophysica Acta (BBA)-Biomembranes* 1838.6 (2014), pp. 1548–1559.

[276] Bala Murali Venkatesan et al., "Lipid bilayer coated Al 2 O 3 nanopore sensors: towards a hybrid biological solid-state nanopore", in: *Biomedical microdevices* 13.4 (2011), pp. 671–682.

[277] Abhinav Srivastava and Ananya Debnath, "Hydration dynamics of a lipid membrane: Hydrogen bond networks and lipid-lipid associations", in: *The Journal of Chemical Physics* 148.9 (2018), p. 094901.

[278] Thomas M Bayerl and Myer Bloom, "Physical properties of single phospholipid bilayers adsorbed to micro glass beads. A new vesicular model system studied by 2H-nuclear magnetic resonance", in: *Biophysical journal* 58.2 (1990), pp. 357–362.

[279] Shirley J Johnson et al., "Structure of an adsorbed dimyristoylphosphatidylcholine bilayer measured with specular reflection of neutrons", in: *Biophysical journal* 59.2 (1991), pp. 289–294.

[280] Bernd W König et al., "Neutron reflectivity and atomic force microscopy studies of a lipid bilayer in water adsorbed to the surface of a silicon single crystal", in: *Langmuir* 12.5 (1996), pp. 1343–1350.

[281] Marion B Hochrein et al., "Structure and mobility of lipid membranes on a thermoplastic substrate", in: *Langmuir* 22.2 (2006), pp. 538–545.

[282] Martin Kreuzer et al., "Polymer-Induced Swelling of Solid-Supported Lipid Membranes", in: *Membranes* 6.1 (2016), p. 2.

[283] William E Truog and John P Kinsella, "Pulmonary gas exchange in the developing lung", in: *Fetal and neonatal physiology*, Elsevier, 2017, pp. 714–724.

[284] Ewald R Weibel, *The pathway for oxygen: structure and function in the mammalian respiratory system*, Harvard University Press, 1984.

[285] Yi Y Zuo et al., "Current perspectives in pulmonary surfactant—inhibition, enhancement and evaluation", in: *Biochimica et Biophysica Acta (BBA)-Biomembranes* 1778.10 (2008), pp. 1947–1977.

[286] JE Hall, *Guyton and Hall textbook of medical physiology. Saunders Elsevier*, 2011.

[287] Robert H Notter, *Lung surfactants: basic science and clinical applications*, CRC Press, 2000.

[288] Peter L Williams et al., *Gray's anatomy*, vol. 378, Churchill livingstone Edinburgh, 1989.

[289] John A Clements and Mary Ellen Avery, "Lung surfactant and neonatal respiratory distress syndrome", in: *American Journal of Respiratory and Critical Care Medicine* 157.4 (1998), S59–S66.

[290] JACOB Bastacky et al., "Alveolar lining layer is thin and continuous: low-temperature scanning electron microscopy of rat lung", in: *Journal of Applied Physiology* 79.5 (1995), pp. 1615–1628.

[291] "Chapter 9 - The Development of the Pulmonary Surfactant System", in: *The Lung (Second Edition)*, ed. by Richard Harding and Kent E. Pinkerton, Second Edition, Boston: Academic Press, 2014, pp. 183–209, ISBN: 978-0-12-799941-8, DOI: https://doi.org/10.1016/B978-0-12-799941-8.00009-2.

[292] James E Hansen and EDGAR P Ampaya, "Human air space shapes, sizes, areas, and volumes", in: *Journal of Applied Physiology* 38.6 (1975), pp. 990–995.

[293] Matthias Ochs et al., "The number of alveoli in the human lung", in: *American journal of respiratory and critical care medicine* 169.1 (2004), pp. 120–124.

[294] Nashwa El-Gendy et al., "Delivery and performance of surfactant replacement therapies to treat pulmonary disorders", in: *Therapeutic delivery* 4.8 (2013), pp. 951–980.

[295] Elena Lopez-Rodriguez and Jesús Pérez-Gil, "Structure-function relationships in pulmonary surfactant membranes: from biophysics to therapy", in: *Biochimica et Biophysica Acta (BBA)-Biomembranes* 1838.6 (2014), pp. 1568–1585.

[296] M Griese, "Pulmonary surfactant in health and human lung diseases: state of the art", in: *European Respiratory Journal* 13.6 (1999), pp. 1455–1476.

[297] Wolfgang Bernhard, "Lung surfactant: Function and composition in the context of development and respiratory physiology", in: *Annals of Anatomy-Anatomischer Anzeiger* 208 (2016), pp. 146–150.

[298] K von Neergard, "Neue auffassungen ueber einen grundbegriff der atemmechanik", in: *Die retraktionskraft der lunge, abhaengig von der oberflaechenspannung in den alveolen* (1929), p. 66.

[299] Jeffrey A Whitsett, "The intersection of surfactant homeostasis and innate host defense of the lung: lessons from newborn infants", in: *Innate immunity* 16.3 (2010), pp. 138–142.

[300] Samuel Schürch, "Surface tension at low lung volumes: dependence on time and alveolar size", in: *Respiration physiology* 48.3 (1982), pp. 339–355.

[301] H Bachofen et al., "Relations among alveolar surface tension, surface area, volume, and recoil pressure", in: *Journal of Applied Physiology* 62.5 (1987), pp. 1878–1887.

[302] Hans Bachofen and Samuel Schürch, "Alveolar surface forces and lung architecture", in: *Comparative Biochemistry and Physiology Part A: Molecular & Integrative Physiology* 129.1 (2001), pp. 183–193.

[303] Henry D Prange, "Laplace's law and the alveolus: a misconception of anatomy and a misapplication of physics", in: *Advances in physiology education* 27.1 (2003), pp. 34–40.

[304] Jeffrey R Basford, "The Law of Laplace and its relevance to contemporary medicine and rehabilitation", in: *Archives of physical medicine and rehabilitation* 83.8 (2002), pp. 1165–1170.

[305] Marie Pierre Krafft, "Overcoming inactivation of the lung surfactant by serum proteins: a potential role for fluorocarbons?", in: *Soft Matter* 11.30 (2015), pp. 5982–5994.

[306] Kent Pinkerton and Richard Harding, *The lung: development, aging and the environment*, Elsevier, 2014.

[307] Fred Possmayer, "Physicochemical aspects of pulmonary surfactant", in: *Fetal and Neonatal Physiology*, Elsevier, 2004, pp. 1014–1034.

[308] Jesús Pérez-Gil, "Structure of pulmonary surfactant membranes and films: the role of proteins and lipid–protein interactions", in: *Biochimica et Biophysica acta (BBA)-Biomembranes* 1778.7-8 (2008), pp. 1676–1695.

[309] Jon Goerke, "Pulmonary surfactant: functions and molecular composition", in: *Biochimica et Biophysica Acta (BBA)-Molecular Basis of Disease* 1408.2-3 (1998), pp. 79–89.

[310] Alicia G Serrano and Jesús Pérez-Gil, "Protein–lipid interactions and surface activity in the pulmonary surfactant system", in: *Chemistry and physics of lipids* 141.1-2 (2006), pp. 105–118.

[311] Ruud Veldhuizen et al., "The role of lipids in pulmonary surfactant", in: *Biochimica et Biophysica Acta (BBA)-Molecular Basis of Disease* 1408.2-3 (1998), pp. 90–108.

[312] Carol J Lang et al., "Dipalmitoylphosphatidylcholine is not the major surfactant phospholipid species in all mammals", in: *American Journal of Physiology-Regulatory, Integrative and Comparative Physiology* 289.5 (2005), R1426–R1439.

[313] Elisa Parra and Jesús Pérez-Gil, "Composition, structure and mechanical properties define performance of pulmonary surfactant membranes and films", in: *Chemistry and physics of lipids* 185 (2015), pp. 153–175.

[314] H Hamm, H Fabel, and W Bartsch, "The surfactant system of the adult lung: physiology and clinical perspectives", in: *The clinical investigator* 70.8 (1992), pp. 637–657.

[315] Sandra Orgeig et al., "Recent advances in alveolar biology: evolution and function of alveolar proteins", in: *Respiratory physiology & neurobiology* 173 (2010), S43–S54.

[316] Antonio Cruz, Cristina Casals, and Jesus Perez-Gil, "Conformational flexibility of pulmonary surfactant proteins SP-B and SP-C, studied in aqueous organic solvents", in: *Biochimica et Biophysica Acta (BBA)-Lipids and Lipid Metabolism* 1255.1 (1995), pp. 68–76.

[317] Fred Possmayer et al., "Recent advances in alveolar biology: some new looks at the alveolar interface", in: *Respiratory physiology & neurobiology* 173 (2010), S55–S64.

[318] Henk P Haagsman and Robert V Diemel, "Surfactant-associated proteins: functions and structural variation", in: *Comparative Biochemistry and Physiology Part A: Molecular & Integrative Physiology* 129.1 (2001), pp. 91–108.

[319] Hitomi Sano and Yoshio Kuroki, "The lung collectins, SP-A and SP-D, modulate pulmonary innate immunity", in: *Molecular immunology* 42.3 (2005), pp. 279–287.

[320] Jeffrey A Whitsett and Timothy E Weaver, "Hydrophobic surfactant proteins in lung function and disease", in: *New England Journal of Medicine* 347.26 (2002), pp. 2141–2148.

[321] Roberta Guagliardo et al., "Pulmonary surfactant and drug delivery: Focusing on the role of surfactant proteins", in: *Journal of controlled release* 291 (2018), pp. 116–126.

[322] Henk P Haagsman et al., "Surfactant collectins and innate immunity", in: *Neonatology* 93.4 (2008), pp. 288–294.

[323] Victoria Goss, Alan N Hunt, and Anthony D Postle, "Regulation of lung surfactant phospholipid synthesis and metabolism", in: *Biochimica et Biophysica Acta (BBA)-Molecular and Cell Biology of Lipids* 1831.2 (2013), pp. 448–458.

[324] Kazuhiro Osanai et al., "Pulmonary surfactant transport in alveolar type II cells", in: *Respirology* 11 (2006), S70–S73.

[325] Timothy E Weaver, "Synthesis, processing and secretion of surfactant proteins B and C", in: *Biochimica et Biophysica Acta (BBA)-Molecular Basis of Disease* 1408.2-3 (1998), pp. 173–179.

[326] WF Voorhout et al., "Immunocytochemical localization of surfactant protein D (SP-D) in type II cells, Clara cells, and alveolar macrophages of rat lung.", in: *Journal of Histochemistry & Cytochemistry* 40.10 (1992), pp. 1589–1597.

[327] Samuel Hawgood and Francis R Poulain, "The pulmonary collectins and surfactant metabolism", in: *Annual review of physiology* 63.1 (2001), pp. 495–519.

[328] Seamus A Rooney, "Regulation of surfactant secretion", in: *Comparative Biochemistry and Physiology Part A: Molecular & Integrative Physiology* 129.1 (2001), pp. 233–243.

[329] S Schürch, Jon Goerke, and John A Clements, "Direct determination of surface tension in the lung", in: *Proceedings of the National Academy of Sciences* 73.12 (1976), pp. 4698–4702.

[330] Samuel Schürch, Jon Goerke, and John A Clements, "Direct determination of volume-and time-dependence of alveolar surface tension in excised lungs", in: *Proceedings of the National Academy of Sciences* 75.7 (1978), pp. 3417–3421.

[331] Samuel Schürch, Hans Bachofen, and Fred Possmayer, "Surface activity in situ, in vivo, and in the captive bubble surfactometer", in: *Comparative Biochemistry and Physiology Part A: Molecular & Integrative Physiology* 129.1 (2001), pp. 195–207.

[332] Chiara Autilio and Jesús Pérez-Gil, "Understanding the principle biophysics concepts of pulmonary surfactant in health and disease", in: *Archives of Disease in Childhood-Fetal and Neonatal Edition* 104.4 (2019), F443–F451.

[333] Jon Goerke and John A Clements, "Alveolar surface tension and lung surfactant", in: *Comprehensive Physiology* (2011), pp. 247–261.

[334] Harden M McConnell, "Structures and transitions in lipid monolayers at the air-water interface", in: *Annual Review of Physical Chemistry* 42.1 (1991), pp. 171–195.

[335] H Mohwald, "Phospholipid and phospholipid-protein monolayers at the air/water interface", in: *Annual Review of Physical Chemistry* 41.1 (1990), pp. 441–476.

[336] DY Takamoto et al., "Interaction of lung surfactant proteins with anionic phospholipids", in: *Biophysical journal* 81.1 (2001), pp. 153–169.

[337] Joseph A Zasadzinski et al., "The physics and physiology of lung surfactants", in: *Current Opinion in Colloid & Interface Science* 6.5-6 (2001), pp. 506–513.

[338] Mercedes Echaide et al., "Restoring pulmonary surfactant membranes and films at the respiratory surface", in: *Biochimica et Biophysica Acta (BBA)-Biomembranes* 1859.9 (2017), pp. 1725–1739.

[339] Jesús Perez-Gil and Timothy E Weaver, "Pulmonary surfactant pathophysiology: current models and open questions", in: *Physiology* 25.3 (2010), pp. 132–141.

[340] Wolfgang Bernhard et al., "Commercial versus native surfactants: surface activity, molecular components, and the effect of calcium", in: *American Journal of Respiratory and Critical Care Medicine* 162.4 (2000), pp. 1524–1533.

[341] Dennis W Nielson and Margaret B Lewis, "Calcium increases in pulmonary alveolar fluid in lambs at birth", in: *Pediatric research* 24.3 (1988), pp. 322–325.

[342] Jacques R Bourbon, *Pulmonary surfactant: biochemical, functional, regulatory, and clinical concepts*, CRC Press, 2019.

[343] HP Haagsman et al., "The major lung surfactant protein, SP 28-36, is a calcium-dependent, carbohydrate-binding protein.", in: *Journal of Biological Chemistry* 262.29 (1987), pp. 13877–13880.

[344] Yasuhiro Suzuki, Yoko Fujita, Kumiko Kogishi, et al., "Reconstitution of tubular myelin from synthetic lipids and proteins associated with pig pulmonary surfactant", in: *Am Rev Respir Dis* 140.1 (1989), pp. 75–81.

[345] Shou-Hwa Yu and Fred Possmayer, "Effect of pulmonary surfactant protein B (SP-B) and calcium on phospholipid adsorption and squeeze-out of phosphatidylglycerol from binary phospholipid monolayers containing dipalmitoylphosphatidylcholine", in: *Biochimica et Biophysica Acta (BBA)-Lipids and Lipid Metabolism* 1126.1 (1992), pp. 26–34.

[346] Y Christova, E Enchev, and Z Lalchev, "Effects of pulmonary surfactant proteins SP-B and SP-C and calcium ions on the surface properties of hydrophobic fractions of lung surfactant", in: *European biophysics journal* 28.1 (1998), pp. 59–66.

[347] RODERIC G Eckenhoff and ANDREW P Somlyo, "Rat lung type II cell and lamellar body: elemental composition in situ", in: *American Journal of Physiology-Cell Physiology* 254.5 (1988), pp. C614–C620.

[348] AD Bangham, CJ Morley, and MC Phillips, "The physical properties of an effective lung surfactant", in: *Biochimica et Biophysica Acta (BBA)-Lipids and Lipid Metabolism* 573.3 (1979), pp. 552–556.

[349] Brian K Walsh, *Neonatal and Pediatric Respiratory Care-E-Book*, Elsevier Health Sciences, 2018.

[350] Mary Ellen Avery and Jere Mead, "Surface properties in relation to atelectasis and hyaline membrane disease", in: *AMA journal of diseases of children* 97.5_PART_I (1959), pp. 517–523.

[351] William H Northway Jr, Robert C Rosan, and David Y Porter, "Pulmonary disease following respirator therapy of hyaline-membrane disease: bronchopulmonary dysplasia", in: *New England Journal of Medicine* 276.7 (1967), pp. 357–368.

[352] RJ Rodriguez, "Respiratory distress syndrome and its management", in: *Neonatal-perinatal medicine* (2002), pp. 1001–1117.

[353] Rolf F Maier et al., *Neugeborenenintensivmedizin*, Springer, 2011.

[354] O Hjalmarson, "EPIDEMIOLOGY AND CLASSIFICATION OF ACUTE, NEONATAL RESPIRATORY DISORDERS: A Prospective Study 1", in: *Acta Paediatrica* 70.6 (1981), pp. 773–783.

[355] Roger Soll, "Early versus delayed selective surfactant treatment for neonatal respiratory distress syndrome", in: *Cochrane Database of Systematic Reviews* 4 (1999).

[356] Tetsuro Fujiwara et al., "Artificial surfactant therapy in hyaline-membrane disease", in: *The Lancet* 315.8159 (1980), pp. 55–59.

[357] Roger G Spragg et al., "Treatment of acute respiratory distress syndrome with recombinant surfactant protein C surfactant", in: *American journal of respiratory and critical care medicine* 167.11 (2003), pp. 1562–1566.

[358] Charles G Cochrane et al., "The efficacy and safety of KL4-surfactant in preterm infants with respiratory distress syndrome.", in: *American journal of respiratory and critical care medicine* 153.1 (1996), pp. 404–410.

[359] Robert H Notter, "Exogenous lung surfactants: Current and future", in: *Lung Surfactants*, CRC Press, 2000, pp. 332–359.

[360] Yuji Tanaka et al., "Development of synthetic lung surfactants.", in: *Journal of Lipid Research* 27.5 (1986), pp. 475–485.

[361] Katsumi Mizuno et al., "Surfactant protein-B supplementation improves in vivo function of a modified natural surfactant", in: *Pediatric research* 37.3 (1995), pp. 271–276.

[362] Junqi Ding et al., "Effects of lung surfactant proteins, SP-B and SP-C, and palmitic acid on monolayer stability", in: *Biophysical Journal* 80.5 (2001), pp. 2262–2272.

[363] R Veldhuizen, "Nag K, Orgeig S, and Possmayer F", in: *The role of lipids in pulmonary surfactant. Biochim Biophys Acta* 1408 (1998), pp. 90–108.

[364] David Moses et al., "Inhibition of pulmonary surfactant function by meconium", in: *American journal of obstetrics and gynecology* 164.2 (1991), pp. 477–481.

[365] Chiara Autilio et al., "Surfactant Injury in the Early Phase of Severe Meconium Aspiration Syndrome", in: *American Journal of Respiratory Cell and Molecular Biology* ja (2020).

[366] RG Spragg et al., "The future for surfactant therapy of the adult respiratory distress syndrome", in: *Surfactant replacement therapy*, Springer, 1988, pp. 203–211.

[367] ARDS Definition Task Force et al., "Acute respiratory distress syndrome", in: *Jama* 307.23 (2012), pp. 2526–2533.

[368] Susanna Price et al., "Respiratory management in severe acute respiratory syndrome coronavirus 2 infection", in: *European Heart Journal: Acute Cardiovascular Care* (2020), p. 2048872620924613.

[369] Lorraine B Ware and Michael A Matthay, "The acute respiratory distress syndrome", in: *New England Journal of Medicine* 342.18 (2000), pp. 1334–1349.

[370] Ritesh Agarwal et al., "Experience with ARDS caused by tuberculosis in a respiratory intensive care unit", in: *Intensive care medicine* 31.9 (2005), pp. 1284–1287.

[371] Tanu Singhal, "A review of coronavirus disease-2019 (COVID-19)", in: *The Indian Journal of Pediatrics* (2020), pp. 1–6.

[372] Renee D Stapleton et al., "Causes and timing of death in patients with ARDS", in: *Chest* 128.2 (2005), pp. 525–532.

[373] C Blay, C Butler, and A Ataya, "ARDS Secondary to Adenovirus", in: *A48. CRITICAL CARE CASE REPORTS: CAUSES AND COMPLICATIONS OF ACUTE RESPIRATORY FAILURE*, American Thoracic Society, 2019, A1795–A1795.

[374] David Cherkas et al., "Traumatic hemorrhagic shock: advances in fluid management", in: *Emerg Med Pract* 13.11 (2011), pp. 1–19.

[375] Majid Afshar et al., "Injury characteristics and von Willebrand factor for the prediction of acute respiratory distress syndrome in patients with burn injury: Development and Internal Validation", in: *Annals of surgery* 270.6 (2019), pp. 1186–1193.

[376] DG Ashbaugh et al., "Acute respiratory distress in adults", in: *The Lancet* 319 (1967), p. 10.

[377] Chun Pan et al., "Acute respiratory distress syndrome: challenge for diagnosis and therapy", in: *Chinese medical journal* 131.10 (2018), p. 1220.

[378] Robert P Dickson et al., "Enrichment of the lung microbiome with gut bacteria in sepsis and the acute respiratory distress syndrome", in: *Nature microbiology* 1.10 (2016), pp. 1–9.

[379] Ronald B Hirschl et al., "Prospective, randomized, controlled pilot study of partial liquid ventilation in adult acute respiratory distress syndrome", in: *American journal of respiratory and critical care medicine* 165.6 (2002), pp. 781–787.

[380] DF Tierney and RP Johnson, "Altered surface tension of lung extracts and lung mechanics", in: *Journal of Applied Physiology* 20.6 (1965), pp. 1253–1260.

[381] Andreas Günther et al., "Surfactant alteration and replacement in acute respiratory distress syndrome", in: *Respiratory research* 2.6 (2001), p. 353.

[382] Akitoshi Ishizaka et al., "Elevation of KL-6, a lung epithelial cell marker, in plasma and epithelial lining fluid in acute respiratory distress syndrome", in: *American Journal of Physiology-Lung Cellular and Molecular Physiology* 286.6 (2004), pp. L1088–L1094.

[383] G Nakos et al., "Bronchoalveolar lavage fluid characteristics of early intermediate and late phases of ARDS", in: *Intensive care medicine* 24.4 (1998), pp. 296–303.

[384] Philippe G Jorens et al., "Interleukin 8 (IL-8) in the bronchoalveolar lavage fluid from patients with the adult respiratory distress syndrome (ARDS) and patients at risk for ARDS", in: *Cytokine* 4.6 (1992), pp. 592–597.

[385] ROGER G SPRAGG, "Abnormalities of lung surfactant function in patients with acute lung injury: implications for therapy", in: *Lung biology in health and disease* 50 (1991), pp. 381–395.

[386] Patrick C Stenger et al., "Rediscovering the Schulze- hardy rule in competitive adsorption to an air- water Interface", in: *Langmuir* 25.17 (2009), pp. 10045–10050.

[387] BA Holm, "Enhorning G, and Notter RH", in: *A biophysical mechanism by which plasma proteins inhibit lung surfactant activity. Chem Phys Lipids* 49 (1988), pp. 49–55.

[388] HW Taeusch, "Bernardino de la Serna J, Perez-Gil J, Alonso C, Zasadzinski JA. Inactivation of pulmonary surfactant due to serum-inhibited adsorption and reversal by hydrophilic polymers: experimental", in: *Biophys J* 89.3 (2005), pp. 1769–79.

[389] Joseph A Zasadzinski et al., "Inhibition of pulmonary surfactant adsorption by serum and the mechanisms of reversal by hydrophilic polymers: theory", in: *Biophysical journal* 89.3 (2005), pp. 1621–1629.

[390] Lasantha Gunasekara et al., "A comparative study of mechanisms of surfactant inhibition", in: *Biochimica et Biophysica Acta (BBA)-Biomembranes* 1778.2 (2008), pp. 433–444.

[391] Gordon R Bernard et al., "The American-European Consensus Conference on ARDS. Definitions, mechanisms, relevant outcomes, and clinical trial coordination.", in: *American journal of respiratory and critical care medicine* 149.3 (1994), pp. 818–824.

[392] BA Holm, RH Notter, and JN Finkelstein, "Surface property changes from interactions of albumin with natural lung surfactant and extracted lung lipids.", in: *Chemistry and physics of lipids* 38.3 (1985), pp. 287–298.

[393] Giuseppe Colacicco and Mukul K Basu, "Effect of serum albumin on dynamic force-area curve of dipalmitoyl lecithin", in: *Respiration physiology* 32.3 (1978), pp. 265–279.

[394] Chia-Chyi Cheng and Chien-Hsiang Chang, "Retardation effect of tyloxapol on inactivation of dipalmitoyl phosphatidylcholine surface activity by albumin", in: *Langmuir* 16.2 (2000), pp. 437–441.

[395] Xinyun Wen and Elias I Franses, "Adsorption of bovine serum albumin at the air/water interface and its effect on the formation of DPPC surface film", in: *Colloids and Surfaces A: Physicochemical and Engineering Aspects* 190.3 (2001), pp. 319–332.

[396] SA Tabak and RH Notter, "Effect of plasma proteins on the dynamic Π—a characteristics of saturated phospholipid films", in: *Journal of Colloid and Interface Science* 59.2 (1977), pp. 293–300.

[397] Bruce A Holm, Zhengdong Wang, and Robert H Notter, "Multiple mechanisms of lung surfactant inhibition", in: *Pediatric research* 46.1 (1999), p. 85.

[398] Antonio Anzueto et al., "Aerosolized surfactant in adults with sepsis-induced acute respiratory distress syndrome", in: *New England Journal of Medicine* 334.22 (1996), pp. 1417–1422.

[399] Joseph A Zasadzinski et al., "Overcoming rapid inactivation of lung surfactant: analogies between competitive adsorption and colloid stability", in: *Biochimica et Biophysica Acta (BBA)-Biomembranes* 1798.4 (2010), pp. 801–828.

[400] TJ Gregory et al., "Surfactant chemical composition and biophysical activity in acute respiratory distress syndrome.", in: *The Journal of clinical investigation* 88.6 (1991), pp. 1976–1981.

[401] Timothy J Gregory et al., "Bovine surfactant therapy for patients with acute respiratory distress syndrome.", in: *American journal of respiratory and critical care medicine* 155.4 (1997), pp. 1309–1315.

[402] Bruce A Holm et al., "Biophysical inhibition of synthetic lung surfactants", in: *Chemistry and physics of lipids* 52.3-4 (1990), pp. 243–250.

[403] THOMAS M HYERS, "Adult respiratory distress syndrome: definition, risk factors, and outcome", in: *Lung biology in health and disease* 50 (1991), pp. 23–36.

[404] Maria Deja et al., "Epidemiology and Pathophysiology of the acute respiratory distress syndrome (ARDS)", in: *Anasthesiologie, Intensivmedizin, Notfallmedizin, Schmerztherapie: AINS* 43.11-12 (2008), pp. 758–66.

[405] Connor Eichenwald et al., "Neonatal Partial Liquid Ventilation for the Treatment and Prevention of Bronchopulmonary Dysplasia", in: *NeoReviews* 21.4 (2020), e238–e248.

[406] Jörg U Bleyl et al., "Changes in pulmonary function and oxygenation during application of perfluorocarbon vapor in healthy and oleic acid-injured animals", in: *Critical care medicine* 30.6 (2002), pp. 1340–1347.

[407] K Von der Hardt, "Schoof E, Kandler MA, Dotsch J, Rascher W", in: *Aerosolized perfluorocarbon suppresses early pulmonary inflammatory response in a surfactant-depleted piglet model. Pediatr Res* 51 (2002), pp. 177–182.

[408] JU Bleyl et al., "Reduction in the aggressiveness of ventilation by inhalation of perfluorohexane after therapy of oleic acid-induced respiratory failure", in: *Der Anaesthesist* 53.2 (2004), pp. 137–143.

[409] Florian F Kneisel et al., "Effects of perfluorohexan vapor on gas exchange, respiratory mechanics, and lung histology in pigs with lung injury after endotoxin infusion", in: *Anesthesiology* 103.3 (2005), pp. 585–94.

[410] Katharina Von Der Hardt et al., "Aerosolized perfluorocarbon suppresses early pulmonary inflammatory response in a surfactant-depleted piglet model", in: *Pediatric research* 51.2 (2002), pp. 177–182.

[411] Michael Andreas Kandler et al., "Dose response to aerosolized perflubron in a neonatal swine model of lung injury", in: *Pediatric research* 56.2 (2004), pp. 191–197.

[412] Michael A Kandler et al., "Persistent improvement of gas exchange and lung mechanics by aerosolized perfluorocarbon", in: *American journal of respiratory and critical care medicine* 164.1 (2001), pp. 31–35.

[413] Marcelo Gama de Abreu et al., "Vaporized perfluorohexane attenuates ventilator-induced lung injury in isolated, perfused rabbit lungs", in: *Anesthesiology: The Journal of the American Society of Anesthesiologists* 102.3 (2005), pp. 597–605.

[414] U Kaisers, KP Kelly, and T Busch, "Liquid ventilation", in: *British Journal of anaesthesia* 91.1 (2003), pp. 143–151.

[415] William A Pryor et al., "Free radical biology and medicine: it's a gas, man!", in: *American Journal of Physiology-Regulatory, Integrative and Comparative Physiology* 291.3 (2006), R491–R511.

[416] Alain Tressaud and Gunter Haufe, *Fluorine and health: molecular imaging, biomedical materials and pharmaceuticals*, Elsevier, 2008.

[417] Leland C Clark and Frank Gollan, "Survival of mammals breathing organic liquids equilibrated with oxygen at atmospheric pressure", in: *Science* 152.3730 (1966), pp. 1755–1756.

[418] Ronald B Hirschl et al., "Liquid ventilation in adults, children, and full-term neonates", in: *The Lancet* 346.8984 (1995), pp. 1201–1202.

[419] Ronald B Hirschl et al., "Liquid ventilation provides uniform distribution of perfluorocarbon in the setting of respiratory failure.", in: *Surgery* 116.2 (1994), pp. 159–67.

[420] J Craig Jackson et al., "Full-tidal liquid ventilation with perfluorocarbon for prevention of lung injury in newborn non-human primates", in: *Artificial Cells, Blood Substitutes, and Biotechnology* 22.4 (1994), pp. 1121–1132.

[421] BRADLEY P Fuhrman, PAMELA R Paczan, and MARIA DeFrancisis, "Perfluorocarbon-associated gas exchange.", in: *Critical care medicine* 19.5 (1991), pp. 712–722.

[422] Ahmet S Tütüncü, N Simon Faithfull, Burkhard Lachmann, et al., "Comparison of ventilatory support with intratracheal perfluorocarbon administration and conventional mechanical ventilation in animals with acute respiratory failure", in: *American Review of Respiratory Disease* 148 (1993), pp. 785–785.

[423] Ronald B Hirschl et al., "Improvement of gas exchange, pulmonary function, and lung injury with partial liquid ventilation: a study model in a setting of severe respiratory failure", in: *Chest* 108.2 (1995), pp. 500–508.

[424] Lynn J Hernan et al., "Perfluorocarbon-associated gas exchange in normal and acid-injured large sheep", in: *Critical care medicine* 24.3 (1996), pp. 475–481.

[425] Paul G Gauger et al., "Initial experience with partial liquid ventilation in pediatric patients with the acute respiratory distress syndrome", in: *Critical care medicine* 24.1 (1996), pp. 16–22.

[426] Ronald B Hirschl et al., "Initial experience with partial liquid ventilation in adult patients with the acute respiratory distress syndrome", in: *Jama* 275.5 (1996), pp. 383–389.

[427] Marla R Wolfson and Thomas H Shaffer, "Pulmonary applications of perfluorochemical liquids: ventilation and beyond", in: *Paediatric respiratory reviews* 6.2 (2005), pp. 117–127.

[428] Jay S Greenspan et al., "Liquid ventilation of human preterm neonates", in: *The Journal of pediatrics* 117.1 (1990), pp. 106–111.

[429] Corinne Lowe Leach et al., "Partial liquid ventilation with perflubron in premature infants with severe respiratory distress syndrome", in: *New England Journal of Medicine* 335.11 (1996), pp. 761–767.

[430] Thomas Pranikoff, Paul G Gauger, and Ronald B Hirschl, "Partial liquid ventilation in newborn patients with congenital diaphragmatic hernia", in: *Journal of pediatric surgery* 31.5 (1996), pp. 613–618.

[431] Martin A Croce et al., "Partial liquid ventilation decreases the inflammatory response in the alveolar environment of trauma patients", in: *Journal of Trauma and Acute Care Surgery* 45.2 (1998), pp. 273–282.

[432] M Quintel, "Partielle Flüssigkeitsbeatmung", in: *Anaesthesist* 47 (1998), pp. 47–9.

[433] R Bartlett et al., "A phase II randomized, controlled trial of partial liquid ventilation (PLV) in adult patients with acute hypoxemic respiratory failure (AHRF)", in: *Crit Care Med* 25.1 (1997), A35.

[434] Robert M Kacmarek et al., "Partial liquid ventilation in adult patients with acute respiratory distress syndrome", in: *American journal of respiratory and critical care medicine* 173.8 (2006), pp. 882–889.

[435] Imelda M Galvin et al., "Partial liquid ventilation for preventing death and morbidity in adults with acute lung injury and acute respiratory distress syndrome", in: *Cochrane Database of Systematic Reviews* 7 (2013).

[436] Mark W Davies and Philip H Sargent, "Partial liquid ventilation for the prevention of mortality and morbidity in paediatric acute lung injury and acute respiratory distress syndrome", in: *Cochrane Database of Systematic Reviews* 4 (2004).

[437] Alan H Jobe and Suhas G Kallapur, "Long term consequences of oxygen therapy in the neonatal period", in: *Seminars in Fetal and Neonatal Medicine*, vol. 15, 4, Elsevier, 2010, pp. 230–235.

[438] Mary E Revenis and Michael A Kaliner, "Lactoferrin and lysozyme deficiency in airway secretions: association with the development of bronchopulmonary dysplasia", in: *The Journal of pediatrics* 121.2 (1992), pp. 262–270.

[439] Alecia Thompson and Vineet Bhandari, "Pulmonary biomarkers of bronchopulmonary dysplasia", in: *Biomarker insights* 3 (2008), BMI–S834.

[440] Frédéric Gerber et al., "Potential use of fluorocarbons in lung surfactant therapy", in: *Artificial cells, blood substitutes, and biotechnology* 35.2 (2007), pp. 211–220.

[441] Frédéric Gerber et al., "Preventing Crystallization of Phospholipids in Monolayers: A New Approach to Lung-Surfactant Therapy", in: *Angewandte Chemie International Edition* 44.18 (2005), pp. 2749–2752.

[442] Phuc Nghia Nguyen et al., "Counteracting the inhibitory effect of proteins towards lung surfactant substitutes: a fluorocarbon gas helps displace albumin at the air/water interface", in: *Chemical Communications* 50.78 (2014), pp. 11576–11579.

[443] Phuc Nghia Nguyen et al., "Reversing the course of the competitive adsorption between a phospholipid and albumin at an air–water interface", in: *Soft Matter* 9.42 (2013), pp. 9972–9976.

[444] Austin Bassett Thompson et al., "Lower respiratory tract lactoferrin and lysozyme arise primarily in the airways and are elevated in association with chronic bronchitis.", in: *The Journal of laboratory and clinical medicine* 115.2 (1990), pp. 148–158.

[445] Marie Pierre Krafft and Jean G Riess, "Perfluorocarbons: Life sciences and biomedical uses Dedicated to the memory of Professor Guy Ourisson, a true RENAISSANCE man.", in: *Journal of Polymer Science Part A: Polymer Chemistry* 45.7 (2007), pp. 1185–1198.

[446] Marie Pierre Krafft and Jean G Riess, "Chemistry, physical chemistry, and uses of molecular fluorocarbon- hydrocarbon diblocks, triblocks, and related compounds unique "apolar" components for self-assembled colloid and interface engineering", in: *Chemical reviews* 109.5 (2009), pp. 1714–1792.

[447] Günter Haufe, "Handbook of Fluorous Chemistry. Herausgegeben von John A. Gladysz, Dennis P. Curran und István T. Horváth.", in: *Angewandte Chemie* 117.27 (2005), pp. 4191–4192.

[448] BE Smart, "Organofluorine Chemistry", in: *Principles and Commercial Applications* (1994), p. 57.

[449] MP Krafft and JG Riess, "Highly fluorinated amphiphiles and colloidal systems, and their applications in the biomedical field. A contribution", in: *Biochimie* 80.5-6 (1998), pp. 489–514.

[450] Jean G Riess, "Fluorous micro-and nanophases with a biomedical perspective", in: *Tetrahedron* 58.20 (2002), pp. 4113–4131.

[451] Jack D Dunitz and Robin Taylor, "Organic fluorine hardly ever accepts hydrogen bonds", in: *Chemistry–A European Journal* 3.1 (1997), pp. 89–98.

[452] Jack D Dunitz, "Organic fluorine: odd man out", in: *ChemBioChem* 5.5 (2004), pp. 614–621.

[453] F Faude, S Wolf, and P Wiedemann, "Flüssige Perfluorkarbone in der Glaskörper und Netzhautchirurgie", in: *Der Ophthalmologe* 97.9 (2000), pp. 652–661.

[454] John A Gladysz, Dennis P Curran, and István T Horváth, *Handbook of fluorous chemistry*, John Wiley & Sons, 2006.

[455] Peter J Papadakos and Burkhard Lachmann, *Mechanical Ventilation E-Book: Clinical Applications and Pathophysiology*, Elsevier Health Sciences, 2007.

[456] Jürgen P Meinhardt and Michael Quintel, "Liquid ventilation", in: *Mechanical Ventilation E-Book: Clinical Applications and Pathophysiology* (2007), p. 286.

[457] Jean G Riess, "Understanding the fundamentals of perfluorocarbons and perfluorocarbon emulsions relevant to in vivo oxygen delivery", in: *Artificial cells, blood substitutes, and biotechnology* 33.1 (2005), pp. 47–63.

[458] Ashley L Farris, Alexandra N Rindone, and Warren L Grayson, "Oxygen delivering biomaterials for tissue engineering", in: *Journal of materials chemistry B* 4.20 (2016), pp. 3422–3432.

[459] Erik Kissa, "Fluorinated surfactants", in: *Surfactant science series* 50 (1994).

[460] Marie Pierre Krafft, "Fluorocarbons and fluorinated amphiphiles in drug delivery and biomedical research", in: *Advanced drug delivery reviews* 47.2-3 (2001), pp. 209–228.

[461] A van Bondi, "van der Waals volumes and radii", in: *The Journal of physical chemistry* 68.3 (1964), pp. 441–451.

[462] Gordon JT Tiddy, "Concentrated surfactant systems", in: *Modern Trends of Colloid Science in Chemistry and Biology*, Springer, 1985, pp. 148–183.

[463] Milton J Rosen and Joy T Kunjappu, *Surfactants and interfacial phenomena*, John Wiley & Sons, 2012.

[464] H Hoffmann, J Kalus, and H Thurn, "Small angle neutron scattering measurements on micellar solutions of perfluor detergents", in: *Colloid and Polymer Science* 261.12 (1983), pp. 1043–1049.

[465] David F Eaton and Bruce E Smart, "Are fluorocarbon chains stiffer than hydrocarbon chains? Dynamics of end-to-end cyclization in a C8F16 segment monitored by fluorescence", in: *Journal of the American Chemical Society* 112.7 (1990), pp. 2821–2823.

[466] David WR Gruen, "A model for the chains in amphiphilic aggregates. 2. Thermodynamic and experimental comparisons for aggregates of different shape and size", in: *The Journal of Physical Chemistry* 89.1 (1985), pp. 153–163.

[467] O Habler, M Kleen, and K Messmer, "Clinical potential of intravenously administered perfluorocarbons.", in: *Acta anaesthesiologica Scandinavica. Supplementum* 111 (1997), p. 256.

[468] Vishwanath H Dalvi and Peter J Rossky, "Molecular origins of fluorocarbon hydrophobicity", in: *Proceedings of the National Academy of Sciences* 107.31 (2010), pp. 13603–13607.

[469] Jean G Riess, "Perfluorocarbon-based oxygen delivery", in: *Artificial cells, blood substitutes, and biotechnology* 34.6 (2006), pp. 567–580.

[470] Bruce D Spiess, "Perfluorocarbon emulsions as a promising technology: a review of tissue and vascular gas dynamics", in: *Journal of Applied Physiology* 106.4 (2009), pp. 1444–1452.

[471] U Gross, H Reichelt, et al., "Perfluorocarbons: chemically inert but biologically active?", in: *Journal of fluorine chemistry* 53.2 (1991), pp. 155–161.

[472] Thomas H Shaffer et al., "Liquid ventilation in premature lambs: uptake, biodistribution and elimination of perfluorodecalin liquid", in: *Reproduction, fertility and development* 8.3 (1996), pp. 409–416.

[473] BE Smart, "Fluorocarbons", in: *Halides, Pseudo-Halides and Azides (1983) Supplement D: Part 1* 1 (1983), pp. 603–655.

[474] TM REED III, "Physical chemistry of fluorocarbons", in: *Fluorine chemistry*, Elsevier, 1964, pp. 133–236.

[475] Jean G Riess, "Highly fluorinated systems for oxygen transport, diagnosis and drug delivery", in: *Colloids and Surfaces A: Physicochemical and Engineering Aspects* 84.1 (1994), pp. 33–48.

[476] Bruce A Holm and Sadis Matalon, "Role of pulmonary surfactant in the development and treatment of adult respiratory distress syndrome.", in: *Anesthesia and analgesia* 69.6 (1989), pp. 805–818.

[477] Olga Rafikova et al., "Control of plasma nitric oxide bioactivity by perfluorocarbons: physiological mechanisms and clinical implications", in: *Circulation* 110.23 (2004), pp. 3573–3580.

[478] AMA Dias et al., "Solubility of oxygen in liquid perfluorocarbons", in: *Fluid Phase Equilibria* 222 (2004), pp. 325–330.

[479] Thomas H Shaffer, Marla R Wolfson, and Leland C Clark Jr, "Liquid ventilation", in: *Pediatric pulmonology* 14.2 (1992), pp. 102–109.

[480] Kenneth C Lowe, "Fluorinated blood substitutes and oxygen carriers", in: *Journal of Fluorine Chemistry* 109.1 (2001), pp. 59–65.

[481] Jean G Riess, "Oxygen carriers (blood substitutes) Raison dEtre, chemistry, and some physiology Blut ist ein ganz besondrer Saft", in: *Chemical Reviews* 101.9 (2001), pp. 2797–2920.

[482] Yuji Fujino et al., "Partial liquid ventilation ventilates better than gas ventilation", in: *American journal of respiratory and critical care medicine* 162.2 (2000), pp. 650–657.

[483] Cynthia A Cox et al., "Liquid ventilation: Gas exchange, perfluorochemical uptake, and biodistribution in an acute lung injury", in: *Pediatric Critical Care Medicine* 3.3 (2002), pp. 288–296.

[484] Pierandrea Lo Nostro, "Phase separation properties of fluorocarbons, hydrocarbons and their copolymers", in: *Advances in colloid and interface science* 56 (1995), pp. 245–287.

[485] Douglas L Dorset, "Binary phase behavior of perfluoroalkanes", in: *Macromolecules* 23.3 (1990), pp. 894–901.

[486] P Mukerjee, "Fluorocarbon-hydrocarbon interactions in interfacial and micellar systems", in: *Journal of the American Oil Chemists Society* 59.12 (1982), pp. 573–578.

[487] Jean G Riess, "Overview of progress in the fluorocarbon approach to in vivo oxygen delivery", in: *Biomaterials, Artificial Cells and Immobilization Biotechnology* 20.2-4 (1992), pp. 183–202.

[488] Eric T Ahrens and Jia Zhong, "In vivo MRI cell tracking using perfluorocarbon probes and fluorine-19 detection", in: *NMR in biomedicine* 26.7 (2013), pp. 860–871.

[489] Eric Lambert, Vijay S Gorantla, and Jelena M Janjic, "Pharmaceutical design and development of perfluorocarbon nanocolloids for oxygen delivery in regenerative medicine", in: *Nanomedicine* 14.20 (2019), pp. 2697–2712.

[490] Fanny Chapelin, Christian M Capitini, and Eric T Ahrens, "Fluorine-19 MRI for detection and quantification of immune cell therapy for cancer", in: *Journal for immunotherapy of cancer* 6.1 (2018), p. 105.

[491] Junjie Chen et al., "Perfluorocarbon nanoparticles for physiological and molecular imaging and therapy", in: *Advances in chronic kidney disease* 20.6 (2013), pp. 466–478.

[492] Qiyang Chen, Jaesok Yu, and Kang Kim, "optically-triggered phase-transition droplets for photoacoustic imaging", in: *Biomedical engineering letters* 8.2 (2018), pp. 223–229.

[493] Daniel Jirak et al., "Fluorine polymer probes for magnetic resonance imaging: quo vadis?", in: *Magnetic Resonance Materials in Physics, Biology and Medicine* 32.1 (2019), pp. 173–185.

[494] Natalya Rapoport, "Drug loaded perfluorocarbon nanodroplets for ultrasound mediated drug delivery", in: *Therapeutic Ultrasound*, Springer, 2016, pp. 221–241.

[495] Donato Cosco et al., "Perfluorocarbon-loaded micro and nanosystems for medical imaging: A state of the art", in: *Journal of Fluorine Chemistry* 171 (2015), pp. 18–26.

[496] Bruce D Spiess, "Perfluorocarbon gas transport: an overview of medical history with yet unrealized potentials", in: *Shock* 52.1S (2019), pp. 7–12.

[497] Radwa H Abou-Saleh et al., "The influence of intercalating perfluorohexane into lipid shells on nano and microbubble stability", in: *Soft matter* 12.34 (2016), pp. 7223–7230.

[498] Rudin Markus, *Molecular imaging: basic principles and applications in biomedical research*, World Scientific, 2013.

[499] Linsey C Phillips et al., "Phase-shift perfluorocarbon agents enhance high intensity focused ultrasound thermal delivery with reduced near-field heating", in: *The Journal of the Acoustical Society of America* 134.2 (2013), pp. 1473–1482.

[500] Ernest G Schutt et al., "Injectable microbubbles as contrast agents for diagnostic ultrasound imaging: the key role of perfluorochemicals", in: *Angewandte Chemie International Edition* 42.28 (2003), pp. 3218–3235.

[501] Natalya Rapoport, Zhonggao Gao, and Anne Kennedy, "Multifunctional nanoparticles for combining ultrasonic tumor imaging and targeted chemotherapy", in: *Journal of the National Cancer Institute* 99.14 (2007), pp. 1095–1106.

[502] Markus Rudin, "Molecular imaging: basic principles and applications in biomedical research", in: (2005).

[503] Emma Kanbar et al., "Impact of filling gas on subharmonic emissions of phospholipid ultrasound contrast agents", in: *Ultrasound in medicine & biology* 43.5 (2017), pp. 1004–1015.

[504] Eleanor Stride and Mohan Edirisinghe, *Special issue on microbubbles: from contrast enhancement to cancer therapy*, 2009.

[505] Csongor Szíjjártó et al., "Effects of perfluorocarbon gases on the size and stability characteristics of phospholipid-coated microbubbles: osmotic effect versus interfacial film stabilization", in: *Langmuir* 28.2 (2012), pp. 1182–1189.

[506] Gregory M Lanza and Samuel A Wickline, "Targeted ultrasonic contrast agents for molecular imaging and therapy", in: *Progress in cardiovascular diseases* 44.1 (2001), pp. 13–31.

[507] Jean G Riess, "Reassessment of criteria for the selection of perfluorochemicals for second-generation blood substitutes: Analysis of structure/property relationships", in: *Artificial organs* 8.1 (1984), pp. 44–56.

[508] Katja B Ferenz, "Artificial oxygen carriers", in: *Current Trends and Future Developments on (Bio-) Membranes*, Elsevier, 2020, pp. 191–213.

[509] Anna Wrobeln et al., "Albumin-derived perfluorocarbon-based artificial oxygen carriers: A physico-chemical characterization and first in vivo evaluation of biocompatibility", in: *European Journal of Pharmaceutics and Biopharmaceutics* 115 (2017), pp. 52–64.

[510] Hohyeon Lee et al., "Microbubbles used for contrast enhanced ultrasound and theragnosis: a review of principles to applications", in: *Biomedical engineering letters* 7.2 (2017), pp. 59–69.

[511] Simona Rossi, Gilles Waton, and Marie Pierre Krafft, "Small Phospholipid-Coated Gas Bubbles Can Last Longer than Larger Ones", in: *ChemPhysChem* 9.14 (2008), pp. 1982–1985.

[512] Simona Rossi, Gilles Waton, and Marie Pierre Krafft, "Phospholipid-coated gas bubble engineering: Key parameters for size and stability control, as determined by an acoustical method", in: *Langmuir* 26.3 (2010), pp. 1649–1655.

[513] JG Riess, "Perfluorochemical emulsions for intravascular use: principles, materials and methods", in: *Fluorine in Medicine, Rapra Technol Ltd., Shawbury, paper* 20 (1994).

[514] Camila Irene Castro and Juan Carlos Briceno, "Perfluorocarbon-based oxygen carriers: review of products and trials", in: *Artificial organs* 34.8 (2010), pp. 622–634.

[515] Harvey S Uy, Miguel D de Leon, and Pearl T Villalon, "Comparison of two techniques for perfluoropropane gas fill in the management of retinal detachment", in: *Philippine Journal of Ophthalmology* 32.2 (2007), pp. 66–69.

[516] Stanley Chang et al., "Perfluorocarbon gases in vitreous surgery", in: *Ophthalmology* 92.5 (1985), pp. 651–656.

[517] Harvey Lincoff et al., "Intravitreal longevity of three perfluorocarbon gases", in: *Archives of ophthalmology* 98.9 (1980), pp. 1610–1611.

[518] M Bonnet, E Santamaria, and J Mouche, "Intraoperative use of pure perfluoropropane gas in the management of proliferative vitreoretinopathy", in: *Graefe's archive for clinical and experimental ophthalmology* 225.4 (1987), pp. 299–302.

[519] Sanford M Meyers et al., "Variation of perfluoropropane disappearance after vitrectomy.", in: *Retina (Philadelphia, Pa.)* 12.4 (1992), pp. 359–363.

[520] Steven G Kramer et al., "Perfluorocarbon liquids in ophthalmology", in: *Survey of ophthalmology* 39.5 (1995), pp. 375–395.

[521] Bernd Kirchhof et al., "Use of perfluorohexyloctane as a long-term internal tamponade agent in complicated retinal detachment surgery", in: *American journal of ophthalmology* 133.1 (2002), pp. 95–101.

[522] Emanuel Bertrand et al., "First-order and critical wetting of alkanes on water", in: *Physical review letters* 85.6 (2000), p. 1282.

[523] Daniel Bonn, "Wetting transitions", in: *Current opinion in colloid & interface science* 6.1 (2001), pp. 22–27.

[524] Joseph O Indekeu et al., "Wetting of alkanes on water from a Cahn-type theory: effects of long-range forces", in: *Journal of statistical physics* 95.5-6 (1999), pp. 1009–1043.

[525] Jacob N Israelachvili, "Adhesion forces between surfaces in liquids and condensable vapours", in: *Surface Science Reports* 14.3 (1992), pp. 109–159.

[526] M Paulus, C Gutt, and M Tolan, "Surface roughness and adsorption isotherms of molecularly thin liquid films: An x-ray reflectivity study", in: *Physical Review E* 72.6 (2005), p. 061601.

[527] Lars Boewer et al., "Concentration-Induced Wetting Transition in Water-Tetrahydrofuran-Isobutane Systems", in: *The Journal of Physical Chemistry C* 115.37 (2011), pp. 18235–18238.

[528] Daniel Bonn et al., "Wetting and spreading", in: *Reviews of modern physics* 81.2 (2009), p. 739.

[529] Erle C Donaldson and Waqi Alam, *Wettability*, Elsevier, 2013.

[530] Bijoyendra Bera, *Ion and surfactant induced wetting transition*, University of Twente, 2016.

[531] J Frenkel, *Kinetic Theory of Liquids, 219–264 Oxford University Press*, 1946.

[532] George Halsey, "Physical adsorption on non-uniform surfaces", in: *The Journal of chemical physics* 16.10 (1948), pp. 931–937.

[533] Terrell L Hill, "Physical adsorption and the free volume model for liquids", in: *The Journal of Chemical Physics* 17.6 (1949), pp. 590–590.

[534] Werner Kunz, JWNB Henle, and Barry W Ninham, ""Zur Lehre von der Wirkung der Salze"(about the science of the effect of salts): Franz Hofmeister's historical papers", in: *Current Opinion in Colloid & Interface Science* 9.1-2 (2004), pp. 19–37.

[535] Franz Hofmeister, "Zur lehre von der wirkung der salze", in: *Archiv für experimentelle Pathologie und Pharmakologie* 25.1 (1888), pp. 1–30.

[536] Kim D Collins and Michael W Washabaugh, "The Hofmeister effect and the behaviour of water at interfaces", in: *Quarterly reviews of biophysics* 18.4 (1985), pp. 323–422.

[537] Ronald Wilfrid Gurney and Ronald W Gurney, "Ionic processes in solution", in: (1953).

[538] Yizhak Marcus, "Effect of ions on the structure of water: structure making and breaking", in: *Chemical reviews* 109.3 (2009), pp. 1346–1370.

[539] N Galamba, "On the effects of temperature, pressure, and dissolved salts on the hydrogen-bond network of water", in: *The Journal of Physical Chemistry B* 117.2 (2013), pp. 589–601.

[540] Jagadish Chandra Roy, Shuvo Das, and Md Nazrul Islam, "Influence of Kosmotropes and Chaotropes on the Krafft Temperature and Critical Micelle Concentration of Tetradecyltrimethylammonium Bromide in Aqueous Solution", in: *Journal of Solution Chemistry* 48.5 (2019), pp. 758–773.

[541] Jared D Smith, Richard J Saykally, and Phillip L Geissler, "The effects of dissolved halide anions on hydrogen bonding in liquid water", in: *Journal of the American Chemical Society* 129.45 (2007), pp. 13847–13856.

[542] Anne Willem Omta et al., "Negligible effect of ions on the hydrogen-bond structure in liquid water", in: *Science* 301.5631 (2003), pp. 347–349.

[543] Michel F Kropman and Huib J Bakker, "Effect of ions on the vibrational relaxation of liquid water", in: *Journal of the American Chemical Society* 126.29 (2004), pp. 9135–9141.

[544] MF Kropman and HJ Bakker, "Femtosecond mid-infrared spectroscopy of aqueous solvation shells", in: *The Journal of Chemical Physics* 115.19 (2001), pp. 8942–8948.

[545] Drew F Parsons et al., "Hofmeister effects: interplay of hydration, nonelectrostatic potentials, and ion size", in: *Physical Chemistry Chemical Physics* 13.27 (2011), pp. 12352–12367.

[546] Yanjie Zhang and Paul S Cremer, "Interactions between macromolecules and ions: the Hofmeister series", in: *Current opinion in chemical biology* 10.6 (2006), pp. 658–663.

[547] Chang Q Sun, Yongli Huang, and Xi Zhang, "Hydration of Hofmeister ions", in: *Advances in colloid and interface science* (2019).

[548] Werner Kunz, P Lo Nostro, and Barry W Ninham, "The present state of affairs with Hofmeister effects", in: *Current opinion in colloid & interface science* 9.1-2 (2004), pp. 1–18.

[549] Pierandrea Lo Nostro and Barry W Ninham, "Hofmeister phenomena: an update on ion specificity in biology", in: *Chemical reviews* 112.4 (2012), pp. 2286–2322.

[550] Epameinondas Leontidis, "Chaotropic salts interacting with soft matter: beyond the lyotropic series", in: *Current Opinion in Colloid & Interface Science* 23 (2016), pp. 100–109.

[551] Peter Atkins and Tina Overton, *Shriver and Atkins' inorganic chemistry*, Oxford University Press, USA, 2010.

[552] John O'M Bockris, *Modern electrochemistry 2B: electrodics in chemistry, engineering, biology and environmental science*, vol. 2, Springer Science & Business Media, 2000.

[553] Terence Cosgrove, *Colloid science: principles, methods and applications*, John Wiley & Sons, 2010.

[554] Pierandrea Lo Nostro and Barry W Ninham, "Electrolytes and specific ion effects. New and old horizons", in: *Current Opinion in Colloid & Interface Science* 100.23 (2016), A1–A5.

[555] Barry W Ninham, "On progress in forces since the DLVO theory", in: *Advances in colloid and interface science* 83.1-3 (1999), pp. 1–17.

[556] M Boström, DRM Williams, and BW Ninham, "Specific ion effects: why DLVO theory fails for biology and colloid systems", in: *Physical review letters* 87.16 (2001), p. 168103.

[557] T Markovich, David Andelman, and Rudolf Podgornik, *Handbook of Lipid Membranes*, 2016.

[558] Kim D Collins, "Charge density-dependent strength of hydration and biological structure", in: *Biophysical journal* 72.1 (1997), pp. 65–76.

[559] John David Lee, *Concise inorganic chemistry*, John Wiley & Sons, 2008.

[560] Kim D Collins, "Ions from the Hofmeister series and osmolytes: effects on proteins in solution and in the crystallization process", in: *Methods* 34.3 (2004), pp. 300–311.

[561] WenJun Xie et al., "On the molecular mechanism of ion specific Hofmeister series", in: *Science China Chemistry* 57.1 (2014), pp. 36–47.

[562] Andrea Salis and Barry W Ninham, "Models and mechanisms of Hofmeister effects in electrolyte solutions, and colloid and protein systems revisited", in: *Chemical Society Reviews* 43.21 (2014), pp. 7358–7377.

[563] C Wm Outhwaite, "Extension of the Debye–Hückel theory of electrolyte solutions", in: *The Journal of Chemical Physics* 50.6 (1969), pp. 2277–2288.

[564] Zareen Abbas et al., "Corrected Debye- Hückel Theory of Salt Solutions: Size Asymmetry and Effective Diameters", in: *The Journal of Physical Chemistry B* 106.6 (2002), pp. 1403–1420.

[565] Kim D Collins, "Sticky ions in biological systems", in: *Proceedings of the National Academy of Sciences* 92.12 (1995), pp. 5553–5557.

[566] Mikael Lund, Luboš Vrbka, and Pavel Jungwirth, "Specific ion binding to nonpolar surface patches of proteins", in: *Journal of the American Chemical Society* 130.35 (2008), pp. 11582–11583.

[567] Rupali S Patil et al., "The viscosity B and D coefficient (Jones–Dole equation) studies in aqueous solutions of alkyltrimethylammonium bromides at 298.15 K", in: *Journal of Molecular Liquids* 200 (2014), pp. 416–424.

[568] Robert L Baldwin, "How Hofmeister ion interactions affect protein stability", in: *Biophysical journal* 71.4 (1996), pp. 2056–2063.

[569] Peter H Von Hippel and Thomas Schleich, "Ion effects on the solution structure of biological macromolecules", in: *Accounts of Chemical Research* 2.9 (1969), pp. 257–265.

[570] Nina Ni and Samuel H Yalkowsky, "Prediction of Setschenow constants", in: *International journal of pharmaceutics* 254.2 (2003), pp. 167–172.

[571] Barry W Ninham and Vassili Yaminsky, "Ion binding and ion specificity: the Hofmeister effect and Onsager and Lifshitz theories", in: *Langmuir* 13.7 (1997), pp. 2097–2108.

[572] M Boström, DRM Williams, and BW Ninham, "Ion specificity of micelles explained by ionic dispersion forces", in: *Langmuir* 18.16 (2002), pp. 6010–6014.

[573] Mathias Boström et al., "Hofmeister effects in membrane biology: the role of ionic dispersion potentials", in: *Physical Review E* 68.4 (2003), p. 041902.

[574] Nina Vlachy et al., "Hofmeister series and specific interactions of charged headgroups with aqueous ions", in: *Advances in colloid and interface science* 146.1-2 (2009), pp. 42–47.

[575] Werner Kunz, "Specific ion effects in colloidal and biological systems", in: *Current Opinion in Colloid & Interface Science* 15.1-2 (2010), pp. 34–39.

[576] Juan J Garcia-Celma et al., "Specific anion and cation binding to lipid membranes investigated on a solid supported membrane", in: *Langmuir* 23.20 (2007), pp. 10074–10080.

[577] Ran Friedman, "Membrane–ion interactions", in: *The Journal of membrane biology* 251.3 (2018), pp. 453–460.

[578] Ran Friedman, "Electrolyte solutions and specific ion effects on interfaces", in: *Journal of Chemical Education* 90.8 (2013), pp. 1018–1023.

[579] Benjamin Klasczyk et al., "Interactions of alkali metal chlorides with phosphatidylcholine vesicles", in: *Langmuir* 26.24 (2010), pp. 18951–18958.

[580] Rainer A Böckmann and Helmut Grubmüller, "Multistep binding of divalent cations to phospholipid bilayers: a molecular dynamics study", in: *Angewandte Chemie International Edition* 43.8 (2004), pp. 1021–1024.

[581] Hermann Träuble and Hansjörg Eibl, "Electrostatic effects on lipid phase transitions: membrane structure and ionic environment", in: *Proceedings of the National Academy of Sciences* 71.1 (1974), pp. 214–219.

[582] AL Hodgkin and Pv Horowicz, "The influence of potassium and chloride ions on the membrane potential of single muscle fibres", in: *The Journal of physiology* 148.1 (1959), pp. 127–160.

[583] Moises Eisenberg et al., "Adsorption of monovalent cations to bilayer membranes containing negative phospholipids", in: *Biochemistry* 18.23 (1979), pp. 5213–5223.

[584] Ronald J Clarke and Christian Lüpfert, "Influence of anions and cations on the dipole potential of phosphatidylcholine vesicles: a basis for the Hofmeister effect", in: *Biophysical journal* 76.5 (1999), pp. 2614–2624.

[585] Jonathan N Sachs et al., "Changes in phosphatidylcholine headgroup tilt and water order induced by monovalent salts: molecular dynamics simulations", in: *Biophysical journal* 86.6 (2004), pp. 3772–3782.

[586] Wei Zhao et al., "Atomic-scale structure and electrostatics of anionic palmitoyloleoylphosphatidylglycerol lipid bilayers with Na+ counterions", in: *Biophysical journal* 92.4 (2007), pp. 1114–1124.

[587] Jinsuk Song et al., "Specific ions modulate diffusion dynamics of hydration water on lipid membrane surfaces", in: *Journal of the American Chemical Society* 136.6 (2014), pp. 2642–2649.

[588] Horia I Petrache et al., "Salt screening and specific ion adsorption determine neutral-lipid membrane interactions", in: *Proceedings of the National Academy of Sciences* 103.21 (2006), pp. 7982–7987.

[589] Zhen Yang, "Hofmeister effects: an explanation for the impact of ionic liquids on biocatalysis", in: *Journal of biotechnology* 144.1 (2009), pp. 12–22.

[590] Beibei Kang et al., "Hofmeister Series: Insights of Ion Specificity from Amphiphilic Assembly and Interface Property", in: *ACS omega* 5.12 (2020), pp. 6229–6239.

[591] Epameinondas Leontidis, "Investigations of the Hofmeister series and other specific ion effects using lipid model systems", in: *Advances in colloid and interface science* 243 (2017), pp. 8–22.

[592] Virginia Mazzini and Vincent SJ Craig, "What is the fundamental ion-specific series for anions and cations? Ion specificity in standard partial molar volumes of electrolytes and electrostriction in water and non-aqueous solvents", in: *Chemical science* 8.10 (2017), pp. 7052–7065.

[593] Barry W Ninham and Pierandrea Lo Nostro, *Molecular forces and self assembly: in colloid, nano sciences and biology*, Cambridge University Press, 2010.

[594] R John Ellis, "Macromolecular crowding: obvious but underappreciated", in: *Trends in biochemical sciences* 26.10 (2001), pp. 597–604.

[595] Thomas J Jentsch, "VRACs and other ion channels and transporters in the regulation of cell volume and beyond", in: *Nature Reviews Molecular Cell Biology* 17.5 (2016), p. 293.

[596] Ove Sten-Knudsen, *Biological Membranes: Theory of transport, potentials and electric impulses*, Cambridge University Press, 2002.

[597] Harvey Lodish et al., "Intracellular ion environment and membrane electric potential", in: *Molecular Cell Biology. 4th edition*, WH Freeman, 2000.

[598] Jeremy M Berg, Lubert Stryer, and John L Tymoczko, *Stryer Biochemie*, Springer-Verlag, 2015.

[599] Bradley J Benson, Samuel Hawgood, and Mary C Williams, "Role of apoprotein and calcium ions in surfactant function", in: *Experimental lung research* 6.3-4 (1984), pp. 223–236.

[600] Agnieszka Olzynska et al., "Properties of Lipid Models of Lung Surfactant Containing Cholesterol and Oxidized Lipids: a Mixed Experimental and Computational Study", in: *Langmuir* (2020).

[601] Y Kuroki and Toyoaki Akino, "Pulmonary surfactant protein A (SP-A) specifically binds dipalmitoylphosphatidylcholine.", in: *Journal of Biological Chemistry* 266.5 (1991), pp. 3068–3073.

[602] Haihong Yang et al., "Regulation of calcium signaling in lung cancer", in: *Journal of thoracic disease* 2.1 (2010), p. 52.

[603] Teneale A Stewart, Kunsala TDS Yapa, and Gregory R Monteith, "Altered calcium signaling in cancer cells", in: *Biochimica et Biophysica Acta (BBA)-Biomembranes* 1848.10 (2015), pp. 2502–2511.

[604] Demetrios Papahadjopoulos, Shlomo Nir, and Nejat Düzgünes, "Molecular mechanisms of calcium-induced membrane fusion", in: *Journal of bioenergetics and biomembranes* 22.2 (1990), pp. 157–179.

[605] Ineke Brouwer et al., "Direct quantitative detection of Doc2b-induced hemifusion in optically trapped membranes", in: *Nature communications* 6.1 (2015), pp. 1–8.

[606] Xiaoshan Shi et al., "Ca 2+ regulates T-cell receptor activation by modulating the charge property of lipids", in: *Nature* 493.7430 (2013), pp. 111–115.

[607] Mark A Lemmon, "Membrane recognition by phospholipid-binding domains", in: *Nature reviews Molecular cell biology* 9.2 (2008), pp. 99–111.

[608] Robert D Nielsen et al., "A ruler for determining the position of proteins in membranes", in: *Journal of the American Chemical Society* 127.17 (2005), pp. 6430–6442.

[609] Alex Rcom-H'cheo-Gauthier, Jacob Goodwin, and Dean L Pountney, "Interactions between calcium and alpha-synuclein in neurodegeneration", in: *Biomolecules* 4.3 (2014), pp. 795–811.

[610] Michael J Berridge, Martin D Bootman, and Peter Lipp, "Calcium-a life and death signal", in: *Nature* 395.6703 (1998), pp. 645–648.

[611] MJ Berridge, "'Neuron-within-neuron'concept of calcium signalling", in: *JOURNAL OF PHYSIOLOGY-LONDON*, vol. 523, CAMBRIDGE UNIV PRESS 40 WEST 20TH STREET, NEW YORK, NY 10011-4211 USA, 2000, 95S–95S.

[612] Jang Won Seo and Tae Jin Park, "Magnesium metabolism", in: *Electrolyte & blood pressure* 6.2 (2008), pp. 86–95.

[613] Andrea MP Romani, "Cellular magnesium homeostasis", in: *Archives of biochemistry and biophysics* 512.1 (2011), pp. 1–23.

[614] HW Huang, D Li, and JA Cowan, "Biostructural chemistry of magnesium. regulation of mithramycin-DNA interactions by Mg2+ coordination", in: *Biochimie* 77.9 (1995), pp. 729–738.

[615] Eva Bilkova et al., "Calcium directly regulates phosphatidylinositol 4, 5-bisphosphate headgroup conformation and recognition", in: *Journal of the American Chemical Society* 139.11 (2017), pp. 4019–4024.

[616] Andrea MP Romani and Michael E Maguire, "Hormonal regulation of Mg 2+ transport and homeostasis in eukaryotic cells", in: *Biometals* 15.3 (2002), pp. 271–283.

[617] H Ebel and T Günther, "Magnesium metabolism: a review", in: *Clinical Chemistry and Laboratory Medicine* 18.5 (1980), pp. 257–270.

[618] Or Szekely et al., "The structure of ions and zwitterionic lipids regulates the charge of dipolar membranes", in: *Langmuir* 27.12 (2011), pp. 7419–7438.

[619] Alexandra Yu Antipina and Andrey A Gurtovenko, "Molecular mechanism of calcium-induced adsorption of DNA on zwitterionic phospholipid membranes", in: *The Journal of Physical Chemistry B* 119.22 (2015), pp. 6638–6645.

[620] Matti Javanainen et al., "Two cations, two mechanisms: interactions of sodium and calcium with zwitterionic lipid membranes", in: *Chemical Communications* 53.39 (2017), pp. 5380–5383.

[621] JA Cowan, *Introduction to the biological chemistry ofmagnesium*, 1995.

[622] Jan Wilschut et al., "Studies on the mechanism of membrane fusion: kinetics of calcium ion induced fusion of phosphatidylserine vesicles followed by a new assay for mixing of aqueous vesicle contents", in: *Biochemistry* 19.26 (1980), pp. 6011–6021.

[623] B Roy Frieden and Robert Gatenby, "Ion-Based Cellular Signal Transmission, Principles of Minimum Information Loss, and Evolution by Natural Selection", in: *International Journal of Molecular Sciences* 21.1 (2020), p. 9.

[624] Takashi Kodama et al., "Graded Coexpression of Ion Channel, Neurofilament, and Synaptic Genes in Fast-Spiking Vestibular Nucleus Neurons", in: *Journal of Neuroscience* 40.3 (2020), pp. 496–508.

[625] Adéla Melcrová et al., "The complex nature of calcium cation interactions with phospholipid bilayers", in: *Scientific reports* 6 (2016), p. 38035.

[626] Andrea Catte et al., "Molecular electrometer and binding of cations to phospholipid bilayers", in: *Physical Chemistry Chemical Physics* 18.47 (2016), pp. 32560–32569.

[627] Chanh Thi Minh Le et al., "Interaction of small ionic species with phospholipid membranes: the role of metal coordination", in: *Frontiers in Materials* 5 (2019), p. 80.

[628] Josef Melcr et al., "Accurate binding of sodium and calcium to a POPC bilayer by effective inclusion of electronic polarization", in: *The Journal of Physical Chemistry B* 122.16 (2018), pp. 4546–4557.

[629] LJ Lis et al., "Adsorption of divalent cations to a variety of phosphatidylcholine bilayers", in: *Biochemistry* 20.7 (1981), pp. 1771–1777.

[630] Joachim Seelig, "Interaction of phospholipids with Ca2+ ions. On the role of the phospholipid head groups", in: *Cell biology international reports* 14.4 (1990), pp. 353–360.

[631] Peter G Scherer and Joachim Seelig, "Structure and dynamics of the phosphatidylcholine and the phosphatidylethanolamine head group in L-M fibroblasts as studied by deuterium nuclear magnetic resonance.", in: *The EMBO journal* 6.10 (1987), pp. 2915–2922.

[632] Lisa B Dreier et al., "Saturation of charge-induced water alignment at model membrane surfaces", in: *Science advances* 4.3 (2018), eaap7415.

[633] S Kundu, A Datta, and S Hazra, "Effect of metal ions on monolayer collapses", in: *Langmuir* 21.13 (2005), pp. 5894–5900.

[634] Dong June Ahn and Elias I Franses, "Interactions of charged Langmuir monolayers with dissolved ions", in: *The Journal of chemical physics* 95.11 (1991), pp. 8486–8493.

[635] Ting Zhang et al., "Cation effects on phosphatidic acid monolayers at various pH conditions", in: *Chemistry and physics of lipids* 200 (2016), pp. 24–31.

[636] Piotr Jurkiewicz et al., "Structure, dynamics, and hydration of POPC/POPS bilayers suspended in NaCl, KCl, and CsCl solutions", in: *Biochimica et Biophysica Acta (BBA)-Biomembranes* 1818.3 (2012), pp. 609–616.

[637] Juan M Ruso et al., "Interactions between liposomes and cations in aqueous solution", in: *Journal of liposome research* 13.2 (2003), pp. 131–145.

[638] J Sabın et al., "Size and stability of liposomes: a possible role of hydration and osmotic forces", in: *The European Physical Journal E* 20.4 (2006), pp. 401–408.

[639] Juan Sabın et al., "On the effect of Ca2+ and La3+ on the colloidal stability of liposomes", in: *Langmuir* 21.24 (2005), pp. 10968–10975.

[640] Andria Aroti et al., "Monolayers, bilayers and micelles of zwitterionic lipids as model systems for the study of specific anion effects", in: *Colloids and Surfaces A: Physicochemical and Engineering Aspects* 303.1-2 (2007), pp. 144–158.

[641] Malcolm N Jones, "The surface properties of phospholipid liposome systems and their characterisation", in: *Advances in colloid and interface science* 54 (1995), pp. 93–128.

[642] Josef Melcr et al., "Transmembrane potential modeling: comparison between methods of constant electric field and ion imbalance", in: *Journal of chemical theory and computation* 12.5 (2016), pp. 2418–2425.

[643] Jean-François Tocanne and Justin Teissié, "Ionization of phospholipids and phospholipid-supported interfacial lateral diffusion of protons in membrane model systems", in: *Biochimica et Biophysica Acta (BBA)-Reviews on Biomembranes* 1031.1 (1990), pp. 111–142.

[644] Hans Binder and Olaf Zschörnig, "The effect of metal cations on the phase behavior and hydration characteristics of phospholipid membranes", in: *Chemistry and physics of lipids* 115.1-2 (2002), pp. 39–61.

[645] Epameinondas Leontidis and Andria Aroti, "Liquid expanded monolayers of lipids as model systems to understand the anionic Hofmeister series: 2. Ion partitioning is mostly a matter of size", in: *The Journal of Physical Chemistry B* 113.5 (2009), pp. 1460–1467.

[646] Robert Vácha et al., "Effects of alkali cations and halide anions on the DOPC lipid membrane", in: *The journal of physical chemistry A* 113.26 (2009), pp. 7235–7243.

[647] Frédéric F Harb and Bernard Tinland, "Effect of ionic strength on dynamics of supported phosphatidylcholine lipid bilayer revealed by FRAPP and Langmuir–Blodgett transfer ratios", in: *Langmuir* 29.18 (2013), pp. 5540–5546.

[648] Georg Pabst et al., "Rigidification of neutral lipid bilayers in the presence of salts", in: *Biophysical journal* 93.8 (2007), pp. 2688–2696.

[649] Andrey Filippov, Greger Orädd, and Göran Lindblom, "Effect of NaCl and CaCl2 on the lateral diffusion of zwitterionic and anionic lipids in bilayers", in: *Chemistry and physics of lipids* 159.2 (2009), pp. 81–87.

[650] Sergi Garcia-Manyes, Gerard Oncins, and Fausto Sanz, "Effect of ion-binding and chemical phospholipid structure on the nanomechanics of lipid bilayers studied by force spectroscopy", in: *Biophysical journal* 89.3 (2005), pp. 1812–1826.

[651] Sergi Garcia-Manyes, Gerard Oncins, and Fausto Sanz, "Effect of pH and ionic strength on phospholipid nanomechanics and on deposition process onto hydrophilic surfaces measured by AFM", in: *Electrochimica Acta* 51.24 (2006), pp. 5029–5036.

[652] Takeshi Fukuma, Michael J Higgins, and Suzanne P Jarvis, "Direct imaging of lipid-ion network formation under physiological conditions by frequency modulation atomic force microscopy", in: *Physical Review Letters* 98.10 (2007), p. 106101.

[653] Urs M Ferber, Gillian Kaggwa, and Suzanne P Jarvis, "Direct imaging of salt effects on lipid bilayer ordering at sub-molecular resolution", in: *European Biophysics Journal* 40.3 (2011), pp. 329–338.

[654] Lorena Redondo-Morata, Gerard Oncins, and Fausto Sanz, "Force spectroscopy reveals the effect of different ions in the nanomechanical behavior of phospholipid model membranes: the case of potassium cation", in: *Biophysical journal* 102.1 (2012), pp. 66–74.

[655] Max L Berkowitz, David L Bostick, and Sagar Pandit, "Aqueous solutions next to phospholipid membrane surfaces: insights from simulations", in: *Chemical reviews* 106.4 (2006), pp. 1527–1539.

[656] Arnau Cordomı, Olle Edholm, and Juan J Perez, "Effect of ions on a dipalmitoyl phosphatidylcholine bilayer. A molecular dynamics simulation study", in: *The Journal of Physical Chemistry B* 112.5 (2008), pp. 1397–1408.

[657] Arnau Cordomi, Olle Edholm, and Juan J Perez, "Effect of force field parameters on sodium and potassium ion binding to dipalmitoyl phosphatidylcholine bilayers", in: *Journal of chemical theory and computation* 5.8 (2009), pp. 2125–2134.

[658] Christopher C Valley et al., "NaCl interactions with phosphatidylcholine bilayers do not alter membrane structure but induce long-range ordering of ions and water", in: *The Journal of membrane biology* 244.1 (2011), p. 35.

[659] Max L Berkowitz and Robert Vácha, "Aqueous solutions at the interface with phospholipid bilayers", in: *Accounts of chemical research* 45.1 (2012), pp. 74–82.

[660] Hideo Akutsu and Joachim Seelig, "Interaction of metal ions with phosphatidylcholine bilayer membranes", in: *Biochemistry* 20.26 (1981), pp. 7366–7373.

[661] Christian Altenbach and Joachim Seelig, "Calcium binding to phosphatidylcholine bilayers as studied by deuterium magnetic resonance. Evidence for the formation of a calcium complex with two phospholipid molecules", in: *Biochemistry* 23.17 (1984), pp. 3913–3920.

[662] Daniela Uhrıková et al., "Structural changes in dipalmitoylphosphatidylcholine bilayer promoted by Ca2+ ions: a small-angle neutron scattering study", in: *Chemistry and physics of lipids* 155.2 (2008), pp. 80–89.

[663] H Hauser et al., "Conformation of the lecithin polar group in charged vesicles", in: *Nature* 261.5559 (1976), pp. 390–394.

[664] H Hauser et al., "The conformation of the polar group of lysophosphatidylcholine in H2O; conformational changes induced by polyvalent cations", in: *Biochimica et Biophysica Acta (BBA)-Biomembranes* 508.3 (1978), pp. 450–463.

[665] L Herbette, CA Napolitano, and RV McDaniel, "Direct determination of the calcium profile structure for dipalmitoyllecithin multilayers using neutron diffraction", in: *Biophysical journal* 46.6 (1984), pp. 677–685.

[666] Siewert J Marrink et al., "Computational modeling of realistic cell membranes", in: *Chemical reviews* 119.9 (2019), pp. 6184–6226.

[667] OH Samuli Ollila and Georg Pabst, "Atomistic resolution structure and dynamics of lipid bilayers in simulations and experiments", in: *Biochimica et Biophysica Acta (BBA)-Biomembranes* 1858.10 (2016), pp. 2512–2528.

[668] David Poger, Bertrand Caron, and Alan E Mark, "Validating lipid force fields against experimental data: Progress, challenges and perspectives", in: *Biochimica et Biophysica Acta (BBA)-Biomembranes* 1858.7 (2016), pp. 1556–1565.

[669] Giray Enkavi et al., "Multiscale simulations of biological membranes: the challenge to understand biological phenomena in a living substance", in: *Chemical reviews* 119.9 (2019), pp. 5607–5774.

[670] DWCSKGR Papahadjopoulos et al., "Studies on membrane fusion. III. The role of calcium-induced phase changes", in: *Biochimica et Biophysica Acta (BBA)-Biomembranes* 465.3 (1977), pp. 579–598.

[671] Carolyn Newton et al., "Specificity of Ca2+ and Mg2+ binding to phosphatidylserine vesicles and resultant phase changes of bilayer membrane structure", in: *Biochimica et Biophysica Acta (BBA)-Biomembranes* 506.2 (1978), pp. 281–287.

[672] Christopher Brasnett et al., "Effects of cations on the behaviour of lipid cubic phases", in: *Scientific reports* 7.1 (2017), pp. 1–7.

[673] Imad Younus Hasan and Adam Mechler, "Nanoviscosity measurements revealing domain formation in biomimetic membranes", in: *Analytical chemistry* 89.3 (2017), pp. 1855–1862.

[674] Patrick Garidel and Alfred Blume, "1, 2-Dimyristoyl-sn-glycero-3-phosphoglycerol (DMPG) monolayers: influence of temperature, pH, ionic strength and binding of alkaline earth cations", in: *Chemistry and physics of lipids* 138.1-2 (2005), pp. 50–59.

[675] Karin A Riske, Lia Q Amaral, and M Teresa Lamy, "Extensive bilayer perforation coupled with the phase transition region of an anionic phospholipid", in: *Langmuir* 25.17 (2009), pp. 10083–10091.

[676] Michael Rappolt et al., "Salt-induced phase separation in the liquid crystalline phase of phosphatidylcholines", in: *Colloids and Surfaces A: Physicochemical and Engineering Aspects* 183 (2001), pp. 171–181.

[677] Kazuo Ohki, "Ca2+-induced lateral phase separation in ternary mixtures of phosphatidic acid, phosphatidylcholine, and phosphatidylethanolamine inferred by calorimetry", in: *The Journal of Biochemistry* 104.1 (1988), pp. 14–17.

[678] F Tölgyesi, S Györgyi, and IP Sugár, "Effect of Monovalent Ions on the Phase Transition Behavior of DPPC-Water Dispersion", in: *Molecular crystals and liquid crystals* 128.3-4 (1985), pp. 263–275.

[679] Helmut Hauser and G Graham Shipley, "Interactions of divalent cations with phosphatidylserine bilayer membranes", in: *Biochemistry* 23.1 (1984), pp. 34–41.

[680] Jairajh Mattai et al., "Interactions of metal ions with phosphatidylserine bilayer membranes: effect of hydrocarbon chain unsaturation", in: *Biochemistry* 28.5 (1989), pp. 2322–2330.

[681] Helmut Hauser and G Graham Shipley, "Comparative structural aspects of cation binding to phosphatidylserine bilayers", in: *Biochimica et Biophysica Acta (BBA)-Biomembranes* 813.2 (1985), pp. 343–346.

[682] MMAE Claessens et al., "Charged lipid vesicles: effects of salts on bending rigidity, stability, and size", in: *Biophysical journal* 87.6 (2004), pp. 3882–3893.

[683] Sarka Pokorna et al., "Interactions of monovalent salts with cationic lipid bilayers", in: *Faraday discussions* 160 (2013), pp. 341–358.

[684] MARGOT E Loosley-Millman, R PETER Rand, and VA Parsegian, "Effects of monovalent ion binding and screening on measured electrostatic forces between charged phospholipid bilayers.", in: *Biophysical journal* 40.3 (1982), p. 221.

[685] BA Cunningham and LJ Lis, "Interactive forces between phosphatidylcholine bilayers in monovalent salt solutions", in: *Journal of colloid and interface science* 128.1 (1989), pp. 15–25.

[686] Peter W Sanderson et al., "The Hofmeister effect in relation to membrane lipid phase stability", in: *Biochimica et Biophysica Acta (BBA)-Biomembranes* 1067.1 (1991), pp. 43–50.

[687] Horia I Petrache et al., "Swelling of phospholipids by monovalent salt", in: *Journal of lipid research* 47.2 (2006), pp. 302–309.

[688] Norbert Kucerka et al., "Calcium and zinc differentially affect the structure of lipid membranes", in: *Langmuir* 33.12 (2017), pp. 3134–3141.

[689] Richard J Alsop, Rafaëla Maria Schober, and Maikel C Rheinstädter, "Swelling of phospholipid membranes by divalent metal ions depends on the location of the ions in the bilayers", in: *Soft Matter* 12.32 (2016), pp. 6737–6748.

[690] VS Gallicchio, "Lithium-still interesting after all these years.", in: *Trace Elements & Electrolytes* 28.1 (2011).

[691] Birsen Aydemir, AR Kiziler, and MC Akyolcu, "Determination of optimal lithium concentration in fractions of blood in atomic absorption spectrophotometer.", in: *Trace Elements & Electrolytes* 24.2 (2007).

[692] Marlene P Freeman and Scott A Freeman, "Lithium: clinical considerations in internal medicine", in: *The American journal of medicine* 119.6 (2006), pp. 478–481.

[693] Nicholas J Birch, *Lithium and the cell: pharmacology and biochemistry*, Academic Press, 2012.

[694] Juan Undurraga et al., "Lithium treatment for unipolar major depressive disorder: Systematic review", in: *Journal of Psychopharmacology* 33.2 (2019), pp. 167–176.

[695] Michel Roux and Myer Bloom, "Ca2 Li+, Na+, and K Distributions in the Headgroup Region of Binary Membranes of Phosphatidylcholine and Phosphatidylserine As Seen by Deuterium NMR", in: *Biochemistry* 29 (1990), pp. 7077–7089.

[696] Joanna Kotyńska, Izabela Dobrzyńska, and Zbigniew A Figaszewski, "Association of alkali metal cations with phosphatidylcholine liposomal membrane surface", in: *European Biophysics Journal* 46.2 (2017), pp. 149–155.

[697] Pabitra Maity et al., "Binding of monovalent alkali metal ions with negatively charged phospholipid membranes", in: *Biochimica et Biophysica Acta (BBA)-Biomembranes* 1858.4 (2016), pp. 706–714.

[698] Eric Jakobsson et al., "Towards a unified understanding of lithium action in basic biology and its significance for applied biology", in: *The Journal of membrane biology* 250.6 (2017), pp. 587–604.

[699] Keisuke Kimura et al., "Transport of cesium and potassium ions across bilayer lipid membranes—Cesium accumulation in biological cells according to the membrane potential", in: *Journal of Electroanalytical Chemistry* 779 (2016), pp. 131–136.

[700] Osamu Shirai et al., "Transport of cesium ion across a bilayer lipid membrane and its facilitation in the presence of iodide ion", in: *Electroanalysis* 25.8 (2013), pp. 1823–1826.

[701] H von Helmholtz, "Ueber einige Gesetze der Vertheilung elektrischer Ströme in körperlichen Leitern, mit Anwendung auf die thierisch-elektrischen Versuche (Schluss.)", in: *Annalen der Physik* 165.7 (1853), pp. 353–377.

[702] David Leonard Chapman, "LI. A contribution to the theory of electrocapillarity", in: *The London, Edinburgh, and Dublin philosophical magazine and journal of science* 25.148 (1913), pp. 475–481.

[703] M Gouy, "Sur la constitution de la charge électrique à la surface d'un électrolyte", in: (1910).

[704] O Stern, "Theory of a double-electric layer with the consideration of the adsorption processes", in: *Z. Electrochem* 30 (1924), pp. 508–516.

[705] Hans-Jürgen Butt, Karlheinz Graf, and Michael Kappl, *Physics and chemistry of interfaces*, John Wiley & Sons, 2013.

[706] Sagar A Pandit, David Bostick, and Max L Berkowitz, "Mixed bilayer containing dipalmitoylphosphatidylcholine and dipalmitoylphosphatidylserine: lipid complexation, ion binding, and electrostatics", in: *Biophysical journal* 85.5 (2003), pp. 3120–3131.

[707] Jacob N Israelachvili, *Intermolecular and surface forces*, Academic press, 2011.

[708] Jeremy M Berg, John L Tymoczko, and L Stryer, "Protein structure and function", in: *Biochemistry* 262 (2002), pp. 159–173.

[709] Acacia F Dishman and Brian F Volkman, "Unfolding the mysteries of protein metamorphosis", in: *ACS chemical biology* 13.6 (2018), pp. 1438–1446.

[710] Leo C James and Dan S Tawfik, "Conformational diversity and protein evolution-a 60-year-old hypothesis revisited", in: *Trends in biochemical sciences* 28.7 (2003), pp. 361–368.

[711] Prakash Kulkarni et al., "Structural metamorphism and polymorphism in proteins on the brink of thermodynamic stability", in: *Protein Science* 27.9 (2018), pp. 1557–1567.

[712] BeiBei Luo et al., "Evolution of metamorphism in thymidylate synthases within the primate lineages", in: *Journal of molecular evolution* 72.3 (2011), pp. 306–314.

[713] Sophia C Goodchild, Paul MG Curmi, and Louise J Brown, "Structural gymnastics of multifunctional metamorphic proteins", in: *Biophysical reviews* 3.3 (2011), p. 143.

[714] Alexey G Murzin, "Metamorphic proteins", in: *Science* 320.5884 (2008), pp. 1725–1726.

[715] Katherine Henzler-Wildman and Dorothee Kern, "Dynamic personalities of proteins", in: *Nature* 450.7172 (2007), pp. 964–972.

[716] Katherine A Henzler-Wildman et al., "A hierarchy of timescales in protein dynamics is linked to enzyme catalysis", in: *Nature* 450.7171 (2007), pp. 913–916.

[717] H Jane Dyson and Peter E Wright, "Intrinsically unstructured proteins and their functions", in: *Nature reviews Molecular cell biology* 6.3 (2005), p. 197.

[718] A Keith Dunker et al., "Intrinsic disorder and protein function", in: *Biochemistry* 41.21 (2002), pp. 6573–6582.

[719] Vladimir N Uversky, "Natively unfolded proteins: a point where biology waits for physics", in: *Protein science* 11.4 (2002), pp. 739–756.

[720] Robin Van Der Lee et al., "Classification of intrinsically disordered regions and proteins", in: *Chemical reviews* 114.13 (2014), pp. 6589–6631.

[721] Peter E Wright and H Jane Dyson, "Intrinsically unstructured proteins: reassessing the protein structure-function paradigm", in: *Journal of molecular biology* 293.2 (1999), pp. 321–331.

[722] Ruth S Spolar and M Thomas Record, "Coupling of local folding to site-specific binding of proteins to DNA", in: *Science* 263.5148 (1994), pp. 777–784.

[723] Mikio Ohgushi and Akiyoshi Wada, "'Molten-globule state': a compact form of globular proteins with mobile side-chains", in: *FEBS letters* 164.1 (1983), pp. 21–24.

[724] DA Dolgikh et al., "α-Lactalbumin: compact state with fluctuating tertiary structure?", in: *FEBS letters* 136.2 (1981), pp. 311–315.

[725] Saskia M Van der Vies et al., "Conformational states of ribulose bisphosphate carboxylase and their interaction with chaperonin 60", in: *Biochemistry* 31.14 (1992), pp. 3635–3644.

[726] Jörg Martin et al., "Chaperonin-mediated protein folding at the surface of groEL through a'molten globule'-like intermediate", in: *Nature* 352.6330 (1991), pp. 36–42.

[727] Himangshu S Bose et al., "The active form of the steroidogenic acute regulatory protein, StAR, appears to be a molten globule", in: *Proceedings of the National Academy of Sciences* 96.13 (1999), pp. 7250–7255.

[728] Cyrus Levinthal, "Are there pathways for protein folding?", in: *Journal de chimie physique* 65 (1968), pp. 44–45.

[729] F Ulrich Hartl, Andreas Bracher, and Manajit Hayer-Hartl, "Molecular chaperones in protein folding and proteostasis", in: *Nature* 475.7356 (2011), pp. 324–332.

[730] Jan Kubelka, James Hofrichter, and William A Eaton, "The protein folding speed limit", in: *Current opinion in structural biology* 14.1 (2004), pp. 76–88.

[731] Furqan M Fazal and Steven M Block, "Optical tweezers study life under tension", in: *Nature photonics* 5.6 (2011), p. 318.

[732] J Christof M Gebhardt, Thomas Bornschlögl, and Matthias Rief, "Full distance-resolved folding energy landscape of one single protein molecule", in: *Proceedings of the National Academy of Sciences* 107.5 (2010), pp. 2013–2018.

[733] Jiawei Chen, Don L Rempel, and Michael L Gross, "Temperature jump and fast photochemical oxidation probe submillisecond protein folding", in: *Journal of the American Chemical Society* 132.44 (2010), pp. 15502–15504.

[734] Yiwen Chen et al., "Protein folding: then and now", in: *Archives of biochemistry and biophysics* 469.1 (2008), pp. 4–19.

[735] Aaron R Dinner et al., "Understanding protein folding via free-energy surfaces from theory and experiment", in: *Trends in biochemical sciences* 25.7 (2000), pp. 331–339.

[736] Alan R Fersht and Valerie Daggett, "Protein folding and unfolding at atomic resolution", in: *Cell* 108.4 (2002), pp. 573–582.

[737] Avijit Ghosh, Ron Elber, and Harold A Scheraga, "An atomically detailed study of the folding pathways of protein A with the stochastic difference equation", in: *Proceedings of the National Academy of Sciences* 99.16 (2002), pp. 10394–10398.

[738] Yong Duan and Peter A Kollman, "Pathways to a protein folding intermediate observed in a 1-microsecond simulation in aqueous solution", in: *Science* 282.5389 (1998), pp. 740–744.

[739] OB Ptitsyn and AA Rashin, "A model of myoglobin self-organization", in: *Biophysical chemistry* 3.1 (1975), pp. 1–20.

[740] Peter S Kim and Robert L Baldwin, "Specific intermediates in the folding reactions of small proteins and the mechanism of protein folding", in: *Annual review of biochemistry* 51.1 (1982), pp. 459–489.

[741] Ryan Day et al., "Increasing temperature accelerates protein unfolding without changing the pathway of unfolding", in: *Journal of molecular biology* 322.1 (2002), pp. 189–203.

[742] Donald B Wetlaufer, "Nucleation, rapid folding, and globular intrachain regions in proteins", in: *Proceedings of the National Academy of Sciences* 70.3 (1973), pp. 697–701.

[743] Alan R Fersht, "Optimization of rates of protein folding: the nucleation-condensation mechanism and its implications", in: *Proceedings of the National Academy of Sciences* 92.24 (1995), pp. 10869–10873.

[744] Alan R Fersht, "Nucleation mechanisms in protein folding", in: *Current opinion in structural biology* 7.1 (1997), pp. 3–9.

[745] Ken A Dill and Hue Sun Chan, "From Levinthal to pathways to funnels", in: *Nature structural biology* 4.1 (1997), p. 10.

[746] Anna T Gres et al., "X-ray crystal structures of native HIV-1 capsid protein reveal conformational variability", in: *Science* 349.6243 (2015), pp. 99–103.

[747] Yanyong Kang et al., "Crystal structure of rhodopsin bound to arrestin by femtosecond X-ray laser", in: *Nature* 523.7562 (2015), p. 561.

[748] Francesca M Marassi and Stanley J Opella, "A solid-state NMR index of helical membrane protein structure and topology", in: *Journal of magnetic resonance (San Diego, Calif.: 1997)* 144.1 (2000), p. 150.

[749] Vitali Tugarinov, Voula Kanelis, and Lewis E Kay, "Isotope labeling strategies for the study of high-molecular-weight proteins by solution NMR spectroscopy", in: *Nature protocols* 1.2 (2006), p. 749.

[750] Leonid Breydo and Vladimir N Uversky, "Structural, morphological, and functional diversity of amyloid oligomers", in: *FEBS letters* 589.19 (2015), pp. 2640–2648.

[751] AA Nizhnikov, KS Antonets, and SG Inge-Vechtomov, "Amyloids: from pathogenesis to function", in: *Biochemistry (Moscow)* 80.9 (2015), pp. 1127–1144.

[752] Thomas R Jahn and Sheena E Radford, "The Yin and Yang of protein folding", in: *The FEBS journal* 272.23 (2005), pp. 5962–5970.

[753] Thomas R Jahn and Sheena E Radford, "Folding versus aggregation: polypeptide conformations on competing pathways", in: *Archives of biochemistry and biophysics* 469.1 (2008), pp. 100–117.

[754] Kazuhiro Nakanishi, Takaharu Sakiyama, and Koreyoshi Imamura, "On the adsorption of proteins on solid surfaces, a common but very complicated phenomenon", in: *Journal of bioscience and bioengineering* 91.3 (2001), pp. 233–244.

[755] Vladimir Hlady and Jos Buijs, "Protein adsorption on solid surfaces", in: *Current Opinion in Biotechnology* 7.1 (1996), p. 72.

[756] Raffaele Mezzenga and Peter Fischer, "The self-assembly, aggregation and phase transitions of food protein systems in one, two and three dimensions", in: *Reports on Progress in Physics* 76.4 (2013), p. 046601.

[757] Jeffrey J Gray, "The interaction of proteins with solid surfaces", in: *Current opinion in structural biology* 14.1 (2004), pp. 110–115.

[758] Jeremiah F Kelly et al., "Amyloid beta-peptide disrupts carbachol-induced muscarinic cholinergic signal transduction in cortical neurons", in: *Proceedings of the National Academy of Sciences* 93.13 (1996), pp. 6753–6758.

[759] Anant K Menon et al., "Clustering, mobility, and triggering activity of small oligomers of immunoglobulin E on rat basophilic leukemia cells.", in: *The Journal of cell biology* 102.2 (1986), pp. 534–540.

[760] Niels Gregersen and Peter Bross, "Protein misfolding and cellular stress: an overview", in: *Protein Misfolding and Cellular Stress in Disease and Aging*, Springer, 2010, pp. 3–23.

[761] Niels Gregersen, Lars Bolund, and Peter Bross, "Protein misfolding, aggregation, and degradation in disease", in: *Molecular Biotechnology* 31.2 (2005), p. 141.

[762] Christopher A Ross and Michelle A Poirier, "Protein aggregation and neurodegenerative disease", in: *Nature medicine* 10.7s (2004), S10.

[763] Michael Rabe, Dorinel Verdes, and Stefan Seeger, "Understanding protein adsorption phenomena at solid surfaces", in: *Advances in colloid and interface science* 162.1-2 (2011), pp. 87–106.

[764] Myo T Tyn and Todd W Gusek, "Prediction of diffusion coefficients of proteins", in: *Biotechnology and bioengineering* 35.4 (1990), pp. 327–338.

[765] W Norde, *Physical Chemistry of Biological Interfaces (Baszkin, A., and Norde, W., Eds.), p 115*, 2000.

[766] Vladimir A Basiuk, "Adsorption of biomolecules at silica", in: *Encyclopedia of Surface and Colloid Science* (2002), pp. 277–293.

[767] Arthur T Hubbard, *Encyclopedia of surface and colloid science*, vol. 1, CRC press, 2002.

[768] Simon J Attwood et al., "Understanding how charge and hydrophobicity influence globular protein adsorption to alkanethiol and material surfaces", in: *Journal of Materials Chemistry B* 7.14 (2019), pp. 2349–2361.

[769] Willem Norde, *Driving forces for protein adsorption at solid surfaces*, Wiley Online Library, 1996.

[770] JJ Ramsden, "Puzzles and paradoxes in protein adsorption", in: *Chemical Society Reviews* 24.1 (1995), pp. 73–78.

[771] Martin Malmsten, "Formation of adsorbed protein layers", in: *Journal of colloid and interface science* 207.2 (1998), pp. 186–199.

[772] Jorgen M Mollerup, "A review of the thermodynamics of protein association to ligands, protein adsorption, and adsorption isotherms", in: *Chemical Engineering & Technology: Industrial Chemistry-Plant Equipment-Process Engineering-Biotechnology* 31.6 (2008), pp. 864–874.

[773] Allen P Minton, "Effects of excluded surface area and adsorbate clustering on surface adsorption of proteins: I. Equilibrium models", in: *Biophysical chemistry* 86.2-3 (2000), pp. 239–247.

[774] Irving Langmuir, "The adsorption of gases on plane surfaces of glass, mica and platinum.", in: *Journal of the American Chemical society* 40.9 (1918), pp. 1361–1403.

[775] P Schaaf and J Talbot, "Kinetics of random sequential adsorption", in: *Physical review letters* 62.2 (1989), p. 175.

[776] Pierre Schaaf, Jean-Claude Voegel, and Bernard Senger, *From random sequential adsorption to ballistic deposition: a general view of irreversible deposition processes*, 2000.

[777] Willem Norde and Charles A Haynes, *Reversibility and the mechanism of protein adsorption*, 1995.

[778] GJ Szöllősi, Imre Derenyi, and Janos Vörös, "Reversible mesoscopic model of protein adsorption: From equilibrium to dynamics", in: *Physica A: Statistical Mechanics and its Applications* 343 (2004), pp. 359–375.

[779] Blake B Langdon et al., "Interfacial protein-protein associations", in: *Biomacromolecules* 15.1 (2013), pp. 66–74.

[780] Wei Dai et al., "A negative correlation between water content and protein adsorption on polymer brushes", in: *Journal of materials chemistry B* 7.13 (2019), pp. 2162–2168.

[781] Songming Chen, Frank A Ferrone, and Ronald Wetzel, "Huntington's disease age-of-onset linked to polyglutamine aggregation nucleation", in: *Proceedings of the National Academy of sciences* 99.18 (2002), pp. 11884–11889.

[782] Euridice P Vieira et al., "Adsorption and diffusion of plasma proteins on hydrophilic and hydrophobic surfaces: effect of trifluoroethanol on protein structure", in: *Langmuir* 25.17 (2009), pp. 9879–9886.

[783] Mimi Gao et al., "Modulation of human IAPP fibrillation: cosolutes, crowders and chaperones", in: *Physical Chemistry Chemical Physics* 17.13 (2015), pp. 8338–8348.

[784] Charles A Haynes and Willem Norde, "Globular proteins at solid/liquid interfaces", in: *Colloids and surfaces B: Biointerfaces* 2.6 (1994), pp. 517–566.

[785] Mohamed Refaee et al., "Pressure-dependent changes in the solution structure of hen egg-white lysozyme", in: *Journal of molecular biology* 327.4 (2003), pp. 857–865.

[786] Lien Callewaert and Chris W Michiels, "Lysozymes in the animal kingdom", in: *Journal of biosciences* 35.1 (2010), pp. 127–160.

[787] Hugues Lelouard et al., "Pathogenic bacteria and dead cells are internalized by a unique subset of Peyer's patch dendritic cells that express lysozyme", in: *Gastroenterology* 138.1 (2010), pp. 173–184.

[788] Stephanie A Ragland and Alison K Criss, "From bacterial killing to immune modulation: Recent insights into the functions of lysozyme", in: *PLoS pathogens* 13.9 (2017).

[789] RK Pipe, "Hydrolytic enzymes associated with the granular haemocytes of the marine musselMytilus edulis", in: *The Histochemical Journal* 22.11 (1990), pp. 595–603.

[790] Rajaram Swaminathan et al., "Lysozyme: a model protein for amyloid research", in: *Advances in protein chemistry and structural biology*, vol. 84, Elsevier, 2011, pp. 63–111.

[791] Erica Frare et al., "A highly amyloidogenic region of hen lysozyme", in: *Journal of molecular biology* 340.5 (2004), pp. 1153–1165.

[792] Aoneng Cao, Daoying Hu, and Luhua Lai, "Formation of amyloid fibrils from fully reduced hen egg white lysozyme", in: *Protein science* 13.2 (2004), pp. 319–324.

[793] Galyna P Gorbenko, Valeriya M Ioffe, and Paavo KJ Kinnunen, "Binding of lysozyme to phospholipid bilayers: evidence for protein aggregation upon membrane association", in: *Biophysical journal* 93.1 (2007), pp. 140–153.

[794] S Adams, AM Higgins, and RAL Jones, "Surface-mediated folding and misfolding of proteins at lipid/water interfaces", in: *Langmuir* 18.12 (2002), pp. 4854–4861.

[795] Hongxia Zhao, Esa KJ Tuominen, and Paavo KJ Kinnunen, "Formation of amyloid fibers triggered by phosphatidylserine-containing membranes", in: *Biochemistry* 43.32 (2004), pp. 10302–10307.

[796] Grazia Sessa and Gerald Weissmann, "Incorporation of lysozyme into liposomes a model for structure-linked latency", in: *Journal of Biological Chemistry* 245.13 (1970), pp. 3295–3301.

[797] Hisham R Ibrahim, Ursula Thomas, and Antonio Pellegrini, "A helix-loop-helix peptide at the upper lip of the active site cleft of lysozyme confers potent antimicrobial activity with membrane permeabilization action", in: *Journal of Biological Chemistry* 276.47 (2001), pp. 43767–43774.

[798] Olaf Zschörnig et al., "Modulation of lysozyme charge influences interaction with phospholipid vesicles", in: *Colloids and Surfaces B: Biointerfaces* 42.1 (2005), pp. 69–78.

[799] Joep J Bergers et al., "The role of protein charge in protein-lipid interactions. pH-dependent changes of the electrophoretic mobility of liposomes through adsorption of water-soluble, globular proteins", in: *Biochemistry* 32.17 (1993), pp. 4641–4649.

[800] Alice R Walker, Nikhil Baddam, and G Andreés Cisneros, "Unfolding Pathways of Hen Egg-White Lysozyme in Ethanol", in: *The Journal of Physical Chemistry B* 123.15 (2019), pp. 3267–3271.

[801] David R Booth et al., "Instability, unfolding and aggregation of human lysozyme variants underlying amyloid fibrillogenesis", in: *Nature* 385.6619 (1997), p. 787.

[802] Alexander K Buell et al., "Population of nonnative states of lysozyme variants drives amyloid fibril formation", in: *Journal of the American Chemical Society* 133.20 (2011), pp. 7737–7743.

[803] Christopher M Dobson, "The structural basis of protein folding and its links with human disease", in: *Philosophical Transactions of the Royal Society of London. Series B: Biological Sciences* 356.1406 (2001), pp. 133–145.

[804] Christopher M Dobson, "Principles of protein folding, misfolding and aggregation", in: *Seminars in cell & developmental biology*, vol. 15, 1, Elsevier, 2004, pp. 3–16.

[805] Tuo Zhang et al., "Intrinsically semi-disordered state and its role in induced folding and protein aggregation", in: *Cell biochemistry and biophysics* 67.3 (2013), pp. 1193–1205.

[806] Mireille Dumoulin et al., "Reduced global cooperativity is a common feature underlying the amyloidogenicity of pathogenic lysozyme mutations", in: *Journal of molecular biology* 346.3 (2005), pp. 773–788.

[807] Erica Frare et al., "Identification of the core structure of lysozyme amyloid fibrils by proteolysis", in: *Journal of molecular biology* 361.3 (2006), pp. 551–561.

[808] Theo L Peeters, Yvan R Depraetere, and Gaston R Vantrappen, "Radioimmunoassay for urinary lysozyme in human serum from leukemic patients.", in: *Clinical chemistry* 24.12 (1978), pp. 2155–2157.

[809] Ana Puinhas et al., "Comparison of IgA, TNF-α and surface tension of the tear film in two different times of the day", in: *Contact Lens and Anterior Eye* 36.3 (2013), pp. 140–145.

[810] Fausto Miano et al., "Insertion of tear proteins into a meibomian lipids film", in: *Colloids and Surfaces B: Biointerfaces* 44.1 (2005), pp. 49–55.

[811] Sophia T Tragoulias et al., "Surface pressure measurements of human tears and individual tear film components indicate that proteins are major contributors to the surface pressure", in: *Cornea* 24.2 (2005), pp. 189–200.

[812] Thomas J Millar et al., "The surface activity of purified ocular mucin at the air-liquid interface and interactions with meibomian lipids", in: *Cornea* 25.1 (2006), pp. 91–100.

[813] Poonam Mudgil, Margaux Torres, and Thomas J Millar, "Adsorption of lysozyme to phospholipid and meibomian lipid monolayer films", in: *Colloids and surfaces B: Biointerfaces* 48.2 (2006), pp. 128–137.

[814] Fausto Miano et al., "Coadsorption of human milk lactoferrin into the dipalmitoylglycerolphosphatidylcholine phospholipid monolayer spread at the air/water interface", in: *Biophysical journal* 92.4 (2007), pp. 1254–1262.

[815] J Daniel Nelson et al., "The international workshop on meibomian gland dysfunction: report of the definition and classification subcommittee", in: *Investigative ophthalmology & visual science* 52.4 (2011), pp. 1930–1937.

[816] Philipp Steven et al., "Semifluorinated alkane eye drops for treatment of dry eye disease—a prospective, multicenter noninterventional study", in: *Journal of Ocular Pharmacology and Therapeutics* 31.8 (2015), pp. 498–503.

[817] Michelle Stephenson, *Dry Eye: What's in The Pipeline?*, 2020, URL: https://www.reviewofophthalmology.com/article/dry-eye-whats-in-the-pipeline-2020.

[818] *Bausch Health Licenses Novaliq's NOV03 Investigational Treatment For Dry Eye Disease*, 2020, URL: https://www.prnewswire.com/news-releases/bausch-health-licenses-novaliqs-nov03-investigational-treatment-for-dry-eye-disease-associated-with-meibomian-gland-dysfunction-300978312.html.

[819] Henry Ancell, "ON THE FUNCTION AND DISEASES OF THE LIVER.", in: *The Lancet* 32.822 (1839), pp. 363–368.

[820] Daniel C Carter and Joseph X Ho, "Structure of serum albumin", in: *Advances in protein chemistry*, vol. 45, Elsevier, 1994, pp. 153–203.

[821] Theodore Peters Jr, "Serum albumin", in: *Advances in protein chemistry*, vol. 37, Elsevier, 1985, pp. 161–245.

[822] Stephen Curry et al., "Crystal structure of human serum albumin complexed with fatty acid reveals an asymmetric distribution of binding sites", in: *Nature structural biology* 5.9 (1998), pp. 827–835.

[823] Ryuichi Narazaki, Toru Maruyama, and Masaki Otagiri, "Probing the cysteine 34 residue in human serum albumin using fluorescence techniques", in: *Biochimica et Biophysica Acta (BBA)-Protein Structure and Molecular Enzymology* 1338.2 (1997), pp. 275–281.

[824] Neil Chadborn et al., "Ligand-dependent conformational equilibria of serum albumin revealed by tryptophan fluorescence quenching", in: *Biophysical journal* 76.4 (1999), pp. 2198–2207.

[825] Jacqueline A Reynolds et al., "The binding of divers detergent anions to bovine serum albumin", in: *Biochemistry* 6.3 (1967), pp. 937–947.

[826] P Bourassa et al., "Resveratrol, genistein, and curcumin bind bovine serum albumin", in: *The Journal of Physical Chemistry B* 114.9 (2010), pp. 3348–3354.

[827] Stephen Curry, "Lessons from the crystallographic analysis of small molecule binding to human serum albumin", in: *Drug metabolism and pharmacokinetics* 24.4 (2009), pp. 342–357.

[828] Olga Rafikova, Ruslan Rafikov, and Evgeny Nudler, "Catalysis of S-nitrosothiols formation by serum albumin: the mechanism and implication in vascular control", in: *Proceedings of the National Academy of Sciences* 99.9 (2002), pp. 5913–5918.

[829] Florian Hollfelder et al., "Characterization of proton-transfer catalysis by serum albumins", in: *Journal of the American Chemical Society* 122.6 (2000), pp. 1022–1029.

[830] Jinsheng Yang et al., "Structural insights into human serum albumin-mediated prostaglandin catalysis", in: *Protein science* 11.3 (2002), pp. 538–545.

[831] Miguel A Sogorb et al., "Rabbit serum albumin hydrolyzes the carbamate carbaryl", in: *Chemical research in toxicology* 15.4 (2002), pp. 520–526.

[832] Marjolaine Roche et al., "The antioxidant properties of serum albumin", in: *FEBS letters* 582.13 (2008), pp. 1783–1787.

[833] Myriam Taverna et al., "Specific antioxidant properties of human serum albumin", in: *Annals of intensive care* 3.1 (2013), p. 4.

[834] IS Young and JV Woodside, "Antioxidants in health and disease", in: *Journal of clinical pathology* 54.3 (2001), pp. 176–186.

[835] Thomas E Finn et al., "Serum albumin prevents protein aggregation and amyloid formation and retains chaperone-like activity in the presence of physiological ligands", in: *Journal of Biological Chemistry* 287.25 (2012), pp. 21530–21540.

[836] Yu-Min Kuo et al., "Amyloid-β peptides interact with plasma proteins and erythrocytes: implications for their quantitation in plasma", in: *Biochemical and biophysical research communications* 268.3 (2000), pp. 750–756.

[837] Bernd Bohrmann et al., "Endogenous proteins controlling amyloid β-peptide polymerization possible implications for β-amyloid formation in the central nervous system and in peripheral tissues", in: *Journal of Biological Chemistry* 274.23 (1999), pp. 15990–15995.

[838] Luciano Galeazzi et al., "Albumin protects human red blood cells against Aβ25–35-induced lysis more effectively than ApoE", in: *Neuroreport* 13.16 (2002), pp. 2149–2154.

[839] Tue Rasmussen et al., "The molecular chaperone α-crystallin as an excipient in an insulin formulation", in: *Pharmaceutical research* 27.7 (2010), pp. 1337–1347.

[840] Nikolaj K Holm et al., "Aggregation and fibrillation of bovine serum albumin", in: *Biochimica et Biophysica Acta (BBA)-Proteins and Proteomics* 1774.9 (2007), pp. 1128–1138.

[841] Pablo Taboada et al., "Effect of solvation on the structure conformation of human serum albumin in aqueous–alcohol mixed solvents", in: *Chemical Physics* 340.1-3 (2007), pp. 59–68.

[842] Silvia Barbosa, Pablo Taboada, and Víctor Mosquera, "Fibrillation and polymorphism of human serum albumin", in: *Bio-nanoimaging*, Elsevier, 2014, pp. 345–362.

[843] Henrike Heise et al., "Molecular-level secondary structure, polymorphism, and dynamics of full-length α-synuclein fibrils studied by solid-state NMR", in: *Proceedings of the National Academy of Sciences* 102.44 (2005), pp. 15871–15876.

[844] Motomasa Tanaka et al., "Conformational variations in an infectious protein determine prion strain differences", in: *Nature* 428.6980 (2004), pp. 323–328.

[845] Aneta T Petkova et al., "Self-propagating, molecular-level polymorphism in Alzheimer's ß-amyloid fibrils", in: *Science* 307.5707 (2005), pp. 262–265.

[846] Constance J Jeffery, "Moonlighting proteins", in: *Trends in biochemical sciences* 24.1 (1999), pp. 8–11.

[847] Shelley D Copley, "Enzymes with extra talents: moonlighting functions and catalytic promiscuity", in: *Current opinion in chemical biology* 7.2 (2003), pp. 265–272.

[848] Ekaterina A Litus et al., "Intrinsically disordered regions in serum albumin: what are they for?", in: *Cell biochemistry and biophysics* 76.1-2 (2018), pp. 39–57.

[849] Jamie Ghuman et al., "Structural basis of the drug-binding specificity of human serum albumin", in: *Journal of molecular biology* 353.1 (2005), pp. 38–52.

[850] Koji Nishi, Keishi Yamasaki, and Masaki Otagiri, "Serum Albumin, Lipid and Drug Binding", in: *Vertebrate and Invertebrate Respiratory Proteins, Lipoproteins and other Body Fluid Proteins*, Springer, 2020, pp. 383–397.

[851] Karolina A Majorek et al., "Structural and immunologic characterization of bovine, horse, and rabbit serum albumins", in: *Molecular immunology* 52.3-4 (2012), pp. 174–182.

[852] Helen M Berman et al., "The protein data bank", in: *Nucleic acids research* 28.1 (2000), pp. 235–242.

[853] S Sugio et al., "Crystal structure of human serum albumin at 2.5 Å resolution", in: *Protein engineering* 12.6 (1999), pp. 439–446.

[854] Yasar Akdogan, Jörg Reichenwallner, and Dariush Hinderberger, "Evidence for Water-Tuned Structural Differences in Proteins: An Approach Emphasizing Variations in Local Hydrophilicity", in: *PloS one* 7 (Sept. 2012), e45681, DOI: 10.1371/journal.pone.0045681.

[855] Xiao Min He and Daniel C Carter, "Atomic structure and chemistry of human serum albumin", in: *Nature* 358.6383 (1992), p. 209.

[856] Ulrich Kragh-Hansen, Victor Tuan Giam Chuang, and Masaki Otagiri, "Practical aspects of the ligand-binding and enzymatic properties of human serum albumin", in: *Biological and Pharmaceutical Bulletin* 25.6 (2002), pp. 695–704.

[857] GDJB Sudlow, DJ Birkett, and DN Wade, "The characterization of two specific drug binding sites on human serum albumin", in: *Molecular Pharmacology* 11.6 (1975), pp. 824–832.

[858] GDJB Sudlow, DJ Birkett, and DN Wade, "Further characterization of specific drug binding sites on human serum albumin", in: *Molecular pharmacology* 12.6 (1976), pp. 1052–1061.

[859] Gregory J Quinlan, Greg S Martin, and Timothy W Evans, "Albumin: biochemical properties and therapeutic potential", in: *Hepatology* 41.6 (2005), pp. 1211–1219.

[860] Jin Lu et al., *Albumin as a zinc carrier: properties of its high-affinity zinc-binding site*, 2008.

[861] Wojciech Bal et al., "Multi-metal binding site of serum albumin", in: *Journal of inorganic biochemistry* 70.1 (1998), pp. 33–39.

[862] Ulrich Kragh-Hansen et al., "Chain length-dependent binding of fatty acid anions to human serum albumin studied by site-directed mutagenesis", in: *Journal of molecular biology* 363.3 (2006), pp. 702–712.

[863] Haritha Mandula et al., "Role of site-specific binding to plasma albumin in drug availability to brain", in: *Journal of Pharmacology and Experimental Therapeutics* 317.2 (2006), pp. 667–675.

[864] Kine Marita Knudsen Sand et al., "Unraveling the interaction between FcRn and albumin: opportunities for design of albumin-based therapeutics", in: *Frontiers in immunology* 5 (2015), p. 682.

[865] John A Luetscher, "Serum albumin. II. Identification of more than one albumin in horse and human serum by electrophoretic mobility in acid solution", in: *Journal of the American Chemical Society* 61.10 (1939), pp. 2888–2890.

[866] A Kent Wright and MR Thompson, "Hydrodynamic structure of bovine serum albumin determined by transient electric birefringence.", in: *Biophysical journal* 15.2 Pt 1 (1975), p. 137.

[867] JL Oncley, G Scatchard, and A Brown, "Physical-chemical characteristics of certain of the proteins of normal human plasma.", in: *The Journal of Physical Chemistry* 51.1 (1947), pp. 184–198.

[868] Charles Tanford and John G Buzzell, "The viscosity of aqueous solutions of bovine serum albumin between pH 4.3 and 10.5.", in: *The Journal of Physical Chemistry* 60.2 (1956), pp. 225–231.

[869] M Champagne, "The structure of serum albumin in dilute solution. I. Serum albumin at the isoionic point", in: *J. chim. phys* 54 (1957), pp. 378–392.

[870] A Kent Wright, Michael R Thompson, and Ronald L Miller, "Study of protein-sodium dodecyl sulfate complexes by transient electric birefringence", in: *Biochemistry* 14.14 (1975), pp. 3224–3228.

[871] V Luzzati, J Witz, and A Nicolaieff, "The structure of bovine serum albumin in solution at pH 5, 3 and 3, 6: study by the absolute central diffusion of x-rays", in: *Journal of molecular biology* 3 (1961), p. 379.

[872] Victor Bloomfield, "The structure of bovine serum albumin at low pH", in: *Biochemistry* 5.2 (1966), pp. 684–689.

[873] L Feng, CZ Hu, and JD Andrade, "Scanning tunneling microscopic images of adsorbed serum albumin on highly oriented pyrolytic graphite", in: *Journal of colloid and interface science* 126.2 (1988), pp. 650–653.

[874] JOSEPH F FostER, "Plasma albumin", in: *The plasma proteins*, Elsevier, 1960, pp. 179–239.

[875] JF Foster, "Albumin Structure, Function and Uses.", in: *Search PubMed* (1977), pp. 53–84.

[876] Daniel C Carter and Xiao-Min He, "Structure of human serum albumin", in: *Science* 249.4966 (1990), pp. 302–303.

[877] H Durchschlag and P Zipper, "Calculation of hydrodynamic parameters of biopolymers from scattering data using whole-body approaches", in: *Analytical Ultracentrifugation IV*, Springer, 1997, pp. 43–57.

[878] Daumantas Matulis et al., "1-Anilino-8-naphthalene sulfonate as a protein conformational tightening agent", in: *Biopolymers: Original Research on Biomolecules* 49.6 (1999), pp. 451–458.

[879] Guy Ladam et al., "Protein interactions with polyelectrolyte multilayers: interactions between human serum albumin and polystyrene sulfonate/polyallylamine multilayers", in: *Biomacromolecules* 1.4 (2000), pp. 674–687.

[880] Sonia F Santos et al., "A systematic study of bovine serum albumin (BSA) and sodium dodecyl sulfate (SDS) interactions by surface tension and small angle X-ray scattering", in: *Journal of colloid and interface science* 262.2 (2003), pp. 400–408.

[881] M Luisa Ferrer et al., "The conformation of serum albumin in solution: a combined phosphorescence depolarization-hydrodynamic modeling study", in: *Biophysical Journal* 80.5 (2001), pp. 2422–2430.

[882] C Ted Lee, Kenneth A Smith, and T Alan Hatton, "Photocontrol of protein folding: the interaction of photosensitive surfactants with bovine serum albumin", in: *Biochemistry* 44.2 (2005), pp. 524–536.

[883] Barbara Jachimska et al., "Structure of bovine serum albumin adsorbed on silica investigated by quartz crystal microbalance", in: *Colloids and Surfaces A: Physicochemical and Engineering Aspects* 489 (2016), pp. 163–172.

[884] Dalila Bendedouch and Sow Hsin Chen, "Structure and interparticle interactions of bovine serum albumin in solution studied by small-angle neutron scattering", in: *The Journal of Physical Chemistry* 87.9 (1983), pp. 1473–1477.

[885] Theodore Peters Jr, *All about albumin: biochemistry, genetics, and medical applications*, Academic press, 1995.

[886] K Baler et al., "Electrostatic unfolding and interactions of albumin driven by pH changes: a molecular dynamics study", in: *The Journal of Physical Chemistry B* 118.4 (2014), pp. 921–930.

[887] S Servagent-Noinville et al., "Conformational changes of bovine serum albumin induced by adsorption on different clay surfaces: FTIR analysis", in: *Journal of colloid and interface science* 221.2 (2000), pp. 273–283.

[888] Turkan Kopac, Kadriye Bozgeyik, and Julide Yener, "Effect of pH and temperature on the adsorption of bovine serum albumin onto titanium dioxide", in: *Colloids and Surfaces A: Physicochemical and Engineering Aspects* 322.1-3 (2008), pp. 19–28.

[889] Bijay K Sah, Kaushik Das, and Sarathi Kundu, "pH-dependent structure, pattern and hysteresis behaviour of lipid (DMPA)-protein (BSA) monolayer complex", in: *Colloids and Surfaces A: Physicochemical and Engineering Aspects* 579 (2019), p. 123663.

[890] MN Jones, HA Skinner, and E Tipping, "The interaction between bovine serum albumin and surfactants", in: *Biochemical Journal* 147.2 (1975), pp. 229–234.

[891] MICHAEL J Geisow and GILBERT H Beaven, "Physical and binding properties of large fragments of human serum albumin", in: *Biochemical Journal* 163.3 (1977), pp. 477–484.

[892] M Yahiya Khan, "Direct evidence for the involvement of domain III in the NF transition of bovine serum albumin", in: *Biochemical journal* 236.1 (1986), pp. 307–310.

[893] SEIICHI ERA et al., "Structural transition of bovine plasma albumin in the alkaline region the N-B transition", in: *International journal of peptide and protein research* 35.1 (1990), pp. 1–11.

[894] S Era and M Sogami, "1H-NMR and CD studies on the structural transition of serum albumin in the acidic region—The N-F transition", in: *The Journal of peptide research* 52.6 (1998), pp. 431–442.

[895] Michael Dockal, Daniel C Carter, and Florian Rüker, "Conformational transitions of the three recombinant domains of human serum albumin depending on pH", in: *Journal of Biological Chemistry* 275.5 (2000), pp. 3042–3050.

[896] Svetlana A Tankovskaia, Karina V Abrosimova, and Sofia V Paston, "Spectral demonstration of structural transitions in albumins", in: *Journal of Molecular Structure* 1171 (2018), pp. 243–252.

[897] Carla E Giacomelli and Willem Norde, "The adsorption–desorption cycle. Reversibility of the BSA–silica system", in: *Journal of Colloid and Interface Science* 233.2 (2001), pp. 234–240.

[898] Luis G Cascão Pereira et al., "Dilatational rheology of BSA conformers at the air/water interface", in: *Langmuir* 19.6 (2003), pp. 2349–2356.

[899] Brittany E Givens et al., "Bovine serum albumin adsorption on SiO2 and TiO2 nanoparticle surfaces at circumneutral and acidic pH: A tale of two nano-bio surface interactions", in: *Journal of colloid and interface science* 493 (2017), pp. 334–341.

[900] Fayezeh Samari et al., "Affinity of two novel five-coordinated anticancer Pt (II) complexes to human and bovine serum albumins: a spectroscopic approach", in: *Inorganic chemistry* 51.6 (2012), pp. 3454–3464.

[901] Hassan A Alhazmi, "FT-IR spectroscopy for the identification of binding sites and measurements of the binding interactions of important metal ions with bovine serum albumin", in: *Scientia Pharmaceutica* 87.1 (2019), p. 5.

[902] Tamara Topală et al., "Bovine serum albumin interactions with metal complexes", in: *Clujul medical* 87.4 (2014), p. 215.

[903] Namrata Singh et al., "Interaction of copper (II) complexes by bovine serum albumin: Spectroscopic and calorimetric insights", in: *Journal of Biomolecular Structure and Dynamics* 36.9 (2018), pp. 2449–2462.

[904] ANATOLE Besarab and JOSE F Caro, "Increased absolute calcium binding to albumin in hypoalbuminaemia.", in: *Journal of clinical pathology* 34.12 (1981), pp. 1368–1374.

[905] NH Martin and DJ Perkins, "The calcium binding of human serum albumin in health and disease", in: *Biochemical Journal* 54.4 (1953), p. 642.

[906] Wojciech Bal et al., "Binding of transition metal ions to albumin: sites, affinities and rates", in: *Biochimica et Biophysica Acta (BBA)-General Subjects* 1830.12 (2013), pp. 5444–5455.

[907] M. Tolan, *X-ray scattering from soft-matter thin films: materials science and basic research*, Springer, 1999.

[908] Jens Als-Nielsen and Des McMorrow, *Elements of modern X-ray physics*, John Wiley & Sons, 2011.

[909] A Braslau et al., "Surface roughness of water measured by x-ray reflectivity", in: *Physical review letters* 54.2 (1985), p. 114.

[910] SK Sinha et al., "X-ray and neutron scattering from rough surfaces", in: *Physical Review B* 38.4 (1988), p. 2297.

[911] Jens Als-Nielsen et al., "Principles and applications of grazing incidence x-ray and neutron scattering from ordered molecular monolayers at the air-water interface", in: *Physics Reports* 246.5 (1994), p. 254.

[912] Siegfried Dietrich and Andreas Haase, "Scattering of x-rays and neutrons at interfaces", in: *Physics Reports* 260.1-2 (1995), pp. 1–138.

[913] Torben René Jensen and Kristian Kjær, "Structural properties and interactions of thin films at the air-liquid interface explored by synchrotron X-ray scattering", in: *Novel methods to study interfacial layers* 11 (2001), p. 2054.

[914] Torben R Jensen et al., "Novel methods for studying lipids and lipases and their mutual interaction at interfaces. Part II. Surface sensitive synchrotron X-ray scattering", in: *Biochimie* 83.5 (2001), pp. 399–408.

[915] CE Miller et al., "Probing the local order of single phospholipid membranes using grazing incidence x-ray diffraction", in: *Physical review letters* 100.5 (2008), p. 058103.

[916] Sebastian Aeffner et al., "Energetics of stalk intermediates in membrane fusion are controlled by lipid composition", in: *Proceedings of the National Academy of Sciences* 109.25 (2012), E1609–E1618.

[917] Britta Weinhausen et al., "Acyl-chain correlation in membrane fusion intermediates: x-ray diffraction from the rhombohedral lipid phase", in: *Biophysical journal* 102.9 (2012), pp. 2121–2129.

[918] Tim Salditt and Sebastian Aeffner, "X-ray structural investigations of fusion intermediates: lipid model systems and beyond", in: *Seminars in cell & developmental biology*, vol. 60, Elsevier, 2016, pp. 65–77.

[919] Heinz Kiessig, "Interferenz von Röntgenstrahlen an dünnen Schichten", in: *Annalen der Physik* 402.7 (1931), pp. 769–788.

[920] Lyman G Parratt, "Surface studies of solids by total reflection of X-rays", in: *Physical review* 95.2 (1954), p. 359.

[921] SH Anastasiadis et al., "Neutron reflectivity studies of the surface-induced ordering of diblock copolymer films", in: *Physical Review Letters* 62.16 (1989), p. 1852.

[922] K Binder, "Collective diffusion, nucleation, and spinodal decomposition in polymer mixtures", in: *The Journal of chemical physics* 79.12 (1983), pp. 6387–6409.

[923] Daniel Broseta et al., "Molecular weight and polydispersity effects at polymer-polymer interfaces", in: *Macromolecules* 23.1 (1990), pp. 132–139.

[924] S Fisk and B Widom, "Structure and free energy of the interface between fluid phases in equilibrium near the critical point", in: *The Journal of Chemical Physics* 50.8 (1969), pp. 3219–3227.

[925] Stanislav Iatsevitch and Frank Forstmann, "Density profiles at liquid–vapor and liquid–liquid interfaces: An integral equation study", in: *The Journal of chemical physics* 107.17 (1997), pp. 6925–6935.

[926] LB Lurio et al., "Liquid-vapor density profile of helium: An X-ray study", in: *Physical review letters* 68.17 (1992), p. 2628.

[927] O.H. Seeck, *LSFit: Available on request from the author. Software for X-ray and neutron reflectivity calculation.* 1999.

[928] K Kjaer et al., "Ordering in lipid monolayers studied by synchrotron x-ray diffraction and fluorescence microscopy", in: *Physical review letters* 58.21 (1987), p. 2224.

[929] Pulak Dutta et al., "X-ray diffraction studies of organic monolayers on the surface of water", in: *Physical review letters* 58.21 (1987), p. 2228.

[930] Helmut Dosch, BW Batterman, and DC Wack, "Depth-controlled grazing-incidence diffraction of synchrotron x radiation", in: *Physical review letters* 56.11 (1986), p. 1144.

[931] Helmut Dosch, "Evanescent absorption in kinematic surface Bragg diffraction", in: *Physical Review B* 35.5 (1987), p. 2137.

[932] Pulak Dutta, "Grazing incidence X-ray diffraction", in: *Current Science* (2000), pp. 1478–1483.

[933] Kerstin de Meijere, Gerald Brezesinski, and Helmuth Möhwald, "Polyelectrolyte coupling to a charged lipid monolayer", in: *Macromolecules* 30.8 (1997), pp. 2337–2342.

[934] Martina Dyck, Peter Krüger, and Mathias Lösche, "Headgroup organization and hydration of methylated phosphatidylethanolamines in Langmuir monolayers", in: *Physical Chemistry Chemical Physics* 7.1 (2005), pp. 150–156.

[935] Wei Bu and Mark L Schlossman, "Synchrotron X-ray scattering from liquid surfaces and interfaces", in: *Synchrotron Light Sources and Free-Electron Lasers: Accelerator Physics, Instrumentation and Science Applications* (2014), pp. 1–33.

[936] Kristian Kjaer, "Some simple ideas on x-ray reflection and grazing-incidence diffraction from thin surfactant films", in: *Physica B: Condensed Matter* 198.1-3 (1994), pp. 100–109.

[937] Pulak Dutta, "What X-rays tell us about the ordering of molecular backbones in Langmuir monolayers", in: *Colloids and Surfaces A: Physicochemical and Engineering Aspects* 171.1-3 (2000), pp. 59–63.

[938] Mrinal K. Bera, Wei Bu, and Ahmet Uysal, "Chapter 7 - Liquid Surface X-Ray Scattering", in: *Physical Chemistry of Gas-Liquid Interfaces*, ed. by Jennifer A. Faust and James E. House, Developments in Physical & Theoretical Chemistry, Elsevier, 2018, pp. 167–194.

[939] Mrinal K Bera, Wei Bu, and Ahmet Uysal, "Liquid Surface X-Ray Scattering", in: *Physical Chemistry of Gas-Liquid Interfaces*, Elsevier, 2018, pp. 167–194.

[940] J Als-Nielsen and H Möhwald, "Handbook of synchrotron radiation", in: *Ebashi, S., Koch, M., Rubenstein, E., Eds* (1991), pp. 1–53.

[941] Didier Jacquemain et al., "Two-dimensional crystallography of amphiphilic molecules at the air–water interface", in: *Angewandte Chemie International Edition in English* 31.2 (1992), pp. 130–152.

[942] Ivan Kuzmenko et al., "Design and characterization of crystalline thin film architectures at the air- liquid interface: Simplicity to complexity", in: *Chemical Reviews* 101.6 (2001), pp. 1659–1696.

[943] Peter S Pershan and Mark Schlossman, *Liquid surfaces and interfaces: synchrotron x-ray methods*, Cambridge University Press, 2012.

[944] D Jacquemain et al., "Dynamics of two-dimensional self-aggregation: pressure and pH-induced structural changes in a fluorocarbon amphiphile at liquid-air interfaces. An x-ray synchrotron study", in: *Journal of the American Chemical Society* 112.21 (1990), pp. 7724–7736.

[945] Cristina Stefaniu and Gerald Brezesinski, "Grazing incidence X-ray diffraction studies of condensed double-chain phospholipid monolayers formed at the soft air/water interface", in: *Advances in colloid and interface science* 207 (2014), pp. 265–279.

[946] VM Kaganer et al., "Positional order in Langmuir monolayers", in: *Physical review letters* 81.26 (1998), p. 5864.

[947] VM Kaganer et al., "Positional order in Langmuir monolayers: An x-ray diffraction study", in: *Physical Review E* 59.2 (1999), p. 2141.

[948] M von Laue, "Eine quantitative Prüfung der Theorie für die Interferenzerscheinungen bei Röntgenstrahlen", in: *Annalen der Physik* 346.10 (1913), pp. 989–1002.

[949] William Henry Bragg and William Lawrence Bragg, "The reflection of X-rays by crystals", in: *Proceedings of the Royal Society of London. Series A, Containing Papers of a Mathematical and Physical Character* 88.605 (1913), pp. 428–438.

[950] André Guinier, *X-ray diffraction in crystals, imperfect crystals, and amorphous bodies*, English, Includes bibliographical references, Freeman, 1963, ISBN: 0716703076.

[951] AL Patterson, "The Scherrer formula for X-ray particle size determination", in: *Physical review* 56.10 (1939), p. 978.

[952] J Il Langford and AJC Wilson, "Scherrer after sixty years: a survey and some new results in the determination of crystallite size", in: *Journal of applied crystallography* 11.2 (1978), pp. 102–113.

[953] Alain Zachowski, "Phospholipids in animal eukaryotic membranes: transverse asymmetry and movement.", in: *Biochemical Journal* 294.Pt 1 (1993), p. 1.

[954] Jos AF Op den Kamp, "Lipid asymmetry in membranes", in: *Annual review of biochemistry* 48.1 (1979), pp. 47–71.

[955] Andrey A Gurtovenko and Ilpo Vattulainen, "Effect of NaCl and KCl on phosphatidylcholine and phosphatidylethanolamine lipid membranes: insight from atomic-scale simulations for understanding salt-induced effects in the plasma membrane", in: *The Journal of Physical Chemistry B* 112.7 (2008), pp. 1953–1962.

[956] W Stillwell, "Membrane polar lipids", in: *An Introduction to Biological Membranes. 2nd edition. Elsevier, New York* (2016), pp. 63–87.

[957] Rodney L Biltonen and Dov Lichtenberg, "The use of differential scanning calorimetry as a tool to characterize liposome preparations", in: *Chemistry and physics of lipids* 64.1-3 (1993), pp. 129–142.

[958] Martin Caffrey and Jacqueline Hogan, "LIPIDAT: A database of lipid phase transition temperatures and enthalpy changes. DMPC data subset analysis", in: *Chemistry and physics of lipids* 61.1 (1992), pp. 1–109.

[959] Edwin JA Veldhuizen and Henk P Haagsman, "Role of pulmonary surfactant components in surface film formation and dynamics", in: *Biochimica et Biophysica Acta (BBA)-Biomembranes* 1467.2 (2000), pp. 255–270.

[960] Paul O Nkadi, T Allen Merritt, and De-Ann M Pillers, "An overview of pulmonary surfactant in the neonate: genetics, metabolism, and the role of surfactant in health and disease", in: *Molecular genetics and metabolism* 97.2 (2009), pp. 95–101.

[961] B Munteanu et al., "Charged particles interacting with a mixed supported lipid bilayer as a biomimetic pulmonary surfactant", in: *The European Physical Journal E* 37.8 (2014), p. 72.

[962] J Goerke and J Gonzales, "Temperature dependence of dipalmitoyl phosphatidylcholine monolayer stability", in: *Journal of Applied Physiology* 51.5 (1981), pp. 1108–1114.

[963] F Possmayer, "Biochemistry of pulmonary surfactant during fetal development and in the perinatal period", in: *Pulmonary surfactant* (1984), pp. 295–355.

[964] T Akino, "Lipid components of the surfactant system", in: *The Pulmonary Surfactant System* (1992), pp. 19–31.

[965] Koji Kuronuma et al., "Anionic pulmonary surfactant phospholipids inhibit inflammatory responses from alveolar macrophages and U937 cells by binding the lipopolysaccharide-interacting proteins CD14 and MD-2", in: *Journal of Biological Chemistry* 284.38 (2009), pp. 25488–25500.

[966] Hansjörg Eibl and Alfred Blume, "The influence of charge on phosphatidic acid bilayer membranes", in: *Biochimica et Biophysica Acta (BBA)-Biomembranes* 553.3 (1979), pp. 476–488.

[967] Edgar E Kooijman et al., "An electrostatic/hydrogen bond switch as the basis for the specific interaction of phosphatidic acid with proteins", in: *Journal of Biological Chemistry* 282.15 (2007), pp. 11356–11364.

[968] S Ghosh and RM Bell, *Regulation of raf-i kinase by interaction with the lipid second messenger, phosphatidic acid*, 1997.

[969] Wenjie Wang et al., "Regulation of the electric charge in phosphatidic acid domains", in: *The Journal of Physical Chemistry B* 116.24 (2012), pp. 7213–7220.

[970] David Vaknin, Peter Krüger, and Mathias Lösche, "Anomalous X-ray reflectivity characterization of ion distribution at biomimetic membranes", in: *Physical review letters* 90.17 (2003), p. 178102.

[971] Wei Bu et al., "Preferential affinity of calcium ions to charged phosphatidic acid surface from a mixed calcium/barium solution: X-ray reflectivity and fluorescence studies", in: *Langmuir* 25.2 (2009), pp. 1068–1073.

[972] Ting Zhang et al., "Effect of PH and Salt on Surface p K a of Phosphatidic Acid Monolayers", in: *Langmuir* 34.1 (2018), pp. 530–539.

[973] Patrick Garidel and Alfred Blume, "Electrostatic interactions of alkaline earth cations with 1, 2-dimyristoyl-sn-glycero-3-phosphatidic acid (DMPA) model membranes at neutral and acidic pH", in: *European Biophysics Journal* 48.8 (2019), pp. 757–772.

[974] Gajanan S Patil, Nancy J Dorman, and David G Cornwell, "Effects of ionization and counterion binding on the surface areas of phosphatidic acids in monolayers.", in: *Journal of lipid research* 20.5 (1979), pp. 663–668.

[975] Demmelash H Mengistu, Edgar E Kooijman, and Sylvio May, "Ionization properties of mixed lipid membranes: A Gouy–Chapman model of the electrostatic–hydrogen bond switch", in: *Biochimica et Biophysica Acta (BBA)-Biomembranes* 1808.8 (2011), pp. 1985–1992.

[976] E Yu Smirnova et al., "Permeability of bilayer lipid membranes in phase transition. The significance of intermolecular phosphate-phosphate hydrogen bonding", in: *Chemistry and physics of lipids* 41.2 (1986), pp. 173–180.

[977] Alfred Blume and Hansjörg Eibl, "The influence of charge on bilayer membranes calorimetric investigations of phosphatidic acid bilayers", in: *Biochimica et Biophysica Acta (BBA)-Biomembranes* 558.1 (1979), pp. 13–21.

[978] NIST Office of Data and Informatics, *NIST Chemistry WebBook*, en, DOI: `https://doi.org/10.18434/T4D303`, URL: `https://webbook.nist.gov/chemistry/`.

[979] E. W. Lemmon et al., *NIST Standard Reference Database 23: Reference Fluid Thermodynamic and Transport Properties-REFPROP, Version 10.0, National Institute of Standards and Technology*, 2018, DOI: `https://dx.doi.org/10.18434/T4JS3C`, URL: `https://www.nist.gov/srd/refprop`.

[980] Sunghwan Kim et al., "PubChem substance and compound databases", in: *Nucleic acids research* 44.D1 (2016), pp. D1202–D1213.

[981] Paul Ruelle, "The n-octanol and n-hexane/water partition coefficient of environmentally relevant chemicals predicted from the mobile order and disorder (MOD) thermodynamics", in: *Chemosphere* 40.5 (2000), pp. 457–512.

[982] Michael H Abraham et al., "Hydrogen bonding. 32. An analysis of water-octanol and water-alkane partitioning and the Δlog P parameter of Seiler", in: *Journal of pharmaceutical sciences* 83.8 (1994), pp. 1085–1100.

[983] Sheldon K Hall et al., "Modeling the dynamics of tamponade multicomponent gases during retina reattachment surgery", in: *AIChE Journal* 63.9 (2017), pp. 3651–3662.

[984] Sujit Banerjee, "Estimating water solubilities of organics as a function of temperature", in: *Water Research* 30.9 (1996), pp. 2222–2225.

[985] Samuel Hyman Yalkowsky and Sujit Banerjee, *Aqueous solubility: Methods of estimation for organic compounds*, Marcel Dekker, 1992.

[986] AMA Dias et al., "Thermodynamic characterization of pure perfluoroalkanes, including interfacial and second order derivative properties, using the crossover soft-SAFT EoS", in: *Fluid phase equilibria* 286.2 (2009), pp. 134–143.

[987] Alexey Kabalnov et al., "Dissolution of multicomponent microbubbles in the bloodstream: 2. Experiment", in: *Ultrasound in medicine & biology* 24.5 (1998), pp. 751–760.

[988] Hong Lin and Yuan-Yuan Duan, "Surface tension measurements of propane (R-290) and isobutane (R-600a) from (253 to 333) K", in: *Journal of Chemical & Engineering Data* 48.5 (2003), pp. 1360–1363.

[989] Ian A McLure, Virgilio AM Soares, and Beryl Edmonds, "Surface tension of perfluoropropane, perfluoro-n-butane, perfluoro-n-hexane, perfluoro-octane, perfluorotributylamine and n-pentane. Application of the principle of corresponding states to the surface tension of perfluoroalkanes", in: *Journal of the Chemical Society, Faraday Transactions 1: Physical Chemistry in Condensed Phases* 78.7 (1982), pp. 2251–2257.

[990] Tiejun Cheng et al., "Computation of octanol- water partition coefficients by guiding an additive model with knowledge", in: *Journal of chemical information and modeling* 47.6 (2007), pp. 2140–2148.

[991] A Gavezzotti, "The calculation of molecular volumes and the use of volume analysis in the investigation of structured media and of solid-state organic reactivity", in: *Journal of the American Chemical Society* 105.16 (1983), pp. 5220–5225.

[992] George Famini, "Using Theoretical Descriptors in Structural Activity Relationships. 1. Molecular Volume", in: (Jan. 1988), p. 30.

[993] Corwin Hansch and Toshio Fujita, "p-σ-π Analysis. A method for the correlation of biological activity and chemical structure", in: *Journal of the American Chemical Society* 86.8 (1964), pp. 1616–1626.

[994] Toshio Fujita, Junkichi Iwasa, and Corwin Hansch, "A new substituent constant, π, derived from partition coefficients", in: *Journal of the American Chemical Society* 86.23 (1964), pp. 5175–5180.

[995] Albert Leo, Corwin Hansch, and David Elkins, "Partition coefficients and their uses", in: *Chemical reviews* 71.6 (1971), pp. 525–616.

[996] Hemi Cumming and Christoph Rücker, "Octanol–water partition coefficient measurement by a simple 1H NMR method", in: *ACS omega* 2.9 (2017), pp. 6244–6249.

[997] Bruce E Smart, "Fluorine substituent effects (on bioactivity)", in: *Journal of Fluorine Chemistry* 109.1 (2001), pp. 3–11.

[998] Peer Kirsch, *Modern fluoroorganic chemistry: synthesis, reactivity, applications*, John Wiley & Sons, 2013.

[999] Mara G Freire et al., "Surface tension of liquid fluorocompounds", in: *Journal of Chemical & Engineering Data* 51.5 (2006), pp. 1820–1824.

[1000] Carl L Yaws, *Yaws' Thermophysical Properties of Chemicals and Hydrocarbons*, Knovel, 2009.

[1001] Carl L Yaws, *Thermophysical properties of chemicals and hydrocarbons*, William Andrew, 2008.

[1002] Corwin Hansch, Albert Leo, DH Hoekman, et al., *Exploring QSAR: fundamentals and applications in chemistry and biology*, vol. 557, American Chemical Society Washington, DC, 1995.

[1003] Jerome L Gabriel et al., "Quantitative structure-activity relationships of perfluorinated hetero-hydrocarbons as potential respiratory media. Application to oxygen solubility, partition coefficient, viscosity, vapor pressure, and density.", in: *ASAIO journal (American Society for Artificial Internal Organs: 1992)* 42.6 (1996), pp. 968–973.

[1004] Alanas A Petrauskas and Eduard A Kolovanov, "ACD/Log P method description", in: *Perspectives in drug discovery and design* 19.1 (2000), pp. 99–116.

[1005] Harry E Pence and Antony Williams, *ChemSpider: an online chemical information resource*, 2010.

[1006] Aiman Al-Rahmani et al., "Effects of partial liquid ventilation with perfluorodecalin in the juvenile rabbit lung after saline injury", in: *Critical care medicine* 28.5 (2000), pp. 1459–1464.

[1007] Cynthia A Cox et al., "Intratracheal administration of perfluorochemical-gentamicin suspension: A comparison to intravenous administration in normal and injured lungs", in: *Pediatric pulmonology* 32.2 (2001), pp. 142–151.

[1008] C Wohlfahrt, *Springer Materials–The Landolt-Börnstein-Database*, 2008.

[1009] Hans-Georg Mack and Heinz Oberhammer, "The gas-phase structures of trans- and cis-perfluorodecalin", in: *Journal of Molecular Structure* 197 (1989), pp. 321–328.

[1010] Ned Bowden et al., "Mesoscale self-assembly of hexagonal plates using lateral capillary forces: synthesis using the capillary bond", in: *Journal of the American Chemical Society* 121.23 (1999), pp. 5373–5391.

[1011] Sun-Joo Lee et al., "Characterization of perfluorooctylbromide-based nanoemulsion particles using atomistic molecular dynamics simulations", in: *The Journal of Physical Chemistry B* 114.31 (2010), pp. 10086–10096.

[1012] Viktor V Obraztsov et al., "In vitro cellular effects of perfluorochemicals correlate with their lipid solubility", in: *American Journal of Physiology-Lung Cellular and Molecular Physiology* 278.5 (2000), pp. L1018–L1024.

[1013] D Smith, "Effects of perflubron (LiquiVent) on human leukocyte activation in vitro", in: *Am J Respir Crit Care Med* 155 (1997), A752.

[1014] Tara M Smith et al., "A liquid perfluorochemical decreases the in vitro production of reactive oxygen species by alveolar macrophages", in: *Critical care medicine* 23.9 (1995), pp. 1533–1539.

[1015] Catherine M Woods et al., "Perflubron attenuates neutrophil adhesion to activated endothelial cells in vitro", in: *American Journal of Physiology-Lung Cellular and Molecular Physiology* 278.5 (2000), pp. L1008–L1017.

[1016] Brian C Tripp, Jules John Magda, and Joseph D Andrade, "Adsorption of globular proteins at the air/water interface as measured via dynamic surface tension: concentration dependence, mass-transfer considerations, and adsorption kinetics", in: *Journal of colloid and interface science* 173.1 (1995), pp. 16–27.

[1017] Mitaben D Lad et al., "The adsorbed conformation of globular proteins at the air/water interface", in: *Physical Chemistry Chemical Physics* 8.18 (2006), pp. 2179–2186.

[1018] Rosangela Itri et al., "Effect of urea on bovine serum albumin in aqueous and reverse micelle environments investigated by small angle X-ray scattering, fluorescence and circular dichroism", in: *Brazilian journal of physics* 34.1 (2004), pp. 58–63.

[1019] Leandro RS Barbosa et al., "The importance of protein-protein interactions on the pH-induced conformational changes of bovine serum albumin: a small-angle X-ray scattering study", in: *Biophysical journal* 98.1 (2010), pp. 147–157.

[1020] Anna Derylo-Marczewska, Agnieszka Chrzanowska, and Adam W Marczewski, "Morphological, structural and physicochemical characteristics of the surface of mesocellular silica foam with the adsorbed OVA and BSA proteins", in: *Microporous and Mesoporous Materials* 293 (2020), p. 109769.

[1021] Helen M Berman et al., "The protein data bank", in: *Acta Crystallographica Section D: Biological Crystallography* 58.6 (2002), pp. 899–907.

[1022] Shaun D Hooke, Sheena E Radford, and Christopher M Dobson, "The refolding of human lysozyme: a comparison with the structurally homologous hen lysozyme", in: *Biochemistry* 33.19 (1994), pp. 5867–5876.

[1023] Taiji Imoto et al., "21 vertebrate lysozymes", in: *The enzymes*, vol. 7, Elsevier, 1972, pp. 665–868.

[1024] Wolfgang Kabsch and Christian Sander, "Dictionary of protein secondary structure: pattern recognition of hydrogen-bonded and geometrical features", in: *Biopolymers: Original Research on Biomolecules* 22.12 (1983), pp. 2577–2637.

[1025] Christopher M Dobson and Alan R Fersht, *Protein folding*, vol. 348, Cambridge University Press, 1996.

[1026] Kengo Kinoshita and Haruki Nakamura, "eF-site and PDBjViewer: database and viewer for protein functional sites", in: *Bioinformatics* 20.8 (2004), pp. 1329–1330.

[1027] Michael L Connolly, "The molecular surface package", in: *Journal of molecular graphics* 11.2 (1993), pp. 139–141.

[1028] ZG Peng, K Hidajat, and MS Uddin, "Adsorption of bovine serum albumin on nanosized magnetic particles", in: *Journal of colloid and interface science* 271.2 (2004), pp. 277–283.

[1029] Kyoung-Yong Chun and Pieter Stroeve, "Protein transport in nanoporous membranes modified with self-assembled monolayers of functionalized thiols", in: *Langmuir* 18.12 (2002), pp. 4653–4658.

[1030] Chaiyavat Chaiyasut and Takao Tsuda, "Isoelectric points estimation of proteins by electroosmotic flow: pH relationship using physically adsorbed proteins on silica gel", in: *CHROMATOGRAPHY-TOKYO-SOCIETY FOR CHROMATOGRAPHIC SCIENCES* 22.2 (2001), pp. 91–96.

[1031] Xuanting Liu et al., "Mg2+ inhibits heat-induced aggregation of BSA: The mechanism and its binding site", in: *Food Hydrocolloids* 101 (2020), p. 105450.

[1032] Catherine Harford and Bibudhendra Sarkar, "Amino terminal Cu (II)-and Ni (II)-binding (ATCUN) motif of proteins and peptides: metal binding, DNA cleavage, and other properties", in: *Accounts of chemical research* 30.3 (1997), pp. 123–130.

[1033] M Bellion et al., "Protein adsorption on tailored substrates: long-range forces and conformational changes", in: *Journal of Physics: Condensed Matter* 20.40 (2008), p. 404226.

[1034] George A Parks, "The isoelectric points of solid oxides, solid hydroxides, and aqueous hydroxo complex systems", in: *Chemical Reviews* 65.2 (1965), pp. 177–198.

[1035] Alexandra Teleki, M Kamal Akhtar, and Sotiris E Pratsinis, "The quality of SiO 2-coatings on flame-made TiO 2-based nanoparticles", in: *Journal of Materials Chemistry* 18.30 (2008), pp. 3547–3555.

[1036] Hendrik Hähl et al., "Subsurface influence on the structure of protein adsorbates as revealed by in situ X-ray reflectivity", in: *Langmuir* 28.20 (2012), pp. 7747–7756.

[1037] Peter J Scales et al., "Electrokinetics of the silica-solution interface: a flat plate streaming potential study", in: *Langmuir* 8.3 (1992), pp. 965–974.

[1038] GL Tan et al., "Optical properties and London dispersion interaction of amorphous and crystalline SiO 2 determined by vacuum ultraviolet spectroscopy and spectroscopic ellipsometry", in: *Physical Review B* 72.20 (2005), p. 205117.

[1039] Walter R Carmody, "Easily prepared wide range buffer series", in: *Journal of Chemical Education* 38.11 (1961), p. 559.

[1040] Søren Peter Lauritz Sörensen, "Über die Messung und Bedeutung der Wasserstoffionen-konzentration bei biologischen Prozessen", in: *Ergebnisse der Physiologie* 12.1 (1912), pp. 393–532.

[1041] Andrew S Thomas and Adrian H Elcock, "Molecular dynamics simulations of hydrophobic associations in aqueous salt solutions indicate a connection between water hydrogen bonding and the Hofmeister effect", in: *Journal of the American Chemical Society* 129.48 (2007), pp. 14887–14898.

[1042] James Kruczek et al., "Effects of lithium and other monovalent ions on palmitoyl oleoyl phosphatidylcholine bilayer", in: *Langmuir* 33.4 (2017), pp. 1105–1115.

[1043] John C Slater, "Atomic radii in crystals", in: *The Journal of Chemical Physics* 41.10 (1964), pp. 3199–3204.

[1044] Boris K Vainshtein, Vladimir M Friedkin, and Vladimir L Indenbom, *Structure of crystals*, Springer Science & Business Media, 2013.

[1045] Enrico Clementi and D.L. Raimondi, "Atomic screening constants from SCF functions", in: *The Journal of Chemical Physics* 38.11 (1963), pp. 2686–2689.

[1046] Yizhak Marcus, "Thermodynamics of solvation of ions. Part 5. -Gibbs free energy of hydration at 298.15 K", in: *Journal of the Chemical Society, Faraday Transactions* 87.18 (1991), pp. 2995–2999.

[1047] Manjeera Mantina et al., "Consistent van der Waals radii for the whole main group", in: *The Journal of Physical Chemistry A* 113.19 (2009), pp. 5806–5812.

[1048] Friederike Giebel et al., "The interaction between stearic acid monolayers and butane under elevated pressures", in: *Colloids and Surfaces A: Physicochemical and Engineering Aspects* 504 (2016), pp. 126–130.

[1049] Friederike Giebel et al., "The adsorption behavior of octafluoropropane at the water/gas interface", in: *Journal of Applied Physics* 116.22 (2014), p. 222204.

[1050] KELLER AG für Druckmesstechnik, *Digital manometers and display units.* URL: `http://www.keller-druck.com/picts/pdf/engl/leaflet_mano_e.pdf`.

[1051] Christian Albers, *Gasadsorption an Grenzflächen*, de, 2017.

[1052] Y. Forov, *X-ray studies on adsorption processes at solid-liquid interfaces and ultrafast dynamics in water*, 2018.

[1053] H Reichert et al., "A new X-ray transmission-reflection scheme for the study of deeply buried interfaces using high-energy microbeams", in: *Physica B: Condensed Matter* 336.1-2 (2003), pp. 46–55.

[1054] V Honkimäki et al., "X-ray optics for liquid surface/interface spectrometers", in: *Journal of synchrotron radiation* 13.6 (2006), pp. 426–431.

[1055] Thomas Arnold et al., "Implementation of a beam deflection system for studies of liquid interfaces on beamline I07 at Diamond", in: *Journal of synchrotron radiation* 19.3 (2012), pp. 408–416.

[1056] Bridget M Murphy et al., "A novel X-ray diffractometer for studies of liquid–liquid interfaces", in: *Journal of synchrotron radiation* 21.1 (2014), pp. 45–56.

[1057] Michael Paulus et al., "An access to buried interfaces: the X-ray reflectivity set-up of BL9 at DELTA", in: *Journal of synchrotron radiation* 15.6 (2008), pp. 600–605.

[1058] Metin Tolan et al., "DELTA: Synchrotron light in nordrhein-westfalen", in: (2003).

[1059] U Berges et al., "Status of the synchrotron light source DELTA", in: *AIP conference proceedings*, vol. 879, 1, AIP, 2007, pp. 30–33.

[1060] Michael Paulus et al., "An internet-based synchrotron experiment for students measuring the X-ray magnetic circular dichroism of a PtFe alloy", in: *Journal of synchrotron radiation* 12.2 (2005), pp. 246–250.

[1061] Christof Krywka et al., "The new diffractometer for surface X-ray diffraction at beamline BL9 of DELTA", in: *Journal of synchrotron radiation* 13.1 (2006), pp. 8–13.

[1062] Christina Krywka et al., "The small-angle and wide-angle X-ray scattering set-up at beamline BL9 of DELTA", in: *Journal of synchrotron radiation* 14.3 (2007), pp. 244–251.

[1063] Christian Reich et al., "A microfluidic setup for studies of solid-liquid interfaces using x-ray reflectivity and fluorescence microscopy", in: *Review of scientific instruments* 76.9 (2005), p. 095103.

[1064] Chad E Miller et al., "Characterization of biological thin films at the solid-liquid interface by x-ray reflectivity", in: *Physical review letters* 94.23 (2005), p. 238104.

[1065] OH Seeck et al., "The high-resolution diffraction beamline P08 at PETRA III", in: *Journal of synchrotron radiation* 19.1 (2012), pp. 30–38.

[1066] BM Murphy et al., "A new Diffractometer for Studies of Liquid Liquid Interfaces", in: *AIP Conference Proceedings*, vol. 1234, 1, AIP, 2010, pp. 155–158.

[1067] Gerhard Materlik, Trevor Rayment, and David I Stuart, *Diamond Light Source: status and perspectives*, 2015.

[1068] Chris Nicklin et al., "Diamond beamline I07: a beamline for surface and interface diffraction", in: *Journal of synchrotron radiation* 23.5 (2016), pp. 1245–1253.

[1069] Alfred G Emslie, Francis T Bonner, and Leslie G Peck, "Flow of a viscous liquid on a rotating disk", in: *Journal of Applied Physics* 29.5 (1958), pp. 858–862.

[1070] Andreas Acrivos, MJ Shah, and EE Petersen, "Momentum and heat transfer in laminar boundary-layer flows of non-Newtonian fluids past external surfaces", in: *AIChE Journal* 6.2 (1960), pp. 312–317.

[1071] A Acrivos, MJ Shah, and EE Petersen, "On the flow of a non-Newtonian liquid on a rotating disk", in: *Journal of Applied Physics* 31.6 (1960), pp. 963–968.

[1072] Dietrich Meyerhofer, "Characteristics of resist films produced by spinning", in: *Journal of Applied Physics* 49.7 (1978), pp. 3993–3997.

[1073] Marc D Porter, *Combinatorial materials science*, John Wiley & Sons, 2007.

[1074] Karen Ashley et al., "Combinatorial Mapping of Polymer Film Wettability On Gradient Energy Surfaces", in: *MRS Online Proceedings Library Archive* 700 (2001).

[1075] Karen M Ashley et al., "Combinatorial Methods and Their Application to Mapping Wetting-Dewetting Transition Lines on Gradient Surface Energy Substrates1", in: *Balaji Narasimhan* (2007), p. 201.

[1076] Changwon Suh et al., "Informatics methods for combinatorial materials science", in: *Combinatorial Materials Science* (2007), pp. 109–119.

[1077] Christian Reich, "Structure, Fluidity and Phase Behavior of Supported Lipid Membranes: An Investigation by X-ray Reflectivity and Fluorescence Microscopy", PhD thesis, lmu, 2007.

[1078] T Salditt et al., "X-ray reflectivity of solid-supported, multilamellar membranes", in: *The European Physical Journal E* 7.2 (2002), pp. 105–116.

[1079] L Perino-Gallice et al., "Dewetting of solid-supported multilamellar lipid layers", in: *The European Physical Journal E* 8.3 (2002), pp. 275–282.

[1080] Lukas K Tamm and Harden M McConnell, "Supported phospholipid bilayers", in: *Biophysical journal* 47.1 (1985), pp. 105–113.

[1081] Warren W Flack et al., "A mathematical model for spin coating of polymer resists", in: *Journal of Applied Physics* 56.4 (1984), pp. 1199–1206.

[1082] Gareth Roberts, *Langmuir-blodgett films*, Springer Science & Business Media, 2013.

[1083] Abraham Ulman, *An Introduction to Ultrathin Organic Films: From Langmuir–Blodgett to Self–Assembly*, Academic press, 2013.

[1084] Syed Arshad Hussain et al., "Unique supramolecular assembly through Langmuir–Blodgett (LB) technique", in: *Heliyon* 4.12 (2018), e01038.

[1085] Osvaldo N Oliveira Jr et al., "Langmuir-Blodgett films-properties and possible applications", in: *Braz J Phys* 22.2 (1992), pp. 60–69.

[1086] RH Tredgold, "The physics of Langmuir-Blodgett films", in: *Reports on Progress in Physics* 50.12 (1987), p. 1609.

[1087] Burton L Henke, Eric M Gullikson, and John C Davis, "X-ray interactions: photoabsorption, scattering, transmission, and reflection at E= 50-30,000 eV, Z= 1-92", in: *Atomic data and nuclear data tables* 54.2 (1993), pp. 181–342.

[1088] 6002 Luzern Suva Gesundheitsschutz, *Sicherheitstechnische Kenngroessen Kenngroessen*, de, URL: `https://www.suva.ch/` (visited on 10/02/2019).

[1089] Maria Molnarne and Wolfgang Möller, "CHEMSAFE–Eine Datenbank für bewertete sicherheitstechnische Kenngrössen", in: *Chemie Ingenieur Technik* 81.1-2 (2009), pp. 45–47.

[1090] IM Tidswell et al., "X-ray specular reflection studies of silicon coated by organic monolayers (alkylsiloxanes)", in: *Physical Review B* 41.2 (1990), p. 1111.

[1091] Susanne Dogan et al., "Human apolipoprotein a1 at solid/liquid and liquid/gas interfaces", in: *The Journal of Physical Chemistry B* 122.14 (2018), pp. 3953–3960.

[1092] Irena Kiesel et al., "Temperature-driven adsorption and desorption of proteins at solid–liquid interfaces", in: *Langmuir* 30.8 (2014), pp. 2077–2083.

[1093] Hans-Georg Steinrück et al., "Nanoscale structure of Si/SiO2/organics interfaces", in: *ACS nano* 8.12 (2014), pp. 12676–12681.

[1094] Yury Forov et al., "Adsorption Behavior of Lysozyme at Titanium Oxide–Water Interfaces", in: *Langmuir* 34.19 (2018), pp. 5403–5408.

[1095] Wolf-Dieter Deckwer et al., *Römpp online*, 2006.

[1096] Anne K Hüsecken et al., "Effect of urea and glycerol on the adsorption of ribonuclease A at the air- water interface", in: *Langmuir* 26.16 (2010), pp. 13429–13435.

[1097] Holger Göhring et al., "Salt induced reduction of lysozyme adsorption at charged interfaces", in: *Journal of Physics: Condensed Matter* 27.23 (2015), p. 235103.

[1098] Andrew G Richter and Ivan Kuzmenko, "Using in situ X-ray reflectivity to study protein adsorption on hydrophilic and hydrophobic surfaces: benefits and limitations", in: *Langmuir* 29.17 (2013), pp. 5167–5180.

[1099] Florian Evers et al., "Exploring the interfacial structure of protein adsorbates and the kinetics of protein adsorption: an in situ high-energy x-ray reflectivity study", in: *Langmuir* 24.18 (2008), pp. 10216–10221.

[1100] Fabian Jirasek et al., "Influence of pH and Salts on Partial Molar Volume of Lysozyme and Bovine Serum Albumin in Aqueous Solutions", in: *Chemical engineering & technology* 41.12 (2018), pp. 2337–2345.

[1101] Frank Putnam, *The Plasma Proteins V2: Structure, Function, and Genetic Control*, Academic Press, 1975, pp. 141–147.

[1102] Thomas E Creighton, *Proteins: structures and molecular properties*, Macmillan, 1993.

[1103] Oliver Hollmann, Thomas Gutberlet, and Claus Czeslik, "Structure and protein binding capacity of a planar PAA brush", in: *Langmuir* 23.3 (2007), pp. 1347–1353.

[1104] Mario Birkholz, *Thin film analysis by X-ray scattering*, John Wiley & Sons, 2006.

[1105] CM Teodorescu et al., "An approximation of the Voigt I profile for the fitting of experimental X-ray absorption data", in: *Nuclear Instruments and Methods in Physics Research Section A: Accelerators, Spectrometers, Detectors and Associated Equipment* 345.1 (1994), pp. 141–147.

[1106] Irina Estrela-Lopis, Gerald Brezesinski, and Helmuth Möhwald, "Influence of model membrane structure on phospholipase D activity", in: *Physical Chemistry Chemical Physics* 2.20 (2000), pp. 4600–4604.

[1107] Laurence Ramos et al., "Electrostatic interactions between polyelectrolyte and amphiphiles in two-and three-dimensional systems", in: *Colloids and Surfaces A: Physicochemical and Engineering Aspects* 303.1-2 (2007), pp. 79–88.

[1108] Frédéric Gerber, Thierry F Vandamme, and Marie Pierre Krafft, "Impact of perfluorooctylethane on the formation of a semi-crystalline liquid-condensed phase in a phospholipid monolayer and of perfluorooctyl bromide on the adsorption of albumin on such a monolayer", in: *Comptes Rendus Chimie* 12.1-2 (2009), pp. 180–187.

[1109] Valentina Dichiarante, Roberto Milani, and Pierangelo Metrangolo, "Natural surfactants towards a more sustainable fluorine chemistry", in: *Green Chemistry* 20.1 (2018), pp. 13–27.

[1110] Andrea Giehl et al., "Interaction of the GM2-activator protein with phospholipid–ganglioside bilayer membranes and with monolayers at the air–water interface", in: *European journal of biochemistry* 261.3 (1999), pp. 650–658.

[1111] Harald R Seitz et al., "Molecular determinants of the reversible membrane anchorage of the G-protein transducin", in: *Biochemistry* 38.25 (1999), pp. 7950–7960.

[1112] Gerald Brezesinski and Helmuth Möhwald, "Langmuir monolayers to study interactions at model membrane surfaces", in: *Advances in colloid and interface science* 100 (2003), pp. 563–584.

[1113] Fred Possmayer et al., "Pulmonary surfactant", in: *Canadian journal of biochemistry and cell biology* 62.11 (1984), pp. 1121–1133.

[1114] Yun-Ta Yang et al., "Ultra-thin phospholipid layers physically adsorbed upon glass characterized by nano-indentation at the surface contact level", in: *Nanotechnology* 20.19 (2009), p. 195702.

[1115] Matthew Patterson, Hans J Vogel, and Elmar J Prenner, "Biophysical characterization of monofilm model systems composed of selected tear film phospholipids", in: *Biochimica et Biophysica Acta (BBA)-Biomembranes* 1858.2 (2016), pp. 403–414.

[1116] D Grigoriev et al., "A novel method to evaluate the phase transition thermodynamics of Langmuir monolayers. Application to DPPG monolayers affected by subphase composition", in: *The Journal of Physical Chemistry B* 107.51 (2003), pp. 14283–14288.

[1117] Heejung Yun et al., "Physicochemical properties of phosphatidylcholine (PC) monolayers with different alkyl chains, at the air/water interface", in: *Bulletin-Korean Chemical Society* 24.3 (2003), pp. 377–383.

[1118] Xiaoli Wang et al., "Structural changes of phospholipid monolayers caused by coupling of human serum albumin: a GIXD study at the air/water interface", in: *The Journal of Physical Chemistry B* 108.37 (2004), pp. 14171–14177.

[1119] J Miñones Jr et al., "The effect of polar groups on structural characteristics of phospholipid monolayers spread at the air–water interface", in: *Colloids and Surfaces A: Physicochemical and Engineering Aspects* 203.1-3 (2002), pp. 273–286.

[1120] Mutsuo Matsumoto et al., "A trough with radial compression for studies of monolayers and fabrication of Langmuir-Blodgett films", in: *Thin Solid Films* 280.1-2 (1996), pp. 238–243.

[1121] Cary W McConlogue, Daniel Malamud, and T Kyle Vanderlick, "Interaction of DPPC monolayers with soluble surfactants: electrostatic effects of membrane perturbants", in: *Biochimica et Biophysica Acta (BBA)-Biomembranes* 1372.1 (1998), pp. 124–134.

[1122] Yasushi Yamamoto et al., "Interactions between Phospholipid Monolayers (DPPC and DMPC) and Anesthetic Isoflurane Observed by Quartz Crystal Oscillator", in: *Journal of Biophysical Chemistry* 6.02 (2015), p. 42.

[1123] Daisuke Yoshida et al., "Morphology observation of dipalmitoyl phosphatidyl choline (DPPC) monolayer on water surface by dropping method", in: (2013).

[1124] Pasupati Mukerjee, "Fluorocarbon—hydrocarbon interactions in micelles and other lipid assemblies, at interfaces, and in solutions", in: *Colloids and Surfaces A: Physicochemical and engineering aspects* 84.1 (1994), pp. 1–10.

[1125] A Braslau et al., "Capillary waves on the surface of simple liquids measured by x-ray reflectivity", in: *Physical Review A* 38.5 (1988), p. 2457.

[1126] Sebastian Tiemeyer, Michael Paulus, and Metin Tolan, "Effect of surface charge distribution on the adsorption orientation of proteins to lipid monolayers", in: *Langmuir* 26.17 (2010), pp. 14064–14067.

[1127] David Vaknin et al., "Structural properties of phosphatidylcholine in a monolayer at the air/water interface: Neutron reflection study and reexamination of x-ray reflection measurements", in: *Biophysical journal* 59.6 (1991), pp. 1325–1332.

[1128] Guohui Wu et al., "Interaction between lipid monolayers and poloxamer 188: an X-ray reflectivity and diffraction study", in: *Biophysical journal* 89.5 (2005), pp. 3159–3173.

[1129] Andrew R McCluskey et al., "Bayesian determination of the effect of a deep eutectic solvent on the structure of lipid monolayers", in: *Physical Chemistry Chemical Physics* 21.11 (2019), pp. 6133–6141.

[1130] CA Helm et al., "Phospholipid monolayer density distribution perpendicular to the water surface. A synchrotron X-ray reflectivity study", in: *EPL (Europhysics Letters)* 4.6 (1987), p. 697.

[1131] Frances Neville et al., "Protegrin interaction with lipid monolayers: grazing incidence X-ray diffraction and X-ray reflectivity study", in: *Soft matter* 4.8 (2008), pp. 1665–1674.

[1132] Haim Diamant et al., "Unstable topography of biphasic surfactant monolayers", in: *EPL (Europhysics Letters)* 52.2 (2000), p. 171.

[1133] DC Florian Wieland et al., "Structure of DPPC–hyaluronan interfacial layers–effects of molecular weight and ion composition", in: *Soft Matter* 12.3 (2016), pp. 729–740.

[1134] Waldemar Kulig et al., "Complex Behavior of Phosphatidylcholine–Phosphatidic Acid Bilayers and Monolayers: Effect of Acyl Chain Unsaturation", in: *Langmuir* 35.17 (2019), pp. 5944–5956.

[1135] CE Miller et al., "Integration of ganglioside GT1b receptor into DPPE and DPPC phospholipid monolayers: an X-ray reflectivity and grazing-incidence diffraction study", in: *Biophysical journal* 95.7 (2008), pp. 3278–3286.

[1136] Bernd Struth et al., "Organization of two-dimensional phospholipid monolayers on a gel-forming substrate", in: *Physical review letters* 88.2 (2001), p. 025502.

[1137] Marie Pierre Krafft, Valentin B Fainerman, and Reinhard Miller, "Modeling of the effect of fluorocarbon gases on the properties of phospholipid monolayers and the adsorption dynamics of their aqueous solutions or dispersions", in: *Colloid and Polymer Science* 293.11 (2015), pp. 3091–3097.

[1138] Simona Rossi, Gilles Waton, and Marie Pierre Krafft, "Phospholipid-coated gas bubble engineering: Key parameters for size and stability control, as determined by an acoustical method", in: *Langmuir* 26.3 (2010), pp. 1649–1655.

[1139] E Maillard et al., "Perfluorocarbons: new tool for islets preservation in vitro", in: *Transplantation proceedings*, vol. 40, 2, Elsevier, 2008, pp. 372–374.

[1140] Norbert Kučerka, Mu-Ping Nieh, and John Katsaras, "Fluid phase lipid areas and bilayer thicknesses of commonly used phosphatidylcholines as a function of temperature", in: *Biochimica et Biophysica Acta (BBA)-Biomembranes* 1808.11 (2011), pp. 2761–2771.

[1141] Stephanie Tristram-Nagle, Horia I Petrache, and John F Nagle, "Structure and interactions of fully hydrated dioleoylphosphatidylcholine bilayers", in: *Biophysical journal* 75.2 (1998), pp. 917–925.

[1142] Horia I Petrache, Steven W Dodd, and Michael F Brown, "Area per lipid and acyl length distributions in fluid phosphatidylcholines determined by 2H NMR spectroscopy", in: *Biophysical journal* 79.6 (2000), pp. 3172–3192.

[1143] Martin Kreuzer, "Solid-supported lipid membranes and their response to varied environmental conditions", PhD thesis, 2012.

[1144] Göran Surmeier, *Cholesterolhaltige Lipidmembranen unter Druck*, de, 2016.

[1145] Isabel Maria Gernhold, *Der Einfluss von Gasen auf die Proteinadsorption an der Flüssig/Gas-Grenzfläche*, de, 2019.

[1146] Canan Orak, *BSA an hydrophoben Grenzflächen unter Einfluss von Perfluordecalin an der Wasser/Luft-Grenzfläche*, de, 2019.

[1147] Andrew G Buckland and David C Wilton, "Anionic phospholipids, interfacial binding and the regulation of cell functions", in: *BBA-Molecular and Cell Biology of Lipids* 2.1483 (2000), pp. 199–216.

[1148] Xiaolong Lu et al., "Behavior of lysozyme adsorbed onto biological liquid crystal lipid monolayer at the air/water interface", in: *Chinese Physics B* 25.9 (2016), p. 090506.

[1149] Juan Torrent Burgués and Rekha Raju, "Effect of lysozyme subphase and insertion on several lipid films", in: *Advanced Materials science* 4.1 (2019), pp. 1–7.

[1150] Joseph T Jarrett and Peter T Lansbury Jr, "Seeding "one-dimensional crystallization" of amyloid: a pathogenic mechanism in Alzheimer's disease and scrapie?", in: *Cell* 73.6 (1993), pp. 1055–1058.

[1151] Yohko F Yano et al., "Initial Conformation of Adsorbed Proteins at an Air–Water Interface", in: *The Journal of Physical Chemistry B* 122.17 (2018), pp. 4662–4666.

[1152] *The crystal structure of the orthorhombic form of hen egg white lysozyme at 1.5 angstroms resolution*, en, DOI: 10.2210/pdb1vdq/pdb.

[1153] Christian F Wertz and Maria M Santore, "Adsorption and reorientation kinetics of lysozyme on hydrophobic surfaces", in: *Langmuir* 18.4 (2002), pp. 1190–1199.

[1154] DE Graham and MC Phillips, "Proteins at liquid interfaces: I. Kinetics of adsorption and surface denaturation", in: *Journal of colloid and interface science* 70.3 (1979), pp. 403–414.

[1155] JR Lu et al., "Structural conformation of lysozyme layers at the air/water interface studied by neutron reflection", in: *Journal of the Chemical Society, Faraday Transactions* 94.21 (1998), pp. 3279–3287.

[1156] C Postel, O Abillon, and B Desbat, "Structure and denaturation of adsorbed lysozyme at the air–water interface", in: *Journal of colloid and interface science* 266.1 (2003), pp. 74–81.

[1157] Caroline Postel and Olivier Abillon, "Adsorption of Lysozyme and Methylated Lysozyme at the Air- Water Interface: An X-ray Reflectivity Study", in: *Langmuir* 14.19 (1998), pp. 5649–5651.

[1158] Adam W Perriman et al., "Effect of the air- water interface on the structure of lysozyme in the presence of guanidinium chloride", in: *The Journal of Physical Chemistry B* 112.31 (2008), pp. 9532–9539.

[1159] Shuqian Xu and Srinivasan Damodaran, "The role of chemical potential in the adsorption of lysozyme at the air-water interface", in: *Langmuir* 8.8 (1992), pp. 2021–2027.

[1160] H William Taeusch et al., "Inactivation of pulmonary surfactant due to serum-inhibited adsorption and reversal by hydrophilic polymers: experimental", in: *Biophysical journal* 89.3 (2005), pp. 1769–1779.

[1161] Joseph A Zasadzinski et al., "Inhibition of pulmonary surfactant adsorption by serum and the mechanisms of reversal by hydrophilic polymers: theory", in: *Biophysical journal* 89.3 (2005), pp. 1621–1629.

[1162] JR Lu, TJ Su, and J Penfold, "Adsorption of serum albumins at the air/water interface", in: *Langmuir* 15.20 (1999), pp. 6975–6983.

[1163] M Paulsson and P Dejmek, "Surface film pressure of β-lactoglobulin, α-lactalbumin and bovine serum albumin at the air/water interface studied by Wilhelmy plate and drop volume", in: *Journal of colloid and interface science* 150.2 (1992), pp. 394–403.

[1164] J Mitchell, L Irons, GJ Palmer, et al., "A study of the spread and adsorbed films of milk proteins.", in: *Biochimica et biophysica acta* 200.1 (1970), pp. 138–50.

[1165] Kamlesh Anand and Srinivasan Damodaran, "Kinetics of adsorption of lysozyme and bovine serum albumin at the air–water interface from a binary mixture", in: *Journal of colloid and interface science* 176.1 (1995), pp. 63–73.

[1166] Sam Lear and Steven L Cobb, "Pep-Calc. com: a set of web utilities for the calculation of peptide and peptoid properties and automatic mass spectral peak assignment", in: *Journal of computer-aided molecular design* 30.3 (2016), pp. 271–277.

[1167] Kurosch Rezwan, Lorenz P Meier, and Ludwig J Gauckler, "A prediction method for the isoelectric point of binary protein mixtures of bovine serum albumin and lysozyme adsorbed on colloidal titania and alumina particles", in: *Langmuir* 21.8 (2005), pp. 3493–3497.

[1168] Barbara Jachimska, Monika Wasilewska, and Zbigniew Adamczyk, "Characterization of globular protein solutions by dynamic light scattering, electrophoretic mobility, and viscosity measurements", in: *Langmuir* 24.13 (2008), pp. 6866–6872.

[1169] Andrzej Kudelski, "Influence of electrostatically bound proteins on the structure of linkage monolayers: adsorption of bovine serum albumin on silver and gold substrates coated with monolayers of 2-mercaptoethanesulphonate", in: *Vibrational Spectroscopy* 33.1-2 (2003), pp. 197–204.

[1170] BA Noskov et al., "Bovine serum albumin unfolding at the air/water interface as studied by dilational surface rheology", in: *Langmuir* 26.22 (2010), pp. 17225–17231.

[1171] Roderic G Eckenhoff and Jonathan W Tanner, "Differential halothane binding and effects on serum albumin and myoglobin", in: *Biophysical journal* 75.1 (1998), pp. 477–483.

[1172] Paul D Jones et al., "Binding of perfluorinated fatty acids to serum proteins", in: *Environmental Toxicology and Chemistry: An International Journal* 22.11 (2003), pp. 2639–2649.

[1173] Orion Shih et al., "Membrane Charging and Swelling upon Calcium Adsorption as Revealed by Phospholipid Nanodiscs", in: *The journal of physical chemistry letters* 9.15 (2018), pp. 4287–4293.

[1174] Melina Helfrich, *Der Einfluss von Ionen auf die Struktur von Lipidmembranen*, de, 2018.

[1175] Carolin Olbrisch, *Proteinadsorption an der Flüssigkeits-Gas-Grenzfläche: Der Einfluss von $MgCl_2$ auf das Adsorptionsverhalten von BSA an DPPA-Langmuirfilmen*, de, 2019.

[1176] Robert Vácha et al., "Mechanism of interaction of monovalent ions with phosphatidylcholine lipid membranes", in: *The Journal of Physical Chemistry B* 114.29 (2010), pp. 9504–9509.

[1177] Adela Melcrova et al., "Concurrent compression of phospholipid membranes by calcium and cholesterol", in: *Langmuir* 35.35 (2019), pp. 11358–11368.

[1178] Jordi Faraudo and Alex Travesset, "Phosphatidic acid domains in membranes: effect of divalent counterions", in: *Biophysical journal* 92.8 (2007), pp. 2806–2818.

[1179] J Pittler et al., "Charge inversion at minute electrolyte concentrations", in: *Physical review letters* 97.4 (2006), p. 046102.

[1180] Rumiana Dimova, "Recent developments in the field of bending rigidity measurements on membranes", in: *Advances in colloid and interface science* 208 (2014), pp. 225–234.

[1181] Zishuai Huang et al., "Influence of salt purity on Na+ and palmitic acid interactions", in: *The Journal of Physical Chemistry A* 117.50 (2013), pp. 13412–13418.

[1182] Wilhelm R Glomm et al., "Same System- Different Results: The Importance of Protein-Introduction Protocols in Langmuir-Monolayer Studies of Lipid-Protein Interactions", in: *Analytical chemistry* 81.8 (2009), pp. 3042–3050.

[1183] Miyuki Yamasaki, Hiroshige Yano, and Koichiro Aoki, "Differential scanning calorimetric studies on bovine serum albumin: I. Effects of pH and ionic strength", in: *International journal of biological macromolecules* 12.4 (1990), pp. 263–268.

[1184] Pin Zhang et al., "Molecular interactions of phospholipid monolayers with a model phospholipase", in: *Soft matter* 15.20 (2019), pp. 4068–4077.

[1185] Felix Franks, *Water: a matrix of life*, Royal Society of Chemistry, 2007.

[1186] Wenjie Wang et al., "Ionic specificity in pH regulated charged interfaces: Fe3+ versus La3+", in: *Langmuir* 27.19 (2011), pp. 11917–11924.

[1187] Wenjie Wang et al., "Ion-specific induced charges at aqueous soft interfaces", in: *Physical review letters* 106.5 (2011), p. 056102.

[1188] Alex Travesset and David Vaknin, "Bjerrum pairing correlations at charged interfaces", in: *EPL (Europhysics Letters)* 74.1 (2006), p. 181.

[1189] Hitoshi Ohtaki and Tamas Radnai, "Structure and dynamics of hydrated ions", in: *Chemical Reviews* 93.3 (1993), pp. 1157–1204.

[1190] Farideh Jalilehvand et al., "Hydration of the calcium ion. An EXAFS, large-angle X-ray scattering, and molecular dynamics simulation study", in: *Journal of the American Chemical Society* 123.3 (2001), pp. 431–441.

[1191] I Bako, J Hutter, and G Palinkas, "Car–Parrinello molecular dynamics simulation of the hydrated calcium ion", in: *The Journal of chemical physics* 117.21 (2002), pp. 9838–9843.

[1192] Gaetan Laroche et al., "Structure and dynamics of dimyristoylphosphatidic acid/calcium complexes by deuterium NMR, infrared, and Raman spectroscopies and small-angle x-ray diffraction", in: *Biochemistry* 30.12 (1991), pp. 3105–3114.

[1193] A Jeremic, WJ Cho, and BP Jena, "Membrane fusion: what may transpire at the atomic level", in: *J Biol Phys Chem* 4 (2004), pp. 139–142.

[1194] Demetrios Papahadjopoulos, "Surface properties of acidic phospholipids: interaction of monolayers and hydrated liquid crystals with uni-and bi-valent metal ions", in: *Biochimica et Biophysica Acta (BBA)-Biomembranes* 163.2 (1968), pp. 240–254.

[1195] Kari K Eklund et al., "Calcium-induced lateral phase separation in phosphatidic acid/phosphatidylcholine monolayers as revealed by fluorescence microscopy", in: *Biochemistry* 27.9 (1988), pp. 3433–3437.

[1196] Maria Sovago et al., "Calcium-induced phospholipid ordering depends on surface pressure", in: *Journal of the American Chemical Society* 129.36 (2007), pp. 11079–11084.

[1197] Hiroshi Takahashi et al., "Structural and thermotropic properties of calcium-di-myristoyl-phosphatidic acid complexes at acidic and neutral pH conditions", in: *Biophysical journal* 69.4 (1995), pp. 1464–1472.

[1198] Daniel Huster, Klaus Arnold, and Klaus Gawrisch, "Strength of Ca2+ binding to retinal lipid membranes: consequences for lipid organization", in: *Biophysical journal* 78.6 (2000), pp. 3011–3018.

[1199] Abdel Boughriet, Meriem Ladjadj, and E Bicknell-Brown, "Calcium-induced condensation-reorganization phenomena in multilamellar vesicles of phosphatidic acid. pH potentiometric and 31P-NMR, Raman and ESR spectroscopic studies", in: *Biochimica et Biophysica Acta (BBA)-Biomembranes* 939.3 (1988), pp. 523–532.

[1200] ZT Graber et al., "Competitive cation binding to phosphatidylinositol-4, 5-bisphosphate domains revealed by X-ray fluorescence", in: *RSC Advances* 5.129 (2015), pp. 106536–106542.

[1201] Edgar E Kooijman et al., "Ionization properties of phosphatidylinositol polyphosphates in mixed model membranes", in: *Biochemistry* 48.40 (2009), pp. 9360–9371.

[1202] Nadia N Casillas-Ituarte et al., "Na+ and Ca2+ effect on the hydration and orientation of the phosphate group of DPPC at air- water and air- hydrated silica interfaces", in: *The Journal of Physical Chemistry B* 114.29 (2010), pp. 9485–9495.

[1203] Andria Aroti et al., "Effects of Hofmeister anions on DPPC Langmuir monolayers at the air- water interface", in: *The Journal of Physical Chemistry B* 108.39 (2004), pp. 15238–15245.

[1204] P Thomas Vernier, Matthew J Ziegler, and Rumiana Dimova, "Calcium binding and head group dipole angle in phosphatidylserine- phosphatidylcholine bilayers", in: *Langmuir* 25.2 (2009), pp. 1020–1027.

[1205] Tao Hu and Zhiguo Su, "A solid phase adsorption method for preparation of bovine serum albumin–bovine hemoglobin conjugate", in: *Journal of biotechnology* 100.3 (2003), pp. 267–275.

[1206] Jessica E DiCiccio and Benjamin E Steinberg, "Lysosomal pH and analysis of the counter ion pathways that support acidification", in: *Journal of General Physiology* 137.4 (2011), pp. 385–390.

[1207] Haoxing Xu and Dejian Ren, "Lysosomal physiology", in: *Annual review of physiology* 77 (2015), pp. 57–80.

[1208] Matthew Bui, Gary Whittaker, and Ari Helenius, "Effect of M1 protein and low pH on nuclear transport of influenza virus ribonucleoproteins.", in: *Journal of virology* 70.12 (1996), pp. 8391–8401.

[1209] Santiago Di Lella, Andreas Herrmann, and Caroline M Mair, "Modulation of the pH stability of influenza virus hemagglutinin: a host cell adaptation strategy", in: *Biophysical journal* 110.11 (2016), pp. 2293–2301.

[1210] Mohamad R Kalani et al., "Characterizing a histidine switch controlling pH-dependent conformational changes of the influenza virus hemagglutinin", in: *Biophysical journal* 105.4 (2013), pp. 993–1003.

[1211] Xu Dong et al., "Ubiquitin S65 phosphorylation engenders a pH-sensitive conformational switch", in: *Proceedings of the National Academy of Sciences* 114.26 (2017), pp. 6770–6775.

[1212] Philipp Bräuer et al., "Structural basis for pH-dependent retrieval of ER proteins from the Golgi by the KDEL receptor", in: *Science* 363.6431 (2019), pp. 1103–1107.

[1213] Giovanna Navarra et al., "Thermal aggregation and ion-induced cold-gelation of bovine serum albumin", in: *European Biophysics Journal* 38.4 (2009), pp. 437–446.

[1214] Valeria Militello et al., "Aggregation kinetics of bovine serum albumin studied by FTIR spectroscopy and light scattering", in: *Biophysical chemistry* 107.2 (2004), pp. 175–187.

[1215] Mily Bhattacharya, Neha Jain, and Samrat Mukhopadhyay, "Insights into the mechanism of aggregation and fibril formation from bovine serum albumin", in: *The Journal of Physical Chemistry B* 115.14 (2011), pp. 4195–4205.

[1216] Ashley I Bush et al., "Rapid induction of Alzheimer A beta amyloid formation by zinc", in: *Science* 265.5177 (1994), pp. 1464–1467.

[1217] Xudong Huang et al., "Zinc-induced Alzheimer's Aβ1–40 aggregation is mediated by conformational factors", in: *Journal of Biological Chemistry* 272.42 (1997), pp. 26464–26470.

[1218] Kevin J Barnham, Colin L Masters, and Ashley I Bush, "Neurodegenerative diseases and oxidative stress", in: *Nature reviews Drug discovery* 3.3 (2004), pp. 205–214.

[1219] K Garai et al., "Selective destabilization of soluble amyloid β oligomers by divalent metal ions", in: *Biochemical and biophysical research communications* 345.1 (2006), pp. 210–215.

[1220] Giovanna Navarra et al., "Influence of metal ions on thermal aggregation of bovine serum albumin: aggregation kinetics and structural changes", in: *Journal of inorganic biochemistry* 103.12 (2009), pp. 1729–1738.

[1221] Marcus Fändrich, Matthew A Fletcher, and Christopher M Dobson, "Amyloid fibrils from muscle myoglobin", in: *Nature* 410.6825 (2001), pp. 165–166.

[1222] Pablo Taboada et al., "Amyloid fibril formation and other aggregate species formed by human serum albumin association", in: *The Journal of physical chemistry B* 110.42 (2006), pp. 20733–20736.

[1223] Ivan Usov, Jozef Adamcik, and Raffaele Mezzenga, "Polymorphism complexity and handedness inversion in serum albumin amyloid fibrils", in: *ACS nano* 7.12 (2013), pp. 10465–10474.

[1224] Jesús Zurdo et al., "Dependence on solution conditions of aggregation and amyloid formation by an SH3 domain", in: *Journal of molecular biology* 311.2 (2001), pp. 325–340.

[1225] Wolfgang Hoyer et al., "Dependence of α-synuclein aggregate morphology on solution conditions", in: *Journal of molecular biology* 322.2 (2002), pp. 383–393.

[1226] Fabrizio Chiti et al., "Studies of the aggregation of mutant proteins in vitro provide insights into the genetics of amyloid diseases", in: *Proceedings of the National Academy of Sciences* 99.suppl 4 (2002), pp. 16419–16426.

[1227] Josué Juárez et al., "Influence of electrostatic interactions on the fibrillation process of human serum albumin", in: *The Journal of Physical Chemistry B* 113.30 (2009), pp. 10521–10529.

[1228] Nooshin Alizadeh-Pasdar and Eunice CY Li-Chan, "Comparison of protein surface hydrophobicity measured at various pH values using three different fluorescent probes", in: *Journal of Agricultural and Food Chemistry* 48.2 (2000), pp. 328–334.

[1229] Bijay K Sah and Sarathi Kundu, "Behaviour of protein (BSA)-lipid (DMPA) mixed monolayer on the spreading order of the individual component", in: *Chemistry and physics of lipids* 225 (2019), p. 104810.

[1230] P Chen et al., "Interfacial tensions of protein solutions using axisymmetric drop shape analysis", in: *Studies in Interface Science*, vol. 7, Elsevier, 1998, pp. 303–339.

[1231] Dietmar Möbius and Reinhard Miller, *Proteins at liquid interfaces*, Elsevier, 1998.

[1232] Patricia Pedraz et al., "Characterization of Langmuir biofilms built by the biospecific interaction of arachidic acid with bovine serum albumin", in: *Thin Solid Films* 525 (2012), pp. 121–131.

[1233] Guoqing Xu et al., "The interaction between BSA and DOTAP at the air-buffer interface", in: *Scientific reports* 8.1 (2018), pp. 1–11.

[1234] Kurosch Rezwan et al., "Bovine serum albumin adsorption onto colloidal Al2O3 particles: a new model based on zeta potential and UV- Vis measurements", in: *Langmuir* 20.23 (2004), pp. 10055–10061.

[1235] Ute Böhme and Ulrich Scheler, "Effective charge of bovine serum albumin determined by electrophoresis NMR", in: *Chemical Physics Letters* 435.4-6 (2007), pp. 342–345.

[1236] Wenjing Zhang et al., "Structure and effective charge characterization of proteins by a mobility capillary electrophoresis based method", in: *Chemical science* 10.33 (2019), pp. 7779–7787.

[1237] Woo-Kul Lee, Jea-Seung Ko, and Hyun-Man Kim, "Effect of electrostatic interaction on the adsorption of globular proteins on octacalcium phosphate crystal film", in: *Journal of colloid and interface science* 246.1 (2002), pp. 70–77.

[1238] Koichi Murayama and Mihoko Tomida, "Heat-induced secondary structure and conformation change of bovine serum albumin investigated by Fourier transform infrared spectroscopy", in: *Biochemistry* 43.36 (2004), pp. 11526–11532.

[1239] Octaaf JM Bos et al., "Drug-binding and other physicochemical properties of a large tryptic and a large peptic fragment of human serum albumin", in: *Biochimica et Biophysica Acta (BBA)-Protein Structure and Molecular Enzymology* 953 (1988), pp. 37–47.

[1240] Jyotsana Pathak, Kamla Rawat, and HB Bohidar, "Thermo-reversibility, ergodicity and surface charge–temperature dependent phase diagram of anionic, cationic and neutral co-gels of gelatin–BSA complexes", in: *RSC advances* 6.46 (2016), pp. 40123–40136.

[1241] Michiyo Murata et al., "Heat-induced transparent gel formation of bovine serum albumin", in: *Bioscience, biotechnology, and biochemistry* 57.1 (1993), pp. 43–46.

[1242] Rui Li et al., "Role of pH-induced structural change in protein aggregation in foam fractionation of bovine serum albumin", in: *Biotechnology Reports* 9 (2016), pp. 46–52.

[1243] G Scanavachi et al., "Aggregation features of partially unfolded bovine serum albumin modulated by hydrogenated and fluorinated surfactants: Molecular dynamics insights and experimental approaches", in: *Journal of Colloid and Interface Science* (2020).

[1244] Guo-qing Xu et al., "Dynamic Behaviors and Morphology Change of Anionic Phospholipid DPPG Monolayer Caused by Bovine Serum Albumin at Air-Water Interface", in: *Chinese Journal of Chemical Physics* 30.5 (2017), p. 595.

[1245] Nara C de Souza et al., "Interaction of small amounts of bovine serum albumin with phospholipid monolayers investigated by surface pressure and atomic force microscopy", in: *Journal of colloid and interface science* 297.2 (2006), pp. 546–553.

[1246] Jochen S Hub et al., "Short-range order and collective dynamics of DMPC bilayers: a comparison between molecular dynamics simulations, x-ray, and neutron scattering experiments", in: *Biophysical journal* 93.9 (2007), pp. 3156–3168.

[1247] Nanjun Chu et al., "Anomalous swelling of lipid bilayer stacks is caused by softening of the bending modulus", in: *Physical review E* 71.4 (2005), p. 041904.

[1248] Barbara A Lewis and Donald M Engelman, "Lipid bilayer thickness varies linearly with acyl chain length in fluid phosphatidylcholine vesicles", in: *Journal of molecular biology* 166.2 (1983), pp. 211–217.

[1249] TA Harroun et al., "Relationship between the unbinding and main transition temperatures of phospholipid bilayers under pressure", in: *Physical Review E* 69.3 (2004), p. 031906.

[1250] Thomas Zander et al., "Influence of high hydrostatic pressure on solid supported DPPC bilayers with hyaluronan in the presence of Ca 2+ ions", in: *Soft matter* 15.36 (2019), pp. 7295–7304.

[1251] Christoph Naumann, Thomas Brumm, and Thomas M Bayerl, "Phase transition behavior of single phosphatidylcholine bilayers on a solid spherical support studied by DSC, NMR and FT-IR", in: *Biophysical journal* 63.5 (1992), pp. 1314–1319.

[1252] Eva Novakova, Klaus Giewekemeyer, and Tim Salditt, "Structure of two-component lipid membranes on solid support: An x-ray reflectivity study", in: *Physical Review E* 74.5 (2006), p. 051911.

[1253] Bert Nickel, "Nanostructure of supported lipid bilayers in water", in: *Biointerphases* 3.3 (2008), FC40–FC46.

[1254] SK Ghosh et al., "In vitro study of interaction of synaptic vesicles with lipid membranes", in: *New Journal of Physics* 12.10 (2010), p. 105004.

[1255] Horia I Petrache, Stephanie Tristram-Nagle, and John F Nagle, "Fluid phase structure of EPC and DMPC bilayers", in: *Chemistry and physics of lipids* 95.1 (1998), pp. 83–94.

[1256] Bernd W Koenig, Helmut H Strey, and Klaus Gawrisch, "Membrane lateral compressibility determined by NMR and x-ray diffraction: effect of acyl chain polyunsaturation", in: *Biophysical journal* 73.4 (1997), pp. 1954–1966.

[1257] Jeffery B Klauda et al., "Simulation-based methods for interpreting x-ray data from lipid bilayers", in: *Biophysical journal* 90.8 (2006), pp. 2796–2807.

[1258] Norbert Kučerka et al., "Structure of fully hydrated fluid phase DMPC and DLPC lipid bilayers using X-ray scattering from oriented multilamellar arrays and from unilamellar vesicles", in: *Biophysical journal* 88.4 (2005), pp. 2626–2637.

[1259] Pouyan Khakbaz and Jeffery B Klauda, "Investigation of phase transitions of saturated phosphocholine lipid bilayers via molecular dynamics simulations", in: *Biochimica et Biophysica Acta (BBA)-Biomembranes* 1860.8 (2018), pp. 1489–1501.

[1260] Drew Marquardt et al., "Lipid bilayer thickness determines cholesterol's location in model membranes", in: *Soft Matter* 12.47 (2016), pp. 9417–9428.

[1261] G Pabst et al., "Structure and fluctuations of phosphatidylcholines in the vicinity of the main phase transition", in: *Physical Review E* 70.2 (2004), p. 021908.

[1262] C Scomparin et al., "Diffusion in supported lipid bilayers: Influence of substrate and preparation technique on the internal dynamics", in: *The European Physical Journal E* 28.2 (2009), pp. 211–220.

[1263] Marie-Cécile Giocondi et al., "Surface topography of membrane domains", in: *Biochimica et Biophysica Acta (BBA)-Biomembranes* 1798.4 (2010), pp. 703–718.

[1264] Jie Yang and Jennifer Appleyard, "The main phase transition of mica-supported phosphatidylcholine membranes", in: *The Journal of Physical Chemistry B* 104.34 (2000), pp. 8097–8100.

[1265] Fuyuki Tokumasu, Albert J Jin, and James A Dvorak, "Lipid membrane phase behaviour elucidated in real time by controlled environment atomic force microscopy", in: *Microscopy* 51.1 (2002), pp. 1–9.

[1266] Agustın Mangiarotti and Natalia Wilke, "Energetics of the phase transition in free-standing versus supported lipid membranes", in: *The Journal of Physical Chemistry B* 119.28 (2015), pp. 8718–8724.

[1267] ZV Leonenko et al., "Investigation of temperature-induced phase transitions in DOPC and DPPC phospholipid bilayers using temperature-controlled scanning force microscopy", in: *Biophysical journal* 86.6 (2004), pp. 3783–3793.

[1268] John F Nagle, "Chain model theory of lipid monolayer transitions", in: *The Journal of Chemical Physics* 63.3 (1975), pp. 1255–1261.

[1269] D Marsh, A Watts, and PF Knowles, "Cooperativity of the phase transition in single-and multibilayer lipid vesicles", in: *Biochimica et Biophysica Acta (BBA)-Biomembranes* 465.3 (1977), pp. 500–514.

[1270] Fuyuki Tokumasu et al., "Atomic force microscopy of nanometric liposome adsorption and nanoscopic membrane domain formation", in: *Ultramicroscopy* 97.1-4 (2003), pp. 217–227.

[1271] Ross F Flewelling and WAYNE L Hubbell, "Hydrophobic ion interactions with membranes. Thermodynamic analysis of tetraphenylphosphonium binding to vesicles", in: *Biophysical journal* 49.2 (1986), pp. 531–540.

[1272] Robert J Donati et al., "Differential effects of antidepressants escitalopram versus lithium on Gs alpha membrane relocalization", in: *BMC neuroscience* 16.1 (2015), p. 40.

[1273] Patrick Garidel, Alfred Blume, and Wigand Hübner, "A Fourier transform infrared spectroscopic study of the interaction of alkaline earth cations with the negatively charged phospholipid 1, 2-dimyristoyl-sn-glycero-3-phosphoglycerol", in: *Biochimica et Biophysica Acta (BBA)-Biomembranes* 1466.1-2 (2000), pp. 245–259.

Publications and conference contributions

Publications

- Dogan, S., Paulus, M., Forov, Y., Weis, C., Kampmann, M., Cewe, C., ... & Tolan, M. (2018). Human apolipoprotein a1 at solid/liquid and liquid/gas interfaces. *The Journal of Physical Chemistry B*, 122(14), 3953-3960.

- Forov, Y., Paulus, M., Dogan, S., Salmen, P., Weis, C., Gahlmann, T., ... & Egger, S. (2018). Adsorption Behavior of Lysozyme at Titanium Oxide-Water Interfaces. *Langmuir*, 34(19), 5403-5408.

- Surmeier, G., Paulus, M., Salmen, P., Dogan, S., Sternemann, C., & Nase, J. (2019). Cholesterol modulates the pressure response of DMPC membranes. *Biophysical Chemistry*, 106210.

- Degen, P., Paulus, M., Zwar, E., Jakobi, V., Dogan, S., Tolan, M., & Rehage, H. (2019). Surfactant-mediated formation of alginate layers at the water-air interface. *Surface and Interface Analysis*.

- Zander, T., Wieland, D. F., Raj, A., Salmen, P., Dogan, S., Dėdinaitė, A., ... & Willumeit-Römer, R. (2019). Influence of high hydrostatic pressure on solid supported DPPC bilayers with hyaluronan in the presence of Ca^{2+} ions. *Soft matter*.

- Gao, M., Estel, K., Seeliger, J., Friedrich, R. P., Dogan, S., Wanker, E. E., ... & Ebbinghaus, S. (2015). Modulation of human IAPP fibrillation: cosolutes, crowders and chaperones. *Physical Chemistry Chemical Physics*, 17(13), 8338-8348.

Conference contributions

- DPG - Spring conference (2016, Deutsche Physikalische Gesellschaft e.V., Germany)
  Human apolipoprotein A1 at water-solid and water-gas interfaces

- SXNS-14 (2016, Stony Brook University, New York, USA)
  pH-and surface pressure depend adsorption of human apolipoprotein A1 at solid/liquid- and gas/liquid-interfaces

- ECM-30 (2016, European Crystallographic Association, Basel, Switzerland)
  pH-and surface pressure depend adsorption of human apolipoprotein A1 at solid/liquid- and gas/liquid-interfaces

- Colloids (2016, 8th International Colloids Conference, Berlin, Germany)
  pH-and surface pressure depend adsorption of human apolipoprotein A1

- DELTA User meeting (2016, Dortmund Electron Accelerator, Dortmund, Germany)
  pH-and surface pressure depend adsorption of human apolipoprotein A1

- DESY User meeting (2017, Deutsche Elektronen-Synchrotron, Hamburg, Germany)
  Effect of compressed gaseous decafluorobutane on DPPC monolayers

- 42nd Lorne Conference on Protein Structure and Function (2017, Lorne, Australia)
  Apolipoprotein A1 adsorption at solid/liquid and liquid/air-interfaces

- DPG - Spring conference (2018, Deutsche Physikalische Gesellschaft e.V., Berlin, Germany)
  Structural changes of lung surfactant Langmuir films in contact with compressed fluorocarbon gases

- SXNS-15 (2018, Science Hall, Pohang Accelerator Lab, Pohang, Korea)
  Effect of fluorocarbon gases on model membranes
  Winner of the poster price in the section: Biological interfaces

Acknowledgements

Without the support of numerous people, this work could not have been carried out in this form. I would like to take this opportunity to express my sincere thanks for the help I have received in many ways.

First of all I would like to thank Prof. Dr. Metin Tolan for the opportunity to write my thesis in his working group E1a, for constructive criticism and for believing in me and giving me the freedom to make my own decisions. I would like to thank Prof. Dr. Matthias Schneider for co-supervising my thesis and Prof. Dr. Johannes Albrecht and Dr. Jens Weingarten for taking part in the examination committee. I would also like to express a big thanks to Dr. Michael Paulus for the scientific input, constructive ideas, efficient discussions, proof-reading and invaluable support during the last years on a professional and personal level. I would also like to thank Manuela Linke, who takes care of all administrative and more!

Experiments at synchrotron radiation facilities cannot be carried out alone and require a team that works well together - and so I would like to thank all those who helped me and who stood by my side with advice and action through the beamtimes at DELTA, DESY and DIAMOND. In particular, Dr. Michael Paulus, Göran Surmeier, Christian Albers, Dr. Yury Forov, Dr. Christopher Weis, Dr. Julia Nase, Mike Moron, Kevin Foryt and Lukas Tepper. My bachelor and master students I want to give a huge "Thank you" for the time and measurements!

Furthermore, I appreciate the support during experiments by beamline staff of the experimental facilities: Dr. Christian Sternemann and Dr. Michael Paulus at BL9 (DELTA), Dr. Uta Rütt, Jonas Warias and Dr. Bridget Murphy at the LISA setup (University of Kiel and PETRA III., DESY.), Francesco Carlà and Jonathan Rawle at the DCD setup (DIAMOND). Great thanks to the facilities for providing the synchrotron radiation.

Many thanks to Dr. Simo Huotari and Dr. Waldemar Kulig (University of Helsinki) for the great cooperation in the research topic: Salt adsorption on model membranes. I am very grateful to the construction office and the mechanical workshop of the TU Dortmund, especially Lutz Feldmann and Susanne Kralemann, for the design and production of the sample cells (PTFE sample holder, high-strength steel gas sample cell for solid/gas-interfaces, Delrin sample cell for studies of stimuli transfer in solid-supported lipid multilayer). A great thanks to Dirk Schemionek and Giesela Pike for cutting the silicon wafers.

Furthermore, I want to thank Dr. Yury Forov for the two visits and the great time

in Japan and the introduction in inelastic scattering at the synchrotron facility SPring-8. For the pleasant time in our office I want to thank my office colleagues Christian Albers, Göran Surmeier and the adopted office colleague Kevin Foryt. I just want to say: Thank you for going through good and bad times (and to the gym). Thanks to my former colleagues Dr. Holger Göhring and Dr. Thomas Büning for the weeks full of Gangsta Rap Mondays to Death Metal Fridays and for the pleasant time in the office. For proof-reading this thesis I want to thank: Dr. Michael Paulus, Göran Surmeier, Malte Surmeier and Christian Albers.

Another big thing was my first touch with "Harry Potter" and watching it together (before the COVID-19 pandemic, needless to say) - thanks to Hannah Förster, Christian Albers, Göran Surmeier, Mirko Elbers, Kevin Foryt, Dr. Julian Schulze and Nico König (participiants: mostly from the E1a chair). Furthermore I would like to dedicate a very special line to my parents Yildiz and Yüksel, my caring uncle and aunt Mizrab and Filis, my lovely cousins Selena and Indra: I love you! or Hepinizi seviyorum! Thanks to my very best friends: Jennifer Imöhl and Christian Peller. The last line goes to my favourite person on this planet: Göran Surmeier! Thanks for being the way you are!

Figure B.3: Hulk 77 (from 2005, Marvel Comics): Hulk, he does not depend on oxygen to survive.

Eidesstattliche Versicherung

Ich versichere hiermit an Eides statt, dass ich die vorliegende Dissertation mit dem Titel "*In-situ* analysis of the influence of gases and ions on biological interfaces" selbständig und ohne unzulässige fremde Hilfe erbracht habe. Ich habe keine anderen als die angegebenen Quellen und Hilfsmittel benutzt sowie wörtliche und sinngemäße Zitate kenntlich gemacht. Die Arbeit hat in gleicher oder ähnlicher Form noch keiner Prüfungsbehörde vorgelegen.

Ort, Datum	Susanne Dogan